Polymeric Macroporous Nanocomposites using highly concentrated emulsions as templates

Alejandro Vílchez Villalba

ADVERTIMENT. La consulta d’aquesta tesi queda condicionada a l’acceptació de les següents condicions d'ús: La difusió d’aquesta tesi per mitjà del servei TDX (**www.tdx.cat**) ha estat autoritzada pels titulars dels drets de propietat intel·lectual únicament per a usos privats emmarcats en activitats d’investigació i docència. No s’autoritza la seva reproducció amb finalitats de lucre ni la seva difusió i posada a disposició des d’un lloc aliè al servei TDX. No s’autoritza la presentació del seu contingut en una finestra o marc aliè a TDX (framing). Aquesta reserva de drets afecta tant al resum de presentació de la tesi com als seus continguts. En la utilització o cita de parts de la tesi és obligat indicar el nom de la persona autora.

ADVERTENCIA. La consulta de esta tesis queda condicionada a la aceptación de las siguientes condiciones de uso: La difusión de esta tesis por medio del servicio TDR (**www.tdx.cat**) ha sido autorizada por los titulares de los derechos de propiedad intelectual únicamente para usos privados enmarcados en actividades de investigación y docencia. No se autoriza su reproducción con finalidades de lucro ni su difusión y puesta a disposición desde un sitio ajeno al servicio TDR. No se autoriza la presentación de su contenido en una ventana o marco ajeno a TDR (framing). Esta reserva de derechos afecta tanto al resumen de presentación de la tesis como a sus contenidos. En la utilización o cita de partes de la tesis es obligado indicar el nombre de la persona autora.

WARNING. On having consulted this thesis you’re accepting the following use conditions: Spreading this thesis by the TDX (**www.tdx.cat**) service has been authorized by the titular of the intellectual property rights only for private uses placed in investigation and teaching activities. Reproduction with lucrative aims is not authorized neither its spreading and availability from a site foreign to the TDX service. Introducing its content in a window or frame foreign to the TDX service is not authorized (framing). This rights affect to the presentation summary of the thesis as well as to its contents. In the using or citation of parts of the thesis it’s obliged to indicate the name of the author.

Universitat de Barcelona
Facultad de Química

Consejo Superior de Investigaciones Químicas
Instituto de Química Avanzada de Cataluña
Departamento de Nanotecnología Química y Biomolecular

POLYMERIC MACROPOROUS NANOCOMPOSITES USING HIGHLY CONCENTRATED EMULSIONS AS TEMPLATES

Tesis doctoral dirigida por los doctores:

Jordi Esquena Moret y Carlos Rodríguez Abreu

Alejandro Vílchez Villalba
Barcelona, enero de 2013
Programa de Doctorado de Ciencia y Tecnología de Materiales

Memoria presentada por Alejandro Vílchez Villalba para optar al grado de Doctor por la Universitat de Barcelona.

Alejandro Vílchez Villalba

El Dr. Jordi Esquena Moret, científico titular del Consejo de Investigaciones Científicas (CSIC), el Dr. Carlos Rodríguez-Abreu, *staff researcher* del *Iberian Nanotechnology Laboratory*, y la Dra. Carmen González Azón, profesora titular de la Universidat de Barcelona,

HACEN CONSTAR QUE:

el trabajo de investigación titulado ***Polymeric Macroporous Nanocomposites using highly concentrated emulsions as templates*** que presenta el Licenciado en Ciencias Ambientales Alejandro Vílchez Villalba se ha llevado a cabo en el grupo de Química de Superficies del Instituto de Química Avanzada de Cataluña (Consejo Superior de Investigaciones Científicas) en el marco del programa de Doctorado de Ciencia y Tecnología de Materiales de la Universitat de Barcelona.

Y para que así conste, firman el presente documento

Dr. Jordi Esquena Moret	Dr. Carlos Rodríguez Abreu	Dra.Carmen González Azòn
(director)	(director)	(tutora)

Barcelona, diciembre de 2012

AGRADECIMIENTOS

Este trabajo de tesis existe gracias al apoyo de numerosas personas. Quisiera agradecer a todas ellas la ayuda prestada en la creación de este proyecto.

En primer lugar me gustaría mencionar a mis directores de tesis. A Jordi Esquena por todo su apoyo, por ser un excelente profesor durante estos años y por haberme transmitido su pasión por el mundo de las emulsiones. A Carlos por haber estado siempre presente cuando lo he necesitado, tanto aquí como en Portugal, dispuesto a aclarar cualquier duda y por su total confianza depositada en mí.

En segundo lugar, no podría olvidarme de Pilar Erra, la persona que me abrió las puertas del CID y con quien compartí mis primeros momentos en el centro. También me gustaría agradecer a Conxita la posibilidad de haberme dejado formar parte del grupo desde el primer día. Y como no, a Amalia, por sus sabios consejos y por ayudarme a adentrarme en el mundo de la investigación. Aún recuerdo los sudores en la primera reunión en la sala de Juntas.

También transmito mi más profunda gratitud a todos los miembros del tribunal por haber aceptado formar parte de él, y por dedicar parte de su valioso tiempo a la lectura de esta tesis.

A Alexander Bismarck, y especialmente a Pablo Botta, por haberme acogido tan amablemente en sus laboratorios y por su asesoramiento científico en Londres y Mar del Plata. Esta tesis no habría salido adelante sin el trabajo realizado en sus laboratorios. Lo siento Pablo por no haberte dejado ver el fútbol.

Me gustaría también reconocer el trabajo y la ayuda, no siempre fácil, de Carmen González, mi tutora en la Universidad y de Núria Llorca y Valía en todo el papeleo del nuevo plan de estudios.

Agradezco enormemente a Núria Azemar y Lídia el hacer más fácil y ágil el trabajo diario, aunque creo que las he molestado un poco con tantos sobres y tantas espirales.

Por otra parte, me gustaría dar las gracias a todas las personas con las que he compartido los buenos y los malos momentos en el laboratorio (y en la biblioteca también), que ha sido mi segunda casa durante estos años. A Susana, por ser la primera en enseñarme a desenvolverme en el mundo de las balanzas y los miligramos, y por darme seguridad en los momentos difíciles. Como no a mi hermanita Marichu (M.M.R), por ser una maravillosa amiga y una química excelente. No puedo olvidar a Isabel, parte de las figuras de esta Tesis también le pertenecen; a Jonathan, quien siempre está dispuesto para ayudar. También a Panita, Jon, Ricardo, Pablo, Eva, Hernán, Lulú, Manroshan, Ferrán y la última en llegar, Lupita.

Mi gratitud también para toda la gente del laboratorio 203 y anexos. A Silviting, la desastrillo del grupo, a Neusing, por ofrecerme todo el apoyo durante estos meses tan duros, a Kelly, por su paciencia, comprensión y alegría, a Camille por su optimismo, y también a iron Txell B, Alberto (primis), Jeremie, Gaby, María H, Goutam, Alessandro, Cristina, Steffie, Javier, Sheila y Rodrigo.

A mis compañeros de pasillo, Marina, Jordi, Aurora y Rosi, y a Raúl, Isabel, Gelen, Benci y Maribel, ha sido un verdadero placer compartir todo este tiempo con vosotros.

A todas las personas que me han ayudado en la preparación y caracterización de muestras; gracias por la buena disposición mostrada a lo largo de todo este tiempo.

A mis amigos de Can Serra: Ricky, Javi, Franchu, Mili, Miji y Álex, sé que siempre estaréis ahí cuando lo necesite. No puedo olvidarme de mis amigos de la Facultad, Carol, Nuria, Rebeca, Raquel, Dani y Marta, y como no de mis mexicanos Irepan, Sonia y Clara.

A mis tíos Isabel y Antonio, y a mis primos Pablo, Mario y Javier, quienes han sido como mis hermanos pequeños todos estos años.

A mi segunda familia: Ángeles, Aida, Alhelí, Augusto, Aitor y a la recién nacida Alaita. Gracias por vuestra comprensión y cariño.

Especialmente a Arsinoe Siguerit(-ing), mi compañera de viajes, de ilusiones y de patiments. Gracias por estar siempre a mi lado, por tu infinita paciencia en los momentos más difíciles y por levantarme el ánimo siempre que lo he necesitado. Con tu amor y cariño, este trabajo ha sido más llevadero. Ahora toca continuar con nuestras aventuras y darle un empujoncito al pisito.

Dedico este trabajo también especialmente a mis padres. A los dos, gracias por soportarme todos estos años y por apoyarme en todo momento y en todas mis decisiones. Espero que el esfuerzo haya valido la pena.

TABLE OF CONTENTS

1 INTRODUCTION

1.1 EMULSIONS

Emulsions are heterogeneous systems, thermodynamically unstable and constituted by two immiscible liquid phases, where droplets of the internal phase (so-called dispersed phase) are dispersed in the other phase (known as continuous).[1] Emulsions are commonly found in our daily lives, as in the food industry (e.g. milk or mayonnaise), cosmetics or paints. A very large number or books and/or chapters have been devoted to emulsions and emulsification in the last 50 years, indicating that it is a research area extensively studied due to the potential applications in industry[2-6].

One of the aspects pointed out in the definition is that emulsions are not thermodynamically stable. Consequently, they will eventually separate in two immiscible phases. However, emulsion destabilization can be retarded by the addition of an emulsifier. Even though surfactants are, by far, the most known and most used emulsifiers, macromolecules or finely-divided solids can also confer kinetic stability to emulsions[7].

1.1.1 Classification

Among the several ways to classify emulsions, they can be simply divided in, namely oil-in-water (O/W) or water-in-oil (W/O) as a function of the nature of the two most common phases. So, in the first case the oil constitutes the internal phase droplets while in the second the oil constitutes the continuous phase. These are the most common types of encountered emulsions. However, it is also possible to prepare oil-in-oil emulsions by choosing oils with relatively distinct polarity, as for example decane and furfuryl alcohol.[8]

Another classification is based on the internal phase volume fraction of emulsions.[2] Diluted, concentrated and highly concentration emulsions are generally defined by possessing less than 20%, between 20 and 74% and internal phase volume fractions higher than 74%, respectively (Figure 1-1). In the present work, we have used highly concentrated emulsions, also known highly concentrated phase emulsions (HIPEs), as templates for the synthesis of macroporous polymers. The 74 vol% of internal phase is the maximum packing ratio for monodisperse spherical particles.[9, 10] The limit for diluted emulsions is arbitrary and is related to the rheological properties of each system.

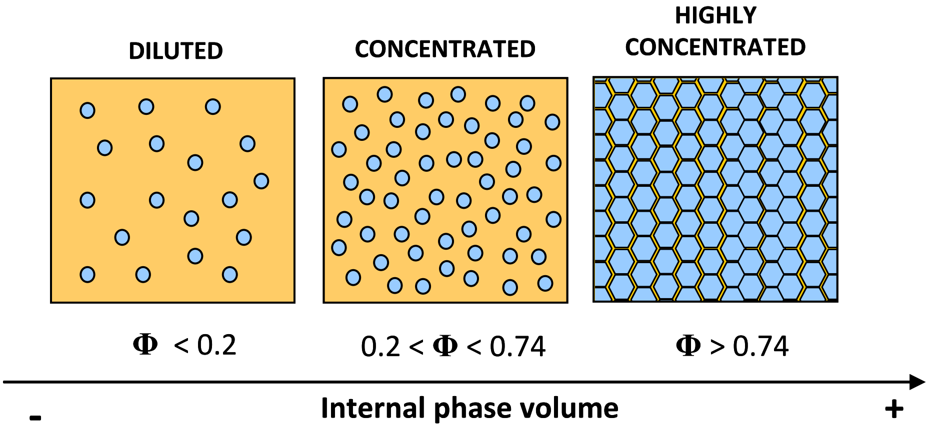

Figure 1-1. Scheme that shows the emulsion sequence as a function of its internal phase volume fraction (ϕ). As indicated in the text, both phases can be indistinctly water or oil.

Emulsions can also be categorized with respect to their internal structure. Simple or multiple emulsions may be distinguished. While the former consists in a dispersed phase within a continuous phase, the second involves a simple emulsion dispersed in a continuous phase. Multiple emulsions, generally double emulsions, can be W/O/W or O/W/O-type.[11]

Finally, two types of emulsions based on the size of the dispersed phase are recognised. Macro-emulsions habitually have droplet sizes ranging from 0.5 to 50 µm, being opaque in appearance. Their observation by means of optical microscopy is straightforward in most cases. By contrast, nano-emulsions possess lower sizes (20-500 nm) and can be accordingly either totally transparent or semi-transparent to the visible light.[12]

1.1.2 Formation and Stability

As illustrated in Figure 1-2, when two separate phases are mixed, interfacial area becomes much larger due to the large number of smaller droplets created. This results in a change of the free surface energy following the equation:

$$\Delta G_{form} = \gamma \Delta A - T\Delta S \qquad \text{1-1}$$

where ΔG_{form} is the free energy of emulsion formation, γ is the interfacial tension between the two phases, ΔA is the interfacial area increment, T is the temperature and the ΔS entropy gain of the transition. The surface energy term ($\gamma \Delta A$) is positive, and generally much higher than the also positive entropic term ($T\Delta S$). Therefore, ΔG_{form} is positive and consequently emulsion formation is not spontaneous, if state variables are kept constants. For this reason, emulsification is usually achieved by applying mechanical energy. The mechanisms of emulsion destabilization that drive emulsions to final phase separation will be explained in a further section.

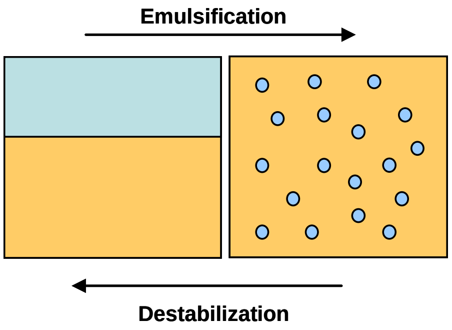

Figure 1-2. Schematic drawing of emulsion formation and destabilization.

Generally, the emulsion preparation procedures are classified in two types: high energy and low energy methods.

1.1.2.1 *High energy or dispersion methods*

On the whole, energy much higher than that described in eq. 1-1 is required when using mechanical agitation, especially for the formation of very small droplets, i.e. submicron (e.g. nanoemulsions droplets). The excess energy stems from the high Laplace pressure gradient (ΔP). This pressure has to be overcome during mechanical emulsification, and is given by the following equation:

$$\Delta P = \gamma\left(\frac{1}{r_{1D}} + \frac{1}{r_{2D}}\right) \approx \frac{2\gamma}{r_D} \tag{1-2}$$

where r_{1D} and r_{2D} are the two radii of droplet curvature. Considering a perfectly spherical droplet ($r_{1D} = r_{2D}$), Laplace pressure gradient becomes $2\gamma/r_D$, where r_D is the radius of the droplet. Therefore, the pressure at each side of a curved interface is different, being greater at the concave side of the interface. As droplets are deformed under shear (see Figure 1-3), ΔP increases, and consequently more energy is required to decrease emulsion droplet size. As it will be shown below, surfactants reduce γ, decreasing the energy required to obtain a certain droplet size.

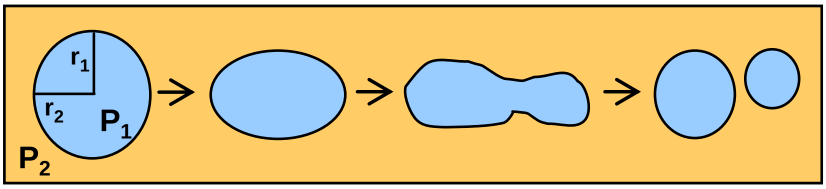

Figure 1-3. Droplet deformation and rupture under shear. Pressure at the concave side of the interface, i.e. inside of the droplet (P_1), is greater than outside (P_2).

In the high energy methods, emulsification is attained by means of mechanical energy. Many devices have been designed for this purpose. Essentially, they differ in the amount of energy given to the system. We can find from low energy systems such a simple pipe flow to high energy devices such as colloidal mills or high pressure homogenizers.[13] One of the devices most often used in laboratory scale is the vibromixer, which is considered as a medium energy device. As aforementioned, a large amount of energy is normally required to overcome the energy barriers during the emulsification stage. This is also caused by the fact that a large extent of this energy is dissipated into heat.

Emulsion formation initiates when the oil-water interface is deformed so that big emulsion droplets form. During mechanical agitation, these initial big droplets break into small ones. In this dynamic process, breakage of the droplets, adsorption of the emulsifier and droplet collision occur simultaneously.[13] Emulsification is generally produced by the application of viscous and inertial forces which generate normal stresses at the drop surfaces. This is normally transmitted via the surrounding liquid (continuous phase).

1.1.2.2 *Condensation or low energy methods*

Contrary to the high energy methods, low energy methods are based on phase transitions produced during emulsification as a result of a change in the spontaneous curvature of surfactants.[14] Such methods make use of chemical potential, instead of mechanical agitation. Phase transitions produce molecular rearrangement, which may lead to the spontaneous formation of droplets. Therefore, formation of emulsions can be achieved with minimum energy inputs or even without mechanical stirring.[15] Specifically, two different routes have been extensively explored: changing composition while keeping temperature constant (Phase Inversion Composition method or PIC),[16, 17] or inversely, composition is kept constant as temperature is modified (Phase Inversion Temperature method or PIT).[15, 18, 19].

1.1.2.3 *Emulsion droplet size distribution*

The determination of drop size distribution and the evaluation of emulsion stability are probably, among others such as viscosity or conductivity, the most often emulsion parameters assessed. Such parameters will be described briefly.

Following emulsion formation, the most common way to determine the droplet size distribution is the use of either laser diffraction or microscopy techniques. The average in number and the corresponding standard deviation can be easily calculated through the following equations:

$$D[1,0] = \frac{\sum_{i=1}^{i=N} D_i}{N} \tag{1-3}$$

$$\sigma = \sqrt{\frac{\sum_{i=1}^{i=N} (D[1,0] - D_i)^2}{N}} \tag{1-4}$$

where $D[1,0]$ represents the average size, D_i the size of each droplet measured, N the total number of droplets and σ the standard deviation.

The effect of the standard deviation in two well-known distribution functions is illustrated in Figure 1-4. The first one (a) corresponds to a Gaussian function distribution that is written as follows:

$$\frac{dP}{dD_i} = \frac{100}{\sigma\sqrt{2\pi}} \exp\left(\frac{(D_i - D_m)^2}{2\sigma^2} \right) \tag{1-5}$$

where P is the percentage of droplets with characteristic diameter D_i, and D_m and σ are the two adjustable parameters, namely arithmetic mean diameter ($D_m = D[1,0]$) and standard deviation, respectively. As clearly shown in the figure, the droplet size distribution becomes narrower as σ is lowered. Since size distributions are seldom symmetric, Gaussian distribution is unlikely to be applicable. If D is replaced by $\log D$, a non-symmetric distribution is obtained. Such function is called the log-normal distribution, and in most cases fits quite well with emulsion droplet diameters obtained from real experimental data.[20] The equation has the form:

$$\frac{dP}{d(D_i)} = \frac{100}{\log\sigma_g\sqrt{2\pi}}\exp\left(\frac{(\log D_i - \log D_m)^2}{2\log{\sigma_g}^2}\right) \qquad \text{1-6}$$

The parameter σ_g is called geometric standard deviation. Corresponding to equation 1.4, is given by:

$$\sigma_g = \sqrt{\frac{\sum_{i=1}^{i=N}\Delta P_i(\log D_i - \log D_m)^2}{N}} \qquad \text{1-7}$$

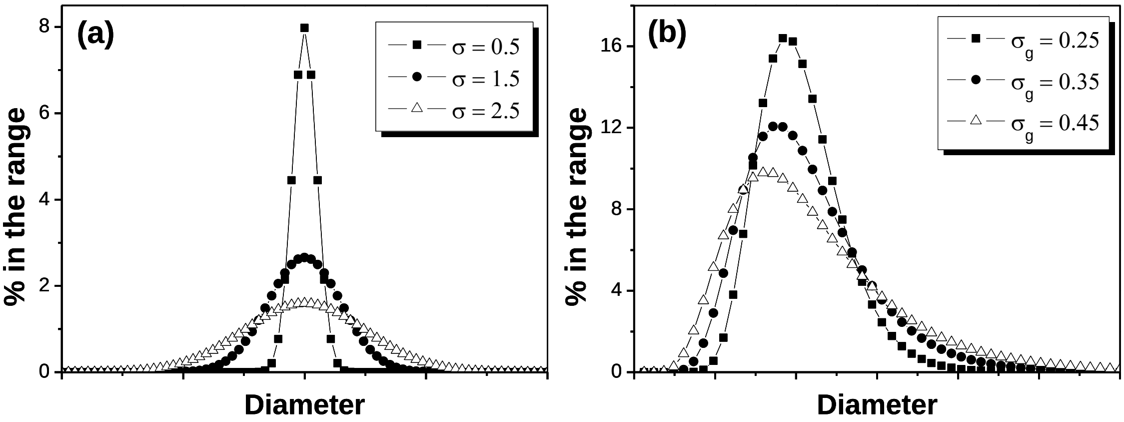

Figure 1-4. (a) Gaussian and (b) log-normal droplet size distributions given for different standard deviation values.

1.1.2.4 *Emulsion stability*

As stated earlier, emulsions are thermodynamically unstable, and in all cases they tend to minimise the surface free energy by reducing interfacial area. However, kinetic stability, which is attained by the addition of an emulsifier, can play an important role over the short time and retard such phase separation. Different destabilization mechanisms exist and are generally divided in five groups, as depicted in Figure 1-5. For convenience the mechanisms will be discussed individually. It is important to recall that the droplet breakdown mechanisms frequently occur simultaneously. For instance, due to the formation of droplet aggregates (flocculation), the rate of sedimentation or creaming increases. The same could happen with coalescence or Ostwald ripening.[13]

Apart from the techniques that are used to quantify emulsion destabilization, such as light scattering, rheology or electrophoretic mobility, emulsion stability can be quickly assessed by monitoring visually the height of residual emulsion as well as the oil and/or water volume fractions resolved at certain time and temperature.[7]

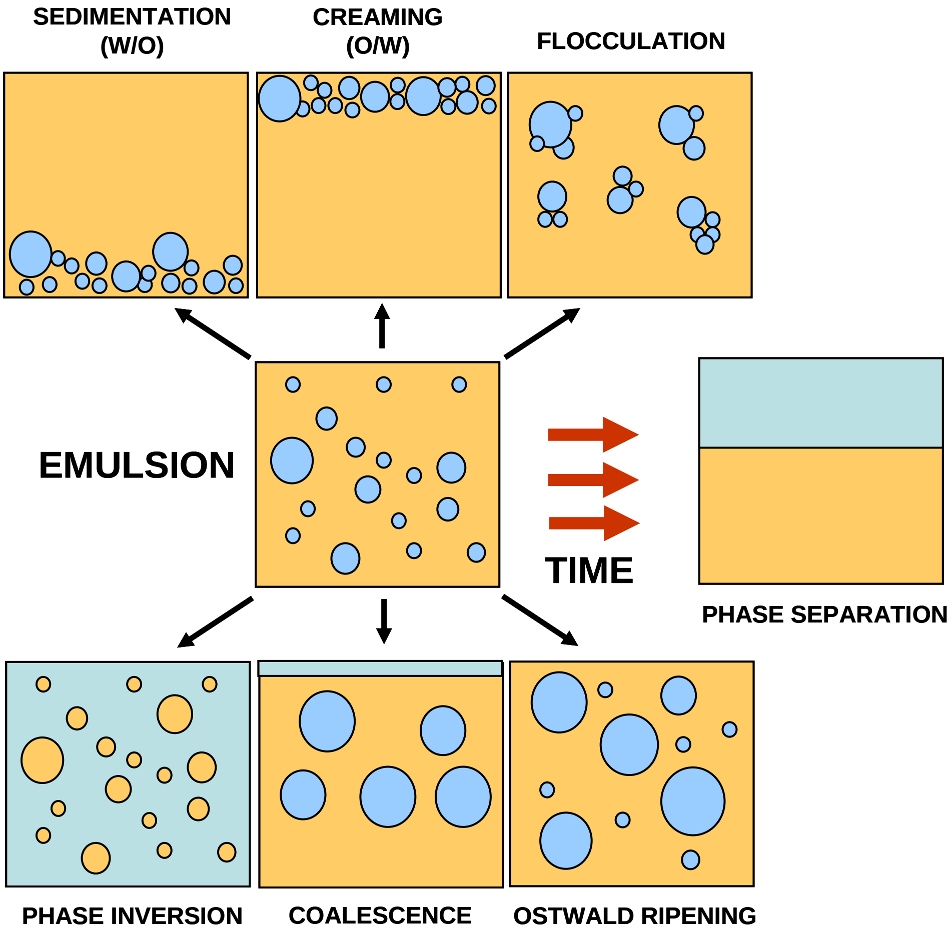

Figure 1-5. Processes involved in emulsion destabilization (adapted from Tadros).[13]

(a) Creaming and emulsion sedimentation

These are processes whereby emulsion droplets progressively migrate and accumulate as a cream or as sediment, as a result of the different densities between water and oil phases. Accordingly, droplets float top when the density of the dispersed phase of the emulsion (for example oil) is lower than that of the continuous phase (water) and inversely, droplets settle when the density of dispersed phase is higher than that of the surrounding medium. Since in practice is rather difficult to produce perfectly monodisperse emulsions, the pictures shown in Figure 1-5 contain emulsion droplets with a relatively wide droplet distribution. Such polydispersity can explain why in real cases in which creaming (or sedimentation) occurs, a completely water (or oil) transparent phase is rarely observed. This is due to the concentration gradient that builds up in the system with the larger oil droplets at the top of the emulsion (in the case of O/W emulsion) and the smaller droplets remaining dispersed in the water, leading to semitransparent or opaque systems. Creaming or sedimentation occur without the loss of individual drop identities. Therefore, emulsion droplet sizes are unaffected and the process is completely reversible by shaking the emulsion, redispersing the droplets again.

It is well known that the creaming or sedimentation velocity (ν_0) depends on droplet radius (r_D), medium viscosity (η_o), gravity (g) and on the density difference between the two emulsion phases ($\Delta\rho$). This dependence is reflected in the Stokes equation:[21]

$$\nu_0 = \frac{2}{9}\frac{\Delta\rho g {r_D}^2}{\eta_o} \qquad \text{1-8}$$

It should be taken into account that this expression is valid for very diluted systems when droplets do not collide (internal phase volume fractions ϕ <0.01).[13] For more concentrated systems the hydrodynamic interactions between droplets should be considered and sedimentation becomes a complex function.[13] In highly concentrated emulsions, ν_0 is reduced by the confinement of droplets and mobility restrictions, due to the high droplet packing ratio (generally ϕ > 0.74). Besides that, destabilization can be partially hindered by the use of thickeners that increase viscosity, by matching the density of both water and oil phases or by reducing droplet size (i.e. nanoemulsions, where Brownian diffusion usually exceed sedimentation rate), as deduced from equation 1.8.

(b) Flocculation

When attraction forces between droplets overcome repulsive interactions, the droplets stick together giving raise to flocs or loose aggregates, in which the individuality of each droplet is maintained.[22, 23] Generally, there are three main interacting energies between droplets: the first is the Van der Waals potential (W_{VdW}), which is generally attractive and results from the addition of three individual contributions: Keesom, Debye and London interactions. Such interactions are based on the existence of dipoles (permanent, induced or fluctuant) on the molecules. The second is the electrostatic repulsion potential (W_E), which is produced by the adsorption of electric charges, and the last is called the steric repulsion potential (W_S) which is caused by the adsorption of nonionic surfactants or polymers. Herein, flocculation will depend on the balance of these forces. Another point that should be considered is that flocculation can be either reversible, whereby the system can go back to the initial state by an input of much less energy that was required for emulsion formation, or irreversible (often called coagulation) if the intensity of the attraction forces is much higher than repulsive forces.

(c) Coalescence

This is one of the mechanisms responsible for the coarsening of droplet emulsions. Coalescence refers to the joining of two or more droplets to form one droplet with higher volume, consequently with less interfacial area.[7] The coalescence is governed by the behaviour of the thin film between the droplets. If there is enough thinning and disruption of such film, an eventual rupture can occur and the identity of the droplets is irreversibly lost.

Meanwhile, as a result of coalescence, emulsions might undergo phase inversion rather than experience phase separation. As shown in Figure 1-5, emulsion can invert from O/W to W/O or vice versa. On the whole, two types can be defined: translational and catastrophic inversion.[13, 24] In the former inversion is induced, among others, by changing emulsifier composition or by adding electrolyte to emulsions at fixed oil-water ratio, whereas in the latter, inversion is originated by increasing the internal phase volume fraction of the emulsion (ϕ).

It was thought that catastrophic inversion was directly related to the maximum packing parameter of monodisperse spherical droplets (ϕ >0.74).[23] Attempts to increase ϕ above this point would result in distortion, breaking or inversion. However, many reports have shown that catastrophic inversion can occur below or above this 74 vol%, depending on the nature and the concentration of emulsifier, and even on the container where the emulsion is prepared.[25-27]

In a typical example, the viscosity of an O/W emulsion gradually increases upon increasing ϕ ; at a certain point, phase inversion occurs leading to a diluted W/O emulsion. This results in a drastic reduction of emulsion viscosity. An interesting study developed by Binks et al.[25] showed that the ϕ at which phase inversion occurred (see Figure 1-6) could be adjusted by modifying the degree of hydrophobicity of the emulsifier (in this case solid silica nanoparticles).

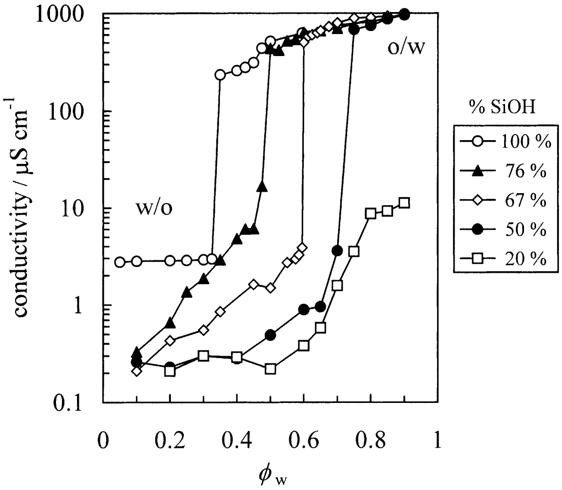

Figure 1-6. Conductivity versus water content (ϕ_w) for emulsions stabilized with silica nanoparticles. The hydrophobicity of the nanoparticles was increased by reducing the silanol groups (% SiOH) on nanoparticle surfaces. Catastrophic inversion can be easily ascribed to a sudden increase of conductivity, indicting the inversion from W/O to O/W emulsions. Reproduced from Binks et al.[25]

Phase inversion can also be induced by temperature changes. By using ethoxylated nonionic surfactants it is possible to obtain preferred emulsion (either O/W or W/O) by simply adjusting the temperature and emulsion composition. Such surfactants change their preferentially solubility from water to oil when increasing temperature, because their poly(ethylene oxide) chains become dehydrated.[28] This concept will be discussed in detail further.

(d) Ostwald Ripening

The driving force of this mechanism is the difference of Laplace pressure between small and large droplets,[29] and takes place when the dispersed phase is soluble enough within the continuous phase of the emulsion. As pointed out earlier (eq. 1-2), Laplace pressure in small droplets is higher than in the larger droplets. As a consequence, depending on the diffusion rate, the bigger droplets will increase in size due to molecular diffusion from smaller to bigger droplets, and a gradual emulsion coarsening occurs. It should be mentioned that in analogy with coalescence, Ostwald ripening is also irreversible.

The theory LSW developed by Lifshitz and Slezov[30] and independently by Wagner,[31] assumes that droplets are perfectly spherical and are separated by a distance much higher than droplet size. Moreover, it considers that the mass transport is limited by molecular diffusion in the continuous phase. According to this theory, the Oswald ripening velocity (ω) can be obtained by the following equation:

$$\omega = \frac{d{r_D}^3}{dt} = \frac{8}{9}\frac{c_\infty \gamma V_m D}{\rho RT} \tag{1-9}$$

where r is the droplet radius, ρ is the density of the dispersed phase, D and c_∞ are the diffusion coefficient and the solubility of the dispersed phase into the continuous phase, respectively, γ is the interfacial tension, and V_m the molar volume of the solute. The equation predicts a linear relation between r^3 and time (t), being the slope the Oswald ripening velocity.

Oswald ripening can be minimized by addition of a second component in the dispersed phase which is insoluble in the continuous phase.[32] This hinders molecular diffusion from smaller to bigger droplets. It should be pointed out that the Ostwald ripening rate is negligible in emulsions possessing droplet sizes > 1 μm and/or in systems where the solubility between both water and oil phases is very low.[29]

1.2 EMULSIFIERS

As pointed out before, emulsions can be stabilized by different means. Surfactants molecules and particles are the most commonly used. Both allow the formation and stabilization of emulsions thanks to their ability to migrate and adsorb spontaneously to liquid-liquid interfaces. The specific properties and the physicochemical aspects related to emulsification will be described in detail for each emulsifier.

1.2.1 Formulation of Emulsions Stabilized with Surfactants

Surfactant molecules have two clearly different parts (Figure 1-7): one lyophilic and another lyophobic.[7] As deduced from the terms, once the molecule is in solvent, the lyophilic part shows affinity whereas the lyophobic has little attraction for it. Such characteristic structure is called amphiphilicity, which means literally “liking both”, indicating that surfactants have affinity for two immiscible phases. Surfactants are therefore surface active.

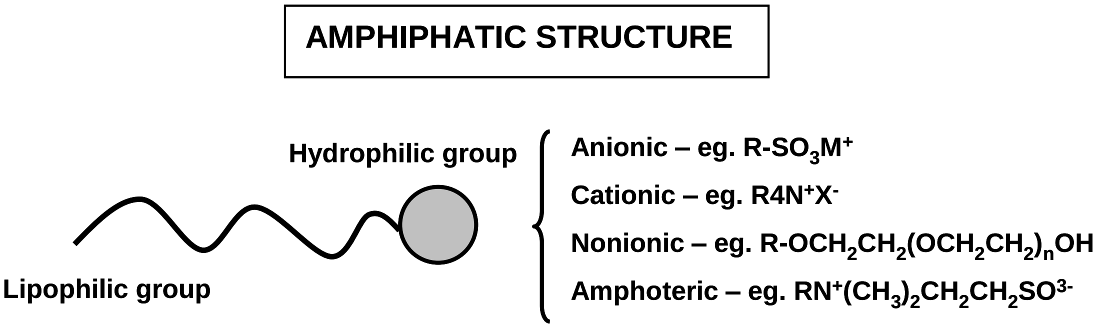

Anionic – eg. R-SO_3M^+
Cationic – eg. R4N^+X^-
Nonionic – eg. R-$OCH_2CH_2(OCH_2CH_2)_nOH$
Amphoteric – eg. $RN^+(CH_3)_2CH_2CH_2SO^{3-}$

Figure 1-7. Representation of a surfactant molecule. In solution, the hydrophilic group (lyophilic) is commonly denoted as “head”, while the lipophilic group (lyophobic) is denominated “tail”.

The ability to adsorb spontaneously at interfaces is the responsible for the interfacial tension reduction, thus reducing the energy necessary to create new surface. The other remarkable feature shown by surfactants unimers is the formation of supramolecular aggregates from very low surfactant concentrations, due their spontaneous self-assembly in solution.[33] Due to these unique characteristics, surfactants are extensively used in cosmetics, detergency, and in the pharmaceutical and food industries.

Surfactants can be generally classified according to the chemical structure of their hydrophilic groups in aqueous solutions, which constitute by far the largest number of surfactant applications.[34] The four groups are listed in Figure 1-7, and can be defined as follows: anionic and cationic hydrophilic groups carry negative or positive charges, respectively, as they dissociate in water. Nonionic groups do not carry charges, and its hydrophilicity is originated by the formation of hydrogen bonds. Amphoteric or zwitterionic surfactants have two or more groups that can be ionized in solution which provide different charges (negative or positive) depending on pH.

1.2.1.1 *Adsorption at interfaces*

The systems that show constant values in their intensive magnitudes are denominated phases. When two phases are put in contact, an interface, i.e. a boundary between two phases, appears. Such interfaces are very thin, in most cases only a few molecular diameter thick. However, rapid changes in density and/or composition across interfaces give them their most important properties, i.e. and excess free energy or lateral stress, which is often called surface (or interfacial) tension.[35] Actually, from a thermodynamic point of view (using the Gibbs´s model), the interfacial tension (γ) can be viewed as the additional surface free energy (∂G^{σ}) per unit area caused by the presence of an interface.[7] At constant temperature and composition:

$$\gamma = \left(\frac{\partial G^{\sigma}}{\partial A} \right)_{T,n_i} \qquad \text{1-10}$$

If interfacial area increases (for a stable interface γ is positive), then G^{σ} increases. When a new interface is formed as in the case of emulsions, the system tends to adopt a configuration of minimum surface (thermodynamically driven), and therefore spheres are formed, since their ratio surface/volume is minimum.

Often, the volume of interfaces is ignored because the number of molecules in these thin regions is negligible compared to the number of molecules in the inner phase. Nevertheless, this does not apply to colloidal systems where the ratio surface/volume is rather high. For instance, when 10 cm^3 of oil are dispersed with an appropriate device, the interface exposed can be 10^6 times higher.

The transition of properties between two phases (air-liquid) is illustrated in Figure 1-8(a). Molecules at the surface have potential energies greater than those in the bulk liquid. This can be explained by the low attractive interactions between the molecules at the interface with those of the surrounding medium (air molecules).[34] Any attempt to increase the surface area will imply a transport of molecules from the inner liquid to the surface. The work that corresponds to such difference in potential energies is defined as the surface free energy, or surface tension.[35] In other words, surface tension is the work required to increase the surface per unit area. This is easily understood if we observe Figure 1-8(b). When a force (F) is applied to expand the surface area, the work (W) applied is equal to:

$$W = \int W = \int F dx = \int \gamma \ell dx = \int \gamma dA \qquad \text{1-11}$$

As deduced from the equation, surface tension possesses dimensions of energy per unit area (J/m^2), though most often it is expressed as the equivalent force per unit of length (mN/m). It should be pointed out that surface tension, as an intensive variable, is influenced by other thermodynamic magnitudes, such as temperature or pressure.

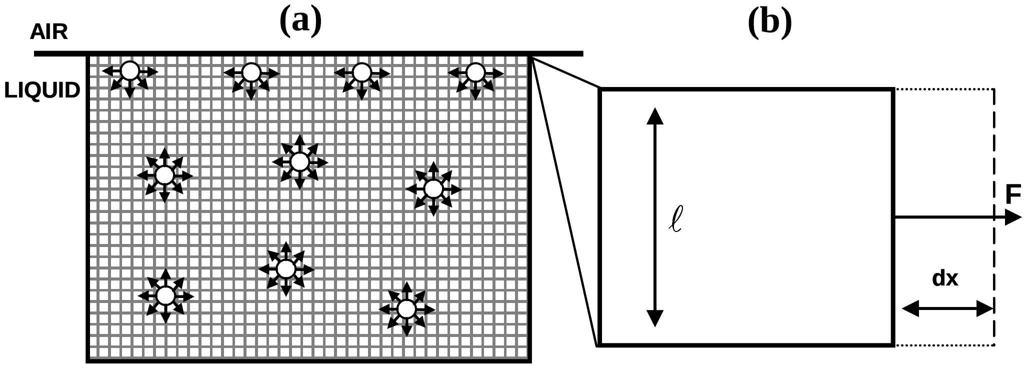

Figure 1-8. (a) Schematic representation of the intermolecular forces between molecules at both the inner phase and the air-liquid interface. The surrounding low attractive medium (gas) represents a high energy situation relative to the bulk. (b) Drawing that represents the creation of a new interface by applying a force. The work per unit area corresponds to the surface tension ($\gamma = dW/dA$).

If the gas phase is replaced by another condensed phase (another liquid), the actual excess of surface free energy will be modified. As in the previous case, the potential energy of the molecules at the interface is different from those in the respective bulk liquids. The interface between two completely or partially immiscible liquid phases is schematized in Figure 1-9(left).

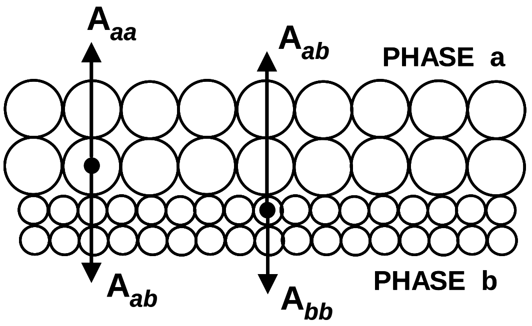

Fluid pair	Interfacial tension (mN/m)
Mercury-water	415
Mercury-benzene	357
n-Octane-water	50.8
Benzene-water	35.0
n-Octanol-water	8.5

Figure 1-9. (Left) Schematic representation of the interface and the molecular interactions involved between two condensed phases (adapted from Rosen).[34] (Right) Interfacial tension values between different liquids. It should be noted that the higher interactions between water and the other phase (from octane to octanol) the lower interfacial tension (values described in Miller and Neogi).[35]

A denotes molecular interactions and *a* and *b* subscripts refer to the molecules of the two phases involved. Accordingly, A_{aa} and A_{ab} indicate molecular interactions between *a* molecules at the interface with *a* molecules in the bulk phase in the first case or with *b* molecules across the interface in the second, respectively. Therefore, A_{aa} - A_{ab} can be defined as the potential increased energy of *a* molecules at the interface, i.e. surface tension of the phase *a* (γ_a).[34] Then, the interfacial tension can be expressed by the equation:

$$\gamma = (A_{aa} - A_{ab}) + (A_{bb} - A_{ab}) = \gamma_a + \gamma_b - 2\gamma_{ab} \qquad \text{1-12}$$

where γ_{ab} is the interaction energy between *a* and *b* molecules per unit area across the interface. It must be underlined that the term γ_{ab} can only be evaluated for totally immiscible liquids, which in practice is a limitation. As deduced from eq. 1.12, if one of the phases (e.g. *b)* is a gas (tension originated by molecular interactions in *b* can be neglected) the interfacial tension becomes the surface tension of the condensed phase *a*, since A_{bb} and γ_{ab} are very close to zero. This large imbalance of forces results in the high surface tension of water (72.8 mN/m), for example. However, on account of the higher molecular density of a liquid, the interactions at the interfacial region are greater and consequently the interfacial tension will significantly be reduced (γ_{ab} increases). As seen in the Table included in Figure 1-9, interfacial tension between water and octane (weak dispersion forces with water) is 50.8 mN/m. If octane is replaced by octanol (polar groups interact more with water) the tension falls to 8.5 mN/m. Obviously, when two liquids are completely miscible, the interface eventually disappears, since tension becomes zero.

In this study, two different methods, among the large variety of existing procedures, have been used in order to measure interfacial tensions: first, the drop-volume method that is based on analysis of capillary-gravity forces, and second, the Du Noüy ring method, which is based on direct measurement using a microbalance. Both will be described in detail in the experimental section.

Surfactants migrate to interfaces (liquid-liquid, liquid-air, etc.) and the driving force for adsorption is decreasing the free energy of that phase boundary. The surfactant molecule orientates such that the hydrophilic part remains in the water while the hydrophobic is oriented away from it (remains in the apolar phase). The displacement of surface liquid molecules by adsorbed surfactant produces a progressive reduction of the free energy of the boundary, and interfacial tension between both phases decreases accordingly. In the case of pure water, the surface tension can be reduced from 72.8 mN/m to 30-35 mN, with low amounts of common surfactants. Surface activity depends basically on the structure of the surfactant, on the nature of the solvent and on the temperature.[33]

In Figure 1-10 the interfacial tension (γ) is plotted as a function of surfactant concentration (log scale). From the figure it is evident that beyond certain surfactant concentration, further increment of concentration does not result in a decrease of γ . The reason lies on the saturation of the interface.

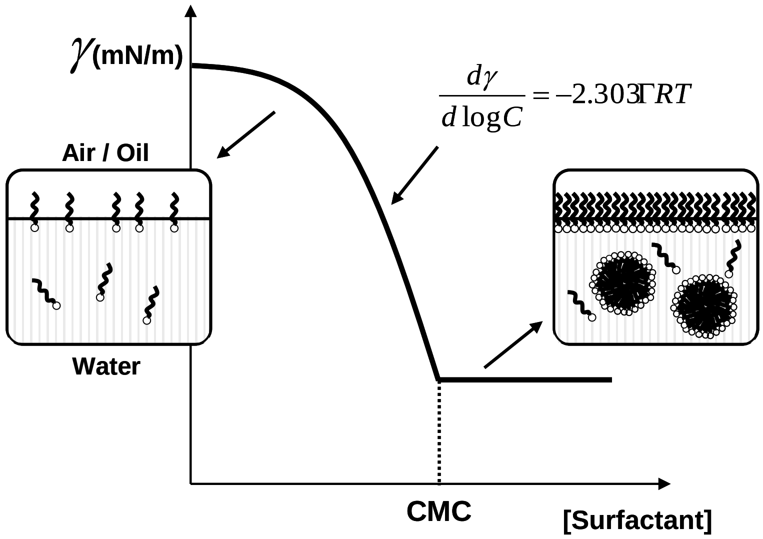

Figure 1-10. Surface (or interfacial) tension variation as a function of surfactant concentration in aqueous solution. Surfactant molecules are schematically shown. The slope is a function of surfactant concentration at the interface (Γ).

As shown in the figure, at low surfactant concentration, the water-oil (or water-air) interface is not fully saturated. Interfacial tension decreases until the interface becomes saturated with surfactant. At this given concentration, the surfactant starts to form aggregates (so-called micelles). Such concentration is known as the critical micelle concentration (or CMC).[34] This aggregation can also be understood in terms of reduction of the free energy. Hydrophobic parts are removed from water since they lay in the inner part of the micelles.[33] It is important to mention that micelles do not contribute to the reduction of interfacial tension.

The increase of surfactant concentration above CMC can produce more complex structures than micelles, such as liquid crystals or vesicles.

The surfactant concentration adsorbed at the interface (denoted as surface excess), can be calculated from the surface or interfacial tension measurements, applying the Gibbs adsorption equation.[13] For diluted solution of nonionic surfactants:

$$\Gamma = -\frac{1}{2.303RT}\left(\frac{\partial \gamma}{\partial \log C_S}\right) \qquad \text{1-13}$$

where Γ (mol/area) is the surface excess, C_S is the bulk surfactant concentration, R is the ideal gas constant and T is the temperature. Therefore, Γ can be obtained from the slope of the interfacial tension vs. concentration plot, specifically from the linear part just before the CMC.[34]

From the surface excess concentration, the surface area per molecule (a) can be calculated from the relationship:

$$a = \frac{10^{16}}{N_A \Gamma} \qquad \text{1-14}$$

where N_A is the Avogadro´s number. The surface area per molecule is a measure of the effectiveness of surfactant adsorption. Lower values of a could mean a close packed surfactant layer at the interface, indicating a high Γ and, in turn, a high adsorption efficiency. Low tension values are a consequence of such high adsorption.

1.2.1.2 *Selection of emulsifier*

The most important point when dealing with emulsions is the selection of an appropriate surfactant in order to achieve appropriate emulsion stabilization of the chosen components. Often in industry, this is made on an empirical basis. In this line, the Bancroft rule,[36] already used at the beginning of the twentieth century, constitutes a simple tool to predict the type of emulsions (either O/W or W/O) that is expected to be obtained. While O/W emulsions will be obtained when using water-soluble surfactants, the use of oil-soluble surfactants will lead to W/O emulsions-type. It should be noted that Bancroft rule is completely qualitative. Later, a semi-empirical scale based on the hydrophilic-lipophilic balance (HLB) number was introduced by Griffin[37, 38] A series of equations were developed for nonionic surfactants. For nonionic ethoxylated surfactants possessing poly(ethylenglycol) as the only hydrophilic group, the HLB can be given as:

$$HLB = \frac{E}{5} \tag{1-15}$$

where E is the wt% of the ethylene oxide group in the surfactant molecule. The HLB numbers (N_{HLB}) required for some specific applications are included in Table 1-1. Obviously, more hydrophilic surfactants are required to obtain O/W emulsions.

Table 1-1. Desired HLB surfactant numbers for various applications (reproduced from Griffin).[37]

N_{HLB} range	**Application**
4-6	W/O emulsion
7-9	Wetting agent
8-18	O/W emulsion
13-15	Detergent
15-18	Solubilizer

It should be stressed that Griffin equation cannot be applied to neither nonionic surfactants containing groups such as propylene oxide, nor ionic surfactants. Other approaches, such as the Davis method,[39] were developed to assign HLB numbers to different functional groups, including ionic groups.

The classification based on the HLB number constitutes a guide to find optimal emulsion stabilization, but it only provides information about the chemical structure of surfactants. Specifically, one could find the most appropriate HLB number in order to emulsify certain oil.

1.2.1.3 *Phase inversion temperature*

This concept was developed by Shinoda and co-workers.[18, 40] They observed that emulsions, stabilized with nonionic surfactants based on poly(oxyethylene) as the hydrophilic group, inverted from O/W to W/O emulsions by simply increasing temperature. Moreover, they found that the phase inversion temperature (abbreviated as PIT or T_{HLB}) was linearly dependent on the HLB number of the surfactant. One of the points of paramount importance concerning this method is that unlike the HLB number defined by Griffin, PIT depends on experimental conditions, such us temperature, oil-water ratio, concentration of the emulsifier, additives, etc.[13]

To understand why inversion occurs we should consider first the effect of temperature on the curvature of the adsorbed monolayer at the oil-water interface. It is well known that the hydration between the hydrophilic poly(oxyethylene) part of the surfactant and the water diminishes at increasing temperature. Initially, surfactant aggregates have convex curvature towards water, as can be appreciated in Figure 1-11(a). The gradual dehydration produced by further increase of temperature, leads to concave curvatures towards water.[41] The PIT is defined as the temperature at which the hydrophilic-lipophilic properties are just balanced. At this given temperature, phase inversion from O/W to W/O emulsion occurs.

A schematic phase behaviour diagram, including the curvature of surfactant aggregates and the variation of volume fractions of the different phases, is included in Figure 1-11(a). Nonionic surfactant dissolves in water forming normal micelles at low temperature. When temperature is increased, the solubilisation of oil inside the micelles increases rapidly, and is followed by an increase of micellar size. As temperature approaches the PIT, solubilisation capacity increases and large amounts of both oil and surfactant can be solubilised. Close to the PIT, the aqueous phase changes continuously to the surfactant phase (denoted as D in the Figure). Therefore, at the PIT three phases coexist: surfactant phase, and water and oil separated phases, with an almost negligible amount of surfactant.[41, 42] It must be remarked that at this temperature the solubility of both water and oil in the surfactant is remarkably high. Above the PIT temperature, the reverse process occurs, since separated water increases gradually, and finally an important fraction of water is dissolved in reverse micelles.

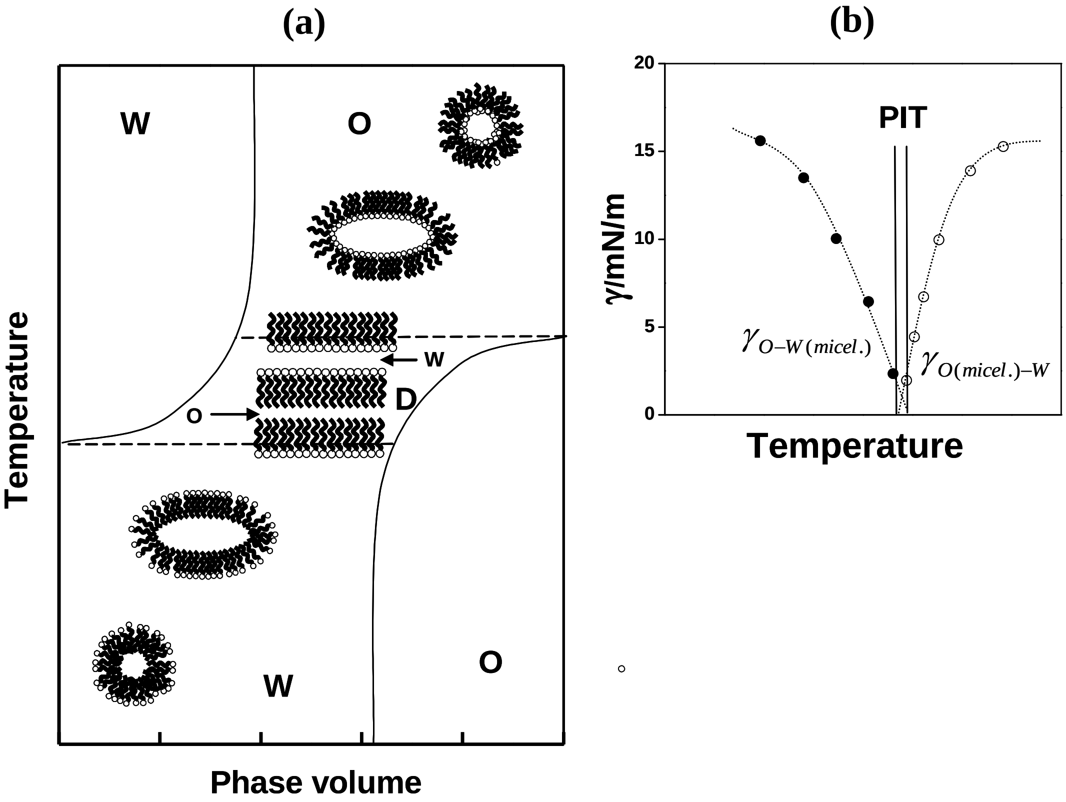

Figure 1-11. (a) Schematic diagram showing the influence of temperature on the poly(oxyethylene) based surfactant aggregates, and the volume of the different phases (O indicates oil, W indicates water and D indicates surfactant phase). At low temperatures hydrophilic micelles are formed, whereas at high temperatures oleophilic micelles appear (reproduced from Shinoda and Kunieda).[41] (b) Interfacial tension versus temperature for the system shown in (a). Very low values are attained at the phase inversion temperature (adapted from Saito and Shinoda).[42]

Another important aspect is the characteristic low interfacial tension attained at the region where the three different phases coexist.[43] The respective interfacial tensions between the micellar solutions (direct and reverse) and the separated water and oil phases, respectively, drastically fall when approaching to the PIT. This is shown in Figure 1-11(b) in the left and right side of the PIT region, respectively. This can be explained by the bicontinuous structure of the D phase in which both the oil and water domains are swollen.[42] Due to the low interfacial tensions at the PIT, emulsions prepared at this temperature possess rather smaller droplet sizes than those prepared by high-energy methods.[14, 15] However, care should be taken because droplets coalesce very rapidly at the PIT, leading to extremely unstable emulsions, due to the low rigidity of surfactant interfaces. For that reason, in order to obtain stable emulsions, they are prepared at the PIT, and then quickly cooled or heated (so-called PIT method).

In a further investigation carried out by Kunieda *et. al*,[44] a relation was established between the PIT and the HLB number (N_{HLB}), for pure polyethylenglycol n-alkylethers nonionic surfactants.

$$PIT = K_{oil}(N_{HLB} - N_{oil}) \tag{1-16}$$

where N_{oil} is a parameter that depends on the "degree" of the hydrophobicity of the oil, and K_{oil} is a constant equal to 17 ºC for most oils. For instance, the N_{oil} for the aliphatic hydrocarbons heptane and hexadecane are 8.9 and 10.0, respectively. K_{oil} and N_{oil} can easily be determined from the slope and the intercept on the y-axis of the straight line of the PIT vs. N_{HLB} plot. Therefore, the use of this equation allows predicting the PIT of a system.

It should be pointed out that in contrast to pure surfactants, PIT for technical grade ethoxylated surfactants depends on composition, such oil-water ratio or surfactant concentration.[19, 45] This is due to the unequal distribution of surfactant at the interface. Commercial surfactants are usually composed of a mixture of homologs or isomers. Herein it is expected that the calculations made from the equation 1.15 slightly deviate from experimental results.[44, 46]

1.2.2 Formulation of Emulsions Stabilized with Colloidal Particles

Although the stabilization of emulsions by solids alone was first reported by Ramsden in 1903,[47] the credit is usually given to Pickering, who in 1907 conducted the first systematic study on the topic.[48] As a consequence, particle-stabilized emulsions are generally known as Pickering emulsions. Despite Pickering emulsions were described long time ago, this topic has been the focus of great attention only during the last 20 years. Several reviews [49-55] and books[56] have recently appeared, which cover the studies conducted in order to explain how particles can promote emulsion stabilization from both experimental and theoretical points of view. Aspects such as the basic stabilization mechanisms and the different parameters that influence emulsion formation are comprehensively discussed.

Pickering emulsions have many technological applications. Particles, sometimes in combination with surfactants, are present in many types of emulsions (or foams), and are important in the food, cosmetic, pharmaceutical, petroleum, mining and agrochemical industries.[49] It is worthy pointing out that undesirable emulsions are also produced by the presence of particles. For instance, in bitumen processing clay particles can contribute to the formation of water-in-bitumen emulsions during bitumen extraction. Removing the particles is necessary in order to demulsify the emulsions and further recovering the bitumen fraction.

1.2.2.1 *General aspects*

It is well established that in analogy with surfactant molecules, colloidal particles (covering from nano- to micro- range) can spontaneously adsorb at interfaces and consequently stabilize emulsions. However, to achieve efficient emulsion formation and stabilization, the hydrophilic and lipophilic properties of the particle surfaces must be balanced. As it will be described below, the wettability of the solids is primarily dictated by the three-phase contact angle, i.e. the contact angle that particles make with the water-oil interface. Such contact angle might be seen equivalent to the HLB parameter for surfactant molecules, which is the most important parameter in determining whether the surfactant resides in either water or oil.[51]

Surfactants and particles, however, differ in the physicochemical aspects related to emulsification. This is basically due to the fact that conventional particles, which usually show homogeneous chemical composition along their surfaces, do not possess two parts with completely different affinity for one solvent, as in the case of amphiphilic molecules. Herein, particles are considered to be surface-active, but not necessarily amphiphilic. This implies that particles, unlike surfactants, do not (at least significantly) reduce the free energy of a liquid-liquid interface by reducing the interfacial tension.[57-59] Since surface (or interfacial) tension is not reduced, it is more difficult to make Pickering emulsions with smaller droplet sizes. By contrast, the surface energy can be reduced when a particle become attached to an interface as the surface area of such interface is reduced.[50, 60] It should be mentioned that another type of particles, known as Janus particles (after the two-faced Roman god of doorways), show two different surfaces regions which make them amphiphilic. However, they are out of the scope of this work.

Besides the interfacial tension effect, another controversial fact is that in most of the reports dealing with the formation of Pickering emulsions, the presence of the particles is seen at the interface after shaking and carrying out the emulsification, but is not clear if the particles would previously diffuse spontaneously to the interface.[52] What is clear is the preference of particles to reside at liquid-liquid interfaces rather than in the bulk phase as it will be described below.

The free energy of detachment (ΔG_d) of a small spherical particle from an oil-water interface (Figure 1-12) into the bulk of one of the two fluids is equal to:[23, 51]

$$\Delta G_d = \pi \, r_p^{\,2} \gamma_{ow} \left(1 \pm \cos\theta_{ow}\right)^2 \qquad 1\text{-}17$$

where the sign in the bracket is positive for removal into oil and negative for removal into water. In the equation, r_p is the particle radius, γ_{ow} is the interfacial tension between the water and the oil phases, and θ_{ow} is the contact angle that the nanoparticle makes with the interface. This equation assumes that the interface remains planar up to the contact line with the nanoparticle, but is also applicable for curved interfaces if the particle radius is much smaller than emulsion droplet radius. Another consideration that should be taken into account is that gravity force is neglected. Calculations made for Dong and Jonson[61] showed that this assumption is generally valid in the case of small particles (less than few microns). For larger particles, gravity would pull such particles down from the interface.

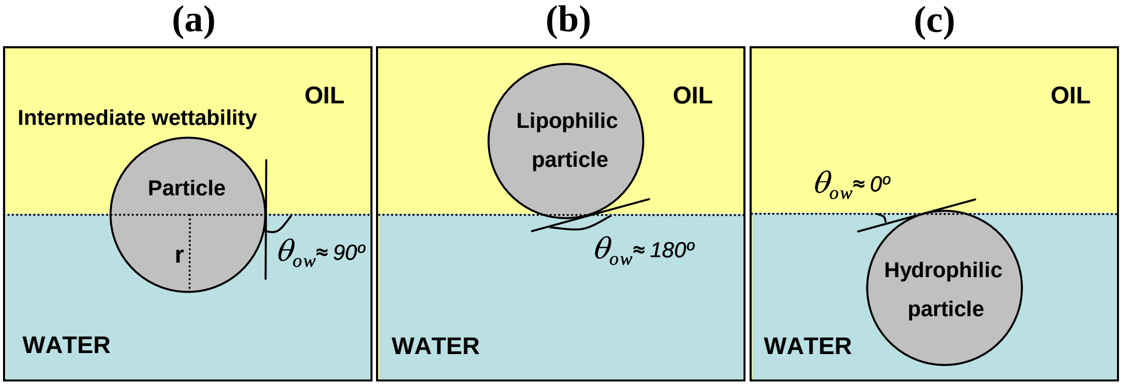

Figure 1-12. Contact angle (θ_{ow}) that a particle with radius r_p makes with the oil-water interface, with respect to its wettability: (a) particle of intermediate wettability (θ_{ow} ≈ 90º); (b) lipophilic particle (θ_{ow} ≈ 180º); (c) hydrophilic particle (θ_{ow} ≈ 0º) (adapted from Binks and Horozov).[56]

According to eq. 1-17, Figure 1-13(up) shows the influence of θ_{ow} on the energy (relative to $k_B T$, where k_B is the Boltzmann constant and T is the temperature) required to detach nanoparticles (of r_p = 10 nm) from an interface at 25ºC. In this example, the interfacial tension between both phases is 36 mNm^{-1}.[25] The first conclusion that can be drawn is that the contact angle is a key parameter when dealing with solid particles at the interfaces. It follows that particles are most strongly held at the interface for θ_{ow} = 90º. Eq. 1.17 also reveals that the free energy of detachment into water is lower for hydrophilic particles (θ_{ow} < 90º) than into oil, and inversely, hydrophobic (θ_{ow} > 90º) particles are more easily detached into oil than into water.

Besides that, data in Figure 1-13(up) suggests that the detachment energy for particles with θ_{ow} = 90º (or around this contact angle) can be several orders of magnitude larger than thermal energy ($k_B T$). This implies that once the particles are adsorbed at the interface, the attachment could be considered as irreversible.[56] The existence of an energy barrier leads to steric repulsion between droplets, and therefore preventing coalescence. Another consequence is that at θ_{ow} = 90° or around this value, the particle adsorption is strongly favoured and spontaneous. This is not the case for nanoparticles with contact angles near 0 or 180 °. It should be mentioned that different interaction forces between particles may play an important role in particle adsorption and in the particle-stabilization mechanisms at emulsion interfaces. However, the simplified model discussed above does not enter into these details, and considers the contact angle as the main parameter.[60, 62] Therefore particle-particle interactions are neglected.

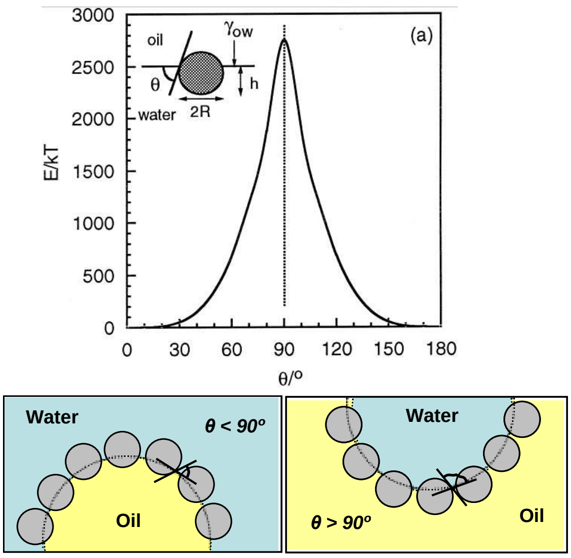

Figure 1-13. (Top) Contact angle vs. required energy to detach a spherical particle ($r = 1\cdot10^{-8}$ m) from the interface (relative to k_BT) according to equation 1-17. The interfacial tension between the water and the oil phases is 36 mN/m^{-1} (reproduced from Binks and Lumsdon).[25] (Bottom) Particles that are preferentially wetted by water (θ_{ow} < 90°) tend to stabilized O/W emulsions and inversely, W/O emulsions are stabilized by particles with θ_{ow} > 90.

This behaviour is significantly different from surfactant molecules, which adsorb and desorb in a relatively short time scale. Once emulsification has been produced, Pickering emulsions are considered in some cases to be more stable than surfactants-based systems. The other important parameter not represented in Figure 1-13 is the particle radius. It is known, and experimentally demonstrated that thermal energy can induced the displacement of sufficiently small nanoparticles (few nanometers in size).[63, 64]

Finkle et al.[65] was the first in relating the three-phase contact angle with the emulsion obtained. In that work it was stated that the phase that preferentially wets the particles is the continuous phase. A further work developed by Shulman et al.[66] quantitatively described the effect of the contact angle of $BaSO_4$ nanoparticles on benzene-water emulsions. The contact angle was systematically varied by adsorbing surface-active molecules (e.g. carboxylic acids) onto the particles. As illustrated in Figure 1-13(down), W/O emulsions are obtained when solids with contact angles made with the interface were higher than 90º, whereas particles with contact angles lower than 90º stabilize O/W emulsions. Other parameters that might influence particle wettability, leading to contact angle hysteresis, are the particle shape or the particle roughness.[51]

According to Young´s equation (eq. 1-18) contact angle is a function of the surface free energies, i.e. interfacial tensions as follows:

$$\cos\theta = \frac{\gamma_{po} - \gamma_{pw}}{\gamma_{ow}} \qquad 1\text{-}18$$

where γ_{po}, γ_{pw} and γ_{ow} are the interfacial tension at the particle-oil, particle-water and oil-water interfaces. While for hydrophilic nanoparticles ($\gamma_{po} > \gamma_{pw}$), θ < 90º, for hydrophobic nanoparticles ($\gamma_{po} < \gamma_{pw}$), θ is higher than 90º. Only in the case that γ_{ow} > ($\gamma_{po} - \gamma_{pw}$) particles will tend to situate at the liquid-liquid interface. If $\gamma_{po} = \gamma_{pw}$, then the contact angle is 90º, which is the most stable situation.

Many kinds of particles (in the micro- or nano- scale), including either organic or inorganic, and either synthetic or naturally-occurring, have been employed as emulsion stabilizers. Several examples are given in Table 1-2.

Table 1-2. Some examples found in the bibliography describing the use of finely-divided solids as emulsifiers. ϕ indicates internal phase volume fraction.

Particles	ϕ (vol%)[a]	Emulsion type	Comments
$BaSO_4$	50	O/W or W/O	Particles of several hundred nm. Contact angle tailored by adding surface-active molecules.[66]
CdSe	Diluted	W/O	Nanoparticles (3 and 5 nm) coated with Tri-*n*-octyl-phosphine-oxide. Larger nanoparticles replace smaller consistently with their adsorption energies.[63, 64]
SiO_2	5-90	O/W or W/O	Emulsion type dictated by wettability of different degree of silane–modified nanoparticles (5-30 nm).[25, 67-71]
TiO_2	20	O/W	Emulsions stabilized with anatase nanoparticles (6 nm). Optimum stability with solids in a state of incipient flocculation.[72]
Fe_3O_4	50	O/W or W/O	Magnetic nanoparticles (≈10 nm) coated with oleic acid. Emulsion inversion induced by changes in pH.[73]
Poly(NIPAM)-co-MAA [a]	30	O/W	Emulsions stabilized by pH and temperature stimuli-responsive particles (150-250 nm).[74]
Chitosan	10	O/W	Surface-active chitosan nanocrystals. Remarkable stable emulsions: dense coverage at the interface and presence of a 3D network in the continuous phase.[75]
Flavonoids	20	O/W	Tiliroside, rutin and naringin particles used as Pickering emulsifiers, simulating human digestion conditions.[76]

[a] Poly(N-isopropylacrylamide) co-polymerized with methacrylic acid.

1.2.2.2 *Emulsion stabilization mechanisms*

The basic requirements for the formation of solid-stabilized emulsions are now well established in the bibliography, and are as follows:[29, 77] i) the size of the particles used as emulsifiers should be considerably lower than the size of the emulsions droplets. ii) particles must be wetted by the two immiscible phases, and the continuous phase of the emulsion will generally be the phase that preferably wets the solids. iii) Some degree of interparticle interaction may be required for effective stabilization.

Interparticle interactions are especially important in nanoparticles that at certain conditions of pH or electrolyte concentration are too hydrophilic (or hydrophobic) to migrate to the interfaces and prefer to remain dispersed in the water (or oil) phases.[78, 79] For instance, SiO_2 nanoparticles at extreme pH, in which particles are highly charged and electrostatic repulsion become important. From early studies, a dense coverage layer of solids at the interface was recognized to be the responsible for the stability of emulsions. Furthermore, some authors suggested that only particles partially flocculated could build up such layer.[80-82]

Figure 1-14 outlines the main stability configurations (i.e. interfacial structures) that may be responsible for the stabilization of Pickering emulsions, consequently impeding emulsion coalescence. By far, complete coverage of droplets with particles, (Figure 1-14(a)) is the configuration most often encountered in experimental studies.[83, 84] The formation of particle dense layers is a result of the attracting forces which dominates the particle interactions at interfaces.[50] The fact that one or more layers might be attached on the droplet surfaces strongly depends on the concentration and nature of nanoparticles. In this sense, the concentration used to stabilize the Pickering emulsions is frequently larger than that required to cover the droplets with a monolayer. One example of such bilayer stabilization is shown in the confocal microscope picture in Figure 1-15(a). In such picture, water droplets in a dodecane medium are stabilized with a closed-packed monolayer of micron-sized poly(methylmethacrylate) spheres. The particles were previously labelled with a fluorescent dye.[85] One of the potential applications that has been explored during last ten years is the use of droplets as sacrificial templates on which particles are assembled into a large structure. The high stability rendered by particles adsorbed at interfaces is a key feature for the preparation of tailored materials. One example are the so-called colloidosomes (by analogy with liposomes) which are semi-permeable capsules with higher potential as encapsulating and drug delivery systems.[86, 87]

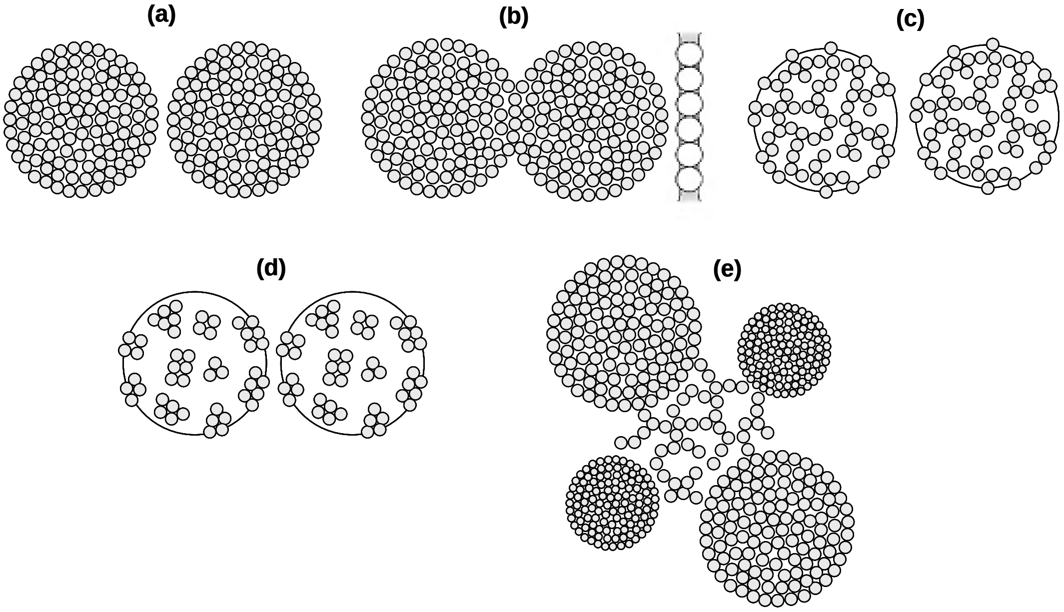

Figure 1-14. Interfacial structures at droplet surfaces, responsible for the stabilization of particle-stabilized emulsions: (a) bilayer; (b) bridging monolayer; (c) aggregated particles forming a 2-D structure; (d) droplets sparsely covered; (e) 3-D particle network in the continuous phase (adapted from Lopetinsky et al.).[6]

Besides the energy of particle detachment commented earlier, which neglects interparticle interactions, other stabilization mechanisms have been proposed to explain the remarkable stability against coalescence of some Pickering emulsions. Tambe et al. [49] argued that lateral displacement of particles away from the drop-drop contact region was likely the main mechanism of particle removal, facilitating coalescence as uncovered surfaces become closer to each other. The magnitude of steric repulsion considers the energy of interaction between particles in the contact regions (i.e. electrostatic, van der Waals and structural components of the interaction forces) and also the energy required to rearrange the particles again on the droplets. As the energy required for the lateral displacement is much lower than that required for particle detachment (the latter is unlikely to be achieved in practice) they conclude that lateral displacement was partially responsible for the stability of emulsions. This mechanism also assumes that particles in the extreme cases of being either completely deflocculated or completely flocculated, those particles may not be effective stabilizers.[49] This model does not explain, however, the stabilization of sparsely covered Pickering emulsion droplets.

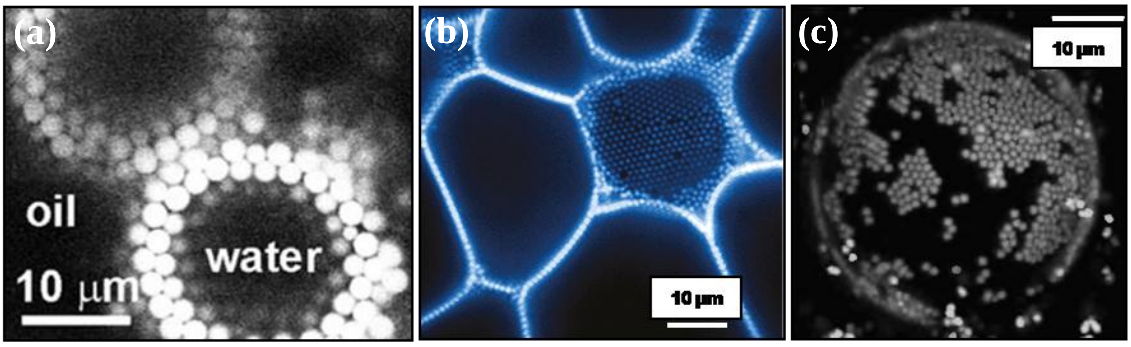

Figure 1-15. Three possible configurations of particles at water-oil interfaces: (a) water-in-dodecane emulsion stabilized with a monolayer of micron-sized poly(methylmethacrylate) spheres; (b) confocal microscope image of a water in oil emulsion stabilized with a bridging monolayer of silica particles 975 nm in size; (c) 1 μm polystyrene spheres partially covering a poly(dimethylsiloxane) droplet. The emulsion is stable, despite having regions lacking of particles. Images are reproduced from (a) Thijssen et al.,[85] (b) Lee et al.,[88] and (c) Tarimala and Dai.[89]

Regarding particle-particle interactions, it is well known from the studies dealing with nanoparticle monolayers at planar oil-water interfaces that such forces (e.g. long range Coulomb and dipole-dipole repulsion) can greatly influence the structure of the nanoparticle layers, the particle-interface attachment as well as emulsion stability.[53]

Ivanov and co-workers were the first in attributing the stability of Pickering emulsions to the presence of capillary pressure, preventing the thinning of the liquid in the continuous phase.[90] Such pressure can be defined as the pressing force required to bring two droplets (or bubbles) to coalescence. It can be also defined as the pressure difference between the droplet and the separating film. Actually, it is considered that as emulsion droplets approach, the film thins until a critical thickness is reached. At this point, the film breaks and droplets can coalesce. The pressure ($P_{c,\max}$) associated with the coalescence event can be given by the relationship:[91]

$$P_{c,\max} = \frac{2\gamma_{ow} - \cos\theta}{br_p} \qquad \text{1-19}$$

where r_p is the particle radius, b is a constant dependent on the packing exhibited by the particles, γ_{ow} is the interfacial tension and θ is the particle contact angle. It should be pointed out that the model predicts lower values for contact angles near 90º, which does not agree with the energies for particle detachment discussed in section 1.2.2.1. Therefore, the two theoretical approaches (theory of capillary pressure and theory of particle detachment) must be taken in combination.[90] In any case, the model based on capillary pressure is limited to densely packed layers.

It should be remarked that both theories do not take into account the influence of interfacial rheology on the stability of the thin film of continuous phase between droplets. Such mechanism has been studied by other authors.[49]

Coming back to the interfacial structures in Pickering emulsions, bridging monolayer (Figure 1-14(b)) is an alternative to the classical bilayer structure. This mechanism was first reported in experiments dealing with fluid interfaces loaded with particles.[92-94] Interestingly, when a water droplet stabilized with hydrophobic polystyrene latex particles (few micrometers size) in an oil medium was slowly approached to a flat oil/water interface, with or without particles, the two water/oil interfaces were suddenly bridged by a stable particle monolayer, leaving a thin oil film separating two aqueous phases, thus preventing coalescence. Attempts to pull away the droplet from the interface resulted in the bridging monolayer holding the two interfaces.[92] Stable films were only observed when the particle wettability fulfils the condition for stable particle bridges, i.e. particles preferentially wetted by oil will tend to stabilize W/O emulsions and inversely. In this interesting case, particles protruding from one droplet can simultaneously adsorb to another droplet (or water/oil interface) and bridge them with a particle monolayer. Consequently, the two extremes of the particles are wetted by the phase forming the droplet, but a major proportion of the nanoparticle is still wetted by the continuous phase.

The number of studies describing bridging monolayers in real emulsions, however, is very limited. One example of a W/O Pickering emulsion gel stabilized with a bridging monolayer of silica particles is depicted in Figure 1-15(b).[88] A parameter that should be considered is that particles should possess a minimum size, which implies that most of the nanoparticles used in

Pickering emulsion studies (up to 100-200 nm) are too small and unlikely to form such bridges. A pioneer study carried out by Binks and Horozov showed the remarkable differences in the ability of both hydrophilic and hydrophobic SiO_2 particles (3 μm of diameter) to adopt such configuration.[69] Consistent with the results obtained previously in octane/water planar monolayers,[93] hydrophobic nanoparticles (θ_{ow} = 152º) gave ordered monolayers at the interface due to the existence of long-range Coloumbic repulsion forces through the oil phase due to charges at the particle-octane interface. In a W/O emulsion, nanoparticles were able to remain at the touching droplet contact points forming a dense-crystalline disk bridge between the two droplet surfaces. Stable emulsions were observed, even with areas outside the contact regions, barely covered by particles. By contrast, as repulsion was absent in the case of more hydrophilic nanoparticles (θ_{ow} = 65º), lateral mobility was greater, and consequently the nanoparticles were easily dragged away from the emulsion contact areas. Therefore, emulsion stabilization (O/W) by bridging monolayer was not observed.[69]

Although Pickering emulsions with a particle bilayer configuration habitually show a homogeneous dense packed particle arrangement, emulsion stabilization is not attributed to individual nanoparticles, but to aggregates of particles. This has been described in works with silica particles.[25, 54] Further definition of the particle network at the oil/water interface is a general encountered problem due to the great difficulty to observe the particle network at the nanoscale. Besides that, it must be stressed that particle-particle interactions before emulsification can be counterbalanced by the energy associated with emulsion formation and also that particles may undergo rearrangement when they attach to the interfaces.[53] Furthermore, it is rather difficult to distinguish particles adsorbing individually or in flocs, or also, if they adsorb simultaneously or progressively. In order to gain insight into the interfacial structure of Pickering emulsions, advanced microscope techniques, such as freeze-fracture TEM[95] or SEM[96] have been recently used.

Despite the difficulty to classify the range of particle structures at low particle concentration, the following division can be made: a) formation of a 2-D structure of aggregated particles on droplet surfaces and b) stabilization of emulsion droplets by sparsely covered domains (Figure 1-14(c-d)). Both cases have been observed experimentally, described at low coverage conditions.[58, 81, 83, 97] One example of an oil emulsion droplet partially stabilized with 1 μm polystyrene spheres with an hexagonally-closed packed structure, but with other completely uncovered areas, is shown in Figure 1-15(c).[89] Despite the not uniform distribution of particles, the emulsion was stable to coalescence. In this line, Vignati et al.[58] has also reported the stabilization of O/W emulsions with silica particles (500 nm in size) with surface coverage as low as 5 % (compared to a packed monolayer). Striking optical microscope observations revealed particle rearrangement and further accumulation at the touching points between droplets, forming a bridging monolayer.

The last configuration included in Figure 1-14(e) consists in the presence of a 3-D network of particles in the continuous phase of the emulsions and it constitutes a secondary structure that improves emulsion stability.[6, 98] This stability mechanism has been described for triglyceride crystals providing long-term stability in food emulsions.[54]

1.2.2.3 *Factors influencing emulsion stability*

(a) Particle surface properties

As pointed out earlier, the type of resulting emulsion is primary dictated by nanoparticle wettability. In turn, the wettability of given nanoparticles can be easily controlled by nanoparticle functionalization. For instance, O/W-type emulsions (at a certain oil-water ratio) stabilized with partially hydrophilic particles can invert to W/O by simply addition of small amounts of stearic acid.[77] The fatty acid, which is dissolved in the oil phase before emulsification, adsorbs at the nanoparticle surface, thus rendering the nanoparticle surfaces more hydrophobic and altering its contact angle. Likewise, surface grafting with molecules with terminal alkyl chains which modifies particle wettability, can be applied to favour the adsorption at the water-oil interfaces of very hydrophilic nanoparticles. Apart from fatty acids,[99, 100] several low-molecular-weight surfactants have been used with the same purpose.[78, 101, 102]

An existing alternative procedure consists in varying the lyophilicity of the solids through prior chemical surface treatment (e.g. silanization of silica particles). Interestingly, Binks and co-workers observed that emulsion phase inversion (see Figure 1-6 in 1.1.2.4) from W/O to O/W emulsions occurred in systems stabilized with SiO_2 nanoparticles at different water volume fractions (ϕ_w), depending on the silanol content on nanoparticle surfaces.[25] Specifically, the ϕ_w at which phase inversion occurred increased with particle hydrophobicity. However, for the particles with the lowest silanol content, the emulsions remained W/O up to 0.9 of internal phase volume (i.e. highly concentrated emulsions).

Finally, an attractive approach of clear technological applications is the use of stimuli-responsive particles for the stabilization of Pickering emulsions. Particles that are swollen by certain solvents (e.g. polystyrene based) and/or particles that are sensitive to temperature (as poly(N-isopropylacrylamide, known as poly(NIPAM)) gives scope for variation of emulsion stability (or type) by external stimuli such as pH or temperature.[74] One example is the incorporation of carboxylate groups, which may lead to pH-sensitive particles. Carboxyl groups are ionized at increasing pH, and particles are thus expected to be more hydrophilic.[103]

(b) Particle size and concentration

The effect of reducing particle size on the enhancement of emulsion stability is well known, and it is recognised that smaller particles give higher packing efficiency.[49, 104] It is considered, however, that the effectiveness of the particles as emulsifier reaches a limit until a minimum particle size is attained. Below this critical size, Brownian motion becomes significant and thermal energy may produce particle detachment from the interface. However, particle-particle interactions, which eventually determine the stability of the dispersion, should also be considered.

Concerning the particle concentration, it has been previously found that the higher amount of particles, the smaller emulsion droplet.[70, 105] This can be explained by the fact that more interfacial area is covered, and consequently smaller droplets can be stabilized. This tendency is also observed in surfactant-stabilized emulsions, whereby an increment of surfactant concentration leads to a progressive reduction of the droplet size. However, when using surfactants, smaller droplet sizes are favoured by interfacial tension reduction.

Contrary to surfactants, when particle concentration is larger than that required to cover the surface of the droplets with a monolayer, particles can often remain disperse in the continuous phase as small aggregates[78] or forming a 3-D network surrounding the droplets.[106] In some cases it has been reported that, even with particle concentrations lower than the interface saturation, nanoparticles remained in the continuous phase instead of being adsorbed at the interface.[60, 107] Masliyah et al.[107] stated that in the case of particles which had been previously surface-modified, some of them could have become more hydrophobic or hydrophilic than others due to a non-homogeneous functionalization.

(c) Interactions between particles and surfactants

Often, in particle-stabilized emulsions, surfactant molecules are added to particles to enhance particle attachment.[82, 102, 108] Even though the inherent ability of surfactants to modify the particle wettability has been studied to some extent, systematic studies of emulsions stabilized with mixtures of both emulsifiers, have generated considerable interest during the last five years.[78, 85, 109-111] Generally, interactions between particles and surfactants with respect to emulsion stability can be classified in two types, namely synergistic or antagonistic.

The first case is typically observed when particle adsorption at the interface is induced by modifying its wettability, as in the study pointed out earlier carried out by Tambe et al.[77] Such adsorption not only might improve emulsion effectiveness, but also might cause particle aggregation and network arrangement at the interface. For instance, Binks and co-workers observed synergistic stabilization when low concentrations of SDS[108] or CTAB[78] surfactants (below the CMC) were mixed with positively or negatively SiO_2 nanoparticles, respectively. Emulsions of gel-like texture were found to be more stable to coalescence when the particles were flocculated, i.e. conditions of zero charge. In these studies, surfactants and particles, both hydrophilic, were mixed in the aqueous phase. However, the synergistic effect has been also described when hydrophilic particles (e.g. Laponite, clay) and hydrophobic surfactants (e.g. Span 80) were mixed for separate, each one in the corresponding phase.[102, 109] Both emulsifiers are therefore able to interact at oil-water interfaces. In this context, it is well known that the preparation method has a significant effect on the resultant Pickering emulsions.[112]

Besides adsorption, the addition of surfactant concentration (below CMC) can also contribute to lower the interfacial tension, therefore facilitating the emulsification and allowing both surfactant and particles to adsorb simultaneously at the oil-water interface. This can impart long-term emulsion stability.[110] In an interesting work, Wang et al.[57] found that the interfacial tension between the oil (containing an ionic surfactant) and the aqueous phase was greater reduced (more than 10 mNm^{-1}) by the presence of oppositely charged kaolinite particles, initially dispersed in water. Such reduction was attributed to the ability of the particles to attract the surfactant at the interface, which then adsorbed at the interface in a greater extent than without nanoparticles. As outlined at the beginning of section 1.2.2.1, nanoparticles do not reduce the free energy of a system by reducing the interfacial tension. However, a small reduction in interfacial (or surface) tension has been reported in some systems. Such reduction has been attributed to partial particle crystallization of hydrophobic particles[113] or to the effect of low concentrated dispersions of charged TiO_2 nanoparticles on surface dynamics.[61] Nonetheless, in most of the reports, the presence of nanoparticles did not change the interfacial tension values.[57-59, 78, 114]

Ravera and coworkers[114, 115] have made a systematic study of the interaction between particles and surfactant at interfaces by means of interfacial tension, ellipsometry and dilational viscoelasticity measurements. Results showed that the interfacial properties remained almost unchanged by the presence of only nanoparticles. Interestingly, partially hydrophobized nanoparticles via CTAB or palmitic acid adsorption accumulate at the water-oil interface driven by Brownian motion. After particle attachment at the interface, surfactant redistributed between the surface of the nanoparticles and the interface, and consequently interfacial tension values decreased. This reduction is illustrated in Figure 1-16(a). From the graph it can be seen that palmitic acid concentrations above $5 \cdot 10^{-5}$ M provide a driving force for particle attachment. Therefore, higher fatty acid concentrations above a threshold value lead to segregated particles at the surface (air-water). It can be also seen that the adsorption is a dynamic process that requires long times to reach equilibrium. Similar results describing particles moving to interfaces as surfactant carriers have been observed by Akartuna et al.[99]

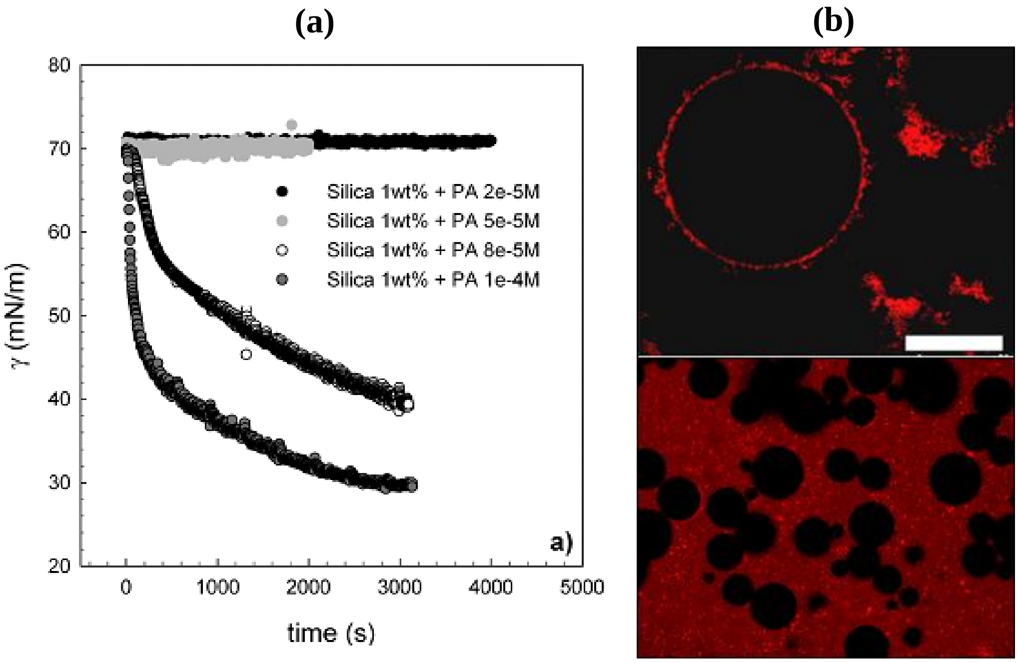

Figure 1-16. (a) Dynamic surface tension for silica dispersions (1 wt%) with different concentrations of palmitic acid (PA in the legend) adsorbed onto their surfaces. Reproduced from Ravera et al.;[114] (b) Two confocal fluorescence images that shows the displacement of silica (12 nm) nanoparticles from the interface of a O/W Pickering emulsion (up), induced by addition of 0.1 M of SDS (down). Rhodamine B dye was attached to the nanoparticle prior emulsification. Initial concentration of silica was 0.54 wt%. Scale bar corresponds to 50 μm. Reproduced from Vashisth et al.[116]

On the contrary, antagonistic interactions can take place when both particles and surfactants compete each other for adsorption at liquid-liquid interfaces. Generally, surfactants adsorb in preference to particles, and consequently surfactant concentrations larger than CMC can produce a desorption of particles from the interface to the continuous phase of emulsions.[117] For example, Vanisth et al.[116] looked into the effect of adding SDS to already-formed O/W emulsions stabilized with partially hydrophobized silica nanoparticles (slightly negatively charged). Complete displacement was attained at the CMC of the surfactant. The sequence is shown in Figure 1-16(b). It should be noted that emulsion droplet size is significantly reduced when surfactant takes the place of nanoparticles. Pichot et al.[110] furthered these findings in systems stabilized with mixtures of silica nanoparticles and both hydrophilic and hydrophobic surfactants. Due to stronger competition for adsorption, they observed particle released from the interface in O/W emulsion only when hydrophilic surfactants were used. On the contrary, Pickering stabilization was maintained when a hydrophobic surfactant was incorporated. Therefore, in the first case a transformation from a Pickering emulsion to a surfactant-stabilized one was observed.

1.2.2.4 *Preparation of inorganic oxide nanoparticles*

This study has investigated the incorporation of two well studied types of inorganic nanoparticles, namely iron oxide (magnetite, Fe_3O_4) and titanium dioxide (TiO_2), in the polymeric walls of macroporous nanocomposites made from W/O highly concentrated emulsions. Both inorganic oxides are naturally occurring minerals on earth. Magnetite is a ferromagnetic mineral while certain crystallographic titanium dioxide phases are photocatallytically active. The integration of such inorganic compounds within polymeric structures is a research field of growing interest due to the potential applications of the resultant functional materials.

1.2.2.4.1 Synthesis of magnetic nanoparticles

The synthetic methods used for the preparation of magnetic nanostructrued materials with nano-scale dimensions can be divided into two main categories:[118] synthesis from molecular precursors, as with most chemical methods such as sol-gel reactions, aerosol/vapor or electrochemical methods, and synthesis by processing of bulk precursors, as for example in mechanical attrition. Among all the techniques available, the classical synthesis by coprecipitation is the simplest and most efficient chemical pathway.[118]

The coprecipitation method is based on aging a stoichiometric mixture of ferrous and ferric salts in aqueous medium, in order to obtain iron oxides (either Fe_3O_4 or γ-Fe_2O_3). In the case of Fe_3O_4, the reaction can be written as follows:[118]

$$Fe^{2+} + 2Fe^{3+} + 8\,OH^- \rightarrow Fe_3O_4 + 4H_2O$$

With a stoichiometric ratio of 2:1 (Fe^{3+}/Fe^{2+}) in a non-oxidizing oxygen environment, complete precipitation of Fe_3O_4 should occur at pH between 8 and 14, taking into account the thermodynamic of the reaction.[119]

Despite the control of particle size distribution is difficult because the growth of the crystals is controlled by kinetic factors,[120] this method allows synthesizing large amounts of product. Another factor that should be taken into account is that magnetite (Fe_3O_4) is sensitive to oxygen and can transformed into maghemite (γ-Fe_2O_3). Generally, particles from 2 to 17 nm can be obtained, and both the particle and shape of the nanoparticles can be somehow controlled by efficient adjustment off temperature, pH, nature of the salts or ratio between Fe^{3+}/Fe^{2+}.[121, 122]

Superparamagnetic iron oxide nanoparticles

From the magnetic point of view, materials can be divided in five different types: diamagnetic, paramagnetic, antiferromagnetic, ferromagnetic and ferrimagnetic.[123] Magnetic effects manifested by the three first types are very weak, though may be detected using the appropriate characterization techniques. On the other hand, ferromagnetic and ferrimagnetic exhibit magnetism to a higher degree. Examples of extensively used ferromagnetic and ferrimagnetic materials are γ-Fe_2O_3 and Fe_3O_4, respectively. As it will be discussed below, superparamagnetism is a purely-finite size effect, which occurs below a critical diameter in which ferromagnetic and ferrimagnetic nanoparticles become single-domain.[124, 125]

Both ferro- and ferrimagnetic materials are characterized by holding spontaneous magnetization, even in absence of any magnetic field. Such magnetization disappears when the material is heated above the Curie temperature (T_C), and the material becomes paramagnetic because of the randomization of the spin magnetic moments.[126] Besides that, in order to explain the unusual dependence of the magnetization (M) with the applied magnetic field (H) observed for ferromagnetic materials, Pierre Weiss postulated that such kind of materials were formed by domains.[127] Within each domain, the direction of M is the same, but the direction varies between domains. It should be noted that average of M may be 0 if parallel and unparallel domains are balanced. The motion of domains under an applied magnetic field of indistinctly, ferro- or ferrimagnetic materials, is schematically shown in Figure 1-17, in which a typical case of M as a function of H is plotted.[128]

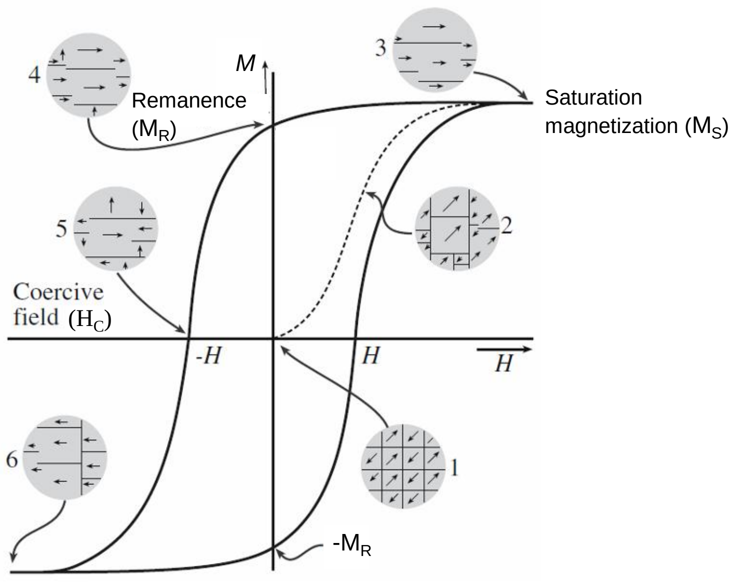

Figure 1-17. Typical magnetization (M) vs. applied magnetic field (H) hysteresis loops for ferromagnetic and ferrimagnetic materials. The insets represent schematically the domain structure and the arrows indicate the spins orientations along the hysteresis curve. Magnetization saturation, remanence and coercive field are denoted as M_s, M_R and H_C, respectively. Reproduced from Carter and Norton.[128]

The experiment starts with the material unmagnetized (1). In a first stage, the process is reversible, as M increases just slightly with H. Consequently, M returns to zero if H is removed. When further increasing H, the oriented domains grow more easily (2) until the saturation magnetization (M_s) is reached, and thus all moments are aligned (3). In this region, if the field is removed the process is not reversible anymore, and there is a resistance to domain wall motion.[128] This results in a material acting as permanent magnet. The residual magnetization at zero H is known as remanence (M_R, point 4). If H is applied in the opposite direction, M continues diminishing until zero magnetization is reached again (5). The H at which domains are completely randomized is known as the coercive field (H_C). Finally, M_s is reached in the opposite direction if H is increased (6). It should be remarked that the curve is completely reproducible at consecutive cycles, and that the area inside the hysteresis loop is equal to the energy consumed in the M vs. H cycle. According to the curve, magnetic materials can be divided in namely soft or hard magnets when H_C is lower than 10^3 A/m or much bigger than this value, respectively.[123]

In 1949, Neel demonstrated that thermal fluctuations could change the orientation of the magnetic moments in single-domain particles when the anisotropic energy is smaller compared with k_BT, where k_B is the Boltzmann constant and is the T temperature.[129] Therefore, while magnetic field tends to align magnetic moments, thermal fluctuations tend to misalign them and the magnetic moment of each nanoparticle fluctuates rapidly with no preferred orientation. This behaviour is essentially the same than that shown by a normal paramagnet, except for the relatively higher value of magnetization of ferro- or ferrimagnetic nanoparticles. This is the reason why such kind of nanoparticles were called superparamagnetic.[130]

The relaxation time (τ) that it takes for a nanoparticle magnetization to randomly flip as a result of thermal fluctuations, is given by the following Arrhenius equation:[131-133]

$$\tau = \tau_0 \exp\left(\frac{E_A}{k_B T}\right) \qquad 1\text{-}20$$

where τ_0 is a time constant characteristic of each material (values normally between 10^{-9} and 10^{-10} seconds), and E_B is the energy anisotropy barrier which separates the two equilibrium states. Following eq. 1-21, such energy barrier is proportional to the particle volume (V_p) and to the uniaxial magnetic anisotropy (K_a):[118]

$$E_A = K_a V_p \qquad 1\text{-}21$$

It is important to stress that one system will be superparamagnetic depending on the characteristically experimental measured time (τ_M).[125] For $\tau_M >> \tau$, the relaxation occurs faster and magnetization will flip many times during the measurement. Consequently, nanoparticles reach the thermodinamical equilibrium and the system will behave as a paramagnet, with zero average magnetization. On the other hand, for $\tau >> \tau_M$, the relaxation is slower and the whole magnetic moment is blocked.[132] The temperature that separates these two different states is known as the blocking temperature (T_B), and it is defined as the temperature at which $\tau = \tau_M$.[134] Since the blocking temperature is associated to the energy barrier, the higher the volume particle, the higher the T_B. Therefore, the following expression can be drawn:

$$T_B = \frac{K_a V_p}{k_B \ln\left(\frac{\tau_M}{\tau_o}\right)} \qquad 1\text{-}22$$

For τ_M = 100 s, which is the typical measuring time when using a superconducting quantum interference device (SQUID), $\ln(\tau_M / \tau_o)$ is 25.

This implies, that for high temperatures or particles extremely small, the nanoparticle relaxation time (τ) is much lower than any measuring time (τ_M), and therefore the particle system is in the superparamagnetic state. As aforementioned, in the magnetization versus applied magnetic field (M vs. H) experiment, ferro- and ferromagnetic materials show hysteresis, coercitivity field and remanence. In the case of superparamagnetic particles, this is also observed below the T_B, in which the whole magnetic is blocked, and thermal fluctuations are not enough to overcome the anisotropy energy. Therefore, the magnetic state depends on previous system conditions. On the other hand, above T_B, moments of each nanoparticle fluctuate rapidly with no preferred orientation and the energy barrier is overcome thermally. As a consequence, demagnetization in superparamagnetic particles occurs without coercitivity. This is because demagnetization is caused by thermal energy, rather than by the action of a magnetic field.[135]

Apart from the M vs. H curves, measurements of superparamagnetic particles as a function of temperature are important and can give additional information about its behaviour.[118, 124] Among them, probably the most widely used are the zero-field cooling (ZFC) and the field cooling (FC) cycles. From this curves, one can obtain with exact precision the average T_B and also a profile of the particle size distribution.

In the ZFC experiment (Figure 1-18(a)), the nanoparticles are cooled down to ca. 0K under H =0.[135] At this given conditions, the magnetic moments are randomly oriented and M =0. Then, a magnetic much lower than a field able to generate any preferential direction is applied and simultaneously, temperature is increased. Initially, thermal energy is not sufficient to overcome E_B, and the magnetic state is the same than at the starting point (line 1). For a modisperse system, the thermal energy satisfies the relation $\tau = \tau_M$ at the T_B. As a result, particles with volume V_p become magnetized as magnetic moments align to the direction of the magnetic field. As temperature is further increased, the random fluctuations from thermal energy begin to dominate and the macrospins become randomly oriented once again (line 2).[135]

In the ZC experiment (Figure 1-18(b)), the same H than in the ZFC experiment is first applied, and then the system is cooled down to ca. 0K. As clearly seen in the plot, the initial magnetization is not zero and it remains constant until the system reaches the T_B (line 1). Further temperature increment produces the same effect than in the ZFC, i.e. a magnetization reduction.

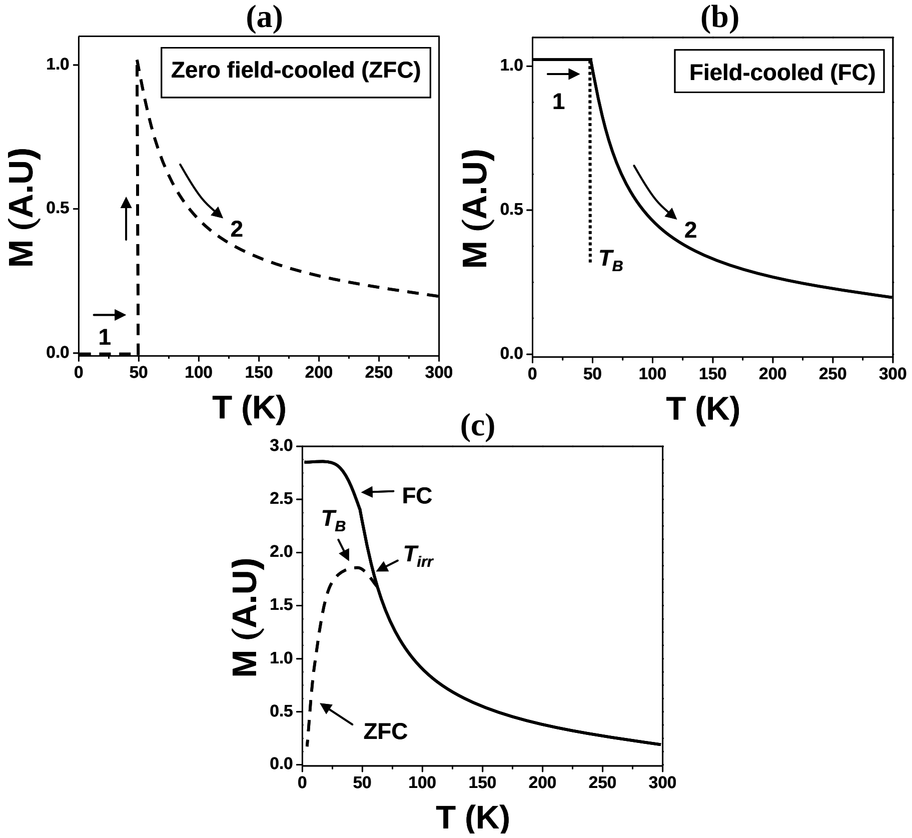

Figure 1-18. Theoretical curves as a function of temperature under (a) zero-field cooled (ZFC) and (b) field cooled (FC) of monodisperse non-interacting magnetic nanoparticles with uniaxial anisotropy. ZFC and ZC curves are plotted together in (c). The average blocking temperature and the irrersivility temperature are denoted as T_B and T_{irr}, respectively.

Figure 1-18(C) shows a typical curve of the whole ZFC-FC experiment. Two characteristic temperatures can be defined: the average blocking temperature (T_B),[133, 135] and the irreversibility temperature (T_{irr}).[136, 137] Comparing the T_B in both Figure 1-18(a) and Figure 1-18(c), we can clearly see that in the last case the peak is broader than in the first case. This can be attributed to the presence of particle polydispersity, which results in a distribution of T_B.[133] Regarding T_{irr}, it should be remarked that it is always above T_B, and is defined as the temperature at which bifurcation between ZFC and ZC occurs.[137] Such temperature is linked to the transition from the blocked to the superparamagnetic state of the larger nanoparticles.

Logically, the real systems are much complicated as particles typically have distinct sizes and morphologies. Moreover, particle interactions must be also considered. It is well-documented that nanoparticle interaction (dipole-dipole and exchange interactions) modifies the anisotropy energy barrier (E_A), altering the magnetic behaviour of fine particle systems.[138, 139] In most of the cases, the blocking temperature (T_B) decreases with weaker interparticle interactions.[133, 134]

Nanosized superparamagnetic iron oxide nanoparticles are attracting much attention in last years because their potential applications in among others, targeted drug delivery[140], magnetic storage media[141] or self-heating processes.[142] The absence of remanence when an external magnetic field is switched off as well as the quick response to such magnetic fields are two of the most remarkable features of superparamagnetic nanoparticles.[118]

1.2.2.4.2 Synthesis of titanium dioxide nanoparticles by mechanochemical methods

One interesting alternative synthesis method for inorganic oxides is the mechanochemical activation of solid-state reactions. The mechanical treament of powder solids in high-energy mills significantly increases the number of defects in the solid structure, leading to much less crystallinity, smaller crystallite size and large surface area.[143] During the high energy ball-milling reaction several types of impact between reactants, balls and container walls of the can occur. An schematic drawing of such possible impacts is depicted in Figure 1-19.

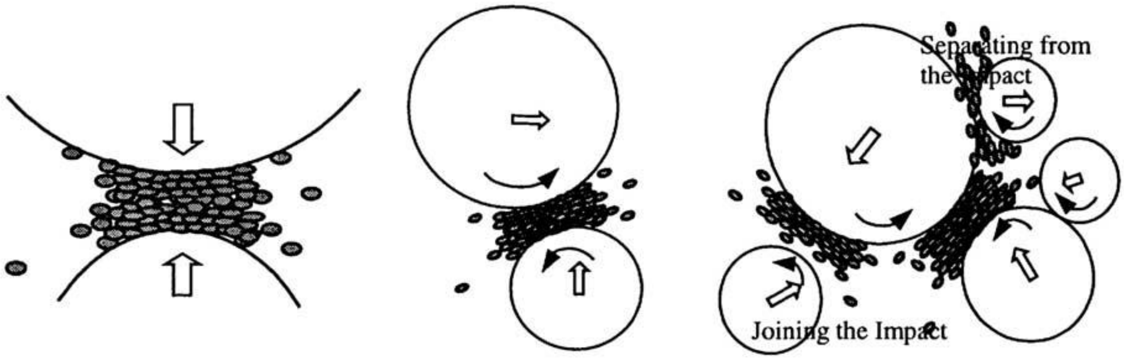

Figure 1-19. Three examples of possible manners by which flying balls in a mill can collide: (a) head-on impact; (b) oblique impact; (c) multi-ball impact. Reproduced from Zhang.[143]

In this way the reactivity of the activated solids is remarkably enhanced. This methodology has been used from some decades as a synthesis tool for different materials, such as special alloys, nanocrystalline powders or metal-ceramic composites.[143] An attractive variation of this method allows obtaining nanometric powders of simple metallic oxides by solid-state reaction between a metallic salt (Lewis acid) and a base. The mechanochemically activated reaction produces low crystallinity oxides immersed in a water soluble salt by-product, which is ulteriorly removed by means of a simple washing procedure.[144, 145] Different oxides (Gd_2O_3, CeO_2, TiO_2, etc.),[146-148] and inclusive metallic nanopowders[149] have been obtained by this technique. In comparison with the most conventional preparative routes, the main advantages of the mechanochemical method are the possibility of obtaining relatively large amounts of product, simplicity of the process, low-cost raw materials and total absence of organic solvents.

Titanium dioxide

The 95 % of titanium that is commercialized over the world is in the form of titanium dioxide (TiO_2). Due to its chemical stability, low cost and availability and a remarkable high refraction index (ca. 2.4), TiO_2 is widely used in paints, cosmetics and in the food industry. Since 1972, when Fujishima[150] and Honda discovered the photocatalytic splitting of water on titanium dioxide electrodes, TiO_2 constitutes the archetypical photocatalyst in heterogeneous photocatalysis due to its relatively high efficiency and chemical stability.[151] Among the three most important TiO_2 polymorphs, i.e. anatase (tetragonal), rutile (tetragonal) and brookite (orthorhombic), only anatase and rutile have demonstrated an appreciable photocatalytic activity. Although all of them are found in nature, rutile is the most abundant and the only thermodynamically stable.[152] In the laboratory, anatase is often obtained by synthesis at low temperature (below 400 ºC), and rutile frequently starts to appear at moderate temperatures, becoming the prevalent phase after annealing at higher temperatures.[153]

Due to the presence of a small amount of oxygen vacancies, TiO_2 is an n-type semiconductor. The valence band of this oxide is mainly formed by the overlapping of the oxygen 2p orbitals, whereas the lower part of the conduction band is mainly constituted by the 3d orbitals of Ti^{4+} cations. The band gaps, i.e. the void region which extends from the top of the filled valence band to the bottom of the vacant conduction band, are 3.2 and 3.0 eV for anatase and rutile, respectively.[154, 155] Therefore, TIO_2 is active under near ultraviolet light (UVA band, from ca. 3.0 to 3.9 eV). These large values avoid the absorption of a significant fraction of visible light, resulting in poor solar-to hydrogen conversion efficiency.

Heterogeneous photocatalysis belongs to the group of Advanced Oxidation Processes (abbreviated as AOP) which refers to procedures to remove organic pollutants (or also inorganic) from water through reactions involving hydroxyl radicals. Specifically, the process of photocatalysis (either in a gaseous or in aqueous medium) is initiated by light energy equal or greater than the band gap of the semiconductor. As a consequence, an excitation of an electron from the valence band to the conduction band is produced, thus generating electron(e^-_{BC})-hole(h^+_{BV}) pairs in the semiconductor material, as illustrated in Figure 1-20 in the case of a TiO_2 particle. Such electron-hole pairs possess an extremely high capacity to oxidize, thus being able to completely mineralize a large variety of both organic and inorganic chemicals.

The lifetime of such electron-hole pairs is in the nanosecond regime.[153] This is sufficient for the created pair to undergo charge transfer to adsorbed species on the semiconductor surface from solution or gas phase contact. However, the electron-hole can also recombine with the release of heat. This process can occur either at the surface of in the particle bulk, and it actually competes with the charge transfer. Recombination depends on parameters such as degree of crystallinity.[156] At the surface, the semiconductor can donate electrons to reduce the oxygen, which is common electron acceptor in aerated solutions.[157] On the other side, the holes can combined with electrons given by the donor species. Two main oxidative paths are nowadays recognised:[154] in the first the holes might directly oxidize the adsorbent compounds, while in the second they might oxide adsorbed water or the hydroxyl groups to form radicals ·OH which eventually are the responsible for the mineralization of the adsorbed species.

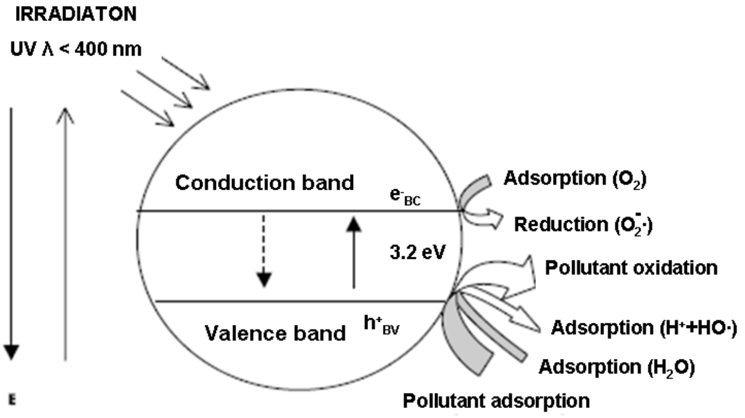

Figure 1-20. Different processes that can undergo in a semiconductor TiO_2 particle under near-UV light irradiation. Adapted from Linsebigler et al.[158]

It should be pointed out that the heterogeneous processes are efficient only when the pollutant concentration is relatively low (up to hundred ppm). Moreover, the reaction is enhanced if the donor species are pre-adsorbed onto the catalyst surface. The performance of a TiO_2 photocatalyst is strongly dependent on crystal phase, particle size, and surface structure (like surface hydroxyl, oxygen vacancy, specific surface area, etc.).[159] In this way the preparation method and process of the photocatalyst have a great influence on the physicochemical properties, which would affect the photocatalytic activity. Heterogeneous photocatalysis show some advantages with respect to other AOP processes such as the efficiency in eliminating toxic halogenated chemicals, the fact that additives are not necessary and that the photocatalyst remains intact after the reaction.

1.3 HIGH INTERNAL PHASE EMULSIONS AS REACTION MEDIA

1.3.1 High Internal Phase Emulsions

High internal phase emulsions (HIPEs), also referred in the literature as high internal phase ratio emulsions[9, 10] or gel emulsions[160] are an interesting class of emulsions having an internal phase volume fraction higher than 0.74, which is considered the maximum compact packing ratio for monodisperse, spherical droplets.[9, 10]. The typical aspect of one HIPE (indistinctly O/W or W/O) is shown in Figure 1-21.

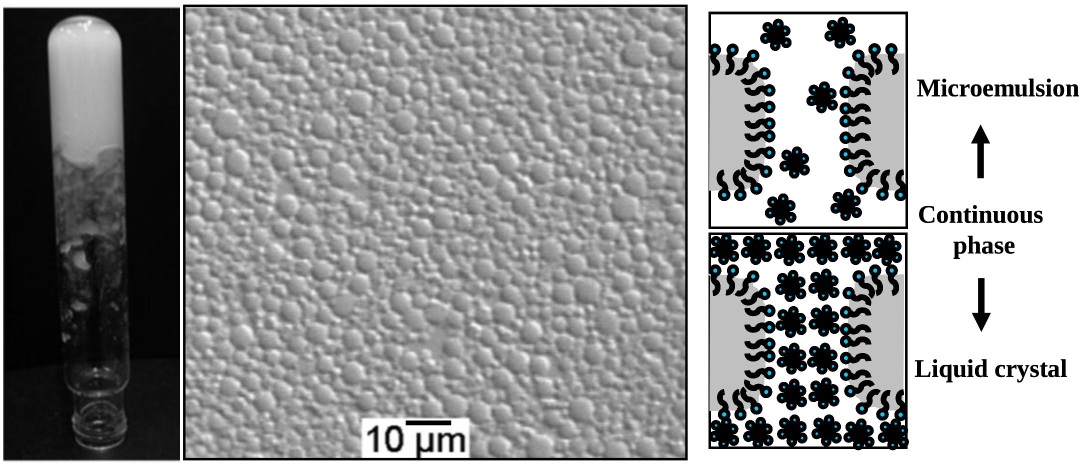

Figure 1-21. Aspect and representative optical microscope picture of a highly internal phase emulsion. Reproduced from Esquena et al.[161] Two pictorial illustrations of the possible configurations, i.e. microemulsion and liquid crystal, in the continuous phase of a HIPE are included.

The structure resembles to gas-liquid foams, and consists of close-packed dispersed droplets separated by a thin layer of continuous phase. Due to the large dispersed phase content, such emulsions are characterized by possessing high viscosities. Specifically, HIPEs are non-Newtonian fluids that can be characterized by a yield stress, i.e. the shear stress required to induce flow of the emulsion.[162] Depending on composition, and factors such as the temperature, HIPEs rheological behaviour range from elastic (solid-like) to viscoelastic.[163] Despite HIPEs are commonly opaque, the preparation of transparent has been reported by matching the refracting indexes of both dispersed and continuous phases.[164] Generally, the droplet size distribution of HIPEs is relatively wide. Droplet polydispersity is rather high because it allows a dense packing with less droplet deformation. Since deformation is reduced the energy associated to the bending of interfacial films is also reduced. Therefore, polydispersity is thermodynamically favoured.

All these features, specially the ability to encapsulate huge amounts of liquids, make HIPEs of great interest for a variety of applications, and their use in many industrial applications has been explored since long ago. Clear examples in daily applications include food emulsions (e.g. mayonnaise) or gel formulations in cosmetics or drug delivery systems.[165] An alternative application that has received a considerable research effort over the last 30 years is the use of HIPEs as templates for the preparation of macroporous polymers.[166, 167]. A brief review of the work that has been done so far is included in next section.

Many different surfactants (nonionic and ionic) have been used to prepare HIPEs. However, nonionic ethoxylated surfactants have been extensively used, because these surfactants are high versatile (different chain lengths are available) and allow both O/W and W/O emulsions. Specifically, systematic works using polyoxyethylene type nonionic surfactants were carried out by the research groups of Kunieda and Solans.[5, 163, 168-170] These works focused on the stability and formation of HIPEs by using detailed phase behaviour studies of the ternary water/nonionic surfactant systems. For instance, it is possible to form W/O HIPEs with very low surfactant concentration (i.e. 0.5 wt%) and with water concentrations as high as 99 wt%.[168] It has also been shown that the continuous phase of HIPEs can have different nanostructures. For instance, it is known that this phase can be a microemulsion,[169] and a liquid crystalline phase.[171] These configurations have been thoroughly characterized by means of several techniques, such as nuclear magnetic resonance (NMR)[169] or small angle X-ray scattering (SAXS).[172] Both microemulsion and liquid crystal configurations are represented in Figure 1-21 between two internal phase droplets.

Other surfactants frequently used to stabilize HIPEs include the nonionic hydrophobic (W/O emulsifiers) sorbitan fatty esters[173] (e.g. Span 80) or block copolymers[8, 174] (e.g. combinations of poly(ethylene oxide) and poly(propylene oxide) units). In addition, the use of ionic surfactants, such as CTAB, for the preparation of O/W HIPEs has been also described.[175] Finally, it should be mentioned that recently, highly concentrated emulsions have been prepared by using particles as stabilizers,[29, 176] in absence of surfactants. This topic will be discussed below.

1.3.1.1 *Formation and stability*

Basically, preparation methods to obtain HIPEs can be divided as follows: the most common used procedure, also called conventional or classical method, consists of dissolving or dispersing the chosen emulsifier, a surfactant(s) or finely-divided solids in the phase continuous phase of the emulsion, followed by dropwise addition of the dispersed phase under stirring. One emulsion prepared by this method is depicted in Figure 1-21. It should be pointed out, that droplet size and polydispersity depends on agitation. Another method is based on mixing all components together in a container and then shaking vigorously at controlled temperature.[160] This method is called the multiple emulsification method because the system passes through various steps, involving a multiple W/O/W emulsion in a certain moment.

These methods involve the use of mechanical devices to emulsify. However, HIPEs can also be prepared by low energy methods, based on phase transitions that induce emulsion formation. For example, the phase inversion method (PIT), already described in section 1.2.1.3, allows obtaining emulsions with droplet sizes smaller than the other two methods mentioned above as well as lower polydispersity values. Regarding the starting point in the formation of HIPEs by the PIT approach, two different strategies have been followed: first, HIPEs have been successfully prepared by heating up or cooling down an isotropic mixture (O/W or O/W microemulsion) from a temperature lower or higher than the PIT to a temperature above or below, respectively.[177] This was attained without mechanical stirring input. The second strategy can be the use of a multi-phase system (e.g. diluted O/W emulsions) as the starting point to obtain the final emulsion (e.g. W/O HIPE) by phase inversion. It must be stressed that in this case an energy input is then required.[178]

As other type of emulsions, HIPEs are thermodynamically unstable and their stability is dependent on composition factors, such as the oil/emulsifier weight ratio, temperature or internal phase volume fraction. Another parameter that should be considered is the nature of the oil. Generally, the larger the differences in polarity between water and oil phases, the higher the stability of the HIPE. For instance, it has been recognised that aromatic molecules (such as the relatively polar styrene) can modify the properties of emulsions, reducing their stability, due to its penetration into the surfactant monolayers.[179] Concerning the addition of electrolytes, one conclusion that can be drawn from the studies is that the emulsion stability can be dramatically enhanced by adding certain salts.[180] In particular, in O/W HIPEs stabilized with nonionic poly(oxyethylene) surfactants, the addition of salt produces a dehydration of the oxyethylene chains in water (and reducing the HLB temperature) and the interactions between surfactant and water are weakened.[168] Herein, molecular interactions between surfactants are very important and the interfacial rheology of the film greatly influences stability.

1.3.2 Macroporous Foams made from Highly Concentrated Emulsions

1.3.2.1 *General aspects*

Since the registration of the first patent on the subject, registered by Unilever in 1982,[181] an extensive research into the synthesis, characterization and exploration of potential applications of macroporous polymers using HIPEs as templates, is being developed. Macroporous polymers are usually obtained by the polymerization of a monomer(s), plus frequently a crosslinker, in the continuous phase of a HIPE.[166, 167, 182] The resulting materials are referred in the literature as polyHIPEs,[181] which is an abbreviation of polymerised HIPEs. Both terms (macroporous polymers and polyHIPEs) will be used indistinctly through this work. It is worth recalling that the same principle can be also applied for the preparation of inorganic macroporous foams (e.g. SiO_2).[183, 184]

A representative scanning electron microscopy (SEM) image of a polyHIPE material is shown in Figure 1-22(a).

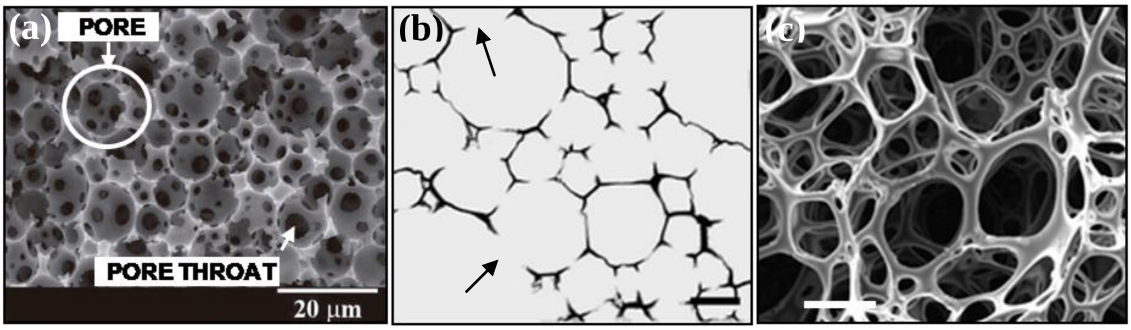

Figure 1-22. Representative (a,c) SEM and (b) TEM images of a polyHIPE. The arrows in (b) indicate pore throats between adjacent pores; polyHIPE in (a) is made of polystyrene, while (b) and (c) shows a gelatine-methacrylate polyHIPE made from a O/W HIPE with a 25 vol% of gelatine in the aqueous phase. (a) Reproduced from Ikem et al.,[185] (b) and (c) reproduced from Barbetta et al.[186] Scale bars in (b) and (c) indicate 40 μm.

As it can be observed, the material consists of individual cells or voids, i.e. macropores, which in fact are a negative exact replica of the initial HIPE droplets (see Figure 1-21).[187] If we have a closer look into the pore structure, some pore throats (also denominated windows or pore connexions) connecting neighbouring pores can be seen. These connexions are clearly visible in the transmission electron microscope (TEM) image of a polyHIPE cross-sectional cut, shown in Figure 1-22(b) (pointed with black arrows). The origin of such interconnectivity will be discussed later on. The open-porosity facilitates the extraction of the internal phase (either water or oil) which remains inside the pores after the polymerization. This allows obtaining materials with characteristic low densities (typically less than 0.1 g/cm^3). Depending on the exact system as well as its stability, the morphology of the pores may be either spherical or polyhedral.

By far, the most widely used polyHIPE base material has been polystyrene (PS), frequently cross-linked with divinylbenzene.[187] This is because styrene is easy to polymerize. Such model system has been used to assess emulsion stability with respect to numerous composition parameters, such as internal phase volume fraction, emulsifier concentration (typically surfactants) or salt concentration. Likewise, the effect of all these parameters on porosity and on porous morphology of the resulting macroporous foams has been exhaustively investigated.[166, 188-191] Since these monomers are hydrophobic, W/O emulsions have been used to prepare the polyHIPEs materials. Taking this system as a model, other monomers/cross-linkers have been included to confer new functionalities to polyHIPEs, such as polyethylene glycol dimethacrylate (PEGDMA)[192] or 2-ethylhexyl methacrylate[193] which impart more elasticity. Other examples described in the literature are the monomer 4-vinylbenzyl chloride, that provides chloromethyl functionalities,[173] and glycidyl methacrylate, which reacts readily with nucleophilies, such as amines[194]. In this line, Piperazine derivatized PolyHIPEs have been applied in water decontamination processes.[195]

On the other hand, O/W emulsions have also been described, but the number of publications is considerable lower because most of the monomers are lipophilic. For instance, some authors have investigated hydrophilic biocompatible and/or biodegradable polyHIPEs as potential tissue engineering scaffolds by polymerization within the continuous phase of O/W emulsions. Examples are 2-Hydroxyethyl methacrylate (HEMA),[196] or gelatine-based[186] (Figure 1-22(c)) polyHIPEs. Alternatively, Silverstein and co-workers have published a number of studies into the successful preparation organic-inorganic polyHIPEs by incorporating polysiloxanes in the polymeric matrix of the HIPEs,[197] and also into the polymerisation in both water (dispersed) and oil (continuous) phases of hydrophilic and hydrophobic monomers, respectively, leading to polyHIPE with remarkable ability to reversibly dry and hydrate.[198] In addition, polyHIPEs constitute a powerful route to synthesize nanocomposites, which typically consist of a polymeric matrix possessing embedded particles (e.g. magnetic) with at least one characteristic length in the nanometer range.[199-201]

All these works have one aspect in common: precursor emulsions were stabilized with surfactants. More recently, Ngai and co-workers and Bismarck and co-workers described the production of polyHIPEs from particle-stabilized HIPEs templating using organic (e.g. PS-co-MAA, Figure 1-23(a))[202, 203] and inorganic (e.g. nano-SiO$_2$, Figure 1-23(b))[100, 204] particles, respectively. Therefore, they took advantage of the ability of the particles to strongly adsorb at liquid-liquid interfaces. This approach presents some important advantages with respect to surfactants-based systems: the first one is that no time-consuming surfactant removal is needed. Secondly, any functionality coming from the solids can be imparted to the pore walls of the resulting materials, and can lead to a variety of further applications. This approach allows for instance to easily emulsify monomers of intermediate hydrophobicity, such as methyl methacrylate (MAA) which has proven difficulty in surfactant-based systems.[187] Interestingly, poly(MAA) particles stabilized water-in-MAA emulsions.[205]. In other cases, particles that are initially stabilizing the emulsions become the continuous polymeric films after removing the liquid non-polymerizable continuous phase.[203] Thus, low initial particle concentrations (e.g. 5 %) might give rise to sufficiently rigid polyHIPEs, as the one depicted in Figure 1-23(a).

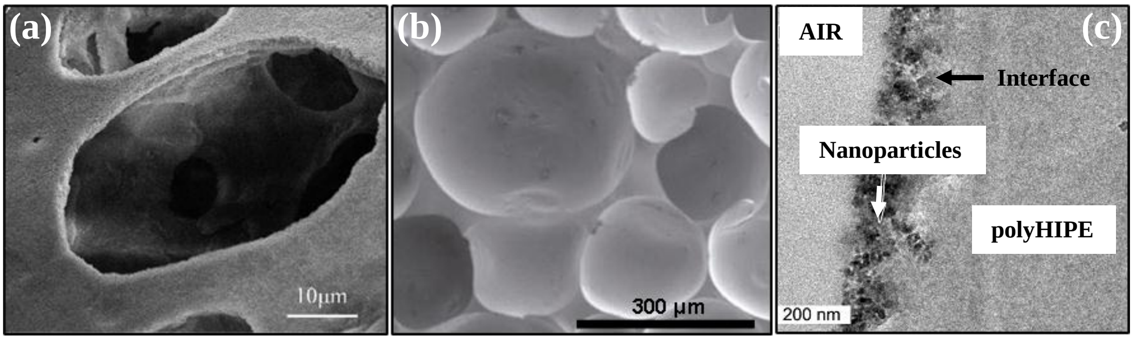

Figure 1-23. (a) PolyHIPE made from a W/O HIPE stabilized with 5 wt% microgel particles (PS-co-MAA). Such particles become the polymer walls after emulsion processing and drying. Image reproduced from Li and Ngai.[203] (b) polyHIPE made from a HIPE (74 vol% of internal phase volume) stabilized with surface-modified SiO_2 (3wt%) nanoparticles. It should be note that its structure is closed-cell and pores are much larger than those shown in Figure 1-22(a). Reproduced from Ikem et al.[185] (c) TEM image of a cross-sectional cut of a polyHIPE made from a HIPE stabilized with functionalized SiO_2 nanoparticles. The particles are located at the resulting polymer-air interface in a multilayer arrangement. Reproduced from Gurevitch and Silverstein.[206]

Regarding inorganic nanoparticles, Bismarck et al. has described the stabilization of HIPEs with high internal phase volume contents (up to 92 vol% internal phase) by using SiO_2[100] and TiO_2 nanoparticles.[204, 207] After the polymerization of the template, macroporous nanocomposites with high porosities, containing nanoparticles embedded in the walls, were obtained. However, two main drawbacks exist when particles are used instead of surfactants: first of all, droplets (i.e. further pores) possess rather larger sizes because particles do not greatly reduce the interfacial tension. Secondly, the porous structure is generally closed-cell, as shown in Figure 1-23(b). This fact can be understood in terms of the thickness of the stabilizing layer, as the relative physical size of particles is much bigger than that of surfactants. Therefore, a close-packed layer of particles, especially in the case of multilayers, is expected to impede the thinning down of the polymer film between original emulsions droplets. One example of such a nanoparticle multilayer at the interface is shown in the TEM image included in Figure 1-23(c), whereby it can be clearly seen that nanoparticles remain at the polymer-air interface after polymerization takes place. Even though these materials are not permeable to gases, small amounts of surfactants might lead to the formation of pore throats on the pore walls.[185] Other research groups,[99, 208] in particular Silverstein et al.[209, 210] are currently working on the topic and exploring new possible applications for this kind of macroporous polymer nanocomposites.

Regarding the formation of pore throats between neighbouring pores, it is generally accepted that connectivity is linked to two main parameters: the type of emulsifier in the precursor emulsion and the internal phase volume fraction.[166] Williams and Gobrelsky[166] observed that surfactant concentration higher than 5 wt% was required to obtain interconnected open-cell macroporous polymers. It seems reasonable to think that it is crucial the thickness of continuous phase around the area of nearest contact between adjacent droplets.[182] This is normally accomplished by droplet size reduction, i.e. increasing surfactant concentration. In this line, Cameron et al.[211] pointed out the importance of the reduction of the polymerizable film thickness to obtain permeable materials. In particular, it was demonstrated that the pore throats started appearing as a result of volume contraction (well known phenomenon in polymerization), on conversion of the monomer styrene into polymer. Moreover, as deduced from Figure 1-22(a), polymerization takes place mainly in the emulsion plateau borders, i.e. the area between three adjacent droplets, which is filled by bulk continuous phase.[182] Other reasons for the formation of pore throats have been proposed.[190] These include mechanical action during the drying step. In some cases, this is induced by the creation of weak points in the polymer walls, as surfactant is pushed to the interface due to the progressive reduction of its solubility in the oil phase as polymerization is taking place. Finally, the connectivity degree also depends on the concentration of the polymerizable monomer in the continuous phase of the HIPE (see Figure 1-22(c)).

1.3.2.2 *Physical characterization*

(a) Porous structure

Conventional polyHIPEs have typically pore sizes ranging from 1 to 50 μm.[187] As pointed out earlier, such values directly depends on the droplet sizes obtained in the precursor emulsions, which in turn basically depends on emulsion composition and preparation conditions.[212] In this line, larger sizes can be achieved by destabilizing the emulsions to some extent,[186] or on the other hand, rather smaller sizes as well as lower polydispersity values can be attained by using the PIT method for emulsion preparation[178]. The morphology and size of the macroporous in the polyHIPEs are normally characterized by SEM, while the pore wall structure is commonly studied by TEM of cross-sectional polymeric slides cut by ultramicrotomy.

Regarding porosity, two distinct densities can be used to define macroporous polymers: skeletal and envelope (also called foam) densities. The first one refers to the ratio of the mass of discrete pieces of solid material to the wall volume including closed (blind) pores. Such density is generally determined on polyHIPE crushed samples, whereby small closed pores/spaces can remain within the polymer walls. Therefore, this parameter should not be confused with the absolute density which does not take into account the closed pores. Regarding envelope density (also denoted as bulk density), it is defined as the mass divided by the total volume, thus including the solid material plus all types of porosity. PolyHIPEs have typically envelope densities as low as 0.02 g/cm^3 and porosities up to 99%.[182, 188, 213] Such factors are influenced by the nature of the polymer as well as the internal phase volume fraction in the initial emulsions. Another two parameters characteristic of all porous materials are its surface area and its permeability. Since the pores exhibited by polyHIPEs are relatively large, surface areas are often lower than 20 m^2/g.[187] However, different approaches have been successfully applied to increase these values, such as the incorporation of porogen agents (increasing up to 550 m^2/g)[189, 214] or via hypercrosslinking[215] (up to 1100 m^2/g). The second parameter, i.e. permeability, is the measure of the ease of fluid flow passing through the medium under an applied pressure gradient[216]. Generally, the permeability is somewhat limited by the small pore sizes found in the materials,[174] but can be tailored to some extent through the control of both pore and pore throat sizes.[185, 217] Such permeability values are one of the aspects to consider for the industrial application of polyHIPEs.

(b) Mechanical properties

Generally, polyHIPEs follow a stress-strain curve in compression like that included in Figure 1-24. It should be pointed out that the mechanical properties of such materials are similar to that exhibited by gas-blown polystyrene foams, but polyHIPEs normally posses higher crush strengths values due to its smaller pore sized and increased spherical symmetry of such pores.[166] The curve is divided in three regions: an initial linear elastic region at low strains, the slope of which is defines as the Young´s modulus, then a stress plateau region and finally a densification region with a steep increase in stress. The crush strength is fixed as the maximum value of the stress-strain curve at the end of the initial linear region. On the other hand, the most common studied polyHIPEs, which are based on divinylbenzene cross-lined polystyrene, are rather brittle and chalky owing to the relatively high glass transition temperature (T_g) of such polymers.[193] This is explains why some polyHIPEs do not show the third compression region. Foams first crack and then break up catastrophically at certain strain. To overcome this, some elastomeric monomers or cross-linkers, such as polyethylene glycol dimethacrylate[192] or 2-ethylhexylacrylate,[193] have been also added to the precursor emulsions. This led to more flexible polyHIPEs since the overall T_g was reduced and the mechanical properties (i.e. Young modulus and crush strength) of the polyHIPEs were also improved. It is relevant to mention the necessity to incorporate a minimum amount of cross-linker into the precursor emulsion formulation. Otherwise the polymeric foam would collapse into a dense material or disintegrate into a powder during polymerization and/or drying.

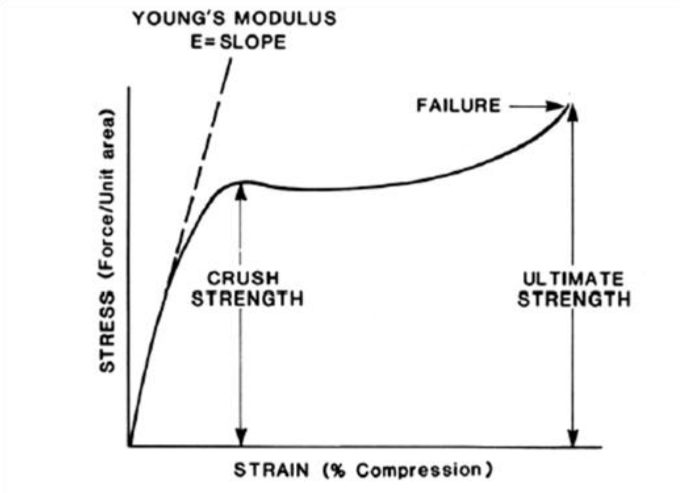

Figure 1-24. Representative stress-strain curve (under compression) of polymeric macroporous foam. Reproduced from Williams and Wroblesky.[166]

On the whole, it is known that the mechanical performance of polyHIPEs is dependent on several factors. On one hand, materials show better properties when their have smaller and narrower pore size distributions,[178] and also when they have thicker polymer walls between neighbouring pores.[186, 192] By contrast, low foam density, which is accomplished by increasing the internal volume fraction of the initial emulsions[218], high material interconnectivity[217, 219] or large pore size distributions inversely affect foam integrity[204] and polyHIPEs tend to fail quicker. In a recent work, Wong et al.[217] described the synthesis of hierarchical macroporous polymers from HIPEs stabilized using nanoparticles and surfactants together, with improved mechanical properties, despite the presence of interconnectivity. It was argued that the pores packed more efficiently.

Another way to improve the mechanical properties of the polymers, such as the hardness or tensile strength is the incorporation of inorganic fillers[220] or by cross-linking silsesquioxane groups with the polymer network.[221] Specially, various groups have recently focused on the addition of inorganic oxide (e.g. silica) nanoparticles,[192] carbon nanotubes[222] or clays[223] to the external phase of W/O HIPEs. In the majority of such studies, the filler is added in the continuous phase of the HIPEs. In order to improve the compatibility between the polymer and the filler the inorganic components are generally surface modified, e.g. by organo-sylanation.[224] In this line, it is well known that effectiveness of the reinforcement depends mainly on particle size and shape and polymer-filler interactions.[225, 226] The reinforcement should even prove more effective if the nanoparticles have double polymerizable double bonds that can react with the monomers forming the oil phase of the HIPEs. Using this approach, Wu et al.[224] achieved a crush strength increase of up to 600 % by incorporating 20 wt% of silica nanoparticles. It should be noted that is of paramount importance that the fillers do not affect emulsion stability. In an interesting work developed by Lepine et al.[223] they found that the mechanical performance of styrene-based polyHIPEs improved by increasing the amount of clay (up to 20 wt%). Despite this improvement, they observed clay aggregates within the polymer walls above 10 wt% which resulted in chalky and brittle materials. Materials with lower concentrations were rather elastic. Moreover, the standard deviation of the different measurements increased upon clay concentration increment which was attributed to an unequal dispersion of the clay layer aggregates.

2 OBJECTIVES & WORK PLAN

2.1 OBJECTIVES

The design of nanocomposites, which typically consist of polymeric matrices with embedded particles having at least one characteristic length in the nanometer range, has recently been the focus of great attention. Nanocomposites, in a large variety of morphologies and distinct compositions, have many technological applications. Examples are micro-optic devices, optical sensors and reinforced plastics such as polyolefin nanocomposites in the automotive industry.[227] In this context, the construction of novel porous nanocomposites, exhibiting hierarchical structures, will allow the development of innovative advanced materials with promising applications in many fields: catalysis, gas/liquid storage, gas purification, subsea oil pipe, etc.

The use of highly concentrated phase emulsions (HIPEs) as templates is an effective route for the preparation of macroporous polymers. Specifically, the use of suitable surface-modified inorganic oxide nanoparticles as emulsions stabilizers (preparing Pickering emulsions in absence of surfactant) provide an alternative approach to the classical surfactant-based systems, to obtain hybrid organic-inorganic nanocomposite porous materials. Thanks to the ability of finely-divided solids to adsorb spontaneously at liquid-liquid interfaces, any functionality coming from the nanoparticles can be imparted to the materials, in a single-step preparation method.

It has been described that the resulting macroporous nanocomposites, obtained in Pickering highly concentrated emulsions, typically exhibit closed-cell structures and rather large pore sizes.[100, 209] These drawbacks are frequently overcome by combining simultaneously surfactants and particles. Nevertheless, there is a lack of systematic study on how the interactions between these two emulsifiers influence the final physicochemical properties of the materials. For instance, contrary to what is often expected, the addition of particles to a surfactant-stabilized emulsion or inversely, the addition of surfactant to a particle-stabilized emulsion can negatively influence its stability, rather than enhance it.

The main objective of this research work was to investigate the formation of polymeric macroporous nanocomposites with embedded functional nanoparticles, using W/O highly concentrated emulsions as templates. For this purpose, two kinds of nanoparticles with interesting functionalities have been used:

- Superparamagnetic iron oxide nanoparticles
- Titanium dioxide photocatalytic nanoparticles

Styrene and the crosslinker divinylbenzene are used in the emulsion continuous phase, as a model monomer system. Macroporous materials are obtained by free-radical polymerization in the continuous phase of W/O HIPEs. In all cases, nanoparticles are incorporated to the emulsions, and three different types of HIPEs are studied using different approaches:

(a) HIPEs stabilized with surfactants and prepared by the phase inversion method, containing nanoparticles in the continuous phase (section 1.1).
(b) HIPEs stabilized with nanoparticles, in absence of surfactant (section 4.3) and prepared by the drop-wise addition method. The use of Pickering HIPE emulsions to obtain nanocomposite materials constitutes a very novel approach, recently described for the first time.[176]
(c) HIPEs stabilized primary with nanoparticles with increasing amounts of surfactant molecules, prepared by the drop-wise addition method (section 4.4).

The main objective implied the following partial objectives:

1. Selection of the appropriate surfactant systems, in order to prepare the surfactant-stabilized emulsions by the PIT and the drop-wise addition methods.

2. Preparation and surface modification with oleic acid of the nanoparticles to be used as W/O stabilizers.

3. Evaluation of the individual contribution of either nanoparticles or surfactants on the (in)stability of the resultant highly concentrated emulsions, and investigation of the precise role that each emulsifier plays, focusing on their interactions and the emulsion stabilization mechanisms.

4. Study of spatial distribution of nanoparticles in the resulting porous nanocomposites, with respect to several parameters such as particle size or surfactant concentration. Study of the influence of such arrangement on the pore interconnectivity of the materials.

5. Comparison of the main physical properties, such as porosity or mechanical strength, of the polymeric macroporous nanocomposites.

6. Study of the magnetic properties and photocatalytic activity of the nanocomposite materials, which contain either iron oxide or titanium dioxide nanoparticles, respectively.

2.2 WORK PLAN

To achieve the above objectives the following work plan was carried out:

1. Preparation and characterization of different types of iron oxide nanoparticles with controlled average sizes.

2. Preparation of titanium dioxide nanoparticles using a mechanochemical-activated solid-state reaction.

3. Surface modification of the resulting hydrophilic nanoparticles with oleic acid, which provides partial hydrophobicity to nanoparticles surface.

4. Selection of the surfactant system in the ternary water / nonionic ethoxylated surfactant / oil (containing styrene and divinylbenzene) systems, by studying the phase inversion temperatures.

5. Study of the interactions between iron oxide nanoparticles and a hydrophobic nonionic surfactant, by interfacial tension determinations and emulsion stability experiments.

6. Emulsification by the phase inversion temperature method using nonionic ethoxylated surfactants, and by the drop-wise addition method, using functionalized inorganic oxide nanoparticles and/or nonionic surfactants as stabilizers.

7. Polymerization of the external phase of the W/O highly concentrated emulsions (HIPEs) to obtain macroporous nanocomposites.

8. Structural and morphological characterization of the polymeric macroporous nanocomposites. The physical properties of the materials are evaluated as a function of several emulsion composition parameters. The following techniques are used:

- Electron microscopy to study the porous structure (scanning electron microscopy) and nanoparticle distribution within the polymeric materials (transmission electron microscopy).
- Picnometry to characterize the porosity of macroporous materials.
- Compression tests to study the mechanical properties of the materials (compression strength and Young modulus).
- Permeability measurements using a homebuilt pressure rise device.

9. Evaluation of the magnetic properties (magnetization saturation and blocking temperature) of the magnetic macroporous polymers containing iron oxide nanoparticles as a function of nanoparticle concentration and nanoparticle distribution within the polymeric walls of the materials. Magnetic properties are compared with those observed for raw nanoparticles.

10. Determination of the photocatalytic activity of the macroporous polymers containing titanium dioxide nanoparticles through a photo-oxidation experiment.

3 EXPERIMENTAL

3.1 MATERIALS

The materials have been classified in three groups: surfactants, reactants, solvents and other chemicals. If not otherwise stated, chemicals received were used without further purification.

3.1.1 Surfactants

Commercial grade nonionic poly(ethylenglycol) n-alkylethers surfactants (abbreviated as $R_m(EO)_n$) were obtained from Croda, United Kingdom (previously known as Uniqema). *m* is the alkyl chain length (R) of the hydrophobic part and *n* is the number of ethylene oxide groups (EO) per molecule (Figure 3-1(a)). Surfactants used were: Renex 30 ($C_{12\text{-}14}(EO)_4$), Synperonic A5 ($C_{13\text{-}15}(EO)_5$), Renex NENA ($C_{13\text{-}15}(EO)_6$) and Synperonic 10/3 ($C_{10}(EO)_3$).

The triblock copolymer surfactant Synperonic PE/L-64 (poly(ethylene glycol)–poly(propylene glycol)–poly(ethylene glycol) (Figure 3-1 (b)) abbreviated as $(EO)_{13}$, $(PO)_{30}$, $(EO)_{13}$) was also obtained from Croda.

Nonionic surfactant Hypermer 2296 (Hydrophilic Lipophilic Balance number = 4.9) was kindly supplied by Croda (USA). This surfactant is a blend of sorbitan ester (Figure 3-1 (c)) and polyisobutylene succinic anhydride (PIBSA) based derivative (Figure 3-1(d)). Such surfactant is an efficient W/O emulsifier and is widely used in the oil industry as a dispersive agent.

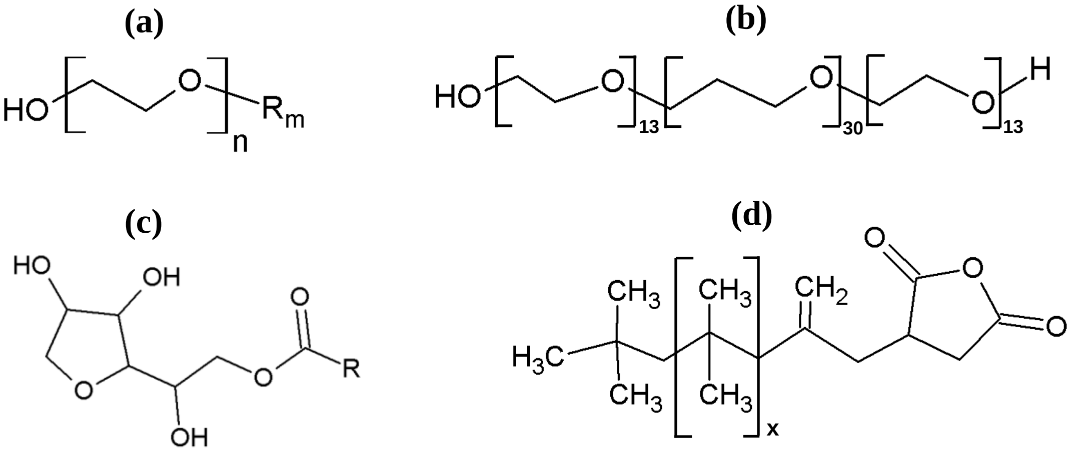

Figure 3-1. (a) Nonionic poly(ethylenglycol) n-alkylether surfactant, where n is the number of ethylene oxide groups and m is the alkyl chain length (R); (b) poly(ethylene glycol)–poly(propylene glycol)–poly(ethylene glycol) triblock copolymer Synperonic PE/L-64; (c) Sorbitan monoester, where R is typically an alkyl chain of 12-18 carbon units; (d) polyisobutylene succinic anhydride (PIBSA), where x is the number of isobutylene units.

3.1.2 Reactants

The monomers styrene (≥99%), acrylic acid (≥99%), and the cross-linker divinylbenzene (technical grade, 55%) were purchased from Sigma-Aldrich. All were purified before use by passing through neutral chromatographic aluminium oxide in order to remove polymerization inhibitors. Three different initiators were selected in order to carry out the polymerizations: the water-soluble potassium persulfate ($K_2S_2O_8$, Merck, ≥99%), and the oil-soluble α,α'-azoisobutyronitrile (AIBN, Merck, ≥96%) were used in emulsion polymerization, whereas the oil-soluble 2,2'-Azobis-(2,4-dimethyl) valeronitrile (ADVN, courtesy of DuPont Iberica S.A., Spain) was used for bulk polymerization. Iron(III) chloride hexahydrate ($FeCl_3 \cdot 6H_2O$, ≥98%), and anhydrous iron (II) chloride ($FeCl_2$, ≥99%) were provided by Sigma-Aldrich. Titanium (IV) oxysulfate ($TiOSO_4$, ≥99.5%) was acquired from Riedel de Haen.

3.1.3 Solvents

Decane ($C_{10}H_{22}$, ≥99%), tetradecane ($C_{14}H_{26}$, ≥99%) and hexadecane ($C_{14}H_{28}$, ≥99%) were obtained from Sigma Aldrich. Pure ethanol (≥99.5%) and toluene (≥99.5%) were supplied by Merck. Water was first passed through a reverse osmosis unit and then a Milli-Q reagent water system.

3.1.4 Other chemicals

Oleic acid ($C_{18}H_{34}O_2$, ≥90%) and sodium hydroxide (NaOH, ≥98%) were obtained from Sigma Aldrich while sodium carbonate (Na_2CO_3, ≥99.9%), ammonium hydroxide (32 wt% NH_3) and methylene blue [($C_{16}H_{18}N_3ClS$), ≥97%)] were purchased from Merck.

3.2 METHODS AND EXPERIMENTAL TECHNIQUES

3.2.1 Preparation and Functionalization of Iron Oxide Nanoparticles

Three kinds of iron oxide nanoparticles (NPs) have been employed in this work. A fully physical characterization will be given in section 4.1.1. NPs are abbreviated hereafter as NP_X, where X is the average size of the nanoparticles. In all cases oleic acid was used as a capping agent to confer hydrophobicity to the NPs. On one hand, iron oxide NPs (NP_3) were synthesized using water-in-oil (W/O) microemulsion droplets as templates following the literature.[228] Larger

NP_8 were prepared using a coprecipitation method as reported by Ramírez et al.[229] Specifically, NP_8 were coprecipitated from an aqueous solution of Fe^{3+}/Fe^{2+} salts (in a 3:2 molar ratio) using excess ammonium hydroxide (NH_4OH). To prevent nanoparticle aggregation, oleic acid was added as a capping agent.

Additionally, as-received commercial magnetite CNP_{32} nanoparticles (Fe_3O_4 nanopowder, <50 nm size, from Sigma) were also functionalized as described in the literature.[100, 176] First, CNP_{32} were dispersed in a mixture of chloroform/oleic acid (1:2 molar ratio), stirred for 3 h, and precipitated from solution with methanol. The excess oleic acid was then removed by repeating the dispersion of nanoparticles in chloroform and precipitating again with methanol prior to drying at 70 ºC.

3.2.1.1 *Characterization of iron oxide nanoparticles*

The weight content of oleic acid attached to the nanoparticle surfaces was determined by thermogravimetric analysis (TGA). The measurements were performed in a TGA/SDTA 851 unit (Mettler Toledo, USA) in a temperature range of 25-550 ºC, at a heating rate of 10 ºC/min in a N_2 atmosphere. Samples were placed in 100 µL aluminum crucibles. Scanning (SEM) and transmission electron microscopy (TEM) images were taken in order to determine the shape and the size of the different type of nanoparticles. For NP_3 and NP_8, a JEM 1010 and a JEM 2011 TEM instruments (both from JEOL, Japan) were used, respectively. Diluted samples were prepared by evaporating a droplet of the dispersion of iron oxide nanoparticles in heptane on a standard TEM copper grid covered with Formvar polymer. On the other hand, a Gemini LEO 1525 field emission GSEM (Carl Zeiss, Netherlands) was used for CNP_{32} characterization. Particle size average and polydispersity were calculated from microscopy images; for improved statistics, at least 500 NPs were measured using the ImageJ software. To confirm the presence of oleic acid on nanoparticle surfaces, samples were analysed by Fourier transform infrared spectroscopy (FTIR) with a Nicolet 510 spectrophotometer (Thermo Scientific, USA). Spectra were collected at 4 cm^{-1} resolution with 64 averaged scans.

Finally, X-ray diffraction (XRD) spectra of the nanoparticles were obtained using a PANalytical X'Pert PRO MPD θ/θ Bragg–Brentano diffractometer with CuK_α radiation ($\lambda = 1.54$Å). The angle range was $2\theta = 5\text{-}120º$. Nanoparticles were finely ground and loaded in a grooved cut silicon substrate. The average crystal size of the nanoparticles was determined according to Scherrer equation,[230] using the full width at half maximum of peaks after correcting the instrumental broadening,

$$D = \frac{0.9\lambda}{\beta \cos \theta} \tag{3-1}$$

where D is the size of crystalline domain, λ is the wavelength of CuK_α radiation (λ = 1.54Å), β is the corrected peak width (in radians) and θ is the diffraction angle.

The magnetic properties of the nanoparticles were studied using an MPMS XL superconducting quantum interference device (SQUID) magnetometer (Quantum Design, USA) at fields ranging from 20 to 20 kOe and at temperatures ranging from 2 to 300 K.

3.2.2 Preparation and Functionalization of Titanium Oxide Nanoparticles

As pointed out in the Introduction, titanium dioxide (TiO_2) nanoparticles were synthesized using a mechanochemical method. Reactive solid mixtures were prepared according to the stoichiometry of the two following reactions:

$$TiOSO_4 \cdot 2H_2O + Na_2CO_3 \rightarrow TiO_2 + Na_2SO_4 + 2H_2O + CO_2 \ (1)$$

$$TiOSO_4 \cdot 2H_2O + 2\,NaOH + Na_2SO_4 \rightarrow TiO_2 + 2Na_2SO_4 + 3H_2O \ (2)$$

Taking into account that the second reaction is highly exothermic, Na_2SO_4 was added (33.3% of the total mixture) in order to avoid excessive increase in the reaction temperature.

Solid mixtures (6 g) were mechanochemically activated in a Fritsch Pulverissette 7 planetary ball-mill (Germany). ZrO_2 vials were rotated at 1500 rpm, each one containing 7 ZrO_2 balls of 15 mm in diameter and 6 g of sample, resulting in a ball-to-powder ratio of 13. Pictures of the equipment used are shown in Figure 3-2. The mechanochemical milling was interrupted at different times (e.g. 15, 30 min) and a small powder sample was then taken for XRD analysis. After reaction, resulting materials were dried at 80ºC for 30 minutes and then calcined in air for 30 minutes at temperatures between 300 and 700 ºC (GHA 12/450, Carbolite, UK). In order to remove the water-soluble by-products, samples were washed twice with distilled water in an ultrasound bath for 15 minutes, filtered and then dried at 80 ºC. TiO_2 nanoparticles were functionalized with oleic acid using the same method described for iron oxide nanoparticles (CNP_{32}).

Figure 3-2. Planetary ball-milling (left) used to carry out the solid-state reactions. Picture on the right shows the vial and the milling-balls, both made of ZrO_2.

3.2.2.1 *Characterization of titanium dioxide nanoparticles*

Evolution of the mixture composition was followed by XRD using a PW 1830/40 diffractometer (Philips, Netherlands) at 40 kV and 30 mA, with CuKα radiation (λ= 1.54 Å). Crystallite size was determined from the peak width using the Scherrer equation (eq. 3-1).

Both the morphology of the aggregates and the nanoparticle size were assessed by high-resolution TEM (300 KV Philips CM30, The Netherlands). Powder materials were analyzed by FTIR (Nicolet 6700 Spectrometer, Thermo Scientific, USA) using Attenuated Total Reflectance (ATR) mode. Spectra were collected at 4 cm^{-1} resolution with 64 averaged scans.

Nitrogen adsorption/desorption isotherms were measured at 77 K using an adsorption porosimeter (Quantachrome Autosorb-1-MP, USA). The samples were degassed in vacuum at 423 K during 4 hours prior the sorption experiments. Specific surface areas (S_{BET}) were calculated by applying the multipoint model to the adsorption isotherm.[231] The total mesopore pore volume was determined also from the adsorption isotherm at relative pressures of 0.94. The S_{BET} values were used to estimate the particle size of TiO_2 nanoparticles. The average particle diameter (D_i) can be related to S_{BET} through the equation:

$$D_i = \frac{6}{S_{BET}\,\rho_{TiO_2}} \qquad 3\text{-}2$$

assuming that nanoparticles are well dispersed, spherical and non-porous. The density of anatase phase (ρ_{TiO_2}) was taken as 3.9 g/cm^3.[232]

In order to test the efficiency of the TiO_2 nanoparticles, a photo-oxidation experiment was carried out in a jacketed photoreactor of 100 mL volume. About 1 wt% dried TiO_2 powder was dispersed in 75 mL of 35 ppm (aqueous) methylene blue solution. The reaction mixture was stirred for 1 hour at 25ºC. Subsequently, the dispersion was irradiated with a light bulb (H125-*BL* 125 W, Iwasaki Electric, Japan), with a maximum emission wavelength of ca. 360 nm (weak ultraviolet light region). Samples (3 mL) were collected for analysis at different intervals of time, and then ultracentrifugated at 19000 r.p.m during 40 minutes to separate the supernatant solution from the precipitated catalyst. The degradation reaction was monitored by measuring the absorbance ($\lambda = 664$) of the samples using a UV-visible scanning spectrophotometer (Varian Cary 300 Bio, USA).

3.2.3 Determination of Phase Inversion Temperature

The so-called hydrophilic lipophilic balance (HLB) or PIT temperature of the water / nonionic / oil systems was determined by conductivity measurements as a function of temperature, in a 50 mL reaction vessel with constant agitation using a magnetic stirrer device. A conductivity meter equipped with Pt electrodes (Crison 525, Spain) was used in the experiments. This method is feasible for surfactants in a narrow range of HLB numbers. As exemplified in Figure 3-3, an abrupt reduction (or increment) in the conductivity can be associated to changes from O/W to W/O (or from W/O to O/W) emulsions due to the change in the preferential affinity of the poly(ethylenglycol) n-alkylethers nonionic surfactants from water to oil as temperature is risen, or inversely, from oil to water when temperature is decreased. Therefore, high and low conductivities indicate O/W and W/O emulsions, respectively

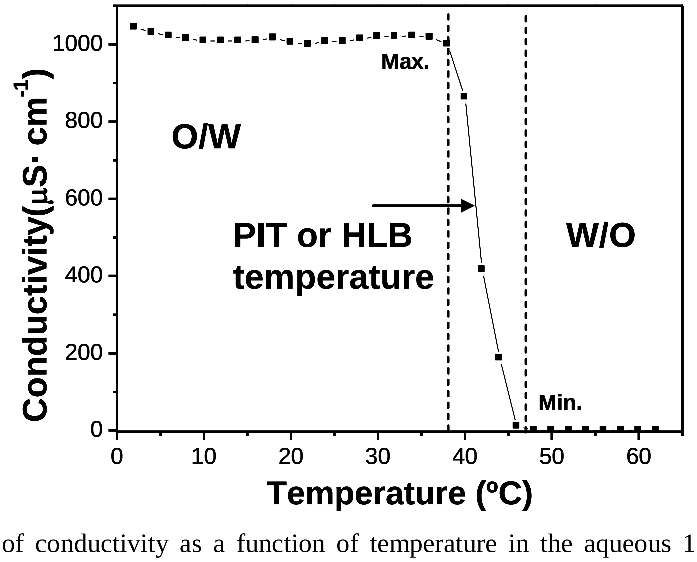

Figure 3-3. Example of conductivity as a function of temperature in the aqueous 10^{-2}M NaCl / $C_{13-15}(EO)_4$) / tetradecane system, at 80 vol% water and 4 wt% surfactant concentration.

Temperature has been modified from 0 to 70 ºC and 0.02 M of salt (NaCl) has been added to emulsions for the purpose of increasing the conductivity signal. In all experiments, the HLB temperature was calculated as the medium point in between the highest and the lowest temperatures observed within the narrow PIT region.

3.2.4 Interfacial Tension Determinations

This method allows evaluating the individual contribution of either nanoparticle or surfactant (at very low concentration) to the overall decrease in interfacial tension. Therefore, it is a useful method to quantify both the free surfactant that remains in solution and the surfactant that adsorbs on nanoparticle surfaces.

The oil-water interface tension was assessed by two different methods, depending on surfactant concentration: in absence or at low surfactant concentrations, interfacial tension were measured using the Du Noüy ring method, while at higher surfactant concentrations, tension determinations were carried out by the droplet-volume method. All measurements have been carried out at 25 º C with distilled water and toluene as the lighter and heavier phase, respectively. Toluene was passed twice through chromatographic alumina to remove impurities. It is important to recall that toluene was used instead the monomers that actually formed the continuous phase of the emulsions, i.e. styrene and divinylbenzene. The reasons were its lower toxicity, its easier manipulation in the laboratory, and their similar chemical structures.

In the interfacial tension determinations, three types of Fe_3O_4 nanoparticles have been used: oleic acid surface-modified NP_8 and NP_{32}, and untreated CNP_{32}. Before the measurements, nanoparticles (1.5 wt%) were dispersed in toluene, containing different concentrations of the nonionic surfactant Hypermer 2296 (0-4 wt%), in an ultrasonic bath for 10 minutes, and then agitated in a water shaking bath (Memmert, Shawaback, Germany) for 60 min. At this point two different approaches were followed, depending on nanoparticle type:

- NP_8: interfacial tension measurements could be performed with NP_8 dispersed in the lighter (toluene) phase due to the stability of nanoparticle dispersions. Therefore, contribution of these nanoparticles to the overall decrease in interfacial tension could be evaluate.

- CNP_{32} and NP_{32}: since both were unstable in the solvent due to fast aggregation, they were separated by simple centrifugation (3000 rpm for 5 min) before the measurements. Otherwise, measurements would have been inaccurate due to the distortion of the interface by nanoparticle sedimentation. This fact implied that interfacial measurements were made on solutions without nanoparticles, and just the free surfactant contribution could be evaluated.

Prior the measurements, sample densities (25 ºC) were determined by using a densimeter DMA4500M from Anton Paar (Austria). Determinations were repeated 5 times for each sample.

3.2.4.1 *Du Noüy ring method*

This method is based on directly measuring the interfacial tension using a microbalance.[233] A Tensiometer K12 from Kruss (Germany) was used for the experiments. It is a simple, quick and high precise alternative to the well-known Wilhelmy plate method. The rectangular plate used in the latter is changed by a wire ring usually made up of platinum or platinum-iridium alloy with a typical radius (r) of 2-3 cm. The wire ranges had a radius which range from 1/30 to 1/60 of that of the ring.[234]

As shown in the picture in Figure 3-4(a), the measurement starts by dipping the ring in the heavier phase (water). Then, the ring is pulled through the interface while measuring the force exerted on the ring (Figure 3-4(b). It is important to ensure a perfect wettability of the surface of the ring (contact angle (θ) ca. 0). Common error sources come from ring surfaces that are not well-cleaned or rings that do not remain parallel to the plain of the interface. To avoid this, the ring was rinsed first with ethanol and later with water before flaming to red heat, after each measurement. In addition, the surface tension of pure water was checked before each measurement to ensure a good cleaning of the ring surface.

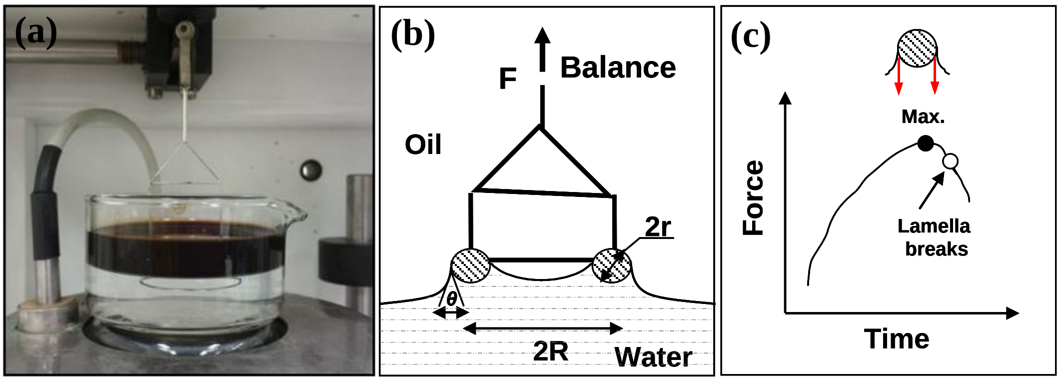

Figure 3-4. (a) Picture showing a Du Noüy ring holding from a microbalance, and dipped into the heavier phase (water), before starting an interfacial tension measurement Light phase is a 1.5 wt% NP_8 toluene dispersion. (b) Schematic drawing that illustrates the ring method (modified from Drelich et al.)[235] (c) Graph representing the force exerting on the ring surface vs. time as the ring is pulled through the interface. Red arrows indicate direction of the force measured.

One advantage compared to the drop-volume method is that non-transparent phases can be measured (see Figure 3-4(a)). As represented in Figure 3-4(c), when the ring is lifted through the surface, the force starts to increase until a maximum force is reached. At this particular point, the force of the vertical constituent is directly proportional to the interfacial (γ) tension. Both are relate through the equation:[235]

$$\gamma = \frac{F}{p\cos\theta} f_N \qquad 3\text{-}3$$

where F is the weight converted to force by the electronic balance, p is the three-phase contact line perimeter, which is twice the circumference of the ring ($4\pi R$), θ is the contact angle of the liquid on the ring, and f_N is a correction factor. The contact angle is assumed to be 0, and as seen in Figure 3-4 (c), this occurs when the maximum force is attained. Unfortunately, a correction factor should be incorporated due to the volume of liquid hanging from the ring as it is pulled above the surface. This explains why values measured without applying the correction factor are generally higher. The correction factor (f_N) can be incorporated directly in the software, and can be calculated by using the following approximate equation developed by Zuidema et al.:[236]

$$f_N = 0.725 + \sqrt{\frac{0.01452\,\gamma}{\frac{U^2}{4}(\rho_H - \rho_L)} + 0.04534 - \frac{1.679}{R/r}} \qquad 3\text{-}4$$

where U is the wetted length, ρ_H and ρ_L are the densities of the heavy and light phases, and R and r are the ring and wire radius, respectively.

Another point that should be considered is that interfacial tension can be determined without breaking the interface. As can be observed in Figure 3-4(c), the lamella does not break when the maximum force is attained. It should be remarked that in presence of surfactant, the ring should be slowly pulled through the interface because the lamella could break due to the initial maximum force might be too great. Therefore, it is necessary to lower the ring into the liquid to relieve the force and then repeat the measurement several times until reached values are constant.

The mean of at least 3 measurements has been used for the calculations of interfacial tension.

3.2.4.2 *Droplet-volume method*

This method is based on analysis of the balance between capillary effects and gravity forces, and is among the oldest surface tension measurements methods in use.[235, 237] Actually, is a modification of the drop-weight method described by Harkins et al. in 1919.[238] Such modification consists in the incorporation of a graduated micrometer attached into the syringe in order to achieve an accurate volume of the droplet. Accurate measurements of static interfacial tension may be made when surfactants are present so that adsorption equilibrium at the interface is only slowly attained.

First of all, a vessel is filled with the lighter phase, while the heavier is placed into a 1 ml syringe (Hamilton, Switzerland). Care should be taken to remove any bubble that might be present inside the syringe. Then, the tip of the needle is submerged into the lighter phase, and the droplet of the heavier phase is created by turning the micrometer screw. It should be noted that for correct measurements the tip should be immersed in the liquid to a depth of about 0.5 cm. It also important to manipulate the micrometer screw carefully in order to create the droplet slowly (from 30 to 60 seconds). The droplet should remain attached to the needle from 2 to 5 minutes, which is sufficient in most cases to attain adsorption equilibrium. Such a droplet may be slowly enlarged until detachment occurs. The measurement finishes when the droplet is released, and its volume can be calculated by comparing the final and the starting point in the micrometer readable scale. Although this method is highly recommended for low interfacial tension values, it is recognised that in cases, where interfacial tension is high and/or when the two phases have quite similar densities, the use of a bigger tip diameter, e.g. > 0.60 mm, could be required. Consequently, a syringe with larger volume must be employed.

Interfacial (or also surface) tension (γ, mN/m) can be calculated from the balance between the drop weight ($V_D \Delta\rho g$) and the force ($2\pi r f_D$) that interfacial tension is exerting on the perimeter of the needle, in the exact moment when the drop is falling from the capillary:

$$\gamma = \frac{V_D \Delta\rho g}{2\pi r f_D} \qquad 3\text{-}5$$

where V_D (cm^3) is the droplet volume when it breaks away, r (cm) the outside needle radius, $\Delta\rho$ (g/cm^3) the density difference between oil and aqueous phases and g the gravity acceleration (9.81 cm/sec^2). A correction factor (f_D) is required because a fraction of droplet remains at the tip of the capillary after detachment, as it is illustrated in Figure 3-5(a). The factor is function of $r/V_D^{1/3}$ and was taken from Harkins et al.[238]

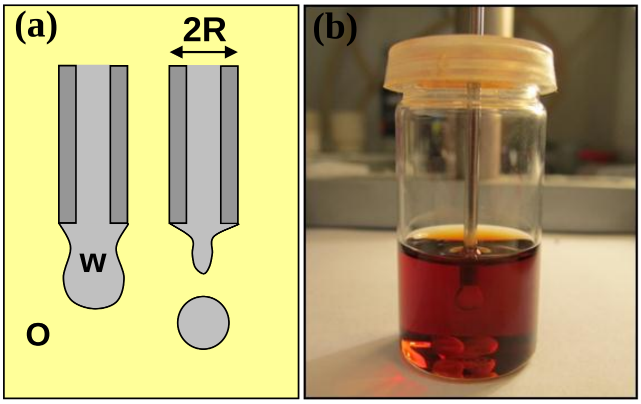

Figure 3-5. (a) Drawing showing the drop detachment sequence from a droplet-volume experiment to determine the oil(O)-water(W) interfacial tension. A fraction of the droplet remains at the tip of the capillary after detachment. Consequently, a correction factor is required. (b) Picture showing a water droplet holding from a syringe (0.1050 cm of radius) in a NP_8 toluene dispersion.

Interfacial tension measurements were performed by forming a drop of water inside an amphiphile (Hypermer 2296) toluene solution (from 0 to 4 wt%) with and without the presence of iron oxide nanoparticles. The mean of at least 8 measurements has been used for the calculations of interfacial tensions.

It should be pointed out that the measurements with NP_8 proved difficult due to the dark colour of the dispersions (see Figure 3-4(a)). Since it was confirmed that NP_8 did not modify the interfacial tension values (using the Du Noüy ring method), NP_8 toluene dispersions were introduced in 15 mL tubes in a DynaMag™-15 (Invitrogen, USA) to remove most of the nanoparticles by magnetic attraction. Consequently, the transparency of the iron oxide dispersions greatly improved, and these solutions were therefore used in the tension determinations (Figure 3-5(b)).

3.2.5 Preparation of Highly Concentrated Emulsions

As pointed out in the objectives and work plan section, different emulsions have been studied in this PhD thesis. Following the approaches described in page 58, highly concentrated emulsions (HIPEs) have been prepared using two different methods, namely phase inversion temperature method (PIT) and dropwise addition method.

3.2.5.1 *Phase Inversion Temperature (PIT) method*

This method of preparation pertains only to results section 4.2.3 and exact emulsion compositions will be given there. After mixing all components, diluted O/W emulsions were first cooled down to 0 ºC by placing 20 mL glass containers into ice. The temperature was then quickly increased to 70 ºC by placing the samples into a water bath at such temperature, with constant and vigorous manual agitation (Figure 3-6). A sudden increase in viscosity was clearly noticed when temperature passed through the PIT, indicating a transition from a diluted emulsion (O/W) to a highly concentrated emulsion (W/O). The phase inversion temperature (PIT) was adjusted experimentally using the conductivity test described in section 3.2.3.

The internal phase volume fraction (water) of emulsions varied from 80 to 90 %, and the continuous phase (oil) contained styrene (ST) and the cross-linker divinylbenzene (DVB) in a weight ratio of 4:1. Divinylbenzene was used as a cross-linker to increase the mechanical strength of nanocomposites prepared later on. It should be pointed out that two kinds of iron oxide nanoparticles (NP_3 and NP_8) were incorporated in the oil phase of the emulsions.

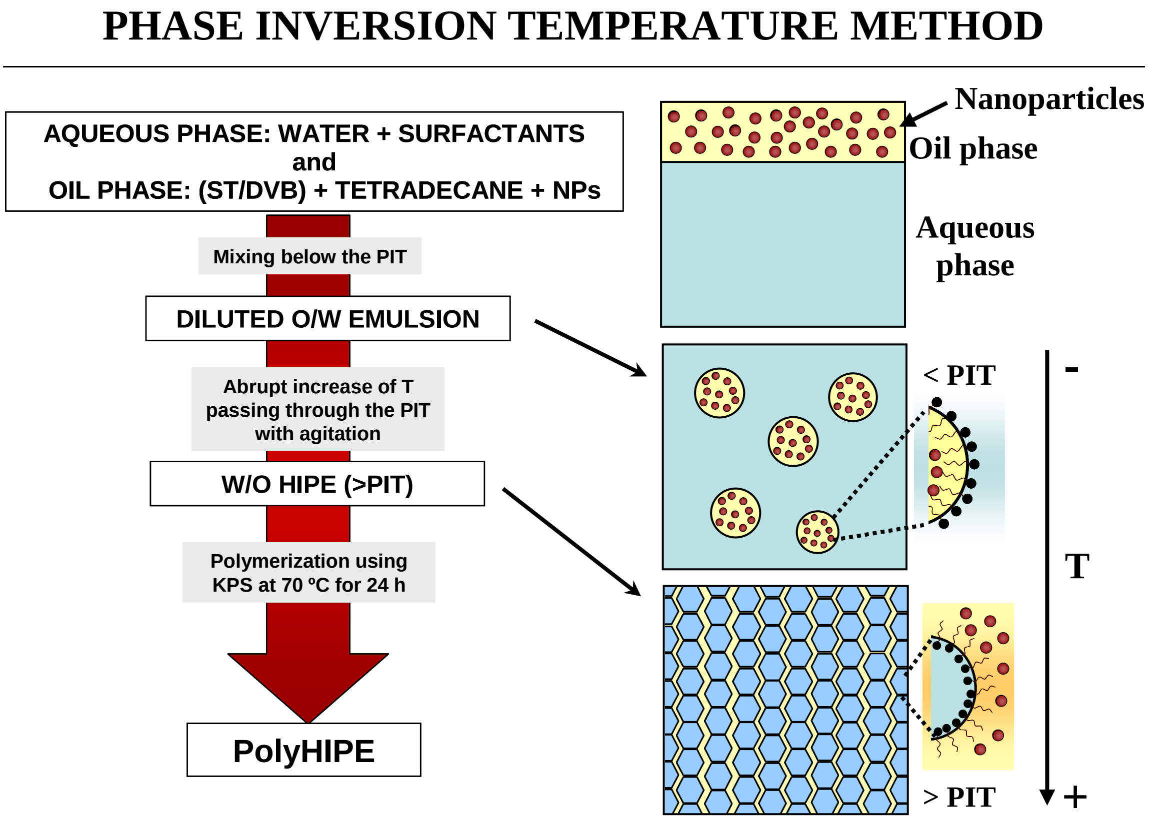

Figure 3-6. Schematic representation showing the formation of highly concentrated emulsions (HIPEs) by the phase inversion temperature (PIT) method. Nanoparticles (NPs) are incorporated in the continuous (oil) phase of the emulsions. ST and DVB indicate styrene and divinylbenzene, respectively.

3.2.5.2 *Dropwise addition method*

Here we summarize the various methods used for preparing HIPEs in sections 4.3 and 4.4. A schematic representation of the dropwise addition method is depicted in Figure 3-7. This method is based on gradual addition of the internal phase of the emulsion (here water) to the continuous (oil) under constant stirring.

(a) Emulsions stabilized with nanoparticles, in absence of surfactant (Pickering emulsions)

Before emulsification, similar to that described elsewhere,[100, 204] dried nanoparticles (either Fe_3O_4 or TiO_2) at different concentrations were dispersed in the oil phase (formed by ST:DVB in 1:1 by weight) of the emulsion using a sonication bath for 10 min. Afterwards, the internal phase formed exclusively by water was added dropwise to the continuous phase under gentle and continuous stirring for 5 min, until the desired volume fraction was reached, with the help of a Vortex Topmix FB15024 (Fisher Scientific, U.K.). Final internal phase volume fraction was varied from 75 % to 92.5 %. The viscous water-in-oil (W/O) HIPEs were prepared directly in either 15 mL or 50 mL standing polypropylene centrifuge (Falcon) tubes.

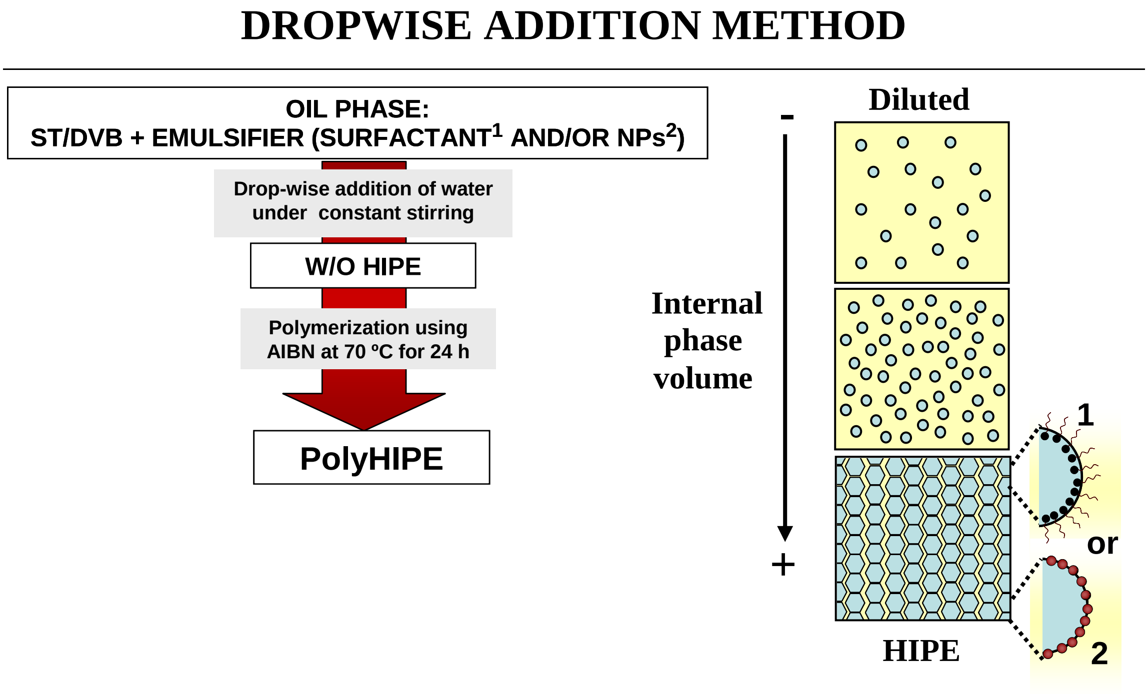

Figure 3-7. Schematic representation showing the formation of highly concentrated emulsions (HIPEs) by the dropwise addition method. The internal phase volume is added dropwise under constant stirring. The emulsions are stabilized by surfactants (case 1) or by nanoparticles (case 2). ST and DVB indicate styrene and divinylbenzene, respectively.

(b) Emulsions stabilized with mixtures of nanoparticles and nonionic surfactant

The only difference compared with the emulsions stabilized solely with nanoparticles described above, is that before emulsification, different amounts of the surfactant Hypermer 2296 (from 0 to 4 wt% with respect to monomers) were mixed with Fe_3O_4 nanoparticles in the oil phase, formed by the styrene and the cross-linker divinylbenzene mixture (weight ratio of 1:1).

3.2.6 Characterization of the Type, Drop Size and Stability of the Emulsion

The type of emulsions (W/O or O/W) was inferred by the drop test and conductivity measurements. The first method is based on observing what happens when a droplet of emulsion is added to either pure water or pure oil. Oil-in-water (water-in-oil) emulsions dispersed in water (oil) and remain as emulsion droplets in oil (water). Therefore is a simple method to know which type of emulsion is.

In order to determine the size of emulsion droplets, images of emulsions were captured using a Reichert Polyvar 2 microscope (Leica, Germany), equipped with a digital camera Sony CCD-Iris. It should be pointed out that an USB horizontal microscope (VMS-001, Veho, UK) was also used for observing HIPEs stabilized mainly or exclusively by nanoparticles. These emulsions were directly imaged inside the tubes, due to attempts to place them in microscope slides resulted in emulsion phase separation. This is explained by the large size of the droplets and their relatively low resistance to any shear stress applied.

The stability of emulsions to creaming or sedimentation was assessed by measuring the height of the emulsion volume fraction (Figure 3-8(a)). Stability to coalescence was evaluated by measuring the heights of resolved water and oil, and residual emulsion over time (Figure 3-8).

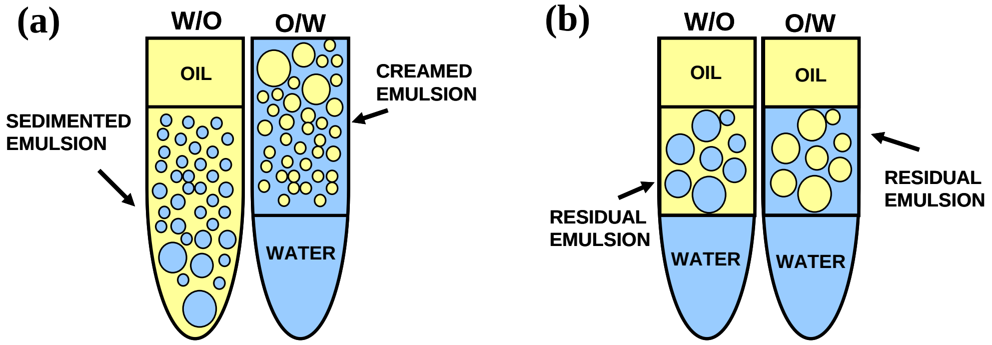

Figure 3-8. Schematic illustration showing W/O and O/W emulsions that have experienced distinct instability processes: (a) sedimentation or creaming; (b) coalescence.

3.2.7 Preparation of Polymeric Macroporous Nanocomposites

Macroporous polymers were obtained by the polymerization of the monomer mixture (styrene-divinylbenzene) in the continuous phase of highly concentrated emulsions (last step in Figure 3-6 and Figure 3-7). As pointed out in the Introduction (section 1.3.2.1), the resulting materials are referred in the literature as polyHIPEs.[181]

Polymerization of the external phase of highly concentrated emulsions prepared by the PIT method (Figure 3-6) was carried out at 70 ºC during 48 hours using the water-soluble initiator $K_2S_2O_8$ (KPS). Such initiator is widely used as a free-radical polymerization initiator in emulsion systems. After polymerization, macroporous solid foams were carefully extracted from the 20 mL glass containers and handled cautiously due to the fragility of the materials at this stage. The materials were then washed thoroughly with water and subsequently purified by soxhlet extraction in ethanol for 12 hours to remove surfactants and unreacted monomer. Finally, macroporous polymers were freeze-dried at -75 ºC and 0.01 mbar for 24 h (Alpha 1-2 Christ instrument, Germany). Shrinkage in porous materials is generally avoided using freeze-drying due to the absence of capillarity forces acting during water sublimation. .

Regarding emulsions prepared by the dropwise addition method (Figure 3-6), the standing polypropylene centrifuge (Falcon) tubes containing the emulsions were placed into an oven for polymerization at 70 ºC for 24 h to yield macroporous polymers (polyHIPEs). In this case, the oil-soluble initiator for free radical polymerization, AIBN, was added (1 wt% with respect to monomers) to iniate the polymerization reaction in the continuous phase of the emulsions. It should be remarked that in these emulsions the weight ratio between the styrene and the crosslinker divinylbenzene was increased from 4:1 (emulsions prepared by the PIT method) to 1:1 in order to increase mechanical strength of polyHIPEs.

After polymerization the macroporous polymers made from emulsions stabilized with particles were rinsed with ethanol to remove unreacted monomers, and then dried until constant weights were reached, using a vacuum oven (Heraeus VT5036, Heraeus Instruments, Germany) at 120 ºC for 12 h. No purification was needed, since emulsions did not contain surfactant. On the other hand, macroporous polymers obtained from highly concentrated emulsions stabilized with mixtures of surfactants and nanoparticles were appropriately purified by soxhlet extraction in ethanol for 12 hours.

3.2.8 Preparation of Nonporous Nanocomposites

For the preparation of monolithic, free-standing non-porous nanocomposites (see 4.2.1), oleic-acid surface-modified iron oxide nanoparticles (NP_3 and NP_8) were dried at 50 ºC and then dispersed with a vortex mixer in a mixture of styrene and divinylbenzene (volume ratio 4:1). To improve the compatibility of iron oxide nanoparticles with respect to the polymer matrix, acrylic acid was added to the monomer mixture (nanoparticles/acrylic acid mass ratio = 3:1). A 1 wt% (with respect to the total monomer weight) of the polymerization initiator ADVN was then dissolved. Samples were kept in glass test tubes at 40 ºC for 24 h allowing polymerization to complete.

The same polymerization reaction was carried out within the internal phase of a diluted O/W emulsion (see 4.2.2). A sodium dodecyl sulfate (SDS) aqueous solution (1.2 wt% surfactant respect aqueous phase) and the same monomer phase described above, containing iron oxide nanoparticles (NP_3), were weighted into a 20 mL glass vessel. Then, an O/W emulsion was prepared by mixing the solution with an Ultraturrax (Ika, Germany) T25 homogenizer (0.7 cm head) at 9.500 rpm for 5 min. Final emulsion had a internal (oil) phase volume fraction equal to 0.05. During polymerization, the emulsion was kept under agitation using a magnetic stirrer device.

3.2.9 Characterization of Polymeric Nanocomposites

3.2.9.1 *Pore structure: scanning and transmission electron microscopy*

Scanning electron microscopy (SEM) micrographs of polyHIPEs were acquired using either a TM-1000 tabletop instrument (Hitachi, Germany) at 15 kV or a JSM-5610 LV microscope (JEOL, Japan) at 20 KV. For observation, samples were coated with a gold layer (ca. 60 nm thick) in an argon atmosphere inside a ScanCoat Six (Edwards Ltd.,U.K), to achieve the necessary electrical conductivity. Pore size distribution of macroporous polymers was determined by measuring at least 500 pores from different regions of the sample using ImageJ software.

For the transmission electron microscopy (TEM) observations, the polymeric samples were first finely divided (few mm in size) and then embedded in a Spurr epoxy resin of low viscosity (60 cps) during 24 hours at 4 ºC. The composition of such a resin was the following: 10 g of ERL 4206 (4-vinylcyclo-hexene dioxide epoxy resin), 6 g of DER 736 (epichlorohydrin-polyglycol epoxi resin, flexibilizer), 26 g of NSA (2-nonenyl succinic anhydride, hardener), 0.4 g of

DMAE S-1 (2-dimethylaminoethanol, accelerator) and 0.8 g of DBP (dibutyl phthalate, plasticizer). Samples were then transferred to a mould and incubated at 65 ºC for 48 hours, to allow polymerization. Afterwards, thin slices (≈400 nm) were cut with freshly-broken-glass knives. The obtained slices were inspected by optical microscopy and the desired areas were selected and marked. Ultrathin sections (about 60 nm) of selected areas were cut with a diamond blade using an ultramicrotome (Leica Ultracut UCT, Austria). Finally, these slices were transferred to a holey copper grid coated with a carbon film. The thickness of the samples is sufficiently small and the polymer becomes transparent to the electron beam. The addition of a contrast agent was not required for the observation of the metal oxide nanoparticles. TEM observations were performed on a JEM 2011F (JEOL, Japan) instrument, working at 200 kV.

3.2.9.2 *Determination of skeletal density, foam density and porosity*

Skeletal density (ρ_s) and foam or envelope density (ρ_f) of the macroporous polymers were determined using pycnometry. A pycnometer is a vessel with a precisely known volume. Despite a pycnometer is used to determine density, or specific gravity, it actually measures volume. As outlined in the Introduction, foam density takes into account the solid material plus all types of porosity (including open and closed pores), while skeletal density only considers the solid fraction and closed pores, which can remain in the polymer walls of the materials. In ideal conditions, the skeletal density of a polystyrene-based macroporous polymer would exactly correspond to the density of polystyrene.

First, skeletal density was obtained using a helium pycnometer (Accupic 1330, Micromeritics, U.K.) based on a gas displacement technique. A gas pycnometer operates by detecting pressure changes as a result of gas displacement by a solid object. Such solid is placed into a sealed chamber of known pressure ($\mathrm{P_s}$) and volume (V_s). A isolated reference chamber (V_r) is then charged with the same gas, reaching a greater pressure ($\mathrm{P_r}$). Finally, a valve that is connecting the two chambers is opened and consequently the pressure in the reference chamber falls. Then, pressure in the system is allowed to equilibrate ($\mathrm{P_{sys}}$). Applying the gas law PV=nRT, the volume of the solid (V_x) can be calculated by the equation,

$$V_x = \frac{(P_{sys}V_s + P_{sys}V_r - P_sV_s - P_rV_r)}{(P_{sys} - P_s)} \qquad 3\text{-}6$$

Skeletal density (ρ_s) can be easily calculated by dividing the known sample weight by V_x. The accuracy of the measurements is high but relies greatly in the absence of air moisture. Moreover, the sample must also be free of volatiles. Helium is generally used in this technique because is able to penetrate readily into the very fine pores. It should be pointed out that prior determinations, macroporous polymer samples are manually ground to break the macroporous structure.

The next step was to determine the foam density of macroporous polymers by means of an envelope density analyzer (GeoPyc 1360, Micrometrics, U.K.). This instrument determines the volume of a solid with known weight, by the displacement of a solid medium composed of small and rigid spheres that close pack efficiently around the object (Figure 3-9).

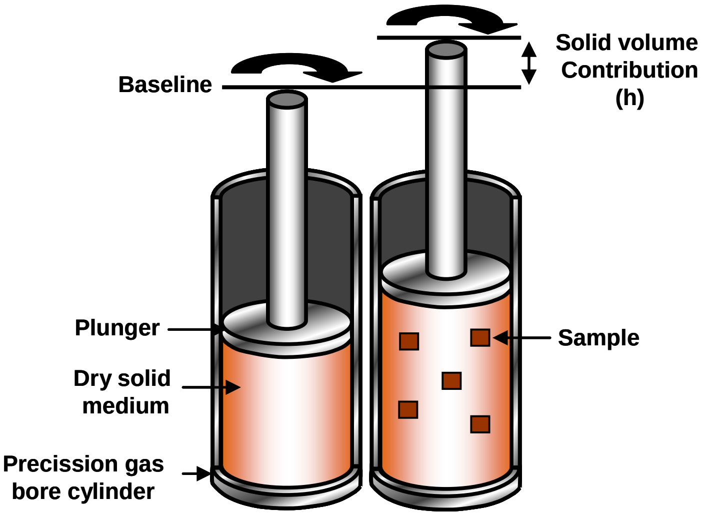

Figure 3-9. Volume determination by displacement of a dry medium in an envelope density analyzer.

First, a plunger compresses a powder (dry solid medium) without sample. The compression force is selectable. If the sample (around 3 cm^3, divided in 3-5 pieces) is incorporated inside the solid medium during compression, a difference in compression length (h) appears as a result of the volume occupied for the sample. This distance (h) is used to calculate the exact volume of the sample. Since the solid medium formed by rigid spheres the do not invade pores of the samples, and conform closely to the surface during consolidation, the envelope volume can be calculated in a controlled manner, according to:

$$V = \pi r^2 h \tag{3-7}$$

where V is the volume displaced of height h and radius r. Envelope density (ρ_f) can be obtained by dividing can be easily calculated knowing the known sample weight by V.

Knowing both skeletal and foam densities, porosity (P) can be obtained using the following equation:

$$P = \left(1 - \frac{\rho_f}{\rho_s}\right) \tag{3-8}$$

At least three replicas of each sample were analyzed in the envelope density measurements to obtain statistically relevant data.

3.2.9.3 *Mechanical characterization: compression test*

Compression tests were performed using a universal Lloyds machine (Lloyds EZ50, Lloyds Instruments, Fareham, UK) equipped with a 50 kN load cell to investigate the mechanical properties of macroporous polymers. At least three samples, which were 10 mm in height and 25 mm in diameter, were cut from the same macroporous polymer monolith. The surface of the samples was smothered using a band saw. Samples were loaded between compression plates at a speed of 1 mm/s until a displacement of half the original sample height was reached. The strain in the stress-strain curves was calculated as follows:

$$Strain = \frac{2d}{h_0} \tag{3-9}$$

where d is the displacement and h_0 is the initial monolith height (10 mm).

The Young's modulus (MPa) is defined as the initial linear slope of the stress–strain curve, and the crush strength (MPa) is the maximum value of the stress–strain curve at the end of the initial linear region. The specific crush strength (MPa·m^{3}·Kg^{-1}) was calculated dividing the crush strength by the foam density. Specific crush strength is used because it is a normalized value, allowing a better comparison of different materials.

3.2.9.4 *Magnetization measurements*

The magnetic properties of both polyHIPEs and iron oxide nanoparticles were studied using an MPMS XL superconducting quantum interference device (SQUID) magnetometer (Quantum Design,US) at fields ranging from -20 to 20 kOe and at temperatures ranging from 2 to 300 K.

3.2.9.5 *Permeability*

The permeability to gases of the macroporous polymers was measured using a homebuilt pressure rise apparatus as described in detail in Manley et al.[239] Following the sample preparation protocol,[174, 224] precursor HIPEs were directly prepared in 15 mL polypropylene centrifuge (Falcon) tubes (Figure 3-10(1)) and then polymerized.

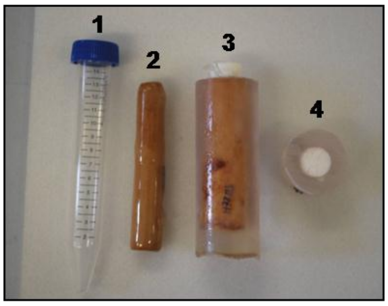

Figure 3-10. Sequence of sample preparation for the permeability test: (1) 15 mL polypropylene tube used as template; (2) resulting polyHIPE after being coated with the first layer of adhesive resin; (3) polyHIPE after coating with epoxy Araldite 2020®; (4) transversal view of the cut sample (25 mm diameter) containing the polyHIPE (15 mm diameter), which is ready for permeability studies.

After purification and drying steps, resulting cylinders of 15 mm in diameter were first coated with a nonpermeable layer of fast curing epoxy resin and allowed to cure at room temperature for about 20 min (Figure 3-10(2)). This is a crucial point in order to avoid the possibility of cross-flow during further permeability determinations. It should be noted that the intrusion of the resin into the porous structure is prevented not only by the high viscosity of the epoxy resin, but also by the characteristic dense skin layer on polyHIPE surface that is formed during polymerization.[240] Afterwards, due to the geometrical requirements of the sample cell in the permeability instrument, the already-coated cylinder was inserted in a poly(tetrafluoreoethylene, PTFE) mould, previously sprayed with a silicon. Then, a two component epoxy adhesive Araldite 2020® was poured into the mould and left at room temperature for 24 h to cure (Figure 3-10(3)). Before the permeability test, the already coated and sealed samples were carefully cut and sand to reach final dimensions of 25 mm in diameter and 31 mm in height (transversal view in Figure 3-10(4)). All different sample preparation steps are shown in Figure 3-10.

A schematic drawing of the permeability instrument is shown in Figure 3-11.

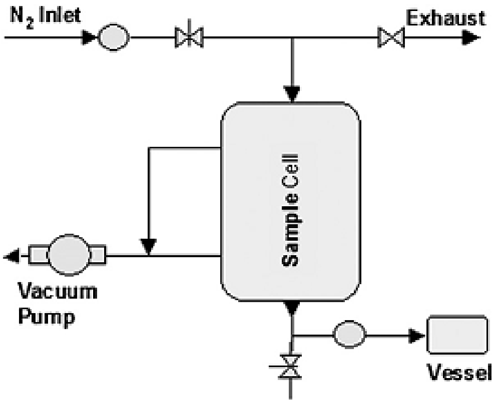

Figure 3-11. Scheme of the homebuilt pressure rise instrument used in this work to determine the permeability of macroporous polymer samples. Reproduced from Manley et al.[174]

First, the sample is introduced in the sample cell. Once the chamber is sealed, both the sample cell and a vessel of known volume are kept at low pressure (ca. 10 Pa) with the help of a vacuum pump. Meanwhile, the pressure at the other side of the sample is kept constant (e.g. 0.4 bar, N_2 inlet). It should be noted that the gas used in all experiments was pure nitrogen (free of oxygen and water vapour). When low pressure is attained, the valve between the sample cell and the N_2 inlet is opened and therefore the gas permeates through the porous sample from the high to the low pressure side (vessel). The gas that permeates thorough the sample is collected in the vessel and accordingly the pressure gradually increases. It should be noted, that during gas permeation, pressure at the high pressure side is kept constant (N_2 inlet).

The rate of pressure rise at the low pressure side is recorded to determine the viscous permeability (k) of the samples, as governed by Darcy´s law. The permeability coefficient (K) can be defined as follows:[239, 241]

$$K = \frac{Q_2 p_2 L}{\Delta p A} = \frac{V(dp_2 / dt)L}{p_1 A} = \frac{k}{\mu} p_m + \frac{4}{3} K_0 \sqrt{\frac{8RT}{\pi M}} \tag{3-10}$$

where Q_2 is the volumetric flow rate at the outlet (low pressure side), p_2 is pressure on the outlet side of the sample, L is the sample length, A is the sample cross-sectional area, Δp is the pressure difference across the sample, V is the fixed (known) volume of the vessel that collects the gas that permeates through the porous material, dp_2 / dt is the rate of pressure rise, p_1 is the pressure on the inlet high pressure side of the sample, μ the gas viscosity, p_m is the mean pressure ($p_1/2$ as p_2 is near 0), K_0 is the Knudsen permeability coefficient, R is the gas constant, T is the temperature and M is the molar mass of nitrogen.

In order to make the calculations, p_2 is plotted vs. t. The relation is linear, thus the slope dp_2 / dt is constant. Generally, dp_2 / dt is recorded for 4 or 5 different values of initial p_1. The range of p_1 (e.g. from 0.4 to 1.4 bars measuring in intervals of 0.2 bars) depends on porous structure of each sample, so that the higher permeability, the lower p_1 that should be fixed. Knowing dp_2 / dt, the permeability coefficient (K) can be calculated as V, L, p_1 and A are known. Finally, permeability (k) can be obtained from the linear relationship of K vs. p_m with $\frac{k}{\mu}$ slope and $\frac{4}{3}K_0\sqrt{\frac{8RT}{\pi M}}$ intercept.

In order to obtain relevant statistical data, measurements were performed on 2 different polyHIPE samples measured from both sides. Determinations were repeated three times per each sample side. The permeability SI units are m^2. However, the most often used unit is the Darcy (D), with an equivalence of 1 D = 10^{-12} m^2.

4 RESULTS & DISCUSSION

4.1 PREPARATION, CHARACTERIZATION AND FUNCTIONALIZATION OF NANOPARTICLES

This section includes a complete description of both iron oxide and titanium dioxide nanoparticles that will be used in next chapters, either as simple fillers in macroporous polymers (section 4.1) or as emulsifiers to stabilize high internal phase emulsions (sections 4.3 and 4.4).

4.1.1 Iron Oxide Nanoparticles

Three kinds of iron oxide nanoparticles with different average sizes and distinct content of oleic acid attached to their surfaces have been used throughout this work. The main characteristics of these nanoparticles are summarized in Table 4-1. Samples of nanoparticles are abbreviated hereafter as NP_X, where X is the average size of the nanoparticles:

- **NP_3**: nanoparticles prepared by coprecipitation of iron salts in a water-in-oil microemulsion.[228] The microemulsion provides a confinement that limits particle nucleation and growth.
- **NP_8**: nanoparticles prepared by coprecipitation of iron salts in aqueous medium.[229]
- **NP_{32}**: nanoparticles acquired from Sigma-Aldrich. To avoid any confusion while reading the text, as-received commercial NP_{32} will be denoted as CNP_{32}, while NP_{32} will always refer to oleic-acid surface modified nanoparticles.

Table 4-1. Main characteristics of the iron oxide nanoparticles used in this work. Crystalline phase was determined by X-ray diffraction. Average particle size was calculated by direct counting from TEM images. Surface area was calculated from N_2 adsorption isotherms applying the BET theory. Oleic acid content was obtained from TGA curves. Oleic acid surface adsorption was calculated using the oleic acid content on nanoparticles, the nanoparticles surface area and the iron oxide density (see text).

Sample	Crystalline phase	Average particle size (nm)	Surface area (m^2/g)	Oleic acid content (wt%)	Oleic acid surface adsorption (molecules/nm^2)
NP_3	Maghemite/ Magnetite	3	Not measured	45	5.9
NP_8	Magnetite	8	Not measured	12.4 ± 1.6	2.5
CNP_{32}	Magnetite	32	48 ± 1	0	0
NP_{32}	Magnetite	32	Not measured	4.2 ± 0.2	2.1

Transmission electron microscopy (TEM) images of both NP_3 and NP_8 nanoparticles are shown in Figure 4-1 (a) and (b), respectively, while the SEM image of as-received CNP_{32} is shown in Figure 4-1(c). In all cases, the nanoparticles are almost spherical. However, they had rather distinct sizes, since the size of NP_3 and NP_8 were between 1-4 and 5-12 nm, with dominant populations at 2 and 8 nm, respectively, whereas the size of CNP_{32} was in the range 10-70 nm, with an average size of 32 nm (see inset graphs in Figure 4-1). The average sizes (x) were calculated as follows:

$$x = \frac{\sum P(\%) \cdot D_i}{100} \qquad \text{4-1}$$

where P (%) is the frequency of each nanoparticle population with a characteristic diameter (D_i).

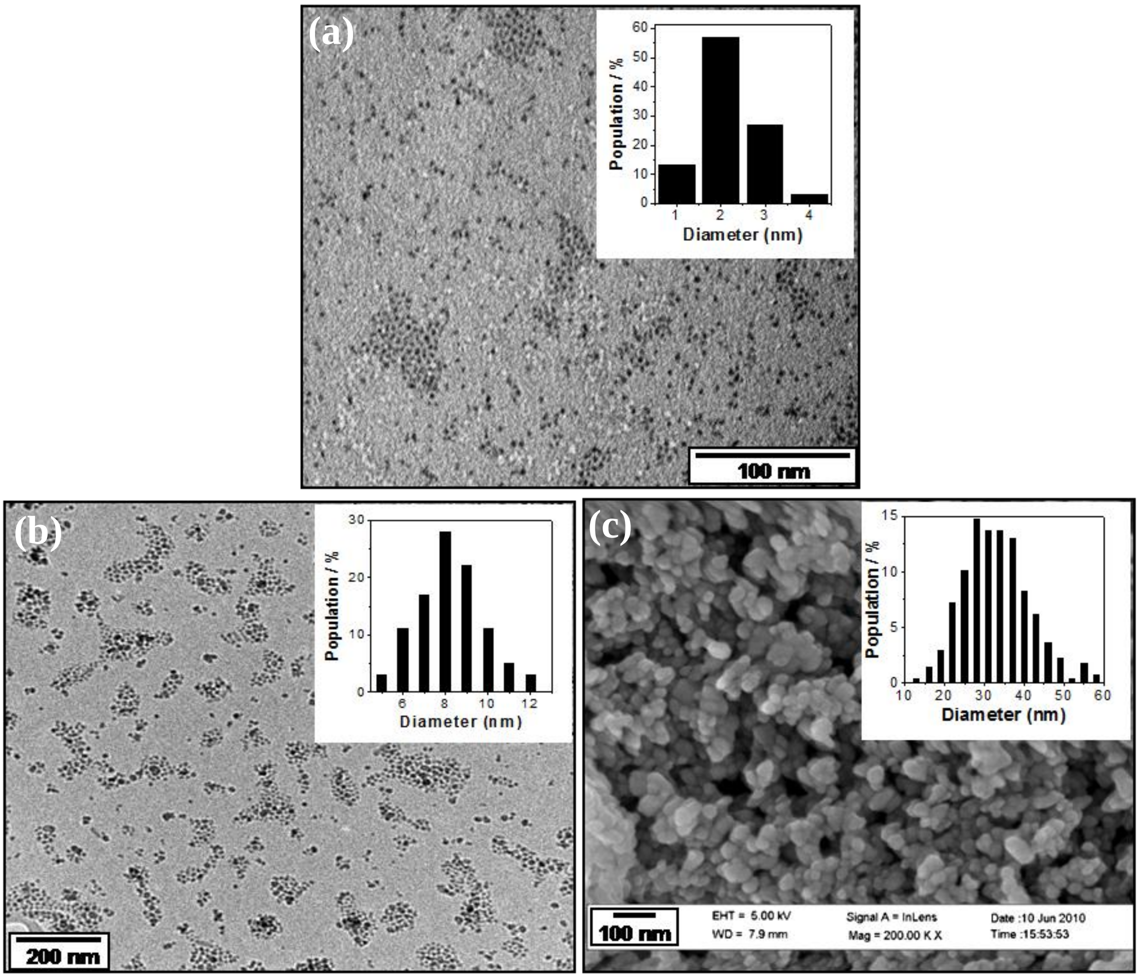

Figure 4-1. TEM images for (a) NP_3 and (b) NP_8 and (c) SEM picture for commercial (CNP_{32}) iron oxide nanoparticles, respectively. The inset graphs show the particle size distributions for the corresponding samples.

Because of the small size of NP_3, X-ray diffraction (XRD) peaks were very broad, making it difficult to differentiate between maghemite (Fe_2O_3) or magnetite (Fe_3O_4) iron oxide phases.[242] On the other hand, XRD peaks for NP_8 could be indexed as the face-centered magnetite (Fe_3O_4) phase (JCPDS 19-629).[208] The crystalline size for NP_3 and NP_8 was estimated to be 2.8 and 7.3 nm, using the Scherrer equation.[230] This is in fair agreement with the TEM observations, which points to single-domain crystalline nanoparticles (Table 4-1). CNP_{32} nanoparticles were also assigned to the same magnetite phase (Fe_3O_4) than NP_8. XRD patterns corresponding to the three kinds of nanoparticles are included as supporting information in Appendix 1 (Figure 10-1).

One of the aims of this work is to incorporate the nanoparticles in hydrophobic polymers. For that reason, nanoparticles were surface-modified with oleic acid in order to increase their hydrophobicity. Oleic acid is a biocompatible monosaturated fatty acid with low melting temperature. For NP_3 and NP_8 the fatty acid was incorporated during the preparation step, whereas commercial CNP_{32} were functionalized as described in section 3.2.1. It is important to recall that more than one preparation batch was used in the case of NP_8 and several functionalization experiments were performed on CNP_{32}. Despite conditions were maintained as uniformly as possible, the amount of oleic acid on nanoparticle surfaces slightly varied for different batches, which explains the small error presented in Table 4-1. Oleic acid content in NP_3 was 45 wt%.[228] Regarding NP_8 nanoparticles, thermogravimetric analysis (TGA) (Figure 4-2(a)) revealed that after the purifying step, the total content of oleic acid attached to the surface of the nanoparticles was 12.4 ± 1.6 wt%. Two different steps of weight loss were detected between 100 and 260 °C, and from 260 and 450 °C. This suggests that oleic acid is presumably attached to the particles in multilayers.[229]

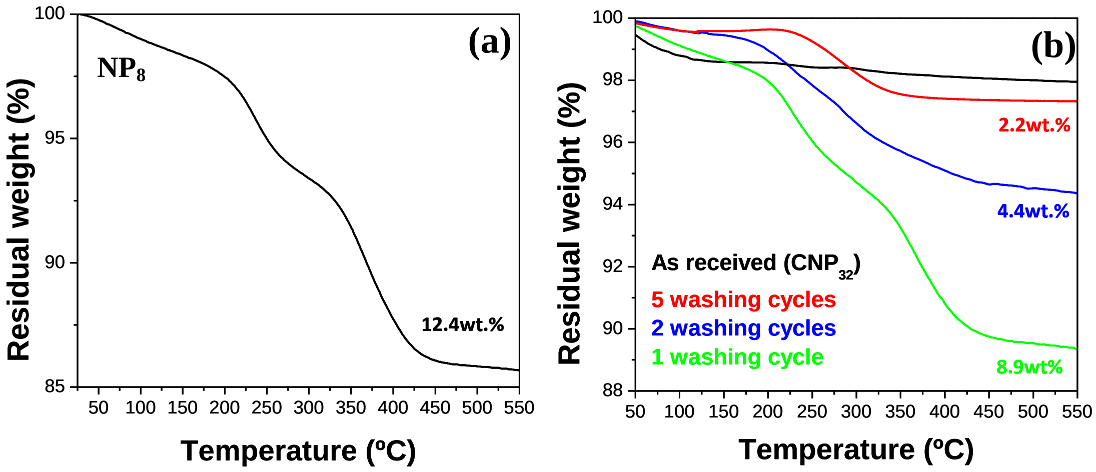

Figure 4-2. Thermogravimetric analysis for oleic acid surface-modified (a) NP_8, (b) CNP_{32} and NP_{32} after several washing cycles. Oleic acid content is indicated above each curve.

Figure 4-2(b) shows the corresponding TGA curves for as-received CNP_{32} and for NP_{32} after several washing cycles. After addition of oleic acid and the first washing cycle, NP_{32} contained 8.9 wt% of oleic acid. Similar to that observed for NP_8, the TGA plot also showed two different steps of weight loss. Probably, adsorption occurs again in multilayers. Successive washing cycles further reduced the content of the fatty acid. NP_{32}, after two washing cycles, showed only one TGA step weight loss, suggesting that oleic acid molecules are arranged in a single monolayer. In contrast with the other two nanoparticles evaluated, the content of oleic acid attached on NP_{32} surface was easily modified by applying washing cycles, which could mean that the fatty acid adsorption on NP_{32} was weaker than for NP_8 and NP_3.

The surface area per molecule (α_c in nm^2/molecules) of the primary layer of oleic acid was estimated for the different nanoparticles. For that purpose, the residual organic fraction determined by TGA, the density of iron oxide (5.16 g/cm^3),[229] and the average particle size obtained from TEM images were taken into account. α_c was calculated following the equations:

$$\alpha_c = \frac{S_{average}}{n_{a.o}} \qquad 4\text{-}2$$

$$S_{average} = \frac{\sum P(\%) \cdot 4\,\pi\, r^2}{100} \qquad 4\text{-}3$$

where $S_{average}$ is the normalized surface area of a nanoparticle, $n_{a.o}$ is the number of oleic acid molecules attached to the surface of such nanoparticle, and $P(\%)$ is the frequency of each nanoparticle population with a characteristic surface ($4\pi r^2$). In order to calculate the surface coverage two crude assumptions were assumed: first, that nanoparticles are completely spherical, and second that nanoparticles are nonporous.

The calculated α_c ranged from 0.19 (NP_3) to 0.47 nm^2/molecule (NP_{32}). The value for NP_3 (0.19) is very close to the cross-sectional area observed in monolayer films with packed straight-chain fatty acids on water (0.20-0.22 nm^2/molecule).[243] This implies that NP_3 are surrounded by a compact monolayer shell. At variance with NP_3, the calculated surface area per molecule in the case of NP_{32} was 0.47, which implies that the surface of NP_{32} nanoparticles is not fully saturated with oleic acid, and therefore a dense monolayer has not been obtained.

The inverse of surface area per molecule is surface adsorption (molecule/nm^2). We have used this parameter to compare the content of oleic acid attached to each kind of nanoparticle. Accordingly, NP_3 showed the higher surface adsorption (5.9 molecules/nm^2), followed by NP_8

(2.5 molecules/nm^2) and NP$_{32}$ (2.1 molecules/nm^2, Table 4-1). As it will be seen in sections 4.3 and 4.4, the degree of surface hydrophobicity is one the factors that most influences the ability of nanoparticles to act as emulsion stabilizers.

Oleic acid surface-modified nanoparticles were also characterized by Fourier Transform Infrared (FTIR) spectroscopy. Figure 4-3(a) shows the FTIR spectra of NP$_3$. The spectra for NP$_8$ and for NP$_{32}$ nanoparticles, before and after functionalization, are plotted in Figure 4-3(b).

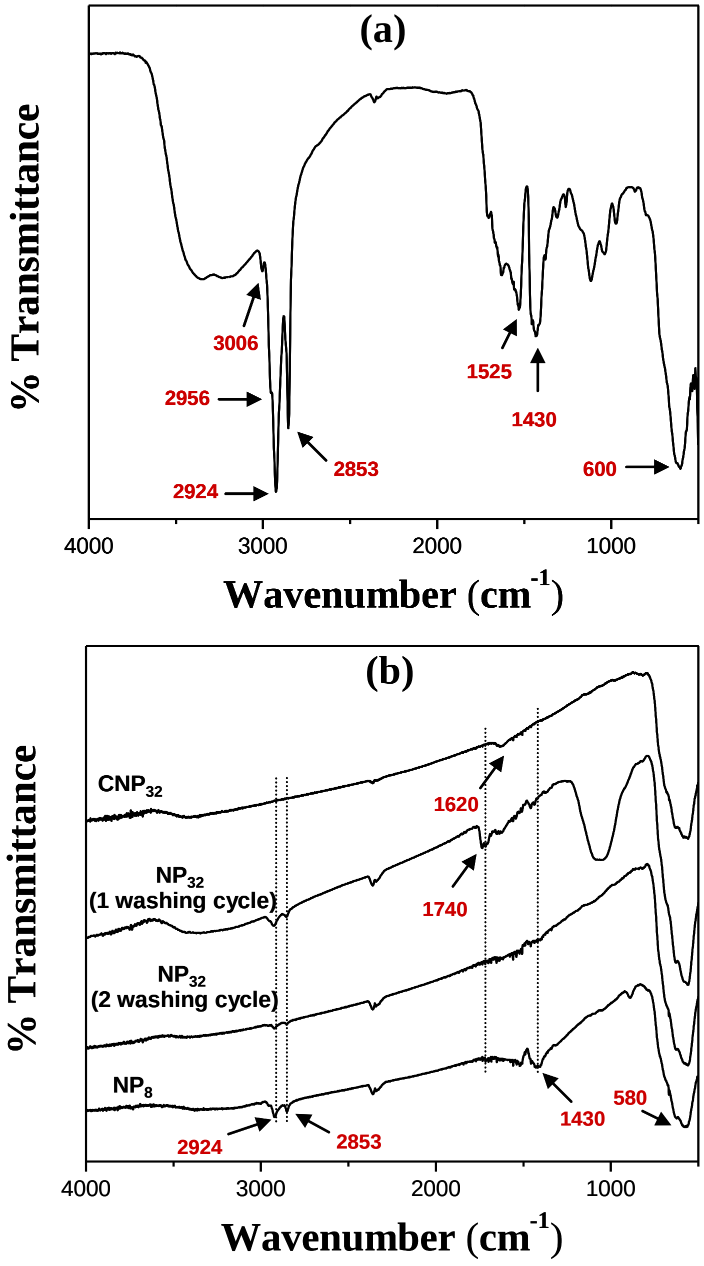

Figure 4-3. FTIR spectra of oleic acid surface-modified (a) NP$_3$, (b) NP$_8$ and NP$_{32}$ after two washing cycles. The oleic acid content was 45, 12.4 and 4.4 wt%, respectively. In (b), the spectra corresponding to as-received CNP$_{32}$ and to NP$_{32}$, after one washing cycle (8.9 wt% oleic acid), were also included as a comparison.

Three intense and characteristic peaks at 2924 ($v_{s.}$ (CH_2)), 2853 (v_a (CH_3)) and 2956 (v_a (CH_2)) cm^{-1} are assigned to C-H stretching, indicating the presence of oleic acid on the surface of nanoparticles. The two peaks with higher intensity were also detected in the case of NP_8 and NP_{32} (1 cycle of washing). For NP_{32} after two washing cycles (4.4 wt% oleic acid), peaks at 2924 and 2843 cm^{-1} practically disappeared. Actually, spectra for as-received CNP_{32} and after two cycles of washings were essentially the same. Although it was difficult to detect the presence of oleic acid in this sample, this was confirmed by TGA determinations (Figure 4-2(a)). Water adsorption in as-received CNP_{32} was attributed to the peak at ≈ 1620 cm^{-1}.

The absence of a peak at 1740 cm^{-1} ((C=O) stretching) in the spectra for NP_3 (Figure 4-3(a)) suggests that no free oleic acid was on the particles. Interestingly, such a peak splits to the broad asymmetric υ_{as} (COO^-) and to the symmetric υ_{as} (COO^-) bands, at 1525 and 1430 cm^{-1}, respectively, which reveals the existence of adsorbed oleic acid as carboxylate on the particle surfaces.[244, 245] This signal was also appreciated in the NP_8 nanoparticles, but missing in the case of NP_{32} (Figure 4-3(b). It should be pointed out that when only one cycle of washing was applied to NP_{32}, the peak at 1740 could be assigned to free oleic acid. It is reasonable to presume that one more cycle of washing was necessary to eliminate all the excess of oleic acid, as demonstrated by the decline in oleic acid content from 8.9 to 4.4 wt% by TGA (Figure 4-2(a). Another characteristic peak (3006 cm^{-1}), assigned to the double bond of the oleic acid was distinguished for NP_3. Finally, a strong vibration corresponding to the Fe^{3+}-oxygen stretching was observed at lower wavenumber region (≈ 580-600 cm^{-1}) in all samples.[246]

Finally, nanoparticles were characterized with respect to their magnetic properties. At first, magnetization versus applied field (M-H) was measured for NP_8 and for as-received NP_{32}, at 300 K. The maximum magnetic field applied was 50 KOe. The plot for NP_8 (Figure 4-4(a), red line) showed that these nanoparticles, as expected, were superparamagnetic, as indicated by the lack of a hysteresis loop and coercivity (nanoparticles do not retain magnetization in the absence of a magnetic field) and the high magnetization saturation (M_s) value reached. M_s, represented in emu per gram of magnetic material (12.4 wt% of the sample was oleic acid) was 58.4 emu/g. Such M_s is appreciably lower than that for theoretical M_s value for bulk magnetite (90-100 emu/g).[247] Reduction of total magnetization partially arises from reduction of particle size, which increases surface spin disorder.[132] Despite the fact that the non-magnetic contribution from the coating organic layer has been subtracted, it is also known that the coordination by non-magnetic layers of polymers or organic molecules with the iron cations might attenuate the net charge on particle surfaces.[248, 249] Therefore, apart from the major reduction caused by the small size of NP_8 nanoparticles, the capping agent (oleic acid) can also has an effect on the M_s value.

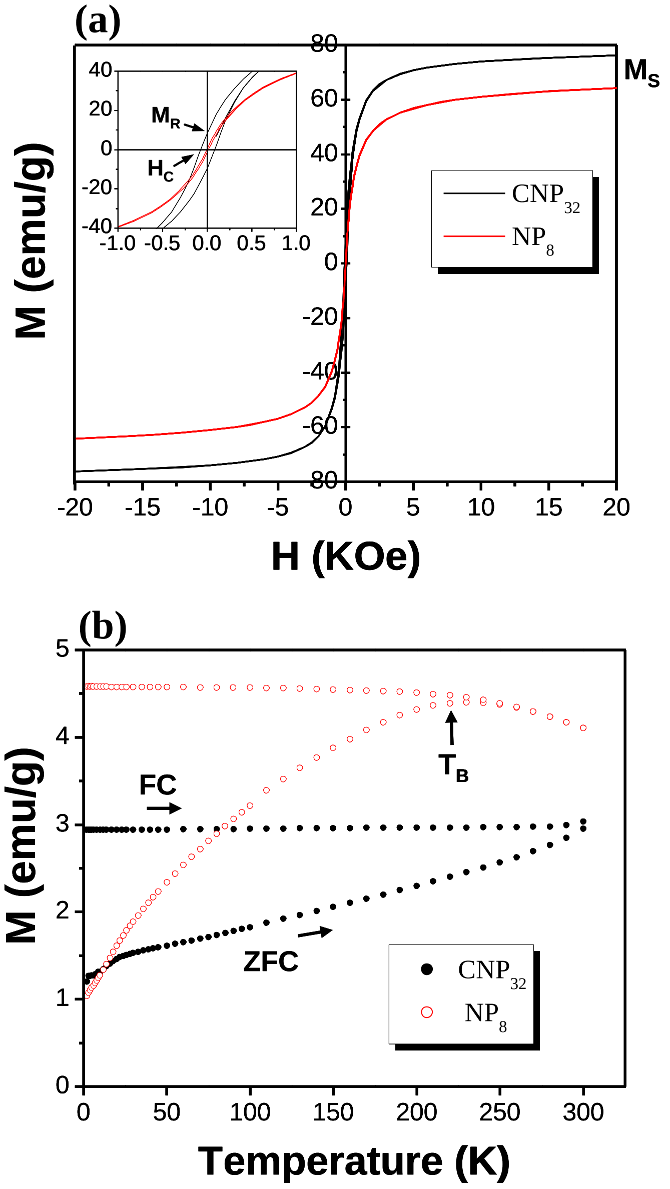

Figure 4-4. (a) Magnetization (M) vs. applied magnetic field at 300 K and (b) field-cooled (FC) and zero field-cooled (ZFC) curves measured at 50 Oe for NP_8 and CNP_{32} nanoparticles. The inset in (a) shows the same results on a larger scale; a hysteresis can be observed in the case of non-superparamagnetic CNP_{32}. Coercive field, remanence and blocking temperature are denoted as H_C, M_R and T_B, respectively.

On the other hand, the M_s for CNP_{32} was 76.2 emu/g (Figure 4-4(a), black line), which was higher than for NP_8 because of its larger size. Moreover, in the case of CNP_{32}, a hysteresis loop was observed in the M-H curves (coercive field (H_C) and remanence (M_R) were 0.08 kOe and 8.7 emu/g, respectively). The hysteresis is clearly seen in the corresponding inset graph.

To detect the transition to the superparamagnetic state, we measured the field-cooled (FC) and the zero field-cooled (ZFC) magnetization versus temperature at a field of H = 50 Oe (Figure 4-4(b)). Confirming the results obtained in M-H plots, no blocking temperature (T_B) could be detected for CNP_{32} (black line), which demonstrates that CNP_{32} do not show superparamagnetic behaviour at room temperature. As seen above, the coercitivity for CNP_{32} opened up below the blocking transition. On the contrary, a maximum in the ZFC magnetization was observed at 230 K for NP_8 nanoparticles (Figure 4-4, red line), which could be attributed to the presence of a T_B.[250] As mentioned in the Introduction (1.2.2.4), one of the properties of single-domain superparamagnetic nanoscopic iron oxide particles is its dependency on temperature.[251] FC and ZFC curves fell on top each other and are reversible, with irreversibility setting the T_B. Such a temperature separates the blocking state (below T_B) from the nanoparticle superparamagnetic state (above T_B), where thermal energy induces rapid fluctuations of the magnetic moments. It is hence evident that the different magnetic behaviours of NP_8 and CNP_{32} are associated with their different particle sizes. M_s and T_B are summarized in Table 4-2.

Table 4-2. Magnetization saturation (M_s) at 300 K and blocking temperature (T_B) at 50 Oe for NP_8 and for CNP_{32} nanoparticles.

Sample	M_s **(emu/ g magnetite)**	T_B **(K)**
NP_8	58.4	230
CNP_{32}	76.2	>300

4.1.2 Titanium Dioxide Nanoparticles

Titanium dioxide nanopowders were synthesized via mechanochemical solid-state reaction. It is well known from the literature, that metal salts (e.g. $FeCl_3$,[252] $Na_2Cr_2O_7$[253]) can undergo reactions with hydroxides or carbonates in low temperature ball-milling reactions, leading to nanocrystalline powders.[144] More recently, the same approach has been followed in the synthesis of TiO_2 nanoparticles, starting from a mixture of a Lewis acid ($TiOSO_4$, metallic salt) and a base.[148, 254]. Generally, these mechanochemically activated reactions produce low crystalline oxides immersed in a water soluble salt by-product which is later removed by means of a simple washing procedure.[145]

As detailed in the experimental section 3.2.2, titanyl sulphate ($TiOSO_4$) was used as titanium precursor, and Na_2CO_3 and NaOH were the bases selected. Figure 4-5 shows the XRD patterns of mixtures, initially formed by $TiOSO_4$ and Na_2CO_3, processed at different ball-milling times (from 15 to 60 minutes). In all experiments, both the initial mass (6 g) introduced in the planetary ball-mill containers (45 cm^3) and the ball-to-powder ratio (13) were kept constant.

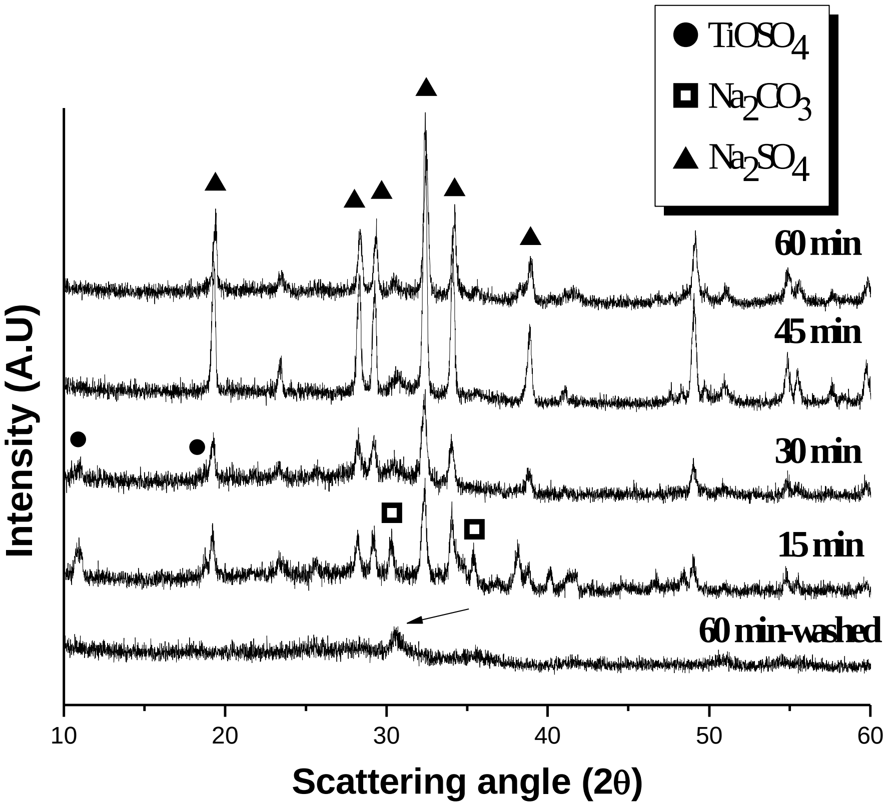

Figure 4-5. XRD patterns of $TiOSO_4$ - Na_2CO_3 powder mixtures milled at different times. The ball-to-powder ratio was 13:1. The curve for the sample milled at 60 min and then washed is also included. The arrow indicates a peak possibly ascribed to a ZrO_2 impurity.

As seen in the figure, after 30 min of mechanochemical treatment, the diffractions signals corresponding to the titanium dioxide precursor (peaks at 17.4 and 21.4º) have almost completely disappeared, indicating that the chemical reaction occurred in a steady-state manner.[147] This was also confirmed by the absence of peaks attributed to the Na_2CO_3 salt in the XRD curve at 30 minutes.

Due to the chemical reaction between $TiOSO_4$ and Na_2CO_3 compounds, Na_2SO_4 was formed and peaks assigned to this salt could be observed from the early stages of the process. Longer processing times (30-45 min) produced $NaSO_4$ with enhanced crystallinity. As a result, the width of the peaks became narrower and the intensity was higher, indicating a growth of the crystal (or grain) size. This is obvious if curves at 30 and 45 min are compared. On the other hand, XRD pattern for even longer mill processing times (60 min), ultimately led to a new decrease in the intensity of such peaks, which became again broader. This means that excessive milling time can microstructurally reduce the crystal size of the Na_2SO_4 salt. It is well known that both grain size and crystallinity are influenced by the mechanochemical reaction conditions, such as milling time or size of the milling-balls.[255] Apart from that, no peaks corresponding to any TiO_2 phase were detected, suggesting that although the reaction has occurred, the TiO_2 had and amorphous structure. This result is in agreement with that reported by Billik et al.[148], who indicated that activation conditions prevent the crystallization of TiO_2.

Therefore, the peaks observed at 60 min of ball-milling were mainly attributed to Na_2SO_4 salt, which is a by-product of the reaction. This salt could be removed by washing with water. The XRD spectrum of the resulting material is shown at the bottom in Figure 4-5. A small peak at 30.5° was detected on each occasion (see black arrow in Figure 4-5), which most likely comes from a ZrO_2 impurity from the milling media. It should be remembered that both, container and milling-balls were made of ZrO_2.

As a conclusion, it has been demonstrated that the reaction can be described as follows:

$$TiOSO_4 \cdot 2H_2O + Na_2CO_3 \rightarrow TiO_2 + Na_2SO_4 + 2H_2O + CO_2$$

Afterwards, aiming at reducing milling times, we decided to change Na_2CO_3 for a stronger base, i.e. NaOH. The first experiment resulted in an abrupt increase of temperature of the container walls after few minutes of ball-milling, because the reaction was highly exothermic. It was also observed that sample fractions remained adhered to the ceramic walls during ball-milling. This could influence the nanostructure formation.[254] In order to reduce this adhesion, a diluent (Na_2SO_4) was added in the initial powder mixture. On one hand diluents can adsorb the collision and heat energies generated during the milling, and simultaneously reduce the collision-rate by increasing the distance between reactants.[145] Furthermore, diluents are generally included with the aim of reducing the effective particle volume fraction, thus hindering hard aggregation.[256]

The reaction could proceed as follows:

$$TiOSO_4 \cdot 2H_2O + 2\,NaOH + Na_2SO_4 \rightarrow TiO_2 + 2Na_2SO_4 + 3H_2O$$

Interestingly, reaction was found to be almost completed after only 15 min of milling (Figure 4-6, curve on top) since peaks corresponding to initial precursors were not observed. This was attributed to the strong solid-state acid-base interaction. From the figure it can be seen that after the washing step, the peak attributed to the ZrO_2 impurity was also present (≈30.5º). Surprisingly, a peak (≈25.3º), that could be assigned to the crystalline anatase TiO_2 phase, was also observed in the XRD pattern. Despite being a broad signal with rather low diffraction intensity, it should be remarked that this has not been reported by other authors studying formation of TiO_2 under mechanochemical processing.[256, 257] In these works, TiO_2 nanoparticles made from mechanochemical-activated solid-state displacement reactions were amorphous, containing occasionally a small fraction of rutile crystalline phase.[148]

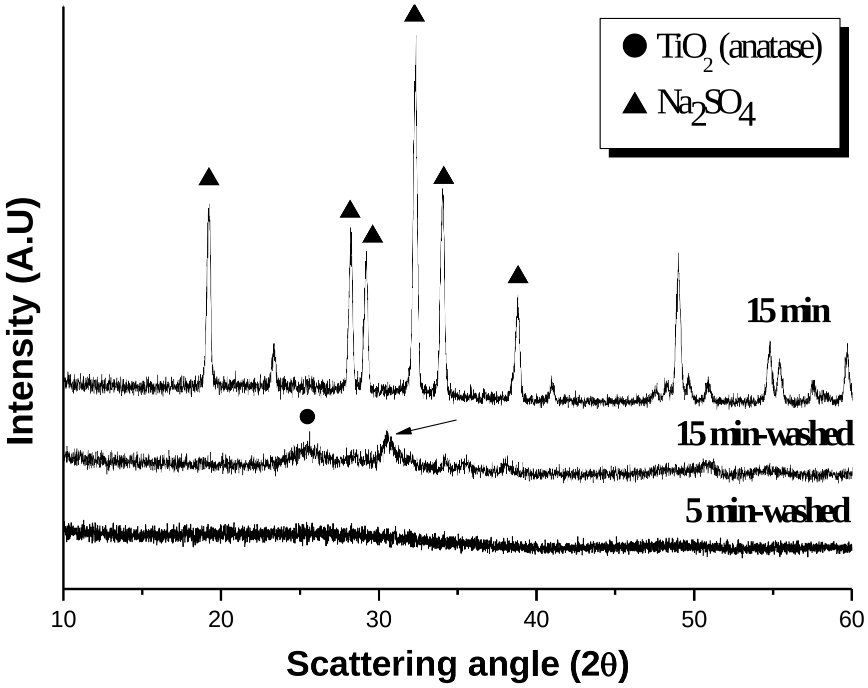

Figure 4-6. Comparison of XRD patterns of the system containing the precursor $TiOSO_4$ and the salt NaOH for different ball-milling times (5 and 15 min). The system also contains Na_2SO_4 as a diluent. The arrow indicates the peak possibly ascribed to a ZrO_2 impurity.

Since it was demonstrated that the reaction had finished after 15 min of milling, the reaction was shortened to 5 min. The XRD (not shown here) profile of the as-milled mixture was exactly the same to that shown in Figure 4-6(up), indicating that 5 min milling were enough to complete the very fast reaction. After washing the sample with water, the corresponding XRD pattern (see curve at the bottom in Figure 4-6) did not show any anatase peak, revealing that the TiO_2 is amorphous. Furthermore, the sample was found to be free of impurities. As seen in the figure, the XRD curve is absolutely flat. All further studies will be based on this system.

Since the TiO_2 obtained so far is amorphous and thus without photocatalytic resulting properties, a calcination treatment was required to obtain the photocatalytic anatase phase. As-milled $TiOSO_4 \cdot 2H_2O + 2NaOH + Na_2SO_4$ powder mixture was calcined at temperatures ranging from 300 to 700 ºC, and subsequently washed. The XRD patterns, displayed in Figure 4-7, show the influence of the treatment temperature on the crystallographic composition of the powders. As clearly seen, a progressive TiO_2 crystallization, producing anatase, starts at approximately 400 ºC. When the annealing temperature was further increased, an increment in the diffraction intensity as well as a decrease of the anatase peaks width is observed. This indicates a higher degree of crystallization and larger grains sizes, as it will be described below. From the curves, it is also evident that the main peak corresponding to the rutile phase (27.5º, assigned to the 110 lattice plain) is observed at temperatures beyond 650 ºC. Such crystallographic phase sequence has been widely studied in the last three decades and is well known that both anatase and brookite phases, irreversibly transforms to rutile at ca. 600 ºC.[153] Even though rutile is, under ambient temperature and pressure conditions, the thermodynamically TiO_2 stable phase, anatase and brookite polymorphs can also be thermodynamically stable for sufficiently smaller particle sizes.[152, 258]

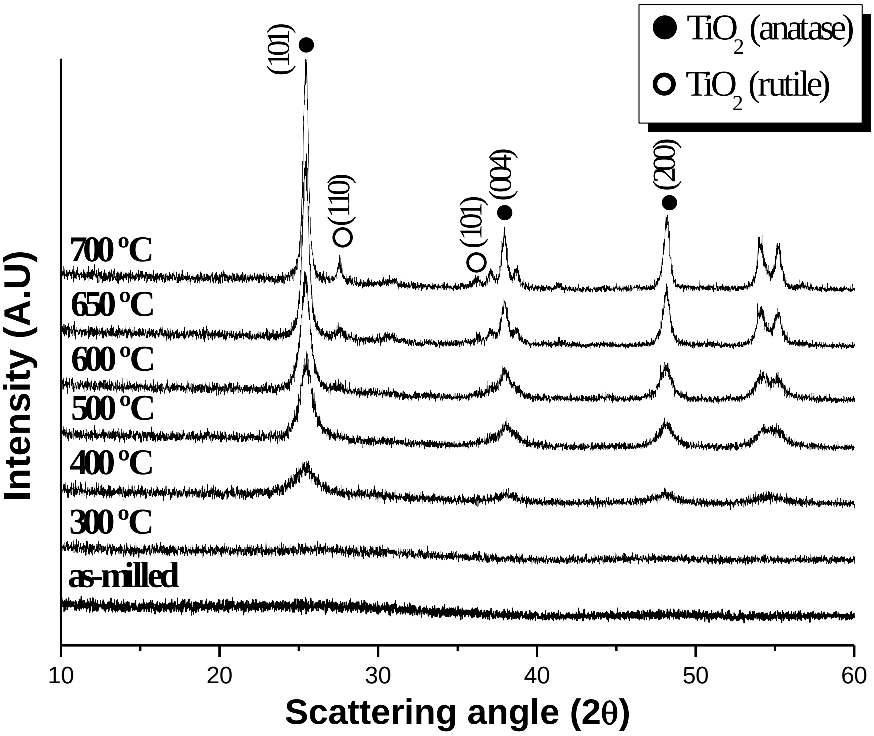

Figure 4-7. X-ray diffraction patterns of the as-milled and subsequent washed $TiO_2 + 2Na_2SO_4 + 3H_2O$ powder mixture, before and after calcination at different temperatures.

The anatase crystallite or grain size presents in each sample was estimated from the XRD peak broadening using the Scherrer equation (eq. 3-2, page 66). The values ranged from 6 nm for the powder calcined at 400 ºC to 20 nm for the sample treated at 700ºC (Table 4-3).

Table 4-3. Influence of calcination temperature on the phase composition and particle size of the TiO_2 nanopowders obtained by mechanochemical processing. Crystalline size was determined using the Scherrer equation. Particle diameter was estimated from TEM images. Surface area was derived from the N_2 adsorption isotherms applying the BET theory. BET particle diameter was calculated from the BET surface area considering spherical monodisperse particles.

Sample	Phase	Crystalline size (nm)	Particle diameter (nm)	Surface area (m^2/g)	BET Particle diameter (nm)
As-milled	Amorphous	-	2 - 4	298	5
400 ºC	Anatase	6	6-11	170	9
500 ºC	Anatase	10	Not measured	121	13
600 ºC	Anatase	13	8-15	78	20
700 ºC	Anatase/Rutile	20	Not measured	35	44

TEM observations were performed to investigate the nanostructure of the as-synthesized powders. Figure 4-8 shows two representative images of the as-milled TiO_2 sample.

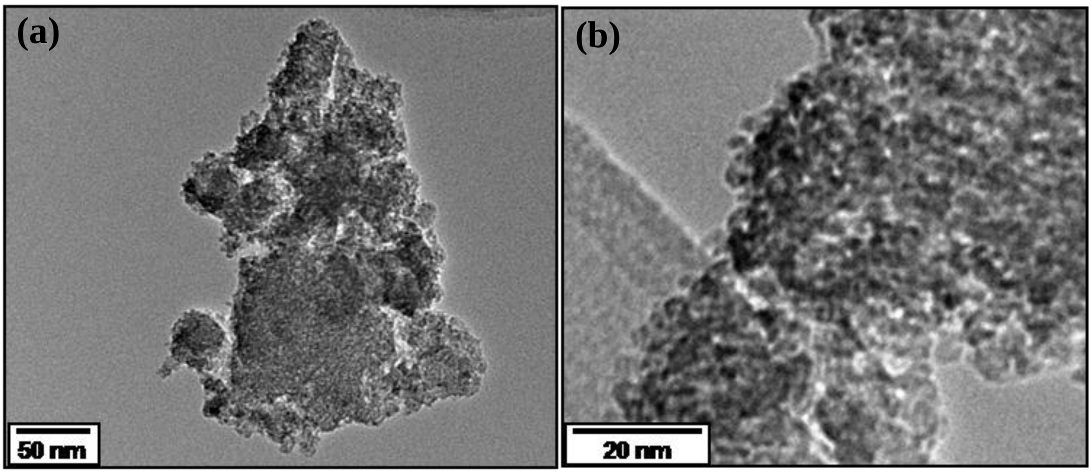

Figure 4-8. TEM images at different magnification of the TiO_2 as-milled powder after washing.

The powder consisted of aggregates 50-500 nm in size, which were actually formed by crystallites 2-4 nm in size. As discussed above, the TiO_2 was amorphous before heat treatment, so that no diffraction peaks were appreciated in the XRD pattern. It should be remarked that in mechanochemical solid-state processes, very fast reactions take place since the nanometer crystallite sizes increases the reaction kinetics.[259]

The reason of the large aggregates formed during ball-milling can be due to several factors: first, the diluent weight fraction (65 % of Na_2SO_4) in the final mixture may not have been high enough to prevent TiO_2 crystallites to be interconnected;[146] second, the high thermal energy generated by the reaction can also be responsible for the formation of such aggregates.[147] Logically, both factors are strongly linked, because a higher diluent fraction incorporated implies a reduction of the temperature in the system while reaction is taking place.

TEM images of the calcined (600 ºC) and subsequently washed TiO_2 powder is shown in Figure 4-9. These TiO_2 nanoparticles are also aggregated. However, individual nanoparticles with irregular shapes can easily be distinguished. As clearly observed, particles are in contact with each other and in some cases are sharing faces (black arrows in Figure 4-9(a)), but it seems that nanoparticles are not fused and they maintain their individuality. If pictures in Figure 4-8 and Figure 4-9 are compared it is obvious that crystals have grown during the heat treatment. The crystal size of the nanopowders before calcination was around 2-4 nm (Table 4-3), and it increased up to 8-15 nm after calcination at 600 ºC. The values extracted from TEM images are in general in fairly agreement with those calculated from the XRD peaks broadening, corroborating that nanoparticles are monocrystalline.

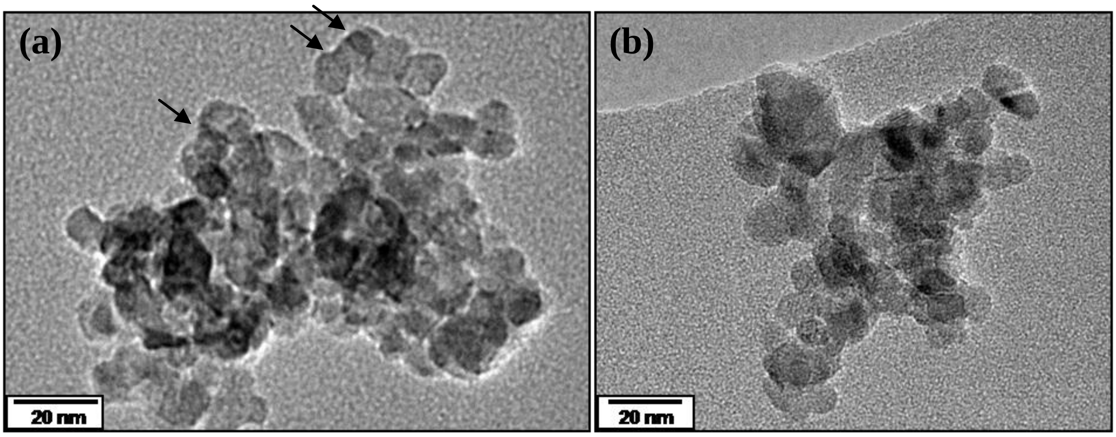

Figure 4-9. TEM images of the as-milled TiO_2 powder after calcination at 600 ºC and following washing. Black arrows indicate particles sharing faces.

Figure 4-10 contains the nitrogen adsorption-desorption isotherms for the TiO_2 powders, before and after calcination at different temperatures. All isotherms show essentially the same behaviour, with the only difference of the amount of adsorbed gas. The higher calcination temperature, the lower amount of adsorbed gas. The isotherms belong to the type II, with no hysteresis at low pressures, which is characteristic of non-porous materials.[260] However, the isotherms presented a hysteresis loop at high pressures, which resembles a type H3.[260] Such hysteresis is ascribed to aggregates (loose assemblies) of plate-like particles leading to slit-shape pores. Generally such loops do not flatten at high p/p_o.[261] The final adsorbed volume at high relative pressures is attributed to capillary condensation in voids between grains. With regards to the morphology of the nanoparticles, is difficult to assess whether they posses a platelike shape just by a closer look to their nanostructure in the TEM images. However, it is rather common to obtain such morphologies in nanoparticles synthesized by mechanochemical processing.[262, 263]

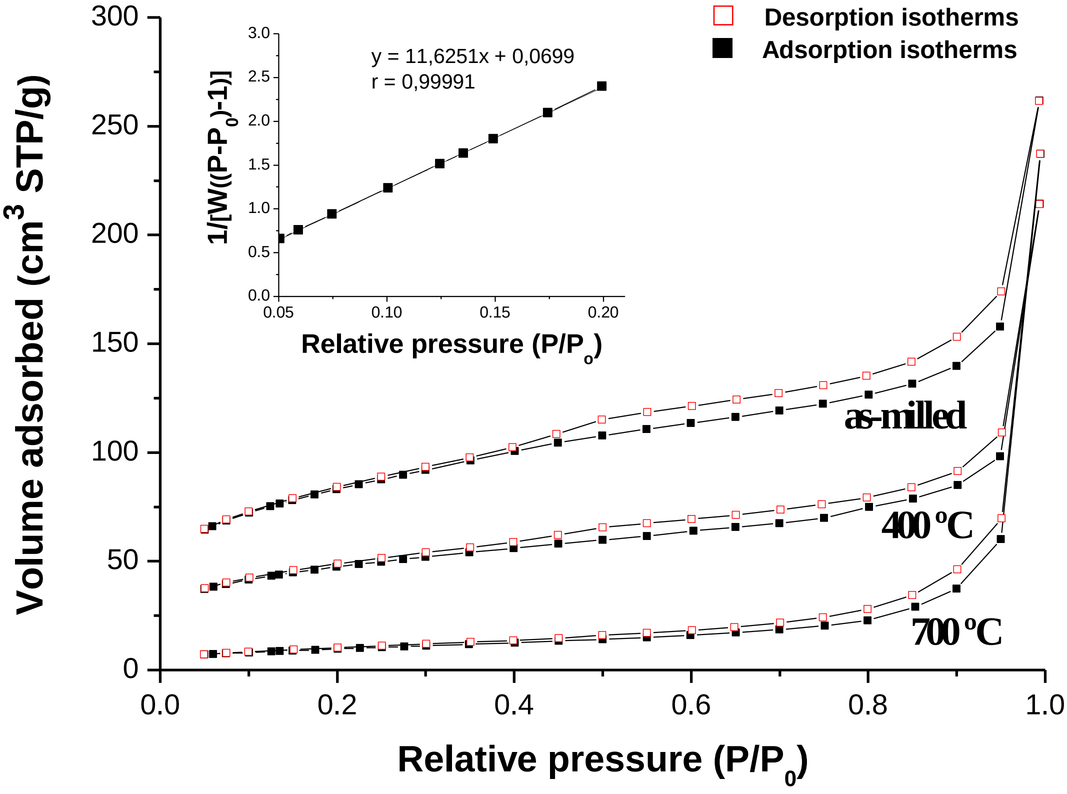

Figure 4-10. Nitrogen adsorption/desorption isotherms for the TiO_2 nanopowders before and after calcination at 400 and 700 ºC. The inset includes an example of a BET plot of the sample without calcination for relative pressures up to 0.20. This plot allowed calculating a surface area of 298 m^2/g.

Based on the TEM observations, one could expect that aggregation could reduce the exposed surface area of the nanoparticles. However, the surface area values determined by the BET theory were considerably high (Table 4-3). As clearly seen, the surface area shows a strong dependence on calcination temperature. The higher calcination temperature, the lower surface area. This can be explained by the growth of the crystals.

Taken the BET surface area values, we calculate the theoretical nanoparticle diameter corresponding to spherical particles. This theoretical size was similar to that observed by TEM. While the BET surface area for the as-milled sample was ca. 300 m^2/g, corresponding to a BET particle size of 5 nm, the crystallite size determined from the TEM images was in the range of 2-4 nm (Table 4-3). Since particles were partially agglomerated, the BET area is therefore slightly lower than it would correspond to well-dispersed and isolated nanoparticles. Nevertheless, the high surface area suggests that there is still a certain extent of nanoparticles surface that is accessible to the nitrogen gas. The same trend was observed for the calcined samples with anatase as the only phase. It should be noted that there is a difference between the particle size observed by TEM and that calculated from the BET surface area, for the sample calcined at 700 ºC (Table 4-3). This discrepancy could be attributed to the fact that the sample contained larger rutile grains, which can be the responsible for giving lower surfaces areas (35 m^2/g).

In conclusion, the results indicate that the nanoparticles are crystalline and non-porous and that the total surface area is related to the external area of the nanocrystals.

4.1.2.1 *Photocatalytic activity*

Titanium dioxide is a semiconductor photocatalyst able to initiate the formation of surface radicals under near UV wavelengths[153] (its band gap energy is around 3.2 eV). In this section, the colour-fading of methylene blue (MB), as a model molecule, was monitored in order to evaluate the photocatalytic activity of the nanopowders synthesized by mechanical processing and subsequent calcination. However, MB adsorption on nanoparticles also may contribute to reduce its concentration. Therefore, prior to evaluate the photocatalytic efficiency, we quantified the amount of dye that nanoparticles can adsorb in the absence of UV radiation (see Table 4-4). In this experiment, the TiO_2 nanoparticles, calcined at temperatures ranging from 400 to 700 ºC, were dispersed in an aqueous solution containing 35 ppm MB with the aid of an ultrasonic bath, which partially disrupted particle aggregates. Concentration of TiO_2 was 1g/L in all cases. After one hour of mechanical agitation, the nanoparticles were separated by centrifugation and the concentration of MB in the supernatant was measured using UV spectroscopy.

Table 4-4. Effect of calcination temperature on the efficiency of titanium dioxide (TiO_2) nanoparticles to adsorb and to degradate methylene blue dye (MB) by a photocatalytic reaction under UV radiation. The concentration of TiO_2 and MB were 1 g/L and 35 ppm, respectively.

Sample (calcination T)	Adsorption (mg dye/mg TiO_2)	% Initial adsorption (wt%)	Reaction constant (min^{-1})
400 ºC	0.020	56.0	0.0018
500 ºC	0.018	48.7	0.0103
600 ºC	0.011	30.2	0.0244
700 ºC	0.006	15.3	0.0170

The % initial adsorption, calculated as the weight fraction of adsorbed methylene blue on TiO_2 nanoparticles with respect to the initial concentration of MB dye in solution, dropped from 56 to 15.3 wt% when calcination temperature was increased from 400 to 700 ºC, respectively (Table 4-4). Such values are particularly high, being the adsorption greater than 50 wt% for the sample calcined at 400 ºC. Although the extent of adsorption is frequently omitted, it needs to be taken in consideration because adsorption is not negligible respect to degradation. This high adsorption seems to be related to the high surface areas that nanoparticles possess, as surface area also decreases when increasing calcination temperature (Table 4-3). Another important parameter that can influence adsorption capacity is the hydrophilicity of TiO_2 surfaces. The hydrophilic properties of TiO_2 surface can be assessed by FTIR spectra, as shown in Figure 4-11.

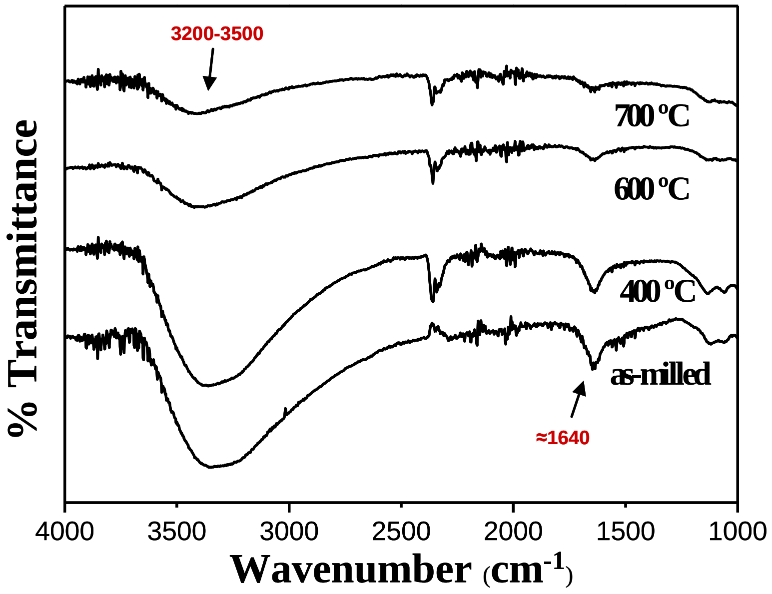

Figure 4-11. FTIR spectra of the as-milled TiO_2 samples before and after calcination at different temperatures. For clarity, the transmittance (in arbitrary units) has been multiplied by arbitrary factors.

The curves strongly indicate the presence of hydroxyl groups, especially for samples treated at lower temperatures. While the band at 1637 cm^{-1} corresponds to O-H bending modes of water molecules, the broad-band peak at 3200-3500 cm^{-1} is attributed to the O-H stretching of physisorbed water. It has been recognized that surface hydroxyl groups play an important role in the efficiency of the photocatalysts.[264]. Therefore, the reduction of dye adsorption can be associated to the reduction of both surface area and pore volume between aggregates and also to the loss of hydroxyl groups as a consequence of the increase of calcination temperature.

Figure 4-12 shows the evolution curves of photocatalytic degradation of MB on various TiO_2 calcined samples at different temperatures. As detailed in the experimental section, the solution was kept under mechanical stirring and was continuously irradiated with a UV lamp of maximum emission wavelength of 360 nm.

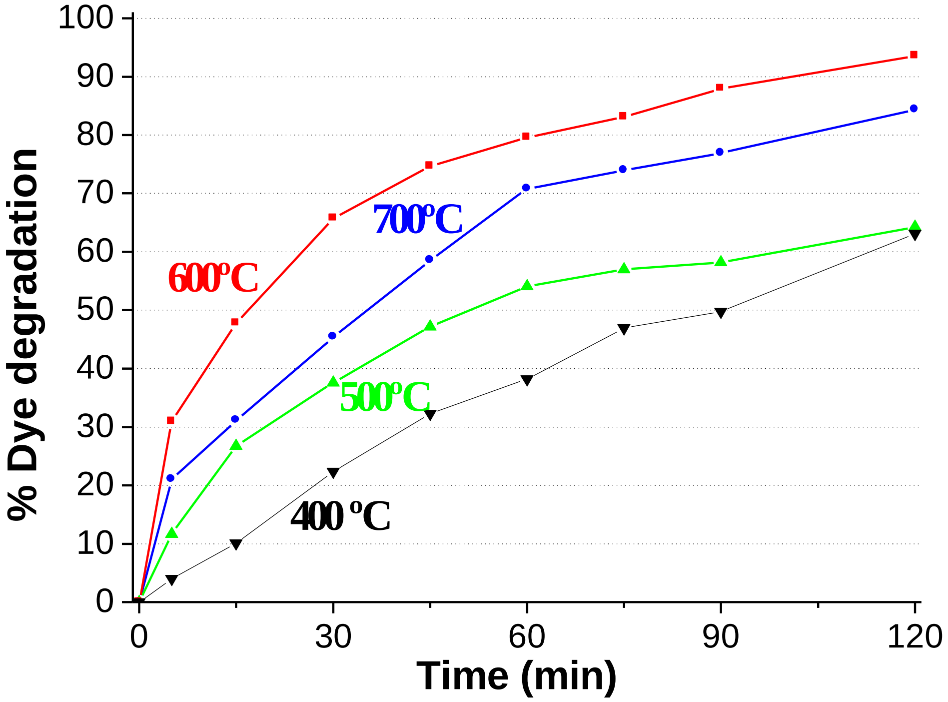

Figure 4-12. Methylene blue (MB) degradation (25 ºC) under UV radiation as a function of time, for samples containing 1g/L of TiO_2 calcined at different temperatures. The initial MB concentration was 35 ppm. The dispersion was stirred in a hot plate at 1100 r.p.m.

Methylene blue degradation is expressed with respect to the initial MB concentration in solution, so that the quantity adsorbed onto the nanoparticles has been already subtracted. It should be mentioned that prior to that, we conducted a blank without TiO_2 nanoparticles. In this experiment, it was confirmed that MB was not oxidized in the absence of photocatalyst. As clearly seen from the Figure 4-12, the higher response to UV was reached with the sample calcined at 600 ºC. It should be pointed out that just after 5 min of reaction, a 30 % of the MB had been degradated and more than 90 % was eliminated at the end of the reaction (120 min). Such values were significantly much higher than the values reached for the sample calcined at 400 ºC, which was the sample with lowest activity (4 and 63% degradation at 5 and 120 min, respectively). Even though the final concentration of MB in the case of nanoparticles treated at 400 and 500 ºC was nearly the same, the degradation ratio was faster for the latter, as deduced from the slope in the first region of the graph.

Since it was demonstrated that the surface area of the nanoparticles dropped upon increasing calcination temperature, one could expect a reduction of the photocatalytic activity if this would be the only parameter playing a role in the activity of the TiO_2 photocatalyst. Nevertheless, it is well known that a higher degree of crystallinity enhances the efficiency of the photocatalytic reactions.[156, 265] Photogenerated electron-hole pairs can recombine in trapping sites before being transferred from TiO_2 to methylene blue molecules. For a given material, the higher crystallinity, the lower trapped sites within the crystal lattice.[254] Almost certainly, this is the reason for the highest activity of the sample calcined at 600 ºC, which possesses a mean crystallite size of 13 nm, determined by XRD peak broadening, and a surface area of 78 m^2/g.

However, a decrease in catalytic activity was observed from 600 ºC to 700 ºC. As observed in the XRD patterns (Figure 4-7), rutile phase appeared at calcination temperatures of ca. 650 ºC. This phase, less active than anatase, is present in the sample calcined at 700 ºC, as expected. This may be responsible for the lower activity of this sample, compared to that reached for the sample calcined at 600ºC, even though rutile phase was in very minor proportion.

With regards to the samples calcined at lower temperatures, it must be underlined that for sufficiently small particles, recombination of electron-hole pairs becomes the predominant effect, which can also have an influence in the lower photocatalytic efficiency showed by these two samples. In one hand, nanoparticles have high surface areas (170 m^2/g for the TiO_2 calcined at 400 ºC), but on the other hand, its crystallinity is rather low.

In the present case, the methylene blue degradation was considered to follow a first order kinetics, following the equation: [266, 267]

$$ln\left(\frac{C}{C_0}\right) = -kt \tag{4-4}$$

where C_0 is the initial concentration, C is the concentration as a function of time (t), and k (min^{-1}) is the reaction constant. The k for the samples calcined at different temperatures, was calculated from the slope in the $ln(C_0/C)$ vs. time plots, as shown in Figure 4-13(a). It is evident that the highest catalytic efficiency corresponds to the sample calcined at 600 ºC, though the MB degradation rate for this sample slightly deviated from the model. This indicates that it may not follow a first order reaction. The correlation coefficients were, however, acceptable in the other cases. For better comparison, reaction constants (k) are plotted in Figure 4-13(b).

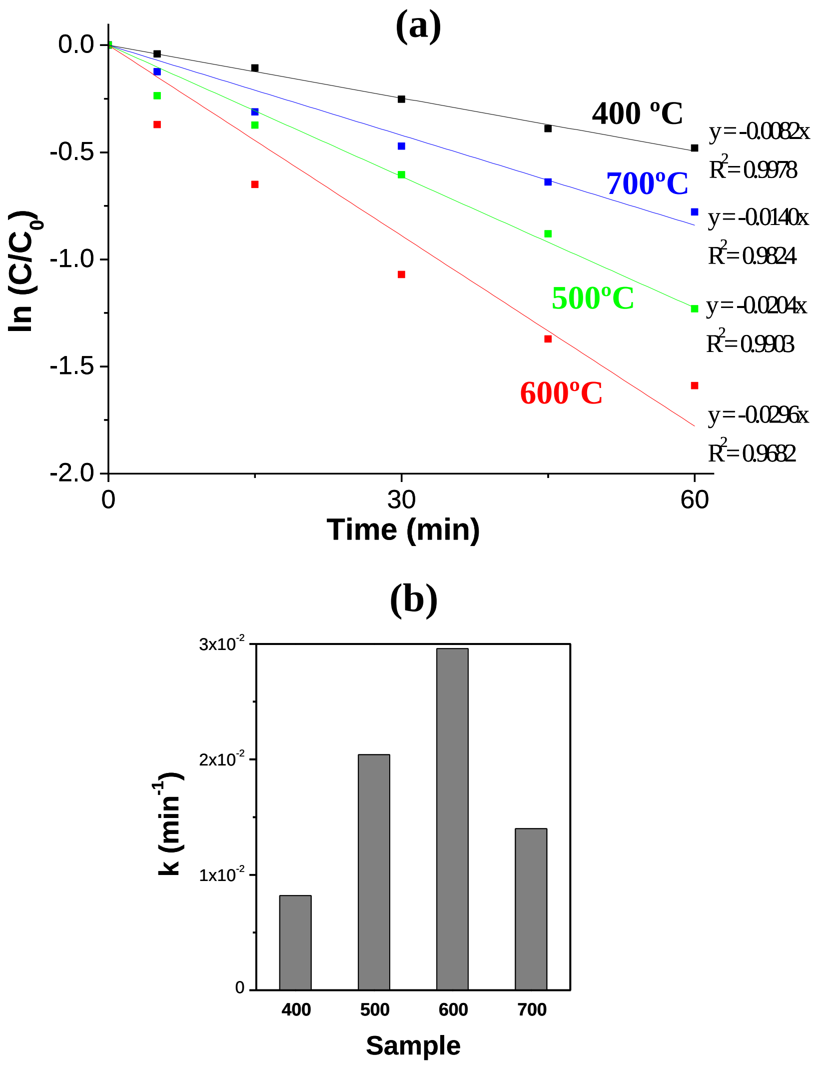

Figure 4-13. (a) First-order kinetics of methylene blue degradation using TiO_2 nanoparticles calcined at different temperatures. The reaction constants (k (min^{-1})) plotted in (b) were obtained from the slopes of the curves shown in (a).

Noticeably, the rate constant (*k*) of the sample calcined at 600 ºC is 3.5 times higher than that showed for the sample calcined at 400 ºC. As mentioned above, further calcination at higher temperatures (700 ºC) reduced the photocatalytic activity of the nanoparticles.

4.2 INCORPORATION OF IRON OXIDE PARTICLES IN POLY(STYRENE-DIVINYLBENZENE) MATERIALS

As mentioned in the Introduction (section 1.3.2), the use of highly concentrated emulsions (also denoted high internal phase emulsions, HIPEs) as templates, has been shown to be an effective route for the preparation of macroporous polymers (referred as polyHIPEs).[181] Over the past two decades, the research has been mainly focused on controlling the open-cell structure of such materials and providing them with new chemical surface functionalities. More recently, several reports have proposed the integration of metal nanostructures (such as gold[199] or palladium[268] nanoparticles) in already formed polyHIPEs. Following a different approach, inorganic oxide nanoparticles were successfully incorporated into the polymer walls of polyHIPEs, by taking advantage of the ability of nanoparticles to stabilize emulsions.[192, 204, 208] However, little attention has been paid to the control of the dispersion of nanoparticles in the polymeric hosts.[223] It is well known that dispersion of nanoparticles in polymer matrices has proven difficulty, often resulting in phase separation or particle-clustering. Hence, particles are generally surface-modified with ligands, which markedly influence particle arrangement within polymer matrices.[269]

Even though polymeric particles[229, 270-274] and colloidosomes[275-277] with magnetic behaviour have deserved increasing attention, little work has been done concerning magnetic macroporous polymeric materials.[251, 278, 279]. In this chapter, surface-modified iron oxide nanoparticles have been incorporated in poly(styrene-divinylbenzene) based materials. The schematic representation in Figure 4-14 illustrates the three different steps adopted for this purpose.

4.2.1 Bulk Polymerization

In a first preliminary step (point 1 in Figure 4-14), non-porous free-standing nanocomposites were synthesized to evaluate the degree of particle dispersability of two different oleic acid surface-modified iron oxide nanoparticles (NP_3 and NP_8, section 4.1.1) in polymeric materials. At first, proof-of-concept experiments were carried out with the aim of selecting a desired oil soluble initiator for the conventional free-radical polymerization of the monomers. For this purpose, either α,α'-azoisobutyronitrile (AIBN) or 2,2'-Azobis-(2,4-dimethyl) valeronitrile (ADVN, used in low temperature polymerizations) were solubilised into the monomer mixture (styrene:divinylbenzene ratio of 4:1 by weight) and then placed into a bath at 60 or 40 ºC, respectively, for 24 hours. Thermal decomposition to two free radicals per initiator molecule is strictly controlled by temperature.

PRELIMINARY EXPERIMENTS

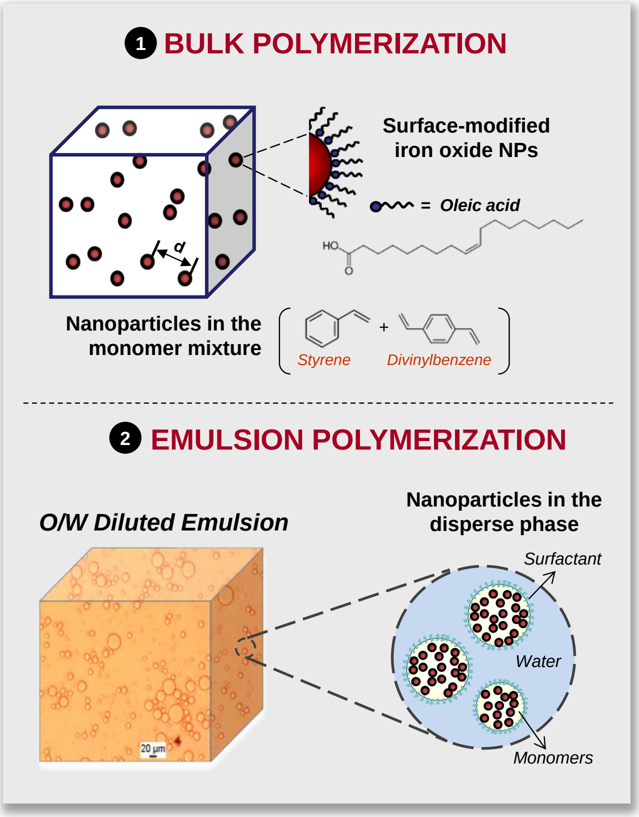

PREPARATION OF POROUS NANOCOMPOSITES

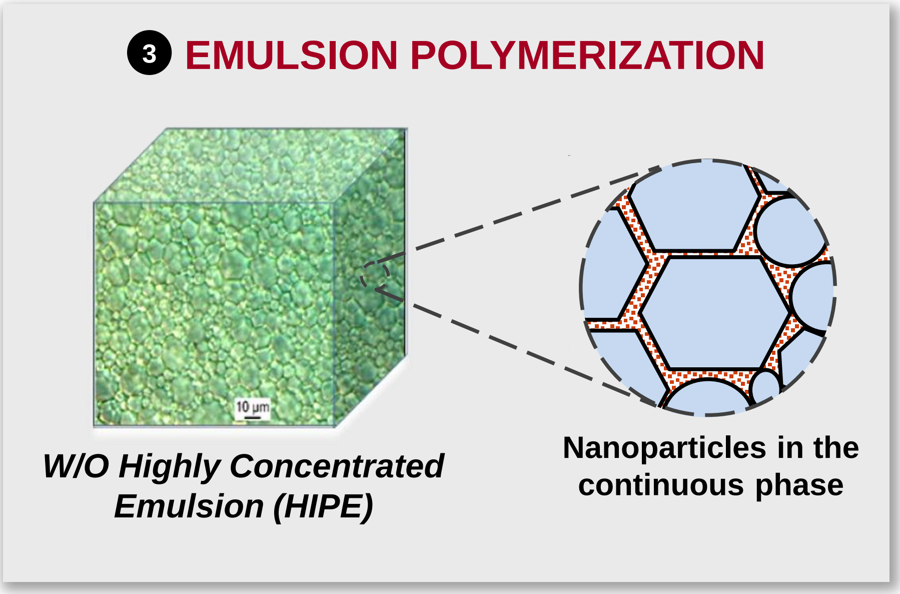

Figure 4-14. Scheme of the three steps developed in this chapter for the synthesis of nanocomposites by incorporating oleic acid surface-modified nanoparticles in poly(styrene-divinylbenzene) based materials. Interparticle spacing (d) is indicated in 1.

While transparent polymers were obtained when ADVN was used, rather turbid materials were observed for AIBN-initiated polymerization. Therefore, ADVN was chosen to initiate the bulk polymerization reactions.

Later on, NP_3 and NP_8 were dispersed in the monomer mixture at different concentrations, and then polymerized at 40 ºC during 24 hours. The appearance of monoliths containing 0.6 and 3.1 wt% NP_3 is shown in Figure 4-15. The optical homogeneity of the sample with lower NP_3 concentration indicates the absence of macrophase separation. Furthermore, it also demonstrates the good dispersability of the nanoparticles. It should be mentioned that acrylic acid was added into the initial nanoparticle suspension (nanoparticles -acrylic acid ratio 3:1 by weight) to enhance the polymer-particle compatibility. Samples with no acrylic acid appeared opaque and turbid due to macroscopic phase separation. Apart from iron oxide nanoparticles, gold and silver nanoparticles have been also included in polystyrene-based non-porous materials using similar approaches. Some of the results obtained are included as supporting information in the Appendix (Figure 10-2 and Figure 10-3).

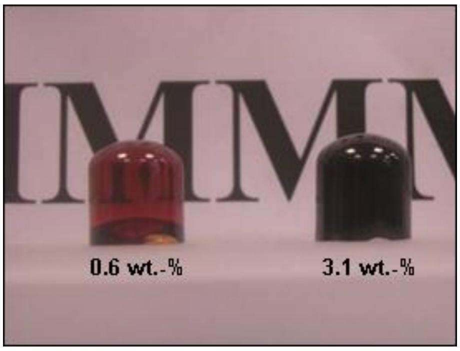

Figure 4-15. Polystyrene-divinylbenzene non-porous monoliths containing 0.6 and 3.1 wt% of NP_3. Acrylic acid was added to increase the polymer NP_3-compatibility (ratio NP_3-acrylic acid 3:1 by weight). Optical homogeneity of the sample with 0.6 wt% NP_3 indicates absence of macrophase separation.

A comparative analysis of samples with 16, 29 and 46 wt% NP_3 (determined by TGA) was carried out by TEM (Figure 4-16). Samples were previously sliced to the same thickness (ca. 60 nm) using an ultramicrotome. As seen in these images, the organic polymer is transparent to the electron beam and particles can be easily distinguished. When NP_3 content was relatively low (Figure 4-16(a)), well-dispersed and homogeneously distributed nanoparticles with low extent of aggregation were observed. It is clear that in the present case, the oleic acid in combination with acrylic acid allowed preventing nanoparticle aggregation.

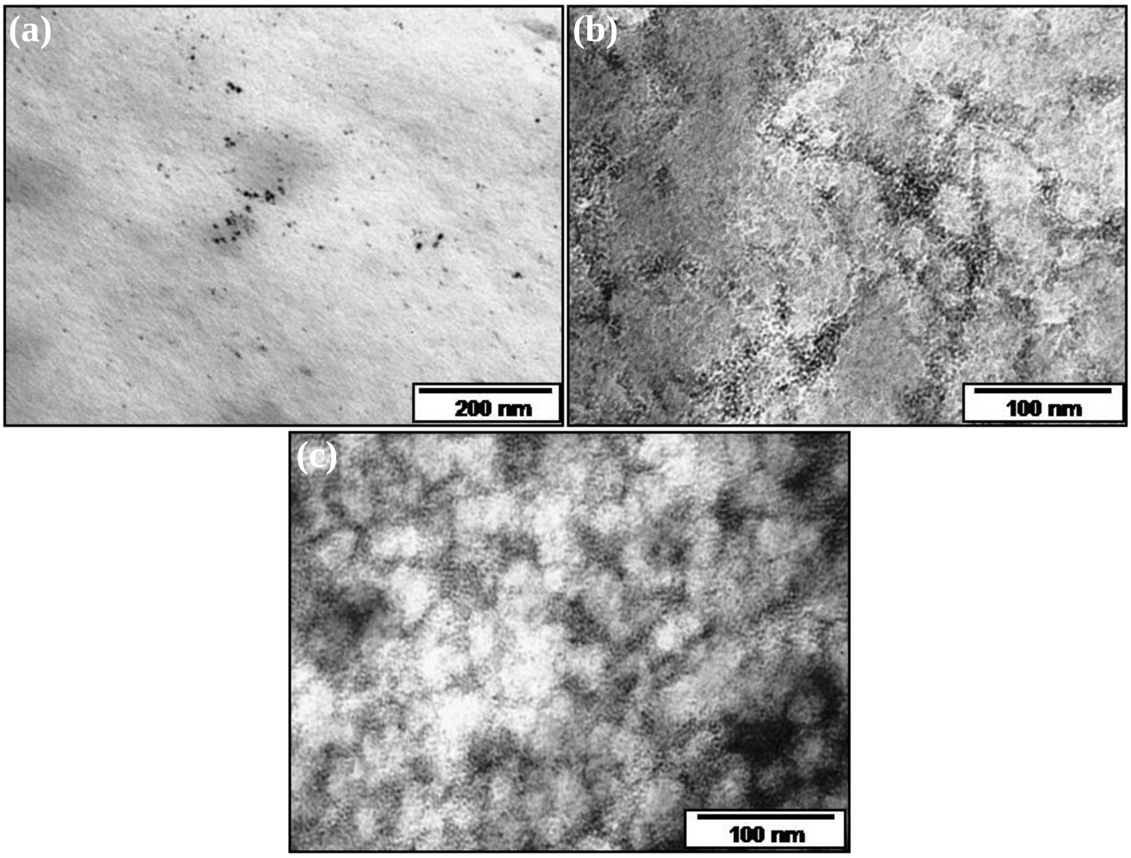

Figure 4-16. Representative transmission electron microscopy images of non-porous nanocomposites with (a) 16 wt%, (b) 29 wt% and (c) 46 wt% NP_3 nanoparticles.

Further increase of NP_3 concentration (29 wt%, Figure 4-16(b)) gave raise to partial aggregation, and a certain degree of clustering forming segregated domains was observed in the entire sample examined. However, it is reasonable to think that oleic acid can act as a physical spacer that prevents sticking of the particles.[280] In this context, it has been described that despite the fact that nanoparticles may physically touch each other, there is still no exchange coupling between them.[281]

As a result of the arrangement adopted by NP_3 at high nanoparticle concentration, a correlation peak appeared in the small angle X-ray scattering (SAXS) intensity profile for the sample with 29 wt% NP_3 (red curve in Figure 4-17). Such sample led to a correlation distance of 5.6 nm. When nanoparticle concentration was increased to 49 wt%, the distance slightly decreased to 5.0 nm, on account of reduction of interparticle distance.

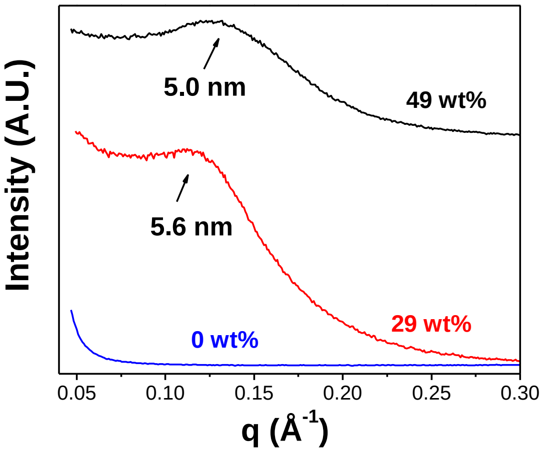

Figure 4-17. Small X-ray scattering (SAXS) spectra for the non-porous nanocomposites, containing distinct NP_3 concentrations. Correlation peaks associated with interparticle distances are indicated next to the SAXS intensity curves.

Non-porous nanocomposites were also prepared by integration of larger nanoparticles (NP_8). It should be remarked here, that materials with NP_8 concentration higher than 25 wt% could not be prepared as they become very soft and fragile. Figure 4-18 shows TEM images for the nanocomposites containing (a) 10 and (b) 25 wt% NP_8. In contrast with the nanocomposites containing NP_3, a homogeneous (random) distribution was observed, with no evidence of micro-segregation. As a consequence, the SAXS results did not show correlation peaks within the experimental q-range for materials containing NP_8 (Figure 4-18(c)). Nevertheless, the possibility that a correlation peak may appear at q values beyond the range of the instrument cannot be ruled out.

The exact reason of cluster formation (Figure 4-16(b,c)) in systems containing NP_3 is not clear. However, weak van der Waals interaction forces may influence such segregation more strongly in the case of smaller and less polydisperse nanoparticles. A major requirement in polymer composites is that the protective nanoparticle coating layer and the polymer should be chemically compatible. In the present work, particle stability is controlled by adsorption of oleic acid on particle surfaces. Generally in the literature, interparticle distance is commonly modulated by either manipulation of the coating layer of self-assembly nanoparticles[282] or by using entities (such as dendrimers)[283] that space and regulate the spacing between nanoparticles. Furthermore, selective dispersion can be achieved by using diblock copolymers; nanoparticles can present high affinity to one specific domain leading to selective dispersion.[284, 285] Other methods found in the literature are based on functionalization of both parts with complementary recognition units, providing efficient specificity.[286] In all of them lowering the nanoparticle size dispersity is considered to be of paramount importance.

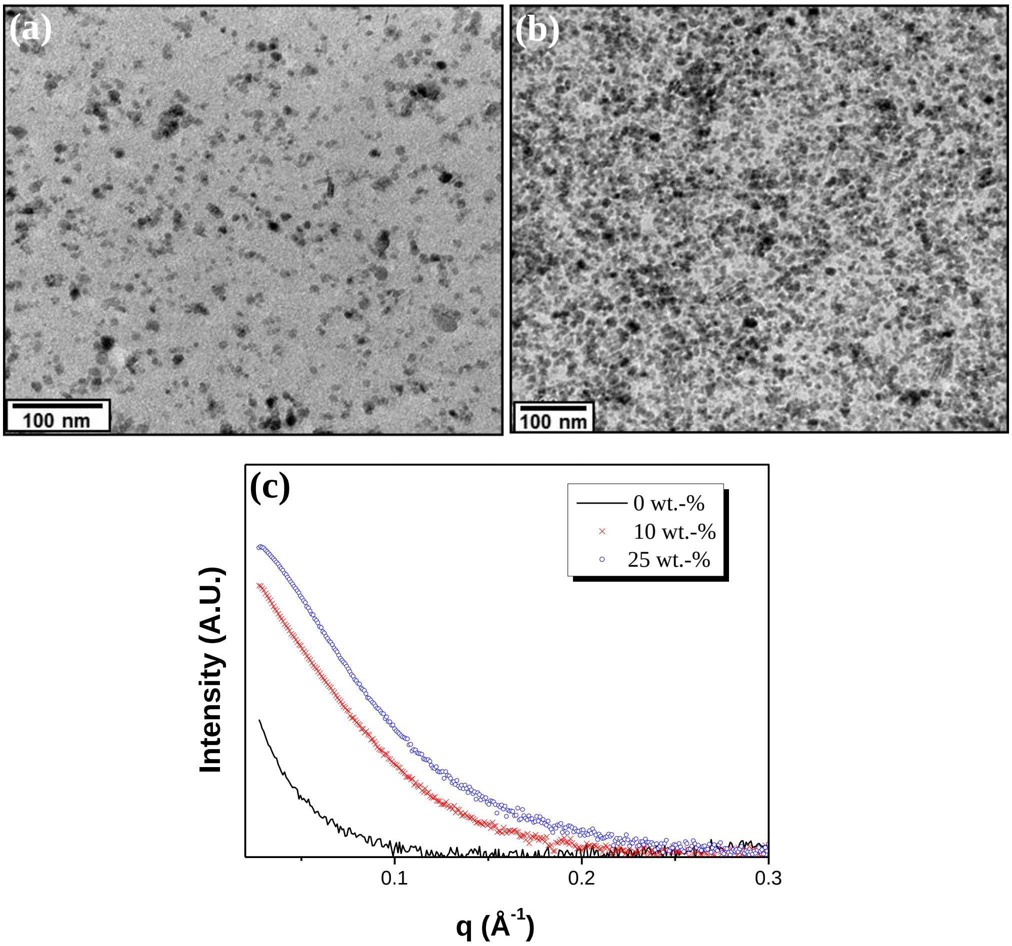

Figure 4-18. Transmission electron microscopy images of non-porous nanocomposites containing (a) 10 wt% and (b) 25 wt% NP_8; (c) SAXS spectra of the nanocomposites shown in (a) and (b); as a comparison one spectra without nanoparticles is also included. No correlation peaks were observed.

4.2.2 Polymerization in the Internal Phase of O/W Diluted Emulsions

Following the procedure described in the experimental section (3.2.8), 10 wt% NP_3 (respect to oil phase) were integrated within polymeric microparticles, via the polymerization of the internal phase of a diluted O/W emulsion (point 2 in Figure 4-14). The emulsion was stabilized with 1.2 wt% sodium dodecyl sulphate surfactant, and the internal phase (5 wt%) consisted of a mixture of styrene:divinylbenzene with weight ratio of 4:1. The resulting polymer particles, containing NP_3 nanoparticles, were then dried, purified and examined by scanning electron microscopy (Figure 4-19). The sample is composed by polydisperse microparticles with sizes ranging from 0.5 to 7 µm, approximately. Such polydispersity arises from the method used to prepare the precursor emulsion, i.e. ultra-turrax homogenizer. As a result of the embedment of the magnetic particles within the polymeric matrix, the material can be attracted and dragged using a strong magnet, as illustrated in the inset in the same figure.

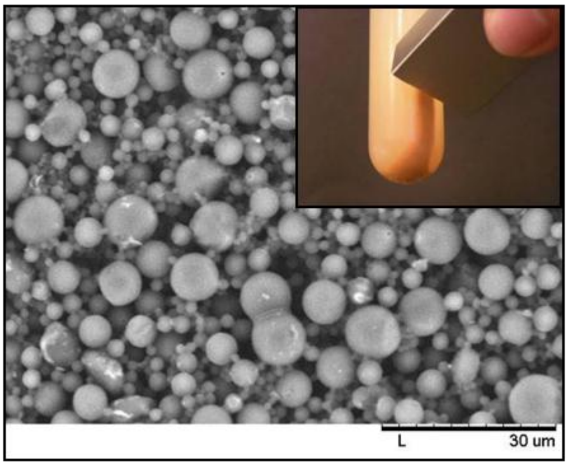

Figure 4-19. Poly(styrene-divinylbenzene) microparticles resulting from the polymerization of the internal phase of a diluted o/w emulsion. The initial monomer weight content in the emulsion was 5 wt% and the surfactant concentration (sodium dodecyl sulfate) was 1.2 wt% with respect to the water content. The inset shows the particles being attracted and dragged using a strong magnet. Magnetic behaviour comes from the presence of 10 wt% NP_3 within the polymeric particles.

The arrangement of NP_3 within the polymeric particles has been proved by TEM observations (Figure 4-20).

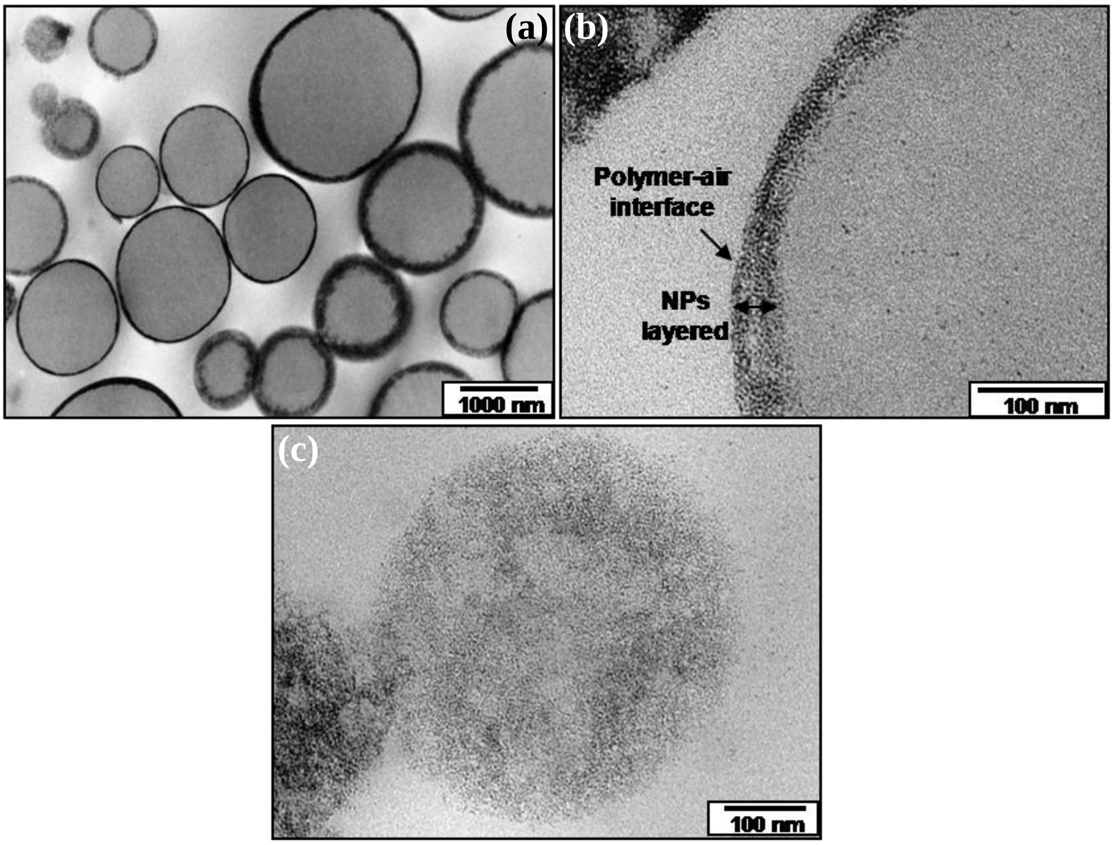

Figure 4-20. TEM images of cross-sectional slices from the same polymeric microparticles. Nanoparticles (NPs) are preferentially located at the polymer-air interfaces (a,b), but they are homogeneously distributed inside small (below 500 μm) polymer microparticles (c).

Now, the powdered samples were first embedded in a Spurr resin and then carefully cut with an ultramicrotome, as described in detail in the experimental part (3.2.9.1). In Figure 4-20(a,b), a predominant pattern is clearly identified. Remarkably, rather than be dispersed in the bulk of the particles, NP_3 were found to be preferentially placed near the polymer-air interfaces. Such an arrangement is most likely due to a partial affinity of the nanoparticles for the interface. The ability of surface-active nanoparticles to migrate spontaneously to water-oil interfaces, and consequently stabilize emulsions is well-documented and has been extensively described since firstly reported more than one hundred years ago.[47, 48] These observations raised the question if oleic acid surface-modified iron oxide nanoparticles are able to act as emulsifiers by themselves. This assumption will be explored in further sections.

In any case, the TEM images clearly demonstrate that nanoparticles arrange themselves forming a thick layer around the interface. The thickness of these layers was estimated to be between 40 and 120 nm. The difference between similar particles can be attributed to the different regions of the particles from where the cuts were made, so that the particle areas which are approximately parallel to the cut plane may give the impression of thicker areas. Despite the affinity for the interface, well-dispersed nanoparticles were also observed in the core of these microparticles. Interestingly, the distribution of NP_3 seems to be more homogeneous in small polymer microparticles. This case, which is exemplified in Figure 4-20(c), confirms that the oleic acid capping prevents aggregation and formation of nanoparticle-clustering. As in non-porous monoliths (Figure 4-16), nanoparticle individuality was preserved.

4.2.3 Polymerization in the Continuous Phase of W/O Highly Concentrated Emulsions prepared by the Phase Inversion Temperature Method

The preparation of macroporous poly(styrene-divinylbenzene) materials (polyHIPEs) using highly concentrated emulsions (HIPEs) as templates, by the phase inversion temperature (PIT) method was firstly reported by Esquena et al.[178] Resultant macroporous polymers were characterized by possessing smaller and less polydisperse pores than others prepared from HIPEs by conventional methods (i.e. dropwise addition). In that work, pure poly(ethylenglycol) n-alkylether non-ionic surfactants were used. However, these pure surfactants are rather expensive and large quantities are not commercially available. Because of the low cost and easier scale production, alternative commercial surfactants of the same type were searched.

4.2.3.1 *Selection of surfactant system*

As outlined in the introduction (section 1.2.1.3), ethoxylated nonionic surfactants change their preferential solubility from water to oil at the hydrophilic-lipophilic balance (HLB) temperature (also called PIT). This allows transforming an initial O/W into a W/O emulsion, by heating up the system across this temperature.

Taking as a reference the work undertook by Esquena et al,[178] several surfactant candidates were initially selected (Table 4-5) aiming to reach a HLB number near 11.4. The respective HLB numbers were determined using the equation developed by Shinoda and Kunieda,[44]

$$PIT = K_{oil}\,(HLB - N_{oil}) \tag{4-5}$$

which relates the phase inversion temperature (PIT) to the HLB number of pure poly(ethylene glycol) alkyl ether type surfactants. K_{oil} is a constant equal to 17 ºC and the parameter N_{oil} indicates the degree of oil hydrophobicity. This equation relates three parameters (PIT, HLB and N_{oil}). If two of them are known (e.g. PIT and N_{oil}), one can calculate the value of the third one (e.g. HLB). For a given system, the lower surfactant HLB number (i.e. more hydrophobic), the lower PIT.

Table 4-5. Experimental PIT and calculated HLB numbers, using the eq. 4-5, for 3 different nonionic ethoxylated surfactants. Water-tetradecane volume ratio and surfactant concentration in emulsions were 80:20 and 4 wt%, respectively.

Surfactant System	Experimental PIT (ºC)	Calculated HLB number
$C_{12\text{-}14}(EO)_4$	31.0	9.7
$C_{13\text{-}15}(EO)_5$	53.8	10.9
$C_{13\text{-}15}(EO)_6$	> 100	Unknown
$C_{13\text{-}15}(EO)_5/C_{13\text{-}15}(EO)_6$ = 70/30 by wt%	63.0	11.4

In these preliminary studies, the PIT of systems with water / nonionic surfactant / tetradecane (Noil = 7.85)[44] was determined, by keeping the water-oil ratio (80:20 by volume) and surfactant concentration (4 wt%) constant. Then, surfactant HLB numbers were calculated using eq. 4-5. For that purpose, conductometric measurements as a function of temperature were carried out in a 50 mL reaction vessel with constant agitation (700 r.p.m), using a magnetic stirrer device. A clear example was given in Figure 3-3 (page 68), in which the increase in temperature induces a three orders-of-magnitude decrease in conductivity. The region with high conductivities corresponds to O/W emulsions, while the region with much lower conductivities, which appear above the PIT, corresponds to W/O emulsions. As a rule, the PIT is taken as the average between the minimum and the maximum values of conductivity. The PIT values were calculated from both the heating and the cooling cycles. Table 4-5 contains the PIT temperatures and the corresponding HLB numbers calculated for the surfactants $C_{12-14}(EO)_4$ (Brij 30 NENA) and $C_{13-15}(EO)_5$ (Synperonic A5). Due to the fact that the PIT of the system containing $C_{13-13}(EO)_6$ (Renex NENA) was higher than 100 ºC, its determination was not made.

In such experiments, a W/O highly concentrated emulsion (80 vol% water) was obtained above the PIT of the system, starting from a diluted O/W emulsion (20 vol% oil). Mechanical agitation was required[178] because the starting point was not a one-phase region (i.e. microemulsion) in the phase diagram.[177] Moreover, the PIT could not be determined for surfactant concentrations lower than 4 wt%. In contrast to pure surfactants, the PIT for technical grade ethoxylated surfactants depends on composition, such the oil-water ratio or the surfactant concentration,[19, 45] due to the unequal distribution of surfactant species at the interface.[44]

Among several possible combinations, a surfactant mixture composed by 70 wt% $C_{13-15}(EO)_5$ and 30 wt% $C_{13-15}(EO)_6$ was chosen initially (Table 4-5). Such a mixture possesses an experimental PIT equal to 63 ºC and a calculated HLB value of 11.4. At this stage, the monomer mixture of styrene and divinylbenzene (ratio 4:1 by weight) was progressively incorporated in the continuous phase of the emulsions, since the main objective here is the obtention of polystyrene-based macroporous polymers. One factor that should be taken into account is that aromatic hydrocarbons have relatively higher solubilities in water. Therefore, they show values of N_{oil} (13.8 for styrene) higher than the values shown by aliphatic hydrocarbons.[178] This implies that such monomers tend to reduce the PIT, and more hydrophilic surfactant and/or the addition of aliphatic hydrocarbons is therefore required. This is the reason by which a surfactant mixture with an initial PIT of 63 ºC was selected. According to eq. 4-5, a theoretical PIT of around 5 ºC is expected when the monomer concentration in the continuous phase of the emulsions is 60 wt%. For higher monomer concentrations, theoretical PIT become negative and therefore phase inversion could not be achieved. However, we need to bear in mind that systems containing commercial surfactants are difficult to be predicted with absolute precision because of the unequal partition of species at the interface.[45]

Therefore, monomer concentration in the continuous phase was progressively increased, and as a consequence a reduction of the PIT was expected. A typical set of runs obtained by heating is depicted in Figure 4-21. As clearly seen, the higher monomer concentration, the lower PIT. It should be noted that in the curves without and with 10 wt% monomers in the continuous phase of the emulsions, a secondary peak before the sharp decrease in conductivity is observed. This could be attributed to the presence of surfactant liquid crystalline phases at certain temperatures.[45] Interestingly, when monomer concentration was 40 wt%, phase inversion occurred at approximately the same temperature than for 30 wt% (PIT of 29.7 and 29.9 ºC respectively), and phase inversion was not observed when monomer concentration was further increased to 50 wt%.

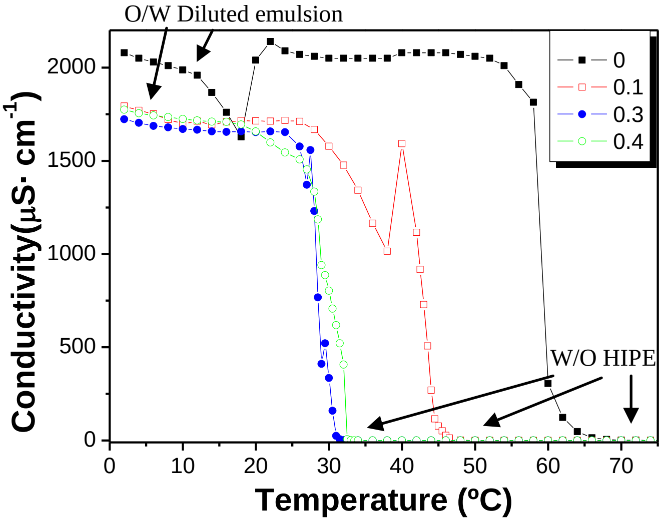

Figure 4-21. Conductivity as a function of temperature in the aqueous 10^{-2} M NaCl / surfactant / tetradecane + monomer systems. Surfactant concentration was 4 wt% (70 % $C_{13\text{-}15}(EO)_5$ - 30 % $C_{13\text{-}15}(EO)_6$) and the water/oil volume ratio was 80/20. NaCl was added to the aqueous phase to increase the conductivity signal. Emulsions were stirred with a magnetic stirrer device at 700 r.p.m. The values included in the legend indicate the monomer weight fraction in the oil phase of the emulsions.

Figure 4-22 shows the comparison of the experimental and theoretical (calculated) PITs temperatures for the systems described above, containing the surfactant mixture 70% $C_{13\text{-}15}(EO)_5$ – 30%$C_{13\text{-}15}(EO)_6$. These values are also summarized in Table 4-6.

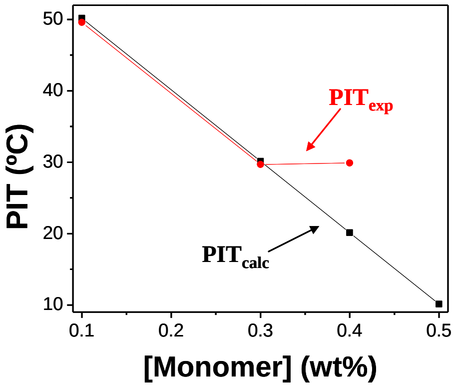

Figure 4-22. Calculated (PIT_{calc}) and experimental PITs (PIT_{exp}), as a function of initial monomer content (up to 50 wt%) in the oil phase of the emulsions evaluated in Figure 4-21. Experimental PITs were calculated from the heating cycle.

It can be seen that both, calculated and experimental PIT (determined from the heating cycle) are in good agreement up to 30 wt% monomer content in the continuous phase of the emulsions. Nevertheless, predicted phase inversion temperatures do not agree with PITs determined experimentally above 30 wt% monomer.

Table 4-6. Calculated and experimental phase inversion temperatures for emulsions containing 4 wt% of surfactant (70% $C_{13-15}(EO)_5$ - 30% $C_{13-15}(EO)_6$). Experimental PITs were determined from both heating and cooling cycles.

Monomers in the continuous phase (wt%)	W/O ratio (vol%)	Agitation (rpm)	Experimental PIT (ºC)		Calculated PIT (ºC)
			Heating cycle	Cooling Cycle	
10	80/20	700	49.6	49.6	50.2
30	80/20	700	29.7	29.7	30.1
40	80/20	700	29.9	29.9	20.1
50	90/10	700	45.0	7.4	10.1
50	90/10	1100	35.0	10.2	10.1

As mentioned above, phase inversion with 50 wt% of monomer in the continuous phase of the emulsions was not achieved. It has been recognised that aromatic molecules (such as styrene) can modify the properties of emulsions, reducing their stability due to its penetration into the surfactant monolayers.[179] We reasoned that with the surfactant system employed, a larger energy input might be required to achieve the desired inversion. Another alternative would be to reduce the monomer content in the overall emulsion by changing the water-oil volume ratio from 80/20 to 90/10, keeping the surfactant concentration constant.

Two new conductometric experiments were performed on emulsions having W/O volume ratios of 90/10, to evaluate the influence of agitation speed (Table 4-6). Two stirring rates were used, 700 and 1100 r.p.m. Concentration of monomers in the oil phase was kept constant at 50 wt%. Both heating (filled symbols) and cooling (empty symbols) cycles are shown in Figure 4-23.

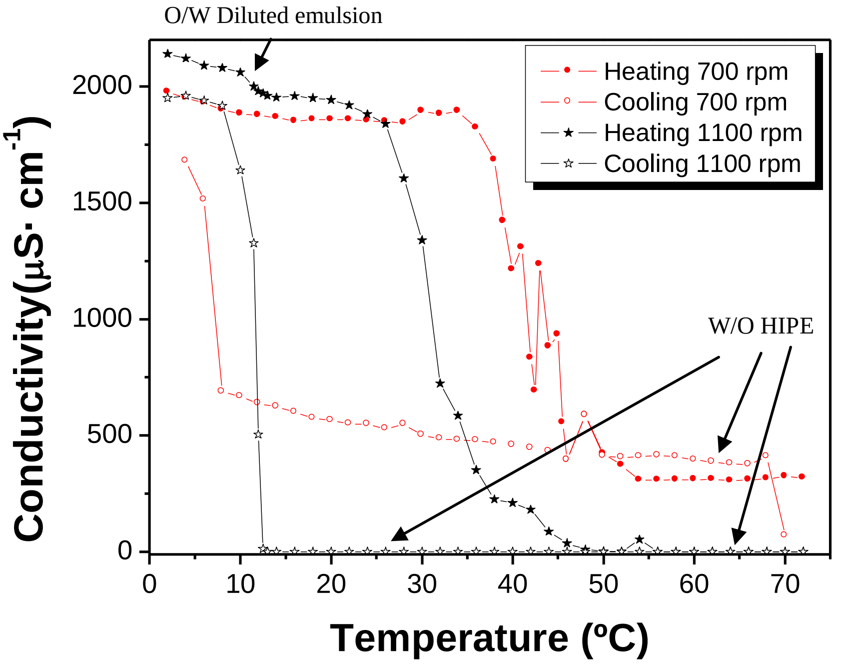

Figure 4-23. Conductivity as a function of temperature on heating and cooling in the aqueous 10^{-2} M NaCl / surfactant/ tetradecane + monomer systems. The effect of agitation speed applied during the experiment is shown. Surfactant concentration was 4 wt% (70% $C_{13-15}(EO)_5$ - 30% $C_{13-15}(EO)_6$), water/oil volume ratio was 90/10 and monomer concentration in the oil phase was 50 wt%. A hysteresis is observed between both heating and cooling cycles.

In these cases, the inversion from diluted O/W emulsions to W/O HIPEs is clearly observed. The results obtained indicate that:

I. Inversion is favoured in emulsions with water-oil volume ratios of 90/10 (Figure 4-23), possibly due to the reduction of total monomer amount in the overall emulsion. Interestingly, a marked hysteresis was detected between the heating and cooling cycles. As a general trend, the higher the stirring velocity, the lower the extent of hysteresis. Another interesting point is that the PIT determined on the cooling cycle agreed with the theoretical PIT calculated using the eq. 1-5 (values included in Table 4-5). This phenomena, firstly described by Esquena et. al,[178] is thought to arise from the different mechanisms involved in the emulsions transitions on heating and cooling respectively. While the inversion from a W/O HIPE to a dilute O/W emulsion can be simply induced by coalescence of water droplets, the opposite requires a bigger energy input. However, such phenomenon was not observed in emulsions with smaller contents of monomer (below 40 wt%) in the continuous phase of the emulsions.

II. The hypothesis that agitation played an important role is beyond doubt confirmed. Besides that the higher agitation speed, the lower hysteresis between heating and cooling cycles, it is also evident that lower conductivity values are attained when increasing the stirring rate. This is rather evident by comparing the heating curves in Figure 4-23, and suggests a more efficient emulsification for the emulsion stirred at 1100 r.p.m.

Both the presence of hysteresis cycles and the high energy-input requirements of the systems with high monomer contents, made the preparation of HIPEs rather difficult, either by mechanical stirring or by hand-shaking. Therefore, at this point we decided to change the $C_{12-14}(EO)_5$ surfactant for the more lipophilic surfactant $C_{12-14}(EO)_4$, in order to favour the formation and stabilization of W/O HIPEs, at lower inversion temperatures. Using the surfactant mixture $C_{12-14}(EO)_4$ - $C_{13-15}(EO)_6$ (1:4 by weight), and keeping all the rest emulsion composition parameters constant, a PIT of 36.8 ºC was obtained. This corresponds to a surfactant HLB number of 10.0. As in the previous emulsion system, monomer concentration in the continuous phase of emulsions was progressively increased. Figure 4-24(a) compares calculated (black line) and experimental PITs (red line) for monomer concentrations ranging from 0 to 60 wt%. According to eq. 4-5, one could expect a negative PIT of -23.2 ºC for monomer concentrations of 60 wt%.

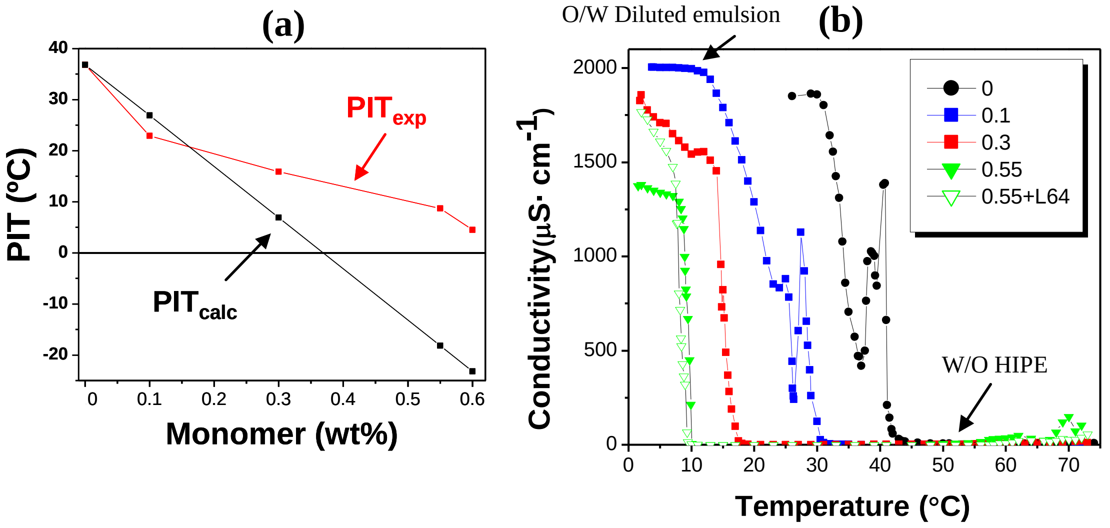

Figure 4-24. (a) Calculated (PIT$_{calc.}$) and experimental (PIT$_{exp.}$) PITs as a function of monomer content in the oil phase of the emulsions. The water-oil volume ratio was 90/10 and the surfactant concentration was 4 wt% (25% $C_{12-14}(EO)_4$ - 75% $C_{13-15}(EO)_6$). Experimental PIT was calculated from the heating cycles shown in (b), in which the conductivity is plotted as a function of the temperature. Differences between both heating and cooling (not shown here) cycles were not detected. L-64 (included in the legend) is a nonionic block copolymer surfactant added to enhance the stability of the HIPEs at high temperatures. Emulsions were stirred at 700 r.p.m.

Surprisingly, inversion occurred in all systems in the range of temperatures studied, up to of 60 wt% monomer concentrations. The corresponding conductometric curves are depicted in Figure 4-24(b). The increase of monomer content led to a reduction of the PIT values, decreasing its value from 36.8 to 4.5 ºC for emulsions without and with 60 wt% monomer, respectively.

However, this reduction was far below from the theoretical reduction determined using eq. 4-5. This strongly indicates that the behaviour of emulsions stabilized with commercial ethoxylated surfactants and containing aromatic molecules is difficult to predict using such equation. Moreover, hysteresis cycles were not observed in the whole range of monomer concentrations, suggesting that the addition of a more hydrophobic surfactant, $C_{12-14}(EO)_4$, in substitution of the more hydrophilic $C_{13-15}(EO)_5$, facilitates and favours inversion from a diluted O/W emulsion to a W/O highly concentrated emulsion.

Next step consisted in selecting the appropriate monomer concentration. It is important to mention that polymerization between styrene and divinylbenzene is carried out at 70 ºC. Therefore, it is of paramount importance that emulsions are stable at this temperature. Although emulsions with 55 wt% of monomer in the oil phase, were stable in a wide range of temperatures, they experienced phase separation in a short time, at temperatures above 65 ºC. This is supported by the sudden rise in conductivity values above such a temperature, and can be attributed to fast coalescence (green-filled triangle curve in Figure 4-24(b)). In order to increase stability, a nonionic block copolymer surfactant (Synperonic PE/L-64), 5 wt% with respect to the total surfactant amount, was included into the formulation. The corresponding conductivity vs. temperature curve was similar to that without PE/L-64 up to 60 ºC (green open curve in Figure 4-24(b)). However, according to conductivity values, the stability of the emulsion containing the block copolymer improved substantially up to temperatures slightly above 70 ºC. Therefore, stable W/O highly concentrated emulsions, containing 55 wt% of monomer in its continuous phase, could be obtained at 70 ºC. This system was selected for further studies on the obtention of macroporous polymeric foams.

Highly concentrated emulsions (HIPEs) were prepared in this system, with a composition H_2O / $K_2S_2O_8$ / $C_{12-14}(EO)_4$ / $C_{13-15}(EO)_6$ / Synperonic L-64 / styrene / divinylbenzene / tetradecane (89.9 / 0.1 / 0.95 / 2.85 / 0.2 / 2.88 / 0.72 / 2.4). Figure 4-25(a,b) shows two representative optical microscope images corresponding to a (a) dilute O/W and a (b) W/O highly concentrated emulsions below and above the phase inversion temperature (PIT) of the system (ca. 10 ºC), respectively. The exceptional small droplet sizes observed in the HIPE (picture b) makes difficult to distinguish the individual droplets. This is a clear advantage of this emulsification method, based on the PIT principle: much smaller sizes can be obtained.[170, 177] This can be explained by the ultralow interfacial tensions attained at the HLB temperature (e.g. 10^{-3} mN/m).[287] For comparison, a typical HIPE, prepared by conventional agitation methods is shown in the introduction section (Figure 1-21, page 45).

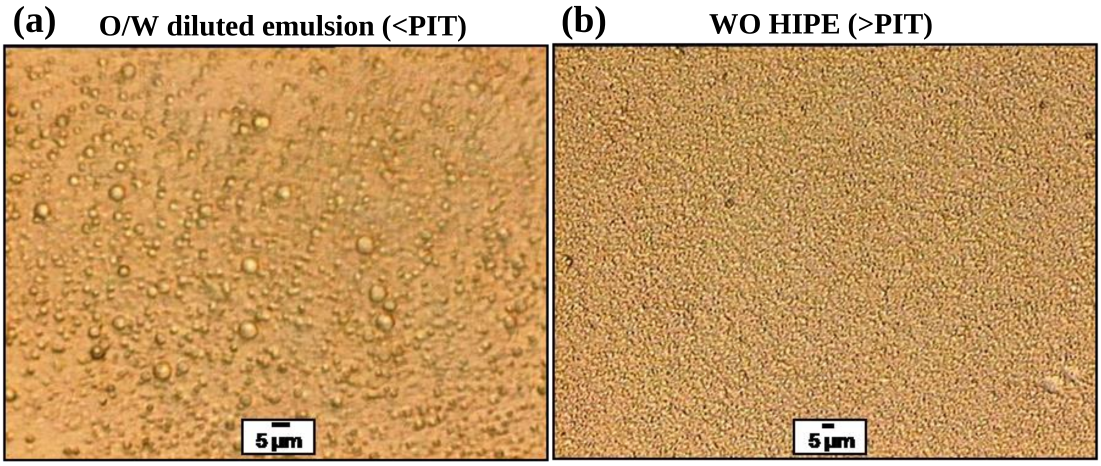

Figure 4-25. Optical microscope images of the emulsions obtained by the PIT method, with composition: H_2O / $K_2S_2O_8$ / C_{12}-14(EO)$_4$ / $C_{13\text{-}15}$(EO)$_6$ / Synperonic L-64 / styrene / divinylbenzene / tetradecane (89.9 / 0.1 / 0.95 / 2.85 / 0.2 / 2.88 / 0.72 / 2.4); (a) O/W diluted emulsion below the PIT; (b) W/O highly concentrated emulsion at room temperature above the PIT.

4.2.3.2 *Macroporous polymers*

Macroporous polymers were obtained by polymerization of the external phase of the highly concentrated emulsion (HIPE) depicted in Figure 4-25(b). As pointed out in the introduction, these materials are generally referred in the literature as polyHIPEs. The free-radical polymerization reaction, initiated by the water soluble $K_2S_2O_8$, was carried out at 70 ºC during 24 hours in cylindrical glass vials. Proof of concept experiments carried out, showed that the minimum monomer (styrene-divinylbenzene weight ratio of 4:1) concentration required in the continuous phase of the emulsions was 50 wt%. Materials prepared with concentrations below this value collapsed, and consequently shrank.

It is interesting that materials can be molded in any shape, just depending on the geometry of the container (Figure 4-26(a)). The pore structure of the monolithic material is seen in Figure 4-26(b), which is characterized by possessing pores ranging from 1 to 5 µm in size. Despite the fact that such pores are smaller than others from different materials found in the literature, if we compare Figure 4-26(b) and Figure 4-25(b), it is clear that emulsion droplets that act as a template experienced a slight increase in size.

It should be pointed out that materials exhibit high degree of interconnectivity, with spherical pore throats from 0.1 to 2 µm in diameter. This high porosity could be associated with the presence of tetradecane (45 wt%) in the continuous phase, acting as a porogen agent.[189]. The total pore volume of the monoliths (20.5 ± 0.8 cm^3/g) was calculated by saturating several pieces of the materials with decane. Taken into account the foam density determined by mass/volume measurements (0.05 g/cm^3), the porosity of the material was estimated to be approximately 95 %.

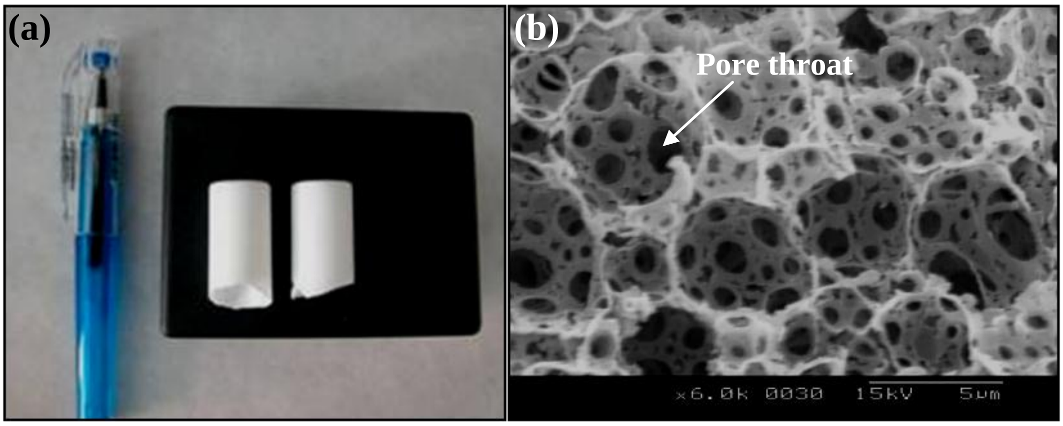

Figure 4-26. (a) Macroporous polymers prepared in glass vials of 1.3 cm in diameter at 70 ºC. (b) SEM image, revealing the pore structure of the material. It is to be noted that once water is removed, 95 % of the total volume is air. The arrow indicates a pore throat, interconnecting neighbouring pores.

Polymerization of the external phase of the HIPEs was also carried out at 60 and 65 ºC (Figure 4-27).

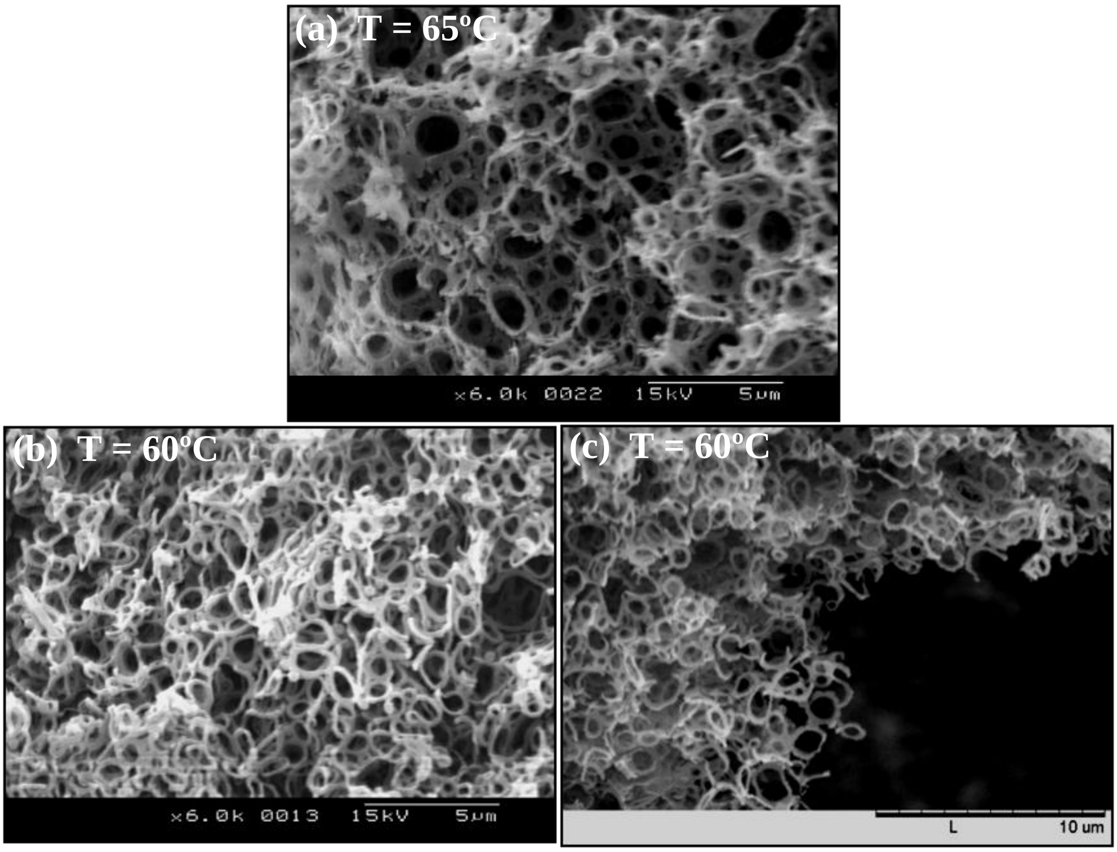

Figure 4-27. SEM images of macroporous polymers prepared from HIPEs with the same composition than that shown in Figure 4-25(b). Polymerization of the external phase of the emulsions was carried out at (a) 65 and (b,c) 60 ºC. Pore structure depends on polymerization temperature.

Interestingly, if we have a closer look to the microstructure shown in the SEM images (Figure 4-27), it is evident that the porous morphology has experienced appreciable changes. Instead of possessing defined macropores with thin polymer walls, the polymer tends to be located around the so-called pore throats when the polymerization temperature is reduced, and foams are formed by rather polymeric rings (pictures b and c in Figure 4-27). Undoubtedly, the comparison of such rings and the pore throats observed in Figure 4-26(b) confirms that all have the same dimensions and presumably all correspond to initial connexions between neighbouring pores during the polymerization reaction. In all cases, materials could be obtained as monoliths and did not shrink during purification and drying steps. This strategy constitutes an attractive route to obtain materials with different porous structures and interconnectivies.

The surface area of the macroporous polymers was calculated from the adsorption isotherms obtained by means of nitrogen adsorption measurements. All values were around 50 m^2/g, with no significant differences among the isotherms (Table 4-7). It must be stressed that values of surface areas for conventional polyHIPEs (macroporous polymers made from HIPEs), are generally lower.[187, 224] This can be explained by several factors: first, the size of the macropores is smaller than generally described in the literature, and this could increase surface area. Second, tetradecane, apart from controlling the PIT, might act as a porogen, as previously described in the literature.[189, 214] Besides that, the micropore total volume is probably rather low, because of little adsorption at low relative pressures, as expected for strictly macroporous polymers.

Table 4-7. Textural parameters derived from the N_2 adsorption isotherms for the macroporous polymers obtained at different polymerization temperatures. S_{BET} is the total surface area and V_t is the total pore volume, taken as the maximum adsorbed volume in the isotherms at relative pressure 0.975.

Polymerization temperature (ºC)	**S_{BET} (m^2/g)**	**V_t (cm^3/g)**
70	49	0.09
65	52	0.11
60	43	0.09

A representative adsorption/desorption isotherm for the material obtained at 70 ºC is included in Figure 4-28. According to the International Union of Pure and Applied Chemistry (IUPAC) terminology, this is a type II isotherm, which is characteristic of non-porous or macroporous materials.

.

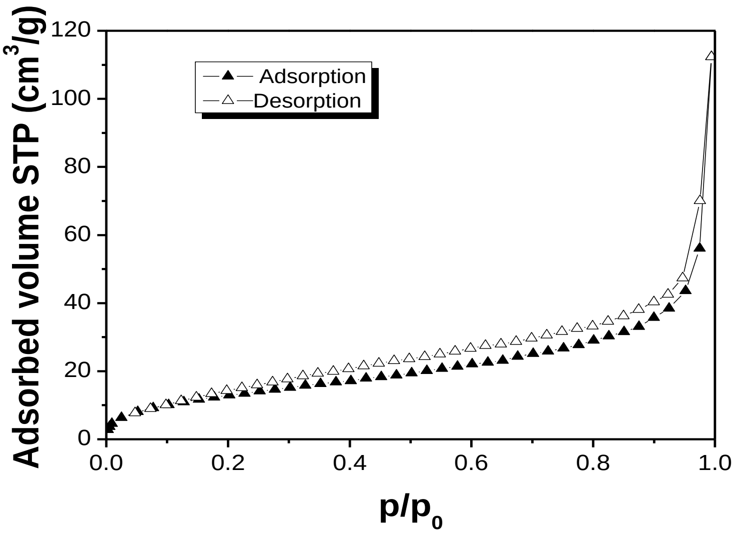

Figure 4-28. N_2 adsorption/desorption isotherm for the macroporous polymer synthesized from a HIPE at 70 ºC.

4.2.3.3 *Polymeric macroporous nanocomposites*

4.2.3.3.1 Preparation of macroporous nanocomposites

NP_3 and NP_8 were dispersed in the continuous phase of the emulsions with a composition H_2O / $K_2S_2O_8$ / $C_{12-14}(EO)_4$ / $C_{13-15}(EO)_6$ /Synperonic L-64 / styrene / divinylbenzene / tetradecane (89.9 / 0.1 / 0.95 / 2.85 / 0.2 / 2.88 / 0.72 / 2.4), and then these emulsions were processed into polymeric macroporous nanocomposites (point 3 in Figure 4-14). Polymerization in the continuous phase of emulsions was identical to that used in previous section. At first, to ensure that the presence of nanoparticles does not affect the PIT of the system, the conductivity vs. temperature of an emulsion containing 7 wt% NP_8 (respect to monomer weight) was compared to that in absence of nanoparticles. Figure 4-29 shows the two curves for the systems with and without nanoparticles. As clearly seen, these curves are very similar. This means that NP_8 do not change the PIT of the system. Therefore, it is confirmed that nanoparticles do not influence the ability of poly(ethylene glycol) alkyl ether type nonionic surfactants to induce inversion from an O/W to a W/O emulsion when temperature is increased. Moreover, emulsions containing NP_8 were also stable at high temperatures.

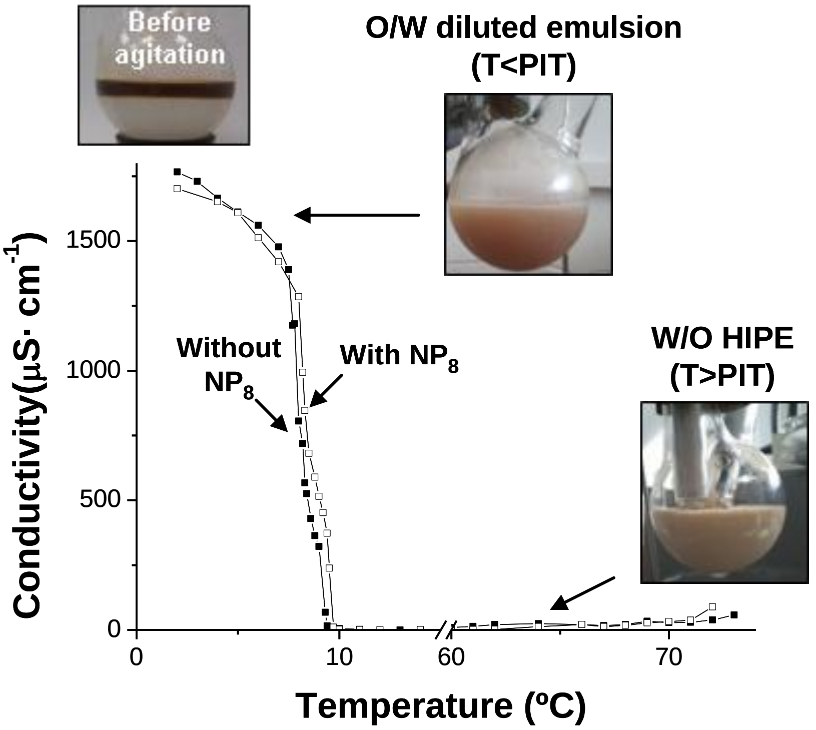

Figure 4-29. Conductivity as a function of increasing temperature in the H_2O / NaCl (10^{-2}M) / $C_{12-14}(EO)_4$ / $C_{13-15}(EO)_6$ / Synperonic L-64 / styrene / divinylbenzene / tetradecane (90.0 / 0.95 / 2.85 / 0.2 / 2.88 / 0.72 / 2.4) systems. Surfactant and monomer concentrations were 4 wt% and 55 wt% (with respect to continuous phase). In one case, 7 wt% NP_8 was added in the continuous phase of emulsions. Pictures illustrate the emulsification process. The brown colour comes from the iron oxide nanoparticles.

4.2.3.3.1 Characterization of porous structure

Macroporous nanocomposite materials were obtained by polymerization at 65 ºC of the continuous phase of the W/O HIPE shown in Figure 4-29. From Figure 4-30 to Figure 4-32 it can be observed that polymeric macroporous nanocomposites were successfully prepared, and that NP_3 and NP_8 were effectively incorporated into the polymer walls of the materials after polymerization. The final loading of both kinds of nanoparticles was 6.4 wt% with respect to the polymer, as confirmed by TGA. Figure 4-30 shows two SEM images of the porous structure of a macroporous polymer containing NP_3. Pores from 3 to 8 µm were distinguished in the entire sample examined, and the material exhibited also a high degree of pore connectivity. In Figure 4-30(b), a SEM image at higher magnification shows typical characteristic elements commonly found in polyHIPEs, as pore throats (indicated as P) and plateau border regions (indicated as B). The texture of the walls indicates the presence of a fine texture, which is difficult to observe clearly by SEM. Despite this texture, the monoliths neither collapse nor shrink after purification and drying processes.

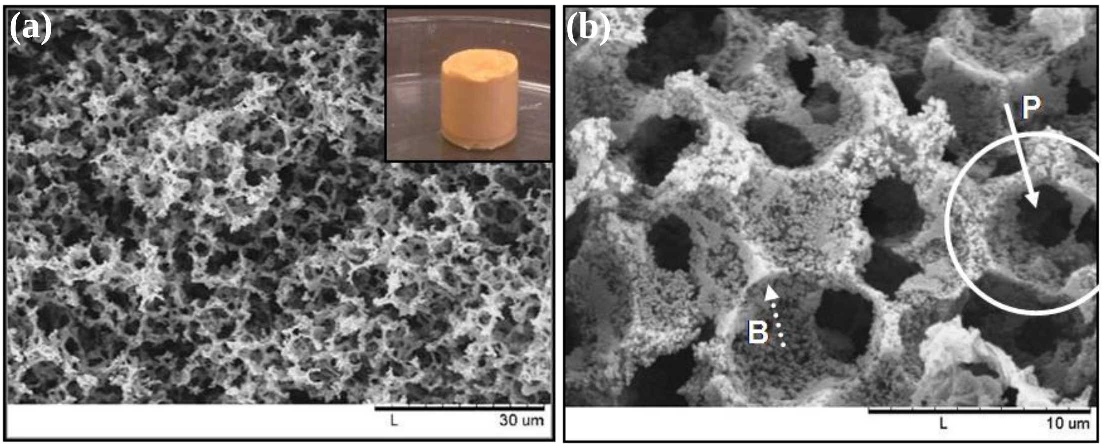

Figure 4-30. SEM images of macroporous polymers made from a highly concentrated emulsion of composition: H_2O / $K_2S_2O_8$ / $C_{12-14}(EO)_4$ / $C_{13-15}(EO)_6$ / Synperonic L-64 / styrene / divinylbenzene / tetradecane (89.9 / 0.1 / 0.95 / 2.85 / 0.2 / 2.88 / 0.72 / 2.4). The polymer walls contain 6.4 wt% NP_3, which were dispersed in the oil phase of the precursor emulsion. The inset in (a) shows the aspect of the macroporous nanocomposite. In (b) P is a pore throat and B is a plateau border region.

Several TEM images of the materials were taken and are shown in Figure 4-31. Undoubtedly, nanoparticles are located within the polystyrene walls, forming some small size clusters.

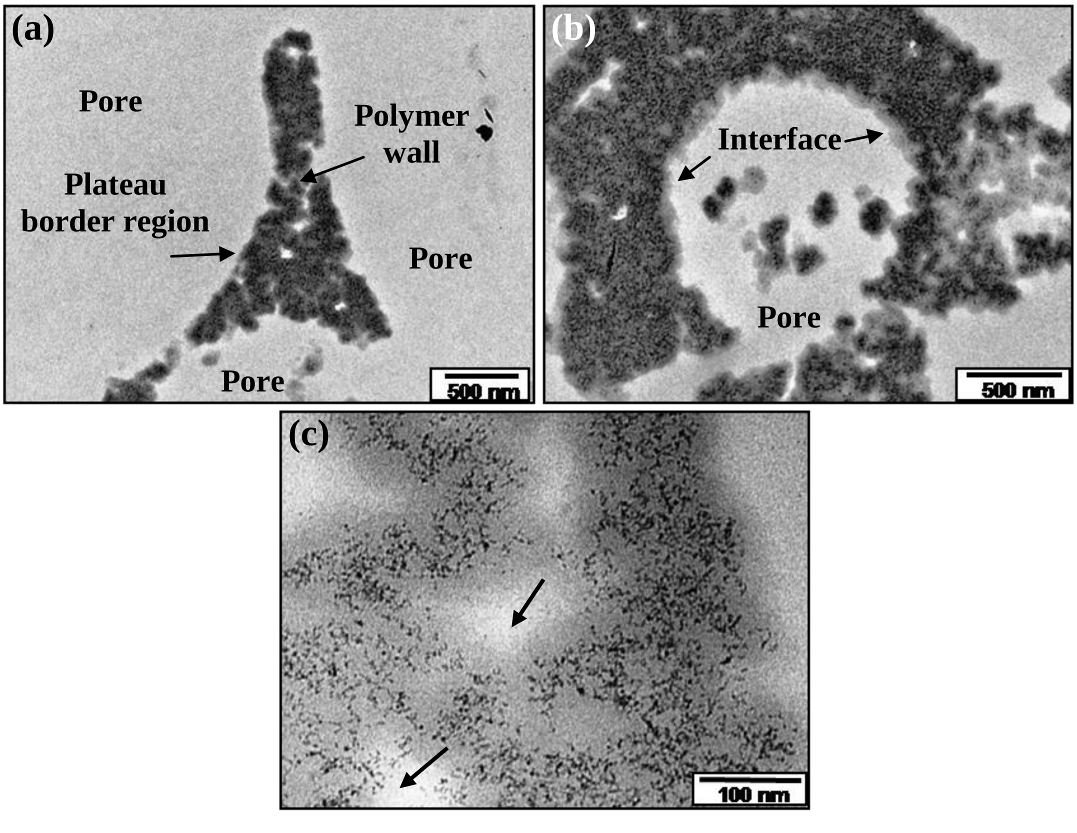

Figure 4-31. TEM images of cross-sectional slices made from the polymeric macroporous nanocomposites depicted in Figure 4-30. Small clusters of NP_3 are dispersed inside the polymer walls of the material. Black arrows in (c) indicate the secondary pore structure generated within the polymer walls, which could be attributed to the presence of tetradecane.

No characteristic peak was detected in the SAXS curves, possibly due to the lower NP_3 concentration compared to the NP_3 concentration in non-porous monoliths prepared in section 4.2.1. Another point that must be underlined is that NP_3 were not located at the polymer-air interface. This is clearly observed having a closer look at the interface region in Figure 4-31(b), in which a grey-thin layer with no nanoparticles can be distinguished. This is in good agreement with the fact that NP_8 did not modify the PIT of the initial emulsion, and more importantly, did not affect its stability.

Moreover, the TEM images strongly confirm that the walls of the polymeric foams posses a secondary pore structure (arrows in Figure 4-31(c)), which could be the same fine texture observed by SEM. These small pores inside polymer walls might have appeared by the presence of tetradecane, acting as a porogen.

Polymeric macroporous nanocomposites were also prepared with NP_8 nanoparticles. The macroporous structure of polyHIPEs as well as the NP_8 spatial distribution within the polymer walls of the materials are shown in Figure 4-32.

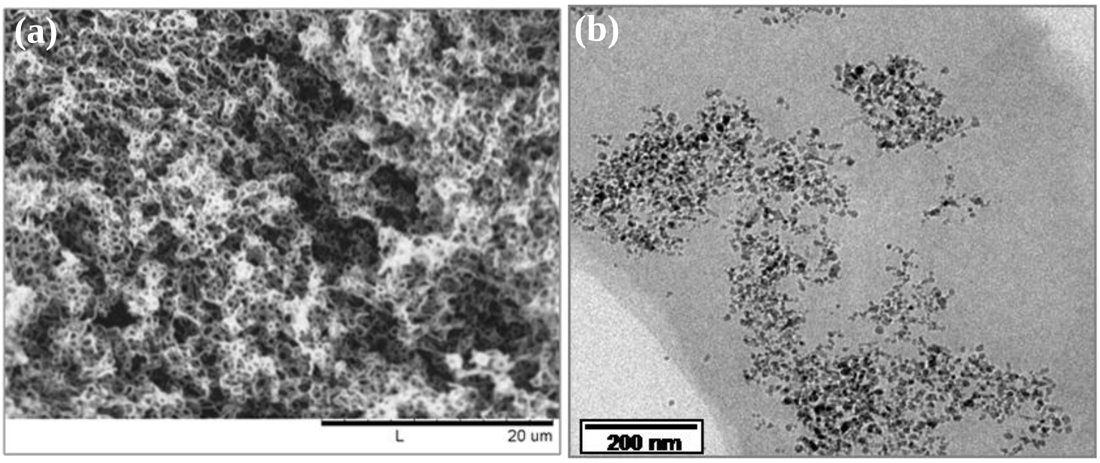

Figure 4-32. (a) SEM and (b) TEM images of a macroporous polymer containing NP_8, made from a highly concentrated emulsion with the same composition than the system included in Figure 4-30, but with NP_8 instead of NP_3.

The porous morphology is rather similar to the structures obtained for the system with NP_3 (Figure 4-30). However, NP_8 were not only concentrated just in some parts of the polymer walls of the materials, but also formation of nanoparticle clusters was more evident. It could be that the emulsification procedure to prepare the porous nanocomposites favours particle aggregation.

4.2.3.3.2 Characterization of magnetic properties

Magnetic properties of the nanocomposites are of outmost importance for any possible commercial application. First, magnetization (M) versus applied magnetic field (H) at 5 K, has been measured for non-porous nanocomposites containing 10 wt% NP_8 (Figure 4-33). The maximum field applied was 20 kOe.

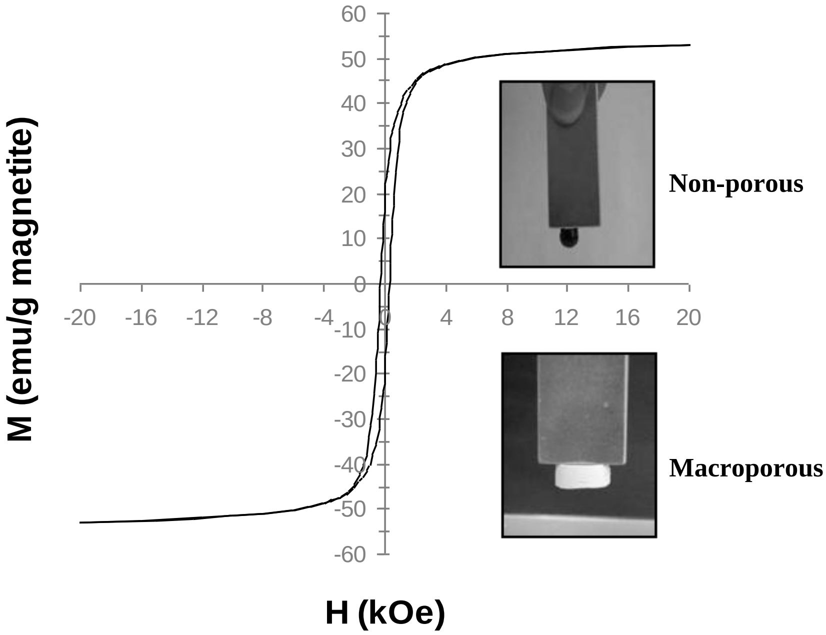

Figure 4-33. Magnetization (M) versus applied magnetic field (H) at 5 K, for non-porous nanocomposite containing 10 wt% NP_8. Maximum applied field was 20 KOe. The insets show the materials being attracted to a permanent magnet.

Saturation magnetization (M_s) reached a value of 52 emu/g (Table 4-8). This is a normalized value dividing M_s by the Fe_3O_4 weight, thus the nonmagnetic contribution from the organic part has been subtracted; if not otherwise stated, M_s values will be given per gram of pure iron-oxide nanoparticles. The M_s determined for the non-porous nanocomposite (52 emu/g) is appreciably lower than M_s measured for as-synthesized NP_8 (77.7 emu/g) at 5 K (Table 4-8). Surface effects from polymer matrix and from the organic coating layer, and oxidative processes occurring during polymerization could be claimed as the reason for further reduction of nanocomposite M_s values. The M - H loop for the macroporous nanocomposites, containing 6.4 wt-% NP_8 was identical to that observed for the non-porous nanocomposite. Therefore, M_s of nanocomposites with NP_8 was the same (52 emu/g) regardless of porosity (non-porous and macroporous). Since both materials are made with the same polymer composition, it is reasonable to assume that surface effects should affect in the same way. TEM images showing the spatial distribution of NP_8 in both non-porous and porous nanocomposites were shown in Figure 4-18(a) and Figure 4-32(b), respectively.

Table 4-8. Magnetic properties of nanoparticles and polymeric nanocomposites (non-porous and macroporous). M_s is the magnetization saturation at 5 K, H_c is the coercivity field also at 5 K and T_B denotes the blocking temperature at 50 Oe.

Material	**Nanoparticles**	**[NP] (wt%)**	M_s **(emu/ g magnetite)**	H_c **(Oe)**	T_B **(K)**
	NP_8	-	78	285	230
Non-porous	NP_8	10	52	300	75
Macroporous	NP_8	6.4	52	350	105
Non-porous	NP_3	16	-	-	3
Macroporous	NP_3	6.4	-	-	8

Coercive fields (H_c) measured for nanocomposites are also shown in Table 4-8. Values of H_c for NP_8 are similar to that for 10 nm magnetite nanoparticles at 5 K reported by another group.[288] Coercivity disappears above the blocking temperature (T_B)[129] and, therefore, all these nanocomposites show superparamagnetic behaviour at room temperature. This transition will be described below. As magnetic properties were imparted to the polymers, both porous and non-porous nanocomposites containing NP_8 are attracted to a strong permanent magnet (see insets in Figure 4-33).

Field-cooled (FC) and zero field-cooled (ZFC) magnetization (M) versus temperature, for NP_8, at a field H = 50 Oe, were measured previously (Figure 4-4(b), page 93). Blocking temperature (T_B) was estimated in 215 K from the maximum exhibited in the ZFC curve. The same measurements were also carried out for non-porous and porous nanocomposites containing either NP_3 or NP_8 (Figure 4-34).

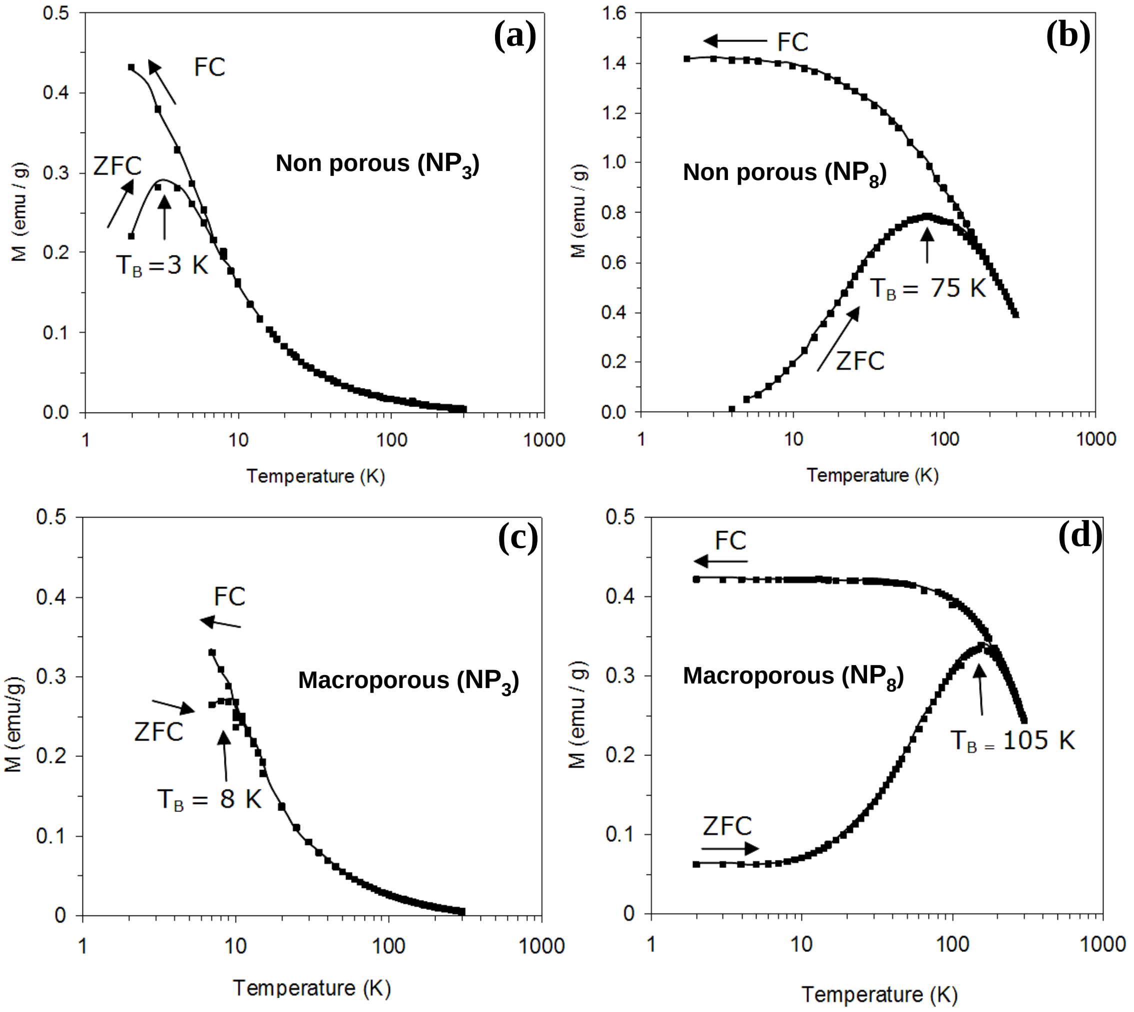

Figure 4-34. Magnetization (M) versus temperature (T) curves of non-porous (a,b) and macroporous nanocomposites (c,d), containing either NP$_3$ or NP$_8$. Zero field-cooled and field-cooled experiments were carried out at H = 50 Oe. Solid lines are only visual guides.

As outlined in the introduction, T_B is directly related to the volume of particles. Therefore, bigger nanoparticles will become superparamagnetic at higher temperatures. This is rather evident by comparing (c) and (d) graphs in Figure 4-34, for example. For a given nanoparticle content in the polymer, i.e. 10 wt%, T_B increases from 8 K to 105 K when increasing the nanoparticle average size from 3 to 8 nm. However, other factors should also be considered. It is well known that interactions between particles (dipole-dipole),[289, 290] and both the size and polydispersity of nanoparticles can significantly influence T_B.[274] In this context, Figure 4-34 shows that porous nanocomposites (b and c) exhibit a higher T_B than those exhibited by non-porous nanocomposites (a and b). We can interpret that the increase of T_B is associated with a higher contribution of particle–particle interactions. Saturation below T_B as well as the proximity between T_B and the FC-ZFC branching temperature also point to stronger interactions in the case of porous nanocomposites ((b) and (d) in Figure 4-34).[291] It could be that the emulsification procedure to prepare the porous nanocomposites favours some particle aggregation.

It should also be noted that T_B for NP_8-containing nanocomposites are lower than T_B for as-synthesized NP_8 (Table 4-8). T_B was significantly reduced from 230 K (as-synthesized NP_8) to 75 K (non-porous nanocomposite), indicating less nanoparticle-interactions when NP_8 are embedded within the polymer matrix.

Summarizing, surface-modified iron oxide nanoparticles have been incorporated in poly(styrene-divinylbenzene) based materials. In particular, nanoparticles were first included in non-porous monoliths. Then, such nanoparticles were embedded in polymeric microparticles and finally in the polymer walls of macroporous polymers by polymerization in diluted and in high internal phase emulsions, respectively. The resultant nanoparticle dispersion within the polymer matrices has been evaluated. At variance with common emulsion preparation procedures, which are based on high-energy methods, here HIPEs were obtained by the phase inversion temperature approach (PIT). This method offers an attractive alternative route and is based on phase transitions produced during the emulsification process.

4.3 MACROPOROUS POLYMERS OBTAINED FROM HIGHLY CONCENTRATED EMULSIONS STABILIZED SOLELY WITH NANOPARTICLES

The main purpose of this section has been to obtain macroporous polymers using W/O high internal phase emulsions (HIPEs) as templates, stabilized solely with either Fe_3O_4 or TiO_2 nanoparticles. As mentioned in the Introduction, emulsions stabilized with particles, in absence of surfactant(s), are known in the literature as Pickering emulsions.[51] Therefore, HIPEs stabilized with particles will be abbreviated hereafter as Pickering HIPEs.

For the preparation of Pickering emulsions, it is required that the particles have balanced hydrophilic-hydrophobic properties, between the oil and the aqueous phase. Usually, balanced properties can be achieved by surface functionalization. For this reason, both kinds of nanoparticles were surface-modified with oleic acid, as described in detail in the experimental part (3.2.1). It is well established that particles that are more wetted by water than by oil can stabilize O/W emulsions, and inversely, particles preferentially wetted by oil can be good emulsifiers for W/O emulsions.[50] Therefore, the contact angle that the nanoparticles exhibit at the oil-water interface plays an important role in the stability of Pickering emulsions. Among the factors that affect this contact angle, the most important are the surface chemistry of particles and the nature of the oil. Here, the surface of the particles has been modified with oleic acid, providing hydrophobicity in order to optimize the stability of W/O Pickering HIPEs.

In this context, Ikem et al. has described the stabilization of Pickering W/O HIPEs with high internal phase volume contents, using small amounts of SiO_2[100] and TiO_2[176, 204] nanoparticles, which were surface-modified with oleic acid. After polymerization of the template, macroporous nanocomposites with high porosities, and containing nanoparticles incorporated within the walls, were obtained. Although a large variety of inorganic nanoparticles have been used to stabilize diluted or concentrated emulsions,[66, 72, 292, 293] only a few types (SiO_2,[100, 206] TiO_2[204] and more recently Fe_3O_4[208] Nanoparticles) have been used to stabilize Pickering HIPEs in order to obtain macroporous polymers. Despite being a research of growing interest, there are still numerous aspects that have not been studied in detail. For instance, there is little evidence about the role that interfacial tension plays in the stabilization of these emulsions. In addition, the spatial distribution of nanoparticles within the resultant macroporous polymers has not been deeply investigated.

In the present section, close attention is paid to all these novel aspects. Furthermore, the main properties of the resultant macroporous polymers have been characterized as a function of oleic acid content and concentration of nanoparticles, and as a function of the internal phase volume in the original HIPEs. The functional nanoparticles used as emulsifiers have been:

- NP_{32} and NP_8 Fe_3O_4 nanoparticles, both surface-modified with 4.4% and 12.4% of oleic acid, respectively (4.1.1).
- TiO_2 nanoparticles synthesized by the mechanochemical solid-state method described in 4.1.2.

4.3.1 Preliminary Studies: Influence of Oleic Acid Functionalization and Interfacial Tension Measurements

Initially, proof-of-concept experiments were carried out to verify the important role of oleic acid onto the surface of nanoparticles. For this purpose, stabilization of Pickering emulsions was studied using either CNP_{32} (unmodified NP_{32}) or NP_{32} (with 4.4 wt% oleic acid). In such experiment, water at neutral pH was added slowly to the oil phase (styrene and divinylbenzene ratio 1:1 by weight), containing 1.5 wt% either CNP_{32} or NP_{32} . Nanoparticle concentrations do not include organic coatings and are expressed as a function of the total monomer weight. The emulsions were prepared using a vortex mixer. Two completely different results were obtained for systems with 75 vol% of water. While in the case of the as-received CNP_{32}, an O/W emulsion was formed, a W/O highly concentration emulsion was obtained in the case of surface-modified NP_{32}. This clearly demonstrated that the nature of the emulsion (O/W or W/O) was dependent on particle functionalization.

Photographs of the emulsions, 15 minutes after preparation, are shown in Figure 4-35(a). Formation of a O/W emulsion (tube 1) is consistent with the hydrophilicity of CNP_{32} nanoparticles.[292] Even though this emulsion creamed rapidly, it did not experience phase separation, at least for 1 month. By contrast, the W/O HIPE formed in the oleic acid modified NP_{32} system (tube 2 in Figure 4-35) must be due to the partial hydrophobicity of the NP_{32} nanoparticles. Figure 4-35(b,c) shows two representative optical microscope images of both emulsions. As seen in both samples, emulsion droplet distributions are quite polydisperse, ranging from 30 to 500 µm. Interestingly, a closer look to the W/O HIPE image (Figure 4-35(c)) allows observing some particle aggregates on emulsion surfaces. Undoubtedly, this is a first indication of the ability of the nanoparticles to migrate to oil-water interfaces. The stability mechanisms involved in Pickering emulsions will be discussed in detail below. Likewise, W/O

Pickering HIPEs were also successfully prepared using NP_8 as emulsifiers, which were previously surface-modified with 12.4 wt% oleic acid (tube 3 in Figure 4-35(a)).

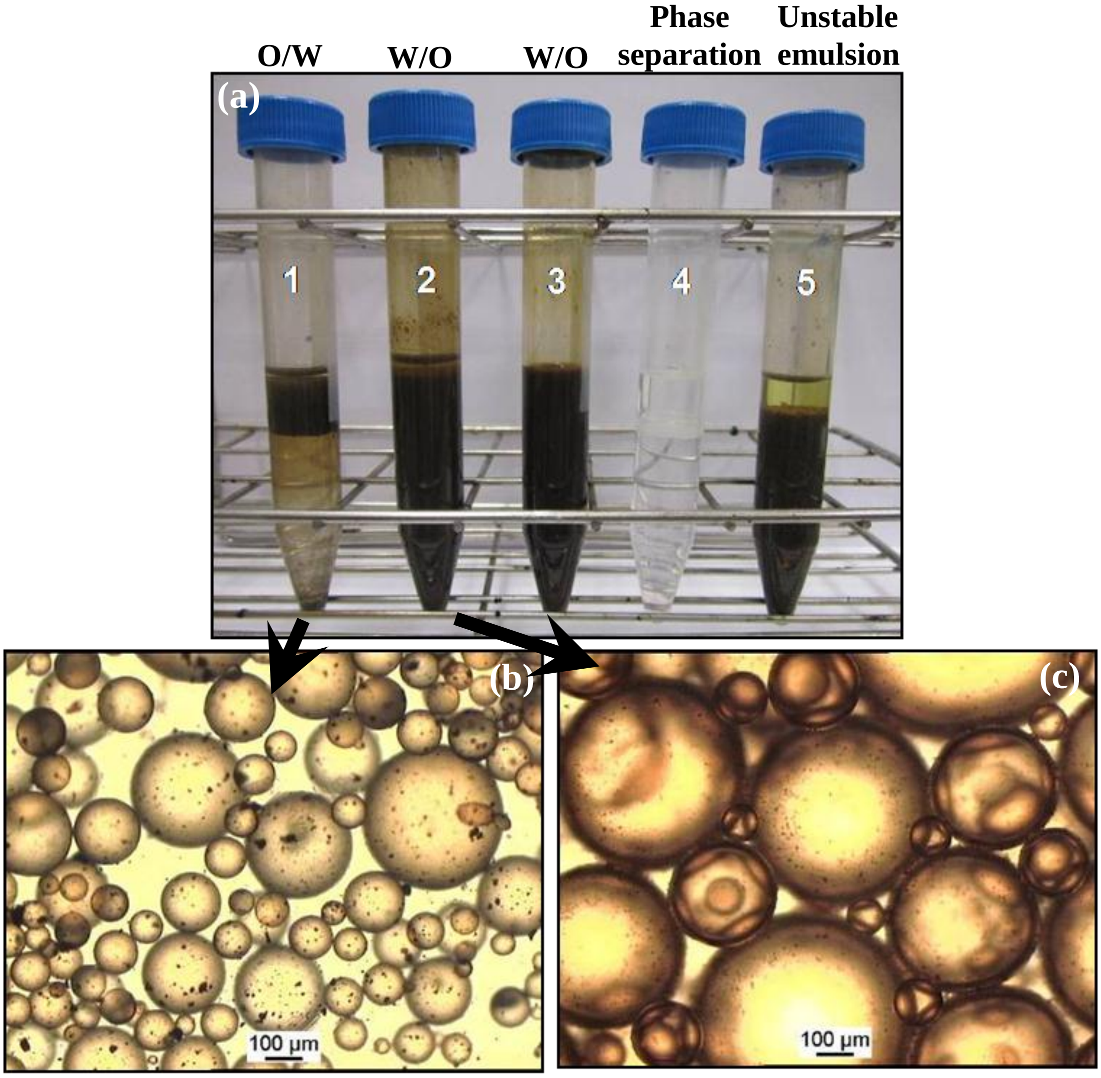

Figure 4-35. a) Photographs of samples consisting of 75 vol% water, 25 vol% oil (monomer mixture) and 1.5 wt% of (1) as-received CNP_{32}, (2) 4.4 wt% oleic acid-modified NP_{32}, and (3) 12.4 wt% oleic acid-modified NP_8.. For comparison, sample (4) did not contain nanoparticles, and only 0.2 wt% oleic acid was added in the oil phase, and sample (5) was prepared using as emulsifier as-received CNP_{32}, mixed with 0.07 wt% oleic acid. The pictures were taken 15 min after mixing. Sample (1) is a diluted O/W emulsion while samples (2), (3) and (5) are W/O emulsions. b) and c) are optical microscopy images of the samples (1) and (2), respectively.

Bearing in mind these results, one hypothesis could be that the oleic acid, desorbed from nanoparticle surfaces, would be the responsible for the successful emulsification. To discard this possibility, emulsions with the same compositions were prepared, but modifying the emulsifier:

I. First, the same amount of oleic acid attached on NP_8 surfaces was added alone, in absence of nanoparticles. It must be stressed that the pH of the aqueous phase was around 6. Tube 4 in Figure 4-35 shows that, after sample preparation, the system separated very quickly into two phases (monomer and water), indicating that emulsion was extremely unstable. Herein, the stability of the W/O emulsions observed in tubes 2 and 3 can be mainly attributed to the surface-modified nanoparticles.

II. Second, instead of using surface-modified NP_{32}, unmodified CNP_{32} and oleic acid were added separately, at the same concentration. Both components were mixed in-situ together in the continuous phase, just before emulsification. In this case, a W/O was obtained (tube 5 in Figure 4-35). However, the emulsion underwent quick sedimentation and phase separation. Moreover, emulsion droplet size was much larger compared to the sample stabilized with surface-modified NP_{32} (tube 2). Such droplets are visible to the naked eye. It can be therefore inferred that oleic acid added just before emulsification, can partially adsorb onto NP_{32} surfaces, slightly modifying their wettability (as seen when comparing tubes 1 and 5). Nevertheless, such adsorption is by far less efficient than that showed by the 4.4 wt% oleic acid modified NP_{32}.

In conclusion, the ability of nanoparticles to act as emulsifiers is, no doubt, merely due the effective adsorption of oleic acid onto the surface of the nanoparticles, which renders the nanoparticle surface partially hydrophobic.

Such assumption has been qualitatively supported by contact angle observations. In the literature, some methods, such as the Washburn,[292, 294] or the gel trapping technique,[295] have been used to estimate the contact angle that individual sub-micron size particles make with an oil-water interface. However, the most employed method in the bibliography, and also used in this work, involves the measurement of the contact angle of a liquid drop on the surface of a powder pellet.[66, 78, 296] The same method may also be used to determine the contact angle that the nanoparticles make with an oil-water interface, if the liquid drop is surrounded by another liquid phase. This method might allow to estimate the efficiency of nanoparticles to act as emulsifiers.[102] The main limitation of this approach is that contact angle depends on the compression of the material. Therefore, the control of film roughness is a critical parameter. Here, compression conditions were maintained constant while preparing flat pellets of CNP_{32}, NP_{32} and NP_8, by compressing the respective nanoparticle powders. A droplet of water was then placed on their surfaces. As seen in the images included in Figure 4-36, water wets the CNP_{32} film (confirming its hydrophilicity), whereas the contact angles observed for NP_{32} and NP_8 are near to 180º. It is thus demonstrated that oleic acid adsorption turns the surface of both NP_{32} and NP_8 nanoparticles more hydrophobic.

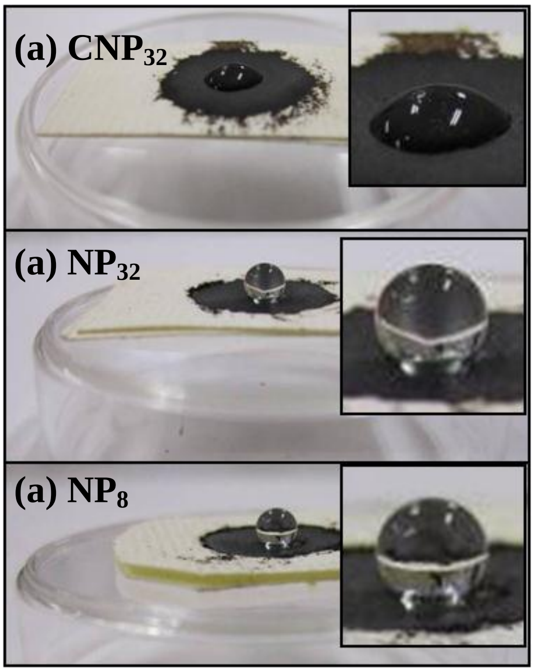

Figure 4-36. Water droplets on (a) CNP_{32}, (b) NP_{32} and (c) NP_8 films.

From the first studies dealing with Pickering emulsions it was generally accepted that only fine-grained structures could act as emulsifiers.[48] Moreover it is known that the ability of particles to adsorb on the interface largely depends of factors such its size or state of dispersion of the solids.[77] For this reason, the stability of nanoparticle suspensions was evaluated in the mixture styrene/divinylbenzene (ratio 1:1 by weight), which will be the continuous phase of the emulsions in further experiments. NP_8 and NP_{32} were dispersed in a sonicator bath for 10 minutes. The appearance of the dispersions after that time is presented in Figure 4-37.

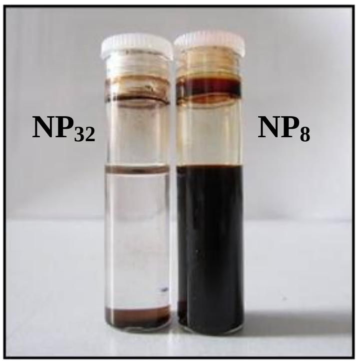

Figure 4-37. Visual aspect of NP_{32} (left vial) and NP_8 (right vial) in a mixture of styrene/divinylbenzene (ratio 1:1 by weight) after ten minutes of sonication. The solid content is 1.5 wt% with respect to weight monomers.

Even though both types of nanoparticles were hydrophobic, they show a remarkable difference in terms of dispersability in the monomer mixture. As clearly seen, NP_{32} experienced sedimentation in a very short period time (<10 minutes), indicating a high degree of particle aggregation. On the contrary, NP_8 remained stable without any sedimentation, as discussed in section 4.2.1. The same trend was observed when nanoparticles were dispersed in either aliphatic (e.g. heptane, decane) or aromatic (e.g. toluene) hydrocarbons.

Interestingly, regardless of these differences, oleic acid functionalized NP_8 and NP_{32} are both efficient emulsifiers to stabilize W/O HIPEs, as it will be shown below.

In an attempt to understand the stabilization mechanisms operating in Pickering emulsions, interfacial tension measurements were performed using the Du Noüy ring method. For these measurements, the monomer mixture styrene-divinylbenzene (1:1 by wt%) was replaced by toluene due to its lower toxicity, similar chemical structure and easier manipulation in the laboratory. Preliminary experiments showed that systems with toluene emulsified very similar as do the monomer mixture, and no differences in emulsion drop size and emulsion stability were observed. Values of interfacial tension determined are listed in Table 4-9.

Table 4-9. Interfacial tension values (25 ºC) obtained using the Du Noüy ring method. Both the average and the standard deviation were calculated over 3 different measurements. NP_8 (1.5 wt%) remained dispersed in the toluene phase during the measurements. NP_{32} were removed from toluene solutions (1.5 wt%) before determinations.

System	Interfacial tension (mN/m)	Surface tension (mN/m)
Toluene // Water	36.2 ± 0.2	-
Toluene + NP_8 // Water	35. 7 ± 0.2	-
Toluene + 0.07 wt% oleic acid // Water	32.0 ± 0.3	-
Toluene + 0.2 wt% oleic acid // Water	29.8 ± 0.2	-
Toluene + NP_{32} // Water	36.4 ± 0.3	-
Toluene // Air	-	28.3 ± 0.2
Toluene + NP_8 // Air	-	27.7 ± 0.2

The interfacial tension between water and toluene (36.2 ± 0.2 mN/m), was in fairly agreement to the literature values).[297] Then, this value was compared to that in presence of 1.5 wt% NP_8 in the toluene phase. The addition of NP_8 nanoparticles decreased very little the oil-water interfacial tension (35.7 ± 0.2 mN/m, Table 4-9). In addition to that, surface tension measurements of toluene, with and without particles, were in agreement with that described above, and no reduction of the tension was observed when NP_8 were dispersed in toluene (Table 4-9). It should be remarked that NP_8 were coated with oleic acid during the synthesis step. It could be possible that part of the oleic acid detached from the surface of the nanoparticles during sample processing, in a similar way to what occurred during the washing cycles described in section 3.2.1.

In order to account for the individual contribution of NP_8 and oleic acid, interfacial tension of the toluene-water system in the presence of free oleic acid was also measured (Table 4-9). This was accomplished by measuring water and toluene containing oleic acid concentrations equivalent to the amount of oleic acid adsorbed on NP_8 (ca. 0.21 wt%). The results show a reduction in the interfacial tension values from 36.2 (pure toluene) to 29.8 mN/m. Interfacial tension for even lower oleic acid concentrations (0.07 wt%) was also determined (32.0 mN/m). These results imply that most of oleic acid molecules remained adsorbed on NP_8 surfaces, since reduction of interfacial tension in the presence of oleic acid functionalized NP_8 was not observed. It is worth pointing out that a previous step of sonication was applied to disperse the nanoparticles in the organic solvent. Therefore, one can conclude that sonication does not pull out oleic acid from the particles surface.

Afterwards, the interfacial tension between water and toluene, the latter having been in contact with NP_{32}, was also measured. Due to the instability of NP_{32} in such solvent (Figure 4-37), NP_{32} were first dispersed using a sonicator and then removed before the measurement. Therefore, the corresponding interfacial tension measurements could not be carried out in the presence of such NP_{32}. Otherwise, the measurements would have been inaccurate due to the distortion of the interface by nanoparticle sedimentation. The value (36.4 ± 0.3 mN/m) was identical within error to the pure water-toluene interfacial tension, confirming the absence of free oleic acid in the toluene phase. In analogy with NP_8, it can be therefore inferred that oleic acid remained almost completely attached to the surface of NP_{32} particles.

These results rule out the possibility that the main stabilization mechanism in Pickering emulsions stabilized with NP_8 is the reduction in interfacial tension, and are consistent with other works in the bibliography, which demonstrate that the presence of the particles has a negligible influence on tensions.[58, 78, 117] In the present case, it can be therefore assumed that particles do not replace molecules of water and oil at the interface, in contrast to surfactant molecules.

4.3.2 Emulsion Formation: Effect of Size, Oleic Acid Content and Concentration of Nanoparticles

The maximum internal phase volume fraction of W/O Pickering emulsions that could be reached for various concentrations of surface-modified NP_8 and NP_{32} is plotted in Figure 4-38(a). Emulsions consisted in water droplets dispersed in the monomer mixture containing nanoparticles. Emulsion type (W/O) was inferred from conductivity measurements. It was observed that with 3 wt% NP_{32} the maximum internal phase volume was 92.5 %. Recently, in a similar study, Ikem et al.[100] reported the stabilization of W/O HIPEs with a 92 % internal phase volume using oleic acid-modified silica nanoparticles. The value corresponding to NP_8 (89 % using 5 wt% of NPs) was slightly lower than that found for NP_{32}.

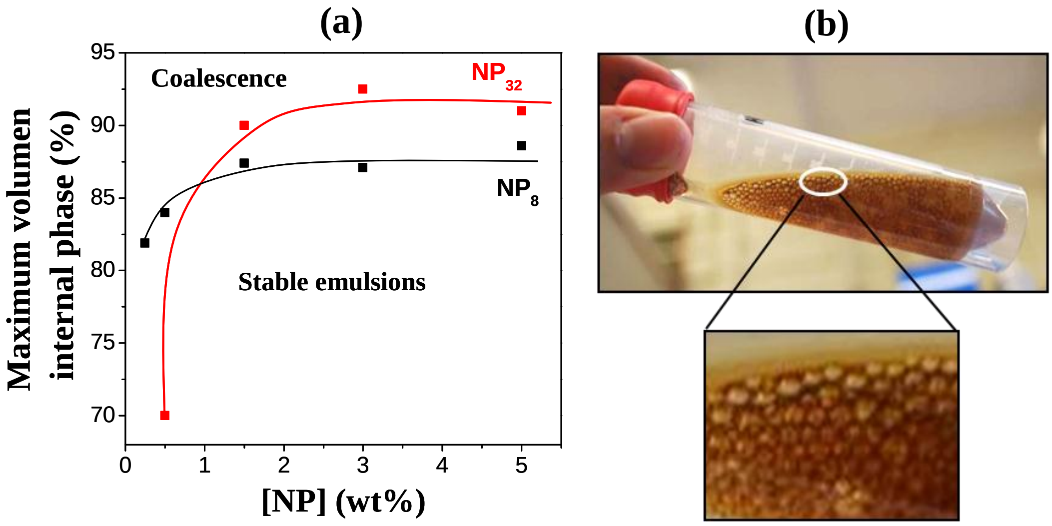

Figure 4-38. (a) Maximum internal phase volume percentage reached in W/O emulsions stabilized with either oleic acid surface-modified (■) NP_8 or (■) NP_{32}, at different nanoparticle concentrations. Lines are simply drawn to guide the eye. The oil phase was formed by a mixture of styrene and divinylbenzene with ratio 1:1 by weight. (b) Images of a Pickering HIPE with an 82 % internal phase volume stabilized with only 0.25 wt% NP_8.

Concentrations of water above the curves depicted in Figure 4-38(a) led to droplet coalescence and fast phase separation. For both types of nanoparticles, the maximum water content reached a constant value at ca. 2 wt% nanoparticle concentration, suggesting that this is the particle concentration required to cover the surface of the droplets. It was attempted to obtain stable emulsions at higher nanoparticle concentrations (e.g. 10 wt%), but the emulsions could not be formed because of high viscosity of the external phase, containing the nanoparticles.[100] It is known that Pickering emulsions with large droplets are not very stable under shear, and thus, high shear cannot be applied during emulsification.[298]

Figure 4-38(a) clearly shows that the maximum volume of internal phase increases with concentration of nanoparticles. Obviously, a larger amount of nanoparticles can cover a bigger surface area, and thus more concentrated emulsions are obtained. An example of a Pickering highly concentrated emulsion (Pickering HIPE) stabilized at low NP_8 concentration (0.25 wt%) is shown in Figure 4-38(b). Due to the low nanoparticle concentration, large emulsion droplet sizes, visible to the naked eye, were obtained. While 0.25 wt% NP_8 was enough to stabilize emulsions with 82 % internal phase volume, 0.5 wt% NP_{32} was necessary to stabilize HIPE emulsions with 70 % internal phase volume. However, it is evident from the results that NP_{32} were more effective, i.e. more internal phase incorporated in the emulsions, when the nanoparticle concentration was increased.

Before emulsification, nanoparticles were dried and redispersed in the oil phase using sonication. As expected, particle suspensions containing NP_8 were significantly more stable than those containing NP_{32}. Large aggregates of nanoparticles due to colloidal aggregation were observed in the case of NP_{32} leading to quick sedimentation. Such aggregates can adsorb to the oil-water interface, greatly influencing Pickering emulsion stabilization,[52] and as consequence preventing droplet coalescence. On the other hand, probably smaller NP_8, which are less aggregated, can cover a much larger interfacial area, thus stabilizing emulsions more efficiently at lower nanoparticle concentrations.

Another point that should be taken into account is the wettability of the nanoparticles. A higher content of oleic acid covering NP_8 surface (12.4 wt%) may induce a preferential dispersion in the oil phase rather than a preferential adsorption in the oil-water interface. This could reduce the ability to stabilize emulsions with higher contents of water compared to NP_{32} (4.4 wt% oleic acid) when the concentration of nanoparticles is high enough. TEM observations (discussed in next section) will provide evidence for different distributions of both types of nanoparticles between the interface and the oil phase.

W/O Pickering HIPEs with a 1.5 wt% NP_{32} concentration (respect to monomer) were selected for a systematic study. Figure 4-39 shows an image of the emulsions, 15 min. after emulsification, as a function of water volume fraction. These Pickering HIPEs were prepared by dispersing water in the monomer mixture, which contained the nanoparticles. The higher internal phase volume (up to 90 vol%), the larger droplet size for a constant nanoparticle concentration in the oil. This was expected because the total concentration of nanoparticles decreases upon increasing the internal phase volume. Consequently, an extra oil-water interface cannot be covered with a sufficient number of adsorbed particles. As seen from the figure, at 95 vol% internal phase, emulsion undergoes complete phase separation.

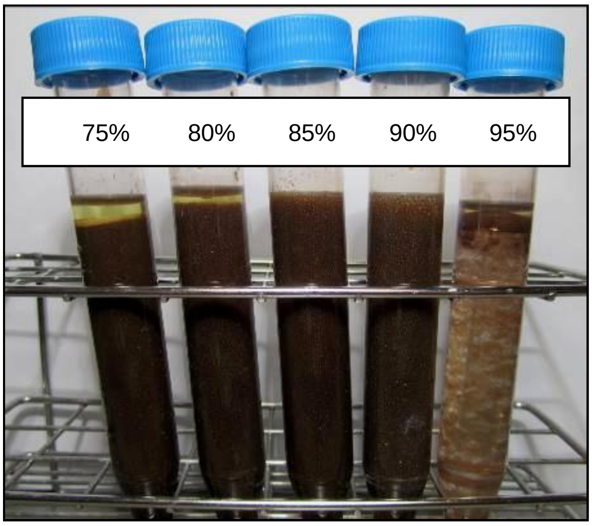

Figure 4-39. Influence of internal phase volume fraction on emulsion stability for Pickering highly concentrated emulsions stabilized with 1.5 wt% NP_{32} (respect to monomer).

Water droplets in emulsions with 75 and 80% internal phase volumes partially sedimented over time and a thin layer of supernatant oil was observed (Figure 4-39). There was no evidence of the presence of particles into the oil released, indicating most likely a complete adsorption of nanoparticles at the oil-water interface. Above 80 vol% water, emulsions were stable against sedimentation. This is due to the high packing of emulsion droplets upon raising the internal-phase volume fraction.[100] Furthermore, when NP_{32} concentration was increased to 3.0 wt %, W/O Pickering HIPEs did not experience sedimentation in the course of time (Figure 10-4 in the Appendix). This feature is common in Pickering emulsions and is generally attributed to the fact that viscosity of the continuous phase increases, retarding or suppressing sedimentation of water drops in the case of W/O emulsions.[24] Meanwhile, the viscosity also increases owing to the reduction in droplet size.

In samples stabilized with 1.5 wt% NP_8, emulsion sedimentation was also not observed. This result was in good agreement with the observations made by Binks and Lumsdon.[104] In their work, a decrease in particle diameter partially hindered sedimentation of W/O Pickering emulsions. Despite this, emulsions prepared with either NP_8 or NP_{32} were stable to coalescence for over 3 months.

Figure 4-40 shows three optical microscopy images corresponding to W/O Pickering HIPEs containing a 75% internal phase volume and stabilized with (a) 1.5 and (b,c) 3.0 wt% NP_8. Both emulsions possessed a wide droplet size distribution ranging from 10 to 300 μm, but droplet size slightly decreased when increasing nanoparticle concentration to 3 wt%. Similar to the emulsion shown in Figure 4-35(c), which was stabilized with oleic-acid surface modified NP_{32}, some NP_8 aggregates were observed on the oil droplets (Figure 4-40(c). However, an important difference was found between the two systems. In NP_8 stabilized emulsions, some nanoparticles were distinguished not only at the interface, but also in the continuous phase. This was observed when the sample on the microscope slide started to dry, and one example can be seen in the background behind the emulsion droplets in Figure 4-40(b). This is in fair agreement with the assumption that NP_8 can partially be dispersed in the continuous phase due to its higher dispersability and hydrophobicity.

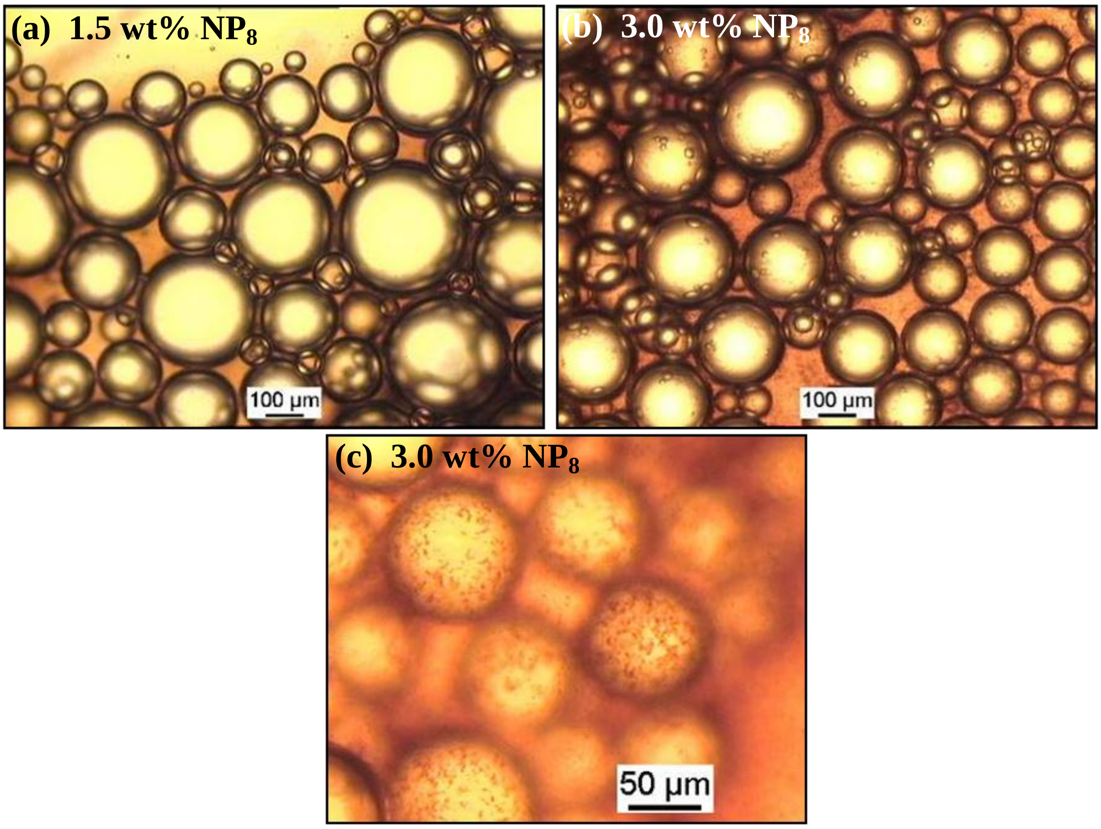

Figure 4-40. Optical microscopy images of Pickering HIPEs, having 75% internal phase volume, and stabilized with (a) 1.5 and (b,c) 3 wt% NP_8.

In Pickering HIPEs, the process that is considered to control droplet size at low-particle-concentrations is the so-called limited coalescence process. Arditty et al.[29] studied the formation of Pickering HIPEs with low particle concentrations, describing that smaller droplets coalesce to form larger droplets until a certain limit is reached in which interfacial area between oil and water is totally covered with nanoparticles. Moreover, they also found that the polydispersity of the resultant large droplets was relatively narrow. This could be the case of the emulsion shown in Figure 4-38(b), and could also explain the big droplet sizes observed in Figure 4-40. Generally, droplets in Pickering emulsions, containing similar contents of water and oil, are in the range of 0.2 to 50 µm.[67, 70, 104, 299] However, at low particle concentrations or at high internal phase volume fractions, droplets become bigger.

It should be pointed out that in all emulsions stabilized using either NP_8 or NP_{32} (with 12.4 and 4.4 wt% oleic acid, respectively), catastrophic phase inversion[67] (from W/O emulsion to O/W emulsion) did not occur during addition of the internal phase. As described in the literature, such an inversion is expected to take place in emulsions stabilized with particles indistinctly partially hydrophilic or partially hydrophobic. This inversion can be controlled in most cases by modulating the hydrophobicity of particles surface,[24] or by modifying pH,[73] temperature[300] or electrolyte concentration[103].

To evaluate the degree of NP_{32} hydrophobicity, emulsions were prepared by varying the oleic acid content on NP_{32} surface while keeping all other parameters constant. NP_{32} covered with a smaller amount of oleic acid (2.2 wt% instead of 4.4 wt%) were used. Such oleic acid concentration was achieved after five washing cycles (TGA curve in Figure 4-2(b), page 89). From TGA analysis, the surface area per molecule was estimated to be 71.8 $Å^2$/molecule. Interestingly, a phase inversion from a W/O to an O/W emulsion was observed when approximately 70% of internal phase volume was added, which was consistent with the results reported by Binks.[67] Here, phase inversion took place when the volume fraction (70 %) of dispersed water was near the close-packing condition, which is 74 %. This value is the limit for monodispersed spherical droplets.[9, 10] Figure 4-41 shows the product of a diluted polymerized O/W Pickering emulsion resulting from catastrophic inversion and leading to cross-linked polystyrene microparticles.

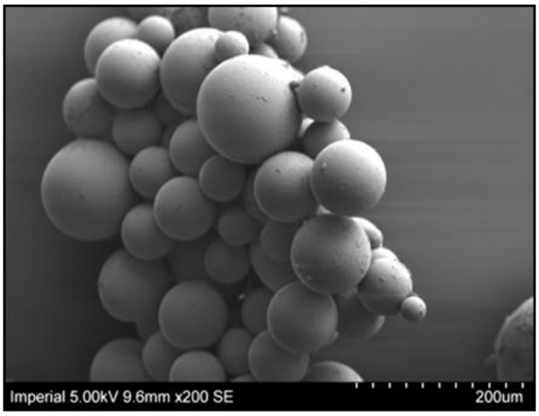

Figure 4-41. SEM image of a polymerized sample after catastrophic inversion from a concentrated Pickering W/O to an O/W diluted Pickering emulsion. Oleic acid content on NP_{32} surfaces was 2.2 wt% and the inversion was observed at 70 % internal phase (water) volume fraction.

Consequently, formation of both W/O Pickering HIPEs and O/W diluted Pickering emulsions can be controlled by adjusting the oleic acid coverage on nanoparticles (NP_{32}) surface.

Despite the good stability exhibited by Pickering emulsions, the presence of a permanent magnetic field has been shown to induce phase separation in systems stabilized with magnetic nanoparticles.[301] This experiment was similarly reproduced by placing Pickering emulsions, stabilized by either NP_{32} or NP_8, into a DynaMag™-15, which can hold tubes and is designed for efficient cell magnetic isolation. Figure 4-42 shows two images of the samples inside the magnet after five minutes and 24 hours. After five minutes, it is seen that the droplets (visible to the naked eye) start to diffuse sidewards. After one day, almost all internal phase (water) has been released, and nanoparticles have been stripped from the interfaces, remaining adhered at the test tube walls, as a result of magnetic attraction. It has been argued that phase separation is induced by droplet compression.[301]

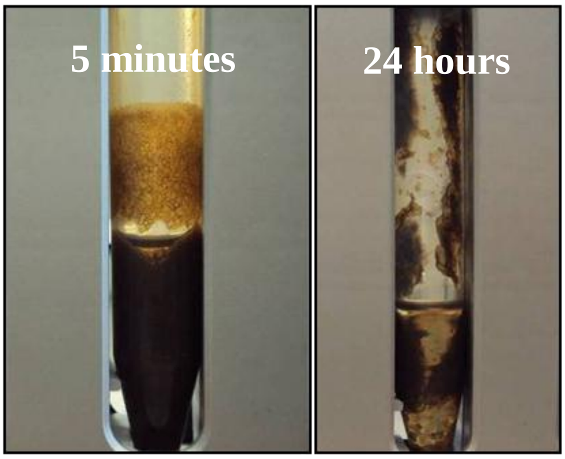

Figure 4-42. Pickering high internal phase emulsion (Pickering HIPE) inside a cell isolation magnet after five minutes (left) and 24 hours (right). The emulsion is stabilized with 1.5 wt% NP_8 (respect to tmonomers) and has a 80:20 water-monomer volume ratio.

One of the interesting points of this experiment is that emulsion droplet alignment can be induced using such magnetic fields. Further work is needed to explore the effect of factors as the type and concentration of particles.

4.3.3 Magnetic Macroporous Polymers Obtained from Pickering High Internal Phase Emulsions

4.3.3.1 *Preparation and characterization of the porous structure*

In this section, we evaluate the influence of several synthesis parameters, such as nanoparticle concentration or internal phase volume fraction in the highly concentrated emulsions (HIPEs), on the physical properties of the macroporous polymers. Details regarding original composition of HIPEs and main physical properties of the macroporous materials are provided in Table 4-10.

Table 4-10. Internal phase volume (ϕ) and nanoparticle concentration (NP wt%, respect to the continuous phase) of Pickering HIPEs prepared in this section and skeletal density (ρ_s), porosity (P) and average pore diameters corresponding to the smaller and the larger size populations of macroporous polymers, obtained after the polymerization of the continuous phase of the HIPEs.

Sample	ϕ **(vol%)**	**NP**	**[NP] (w/w%)**	ρ_s **(g/cm^3)**	**P (%)**	**Average pore size [µm]** Population 1	**Population 2**
1	75	NP_8	0.5	1.09 ± 0.01	83.2 ± 5.3	21 ± 12	436 ± 108
2	75	NP_8	1.5	1.09 ± 0.01	78.8 ± 2.2	22 ± 16	154 ± 38
3	75	NP_8	3.0	1.13 ± 0.01	79.5 ± 2.0	18 ± 13	124 ± 38
4	75	NP_{32}	3.0	1.12 ± 0.01	79.4 ± 2.3	37 ± 22	237 ± 92
5	85	NP_{32}	3.0	1.13 ± 0.01	88.9 ± 1.9	32 ± 22	310 ± 83
6	92.5	NP_{32}	3.0	1.13 ± 0.01	94.0 ± 1.3	27 ± 15	669 ± 189
7	85	NP_{32}	5.0	1.13 ± 0.01	86.9 ± 0.5	30 ± 19	287 ± 75
8	85	NP_8	5.0	1.13 ± 0.01	87.5 ± 0.6	24 ± 15	378 ± 98

Following the method described in the experimental section (3.2.7), macroporous polymers were obtained by free-radical polymerization in the continuous phase of W/O Pickering HIPEs, composed of a mixture of styrene and divinylbenzene (1:1 by weight). Polymerization was induced by adding a initiator (AIBN, 1 wt% respect to the monomer) and heating at 70 ºC for 24 h. As a result, macroporous polymers with no significant shrinkage were obtained after drying. No time-consuming purification was needed because the emulsions did not contain any surfactant. The appearance of the materials is shown in Figure 4-43(a). It is important to mention that the homogeneity of the brown colour along the sample is a first indication of the good dispersion of nanoparticles in the polymer matrix. Furthermore, the dried foams were easily attracted to a magnet, suggesting that materials had a relatively high magnetic moment.

The image shown in Figure 4-43(a) presents the sample sequence 1-3, in which the NP_8 wt% concentrations were 0.5, 1.5, and 3.0, respectively, keeping the internal phase volume fraction constant (75 %, Table 4-10). The larger pores can be clearly seen, especially in the sample made with the lowest nanoparticle concentration. Bulk density and porosity of the same samples were determined by means of pycnometry. The skeletal density increased from 1.09 to 1.13 g/cm^3 upon increasing nanoparticle concentration. Such densities were higher than that of pure polystyrene (1.05 g/cm^3) because of the incorporation of inorganic nanoparticles into the polymer structure. Porosities (P) were always higher than the internal phase volume fractions

(ϕ) added in the original emulsions, which were the same for all of them (75%, Table 4-10). This fact could be due to two possible reasons:

I. An increase in skeletal density during polymerization due to monomer (ρ of styrene 0.91 g/cm^3) to polymer volume contraction (ρ of polystyrene 1.05 g/cm^3), that vinyl monomers undergo on polymerization.[211] Accordingly, for macroporous polymers obtained after polymerization of the continuous phase of emulsions, containing 75, 80 or 85 vol% internal phase, their porosities will be 78.3, 82.6, or 87 %, respectively (porosity equation, eq-2-6, page 81).

II. An incomplete conversion of monomers to polymer can also contribute to cause a small increase of the porosities values.

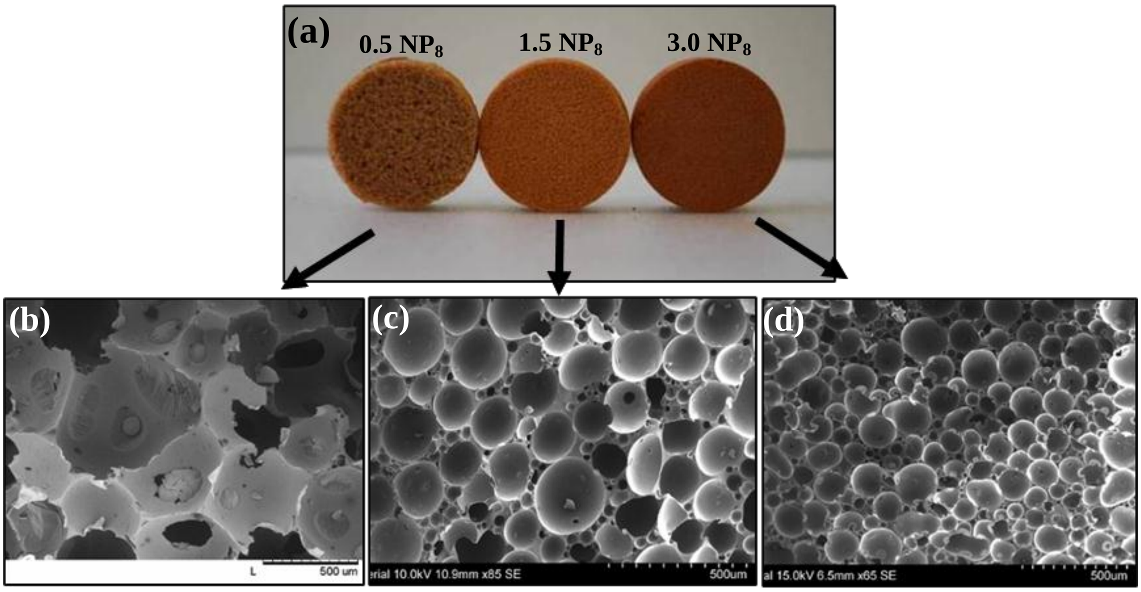

Figure 4-43. (a) Photograph of macroporous polymers synthesized from Pickering HIPEs containing a 75 vol% internal phase (water) and stabilized with 0.5, 1.5 and 3.0 wt% NP$_8$. (b-d) SEM images of the macroporous polymer shown in (a). The scale bars indicate 500 μm.

The same samples shown in Figure 4-43(a) were also characterized by SEM to examine their macroporous structure. The morphologies displayed in Figure 4-43(b-d) are quite similar to other macroporous polymers made from Pickering emulsions described in the literature.[176, 204, 206] These macroporous polymers have a close-cell structure. It is widely accepted that a dense film layer is formed by the nanoparticles at the oil-water interface, creating a rigid film between adjacent droplets in the emulsions. After polymerization, thick polymer films between neighbouring pores are thus obtained, which hinder formation of pore connexions.

In comparing images in Figure 4-43(b-d), it is clear that when nanoparticle concentration is increased, pore size gradually decreased because of the stabilization of a larger interfacial area. The average pore diameter of larger pores decreased from 450 μm in the case of the sample with 0.5 wt% NP_8 (Figure 4-43(b)) to 125 μm for sample with 3 wt% nanoparticles (Figure 4-43(d)). These diameters correspond to the pore population 2 in Table 4-10.

Apart from nanoparticle concentration, the other important parameter influencing droplet size in Pickering emulsions is the volume fraction of the internal phase. The influence of this parameter, studied in macroporous polymers made from Pickering HIPEs stabilized with NP_{32}, is shown in Figure 4-44. In this experiment, emulsions with 75 vol% (sample 4, Table 4-10), 85 vol% (sample 5), and 92.5 vol% (sample 6) water were prepared by keeping NP_{32} concentration constant (3 wt%).

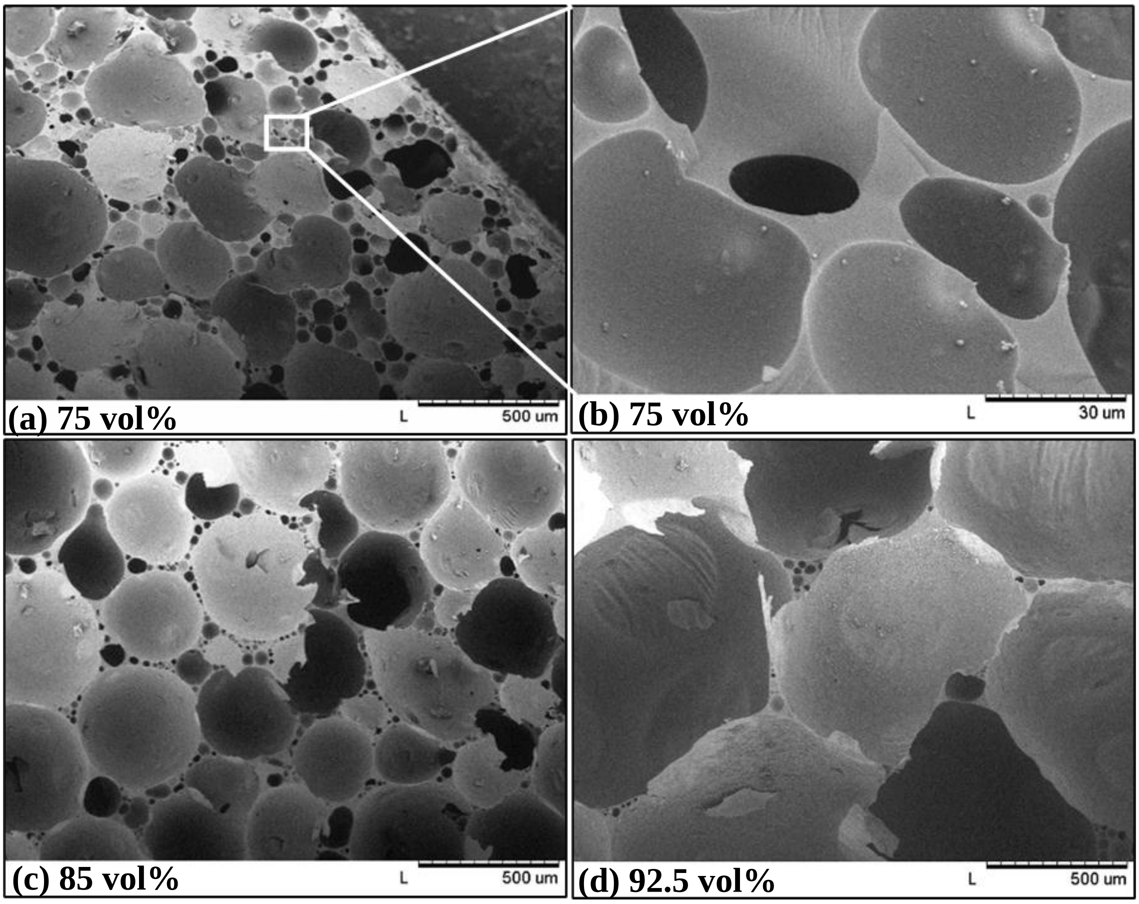

Figure 4-44. SEM images of macroporous polymers synthesized from Pickering HIPEs containing 3.0 wt% NP_{32} and having (a,b) 75, (c) 85, and (d) 92.5 % internal phase volumes. (b) is a higher-magnification image of (a).

As clearly seen in the figure, the higher internal phase volume, the higher pore size. This is because the total nanoparticle content in the emulsions decreases gradually as water (internal phase) fraction increases. Regarding microstructure, SEM images shown in Figure 4-44 revealed that the features observed for poly-Pickering HIPEs made from HIPEs stabilized with NP_{32} were essentially the same as those stabilized using NP_8 (Figure 4-43). It is noteworthy that the integrity of macroporous structure was not affected, even though the size of the NP_{32} is significantly larger than for NP_8. In all cases, SEM images showed a considerably larger number of smaller pores, in line with optical microscope observations of the original HIPEs. A magnified image of the smallest pores of the macroporous polymer shown in Figure 4-44(a) is depicted in Figure 4-44(b). Closed small pores are placed at the plateau borders of larger pores in the materials, and they are separated by polymer walls that are about 1-15 µm thick. As pointed out before, the closed-cell structure is typical of macroporous polymers prepared from Pickering emulsions. The absence of pore throats between neighbouring cells is generally attributed to thicker biliquid films in particle-stabilized systems, in comparison to biliquid films stabilized with surfactants. Pore interconectivity will be discussed in detail in section 4.4.3.2.

The resulting values of bulk density and porosity (Table 4-10) of the samples containing 3 wt% NP_{32} were consistent with the values calculated for poly-Pickering HIPEs containing NP_8. First, skeletal density values remained constant at 1.13 g/cm^3 when using the same nanoparticle concentration. Second, porosities were again slightly higher than the internal phase volume fraction of the initial emulsions. Because the sample prepared from a HIPE with 92.5 vol% internal phase (sample 6) was too brittle and broke during the measurement, the porosity of this sample could not be determined using pycnometry. However, the porosity was estimated to be 94% by measuring the weight and approximate volume of three pieces corresponding to one sample.

Emulsion droplets and pores in the macroporous polymers were similar in size, demonstrating that no destabilization occurred during the polymerization step. As aforementioned, two distinct pore populations were clearly observed, indicating a bimodal pore size distribution of macropores. A quantitative analysis of the pore size distributions was carried out, using the direct pore counting method from SEM images. The pore number distributions are shown in Figure 4-45. Two maximums, which correspond to the distinct populations are observed. The corresponding average sizes for small and large pore populations are listed in Table 4-10.

(a) 75 vol% internal phase at different NP_8 concentrations

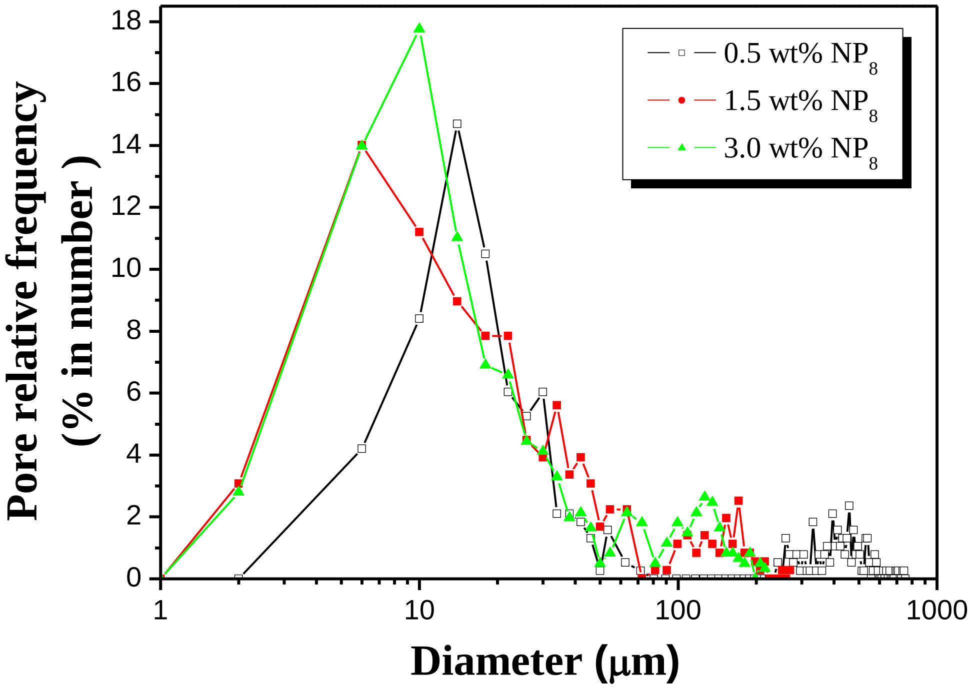

(b) 3 wt% NP_{32} at different internal phase volume fractions

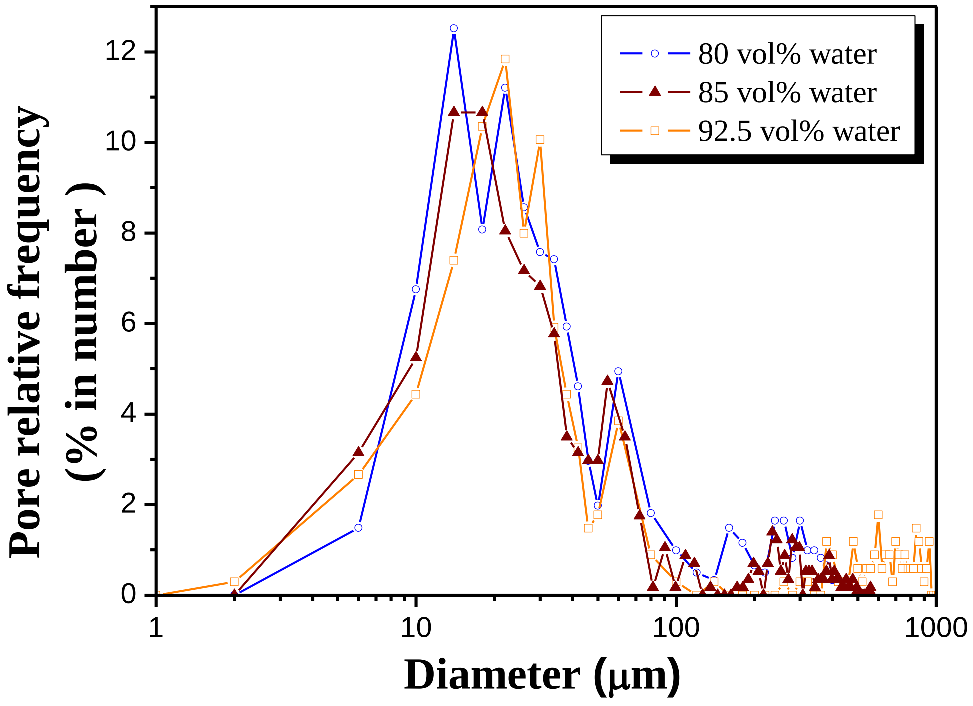

Figure 4-45. Pore size distributions for (a) macroporous polymers synthesized from Pickering HIPEs containing the same internal phase volume fractions (75 %), showing the influence of nanoparticle (NP_8) concentration, and for (b) samples in which the nanoparticle (NP_{32}) concentration (3 wt%) is kept constant, showing the influence of the internal phase volume (water).

Figure 4-45(a) shows that the average size of the population with larger pores, which are easily observed in Figure 4-43(b-d), dropped from values near 420 to 120 µm when the nanoparticle concentration increased from 0.5 wt% to 3 wt%, at constant 75 % emulsion internal phase (Table 4-10). This means that the extent of limiting coalescence in the emulsions decreased gradually, and consequently pore size distribution becomes narrower. Therefore, the size of the larger pores can be used as a qualitative measurement of emulsion stability.

It should be noted that smaller pores are much more numerous than larger pores. Moreover, the size of the smaller size population (maximum peak observed at about 10-15 µm, Figure 4-45(a)) is practically the same in all samples, and it does not depend on nanoparticle concentration. On the other hand, a small fraction of large pores can have most of the total pore volume, and then, it can negatively affect the mechanical integrity of the materials, as will be discussed in detail later on.

Figure 4-45(b) shows the influence of the internal phase volume fraction on pore size distributions of the same macroporous polymers shown in Figure 4-44, which contained NP_{32}. Even though the number of small pores (most of them are from 15 to 35 µm size) is considerably higher in all cases, the size of the large pores shifts to higher values when the internal phase volume increased from 80 to 92.5 vol%. Pores with large sizes, greater than 1000 µm, were found in the sample with 92.5 vol% internal phase, leading to the brittleness of the sample. As expected, the higher water volume fraction, the higher pore size.

As a general trend, pore size distributions of macroporous foams, prepared from HIPEs containing either NP_8 or NP_{32}, exhibited similar patterns. However, average sizes of the smaller pore populations of macroporous polymers containing NP_8, were in all cases smaller than those determined for the materials containing NP_{32} (Table 4-10).

In order to study the internal structure of the macroporous polymers walls, TEM images of sample thin sections embedded in an epoxy resin were taken. First, a macroporous polymer prepared from a Pickering HIPE with 85 vol% internal phase, and stabilized with 5 wt% NP_{32}, was examined (Figure 4-46(a-c). The figure shows representative examples with all of the different regions observed in the ultramicrotome slides.

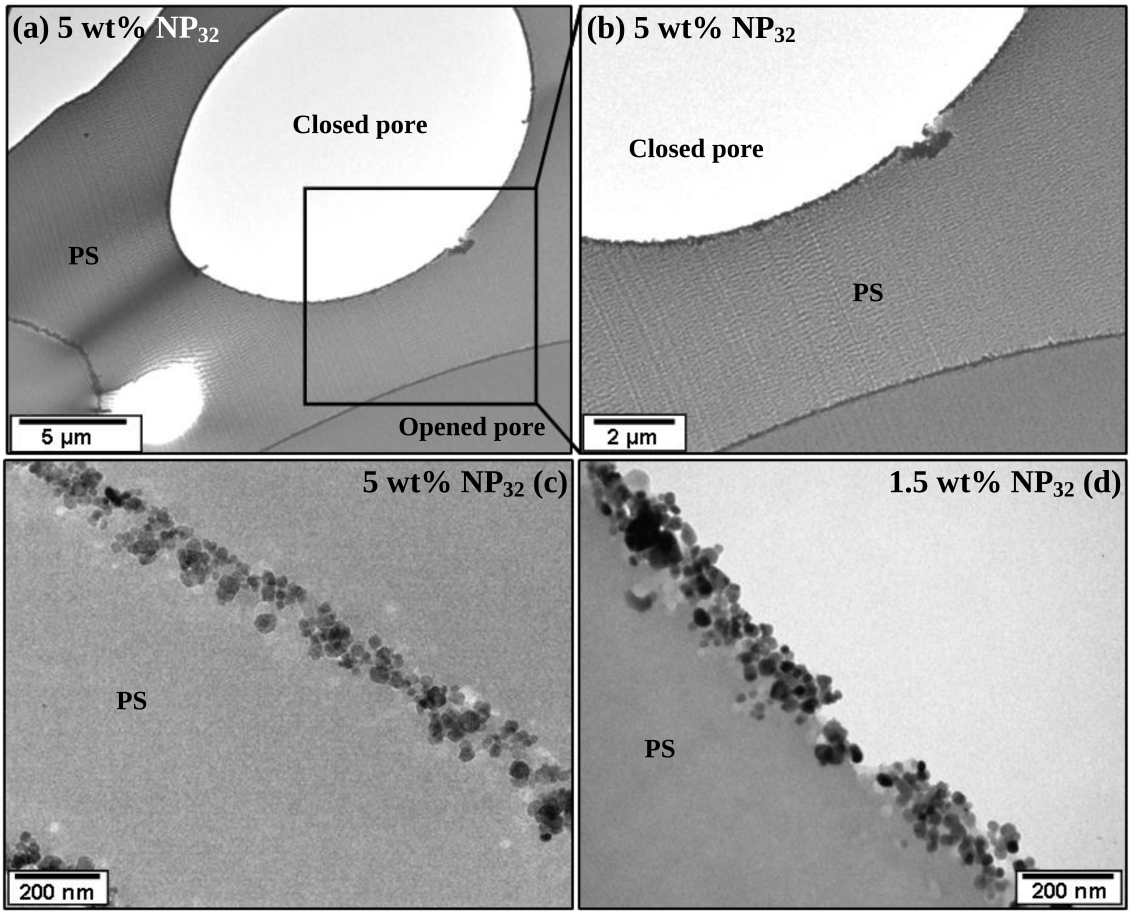

Figure 4-46. Representative TEM images of ultramicrotome slides (around 60 nm thick) showing the distribution of nanoparticles (NP_{32}) in the polymer matrix of a macroporous polymer. Macroporous polymers were obtained from Pickering HIPEs with an 85 % internal phase volume and stabilized with (a-c) 5 wt% and (d) 1.5 wt% NP_{32}, respectively. PS indicates polystyrene wall..

These TEM images show that several micrometer-sized pores are surrounded by polymer walls (indicated in the figure as PS), which is in agreement with the SEM micrographs depicted in Figure 4-44(b). Iron oxide nanoparticles are clearly visible at the pore-polymer interface. It is important to note that the pores are not always filled with the epoxy resin used before the cutting process, and air remained trapped inside closed pores. The low permeability of the materials with respect to such a resin could be explained by the characteristic close-cell structure of the macroporous polymers.

TEM images undoubtedly revealed that aggregated NP_{32} were located exclusively on the polymer surface, which was the former W/O interface in the Pickering highly concentrated emulsions (HIPE) template (Figure 4-46(a-c)). The fact that nanoparticles are aggregated explains why the amount of nanoparticles required for stabilization, was higher than the concentration needed to form a single monolayer.

An interesting point is that hardly any NP_{32} could be found deep inside the pore wall. Therefore, the nanoparticles did not change their wettability during polymerization. Even though NP_{32} were partially aggregated, they could be easily singled out from TEM images (Figure 4-46 (c-d)). It is well known that nanoparticle aggregation might improve the stability of Pickering emulsions. The arrangement exhibited by these nanoparticles was consistent with recent observations made by Gurevitch.[206, 209]

For comparison, Figure 4-46(d) shows a TEM image of a macroporous polymer made from a Pickering HIPE stabilized with 1.5 wt% NP_{32}, rather than with 5 wt%. Similar degree of surface coverage was observed despite the lower nanoparticle concentration used. As discussed previously, pore size of macroporous polymers increases when decreasing nanoparticle concentration. This occurs in a way that particle surface coverage seems to remain approximately constant (Figure 4-46(d)).

The same TEM observations were carried out for samples prepared with NP_8 nanoparticles, which were previously surface-modified with 12.4 wt% oleic acid (Figure 4-47). Even though most of NP_8 were located at the polymer-air interface (Figure 4-47(a,b)), there was a significant number of NP_8 embedded within the polymer walls (Figure 4-47(c)). This behaviour is significantly different than that observed for NP_{32}. Inside the polymer, NP_8 were individually and homogenously dispersed. This evidence indicated that some NP_8 had a higher affinity for the continuous phase of the W/O HIPEs and they could be effectively dispersed into the oil phase. Therefore, it can be assumed that a higher content of oleic acid produced more lipophilic particles and prevented its aggregation within the polymer. Another difference between NP_{32} and NP_8 nanoparticles is that due to the smaller size of NP_8, the number of nanoparticles for a given volume of solid material is considerably higher compared to NP_{32}, i.e. almost 84 times larger. This could explain that the thickness of the several layers trapped at the interface in some regions of the sample is higher in the case of NP_8 (compare Figure 4-47(b) and Figure 4-46(c)).

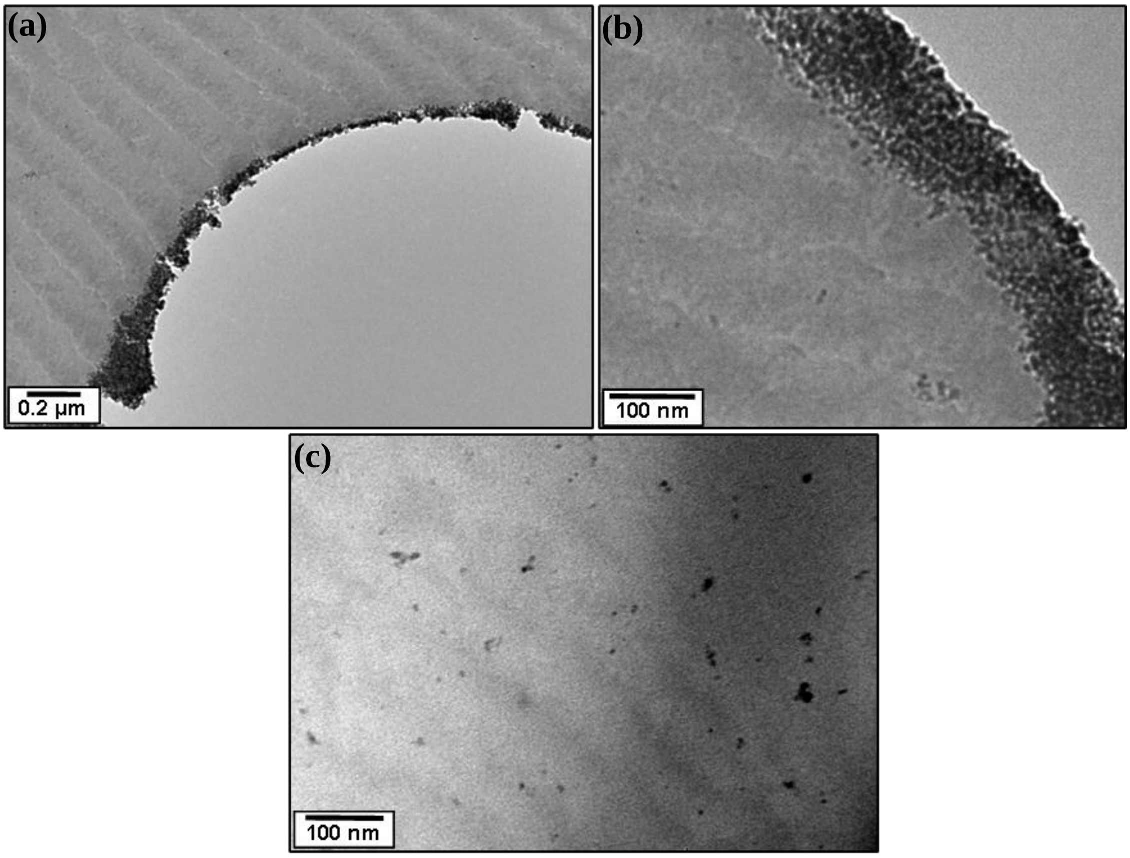

Figure 4-47. Representative TEM images of a macroporous polymer obtained from a Pickering HIPE with an 85% internal phase volume, and stabilized with 5 wt% NP_8 (sample 8, Table 4-10), showing that most nanoparticles are located at the interface (a,b) although many are embedded in the polymer matrix (c).

These results strongly confirm previous observations during formation of the highly concentrated emulsions (HIPEs). The ability of NP_{32} to absorb more effectively at the W/O interface (compared to NP_8) is most likely the reason for the better capacity to incorporate larger internal phase volumes in the emulsions. It should be remarked that regardless of the initial state of dispersion of both solids (NP_{32} and NP_8) they could act as efficient emulsifiers. Based on these experimental findings, it can also be concluded that the stabilization mechanism in these Pickering emulsions is most likely provided by steric (mechanical) hindrance to droplet coalescence,[49] attributed to the complete surface coverage of droplet surfaces by dense particle layers.

4.3.3.2 *Mechanical Properties*

Crush strength (σ) and Young modulus (E) of macroporous polymers were determined under compression load at room temperature. Mechanical properties were characterized with respect to the internal phase volume and type and concentration of nanoparticles in the original HIPEs.

Mechanical properties and initial emulsion compositions are listed in Table 4-11. The average and the standard deviation values of Porosity (P), σ and E were obtained from at least 6 measurements of different parts of two different macroporous polymer monoliths.

Table 4-11. Internal phase volume (ϕ) and nanoparticle concentration (C_p, respect to the continuous phase) of Pickering HIPEs, and porosity (P), crush strength (σ), specific crush strength (σ_s) and Young (elastic) modulus (E) of the macroporous polymers obtained after polymerization of the continuous phase of the HIPEs.

Sample	ϕ (vol%)	NP	C_p (w/w %)	P (%)	σ (MPa)	σ_s ($MPa \cdot m^3 \cdot Kg^{-1}$)	E (MPa)
1	75	NP_8	0.5	83.2 ± 5.3	1.2 ± 0.8	0.006 ± 0.002	29 ± 23
2	75	NP_8	1.5	78.8 ± 2.2	3.4 ± 0.6	0.015 ± 0.001	83 ± 11
3	75	NP_8	3.0	79.5 ± 1.1	3.9 ± 0.7	0.017 ± 0.002	94 ± 21
9	80	NP_8	1.5	83.7 ± 2.5	1.2 ± 0.6	0.007 ± 0.003	26 ± 8
10	80	NP_8	3.0	83.4 ± 1.3	1.5 ± 0.3	0.010 ± 0.001	32 ± 13
11	85	NP_8	1.5	87.7 ± 2.4	0.7 ± 0.3	0.005 ± 0.001	14 ± 3
12	85	NP_8	3.0	88.8 ± 0.9	1.0 ± 0.1	0.007 ± 0.001	20 ± 8
8	85	NP_8	5.0	87.5 ± 0.6	1.0 ± 0.3	0.007 ± 0.002	20 ± 8
4	75	NP_{32}	3.0	79.4 ± 2.3	3.1 ± 0.5	0.013 ± 0.001	67 ± 19
13	80	NP_{32}	3.0	84.6 ± 3.1	1.3 ± 0.5	0.007 ± 0.002	31 ± 14
5	85	NP_{32}	3.0	88.9 ± 1.9	0.5 ± 0.2	0.004 ± 0.001	7 ± 3

Representative stress-strain curves are plotted in Figure 4-48(a). The stress represents the load, i.e. force applied to the monoliths, and the strain represents deformation, which is expressed as twice the displacement respect to the initial sample height. The curves show an initial elastic region, from which Young modulus was calculated, as detailed in the experimental section (3.2.9.3). At higher strain values, the macropororous structure collapses, and the maximum stress at the end of the linear region is taken as the crush strength. The three curves correspond to samples 1-3, in which the concentration of NP_8 in the original Pickering HIPEs (75 vol% water) was increased from 0.5 to 3 wt%. As seen in Table 4-11, the increase of nanoparticle concentration from 0.5 to 3 wt% leads to an increase of crush strength from 1.2 to 3.9 MPa, respectively. This is probably due to a reduction of the average pore diameter corresponding to the larger size population, when nanoparticle concentration is increased. The pore size distributions as a function of nanoparticle concentration (NP_8) can be found in Figure 4-45(a). It is accepted that foams with wide pore size distributions, specially those possessing larger pore sizes are most likely to experience mechanical failure, than those with less polydisperse populations.[178, 218] Apart from that, particles might act as polymer reinforcement.

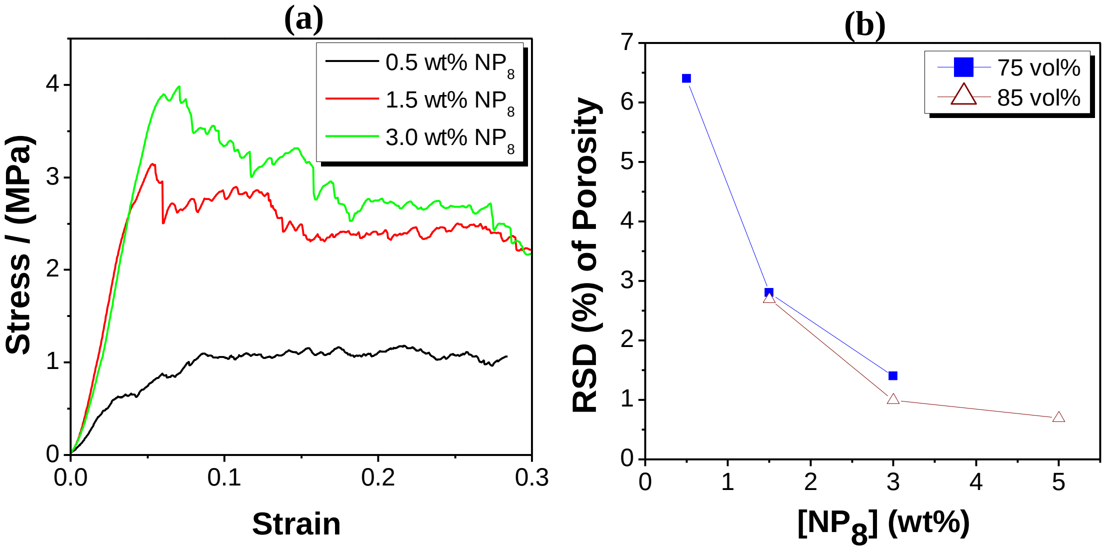

Figure 4-48. (a) Representative stress-strain curves for samples 1, 2 and 3 under compressive load. The samples were prepared from Pickering HIPEs containing 75% internal phase volume (water) and stabilized with different amounts of NP_8. (b) Relative standard deviation (%RSD) of Porosity as a function of NP_8 concentration for macroporous polymers made from HIPEs containing internal phase volume fractions of 75 (samples 1-3, Table 4-11), and 85% (samples 8,11 and 12).

It is relevant to note that both, crush strength and Young modulus standard deviations are quite high, especially in the samples with lower nanoparticle concentrations (Table 4-11). This is mainly due the rather inhomogeneous foam density across the monolithic-shaped macroporous polymers. To examine this effect, the densities of the three (i.e. top, middle and bottom) disks used in the mechanical characterization test, were determined using mass/volume measurements. The porosities (%) of such samples were then calculated taking into account the skeletal densities previously measured using Picnometry (eq. 3-8, page 81). The relative standard deviation (%RSD) of porosity values of macroporous polymers, made from Pickering HIPEs, containing from 0.5 to 5.0 wt% NP_8 and 75 or 85 vol% water are plotted in Figure 4-48(b). As observed in the figure, there is a dramatic decrease in the RSD between replicas of the same material upon increasing nanoparticle concentration. Such a difference dropped from around 6.5% (sample 1) to approximately 0.6 % (sample 8) in the range of NP_8 concentrations studied (0.5-5 wt%). Furthermore, it was found that for the same nanoparticle concentration (e.g. 1.5 wt%, samples 2 and 11) similar variations were found, regardless of the internal phase volume fraction added to the original emulsions.

It is evident from the results that the large variations (RSD) in porosities observed in the macroporous polymers, are mainly due to the drainage of the organic phase when polymerization of the continuous phase of the emulsions is taking place. This drainage produces a decrease of continous phase from top to bottom, as time elapses. However, Figure 4-48(b) indicates that such process is minimum for initial emulsions stabilized with 5 wt% NP_8.

As a consequence of drainage, it seems plausible that samples have different crush strengths values along the sample height. For a sample with homogeneous pore size distribution and nanoparticle concentration, but with inhomogeneous foam density (i.e. porosity), the wall thickness separating neighbour pores will be different along the monolith height. Herein, the higher foam density, the higher toughness will be.

In order to overcome this, crush strength values were normalized by dividing the crush strength by its foam density. As a consequence, standard deviations of the normalized specific crush strength are significantly lower than those observed for crush strength values. Normalized specific crush strength and Young modulus values of samples 1-3 are plotted in Figure 4-49 as a function of nanoparticle (NP_8) concentration.

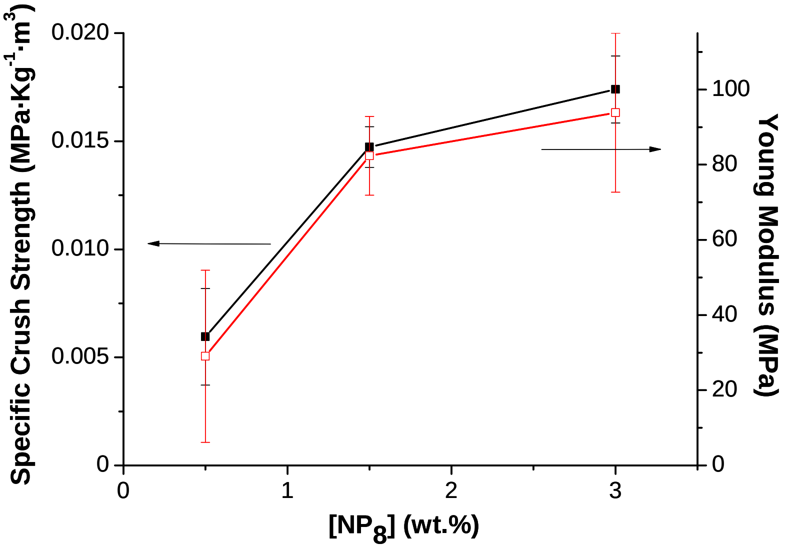

Figure 4-49. Normalized specific crush strength (σ_s , ■) and Young modulus (E , □), for macroporous polymers prepared from Pickering HIPEs containing 75 % internal phase volume (water) and stabilized with different loads of NP_8 (samples 1- 3, Table 4-11). σ_s and E were determined under compressive load.

As expected, there is an increase in specific crush strength as well as in Young modulus from 0.006 to 0.017 $MPa·m^3·Kg^{-1}$ and from 29 to 94 MPa, respectively, when nanoparticle increased from 0.5 to 3.0 wt%. As mentioned before, almost certainly, such increment is due to the fact that pore size distribution becomes narrower as NP_8 concentration increases (see Figure

4-45(a)). It should be noted that standard deviations in the normalized specific crush strength values are smaller than the standard deviations for Young Mudulus.

Figure 4-50 (up) shows the effect of the internal phase volume fraction of Pickering HIPEs stabilized with NP_8, on the specific crush strength of the resultant macroporous polymers. Obviously, the higher internal phase volume fraction, the higher porosity of materials, which inversely affects foam strength. As a result, specific crush strength dropped from 0.015 to 0.005 $MPa \cdot m^3 \cdot Kg^{-1}$, for macroporous polymers prepared from emulsions having internal phase volume fractions of 75 and 85%, at fixed NP_8 concentration (1.5 wt%, samples 2 and 11). It should be noted, that reduction is much more important from 75 to 80 vol% than from 80 to 85 vol%. Moreover, in line with the results described above, the higher NP_8 concentration, the higher specific crush strength in the whole range of internal phase volume fractions studied (75–85 vol%).

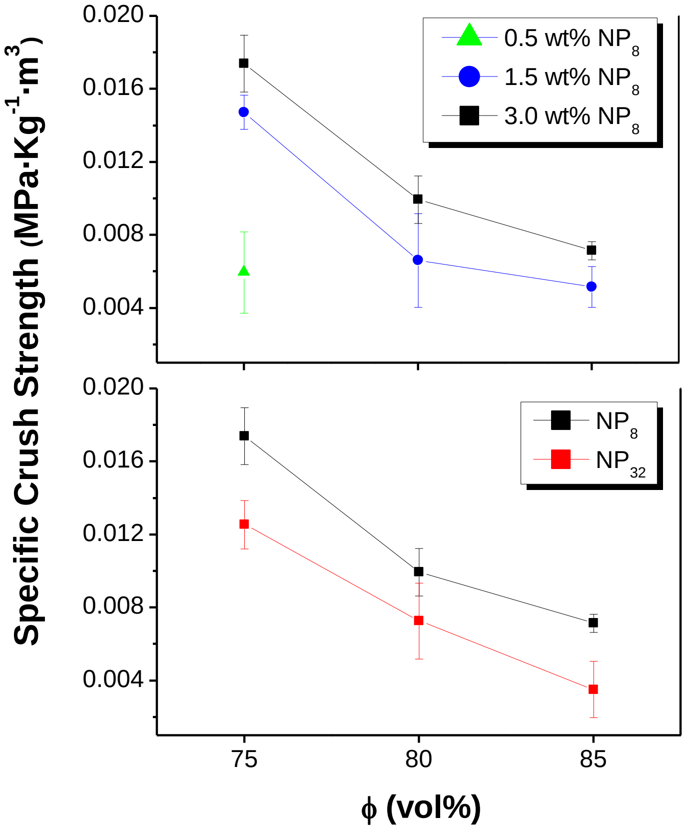

Figure 4-50. Normalized specific crush strength values for macroporous polymers under compressive load as a function of internal phase volume fraction in the Pickering HIPEs. The samples were prepared from HIPEs containing 75-85 % internal phase volume at different NP_8 concentrations (top). Comparison between samples at fixed nanoparticle concentration (3 wt%) containing either NP_{32} or NP_8 is shown at the bottom.

In the previous section, macroporous polymers containing either NP_8 or NP_{32} were compared. It was argued that the corresponding pore size distributions exhibited similar patterns (Figure

4-45). However, the average pore sizes of the smaller pores in the macroporous polymers containing NP_8, were in all cases smaller than those determined for the materials containing NP_{32} (population 1 in Table 4-10). Moreover, differences in nanoparticle distribution after polymerization were also observed. NP_{32} were located exclusively at the polymer-air interface, whereas NP_8 were also found inside polymer walls.

Taking as whole these facts, differences in mechanical performance might be expected. Specific crush strength values for samples with constant nanoparticle contents (3 wt% either NP_8 or NP_{32}), at different internal phase volumes are plotted in Figure 4-50 (down). The toughness of the materials containing NP_8 was higher than those containing NP_{32} in each sample examined. Specifically, specific crush strengths values were about 30-40 % higher for NP_8. It can be therefore inferred that both the better dispersion of NP_8 within the polymeric walls, and the presence of smaller pores, can play an important role in enhancing the mechanical performance of macroporous polymers.

4.3.4 Macroporous Polymers Prepared from High Internal Phase Emulsions Stabilized with TiO_2 Nanoparticles

4.3.4.1 *Preparation and characterization of macroporous polymers*

A detailed description of the titanium dioxide (TiO_2) nanoparticles can be found in 4.1.2. Such nanoparticles were also functionalized with oleic acid using the same method employed for the iron oxide NP_{32} (see 3.2.1). According to that, oleic acid content was adjusted by controlling the number of washing cycles. The TGA curves, corresponding to the as-milled nanoparticles and also to those nanoparticles calcined at 600 ºC, are included as supporting information in the Appendix (Figure 10-5). It should be pointed out that, similarly to that observed for iron oxide NP_{32}, oleic acid surface-modified TiO_2 nanoparticles experienced sedimentation in a short period of time when dispersed in an organic solvent. This was attributed to the strong aggregation they exhibited.

Initially, aiming at evaluating the role of oleic acid attached onto the TiO_2 nanoparticles, we prepared a series of emulsions using as emulsifier nanoparticles with distinct amounts of the fatty acid. Concentration was varied from 1.8 to 25.8 %, thus controlling the hydrophilic-lipophilic properties of nanoparticles surface. This was accomplished by applying 3 and 1 washing cycles, respectively. As-milled nanoparticles (without oleic acid) were also tested as a comparison. The emulsions were prepared by drop-wise addition of the dispersed phase (water) into the monomer phase (styrene and divinylbenzene weight ration 1:1) with the aid of vortex mixer. The nanoparticle concentration and the final internal phase volume fraction were 3 wt% and 80%, respectively. Photographs of the samples 15 min after preparation are shown in Figure 4-51.

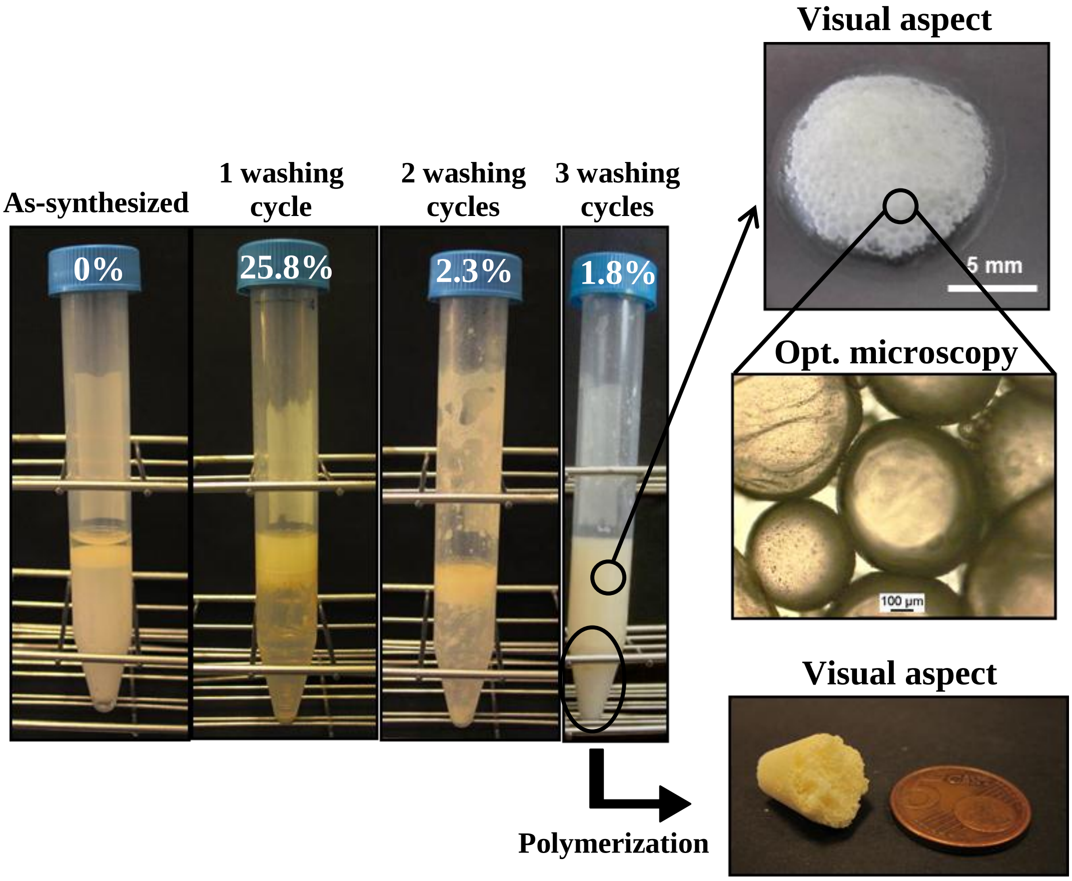

Figure 4-51. Photographs (left side) of samples consisting of 80 vol% water, 20 vol% oil (monomer mixture) and 3.0 wt% of as-milled TiO_2 nanoparticles. The concentration of oleic acid adsorbed on nanoparticles is indicated in each picture. Pictures (right side) from top to bottom: image of the W/O highly concentrated emulsion obtained using nanoparticles with 1.8 wt% oleic acid, optical microscopy image of the same emulsion and picture of the resultant material after polymerization of the external phase of the emulsion.

As one would expect, water cannot be emulsified with as-milled nanoparticles (tube on the left, with absence of oleic acid) in the same way as with functionalized TiO_2 nanoparticles. Even though coalescence was substantial, as deduced from the fraction of oil released, a residual O/W emulsion (inferred by conductivimetrical measurements) was obtained by using untreated nanoparticles. This is in good agreement with the hydrophilicity of TiO_2 surface.[72]

Polymerization of this sample was carried out at 70 ºC by adding the oil soluble initiator AIBN into the oil phase (1 wt%), to confirm wether monomers were constituting the dispersed phase. The resulting powder was examined by SEM (Figure 4-52). The pictures clearly demonstrate the presence of polydisperse polymeric particles with sizes as big as 400 µm. A large fraction of particles was therefore visible to the naked eye. Inspection of the surface of the polymeric particles indicates that TiO_2 nanopowder is strongly attached onto the polymeric surfaces (Figure 4-52(b)). Microparticles were washed several times with water without detecting any residual fraction of detached inorganic material. Undoubtedly, this is an indication of the strong adhesion capacity of these TiO_2 nanoparticles.

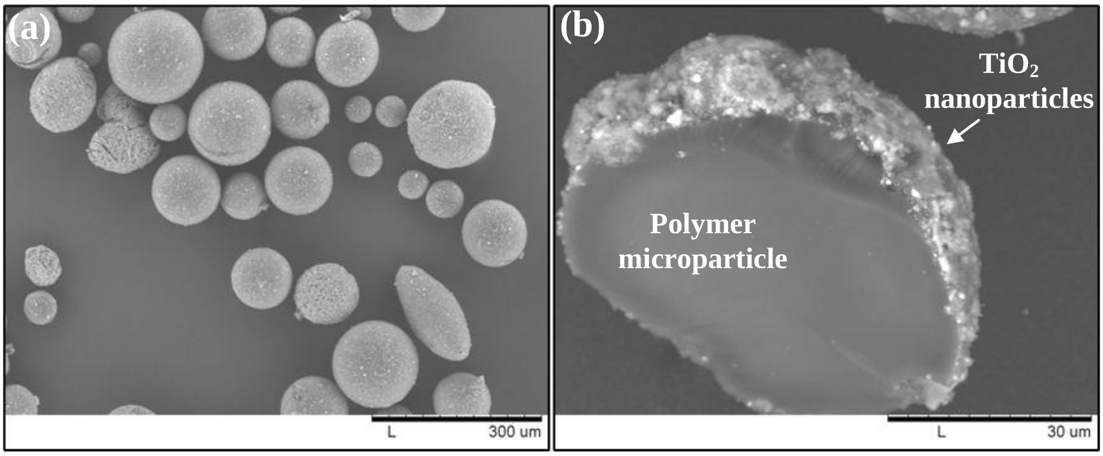

Figure 4-52. SEM images of polymer microparticles prepared from an O/W emulsion, stabilized with 3.0 wt% of as-milled (without oleic acid) TiO_2 nanoparticles. The initial emulsion had a monomer-water volume ratio of 1:4.

When more lipophilic nanoparticles obtained after one washing cycle were used (25.8 wt% oleic acid), no emulsion was obtained. As seen in the corresponding image (Figure 4-51), the nanoparticles remained dispersed in the monomer phase after phase separation. However, they sedimented with time and ended up at the O/W interface. The excess of oleic acid, producing too hydrophobic nanoparticles, may be the responsible for emulsification failure. Oleic acid concentration was further reduced from 25.8 to 2.3 wt% with an additional washing cycle, that presumably eliminated the excess of fatty acid. In this case, even though W/O emulsions could be obtained shortly after mixing, emulsions were unstable and finally a two phase system evolved.

The amount of oleic acid after three washing cycles (1.8 wt%) was nearly the same than after two cycles (2.3 wt%), but the results obtained were completely different: W/O HIPEs were now successfully prepared. More importantly, W/O HIPEs exhibited an outstanding stability, which is a typical feature encountered in Pickering emulsions stabilized with suitable nanoparticles. It should be remarked that emulsion stability can be improved just by reducing 0.5 wt% oleic acid concentration. As discussed previously for Fe_3O_4 nanoparticles (section 4.3.1), the ability of these TiO_2 nanoparticles to act as emulsifier is beyond doubt, merely due to the effective adsorption of oleic acid, which renders the surface of nanoparticles partially hydrophobic. Several drops of the W/O HIPE were carefully placed on a microscope slide and then inspected by optical microscopy. As seen in Figure 4-51, droplet size is quite large. Although further work is needed, if we take into account the nanoparticle concentration used (3 wt%), it could be inferred that the efficiency of TiO_2 nanoparticles was by far lower than that attained by the iron oxide nanoparticles. It seems highly probable that this lower efficiency is a consequence of the strong aggregation experienced by the TiO_2 nanoparticles. As shown in the same figure at the bottom-right part, the material obtained after polymerization of the HIPE preserved the shape of the container, but was rather chalky and brittle. The corresponding SEM image is shown in Figure 4-53(a).

Figure 4-53(b,c) shows two SEM images at different magnifications of a sample made from a Pickering HIPE, stabilized with 3 wt% of oleic acid surface-modified TiO_2 nanoparticles (containing 2.9 wt% oleic acid), which were previously calcined at 600 ºC. At such temperature nanoparticles crystallized into the anatase phase (see Figure 4-7).

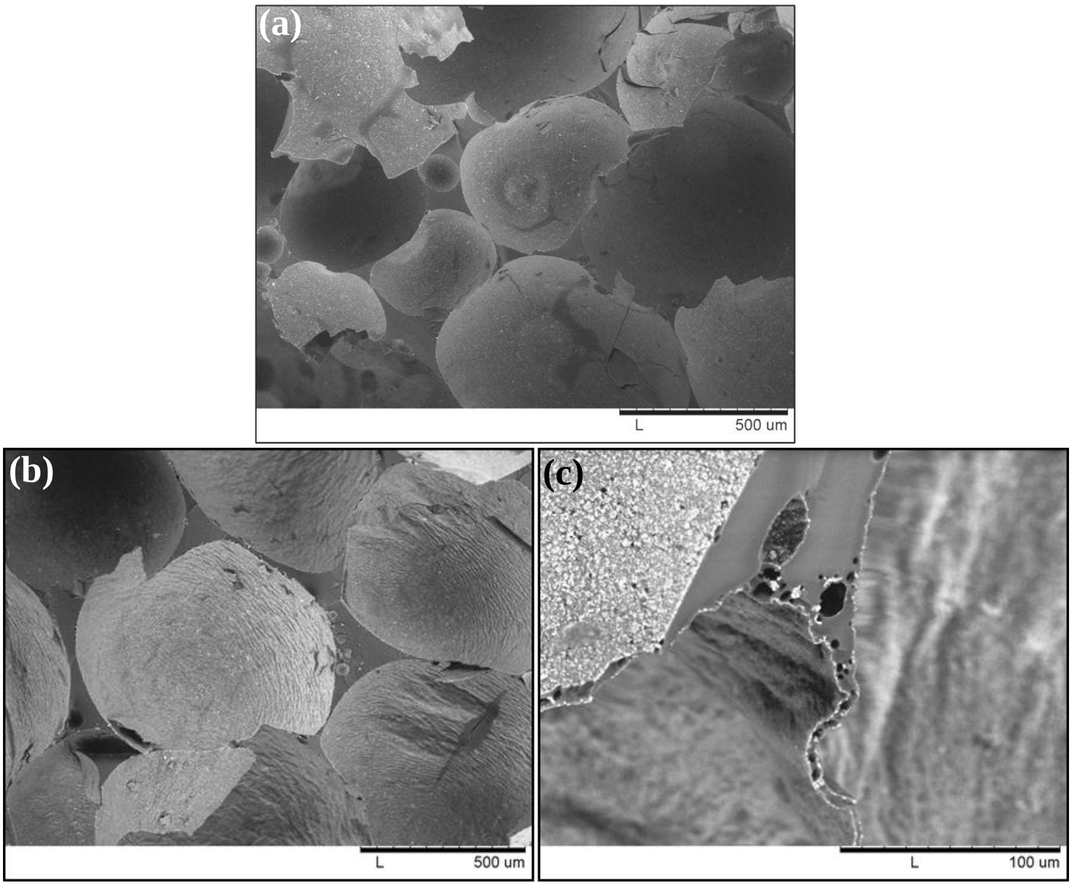

Figure 4-53. Macroporous polymers made from highly concentrated emulsions (monomer-water 1:4 by volume) stabilized with 3 wt% oleic acid surface-modified TiO_2 nanoparticles. (a) As-milled (without calcination) nanoparticles; (b) anatase nanoparticles, previously calcined at 600 ºC; (c) higher magnification of image (b).

The macroporous structure was identical to that obtained by using as-milled nanoparticles (without calcination, Figure 4-53(a)). Macroporous polymers were characterized by possessing numerous closed pores with exceptionally large sizes, i.e. up to 700 µm (Figure 4-53(a,b)) and few pores ranging from several to 20 µm, mainly located at the Plateau border regions (Figure 4-53 (c)). The surface of the pores was totally covered by a dense layer of inorganic powder, which evidently corresponded to the TiO_2 nanoparticles. This produced a high surface roughness which is clearly visible at low magnification SEM. Even though the presence of isolated nanoparticles or clusters within the polymer walls cannot be discarded, SEM images indicate that the emulsifier was preferentially placed at the outer part of the polymer wall, i.e. aqueous side of the O/W interface in initial emulsions. This fact raised the question whether the nanocomposites containing TiO_2 nanoparticles (anatase) retained the photocatalytic activity coming from anatase nanoparticles. It is important to reiterate that the aim was not only stabilize the precursor emulsions, but also confer UV absorption[302] or catalytic activity[303] to the macroporous polymers. In this context, TiO_2 nanoparticles are being investigated in recent years because its ability to photodegradate synthetic polymers, such as polyethylene,[304] poly(vinyl-chloride)[305] or polystyrene,[306, 307] or to accelerate the degradation of biodegradable polymers such as poly(L-lactic acid).[308] However, these effects depend much on nanoparticle characteristics and interactions between polymer and filler.[309]

4.3.4.2 *Photocatalytic activity*

The photocatalytic activity of the nanocomposite containing anatase nanoparticles was qualitatively evaluated by monitoring the colour-fading of methylene blue dye under UV light (see experimental section, 3.2.2.1). In order to increase the surface area exposed to the UV radiation the material was gently crushed with a mortar, obtaining polymeric pieces of few mm in size. Then, the divided material was dispersed in a 5 ppm methylene blue aqueous solution under continuous mechanical stirring. The concentration of TiO_2 nanoparticles was calculated to be approximately 0.25 g/L. As the material is constituted by a hydrophobic polymer matrix, it did not show a good dispersability in water. However, the material adsorbed an important percentage of the hydrophilic dye after two hours of agitation because of the presence of TiO_2 nanoparticles. The corresponding absorbance curve (in the visible range) for the initial methylene blue solution (black line) and for solutions after different times of reaction under UV light are shown in Figure 4-54. The maximum absorbance for methylene blue is at 664 nm.

From the figure it can be seen that the most important reduction of methylene blue concentration occurs before starting the photocatalytic experiment (from the initial solution to the 0 min curve). As mentioned before, this can be explained by dye adsorption on the macroporous material. Despite the degradation kinetics of the dye under UV irradiation is slow, the results show that after 120 min, practically all methylene blue has been removed from solution. The visual aspect of methylene blue solutions after UV treatment for different irradiation times (from 0 to 120 min) is shown in Figure 4-54.

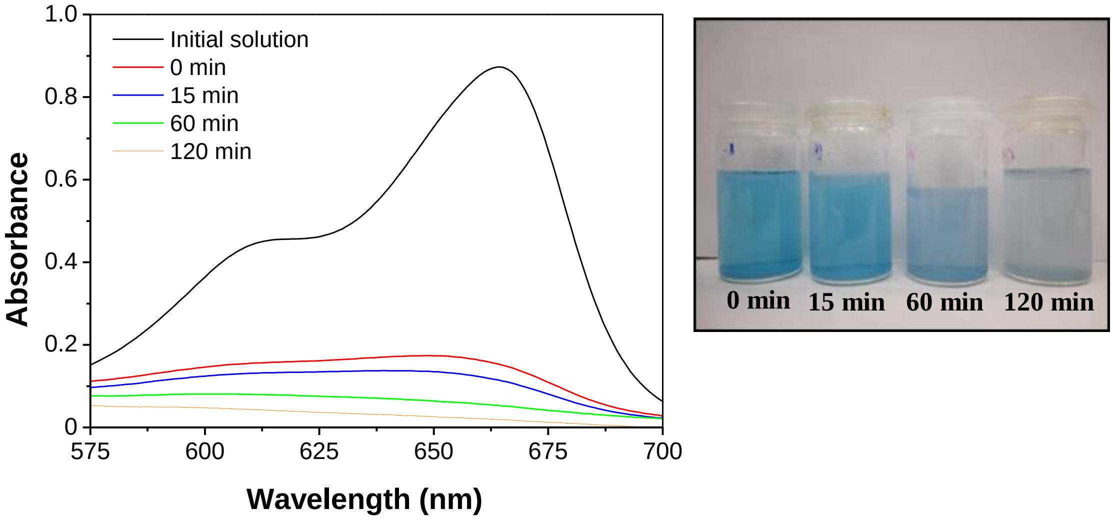

Figure 4-54. Visible adsorption spectra of the initial 5 ppm methylene blue solution and of solutions after different times of UV irradiation in the presence of a dispersed nanocomposite containing anatase nanoparticles. The maximum absorbance for methylene blue is at 664 nm. The picture on the right shows the visual aspect of the solutions at different UV irradiation times.

These results confirm that TiO_2 nanoparticles are accessible to UV irradiation since these particles are located at the surface of the pores. Consequently, the nanocomposites containing anatase nanoparticles are photocatallytically active.

4.4 MACROPOROUS POLYMERS OBTAINED IN HIGHLY CONCENTRATED EMULSIONS STABILIZED WITH MIXTURES OF IRON OXIDE NANOPARTICLES AND NONIONIC SURFACTANT

In the previous section, the preparation of polymeric macroporous nanocomposites with closed-pore structures was described, which resulted in low connectivity and gas permeation. The closed-pore structure was attributed to nanoparticle rigid films covering emulsion droplets. In the present section, the procedure recently developed by Ikem et al.[185] to obtain permeable macroporous polymers has been applied. In that work, permeable materials were obtained by addition of a nonionic surfactant (Hypermer 22296) to already-made Pickering HIPEs. Hypermer 2296 is a nonionic surfactant used as W/O emulsifier,[219, 222] because of its low HLB value (4.9).

The present section is divided as follows: first, the influence of addition of different surfactant (Hypermer 2296) concentrations to Fe_3O_4 nanoparticle toluene dispersions has been studied. Interfacial tension measurements were used to evaluate the degree of surfactant adsorption onto the nanoparticle surfaces (section 4.4.1). Afterwards, highly concentrated W/O emulsions (HIPEs) were prepared using mixtures of surfactant and nanoparticles (section 4.4.2). Then, HIPEs were processed into macroporous polymers (denoted as polyHIPEs) and then characterized with respect to their pore structure and mechanical properties. Moreover, magnetic properties of the macroporous polymers were evaluated for different nanoparticle arrangements within the polymer walls of the materials (section 4.4.3).

Finally, the main features of the materials obtained using the two methods of preparation, i.e. nanoparticles and surfactant mixed before or after emulsification, are compared (4.4.4).

4.4.1 Interfacial Tension Measurements

Interfacial tension determinations allow evaluating the individual contribution of either nanoparticle or surfactant (at very low concentration) to the overall decrease in the interfacial tension values. Therefore, it is a very precise technique to quantify and clearly differentiate both the free surfactant that remains in solution and the surfactant that adsorbs on nanoparticle surfaces. The evaluation of surfactant adsorption on SiO_2 particles by means of tensiometry has been already described in other works dealing with Pickering emulsions.[78, 112]

Two different tensiometry methods, namely a microbalance with a platinum Du Noüy ring and the drop-volume method, were used to determine the whole interfacial tension curves in water-toluene systems, at 25 ºC. As pointed out in the experimental section (3.2.4), nanoparticles at 1.5 wt% in toluene, were mixed with Hypermer 2296 surfactant at different concentrations (from 0 to 4 wt%). Three types of Fe_3O_4 nanoparticles have been used in this study: oleic acid surface-modified NP_8 and NP_{32}, and untreated CNP_{32}. It is important to underline that in the case of NP_8, interfacial measurements could be performed with the nanoparticles dispersed in the toluene, while NP_{32} and CNP_{32} were separated (with surfactant adsorbed onto their surfaces) by simple centrifugation before the measurements, due to the fast aggregation they experienced.

At first, interfacial tension (γ) between pure water and toluene was measured in absence of surfactant, with or without 1.5 wt% of NP_8. As mentioned in section 4.3.1, the value of interfacial tension for pure toluene and water was consistent with that found in the literature (36.2 mN/m).[297] Further addition of oleic acid surface-modified nanoparticles NP_8 decreased very little the oil-water interfacial tension (35.7 ± 0.2 mN/m). These results are consistent with other works in the bibliography, which demonstrate that the presence of particles has a negligible influence on tensions.[58, 78, 117]

The interfacial tension (γ) curves for all systems, as a function of surfactant concentration are shown in Figure 4-55. The curve for the system without nanoparticles (only Hypermer 2296) is also included as a reference. All values are summarized as supporting information in the Appendix (Table 10-1).

As expected, in the system without nanoparticles, the toluene-water interfacial tension was reduced upon increasing surfactant concentration (Figure 4-55, black squares). It is well known, that surfactants adsorb gradually to the oil-water interface up the critical micelle concentration (CMC). It seems that a constant value is reached at approximately 1 wt% surfactant (3.4 mN/m). The minimum value (2.8 mN/m) was achieved at the highest surfactant concentration (4 wt%).

Interestingly, quite large differences in interfacial tension were found in the particle-containing systems compared to the Hypermer 2296 stock solutions, regardless of the type of nanoparticle used. The addition of 1.5 wt% nanoparticles into the toluene phase increases the interfacial tension values at every surfactant concentration up to 1.0 wt%. Such increment can be attributed to the adsorption of surfactant onto the nanoparticle surfaces. Since a fraction of surfactant molecules is adsorbed on nanoparticles, the free surfactant concentration in the toluene is reduced, and therefore the interfacial tension increases. These results confirm the depletion of the surfactant solution due to strong Hypermer 2296 adsorption onto the nanoparticle surfaces.

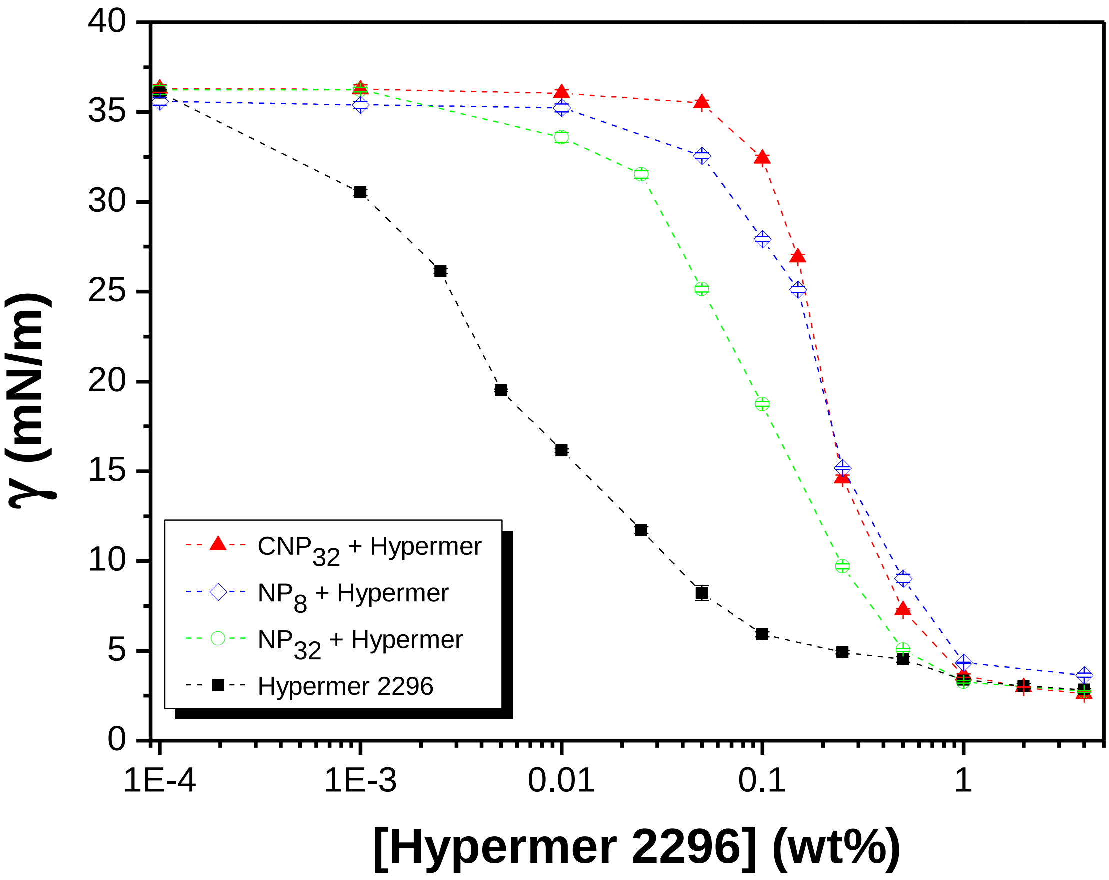

Figure 4-55. Toluene-water interfacial tensions (γ) at 25ºC as a function of Hypermer 2296 concentration in systems prepared with and without nanoparticles. Measurements in the NP_8 + Hypermer system were carried out with 1.5 wt% of well-dispersed NP_8 in the toluene phase. NP_{32} and CNP_{32}, with different surfactant concentration on their surfaces, were removed from toluene solutions (1.5 wt%) prior the measurements. Error bars represent standard deviation. Lines are only given as a guide to the eye.

From the curves of the systems containing nanoparticles in Figure 4-55, it can be clearly seen that the interfacial tension remains approximately constant at low surfactant concentrations. indicating that initially, almost all surfactant molecules are adsorbing on nanoparticles, rather than migrating to the toluene-water interface. At certain surfactant concentration (e.g. 0.05 for CNP_{32}, red triangles curve), a sharp reduction in interfacial tension is observed. It can be assumed that surfactant added above such concentration migrates preferentially to the oil-water interface, possibly because the nanoparticle surfaces are already saturated with surfactant. It is noteworthy that in the case of CNP_{32}, the surfactant concentration needs to be almost three orders of magnitude higher, in order to reduce the interfacial tension, compared with the system without nanoparticles.

Regarding the region at high surfactant concentrations (above 1 wt%), the interfacial tension of all systems become similar. It is accepted that the use of interfacial tension measurements does not allow to find differences once the samples containing nanoparticles reach the constant value at the CMC of the surfactant.[78]

Despite the similarities of the tension curves for particle-containing systems, the total amount of surfactant adsorbed on the three types of nanoparticles examined is greatly different. In Figure 4-56, the differences of interfacial tension values (γ) between the systems with particles and the system without particles (only with surfactant) are plotted, as a function of surfactant concentration. Such differences increase progressively until a maximum value is reached. The maximum difference in tensions occurs at the same surfactant concentration in which interfacial tension starts falling rapidly in the particle-containing systems (Figure 4-55). Clearly, the highest difference ($\gamma_{with\,NPs} - \gamma_{withoutNPs}$) corresponds to CNP_{32} (27.3 mN/m at 0.05 wt% surfactant), followed by NP_8 (24.4 mN/m) and by NP_{32} (19.8 mN/m at 0.03 wt% surfactant). This indicates that surfactant is adsorbed more on CNP_{32} nanoparticles, and the smallest adsorption occurs on NP_{32}.

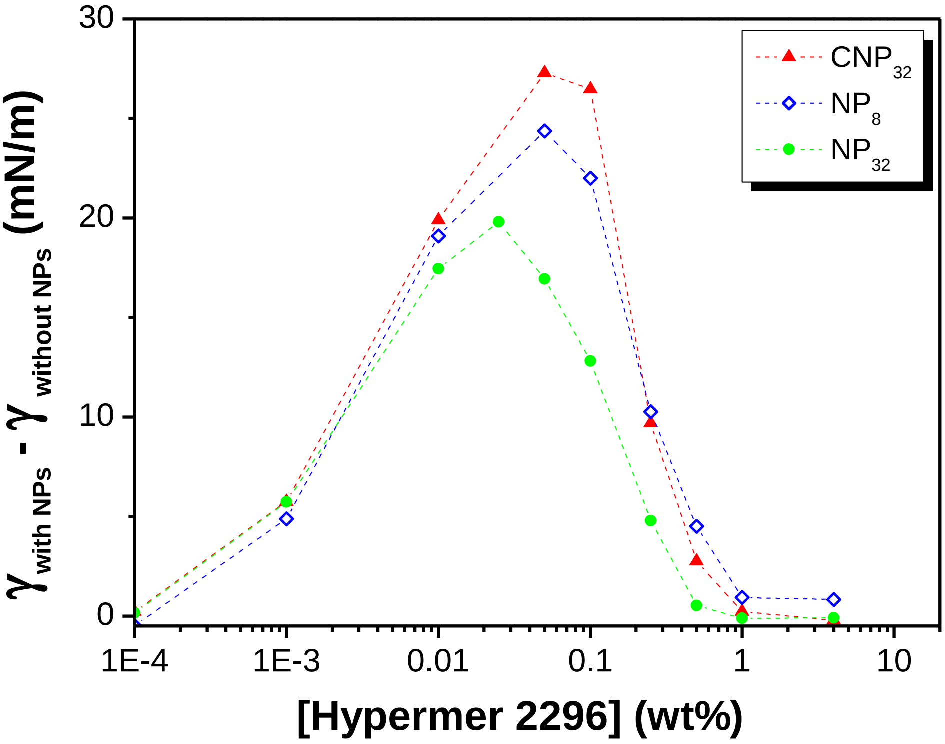

Figure 4-56. Interfacial tension (γ) differences between systems with particles and the system without particles, as a function of Hypermer 2296 concentration. Tension values were taken from Figure 4-55.

The fact that more surfactant is adsorbed on CNP_{32} than on NP_8 and NP_{32}, might be associated to its untreated surface. Despite the surface of NP_8 and NP_{32} was already surface-modified with oleic acid, the surfactant is still able to adsorb on those functionalized nanoparticles, as demonstrated by the interfacial tension curves (Figure 4-55). Apparently, the bigger specific surface of NP_8 nanoparticles could be the reason for the larger adsorption on these particles compared to NP_{32}.

Taking as whole these facts, it can be concluded that the addition of Fe_3O_4 nanoparticles (functionalized or untreated) to surfactant solutions leads to higher interfacial tensions due to surfactant adsorption on nanoparticles.

In addition to the interfacial tension experiment permorfed as a function of surfactant concentration, other measurements were carried out keeping the surfactant concentration constant (1 wt%) but modifying nanoparticle (NP_8) concentration. The corresponding interfacial tension curve (25 ºC) is included as supporting information in the Appendix (Figure 10-6). The resuls also indicate that addition of nanoparticles increases the interfacial tension, probably due to surfactant adsorption on nanoparticles, which reduces the concentration of free surfactant in solution.

4.4.1.1 *Adsorption of surfactant on CNP_{32}*

As mentioned in a previous chapter, CNP_{32} were not suitable to stabilize W/O emulsions due to its very hydrophilic nature (see Figure 4-35 in page 135). Nevertheless, since CNP_{32} are not surface-modified, they are a good candidate to evaluate the degree of adsorption on its “naked” surface. As deduced from the values included in Figure 4-55, almost all Hypermer 2296 added to the system up to 0.05 wt% is adsorbed on the CNP_{32} surfaces. Further addition causes a reduction of the interfacial tension values.

In order to confirm the possible surfactant adsorption, thermogravimetric analysis (TGA), determining the total organic content of the CNP_{32} samples extracted by centrifugation, were undertook. The surfactant adsorbed on CNP_{32} (25 ºC), as a function of Hypermer 2296 concentration, is plotted in Figure 4-57.

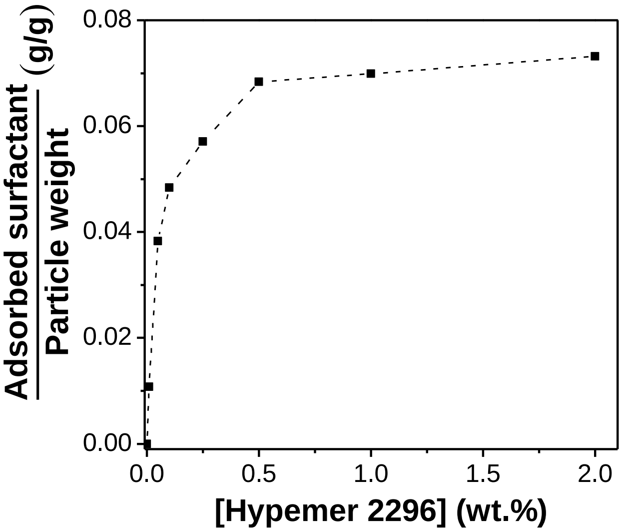

Figure 4-57. Surfactant (Hypermer 2296) adsorbed on CNP_{32} iron oxide nanoparticles. The adsorbed amount was determined by TGA applied to nanoparticles separated by centrifugation.

From 0 to 0.1 wt% surfactant, there is a sharp increase in surfactant adsorption, reaching values of around 0.05 g of surfactant per gram of CNP_{32}. A constant surfactant adsorption value (ca. 0.068 g/g) is reached at approximately 0.5 wt% of surfactant. From these results, two main conclusions can be drawn: first, it is confirmed that in a wide range of surfactant concentration (0.1-0.5 wt%, see Figure 4-55), surfactant not only reduces the interfacial tension, but also adsorbs onto CNP_{32} nanoparticles surface. Second, the constant surfactant adsorption value, reached at 0.5 wt% surfactant, is in good agreement with the trend observed in the interfacial tension differences shown in Figure 4-56. At such surfactant concentrations, the differences between the system with CNP_{32} and the system without particles has been significantly reduced, probably indicating that particle surface is already saturated with surfactant, and the addition of more surfactant contributes only to reduce interfacial tension.

Finally, the same experiment shown in Figure 4-36 was reproduced. For that purpose, two samples of untreated CNP_{32} nanoparticles, were extracted and dried from a toluene solution, in absence or in presence of 4 wt% Hypermer 2296, respectively. Then, the resulting nanoparticle powders were compressed to obtained flat films, and a water droplet was placed on them. The corresponding images are depicted in Figure 4-58.

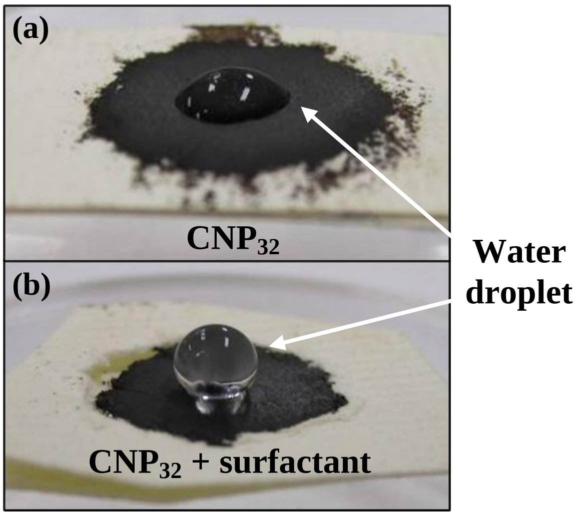

Figure 4-58. (a) Film made of untreated CNP_{32} on a cellulose support. (b) Film, on a cellulose support, made of CNP_{32} nanoparticles extracted by centrifugation and further drying, from a 4 wt% Hypermer solution in toluene. The adsorption of surfactant makes the particles hydrophobic, as deduced from the different wettability exhibited by the water droplet on nanoparticle films.

It can be clearly seen that surfactant adsorption turns the surface of the nanoparticles hydrophobic, which results in a larger contact angle towards water (Figure 4-58). Based on these experimental findings, surfactant adsorption on nanoparticles is indeed confirmed.

4.4.2 W/O Highly Concentrated Emulsions Stabilized with Mixtures of Hypermer 2296 and Fe_3O_4 Nanoparticles

4.4.2.1 *Emulsion stability*

The above results have demonstrated that surfactant adsorption on nanoparticles leads to an increase of interfacial tension. The stability of emulsions prepared with mixtures of surfactant and nanoparticles is described in the present section. For this purpose, water-in-monomer highly concentrated emulsions (HIPEs) have been prepared, with the aim of polymerizing the external phase of the W/O HIPEs. Emulsions were prepared with 80 vol% of water. The monomer system (20 vol%) was a mixture of styrene and divinylbenzene, which was used as a crosslinker (1:1 by weight). Nanoparticle (1.5 wt%) and surfactant concentrations (from 0 to 4 wt%) were the same than those used in the interfacial tension experiments. In all sections, both concentrations were expressed with respect to the continuous phase.

For emulsification, water was added slowly to the monomers containing both particles and surfactant, with the aid of a vibromixer. The visual aspect of emulsions 24 hours after preparation is shown in Figure 4-59. As a comparison, the system without nanoparticles (only surfactant Hypermer 2296) is also included (Figure 4-59(a)). As illustrated, the boundary line between the emulsions and the separated phases allowed us to quantify and compare emulsion stability. The stability of emulsions to creaming, sedimentation and coalescence was assessed by measuring the heights of separated water and oil from the emulsions over time.

The results obtained for each system will be described as follows:

Emulsions stabilized with only Hypermer 2296, in absence of particles (Figure 4-59(a))

A two phase system evolved, consisting of separated monomer and aqueous phases at low surfactant concentrations (up to 0.25 wt%). The progressive increase in emulsion stability when increasing surfactant concentration is due to surfactant adsorption at the water-oil interface, forming a surfactant monolayer around droplets that prevents coalescence. Despite some degree of sedimentation, formation of W/O-type HIPEs was observed from 0.65 wt% surfactant concentration. If surfactant concentration is further increased, sedimentation is completely suppressed. This occurs at 2 wt% Hypermer 2296. Characterization of the emulsion droplet sizes will be described in next section.

Emulsions stabilized with mixtures of untreated CNP_{32} nanoparticles and Hypermer 2296 (Figure 4-59(b))

It was demonstrated earlier that rather than stabilize water-in-oil (W/O), CNP_{32} poorly stabilized oil-in-water emulsions (O/W). This was attributed to the hydrophilic character of its surface. As seen in Figure 4-59(b), the volume of the residual O/W emulsion slighty increased when surfactant concentration was also increased from 0 to 0.05 wt%. It should be mentioned that the toluene-water interfacial tension curve (Figure 4-55) revealed that up to such a surfactant concentration, all Hypermer 2296 incorporated into the system adsorbed on CNP_{32} surfaces, leading to more hydrophobic CNP_{32} surfaces. Therefore, at low surfactant concentration, surfactant adsorption slightly enhances the ability of CNP_{32} as O/W emulsifier, due to partial surface hydrophobization. This finding is consistent with the literature, since one of the methods to improve the efficiency of very hydrophilic nanoparticles (commonly SiO_2) as O/W emulsifier is the addition of amphiphile molecules in order to partially hydrophobize their surfaces.[99, 101, 293]

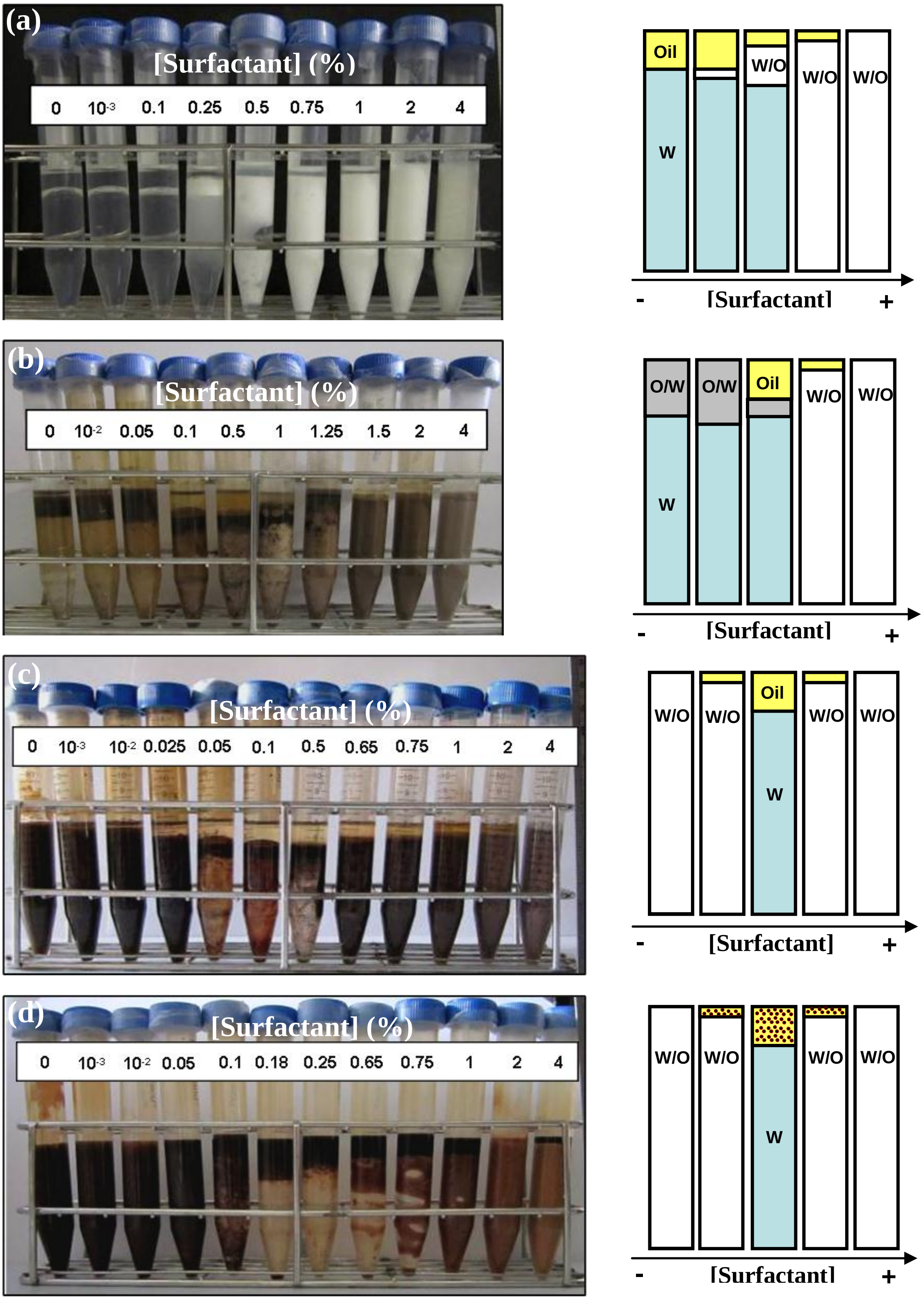

Figure 4-59. Visual aspect of emulsions 24 hours after preparation (25 ºC) containing increasing Hypermer 2296 concentrations (ranging from 0 to 4 wt%) in absence (a) and in presence of 1.5 wt% (b) CNP_{32}, (c) NP_{32} and (d) NP_8 nanoparticles. Schematic drawings showing the same sequences are shown next to each picture (O/W residual emulsions are shaded with grey colour, W/O are white, blue indicates aqueous phase, yellow represents the oil phase and NP_8 nanoparticles are indicated as brown dots).

If surfactant concentration is further increased (from 0.1 to 1%), emulsions eventually undergo phase separation. Presumably, all or at least an important fraction of CNP_{32} has been displaced from the interface at 0.1% surfactant concentration, because the particles are now too hydrophobic. This is the same surfactant concentration in which a sudden decrease in interfacial tension was observed (Figure 4-55). Despite surfactant starts adsorbing on the water-monomer interface, there is still no enough free-surfactant to stabilize W/O highly concentrated emulsions. Therefore, both stability experiments and interfacial tension determinations are in good agreement. Similar silica particle displacement from the oil-water interface has been recently monitorized by other authors in diluted and concentrated emulsions.[110, 116, 117] However, in that studies particle detachment is apparently produced by competition for adsorption at the interface, rather by previous surfactant adsorption on nanoparticle surfaces.

Similar to that observed for the system without nanoparticles (Figure 4-59(a)), when surfactant concentration is further increased, W/O highly concentrated emulsions (HIPEs) are obtained at approximately 1.5 wt% surfactant (Figure 4-59(a)).

Emulsions stabilized with mixtures of oleic acid surface-modified NP_{32} and NP_{8} nanoparticles and Hypermer 2296 (Figure 4-59(c,d))

As detailed in section 4.3.2, stable Pickering W/O HIPEs were successfully obtained by using either functionalized NP_{32} or NP_{8} as emulsifiers. The visual aspect of such emulsions (0 wt% surfactant) is depicted in Figure 4-59(c,d). HIPEs, especially those stabilized with NP_{32}, experienced destabilization upon addition of low surfactant concentrations (sedimentation caused by an increase in droplet size). In line with the emulsions stabilized with CNP_{32}, surfactant adsorbed on partially hydrophobic surfaces of NP_{32} and NP_{8}. But now, such adsorption turns the surface of the nanoparticles even more hydrophobic, and consequently the efficiency of the nanoparticles to adsorb at the water-monomer interface is reduced. This results in less stable emulsions. Particle detachment from interfaces of a W/O emulsion can be understood in terms of an increase in the contact angle (see eq.1-17, page 23), which reduces the energy required for particle detachment from the interface.

Emulsion instability increases dramatically at higher surfactant concentrations added to Pickering emulsions, because again less particles are available to stabilize the emulsions. As a consequence, emulsions experience phase separation (Figure 4-59(c,d)). It should be remarked that emulsions stabilized with NP_{8} were more stable than those stabilized NP_{32} and surfactant concentration that produced phase separation for NP_{8} (0.1 wt%) was twice higher than for NP_{32} (0.05 wt%). Such surfactants concentrations were in fairly agreement with the interfacial tensions, at which surfactant starts adsorbing at the water-oil interface (Figure 4-55), thus reducing abruptly interfacial tension. Interestingly, a clear distinct behaviour between both NP_8 and NP_{32} was observed when respective emulsions underwent phase separation (Figure 4-59(c,d)): while NP_8 remain well-dispersed in the separated monomer phase, NP_{32} sedimented with time and ended up at the O/W interface. Therefore, this demonstrates that NP_8 remain stable at the continuous phase, regardless of the addition (and consequent adsorption) of Hypermer 2296.

The fact that emulsions stabilized with NP_8 are more stable than those stabilized by NP_{32} can be due to two different reasons: first, as aforementioned, the higher surface area (NP_8), the larger extent of surfactant adsorption. Therefore, higher surfactant concentrations are required to displace nanoparticles from the water-monomer interface of the emulsions. Second, we have to bear in mind that not all NP_8 were placed at the monomer-water interface, but also an important fraction was found dispersed within the continuous phase (Figure 4-47, page 154). It may be argued that initial stages of surfactant adsorption on NP_8 do not affect importantly its ability as efficient emulsifier, since surfactant is also adsorbing on NP_8 that are not stabilizing the emulsions.

Consistent with the systems studied earlier, transition to surfactant-stabilized emulsions was also observed. Here, W/O HIPEs were obtained from surfactant concentrations of 0.65 and 1.0 wt% for NP_{32} and NP_8, respectively (Figure 4-59(c,d)).

To summarize, the volumes of residual emulsions were measured for every system, and the results are shown in Figure 4-60. Values above and below the zero value in the Y axis indicate W/O and O/W emulsions, respectively. At low surfactant concentrations, three different results were obtained: by one hand, the use of CNP_{32} (Figure 4-59(b)), in absence of surfactant, led to O/W diluted emulsions. As seen in Figure 4-60, the O/W residual emulsion increased from 20.8 to 32.2 % when Hypermer 2296 surfactant concentration was also increased from 0 to 0.05 wt%. On the other hand, stable Pickering W/O HIPEs were successfully obtained by using either functionalized NP_{32} or NP_8 as emulsifiers. HIPEs, especially those stabilized with NP_{32}, experienced destabilization upon addition of low surfactant concentrations (sedimentation caused by an increase in droplet size), as clearly seen in the volume of residual emulsions plotted in Figure 4-60. Regarding the system without nanoparticles (only surfactant) emulsions undergo phase separation since surfactant concentration is no enough to stabilized emulsions.

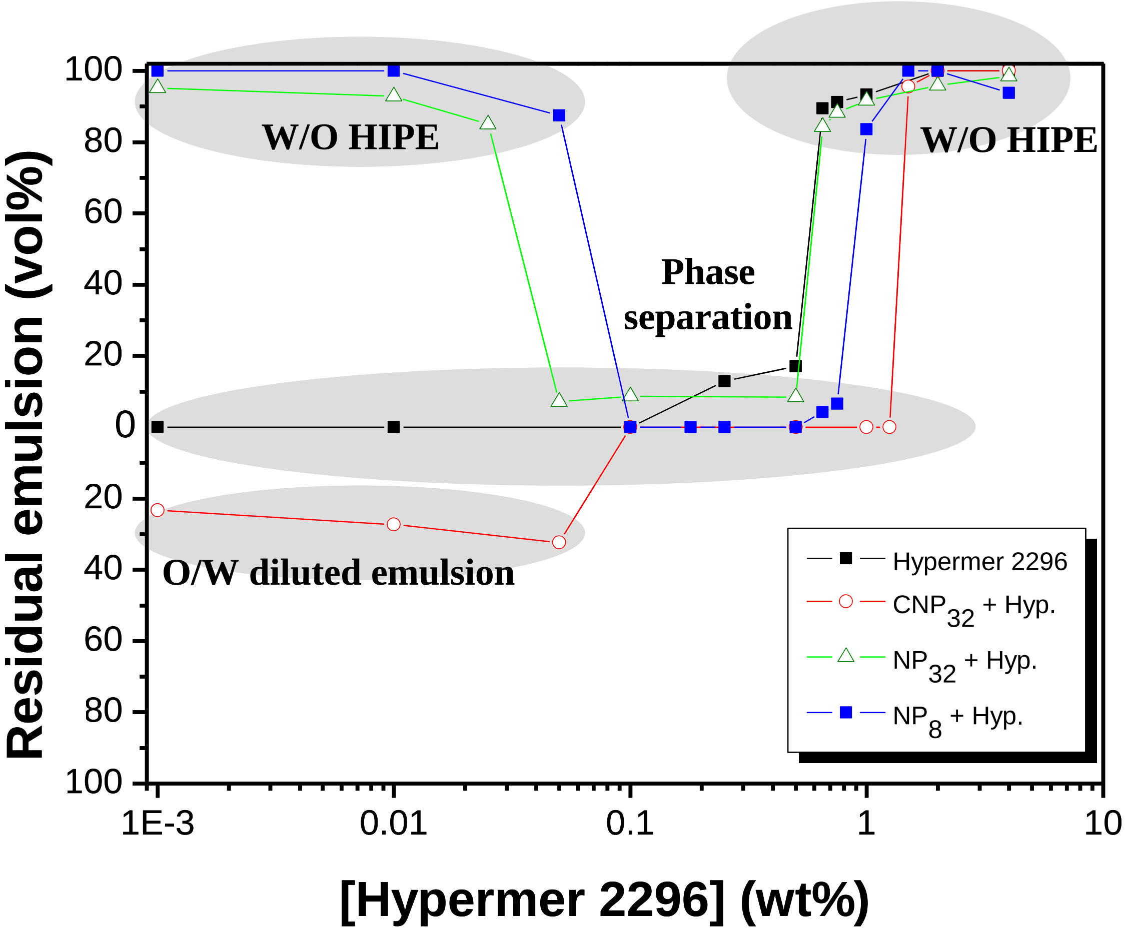

Figure 4-60. Residual emulsions (vol%) as a function of Hypermer 2296 concentration for the systems depicted in Figure 4-59, in the presence of 1.5 wt% nanoparticles (CNP_{32}, NP_{32} or NP_8) and in the absence (just Hypermer 2296) of nanoparticles in the continuous phase of emulsions. The emulsions were kept at 25 ºC during 24 hours. Values above and below the zero value in the Y axis indicate W/O or O/W emulsions, respectively.

At intermediate surfactant concentrations (ca. 0.1 wt%) all emulsions containing nanoparticles eventually undergo phase separation (Figure 4-60). Presumably, all or at least an important fraction of the particles has been displaced from the interface at such surfactant concentration, because the particles are now too hydrophobic.

Finally, regardless of the addition of nanoparticles, W/O highly concentrated emulsions are obtained at higher surfactant concentrations. If residual emulsion curves for the systems with Hypermer 2296 and with nanoparticles are compared, it is clearly seen that the surfactant concentration necessary to achieve again stabilization of W/O HIPEs, shifts to higher surfactant concentrations in the case of NP_8 and CNP_{32} containing systems. While 0.65 wt% surfactant concentration was necessary to obtain such emulsions in the particle-free system, 1 or 1.5 wt% was the minimum required for the NP_8 or CNP_{32}-containing system. This obviously demonstrates that not all surfactant added into the system is acting as emulsifier. These results are consistent with the differences of interfatial tension values between the systems with particles and the systems without particles (only surfactant) shown in Figure 4-56. Therefore, Figure 4-60 also confirms that more surfactant was adsorbed on untreated CNP_{32} than on oleic acid surface-modified NP_8.

It is assumed that at higher surfactant concentrations, there is enough free surfactant in the continuous phase of the emulsions to stabilize W/O HIPEs. However, microscope observations (optical and electronic) are required to verify if all nanoparticles have been pushed out from the water-monomer interfaces of such emulsions. Optical microscopy observations are described in next section.

4.4.2.2 *Characterization of emulsion droplet size*

Due to the different stabilization mechanisms involved in Pickering and in surfactant-stabilized emulsions, the use of either particles or surfactants (or both at the same time) can lead to emulsions with characteristic drop sizes. It is well known that smaller drop sizes are obtained in emulsions stabilized with surfactants due to the lower interfacial tensions attained. Therefore, surfactant and particle-stabilized emulsions can be easily distinguished by using optical microscopy images.

First, highly concentrated Pickering emulsions (HIPEs) stabilized with only NP_{32} (Figure 4-61(a,b)), and the same emulsion with low surfactant concentration added (0.1 wt%, Figure 4-59(c)) were examined by optical microscopy. As pointed out in section 4.3.2, Pickering HIPEs stabilized with either functionalized NP_{32} or NP_8 had very large droplet sizes, with wide size distributions, from 10 to 500 μm (Figure 4-61(a,b)). It is evident by comparing (a) and (c) digital images that emulsion droplet size increases to very large values (up 800-900 μm), upon addition of 0.01 wt% surfactant. This increase is consistent with the progressive emulsion destabilization observed in the stability experiments carried out earlier (Figure 4-59(c).

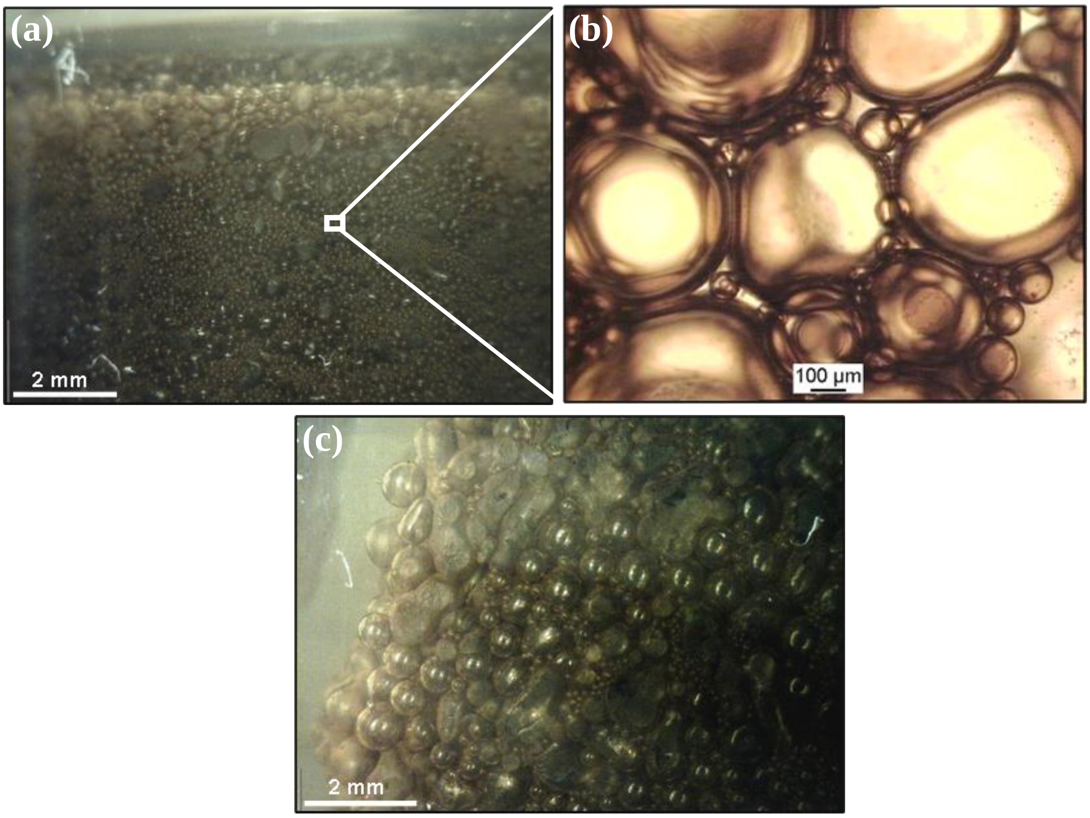

Figure 4-61. Images of W/O HIPEs having 80 % internal phase volume, stabilized with (a,b) solely 1.5 wt% NP_{32} and with (b) a mixture of NP_{32} and Hypermer 2296 surfactant (0.01 wt%). Pictures (a) and (c) were taken with an USB desktop digital camera, while (b) is an optical microscopy image.

Regarding the emulsions stabilized at higher surfactant concentrations, images of emulsions stabilized with mixtures of 1.5 wt% NP_{32} and 1.5 or 4 wt% Hypermer 2296 are shown in Figure 4-62(a,b). It should be noted that emulsion droplet size is significantly lower than that observed in the W/O HIPEs stabilized mainly by nanoparticles (Figure 4-61). This strongly confirms that the emulsions shown in Figure 4-62 are mainly stabilized by surfactant. It is well-known that surfactants reduce the oil-water interfacial tension, thus facilitating the obtention of emulsions with rather small sizes. The range of drop sizes in the emulsions was relatively polydisperse with a population of drops of few micrometers size and a population of larger drops sizes ranging from 15 to 40 µm. As expected, the increase of surfactant concentrations from 1.5 to 4 wt% decreased droplet size (Figure 4-62(b)). It should be remarked that the presence of NP_{32} did not modify appreciable the droplet size distribution of the emulsions, compared to the system stabilized with surfactant, in absence of nanoparticles (see supporting information in the Appendix, Figure 10-8(a,b)).

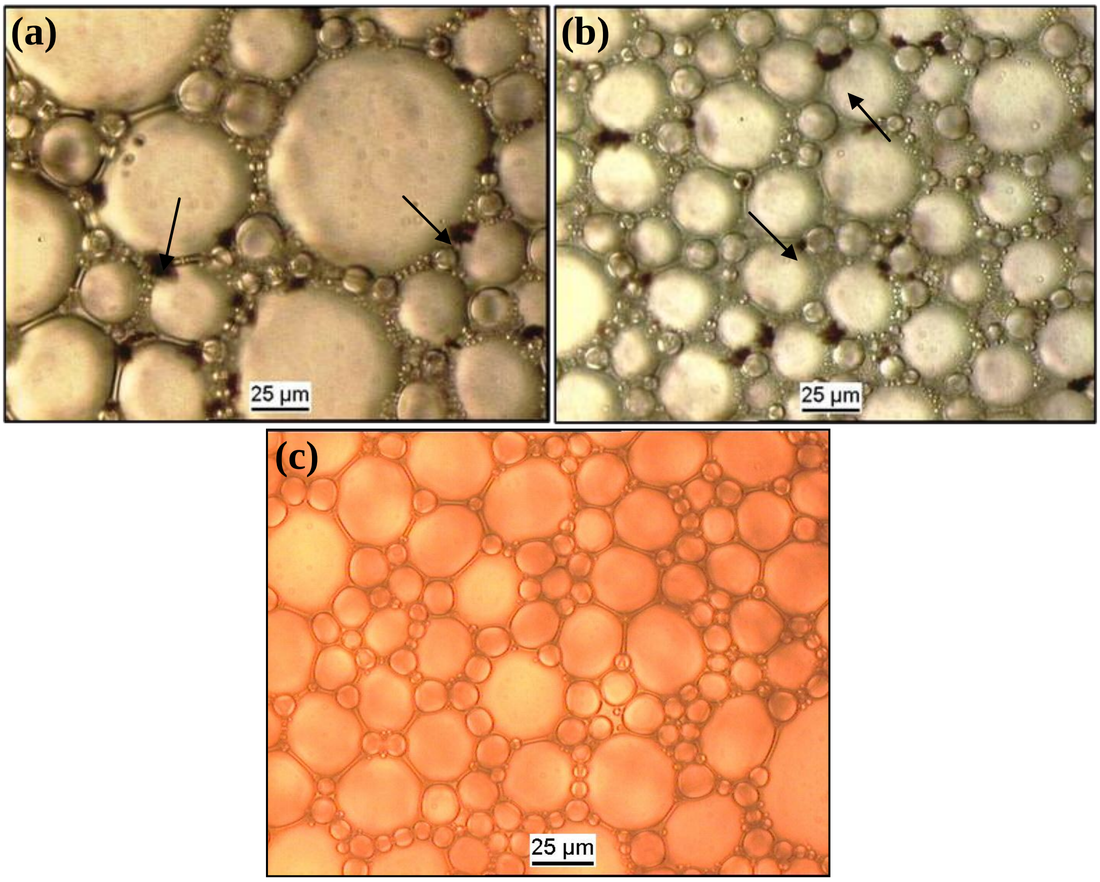

Figure 4-62. Optical microscope images of emulsions consisting of 80 % internal phase volume, and stabilized with different concentrations of nanoparticles and Hypermer 2296 surfactant: (a) 1.5 wt% surfactant and 1.5 wt% NP_{32}; (b) 4 wt% surfactant and 1.5 wt% NP_{32}; (c) 4 wt% surfactant and 1.5 wt% NP_8. Black arrows indicate the presence of NP_{32} aggregates.

Interestingly, some NP_{32} particle aggregates (pointed out with black arrows in Figure 4-62(a,b)) of few micrometers size are seen in the continuous phase of the emulsions, between neighbouring droplets, thus confirming the hypothesis that the particles are pulled out from the interface by surfactant adsorption onto their surfaces. This fact was also observed in the W/O HIPEs stabilized with mixtures of CNP_{32} and Hypermer 2296 at high concentrations, indicating that the surface of CNP_{32}, originally hydrophilic, is rendered rather hydrophobic due to surfactant adsorption, allowing them to transfer to the monomer phase (supporting information, Figure 10-8(c)). The fast aggregation experienced by these two kinds of nanoparticles (NP_{32} and CNP_{32}) in the monomer solution might explain the presence of particle aggregates in the continuous phase of the emulsions.

In analogy with NP_{32} nanoparticles, the presence of NP_8 nanoparticles did not modify the droplet size distribution of the emulsions compared to the systems stabilized with surfactant (Figure 4-62(c)). Nevertheless, nanoparticle distribution in the continuous phase was found to be remarkably different. While big aggregates of NP_{32} appeared, NP_8 could not be distinguished as a result of its better dispersability in the monomer phase (Figure 4-62(c)). In turn, without images at higher magnifications, the presence of some NP_8 at the monomer-water interface can not be discarded. In next section, the spatial distribution of nanoparticles within the polymer walls of the macroporous materials will be inspected by TEM.

As a conclusion, the images provide a clear distinction between both kinds of emulsion stabilization mechanisms: on one hand, large droplets sizes were obtained in Pickering emulsions (Figure 4-61). On the other hand, rather smaller droplet sizes were obtained in emulsions at higher surfactant concentrations (Figure 4-62). Such droplets are from one to two orders of magnitude smaller than those in particle-stabilized emulsions. Therefore, this study provides support that systems “transform” from particle-stabilized emulsions to surfactant-stabilized emulsions, passing for a wide range of surfactant concentrations in which the emulsions experienced phase separation (Figure 4-59). This demonstrates that nanoparticles and surfactant are beyond doubt acting antagonistically.

Figure 4-63 shows schematically the sequence proposed in this section, illustrating the influence of surfactant addition on Pickering emulsions. In one case (1) the starting point is a W/O highly concentrated Pickering emulsion stabilized with oleic acid surface-modified nanoparticles (representing NP_8 or NP_{32}), while in the other (2) is an O/W Pickering emulsion stabilized with hydrophilic untreated nanoparticles (representing hydrophilic CNP_{32}). If concentration of the nonionic Hypermer 2296 surfactant is increased, surfactant adsorbs preferentially on nanoparticles. This produces a progressive hydrophobization of the nanoparticles surface, leading to a gradual detachment of the nanoparticles from the oil-water interface into the oil phase of the emulsions. As a small number of particles are available to stabilize the interface, drop sizes increase, which results in larger droplets curvatures (Figure 4-63). As mentioned avobe, at certain surfactant concentration emulsions eventually undergo phase separation. If surfactant concentration is further increased, surfactant-stabilized emulsions are obtained, possessing rather smaller droplet sizes (greater droplet curvature). Therefore, particles initially adsorbed at the oil-water interface, migrate to the continuous phase of emulsions as a result of surfactant adsporption onto their surfaces. Interestingly, this process occurs for both functionalized with oleic acid nanoparticles and untreated hydrophilic nanoparticles.

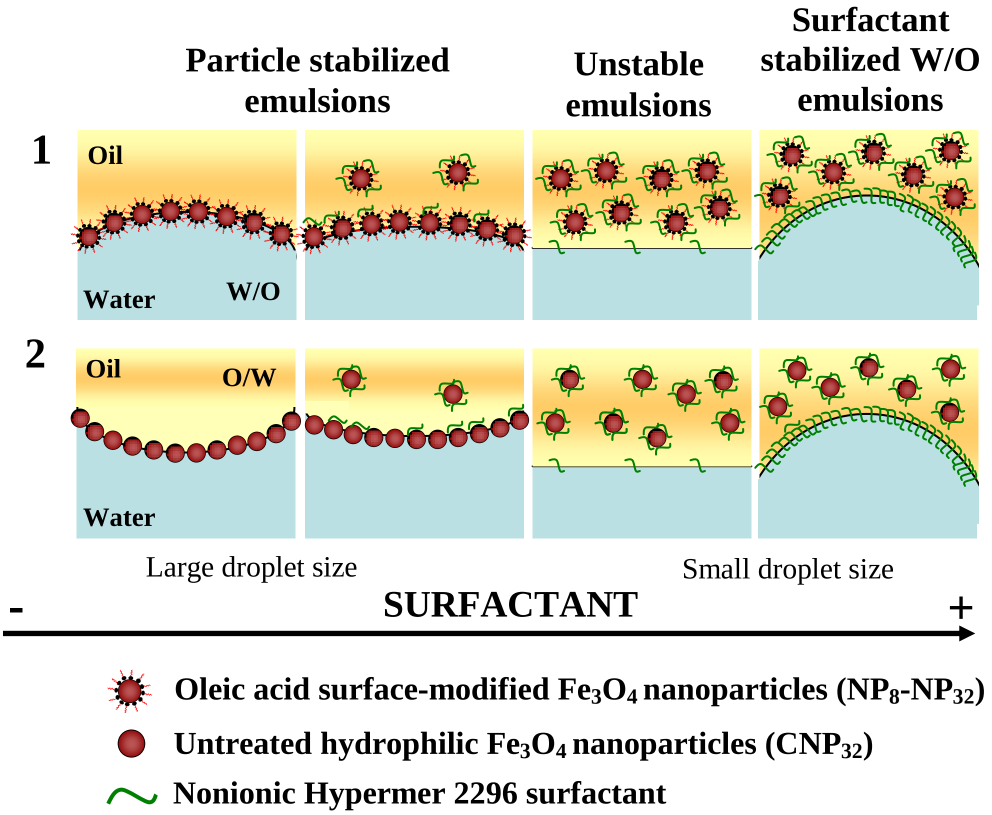

Figure 4-63. Scheme showing the influence of Hypermer 2296 surfactant addition on (1) W/O or (2) O/W Pickering emulsions at fixed nanoparticle concentration, initially stabilized with either oleic acid surface-modified Fe_3O_4 nanoparticles or hydrophilic untreated nanoparticles. Surfactant-stabilized emulsions have greater droplet curvatures than Pickering emulsions due to smaller droplet sizes.

4.4.3 Macroporous Polymers made from HIPEs Stabilized with Mixtures of Magnetic Nanoparticles and Hypermer 2296

This section describes the characterization of macroporous polymers, obtained by polymerization of the continuous phase of W/O HIPEs, stabilized with mixtures of magnetic nanoparticles and Hypermer 2296 surfactant. Transmission electron microscopy (TEM) is used to determine the spatial distribution of nanoparticles and scanning electron microscopy (SEM) is used to study the morphology of macropores. Moreover the physical and magnetic properties of the materials have been examined.

4.4.3.1 *Transmission Electron Microscopy characterization*

The organization of particles at liquid-liquid interfaces and the synergistic effects between nanoparticles and surfactants might be evaluated using microscope techniques, such optical,[69] or freeze-fracture SEM.[96] However, nanoparticles with very small sizes, especially when they are not aggregated, may not be resolved, and TEM is needed. Regarding macroporous polymers materials (polyHIPEs), both SEM[166, 178] and TEM[223, 310] can be used to observe pore and wall structures of polyHIPE materials. However, only a few studies have devoted to study the spatial distribution of nanoparticles in macroporous polymers made from Pickering emulsions. Gurevitch et al.[209] and Vílchez et al.[311] have shown recently how nanoparticles were effectively adsorbed on monomer/air interfaces after polymerization of the external phase of the original Pickering HIPEs. In this section we have examined the internal wall structures by TEM, of samples made from emulsions containing either NP_8 or NP_{32} nanoparticles.

Cross sections of polyHIPEs materials were cut with an ultramicrotome. Firstly, samples made from emulsions containing NP_{32} (1.5 wt%) without and at low Hypermer 2296 surfactant concentration were examined (Figure 4-64).

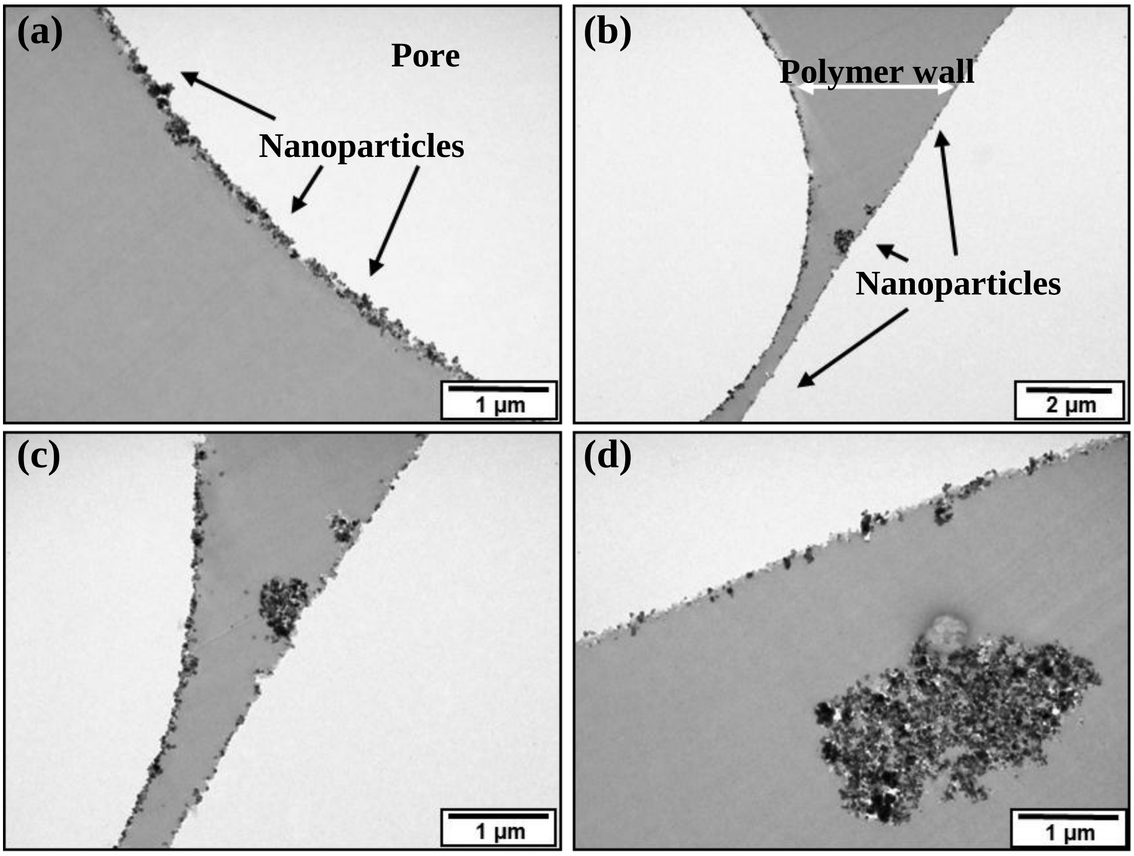

Figure 4-64. Representative TEM images of ultramicrotome slides (around 60 nm thick) showing how the nanoparticles (NP_{32}) are distributed in the polymer matrix of macroporous polymers. Samples were obtained from HIPEs with an 80 % internal phase volume and stabilized solely with 1.5 wt% NP_{32} (a) and with a mixture of 1.5 wt% NP_{32} and 10^{-3} wt% Hypermer 2296 (b-d).

Figure 4-64 shows that when no surfactant was used, i.e. Pickering emulsion as template, NP_{32} were only found at the monomer/air interface (Figure 4-64(a)), confirming that emulsions are stabilized with nanoparticles, as already mentioned in section 4.3.3.1 (Figure 4-46, page 152). Interestingly, NP_{32} aggregates as well as some individual particles were observed within the polymer walls of the polyHIPE materials, as surfactant concentration was slightly increased to 10^{-3} wt% (Figure 4-64(b-d)). As pointed out before, surfactant adsorption on nanoparticle surfaces led to less stable emulsions due to the progressive displacement of nanoparticles from the monomer-water interface. Aggregates are easily seen inside the wall between pores depicted in Figure 4-64(c). Although such images did not allow observing any increment of pore size, the presence of the aggregates is obviously linked with the increment of droplet sizes observed in Figure 4-61(c), because of the lower number of NP_{32} at the oil-water interface, acting as emulsifiers.

Samples made from HIPEs stabilized with mixtures of 1.5 wt% NP_{32} and surfactant at higher concentrations are shown in Figure 4-65(a-b) (1.5 wt%) and Figure 4-65(c-d) (4 wt%).

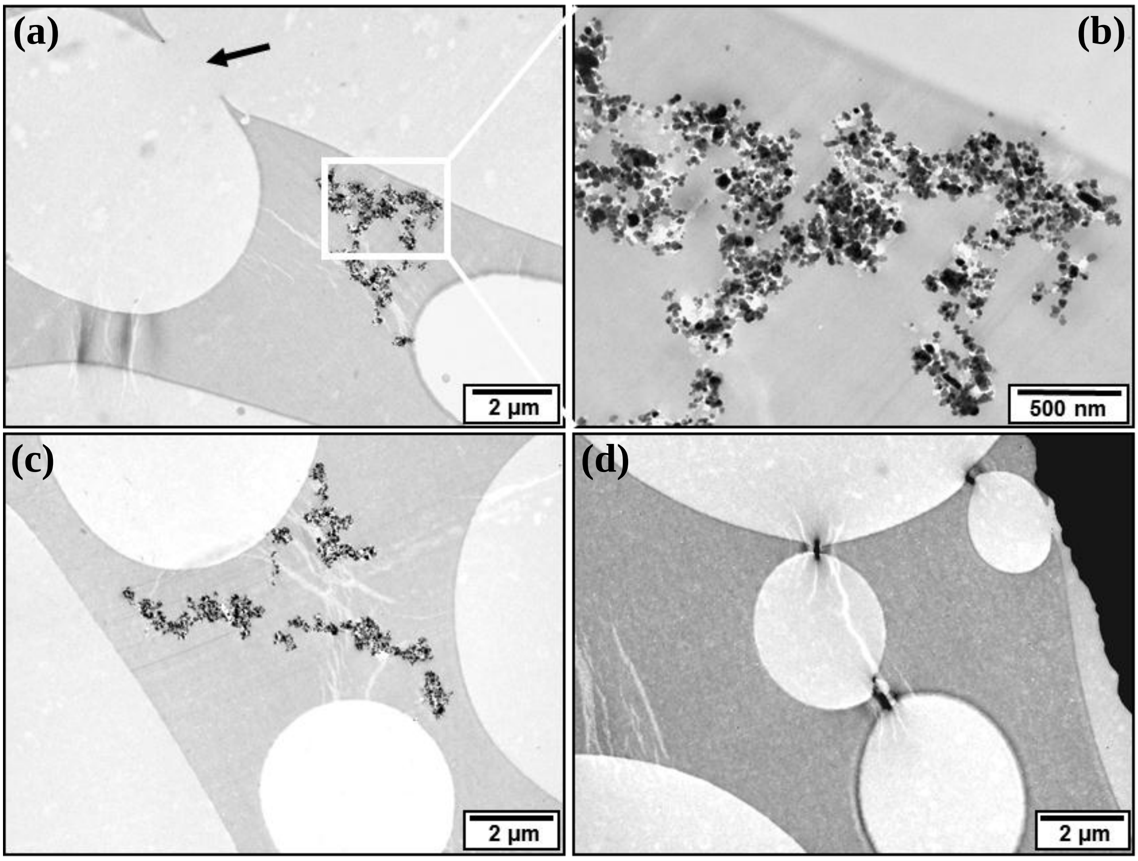

Figure 4-65. Representative TEM images of macroporous polymers obtained from HIPEs with an 80 % internal phase volume, and stabilized with mixtures of NP_{32} (1.5 wt%) and surfactant at 1.5 wt% (a-b) or 4 wt% concentration (c-d). Nanoparticles are not adsorbed on the polymer-air interface, and are located inside the polymer walls forming large aggregates.

These images do not show any NP_{32} located at the polymer-air interface. They do, however, show that NP_{32} aggregates are randomly dispersed inside the polymer walls. This fact could be explained by displacement of NP_{32} nanoparticles from the monomer-water interface. Surfactant at low concentrations adsorbs onto NP_{32}, enhancing its surface hydrophobicity and therefore reducing its ability to adsorb at the O-W interface. As a consequence, emulsion was less stable and sedimentation occurred. As surfactant concentration is progressively increased, particles are completely desorbed from the interface. At 1.5 wt% Hypermer 2296 (Figure 4-65(a,b)), all NP_{32} are already pulled out from the interface, supporting optical microscopy observations (Figure 4-62(a,b)). No differences in nanoparticle distribution within the polymeric walls were found when surfactant concentration was increased to 4 wt% (Figure 4-65(c,d)). It should be noted that, a discontinuity in the polymer film appeared in picture Figure 4-65(a) (see black arrow). This corresponds to a connexion (also called pore throat) between adjacent pores. Pore throat formation will be described in detail in further sections.

As discussed in section 4.3.3.1, in absence of surfactant, although most of NP_8 were located at the polymer-air interface of the resulting materials, there was a significant number of NP_8 embedded within the polymer walls of the macroporous material (see Figure 4-47). This behaviour was significantly different than that observed for NP_{32}, which had a bigger particle size than NP_8. This evidence indicated that some NP_8 had a higher affinity for the continuous phase of the W/O HIPEs and they could be effectively dispersed into the oil phase. Figure 4-66 shows TEM images of a macroporous material, made from a W/O HIPE stabilized with a mixture of 1.5 wt% NP_8 and 10^{-3} wt% Hypermer 2296.

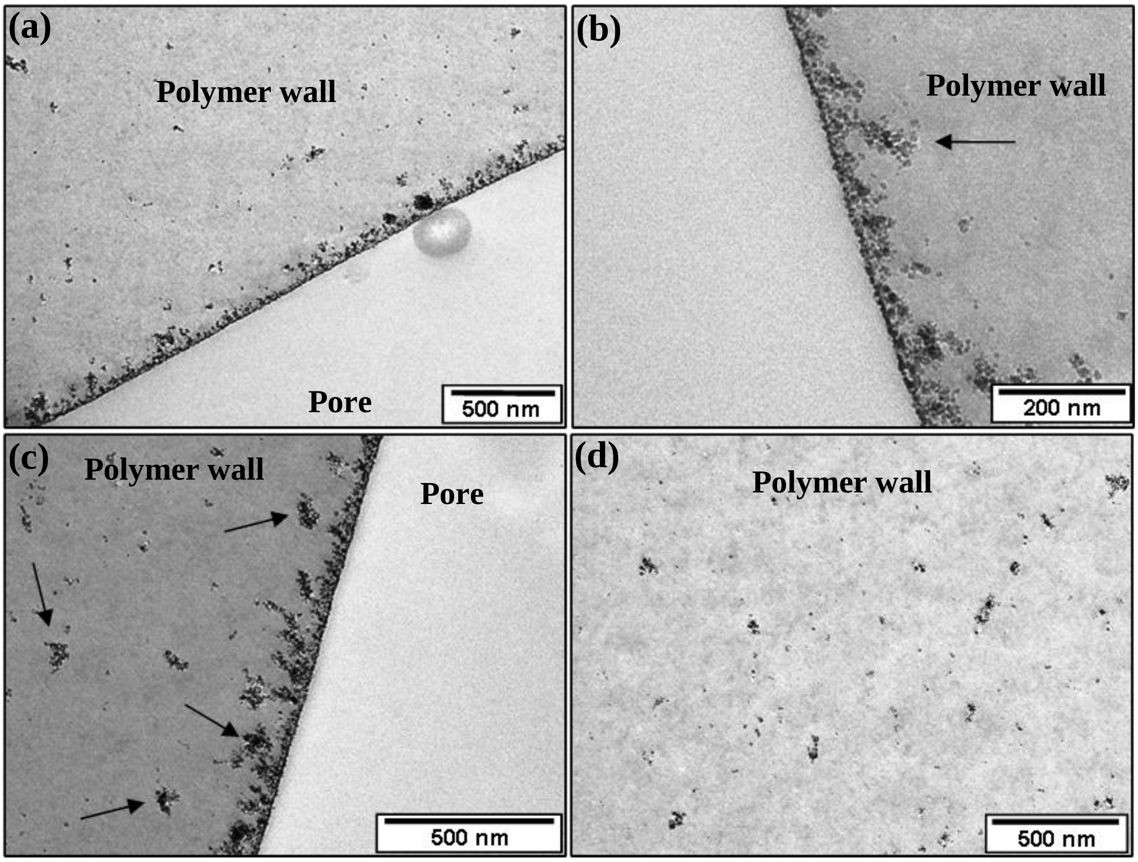

Figure 4-66. Representative TEM images of macroporous polymers obtained from HIPEs with an 80 % internal phase volume, and stabilized with mixtures of 1.5 wt% NP_8 and 10^{-3} wt% surfactant. The arrows indicate the presence of NP_8 aggregates outside the interface.

From the figure, it can be clearly seen that a large fraction of NP_8 is adsorbed on the polymer-air interface of the polyHIPE. However, some particle aggregates are found outside the polymer-air interface (indicated with arrows in Figure 4-66(b,c)). This was not observed in macroporous materials made from Pickering emulsions stabilized solely with 1.5 wt% NP_8, in absence of surfactant (supporting information in Appendix, Figure 10-9). Moreover, it seems that a larger number of NP_8 is dispersed within the polymeric walls of the materials (compare Figure 4-66 (d) and Figure 10-9(d)). In this context, both individual nanoparticles and clusters of up to approximately 80 nanoparticles were found inside the polymer walls. Consistent with that observed in samples containing NP_{32}, it is highly probable that NP_8 are being gradually pulled out from the interface when surfactant is added at low concentrations. In any case, NP_8 adsorbs more on the interface than NP_{32}.

It is well known from the literature, that smaller nanoparticles have smaller adsorption energies, thus being subject to displacement from oil-water interfaces by thermal energy.[63] Therefore, it was considered of interest to evaluate the influence of particle size. NP_8 nanoparticles (≈8 nm) are smaller than NP_{32} (≈32 nm) and both results have been compared.

In this context, Figure 4-67 shows representative TEM images of a macroporous polymer synthesized from a W/O HIPE, stabilized with a mixture of 1.5 wt% NP_8 and 4 wt% surfactant. The corresponding TEM images for the macroporous polymer containing intermediate surfactant concentration (1.5 wt%), are included in Figure 10-10 as supporting information.

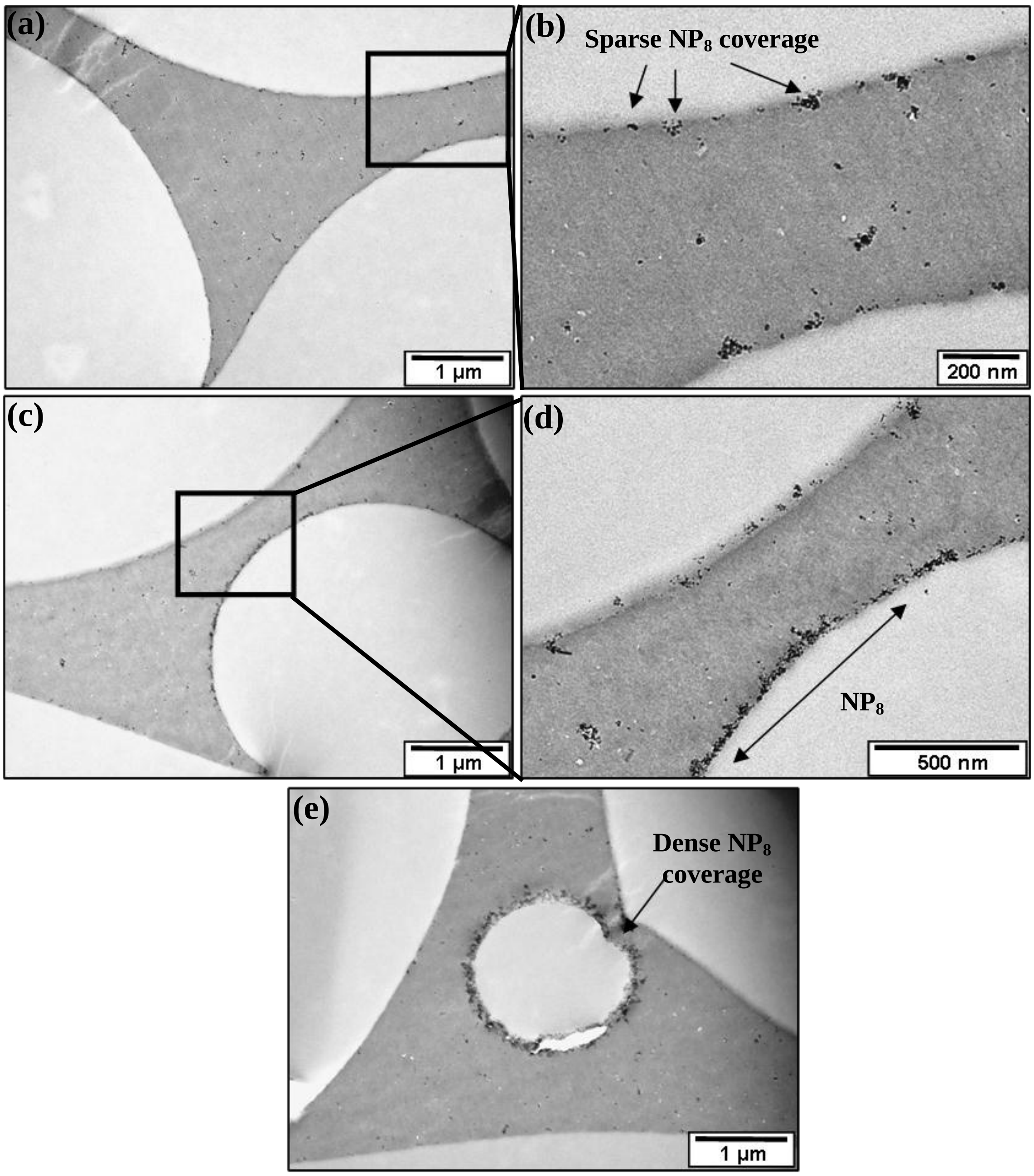

Figure 4-67. Representative TEM images of macroporous polymers obtained from HIPEs with an 80 % internal phase volume, and stabilized with a mixture of NP_8 (1.5 wt%) and 4.0 wt% surfactant. Notice that nanoparticles are in some cases located at the polymer-air interface, but mainly inside the polymer walls. Pictures in (b) and (d) are higher-magnification zooms of the regions delimited with squares in (a) and (c), respectively.

From the TEM observations in Figure 4-67, it can be observed that the lowest NP_8 coverage density was found in the surface of large pore sizes (Figure 4-67(a,b). Nanoparticles were sparsely covering the polymer-air interface, as seen in Figure 4-67(b). However, in some cases the NP_8 coverage density on both sides of larger pore walls was not symmetric. Since the resin used in the ultramicrotome cutting process was successfully embedded in all pores of the sample shown in Figure 4-67(c,d), the possibility that some NP_8 might have squeezed out from the sample during the slide processing can be ruled out. Besides that, numerous small pores were densely covered by several layers of NP_8, whereas the surrounding larger pores were free of them (Figure 4-67(e)).

In any case, it could be concluded that NP_8 nanoparticles are not totally pulled out from the interface as surfactant concentration is increased up to 4.0 wt%. This behaviour is substantially different from that observed for NP_{32} nanoparticles, which can be completely removed from the interface at high surfactant concentrations (Figure 4-65). One possible explanation could be the different size of nanoparticles. Smaller nanoparticles (NP_8) have a larger surface area, which probably requires a larger surfactant concentration to modify its surface properties. In this context, it was shown that removal of particles from the interface occurs at higher surfactant concentrations for NP_8 (Figure 4-59(d)) than for NP_{32} (Figure 4-59(c)).

4.4.3.2 *Characterization of pore structure and mechanical properties*

Details regarding composition of the original HIPEs, as well as porosity, specific crush strength and permeability values, are summarized in Table 4-12. If not otherwise mentioned, both the internal phase volume fraction and nanoparticle concentration were kept constant at 80 % and 1.5 wt%, respectively.

Table 4-12. Composition of HIPEs and physical properties of the macroporous polymers after polymerization of the continuous phase of the HIPEs. Porosity, specific crush strength (σ_s) and nitrogen permeability are indicated. The internal phase volume fraction and the nanoparticle concentration (respect to the continuous phase) of the HIPEs were 80 % and 1.5 wt%, respectively.

Sample	Nanoparticles	Hypermer (wt/wt%)	Porosity (%)	σ_s (MPa·m^3·kg^{-1})	Permeability (Da)
1	NP$_8$	Without	83.7 ± 2.5	0.0066 ± 0.0026	0
2	NP$_8$	10^{-2}	85.2 ± 3.2	0.0057 ± 0.0004	0
3	NP$_8$	1.5	82.8 ± 0.7	0.0181 ± 0.0031	0.38 ± 0.01
4	NP$_8$	2	82.2 ± 0.4	0.0217 ± 0.0004	0.90 ± 0.04
5	NP$_8$	4	82.8 ± 0.4	0.0259 ± 0.0007	0.60 ± 0.06
6	Without	4	82.9 ± 1.1	0.0207 ± 0.0013	0.75 ± 0.02
7	NP$_{32}$	4	84.1 ± 0.1	0.0242 ± 0.0006	Not measured
8	CNP$_{32}$	4	83.7 ± 0.2	0.0218 ± 0.0004	0.77 ± 0.03

In line with the emulsion stability experiments, polyHIPEs (macroporous polymers prepared from HIPEs) have been obtained using either Pickering emulsions, in absence or at low surfactant concentrations, or surfactant-stabilized emulsions, at surfactant concentrations above 1.5 wt%. At first, the system containing NP$_8$ in the whole range of surfactant concentrations was examined. Figure 4-68 shows two SEM images, corresponding to macroporous polymers made from a Pickering emulsion (sample 1 in Table 4-12), and from an emulsion stabilized with a mixture of 1.5 wt% NP$_8$ and 10^{-2} wt% Hypermer 2296 (sample 2 in Table 4-12).

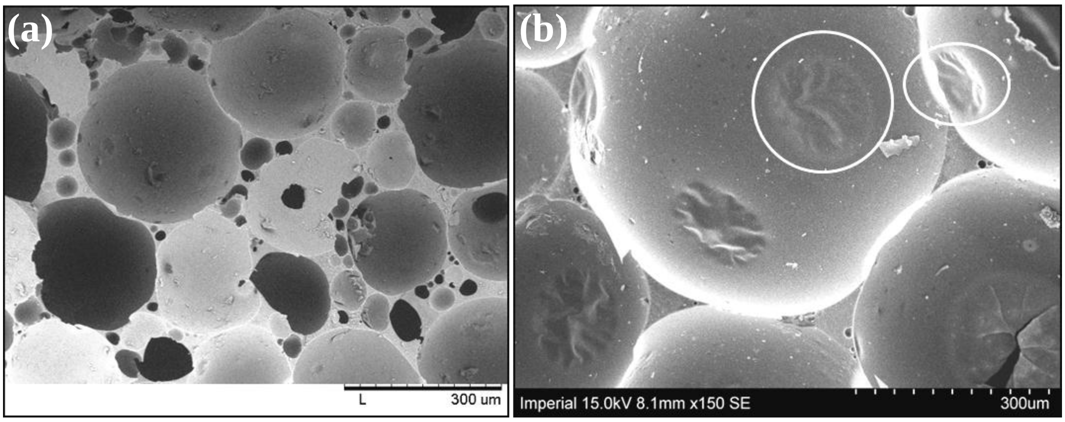

Figure 4-68. SEM images of macroporous polymers synthesized from a (a) Pickering HIPE and from a (b) HIPE containing a mixture of NP_8 nanoparticles and surfactant (10^{-2} wt%). In both cases NP_8 concentration and internal phase volume fraction in the emulsions was 1.5 wt% and 80 %, respectively. The white circle indicate thin film regions.

Figure 4-68 shows a very large increase in pore size when slightly increasing surfactant concentration to 10^{-2} wt%. Sample 2 (Figure 4-68(b)) have pores bigger than 500 μm, much larger than in sample 1, without surfactant (Figure 4-68(b)). Moreover, the walls in sample 2 do not show any visible pore throat, which interconnect neighbouring pores. They did, however, show some thin polymer films which probably correspond to droplet contacts in the original HIPEs (indicated in Figure 4-68(b)). The presence of these thin polymer films, separating neighbouring pores, is most likely associated to the detachment of some NP_8 nanoparticles from the interface to the inner polymer wall, as a consequence of surfactant addition (10^{-2} wt%). This also explains the big increase in pore size by comparing images (a) and (b) in Figure 4-68. Moreover, cracks and flaws were detected within the polymer walls, which could be related to this film thinning. However, permeability experiments verified that both samples 1 and 2 were completely impermeable to nitrogen gas in the pressure range evaluated (up to 1.6 bars). It can be therefore concluded that such materials have an entire closed-cell structure.

Figure 4-69 shows SEM images revealing the macroporous structure of macroporous polymers prepared from HIPEs stabilized with mixtures of 1.5 wt% NP_8 and higher surfactant concentrations, 1.5 wt% (Figure 4-69(a)) or 4 wt% (Figure 4-69(b,c)). In this case, the pore size was reduced as surfactant concentration increased, confirming the observations made by optical microscopy.

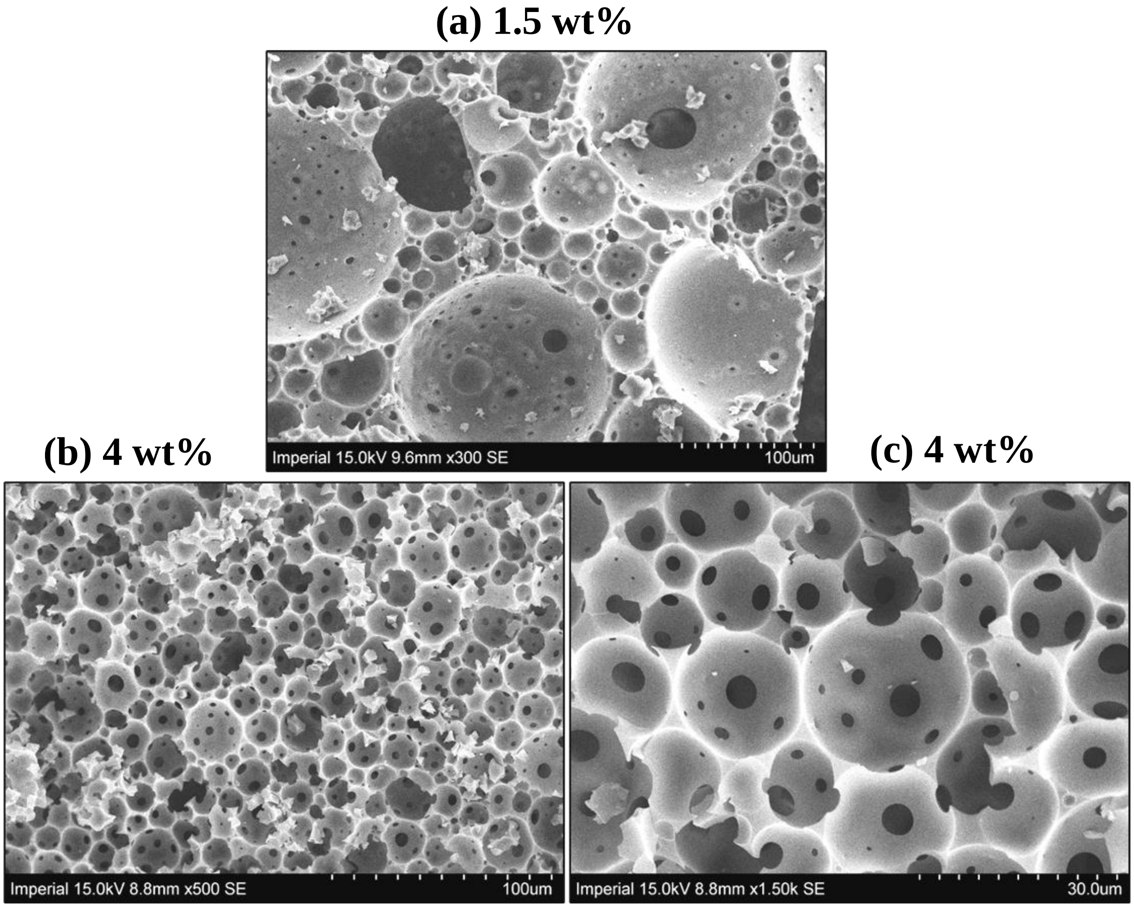

Figure 4-69. SEM images of macroporous polymers synthesized from HIPEs containing a mixture of NP_8 nanoparticles (1.5 wt%) and Hypermer 2296 surfactant: (a) 1.5 wt%; (b) 4wt% and (c) 4 wt%, observed at higher magnification. In all cases the internal phase volume fraction of the emulsions was 80 %.

Apart from pore size reduction, a dramatic change occurred in the microstructure of the pores as surfactant concentration was increased. Small windows began to appear within polymer walls at 1.5 wt% Hypermer 2296 (Figure 4-69(a)). Both the size and the number of such connecting windows increased as surfactant concentration was increased. This fact is evident when comparing pictures (a) and (b) in Figure 4-69. Pore throats in sample 5 (4 wt% surfactant, Figure 4-69(b,c)) had sizes from 0.7 to 5 μm. This has already been described in the literature. Wrobleski[166] first and later Cameron[211] pointed out the importance of the reduction of the polymerizable film by addition of surfactants as emulsifiers to obtain such interconnectivity. In particular, Cameron demonstrated that pore throats began to appear as a result of volume contraction, on conversion of monomer to polymer at the gel point of the polymerization.[211] The difference between the closed-cell structure observed in Figure 4-68 and the opened-cell structure see in Figure 4-69 can be understood in terms of the stabilizing layer thickness, as the size of particles is much bigger than that of surfactants. Therefore, a close-packed layer of particles, especially in the case of multilayers, is expected to impede the thinning down of the film between emulsions droplets.

Pore size distributions of the polyHIPEs characterized above were determined by a direct pore counting method using several SEM images (Figure 4-70) as described in the experimental section (3.2.9.1). Very large pores were found in sample 2 (10^{-2} wt% surfactant, Figure 4-68(b)), compared with those observed in sample 1 (without surfactant, Figure 4-68(a)). As aforementioned, this fact is most likely a consequence of the emulsion destabilization induced by small amounts of surfactant. Pores of this material (sample 2) were highly polydispersed, ranging from several micrometers to approximately 600 µm (blue open triangles in Figure 4-70).

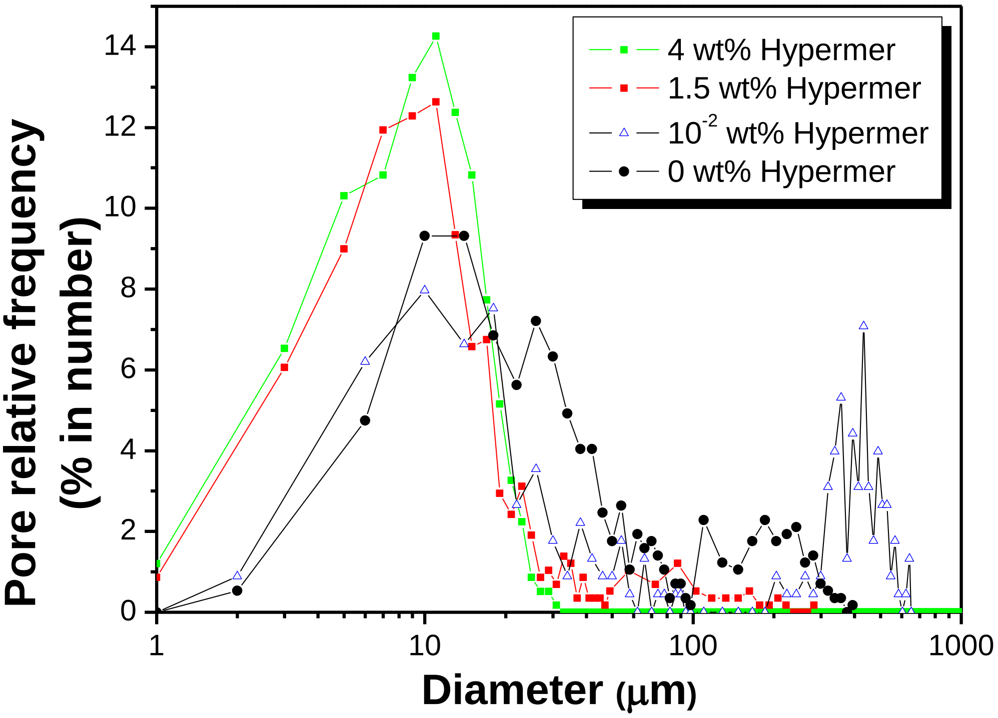

Figure 4-70. Pore size distributions for macroporous polymers prepared from HIPEs, at constant internal phase volume fractions (80 %) and NP_8 concentration (1.5 wt%), for different Hypermer 2296 concentrations. Such concentrations are expressed with respect to the monomer phase.

Pore size distribution shifted to large sizes when adding 10^{-2} wt% Hypermer 2296, but it moved back to small sizes when adding larger amounts of surfactant (Figure 4-70). While in sample 3 (1.5 wt% Hypermer, indicated as red filled squares), pores with 200 µm in diameter can still be observed, the increase in surfactant concentration leads to a single, but polydisperse pore population centered at around 10 µm pore diameter (sample 5, 4 wt% surfactant, green filled squares). These sizes are in good agreement with other polyHIPEs already described in the bibliography[173, 188].

Regarding porosity, values varied from 82 to 85 % (Table 4-12). This again does not exactly fit with the internal phase volume fractions added to the precursor emulsion. The difference between both values was attributed to the increase in skeletal density from monomer to polymer, as explained in section 4.3.3.1. However, the large deviation showed by sample 2 (10^{-2} wt% surfactant, 85.2 % porosity, Table 4-12) cannot be only explained by that reason. As mentioned above, sedimentation occurred during the polymerization of the emulsion in this sample, which resulted in a separated polymer phase. Consequently, there is an increase of foam density, and the porosity of the macroporous polymer is higher than it would be expected.

Similar results concerning pore structure and pore size distribution of polyHIPEs containing NP_8 have also been observed in polyHIPEs containing NP_{32}. Some representative SEM images of such materials are included as supporting information in the Appendix (Figure 10-12).

As regards mechanical properties, it was anticipated that the marked high polydispersity of pore sizes exhibited by both samples 1 and 2 had a significant effect on their specific crush strength values (σ_s). These two samples, made from HIPEs without surfactant (sample 1) and with 10^{-2} wt% surfactant (sample 2) possessed the lowest values among the macroporous polymer examined (Table 4-12 and inset in Figure 4-71). The influence of pore size polydispersity on mechanical properties is in agreement with that described in the literature.[178, 204] The higher polydispersity, the lower crush strength. The specific crush strength was also determined for the polyHIPEs at higher surfactant concentrations. In particular, it increased from 0.0181 (at 1.5 wt% surfactant, sample 3) to 0.0259 $MPa \cdot m^3 \cdot Kg^{-1}$ (at 4 wt% surfactant, sample 5). To better highlight this increase, the specific crush strength values of the samples are plotted in Figure 4-71. These σ_s values are much larger than that showed by the macroporous polymers, made from Pickering HIPEs, in absence of surfactant or at low surfactant concentration, basically due to a reduction in pore size. It is important to recall that from 0.1 to approximately 1 wt% surfactant, emulsions undergo phase separation. Therefore, macroporous polymers could not be obtained in this surfactant concentration region, which is shaded in Figure 4-71.

Another important parameter that may be affected by the reduction of the pore size is the permeability of the materials. The permeability of a macroporous polymer containing NP_8 (1.5 wt%), as a function of surfactant concentration in the initial emulsions, is also plotted in Figure 4-71. As discussed before, the two samples, made from HIPEs without (sample 1) and with 10^{-2} wt% surfactant were completely impermeable to nitrogen gas in the pressure range evaluated (up to 1.6 bars), confirming their entire closed-cell structure.

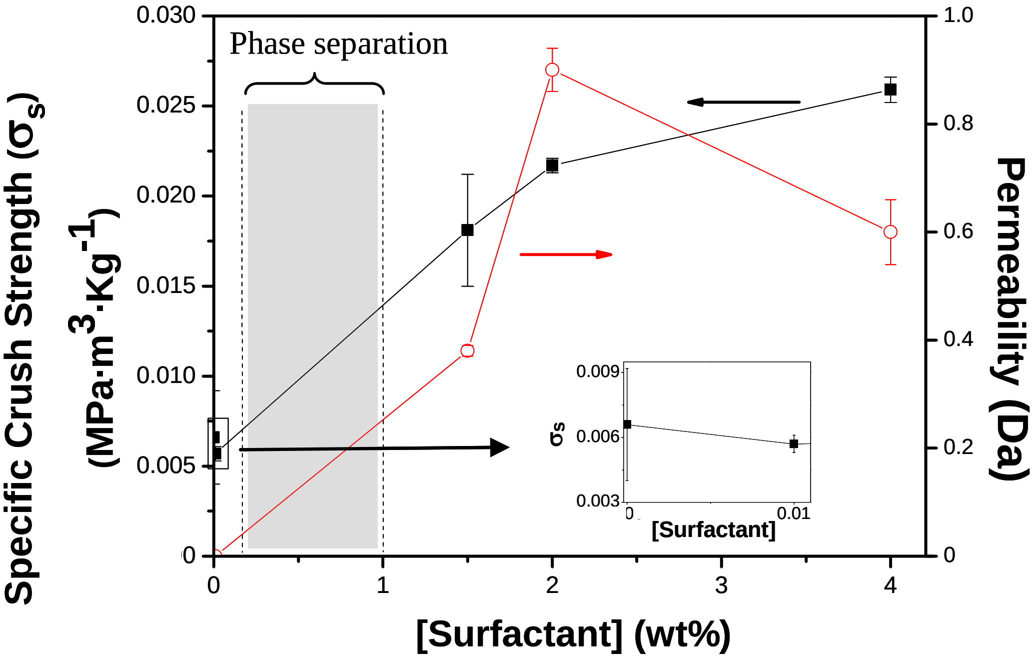

Figure 4-71. Specific crush strength and permeability for polyHIPE materials containing NP_8 nanoparticles, as a function of surfactant concentration in the initial highly concentrated emulsions. NP_8 concentration and internal phase volume fraction in the emulsions were 1.5 wt% and 80%, respectively. The area shaded in the graph, corresponds to surfactant concentrations leading to unstable emulsions (Figure 4-59). The inset graph shows a zoom of the specific crush strength for samples without surfactant and at low surfactant concentration (10^{-2} wt%) on a larger scale.

Regarding macroporous polymers at higher surfactant concentrations, in principle, the larger pore size, the higher permeability considering a constant number and size of pore throats.[217] Nevertheless, this assumption is not valid in this case, because the samples possessed different degrees of interconnectivity as surfactant concentration increased (Figure 4-69). In Figure Figure 4-69(a), it can be observed that, macroporous polymer made from an emulsion containing 1.5 wt% surfactant, despite possessing the larger pores of the sequence at higher surfactant concentrations, most of them were actually found to be rather closed-cell, indicating still the presence of an important number of NP_8 at the interface. The permeability of this sample was 0.38 Da (Figure 4-71). On the other hand, the highest value of permeability (0.90 Da) was reached for the macroporous polymer made from an emulsion containing an intermediate surfactant concentration (2 wt%, sample 4). Further increment in surfactant concentration (4 wt%, sample 5 in Figure 4-69(b,c)) led to a 33 % reduction in the permeability, compared to sample 4 (Figure 4-71). This fact suggests that small pores with small pore throats are limiting gas permeability. Actually, the TEM images in Figure 4-67(e), showed the presence of some small pores densely covered by NP_8 in sample containing 4 wt% surfactant. This could explain the lower permeability (0.60 Da) of this macroporous polymer compared to that exhibited (0.75 Da) by the polyHIPE made with the same surfactant concentration (4 wt%), but without NP_8 (sample 6 in Table 4-12).

Finally, with the aim of assessing whether the mechanical properties of the polyHIPEs might be influenced by the presence of nanoparticles within their polymer walls, macroporous solid foams made from HIPEs stabilized with 4 wt% Hypermer 2296, and in the presence or absence of 1.5 wt% nanoparticles, were prepared and tested, as described in the experimental section.

At this particular surfactant concentration, samples prepared without particles (see Figure 4-72(a)) as well as macroporous polymers containing NP_{32} and CNP_{32} (Figure 10-12 in the Appendix) showed macroporous structures very similar to that containing NP_8 (Figure 4-69(b,c)). In particular, from Figure 4-72(b), it can be seen that the pore size distribution for the sample without nanoparticles (sample 6 in Table 4-12) slightly shifted to lower values compared to that also containing NP_8. This allows ascertaining the individual contribution of each kind of nanoparticles to the overall specific crush strength values.

Stress-strain analysis conducted for samples with and without NP_8 is shown in Figure 4-72(c). As observed, and crush strength was increased by introducing 1.5 wt% oleic acid-capped NP_8. A 22 % higher stress was necessary to be applied to produce a 6 % decrease of the sample thickness when the nanoparticles were acting as reinforcement. These results confirm that particles can strengthen the macroporous polymers.

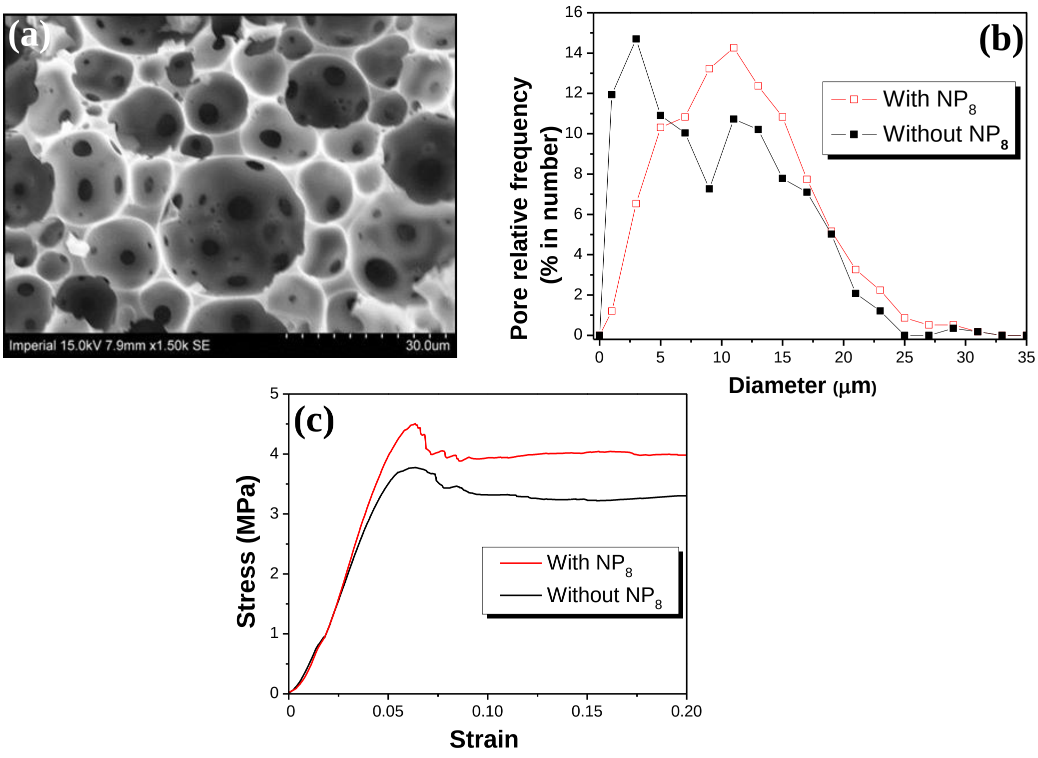

Figure 4-72. (a) SEM image of a polyHIPEs synthesized from a HIPE stabilized with 4 wt% Hypermer 2294, in absence of nanoparticles. (b) Pore size distributions and (c) compression curve for polyHIPEs made from emulsions stabilized with 4 wt% Hypermer 2296 in presence or in absence of 1.5 wt% NP_8.

The values of specific crush strength are represented in Figure 4-73. It can be seen that the value for the polyHIPE containing just 1.5 wt% NP_8 was 20 % higher than that measured for the polyHIPE prepared from a conventional HIPE, stabilized with 4 wt% surfactant. These observations are consistent with that already described in the literature. It is well known that the addition of inorganic fillers enhances the mechanical properties of polymers and specifically those of polyHIPEs[218, 223].

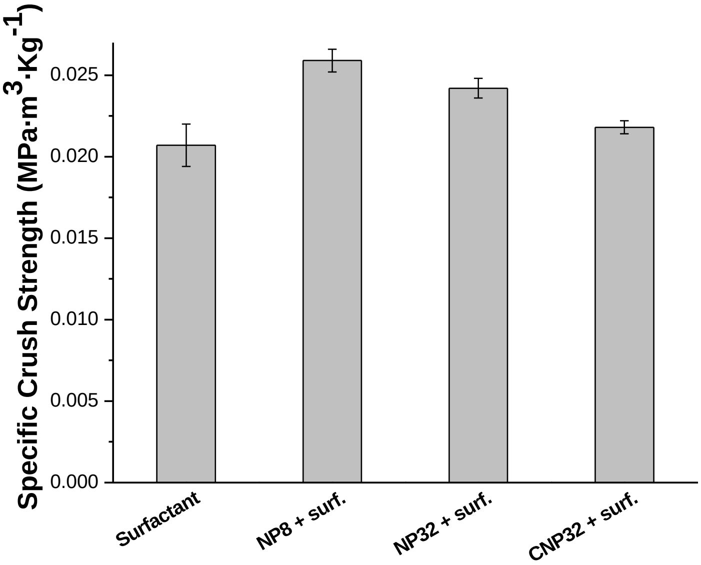

Figure 4-73. Specific crush strength values of the polyHIPEs made from highly concentrated emulsions (HIPEs), stabilized with 4 wt% surfactant in the absence or in the presence of 1.5 wt% NP_8, NP_{32}, or CNP_{32}. From left to right, samples correspond to sample 6, 5, 7 and 8 in Table 4-12. The error bars correspond to the standard deviation calculated over 6 samples measured in the compression test.

Interestingly, the extent of reinforcement seems to be slightly different for the different kind of nanoparticles used. The higher specific crush strength value for the polyHIPE containing NP_8 reinforces the hypothesis that is of paramount importance that nanoparticles are homogeneously distributed and not strongly aggregated within the polymer. The specific crush strength for such sample was 0.0259 $MPa \cdot m^3 \cdot Kg^{-1}$ while values for polyHIPEs containing NP_{32} and CNP_{32}, were 0.0242 and 0.0218, respectively. This represents an overall difference of 7 and 16 % with respect to the sample containing NP_8. The presence of both NP_{32} and CNP_{32} aggregates, confirmed by TEM observations, could produce such differences (Figure 4-65). Moreover, quite large aggregates were found in the case of CNP_{32}, which could explain the large difference with respect to NP_8 (Figure 10-11 in the Appendix, as supporting information). In any case, it is worth mentioning that the yield strength of the polyHIPEs containing nanoparticles was higher than the equivalent nanoparticle-free system, in all cases.

4.4.3.3 *Characterization of magnetic properties*

The main objective was to impart magnetic properties to the polymeric nanocomposites. At first, magnetization saturation (M_s) of macroporous polymers, prepared from Pickering highly concentrated emulsions (Pickering HIPEs), containing different NP$_8$ concentrations, was evaluated as a function of the applied magnetic field at 300 K. The magnetization of polyHIPEs was compared to the magnetization of neat NP$_8$, which is already described in section 4.1.1 (Figure 1-4(a)). Previous results revealed that NP$_8$ are superparamagnetic nanoparticles, reaching M_s of 58.4 emu/g. Magnetization vs. applied field (M-H) curves for the macroporous polymers are plotted in Figure 4-74. NP$_8$ data was likewise included as a reference.

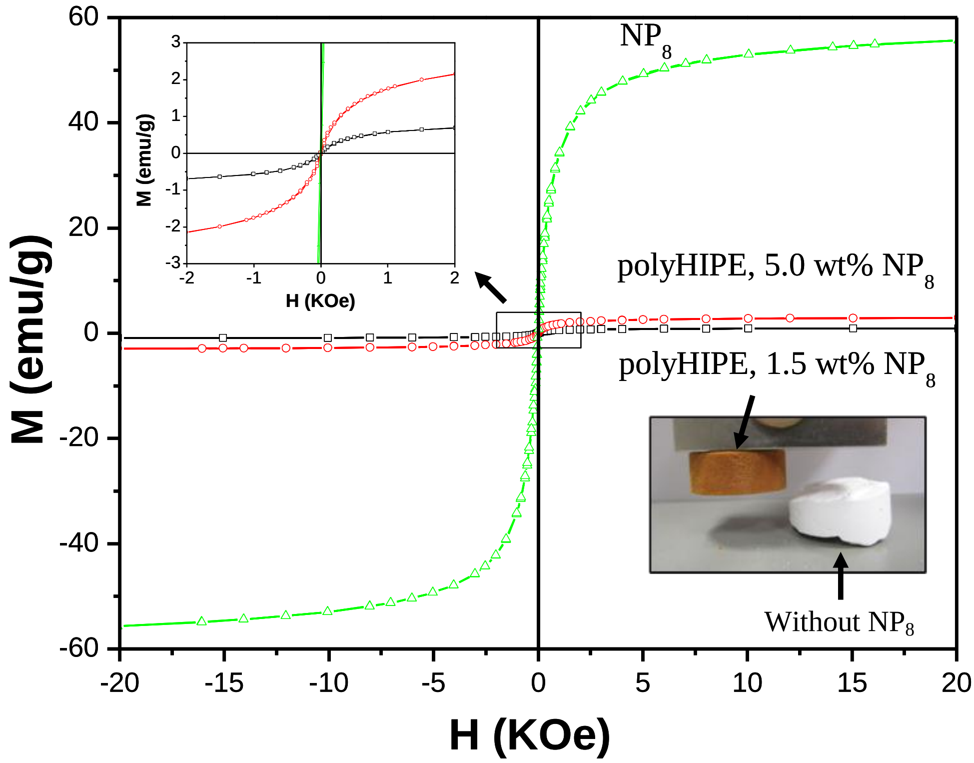

Figure 4-74. Magnetization vs. applied magnetic field for original NP$_8$ (green line) and for macroporous polymers prepared from Pickering HIPEs containing a 80 % internal phase volume and stabilized with either 1.5 (black line) or 5 wt% (red line) of NP$_8$, in absence of surfactant. The inset graph shows a zoom of the same results on a larger scale. The measurements were carried out at 300 K. The picture shows the macroporous polymer containing 1.5 wt% superparamagnetic NP$_8$ being attracted to a permanent magnet.

As deduced from the hysteresis loop measurements shown in Figure 4-74, magnetization (emu) per gram of material further decreased from 58.4 emu/g to 2.9 and to 1.0 with the encapsulation of NP$_8$ in the polymer, for macroporous polymers containing 5.0 and 1.5 wt% NP$_8$, respectively. This reduction is in very well agreement with the concentration of NP$_8$ in the sample. The smaller nanoparticle concentration, the lower magnetization saturation. This result demonstrates that magnetization of nanoparticles is not lost during polymerization. This is in fairly good agreement with other works that report the incorporation of magnetic nanoparticles in polymeric matrices. [270, 271, 274, 312] In such studies, little influence of the polymer on nanoparticles M_s is observed, and M_s per gram of material fits quite well with the corresponding weight fraction of the nanoparticles inside the polymer.

Interestingly, the superparamagnetic behaviour was also retained by the macroporous polymers, as indicated by the lack of hysteresis loop and coercivity (see inset in Figure 4-74). An example of a macroporous polymer or polyHIPE material containing 1.5 wt% of NP_8 being attracted to a magnet is also shown (Figure 4-74). It should be mentioned that the same trend in M-H results were obtained for macroporous polymers made from HIPEs stabilized with mixtures of nanoparticles (NP_8) and 1.5 wt% surfactant. The corresponding M-H curve is included as supporting information in the Appendix (Figure 10-13). This suggests that M_s was not affected by either particle aggregation or location around the oil-water interface. In conclusion, magnetism saturation does not depend on particle spatial distribution.

On the other hand, it is well-documented that nanoparticle interactions may alter the magnetic behaviour of fine particle systems, thus modifying the blocking temperature of the nanoparticles. In this context, it was demonstrated earlier by TEM observations, that the spatial distribution of NP_8 in the polymer could be partially controlled, by selecting the appropriate concentration of nanoparticles and/or surfactant as emulsifiers. Specifically, aggregated nanoparticles were adsorbed preferentially at the oil-water interfaces in absence of surfactant (Figure 4-47). When Hypermer 2296 surfactant concentration was increased, nanoparticles were progressively pulled out from such interfaces, and they remained well-dispersed within the polymeric walls of the macroporous polymers (Figure 4-67). Therefore, it was considered that such systems might be ideal to study the influence of surfactant addition on the blocking temperature of the nanoparticles embedded within the nanocomposites. To ensure the reliability of the results, the same kind of nanoparticles (NP_8) at the same concentration (1.5 wt%) were used in the experiment. Differences in magnetic response will indeed be, merely due to the different nanoparticle spatial arrangement.

Figure 4-75 shows the curves of magnetization as a function of temperature, for three macroporous polymers, prepared from HIPEs with different Hypermer 2296 concentrations, at constant NP_8 concentration (1.5 wt%). The curves are characteristic of weakly interacting systems of superparamagnetic nanoparticles.[291] Experiments were performed both under zero field-cooling (ZFC) and field-cooling (FC) conditions, at H = 50 Oe. The curve corresponding to neat NP_8 nanoparticles is also included for comparison (see inset).

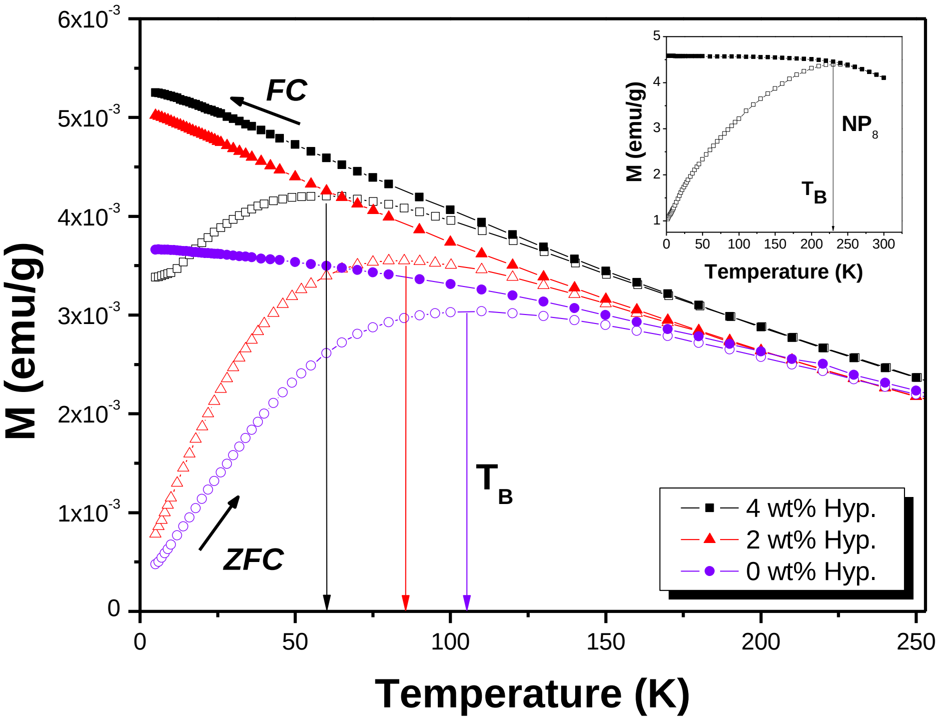

Figure 4-75. Magnetization vs. temperature for polyHIPEs, prepared from HIPEs stabilized with 1.5 wt% NP_8 and different Hypermer 2296 surfactant concentrations. Zero field-cooling (open symbols) and field-cooling (solid symbols) measurements were carried out at H = 50 Oe. The surfactant concentrations indicated in the legend are expressed with respect to the monomer phase weight in the initial emulsions. Lines are only visual guides. The inset shows the same ZFC and FC measurements for neat NP_8, for comparison.

As indicated in the Introduction (1.2.2.4), the (average) blocking temperature (T_B) can be ascribed to the maximum in the ZFC magnetization. T_B for neat NP_8 was estimated to be 230 K (see inset in Figure 4-75). As clearly seen in the figure, the concentration of surfactant in the initial emulsions has a significant effect on the T_B of the nanoparticles embedded in the polymer. When the emulsion used as a template was solely stabilized with 1.5 wt% NP_8, the T_B of the macroporous polymer was 105 K. Further surfactant addition progressively lowered the T_B to 85 and to 60 K for samples prepared from emulsions containing 2 and 4 wt% of surfactant. The displacement of the NP_8 from the interface (Figure 4-76), where NP_8 are strongly aggregated and in contact to each other, to the inner part of the polymer, decreases the interparticle interactions and therefore reduces the temperature for the superparamagnetic transition.

Moreover, in agreement with the progressive increase in the magnetic dipolar interactions,[291] magnetization in FC tends to saturate at lower temperatures[134] as well as the maximum in the ZFC become broader and exhibits low magnetic susceptibility.[280, 313] The characteristic broadness of all curves, including that corresponding to NP$_8$, most likely imply a broad particle-size distribution of the nanoparticles.[132]

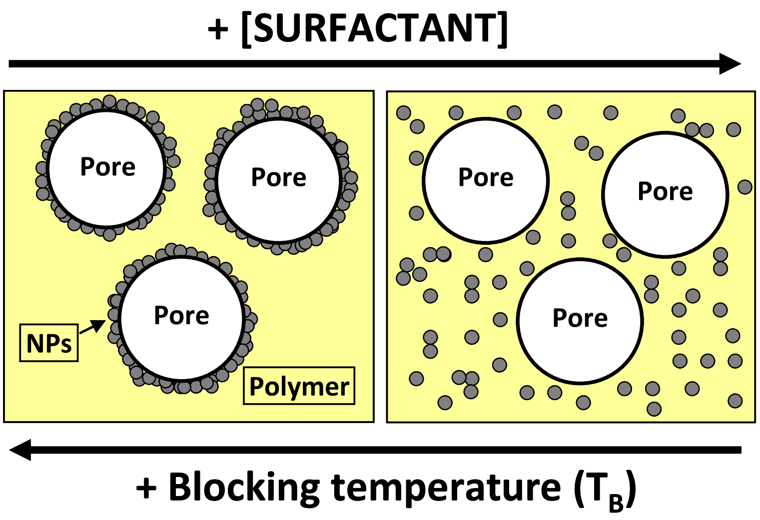

Figure 4-76. Schematic drawing that shows the spatial distribution of NP$_8$ as a function of surfactant concentration in the macroporous polymers. Dipolar interactions are more important when nanoparticles are concentrated at the oil-water interface stabilizing the original emulsions. Consequently, the blocking temperature decreases when increasing surfactant concentration.

Apart from the effect of nanoparticle distribution as a function of surfactant concentration, the influence of NP$_8$ concentration on the T_B, in macroporous polymers made from Pickering HIPEs, was evaluated. The ZFC and FC curves for materials containing 1.5 and 5 wt% (same samples that in Figure 4-74) are compared in Figure 4-77.

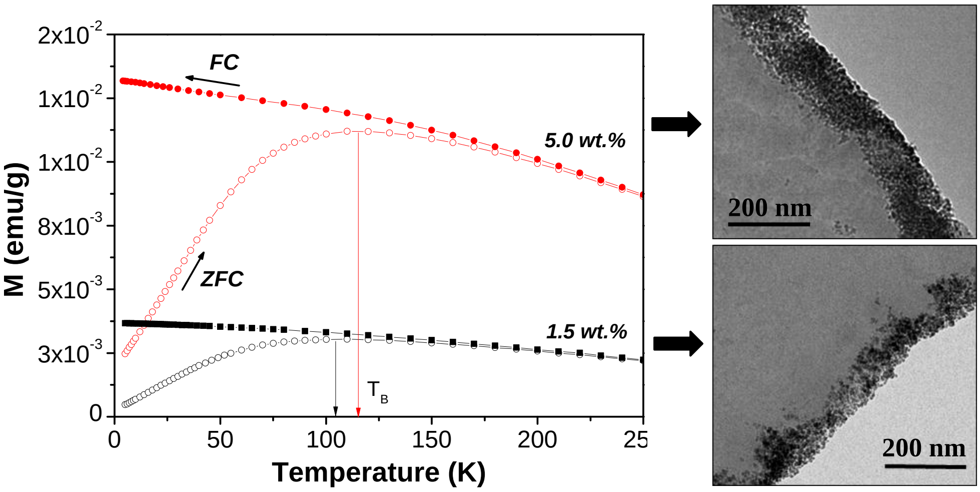

Figure 4-77. Magnetization versus temperature plots of macroporous polymers prepared from HIPEs stabilized with 1.5 and 5wt% NP$_8$. Zero field-cooling (open symbols) and field-cooling (solid symbols) measurements were carried out at H = 50 Oe. Lines are only visual guides. The pictures are TEM representative images showing the nanoparticle spatial distribution at the polymer-air interface.

For both samples, nanoparticles were located in layers at the surface of the pores, the only difference being the thickness of that layers. The results suggest that more interactions are induced by increasing NP_8 concentration. Magnetization clearly increased in the case of the polyHIPE with higher nanoparticle concentration. Moreover, the T_B slightly increased from 105 to 115 K.

The results are in agreement with well-known theory. As mentioned before, it has been described that nanoparticle interactions (dipole-dipole and exchange interactions) modify the anisotropy energy barrier (E_A), influencing the magnetic behaviour of systems consisting of small nanoparticles.[138, 139] Specifically, the contribution of the exchange interactions in the oleic acid surface-modified nanoparticles can be neglected and primary interactions are considered from dipole-dipole coupling.[138] In most cases, the blocking temperature (T_B) decreases with weaker interparticle interactions.[133, 134] This normally occurs by increasing the particle-particle distance either by dilution in liquid mediums[314] or in solid matrices.[280] For a particle of uniaxial anisotropy, the T_B is directly related to the energy barrier ($E_A = K_a V_p$) through the equation already described in the Introduction (section 1.2.2.4):[315]

$$T_B = \frac{K_a V_p}{k_B \ln\left(\frac{\tau_M}{\tau_o}\right)} \qquad \text{4-6}$$

where K_a is the uniaxial magnetic anisotropy density, V_p is the particle volume, k_B is the Boltzmann constant, τ_M is the characteristically experimental measured time, and τ_o is a time constant characteristic of each material. For τ_M =100 s, which is the typical measuring time when using a SQUID device, $\ln(\tau_M / \tau_o)$ is 25. Therefore the thermal energy required to overcome E_A, that separates the blocked from the superparamagnetic state, will be lower if this anisotropy energy is reduced, by reducing the extent of particle aggregation.

4.4.4 Macroporous Polymers Prepared from Pickering HIPEs Stabilized with Magnetic Nanoparticles and Subsequent Addition of Surfactant

In the previous section, the preparation of polymeric macroporous nanocomposites, by using HIPEs stabilized with mixtures of Fe_3O_4 nanoparticles and surfactant, has been described. Such materials exhibited superparamagnetic behaviour and were permeable to nitrogen gas. However, the small pore throats (0.7 to 5 μm) connecting pores reduced gas permeability. As mentioned at the beginning of section 4.4, an alternative approach for the synthesis of highly permeable macroporous polymers was reported recently by Ikem et al.[185] Such method consisted in the addition of a nonionic surfactant (Hypermer 2296) to already-made Pickering emulsions, stabilized with oleic acid surface-modified silica nanoparticles. Even though the materials were successfully obtained using this route, the interactions between both emulsifiers were not studied. The same approach was adopted here, based on mixtures of superparamagnetic nanoparticles (NP_8) and the same surfactant (Hypermer 2296), and a systematic work was carried out, in order to understand the phenomena related to gas permeability.

Emulsions were synthesized using 1.5 wt% of NP_8 as emulsifier, and containing internal phase volume fractions in the range of 75-85 %. Immediately after formation, 1 or 3 wt% Hypermer 2296 (with respect to the monomer phase) was added to the already-made Pickering HIPEs, under gently stirring for a short period of time (10 seconds). Subsequently, polymerization of the external phase of the HIPEs was carried out.

Both the composition of the initial HIPEs and the main physical properties measured for the macroporous polymers are summarized in Table 4-13.

Table 4-13. Composition of HIPEs and physical properties of the resultant macroporous polymers after the polymerization of the continuous phase of the HIPEs. Nanoparticle (NP_8) concentration with respect to the monomer phase was kept constant at 1.5 wt%. In sample 5, surfactant and NP_8 were mixed before emulsification, as described in a previous section (4.4.2). ϕ indicates internal phase volume of the emulsions and σ indicates crush strength.

Sample	ϕ (vol%)	Hypermer 2296 (wt/wt%)	Porosity (%)	σ (MPa)	Permeability (Da)
1	75	1	79.2 ± 0.6	5.1 ± 0.9	0.67 ± 0.03
2	80	1	82.5 ± 0.3	3.3 ± 0.3	1.81 ± 0.14
3	85	1	87.2 ± 0.3	2.1 ± 0.0	2.40 ± 0.32
4	80	0	83.7 ± 2.5	1.2 ± 0.6	0
5	80	1	84.5 ± 2.1	2.4 ± 0.7	0

First, the macroporous structure of macroporous polymers obtained from HIPEs having 80 vol% internal phase, primarily stabilized with 1.5 wt% NP_8 and with subsequent addition of 1 or 3 wt% surfactant, was examined by SEM (Figure 4-78). For comparison, a SEM picture of a macroporous polymer prepared from a Pickering HIPE stabilized solely with 1.5 wt% NP_8, in absence of surfactant, was also included (Figure 4-78(a), sample 4 in Table 4-13). Such sample exhibits the typical closed-cell structure due to the extremely stable films formed by several layers of NP_8. Hence, the sample was completely impermeable to nitrogen gas. Moreover, it showed a bimodal pore size distribution, resulting from the limited coalescence process described in section 4.3.2.

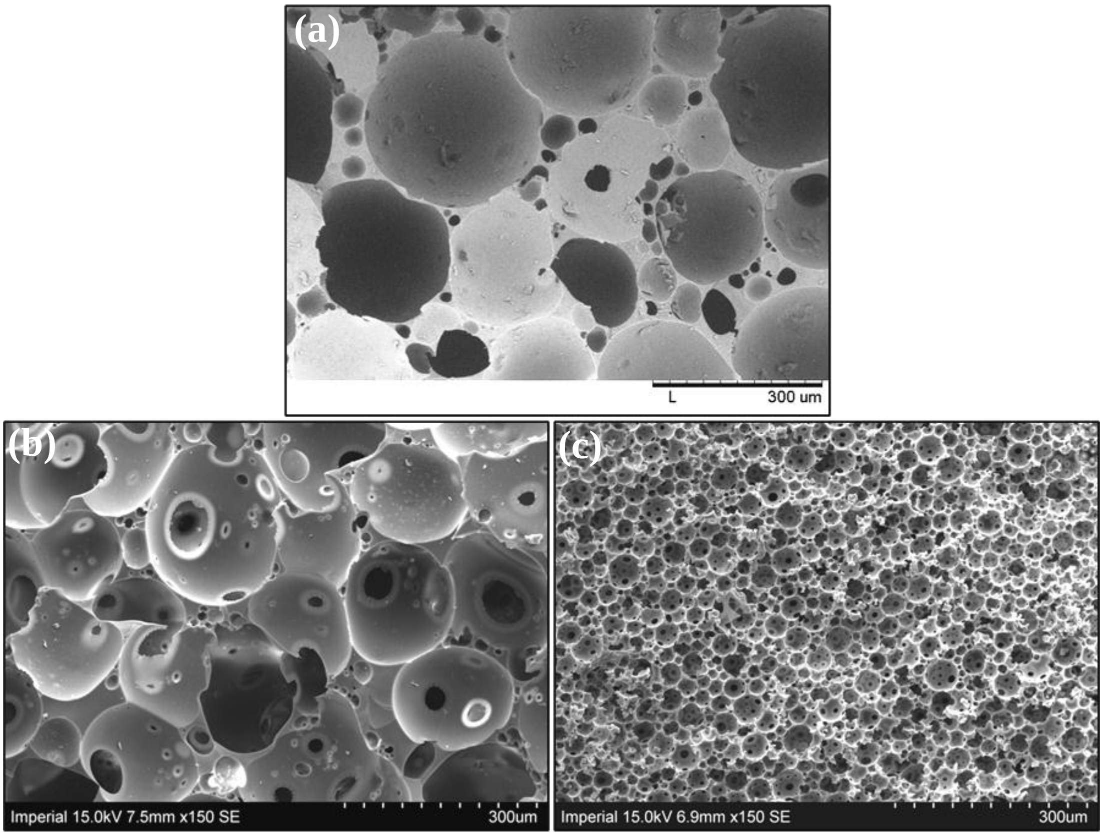

Figure 4-78. SEM images of macroporous polymers synthesized from HIPEs, primarily stabilized with 1.5 wt% NP_8 and having 80 % of internal phase volume fraction: (a) Pickering HIPE, without surfactant; 1 wt% (b) or 3 wt% (c) surfactant added after emulsification to already-made Pickering emulsions.

In fairly agreement with Ikem et al.,[185] quite large pore throats (up to 50 μm) appeared in the wall regions connecting neighbour large pores in the samples with 1 wt% surfactant added (Figure 4-78(b)). By comparing Figure 4-78(a) and Figure 4-78(b) it can be seen that despite the presence of pore throats, the pore size distribution did not change substantially upon surfactant addition. This is represented in Figure 4-79, in which the pore size distributions of samples with the same composition, i.e. NP_8 concentration (1.5 wt%) and internal phase volume fraction (75 %), but one containing surfactant added at the end of the process, are compared. From this figure it becomes evident that the addition of 1 wt% of Hypermer 2296 just led to a rather small reduction of the size of the large pore population in combination with a major percentage of the small pore size population centered at about 10 μm.

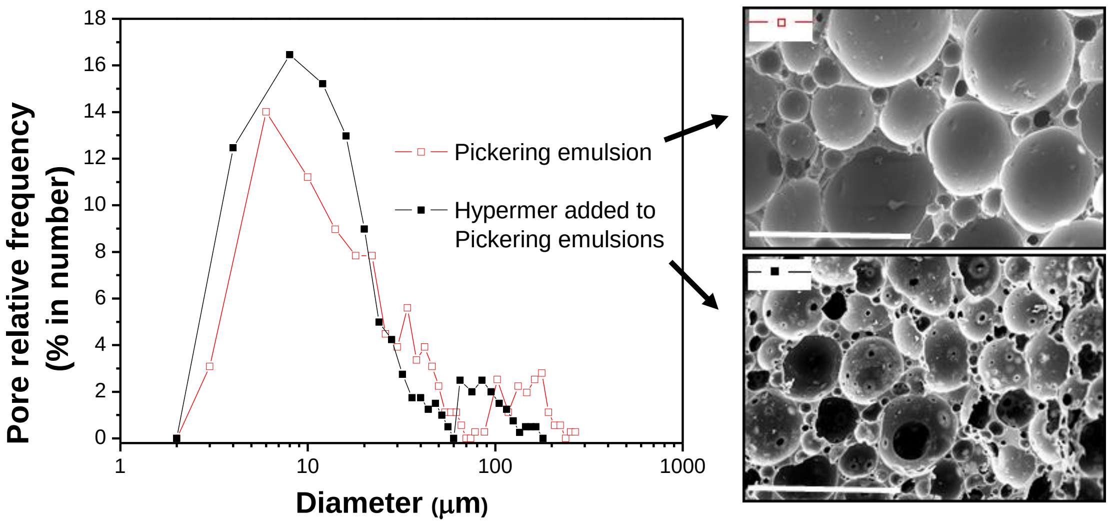

Figure 4-79. Pore size distributions and corresponding SEM images for macroporous polymers prepared from Pickering HIPEs, which contained the same internal phase volume fractions (75 %) and NP_8 concentration (1.5 wt%), with the only difference that in one of the emulsions, 1 wt% of nonionic surfactant Hypermer 2296 was added at the end of the process, just before polymerization took place. Scale bars in the SEM images indicate 300 μm.

The possible explanation for the appearance of pore throats lies on the effect of surfactant addition. On one hand, the fact that pore size is not being drastically reduced as one would expect if surfactant migrates to the O/W interface, suggests that Hypermer 2296 preferentially adsorbs onto NP_8 surfaces, rather than at the O/W interface. However, we should take into consideration that the short stirring time as well as the low surfactant concentration employed do not contribute to droplet size reduction. This hypothesis was tested by increasing the amount of Hypermer 2296 added to the precursor emulsion from 1 to 3 wt%. The corresponding SEM image is shown in Figure 4-78(c). As clearly seen, the droplet size decreased significantly and the porous structure was rather similar to that exhibited by samples with mixtures of NP_8 and high surfactant concentrations (> 2 wt%), in which both emulsifiers were mixed together before emulsification (Figure 4-69(b-c)). Therefore, the use of this method allows obtaining materials with pore sizes similar to those obtained by using Pickering HIPEs as templates, but with open porosity. One important point is that the required surfactant concentration is rather low.

To better elucidate the effect of surfactant addition on the spatial distribution of NP_8 in the polymeric walls of the macroporous polymers, thin sections of the polyHIPE, made from a HIPE primarily stabilized with 1.5 wt% NP_8 and subsequent addition of 1 wt% surfactant (Figure 4-78(b)) were examined by TEM. Representative images are depicted in Figure 4-80.

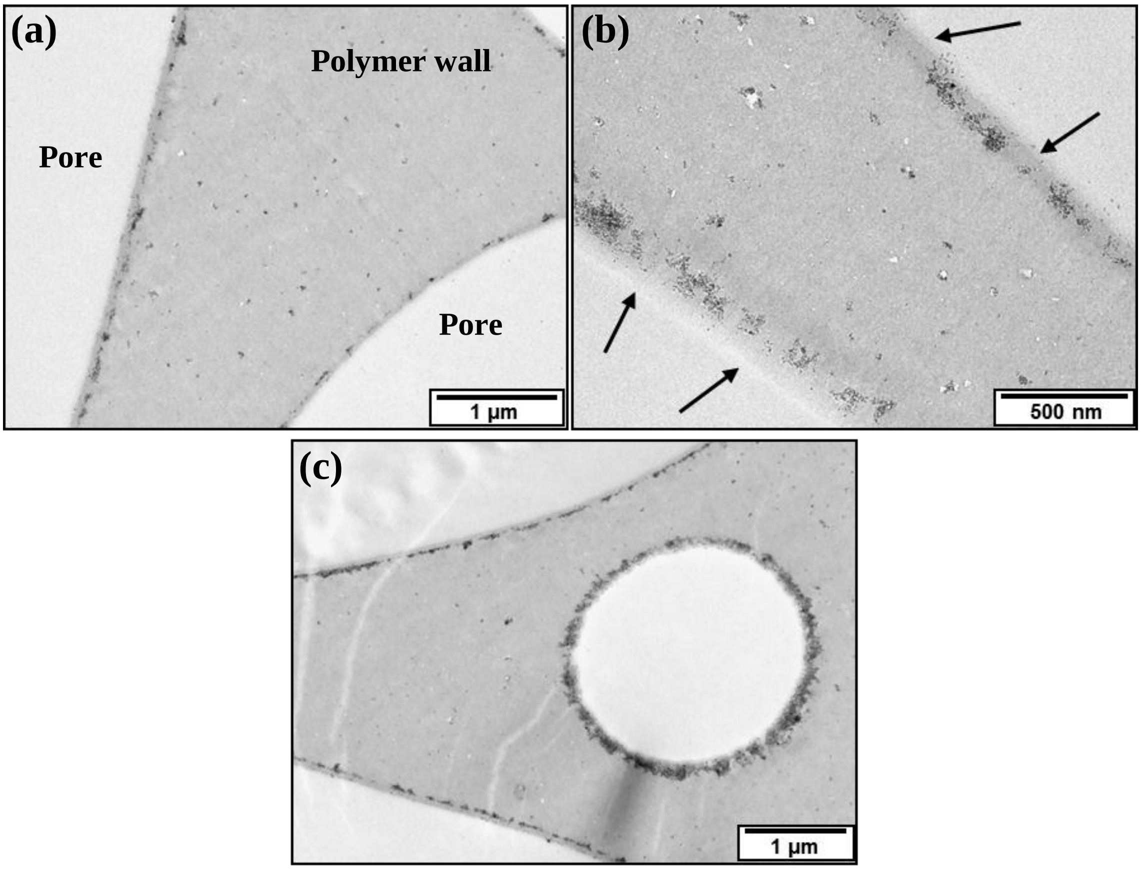

Figure 4-80. Representative TEM images of ultramicrotome slides (around 60 nm thick), in which the distribution of the nanoparticles (NP_8) within a macroporous polymer is shown. The sample (sample 2, see also Figure 4-78(b)) was obtained from a HIPE stabilized with 1.5 wt% NP_8 having an 80 % internal phase volume and subsequent addition of 1 wt% of Hypermer 2296. Arrows indicate a non-homogeneous distribution of nanoparticles at the polymer-aire interface.

The pictures reveal a NP_8 spatial distribution with an intermediate behaviour, between that found for macroporous polymers made from Pickering emulsions (Figure 4-47 in page 154) and that for materials synthesized from HIPEs with surfactant and particles mixed before emulsification (Figure 4-67, page 186). Interestingly, the nanoparticle coverage at the polymer-air interface of the larger pores was not homogeneous, so that regions covered with several layers of aggregated NP_8 coexisted with small regions completely free of NP_8 (see black arrows in Figure 4-80(b)). Based on such findings, it may be assumed that part of NP_8 have been presumably pulled out from the interface to the inner polymer phase due to surfactant adsorption onto their surfaces. Meanwhile, enough NP_8 remained at the interface to stabilize the initial HIPEs. Possibly, surfactant is also present (NP_8 free-areas), since both surfactant adsorption onto NP_8 and surfactant adsorption at the interface can occur simultaneously. Nevertheless, one can find examples in the literature of Pickering emulsions stabilized with very low nanoparticle droplet coverage, i.e. less than 10 % of the surface.[58, 316] In the hypothetic case of surfactant at the interface, the gentle agitation after Hypermer 2966 addition may have hindered the reduction of the emulsion droplet size. Another important point that should be stressed is consistent with that observed in Figure 4-67 (e), the surface area of some smaller pores (few µm in size, see Figure 4-80(c)) was densely covered by NP_8.

As stated earlier regarding pore connectivity, it is known that films between adjacent emulsion droplets should be thin to obtain permeable polymers.[166] Besides from the already mentioned volume contraction of monomer to polymer on polymerization, other reasons for the formation of pore throats have been proposed. These include mechanical action during the drying step. On some occasions this is induced by the creation of weak points in the polymer walls, as surfactant is pushed to the interface due to the progressive reduction of its solubility in the oil phase as polymerization is taking place.[190] Pore throats in the pore walls of the same sample shown in Figure 4-78(b) and Figure 4-80 (with 1 wt% surfactant added) can be observed in Figure 4-81. The bigger pore throats correspond to the contact points of neighbouring droplets, where the thickness of the polymer film is expected to be minimum. The particle-free areas at the surface of the pores (Figure 4-80(b)) may facilitate film breakage since these contact points become thinner. Connections between large pores are the responsible for the remarkable high permeabilities measured for the macroporous polymers made from HIPEs in which the surfactant was added to already-made Pickering emulsions (samples 1-3, Table 4-13). However, there were few connections between small pores, due to the high NP_8 surface coverage.

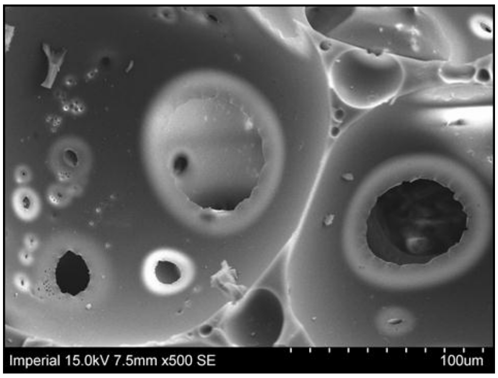

Figure 4-81. SEM image of a macroporous polymer synthesized from a HIPE primarily stabilized with 1.5 wt% NP_8 and subsequent addition of 1 wt% Hypermer 2296. Big pore throats correspond to contact points of neighbouring droplets in the precursor emulsion. It is to be noted that small pores remain, however, rather closed.

Permeability (Da) and crush strength, as a function of internal phase volume fraction for macroporous polymers prepared from Pickering HIPEs stabilized with 1.5 wt% NP_8, and subsequent addition of 1 wt% surfactant, are represented in Figure 4-82. As expected, the higher the internal phase volume fraction (i.e. porosity) led to the highest permeability (2.40 Da, Table 4-13), and inversely, the lowest crush strength value (2.1 MPa). It should be noted that the polyHIPE with 80 vol% internal phase in the initial emulsion reached a permeability of 1.81 Da, which is almost twice than the maximum permeability achieved (0.90 Da, Table 4-12) for the macroporous polymers described in the previous section, which were made from HIPEs stabilized with mixtures of surfactant and nanoparticles mixed before emulsification. The high permeability can be certainly attributed to the large pore throats present in the macroporous polymers (Figure 4-78(b)). Therefore, the results corroborate that the method that consist in the addition of the surfactant to already-made Pickering emulsions, enhances importantly the pore connectivity.

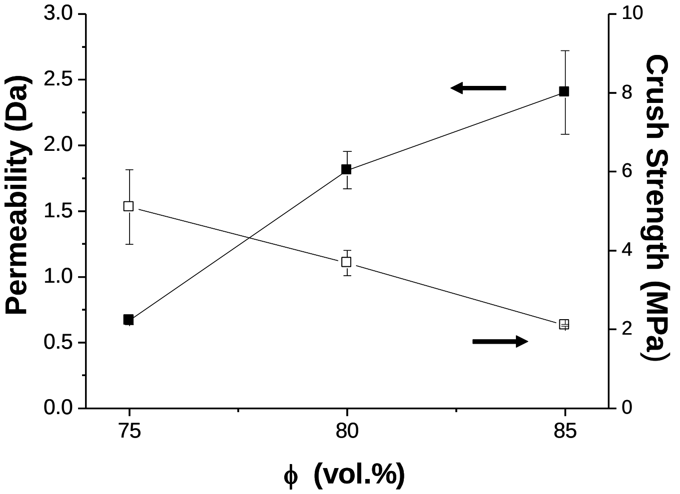

Figure 4-82. Permeability and Crush Strength for polyHIPEs, prepared from HIPEs containing different internal phase volume fractions. The emulsions were stabilized with 1.5 wt% NP_8, and subsequently, 1 wt% Hypermer 2296 was added to the already-made Pickering emulsions. Error bars indicate the standard deviation.

The key problem was to understand the influence of the order of addition in which both nanoparticles and surfactant are incorporated. To conclude, the two distinct methodologies can be summarized as follows:

Both nanoparticles (NP_8) and surfactant mixed in the continuous phase of the emulsions, before emulsification

Based on systematic interfacial tension measurements (Figure 4-55), emulsion stability tests (Figure 4-59) and TEM observations (Figure 4-66 and Figure 4-67) carried out before, it was demonstrated that NP_8 were progressively displaced from the interface upon surfactant addition. As a consequence, three different results were obtained: first, closed-cell macroporous polymers with large pore sizes were prepared at low surfactant concentration. Second, a region where emulsion phase separation occurred, and consequently materials could not be obtained. Finally, macroporous polymers with rather small sizes and low permeabilities were obtained, at higher surfactant concentrations.

Transition from particle-stabilized emulsions to surfactant-estabilized emulsions led to a drastic reduction of the emulsions drop size, wich explains the low permeability values of the resultant materials. It must be stressed, that even though most of the NP_8 were well dispersed within the polymer walls of the macroporous materials, some NP_8 remained at the interface, even for high surfactant concentrations (i.e. 4 wt%, Figure 4-67).

Surfactant added after emulsification to an already-made Pickering HIPE

In this approach, the starting point is a Pickering HIPE, stabilized solely with nanoparticles in absence of surfactant, which possesses characteristic large drop sizes. The addition of small concentrations of surfactant (1 wt%) directly to already-prepared Pickering emulsions, leads to partial displacement of nanoparticles from the interface (Figure 4-80), with only minor changes in drop size distribution of emulsions (Figure 4-79). Despite that not all nanoparticles have been removed from the interface, some areas without nanoparticles allows the formation of pore throats between large macroporous during polymerization. Therefore, this results in macroporous materials with higher permeabities (Figure 4-82).

5 CONCLUSIONS

The main conclusions and major achievements of this work are summarized as follows:

1. Preparation, characterization and functionalization of iron oxide nanoparticles

- Two different types of superparamagnetic nanoparticles have been obtained following co-precipitation methods described in the literature: NP_3 and NP_8, where 3 and 8 denote the average size of the nanoparticles. Such nanoparticles, and NP_{32} (purchased), were successfully surface-modified with oleic acid. Distinct degrees of surface adsorption (oleic acid molecules / nm^2 of nanoparticle) could be attained: 5.9, 2.5 and 2.1 for NP_3, NP_8 and NP_{32}, respectively. NP_3 and NP_8 were easily dispersed in organic solvents such as decane or toluene, whereas NP_{32} showed rather poor stability.

2. Preparation, characterization and functionalization of titanium dioxide nanoparticles

- Anatase TiO_2 nanoparticles were successfully synthesized by means of a simple and effective mechanochemical method. The reaction between the titanium precursor $TiOSO_4$ and NaOH was almost completely ended after five minutes of ball milling.

- In the absence of calcination, poorly crystalline nanoparticles were obtained. The nanoparticles were strongly agglomerated, forming flocs of 50-500 nm in size. The anatase crystalline size increased from 6 to 20 nm upon increasing the calcination temperature from 400 to 700 ºC. Consequently, the specific surface area, S_{BET}, was greatly reduced from 170 to 35 m^2/g.

- Nanoparticles calcined at 600 ºC showed the best efficiency in the photocatalytic test with a reaction constant of 0.0244 min^{-1}. The most important factor affecting the photocatalytic efficiency of anatase nanoparticles was its degree of crystallinity.

- TiO_2 nanoparticles were also functionalized with oleic acid, conferring hydrophobicity to their surfaces. Oleic acid content could by adjusted by applying washing cycles.

3. Incorporation of iron oxide nanoparticles (NP_3 and NP_8) in poly(styrene-divinylbenzene) non-porous based materials

- NP_3 and NP_8 were effectively incorporated (up to concentrations of 49 and 25 wt%, respectively) in polystyrene crosslinked with divinylbenzene (ST-DVB) nonporous materials, via free-radical polymerization. This was attributed to the effective hydrophobization of the nanoparticles surface with oleic acid, which prevented an excess of particle aggregation and the consequent phase separation upon polymerization.

- Poly(ST-DVB) magnetic microparticles were also synthesized by polymerization of an O/W diluted emulsion, which contained NP_3 in the dispersed phase. From the TEM images it was inferred that NP_3 might be contributing to stabilize the initial emulsion.

4. Incorporation of iron oxide nanoparticles (NP_3 and NP_8) in poly(styrene-divinylbenzene) porous based materials, using highly concentrated emulsions (HIPEs) as templates, prepared by the phase inversion temperature (PIT) method

Selection of the surfactant system by HLB temperature (PIT) determinations in water / ethoxylated nonionic surfactants / oil systems

- The initial PIT (61ºC) of the water / 70% $C_{13\text{-}15}(EO)_5$ – 30% $C_{13\text{-}15}(EO)_6$ / tetradecane system decreased upon increasing the monomer (ST-DVB) concentration in the oil phase, which can be explained by the relative hidrophilicity of these monomers. Calculated and experimental PIT were in good agreement up to 30 wt% of monomer in the continuous phase of emulsions, which were stabilized with 4 wt% surfactant and had water-oil volume ratios of 80:20. However, above 40 wt% of monomer in the continuous phase, a marked hysteresis was observed between the heating and the cooling cycles, which was ascribed to the different mechanisms involved in the emulsion transitions on heating and cooling. Coalescence induces inversion from highly concentrated W/O to diluted O/W. However, the inversion from diluted O/W to highly concentrated W/O emulsions is not favoured.

- Phase inversion without hysteresis was observed when a more hydrophobic surfactant was added to the surfactant system ($C_{13\text{-}15}(EO)_4$), and thus favouring the formation of W/O HIPEs. Inversion occurred for monomer concentrations up to 60 wt% in the range of temperatures studied. The droplet sizes of the W/O HIPEs obtained, were remarkably small (1-5 µm). This can be explained by the low interfacial tension values attained at the phase inversion temperature.

Preparation and characterization of the macroporous polymers nanocomposites with incorporated hydrophobic nanoparticles

- These W/O HIPEs were used as templates to obtain macroporous polymers. Such materials had large pore volumes (ca. 20.5 cm^3/g) and low foam densities (ca. 0.05 g/cm^3).

- Addition of either NP_3 or NP_8 into the continuous phase of the HIPEs did not cause any modification on the PIT of the system. It was inferred that nanoparticles did not migrate to the water-oil interface, thus not affecting the ability of the nonionic ethoxylated surfactant to stabilize the emulsions. After polymerization, it was found that both NP_3 and NP_8 were forming clusters in the polymer walls, but the dispersion was much more homogeneous in the case of the smaller NP_3.

- Both the magnetization saturation (M_s) and the blocking temperature (T_B) of the polymeric nanocomposites, determined by magnetometry, were lower than those measured for the as-synthesized superparamagnetic nanoparticles. The reduction in M_s was probably due to surface oxidation effects, while the T_B reduction is explained by the weaker interparticle interactions of the nanoparticles embedded in the polymer. The T_B for non-porous nanocomposites was lower than for macroporous nanocomposites. This was associated to particle aggregation produced during the emulsification process to obtain the macroporous materials.

5. Macroporous polymers nanocomposites obtained in highly concentrated emulsions stabilize with nanoparticles, in absence of surfactant

Highly concentrated Pickering emulsions stabilized with Fe_3O_4 nanoparticles

- W/O Pickering highly concentrated emulsions (Pickering HIPEs) were successfully stabilized using oleic acid surface-modified Fe_3O_4 nanoparticles. The emulsions remained stable over long periods of time. Emulsion formation was achieved because of the partial hydrophobic surface of nanoparticles.

- The adsorption of partially hydrophobic nanoparticles to the water emulsion droplets, thus preventing drop-drop coalescence by steric repulsion, is most likely the mechanism of emulsion stabilization. Tensiometry measurements strongly confirmed that the emulsification using NP_8 was not favoured by reduction of the interfacial tension.

- High internal phase volume fractions (up to 92.5 vol%) were incorporated to the W/O HIPEs when using low concentrations of aggregated NP_{32} (3 wt% in the external phase). Slightly lower values were attained when using NP_8. It was hypothesized that a higher content of oleic acid, covering the NP_8 surfaces, might reduce the particle adsorption on the interface, limiting their ability as emulsifiers.

Characterization of the polymeric macroporous nanocomposites containing Fe_3O_4 nanoparticles

- The resulting polystyrene-based macroporous polymers had a close-cell structure, which is a consequence of the dense film layer formed by nanoparticles at the interface. Therefore, these materials were not permeable to gases despite of their high porosity values (from 77 to 95%). Two well-defined pore populations were clearly observed: one of several microns and the other ranging from 100 to 700 μm. The larger pore size population increased upon increasing the internal phase volume, but decreased with increasing NP concentration. This pore size distribution was a replica of that observed in the emulsions.

- It has been demonstrated that NP_{32} were exclusively located at the polymer-air interface of the obtained materials, forming thick nanoparticle aggregates. On the other hand, a large fraction of NP_8 nanoparticles was effectively and homogeneously dispersed in the bulk polymer, regardless of nanoparticle concentration. This fact was attributed to the greater affinity of NP_8 for the oil phase of the emulsions, due to the presence of the oleic acid capping (12.4 wt%) onto their surfaces.

- Mechanical strength and Young's modulus of the macroporous polymers decreased with increasing the internal phase volume fractions in the initial emulsions, but increased with NP concentration. The mechanical performance of the materials containing NP_8 improved remarkably with respect to those containing NP_{32}. Such improvement possibly comes from the presence of well-dispersed NP_8 inside the polymer walls, acting as a reinforcement.

Polymeric macroporous nanocomposites containing TiO_2 nanoparticles

- The same approach was followed to synthesize macroporous polymers with photocatalytic activity, by incorporating anatase TiO_2 nanoparticles. Formation of highly concentrated Pickering emulsions was severely limited because of the strong nanoparticle aggregation. However, materials with anatase nanoparticles at the surface of the pores were obtained. Consequently, the materials retained part of the photocatalytic capacity of the nanoparticles.

6. Polymeric macroporous nanocomposites obtained in highly concentrated emulsions stabilized with mixtures of iron oxide nanoparticles and nonionic surfactant

Formation of highly concentrated Pickering emulsions

- Three different regions were observed when surfactant (Hypermer 2296) concentration is progressively increased, at fixed nanoparticle concentration (1.5 wt%):

    I. Low surfactant concentration: the surfactant preferentially adsorbed onto nanoparticles surface, thus rendering the surface more hydrophobic. Therefore, surfactant addition leads to particle desorption from the interface, and consequently W/O Pickering emulsions become less stable than in complete absence of surfactant.

II. Intermediate surfactant concentration: emulsions are unstable and phase separation occurs at around 0.1 wt% surfactant in the continuous phase. At this point, nanoparticles have been almost completely pulled out from the interface. Further increase of surfactant concentration leads to a gradual reduction of the interfacial tension values, as surfactant starts adsorbing to the oil-water interface.

III. High surfactant concentration: at surfactant concentrations of about 1 wt% in the continuous phase, W/O conventional highly concentrated emulsions (stabilized with surfactant) are obtained. This greatly decreases the droplet size down to values in the range of 1-30 μm. Therefore, an initial particle-stabilized emulsion “transforms” to a surfactant-stabilized one.

Characterization of the materials

- It has been confirmed by TEM observations that at low surfactant concentrations, both NP_8 and NP_{32}, are progressively pulled out from the interface, as a result of surfactant adsorption onto the nanoparticles surface. At higher surfactant concentrations, two completely different behaviours were observed: first, NP_{32} were totally removed from the interface, and aggregates of several microns in size, were found within the polymer walls. By contrast, displacement of NP_8 was gradual, and even at the highest surfactant concentration examined (4 wt%), some NP_8 remained at the pore surface, especially on the smaller pores of the materials. Moreover, the NP_8 aggregation was substantially lower than for NP_{32}. This was attributed to the larger surface area of NP_8 nanoparticles, in comparison to NP_{32}.

- Pore throats (0.7-5 μm) were created in the macroporous polymers prepared from surfactant-stabilized emulsions. Moreover, both the pore size and pore polydispersity were reduced. The crush strength of the materials improved substantially due to reduction of pore sizes. Interestingly, the crush strength was 20% higher in the materials containing 1.5 wt% of NP_8 than without, confirming the reinforcement effect of the nanoparticles in the polymer. However, the small size of the pore throats limited the permeability of the material to gases (maximum value achieved of 0.9 Da).

- The magnetization saturation of the macroporous polymers was directly proportional to the content of magnetic material (NP_3 or NP_8) inside the polymer, indicating the absence of any polymer matrix effect. The ability to tailor the location of the superparamagnetic NP_8 within the polymer, by an appropriate control of the NP_8-nonionic surfactant

Hypermer 2296 ratio, allowed modulating the blocking temperature of the nanoparticles. Blocking temperature was lowered from 130 to 60 K due to lower contribution of particle-particle interactions, by displacement of aggregated NP_8 from the interface, to the bulk polymer.

Polymeric macroporous nanocomposites prepared from highly concentrated emulsions stabilized with Fe_3O_4 nanoparticles and subsequent addition of nonionic surfactant

- Macroporous polymers with high crush strength values (2-5 MPa) and much higher permeabilities (0.5-2.5 Da) were obtained, by adding 1 wt% of the nonionic Hypermer 2296 surfactant, to a pre-made Pickering W/O HIPE.. A thinning of the film in the areas of nearest contact between droplets in the emulsions was caused by partial displacement of the NP_8. As a consequence, pore throats appeared between neighbouring pores. Interestingly, the droplet size in the emulsions was not substantially reduced, possibly due to the short duration of gentle agitation upon surfactant addition.

6 SUGGESTIONS FOR FUTURE WORK

In this thesis, highly concentrated emulsions stabilized by different methods, have been used for the preparation of macroporous polymer nanocomposites, with incorporated inorganic oxide nanoparticles. Special emphasis has been given to the role of nanoparticles and to the interactions between nanoparticles and surfactants, and their implications on emulsion stabilization. However, some interesting aspects have not been covered in the present work. The following aspects are recommendations for future research:

- Study of the possible technological applications of the materials, investigating the use of superparamagnetic macroporous polymers in water decontamination treatments (e.g. arsenic removal) and self-heating processes.

- A more quantitative study of the wettability of the nanoparticles by means of three-phase contact angle measurements. This could give information about the different hydrophobicity of nanoparticles with different degree of functionalization.

- Extending the work to other surfactants, to evaluate the influence of the HLB number on the surfactant adsorption on nanoparticle surfaces, and consequently on emulsion stability.

- Investigation of the rheological properties of emulsions containing different kinds of inorganic oxide nanoparticles, located either in the interfacial region or in the continuous phase of the emulsions. The influence of particle-clustering could be also assessed.

- Investigation of the preparation of macroporous polymer nanocomposites with nanoparticles incorporated in the polymer walls, but synthesized in single-step processes during emulsification and/or polymerization.

- Investigation of tailored pore morphologies in magnetic macroporous foams induced by magnetic fields.

- Extending the work to other biocompatible macroporous materials, such as polylactic or gelatine-based materials.

7 REFERENCES

1. Sherman, P., *Emulsion Science*. Academic Press: New York, **1968**.

2. Lissant, K. J., *Emulsions and Emulsion Technology*. Dekker: New York, **1974**.

3. Sjoblom, J., *Emulsions and Emulsion Stability*. Marcel Dekker: New York, **1996**.

4. Becher, P., *Emulsions. Theory and Practice*. 3rd ed.; American Chemical Society: Washington, DC, **2001**.

5. Solans, C., Esquena, J., Azemar, N., Rodríguez, C. and H., K., Highly concentrated (gel) emulsions: formation and properties. In *Emulsions: Structure, stability and Interactions*, D. N. Petsev, Ed. Elsevier: Amsterdam, **2004**; Vol. 4, pp 511-545.

6. Lopetinsky, R. J. G., Masliyah, J. H. and Xu, Z., Solids-Stabilized Emulsions: A Review. In *Colloidal Particles at Liquid Interfaces*, B. P. Binks and T. S. Horozov, Eds. Cambride University Press: New York, **2006**; pp 186-224.

7. Myers, D., *Surfaces, Interfaces, and Colloids. Principles and Applications.* 2nd ed.; John Wiley & Sons: New York, **1999**.

8. Vílchez, S., Pérez-Carrillo, L. A., Miras, J., Solans, C. and Esquena, J. Oil-in-alcohol highly concentrated emulsions as templates for the preparation of macroporous materials, *Langmuir* **2012,** *28*, 7614-7621.

9. Lissant, K. J. The geometry of high-internal-phase-ratio emulsions, *J. Colloid Interface Sci.* **1966,** *22*, 462-468.

10. Princen, H. M. Rheology of foams and highly concentrated emulsions. I. Elastic properties and yield stress of a cylindrical model system, *J. Colloid Interface Sci.* **1983,** *91*, 160-175.

11. Matsumoto, S., Kita, Y. and Yonezawa, D. An attempt at preparing water-in-oil-in-water multiple-phase emulsions, *J. Colloid Interface Sci.* **1976,** *57*, 353-361.

12. Solans, C., Izquierdo, P., Nolla, J., Azemar, N. and Garcia-Celma, M. J. Nano-emulsions, *Curr. Opin. Colloid. Interface Sci.* **2005,** *10*, 102-110.

13. Tadros, T. F., Emulsion Science and Technology: A General Introduction. In *Emulsion Science and Technology*, T. F. Tadros, Ed. WILEY-VCH Verlag GmbH & KGaA: Weinheim, **2009**; pp 1-56.

14. Solans, C. and Solé, I. Nano-emulsions: Formation by low-energy methods, *Curr. Opin. Colloid. Interface Sci.* **2012,** *17*, 246-254.

15. Esquena, J. and Solans, C., Highly Concentrated Emulsions as Templates for Solid Foams. In *Emulsions and emulsion stability*, J. Sjoblom, Ed. Marcel Dekker: Amsterdam, **2005**.

16. Forgiarini, A., Esquena, J., González, C. and Solans, C. Formation of nano-emulsions by low-energy emulsification methods at constant temperature, *Langmuir* **2001,** *17*, 2076-2083.

17. Solè, I., Maestro, A., González, C., Solans, C. and Gutiérrez, J. M. Optimization of nano-emulsion preparation by low-energy methods in an ionic surfactant system, *Langmuir* **2006,** *22*, 8326-8332.

18. Shinoda, K. and Saito, H. The effect of temperature on the phase equilibria and the types of dispersions of the ternary system composed of water, cyclohexane, and nonionic surfactant, *J. Colloid Interface Sci.* **1968,** *26*, 70-74.

19. Machado, A. H. E., Lundberg, D., Ribeiro, A. J., Veiga, F. J., Lindman, B., Miguel, M. G. and Olsson, U. Preparation of Calcium Alginate Nanoparticles Using Water-in-Oil (W/O) Nanoemulsions, *Langmuir* **2012,** *28*, 4131-4141.

20. Orr, C., Emulsion Droplet Size Data. In *Encyclopedia of emulsion technology: basic theory*, P. Becher, Ed. Marcel Dekker, Inc: New York, **1983**; Vol. 1, pp 369-404.

21. Stokes, G. G. *Phylos Mag.* **1857,** *1*, 337.

22. Verwey, E. S. W. and Overweek, J. T. G., *Theory of the Stability of Liophobic Colloids*. Elsevier: Amsterdam, **1948**.

23. Thadros, T. F. and Vincent, B., Emulsion stability. In *Encyclopedia of emulsion technology: basic theory*, P. Becher, Ed. Marcel Dekker, Inc.: New York, **1983**; Vol. 1, pp 129-285.

24. Binks, B. P. and Lumsdon, S. O. Transitional phase inversion of solid-stabilized emulsions using particle mixtures, *Langmuir* **2000,** *16*, 3748-3756.

25. Binks, B. P. and Lumsdon, S. O. Influence of particle wettability on the type and stability of surfactant-free emulsions, *Langmuir* **2000,** *16*, 8622-8631.

26. Bouchama, F., Van Aken, G. A., Autin, A. J. E. and Koper, G. J. M. On the mechanism of catastrophic phase inversion in emulsions, *Colloids. Surface. A* **2003,** *231*, 11-17.

27. Dunstan, T. S., Fletcher, P. D. I. and Mashinchi, S. High internal phase emulsions: Catastrophic phase inversion, stability, and triggered destabilization, *Langmuir* **2012,** *28*, 339-349.

28. Schönfeldt, N., *Surface Active Ethylene oxide adducts*. Pergamon Press: Oxford, **1969**.

29. Arditty, S., Whitby, C. P., Binks, B. P., Schmitt, V. and Leal-Calderon, F. Some general features of limited coalescence in solid-stabilized emulsions, *Eur. Phys. J. E* **2003,** *11*, 273-281.

30. Lifshitz, I. M. and Slyozov, V. V. The kinetics of precipitation from supersaturated solid solutions, *J. Phys. Chem. Solids* **1961,** *19*, 35-50.

31. Wagner, C. Theorie der alterung von niederschlagen durch umlosen (Ostwald-reifung), *Electrochem.* **1961,** *35*, 581-591.

32. Tadros, T., Izquierdo, P., Esquena, J. and Solans, C. Formation and stability of nano-emulsions, *Adv. Colloid Interface Sci.* **2004,** *108-109,* 303-318.

33. Jönsson, B., Lindman, B., Holmberg, K. and Kronberg, B., *Surfactants and Polymers in Aqueous Solution*. John Wiley & Sons Ltd,: Chichester, **1998**.

34. Rosen, M. J., *Surfactants and Interfacial Phenomena*. 3rd ed.; John Wiley & Sons, Inc: Hoboken, New Jersey, **2004**.

35. Miller, C. A. and Neogi, P., *Interfacial Phenomena: Equilibrium and Dynamic Effects*. Marcel Dekker, Inc: New York, **1985**; Vol. 17.

36. Bancroft, W. D. The theory of emulsification III, *J. Phys. Chem.* **1912,** *16*, 475-512.

37. Griffin, W. C. Classification of Surface-Active Agents by 'HLB, *J. Soc. Cosmet. Chem.* **1949,** *1,* 311-326.

38. Griffin, W. C. Calculation of HLB values of non-ionic surfactants, *J. Soc. Cosmet. Chem.* **1954,** *5*, 249-256.

39. Davies, J. T. A quantitative kinetic theory of emulsion type. I. Physical chemistry of the emulsifiying agent. Gas/Liquid and Liquid/Liquid Interfaces. In *Congress Surface Activity,* London, **1957**; pp 426-438.

40. Shinoda, K. and Saito, H. The Stability of O/W type emulsions as functions of temperature and the HLB of emulsifiers: The emulsification by PIT-method, *J. Colloid Interface Sci.* **1969,** *30*, 258-263.

41. Shinoda, K. and Kunieda, H., Phase Properties of Emulsions: PIT and HLB. In *Encyclopedia of emulsion technology: basic theory*, P. Becher, Ed. Marcel Dekker, Inc: New York, **1983**; Vol. 1, pp 337-367.

42. Saito, H. and Shinoda, K. The stability of W/O type emulsions as a function of temperature and of the hydrophilic chain length of the emulsifier, *J. Colloid Interface Sci.* **1970,** *32*, 647-651.

43. Shinoda, K., Hanrin, M., Kunieda, H. and Saito, H. Principles of attaining ultra-low interfacial tension: The role of hydrophile-lipophile-balance of surfactant at oil/water interface, *Colloids Surf.* **1981,** *2,* 301-314.

44. Kunieda, H. and Shinoda, K. Evaluation of the hydrophile-lipophile balance (HLB) of nonionic surfactants. I. Multisurfactant systems, *J. Colloid Interface Sci.* **1985,** *107*, 107-121.

45. Izquierdo, P., Feng, J., Esquena, J., Tadros, T. F., Dederen, J. C., Garcia, M. J., Azemar, N. and Solans, C. The influence of surfactant mixing ratio on nano-emulsion formation by the pit method, *J. Colloid Interface Sci.* **2005,** *285*, 388-394.

46. Kunieda, H. and Ishikawa, N. Evaluation of the hydrophile-lipophile balance (HLB) of nonionic surfactants. II. Commercial-surfactant systems, *J. Colloid Interface Sci.* **1985,** *107*, 122-128.

47. Ramsden, W. Separation of Solids in the Surface-Layers of Solutions and 'Suspensions' (Observations on Surface-Membranes, Bubbles, Emulsions, and Mechanical Coagulation). -- Preliminary Account, *Proc. Roy. Soc.* **1903,** *72*, 156-164.

48. Pickering, S. U. CXCVI. - Emulsions, *J. Chem. Soc.* **1907,** *91*, 2001-2021.

49. Tambe, D. E. and Sharma, M. M. The effect of colloidal particles on fluid-fluid interfacial properties and emulsion stability, *Adv. Colloid Interface Sci.* **1994,** *52*, 1-63.

50. Binks, B. P. Particles as surfactants - Similarities and differences, *Curr. Opin. Colloid. Interface Sci.* **2002,** *7*, 21-41.

51. Aveyard, R., Binks, B. P. and Clint, J. H. Emulsions stabilised solely by colloidal particles, *Adv. Colloid Interface Sci.* **2003,** *100-102*, 503-546.

52. Zeng, C., Bissig, H. and Dinsmore, A. D. Particles on droplets: From fundamental physics to novel materials, *Solid State Commun.* **2006,** *139*, 547-556.

53. Hunter, T. N., Pugh, R. J., Franks, G. V. and Jameson, G. J. The role of particles in stabilising foams and emulsions, *Adv. Colloid Interface Sci.* **2008,** *137*, 57-81.

54. Dickinson, E. Food emulsions and foams: Stabilization by particles, *Curr. Opin. Colloid. Interface Sci.* **2010,** *15*, 40-49.

55. Leal-Calderon, F. and Schmitt, V. Solid-stabilized emulsions, *Curr. Opin. Colloid. Interface Sci.* **2008,** *13*, 217-227.

56. Binks, B. P. and Horozov, T. S., *Colloidal Particles at Liquid Interfaces*. Cambride University Press: New York, **2006**.

57. Wang, W., Zhou, Z., Nandakumar, K., Xu, Z. and Masliyah, J. H. Effect of charged colloidal particles on adsorption of surfactants at oil–water interface, *J. Colloid Interface Sci.* **2004,** *274*, 625-630.

58. Vignati, E., Piazza, R. and Lockhart, T. P. Pickering Emulsions: Interfacial Tension, Colloidal Layer Morphology, and Trapped-Particle Motion, *Langmuir* **2003,** *19*, 6650-6656.

59. Pichot, R., Spyropoulos, F. and Norton, I. T. Competitive adsorption of surfactants and hydrophilic silica particles at the oil–water interface: Interfacial tension and contact angle studies, *J. Colloid Interface Sci.* **2012,** *377*, 396-405.

60. Levine, S., Bowen, B. D. and Partridge, S. J. Stabilization of emulsions by fine particles I. Partitioning of particles between continuous phase and oil/water interface, *Colloids Surf.* **1989,** *38*, 325-343.

61. Dong, L. and Johnson, D. T. The study of the surface tension of charge-stabilized colloidal dispersions, *J. Disper. Sci. Technol.* **2004,** *25*, 575-583.

62. Aveyard, R., Clint, J. H. and Horozov, T. S. Aspects of the stabilisation of emulsions by solid particles: Effects of line tension and monolayer curvature energy, *Phys. Chem. Chem. Phys.* **2003,** *5*, 2398-2409.

63. Lin, Y., Skaff, H., Emrick, T., Dinsmore, A. D. and Russell, T. P. Nanoparticle assembly and transport at liquid-liquid interfaces, *Science* **2003,** *299*, 226-229.

64. Lin, Y., Böker, A., Skaff, H., Cookson, D., Dinsmore, A. D., Emrick, T. and Russell, T. P. Nanoparticle assembly at fluid interfaces: Structure and dynamics, *Langmuir* **2005,** *21*, 191-194.

65. Finkle, P., Draper, H. D. and Hildebrand, J. H. The theory of emulsification, *J. Am. Chem. Soc.* **1923,** *45*, 2780-2788.

66. Schulman, J. H. and Leja, J. Control of Contact Angles at the Oil-Water-Solid Interfaces - Emulsions Stabilized by Solid Particles ($BaSO_4$), *J. Trans. Faraday Soc.* **1954,** *50*, 598-605.

67. Binks, B. P. and Lumsdon, S. O. Catastrophic phase inversion of water-in-oil emulsions stabilized by hydrophobie silica, *Langmuir* **2000,** *16*, 2539-2547.

68. Yan, N., Gray, M. R. and Masliyah, J. H. On water-in-oil emulsions stabilized by fine solids, *Colloids. Surface. A* **2001,** *193*, 97-107.

69. Horozov, T. S. and Binks, B. P. Particle-stabilized emulsions: A bilayer or a bridging monolayer?, *Angew. Chem. Int. Ed.* **2006,** *45*, 773-776.

70. Frelichowska, J., Bolzinger, M. A. and Chevalier, Y. Effects of solid particle content on properties of o/w Pickering emulsions, *J. Colloid Interface Sci.* **2010,** *351*, 348-356.

71. Whitby, C. P., Lotte, L. and Lang, C. Structure of concentrated oil-in-water Pickering emulsions, *Soft Matter* **2012,** *8*, 3784-3789.

72. Bachinger, A. and Kickelbick, G. Pickering emulsions stabilized by anatase nanoparticles, *Monatshefte fur Chemie* **2010,** *141*, 685-690.

73. Lan, Q., Liu, C., Yang, F., Liu, S., Xu, J. and Sun, D. Synthesis of bilayer oleic acid-coated Fe_3O_4 nanoparticles and their application in pH-responsive Pickering emulsions, *J. Colloid Interface Sci.* **2007,** *310*, 260-269.

74. Ngai, T., Behrens, S. H. and Auweter, H. Novel emulsions stabilized by pH and temperature sensitive microgels, *Chem. Commun.* **2005,** 331-333.

75. Tzoumaki, M. V., Moschakis, T., Kiosseoglou, V. and Biliaderis, C. G. Oil-in-water emulsions stabilized by chitin nanocrystal particles, *Food Hydrocolloid.* **2011,** *25*, 1521-1529.

76. Luo, Z., Murray, B. S., Ross, A. L., Povey, M. J. W., Morgan, M. R. A. and Day, A. J. Effects of pH on the ability of flavonoids to act as Pickering emulsion stabilizers, *Colloids Surf., B* **2012,** *92*, 84-90.

77. Tambe, D. E. and Sharma, M. M. Factors Controlling the Stability of Colloid-Stabilized Emulsions. I. An Experimental Investigation, *J. Colloid Interface Sci.* **1993,** *157*, 244-253.

78. Binks, B. P., Rodrigues, J. A. and Frith, W. J. Synergistic interaction in emulsions stabilized by a mixture of silica nanoparticles and cationic surfactant, *Langmuir* **2007,** *23*, 3626-3636.

79. Binks, B. P. and Rodrigues, J. A. Double Inversion of Emulsions By Using Nanoparticles and a Di-Chain Surfactant, *Angew. Chem. Int. Ed.* **2007,** *46*, 5389-5392.

80. Briggs, T. R. Emulsions with Finely Divided Solids, *J. Ind. Eng. Chem.* **1921,** *13*, 1008-1010.

81. Midmore, B. R. Preparation of a novel silica-stabilized oil/water emulsion, *Colloids. Surface. A* **1998,** *132*, 257-265.

82. Binks, B. P., Desforges, A. and Duff, D. G. Synergistic stabilization of emulsions by a mixture of surface-active nanoparticles and surfactant, *Langmuir* **2007,** *23*, 1098-1106.

83. Binks, B. P. and Kirkland, M. Interfacial structure of solid-stabilised emulsions studied by scanning electron microscopy, *Phys. Chem. Chem. Phys.* **2002,** *4*, 3727-3733.

84. Simovic, S. and Prestidge, C. A. Adsorption of Hydrophobic Silica Nanoparticles at the PDMS Droplet−Water Interface, *Langmuir* **2003,** *19*, 8364-8370.

85. Thijssen, J. H. J., Schofield, A. B. and Clegg, P. S. How do (fluorescent) surfactants affect particle-stabilized emulsions?, *Soft Matter* **2011,** *7*, 7965-7968.

86. Dinsmore, A. D., Hsu, M. F., Nikolaides, M. G., Marquez, M., Bausch, A. R. and Weitz, D. A. Colloidosomes: Selectively permeable capsules composed of colloidal particles, *Science* **2002,** *298*, 1006-1009.

87. Wang, H., Zhu, X., Tsarkova, L., Pich, A. and Möller, M. All-silica colloidosomes with a particle-bilayer shell, *ACS Nano* **2011,** *5*, 3937-3942.

88. Lee, M. N., Chan, H. K. and Mohraz, A. Characteristics of Pickering Emulsion Gels Formed by Droplet Bridging, *Langmuir* **2011,** *28*, 3085-3091.

89. Tarimala, S. and Dai, L. L. Structure of Microparticles in Solid-Stabilized Emulsions, *Langmuir* **2003,** *20*, 3492-3494.

90. Denkov, N. D., Ivanov, I. B., Kralchevsky, P. A. and Wasan, D. T. A possible mechanism of stabilization of emulsions by solid particles, *J. Colloid Interface Sci.* **1992,** *150*, 589-593.

91. Kruglyakov, P. M., Nushtayeva, A. V. and Vilkova, N. G. Experimental investigation of capillary pressure influence on breaking of emulsions stabilized by solid particles, *J. Colloid Interface Sci.* **2004,** *276*, 465-474.

92. Stancik, E. J., Kouhkan, M. and Fuller, G. G. Coalescence of Particle-Laden Fluid Interfaces, *Langmuir* **2004,** *20*, 90-94.

93. Horozov, T. S., Aveyard, R., Clint, J. H. and Neumann, B. Particle Zips: Vertical Emulsion Films with Particle Monolayers at Their Surfaces, *Langmuir* **2005,** *21,* 2330-2341.

94. Ashby, N. P., Binks, B. P. and Paunov, V. N. Bridging interaction between a water drop stabilised by solid particles and a planar oil/water interface, *Chem. Commun.* **2004,** 436-437.

95. Midmore, B. R. Synergy between silica and polyoxyethylene surfactants in the formation of O/W emulsions, *Colloids. Surface. A* **1998,** *145,* 133-143.

96. Limage, S., Schmitt, M., Vincent-Bonnieu, S., Dominici, C. and Antoni, M. Characterization of solid-stabilized water/oil emulsions by scanning electron microscopy, *Colloids. Surface. A* **2010,** *365,* 154-161.

97. Bucak, S., Destribats, M., Ravaine, S., Heroguez, V., Leal-Calderon, F. and Schmitt, V., Outstanding Stability of Poorly-protected Pickering Emulsions. In *Trends in Colloid and Interface Science* Springer: Berlin, **2010**; Vol. XXIII, pp 13-18.

98. Garcia, P. C. and Whitby, C. P. Laponite-stabilised oil-in-water emulsions: viscoelasticity and thixotropy, *Soft Matter* **2012,** *8,* 1609-1615.

99. Akartuna, I., Studart, A. R., Tervoort, E., Gonzenbach, U. T. and Gauckler, L. J. Stabilization of Oil-in-Water Emulsions by Colloidal Particles Modified with Short Amphiphiles, *Langmuir* **2008,** *24,* 7161-7168.

100. Ikem, V. O., Menner, A. and Bismarck, A. High internal phase emulsions stabilized solely by functionalized silica particles, *Angew. Chem. Int. Ed.* **2008,** *47,* 8277-8279.

101. Gelot, A., Friesen, W. and Hamza, H. A. Emulsification of oil and water in the presence of finely divided solids and surface-active agents, *Colloids Surf.* **1984,** *12,* 271-303.

102. Wang, J., Yang, F., Tan, J., Liu, G., Xu, J. and Sun, D. Pickering emulsions stabilized by a lipophilic surfactant and hydrophilic platelike particles, *Langmuir* **2010,** *26,* 5397-5404.

103. Binks, B. P. and Rodrigues, J. A. Inversion of emulsions stabilized solely by ionizable nanoparticles, *Angew. Chem. Int. Ed.* **2005,** *44,* 441-444.

104. Binks, B. P. and Lumsdon, S. O. Pickering emulsions stabilized by monodisperse latex particles: Effects of particle size, *Langmuir* **2001,** *17,* 4540-4547.

105. Binks, B. P. and Whitby, C. P. Silica Particle-Stabilized Emulsions of Silicone Oil and Water: Aspects of Emulsification, *Langmuir* **2004,** *20,* 1130-1137.

106. Thieme, J., Abend, S. and Lagaly, G. Aggregation in Pickering emulsions, *Colloid Polym. Sci.* **1999,** *277,* 257-260.

107. Yan, Y. and Masliyah, J. H. Solids-stabilized oil-in-water emulsions: Scavenging of emulsion droplets by fresh oil addition, *Colloids. Surface. A* **1993,** *75*, 123-132.

108. Binks, B. P. and Rodrigues, J. A. Enhanced stabilization of emulsions due to surfactant-induced nanoparticle flocculation, *Langmuir* **2007,** *23*, 7436-7439.

109. Whitby, C. P., Fornasiero, D. and Ralston, J. Effect of oil soluble surfactant in emulsions stabilised by clay particles, *J. Colloid Interface Sci.* **2008,** *323*, 410-419.

110. Pichot, R., Spyropoulos, F. and Norton, I. T. O/W emulsions stabilised by both low molecular weight surfactants and colloidal particles: The effect of surfactant type and concentration, *J. Colloid Interface Sci.* **2010,** *352*, 128-135.

111. Lan, Q., Yang, F., Zhang, S., Liu, S., Xu, J. and Sun, D. Synergistic effect of silica nanoparticle and cetyltrimethyl ammonium bromide on the stabilization of O/W emulsions, *Colloids. Surface. A* **2007,** *302*, 126-135.

112. Eskandar, N. G., Simovic, S. and Prestidge, C. A. Interactions of hydrophilic silica nanoparticles and classical surfactants at non-polar oil–water interface, *J. Colloid Interface Sci.* **2011,** *358*, 217-225.

113. Okubo, T. Surface Tension of Structured Colloidal Suspensions of Polystyrene and Silica Spheres at the Air-Water Interface, *J. Colloid Interface Sci.* **1995,** *171*, 55-62.

114. Santini, E., Guzman, E., Ravera, F., Ferrari, M. and Liggieri, L. Properties and structure of interfacial layers formed by hydrophilic silica dispersions and palmitic acid, *Phys. Chem. Chem. Phys.* **2012,** *14*, 607-615.

115. Ravera, F., Santini, E., Loglio, G., Ferrari, M. and Liggieri, L. Effect of Nanoparticles on the Interfacial Properties of Liquid/Liquid and Liquid/Air Surface Layers, *J. Phys. Chem. B* **2006,** *110*, 19543-19551.

116. Vashisth, C., Whitby, C. P., Fornasiero, D. and Ralston, J. Interfacial displacement of nanoparticles by surfactant molecules in emulsions, *J. Colloid Interface Sci.* **2010,** *349*, 537-543.

117. Drelich, A., Gomez, F., Clausse, D. and Pezron, I. Evolution of water-in-oil emulsions stabilized with solid particles: Influence of added emulsifier, *Colloids. Surface. A* **2010,** *365*, 171-177.

118. Laurent, S., Forge, D., Port, M., Roch, A., Robic, C., Vander Elst, L. and Muller, R. N. Magnetic Iron Oxide Nanoparticles: Synthesis, Stabilization, Vectorization, Physicochemical Characterizations, and Biological Applications, *Chem. Rev.* **2008,** *108*, 2064-2110.

119. Jolivet, J. P., Chanéac, C. and Tronc, E. Iron oxide chemistry. From molecular clusters to extended solid networks, *Chem. Commun.* **2004,** *10*, 481-487.

120. Gribanov, N. M., Bibik, E. E., Buzunov, O. V. and Naumov, V. N. Physico-chemical regularities of obtaining highly dispersed magnetite by the method of chemical condensation, *J. Magn. Magn.* **1990,** *85*, 7-10.

121. Babes, L., Denizot, B., Tanguy, G., Le Jeune, J. J. and Jallet, P. Synthesis of iron oxide nanoparticles used as MRI contrast agents: A parametric study, *J. Colloid Interface Sci.* **1999,** *212*, 474-482.

122. Mahmoudi, M., Simchi, A., Imani, M., Milani, A. S. and Stroeve, P. Optimal design and characterization of superparamagnetic iron oxide nanoparticles coated with polyvinyl alcohol for targeted delivery and imaging, *J. Phys. Chem. B* **2008,** *112*, 14470-14481.

123. Coey, J. M. D., *Magnetism and Magnetic Materials*. Cambridge University Press: Cambridge, UK, **2009**.

124. Leslie-Pelecky, D. L. and Rieke, R. D. Magnetic Properties of Nanostructured Materials, *Chem. Mater.* **1996,** *8*, 1770-1783.

125. Tartaj, P. Superparamagnetic Composites: Magnetism with No Memory, *Eur. J. Inorg. Chem.* **2009,** *2009*, 333-343.

126. Cullity, B. D., *Introduction to magnetic materials*. John Wiley & Sons: New Jersey, **2009**.

127. Weiss, P. *J. de Phys. Rad.* **1907,** *6*, 661.

128. Carter, C. B. and Norton, M. G., Using Magnetic Fields and Storing Data. In *Ceramic materials: Science and Technology,* Springer: New York, **2007**; pp 598-618.

129. Néel, L. Théorie du traînage magnétique des ferromagnétiques en grains fins avec applications aux terres cuites, *Ann. Géophys* **1949,** *5*, 99-136.

130. Bean, C. P. and Livingston, J. D. Superparamagnetism, *J. Appl. Phys.* **1959,** *30*, S120-S129.

131. Néel, L. *C. R. Acad. Sci* **1949,** *228*, 664.

132. Sohn, B. H., Cohen, R. E. and Papaefthymiou, G. C. Magnetic properties of iron oxide nanoclusters within microdomains of block copolymers, *J. Magn. Magn.* **1998,** *182*, 216-224.

133. El-Hilo, M., O'Grady, K. and Chantrell, R. W. Susceptibility phenomena in a fine particle system. I. Concentration dependence of the peak, *J. Magn. Magn.* **1992,** *114*, 295-306.

134. Tronc, E., Prené, P., Jolivet, J. P., Fiorani, D., Testa, A. M., Cherkaoui, R., Nogues, M. and Dormann, J. L. Magnetic dynamics of γ-Fe_2O_3 nanoparticles, *Nanostruct. Mater.* **1995,** *6*, 945-948.

135. Papaefthymiou, G. C. Nanoparticle magnetism, *Nano Today* **2009,** *4*, 438-447.

136. Hansen, M. F. and Mørup, S. Estimation of blocking temperatures from ZFC/FC curves, *J. Magn. Magn.* **1999,** *203*, 214-216.

137. Topkaya, R., Akman, O., Kazan, S., Aktaş, B., Durmus, Z. and Baykal, A. Surface spin disorder and spin-glass-like behaviour in manganese- substituted cobalt ferrite nanoparticles, *J. Nanopart. Res.* **2012,** *14*.

138. Held, G. A., Grinstein, G., Doyle, H., Sun, S. and Murray, C. B. Competing interactions in dispersions of superparamagnetic nanoparticles, *Phys. Rev. B* **2001,** *64*, 124081-124084.

139. Batlle, X. and Labarta, A. Finite-size effects in fine particles: Magnetic and transport properties, *J. Phys. D: Appl. Phys.* **2002,** *35*, R15-R42.

140. Jain, T. K., Morales, M. A., Sahoo, S. K., Leslie-Pelecky, D. L. and Labhasetwar, V. Iron Oxide Nanoparticles for Sustained Delivery of Anticancer Agents, *Mol. Pharm.* **2005,** *2*, 194-205.

141. Sun, S., Murray, C. B., Weller, D., Folks, L. and Moser, A. Monodisperse FePt Nanoparticles and Ferromagnetic FePt Nanocrystal Superlattices, *Science* **2000,** *287*, 1989-1992.

142. Kovačič, S., Ferk, G., Drofenik, M. and Krajnc, P. Nanocomposite polyHIPEs with magnetic nanoparticles: Preparation and heating effect, *React. Funct. Polym.* **2012,** *72*, 955-961.

143. Zhang, D. L. Processing of advanced materials using high-energy mechanical milling, *Prog. Mater. Sci.* **2004,** *49*, 537-560.

144. McCormick, P. G., Tsuzuki, T., Robinson, J. S. and Ding, J. Nanopowders synthesized by mechanochemical processing, *Adv. Mater.* **2001,** *13*, 1008-1010.

145. Tsuzuki, T. and McCormick, P. G. Mechanochemical synthesis of nanoparticles, *J. Mater. Sci.* **2004,** *39*, 5143-5146.

146. Tsuzuki, T., Pirault, E. and McCormick, P. G. Mechanochemical synthesis of gadolinium oxide nanoparticles, *Nanostruct. Mater.* **1999,** *11*, 125-131.

147. Tsuzuki, T. and McCormick, P. G. Synthesis of Ultrafine Ceria Powders by Mechanochemical Processing, *J. Am. Ceram. Soc.* **2001,** *84*, 1453-1458.

148. Billik, P. and Plesch, G. Mechanochemical synthesis of anatase and rutile nanopowders from $TiOSO_4$, *Mater. Lett.* **2007,** *61*, 1183-1186.

149. Ding, J., Miao, W. F., McCormick, P. G. and Street, R. Mechanochemical synthesis of ultrafine Fe powder, *Appl. Phys. Lett.* **1995,** *67*, 3804-3806.

150. Fujishima, A. and Honda, K. Electrochemical Photolysis of Water at a Semiconductor Electrode, *Nature* **1972,** *238*, 37-38.

151. Hernandez-Alonso, M. D., Fresno, F., Suarez, S. and Coronado, J. M. Development of alternative photocatalysts to TiO_2: Challenges and opportunities, *Energy Environ. Sci.* **2009,** *2*, 1231-1257.

152. Zhang, H. and F. Banfield, J. Thermodynamic analysis of phase stability of nanocrystalline titania, *J. Mater. Chem.* **1998,** *8*, 2073-2076.

153. Chen, X. and Mao, S. S. Titanium Dioxide Nanomaterials: Synthesis, Properties, Modifications, and Applications, *Chem. Rev.* **2007,** *107*, 2891-2959.

154. Hoffmann, M. R., Martin, S. T., Choi, W. and Bahnemann, D. W. Environmental Applications of Semiconductor Photocatalysis, *Chem. Rev.* **1995,** *95*, 69-96.

155. Herrmann, J.-M. Heterogeneous photocatalysis: fundamentals and applications to the removal of various types of aqueous pollutants, *Catal. Today* **1999,** *53*, 115-129.

156. Tanaka, K., Capule, M. F. V. and Hisanaga, T. Effect of crystallinity of TiO_2 on its photocatalytic action, *Chem. Phys. Lett.* **1991,** *187*, 73-76.

157. Fox, M. A. and Dulay, M. T. Heterogeneous photocatalysis, *Chem. Rev.* **1993,** *93*, 341-357.

158. Linsebigler, A. L., Lu, G. and Yates, J. T. Photocatalysis on TiO_2 Surfaces: Principles, Mechanisms, and Selected Results, *Chem. Rev.* **1995,** *95*, 735-758.

159. Tian, G., Fu, H., Jing, L., Xin, B. and Pan, K. Preparation and Characterization of Stable Biphase TiO_2 Photocatalyst with High Crystallinity, Large Surface Area, and Enhanced Photoactivity, *J. Phys. Chem. C* **2008,** *112*, 3083-3089.

160. Solans, C., Pons, R. and Kunieda, H., Gel emulsions - Relation between Phase Behaviour and Formation. In *Modern Aspects in Emulsion Science*, B. P. Binks, Ed. Cambridge: Royal Society of Chemistry: **1998**; pp 367-394.

161. Esquena, J., Nestor, J., Vílchez, A., Aramaki, K. and Solans, C. Preparation of mesoporous/macroporous materials in highly concentrated emulsions based on cubic phases by a single-step method, *Langmuir* **2012,** *28*, 12334-12340.

162. Princen, H. M. and Kiss, A. D. Rheology of foams and highly concentrated emulsions. III. Static shear modulus, *J. Colloid Interface Sci.* **1986,** *112,* 427-437.

163. Pons, R., Erra, P., Solans, C., Ravey, J. C. and Stébé, M. J. Viscoelastic properties of gel-emulsions: Their relationship with structure and equilibrium properties, *J. Phys. Chem.* **1993,** *97,* 12320-12324.

164. Rodríguez, C., Shigeta, K. and Kunieda, H. Cubic-phase-based concentrated emulsions, *J. Colloid Interface Sci.* **2000,** *223,* 197-204.

165. Calderó, G., Patti, A., Llinàs, M. and García-Celma, M. J. Diffusion in highly concentrated emulsions, *Curr. Opin. Colloid. Interface Sci.* **2012,** *17,* 255-260.

166. Williams, J. M. and Wrobleski, D. A. Spatial-Distribution of the Phases in Water-in-Oil Emulsions - Open and Closed Microcellular Foams from Cross-Linked Polystyrene, *Langmuir* **1988,** *4*, 656-662.

167. Ruckenstein, E. and Park, J. S. Stable Concentrated Emulsions as Precursors for Hydrophilic Hydrophobic Polymer Composites, *Polymer* **1992,** *33*, 405-417.

168. Kunieda, H., Solans, C., Shida, N. and Parra, J. L. The formation of gel-emulsions in a water/nonionic surfactant/oil system, *Colloids Surf.* **1987,** *24*, 225-237.

169. Solans, C., Pons, R., Zhu, S., Davis, H. T., Evans, D. F., Nakamura, K. and Kunieda, H. Studies on macro- and microstructures of highly concentrated water-in-oil emulsions (gel emulsions), *Langmuir* **1993,** *9*, 1479-1482.

170. Kunieda, H., Fukui, Y., Uchiyama, H. and Solans, C. Spontaneous Formation of Highly Concentrated Water-in-Oil Emulsions (Gel-Emulsions), *Langmuir* **1996,** *12*, 2136-2140.

171. Uddin, M. H., Kunieda, H. and Solans, C., Highly concentrated cubic-phase-based emulsions. In *Structure-performance relationships in surfactants*, K. Esumi and M. Ueno, Eds. Marcel Dekker: New York, **2003**; pp 599-626.

172. Pons, R., Ravey, J. C., Sauvage, S., Stébé, M. J., Erra, P. and Solans, C. Structural studies on gel emulsions, *Colloids. Surface. A* **1993,** *76*, 171-177.

173. Barbetta, A., Cameron, N. R. and Cooper, S. J. High internal phase emulsions (HIPEs) containing divinylbenzene and 4- vinylbenzyl chloride and the morphology of the resulting PolyHIPE materials, *Chem. Commun.* **2000,** 221-222.

174. Manley, S. S., Graeber, N., Grof, Z., Menner, A., Hewitt, G. F., Stepanek, F. and Bismarck, A. New insights into the relationship between internal phase level of emulsion templates and gas-liquid permeability of interconnected macroporous polymers, *Soft Matter* **2009,** *5*, 4780-4787.

175. Zhang, S. and Chen, J. Synthesis of open porous emulsion-templated monoliths using cetyltrimethylammonium bromide, *Polymer* **2007,** *48*, 3021-3025.

176. Menner, A., Ikem, V., Salgueiro, M., Shaffer, M. S. P. and Bismarck, A. High internal phase emulsion templates solely stabilised by functionalised titania nanoparticles, *Chem. Commun.* **2007,** 4274-4276.

177. Pons, R., Carrera, I., Erra, P., Kunieda, H. and Solans, C. Novel preparation methods for highly concentrated water-in-oil emulsions, *Colloids. Surface. A* **1994,** *91*, 259-266.

178. Esquena, J., Sankar, G. R. and Solans, C. Highly concentrated W/O emulsions prepared by the PIT method as templates for solid foams, *Langmuir* **2003,** *19*, 2983-2988.

179. Mitchell, D. J. and Ninham, B. W. Micelles, vesicles and microemulsions, *J. Chem. Soc., Faraday Trans. 2* **1981,** *77*, 601-629.

180. Aronson, M. P. and Petko, M. F. Highly Concentrated Water-in-Oil Emulsions: Influence of Electrolyte on Their Properties and Stability, *J. Colloid Interface Sci.* **1993,** *159*, 134-149.

181. Barby, D. and Haq, Z. European Patent. 0060138, 1982.

182. Cameron, N. R. and Sherrington, D. C. High Internal Phase Emulsions (HIPEs) - Structure, Properties and Use in Polymer Preparation, *Adv. Polym. Sci.* **1996,** *126*, 162-214.

183. Imhof, A. and Pine, D. J. Ordered macroporous materials by emulsion templating, *Nature* **1997,** *389*, 948-951.

184. Brun, N., Ungureanu, S., Deleuze, H. and Backov, R. Hybrid foams, colloids and beyond: From design to applications, *Chem. Soc. Rev.* **2011,** *40*, 771-788.

185. Ikem, V. O., Menner, A., Horozov, T. S. and Bismarck, A. Highly permeable macroporous polymers synthesized from pickering medium and high internal phase emulsion templates, *Adv. Mater.* **2010,** *22*, 3588-3592.

186. Barbetta, A., Dentini, M., Zannoni, E. M. and De Stefano, M. E. Tailoring the porosity and morphology of gelatin-methacrylate polyHIPE scaffolds for tissue engineering applications, *Langmuir* **2005,** *21*, 12333-12341.

187. Cameron, N. R. High internal phase emulsion templating as a route to well-defined porous polymers, *Polymer* **2005,** *46*, 1439-1449.

188. Williams, J. M., James Gray, A. and Wilkerson, M. H. Emulsion stability and rigid foams from styrene or divinylbenzene water-in-oil emulsions, *Langmuir* **1990,** *6*, 437-444.

189. Hainey, P., Huxham, I. M., Rowatt, B., Sherrington, D. C. and Tetley, L. Synthesis and ultrastructural studies of styrene-divinylbenzene polyhipe polymers, *Macromolecules* **1991,** *24*, 117-121.

190. Menner, A. and Bismarck, A. New evidence for the mechanism of the pore formation in polymerising high internal phase emulsions or why polyHIPEs have an interconnected pore network structure, *Macromol Symp.* **2006,** *242*, 19-24.

191. Carnachan, R. J., Bokhari, M., Przyborski, S. A. and Cameron, N. R. Tailoring the morphology of emulsion-templated porous polymers, *Soft Matter* **2006,** *2*, 608-616.

192. Menner, A., Haibach, K., Powell, R. and Bismarck, A. Tough reinforced open porous polymer foams via concentrated emulsion templating, *Polymer* **2006,** *47*, 7628-7635.

193. Cameron, N. R. and Sherrington, D. C. Preparation and glass transition temperatures of elastomeric PolyHIPE materials, *J. Mater. Chem.* **1997,** *7*, 2209-2212.

194. Kimmins, S. D. and Cameron, N. R. Functional porous polymers by emulsion templating: Recent advances, *Adv. Funct. Mater.* **2011,** *21*, 211-225.

195. Pulko, I., Kolar, M. and Krajnc, P. Atrazine removal by covalent bonding to piperazine functionalized PolyHIPEs, *Sci. Total Environ.* **2007,** *386*, 114-123.

196. Kulygin, O. and Silverstein, M. S. Porous poly(2-hydroxyethyl methacrylate) hydrogels synthesized within high internal phase emulsions, *Soft Matter* **2007,** *3*, 1525-1529.

197. Amir, N., Levina, A. and Silverstein, M. S. Nanocomposites through copolymerization of a polyhedral oligomeric silsesquioxane and methyl methacrylate, *J. Polym. Sci. Pol. Chem.* **2007,** *45*, 4264-4275.

198. Gitli, T. and Silverstein, M. S. Bicontinuous hydrogel-hydrophobic polymer systems through emulsion templated simultaneous polymerizations, *Soft Matter* **2008,** *4*, 2475-2485.

199. Feral-Martin, C., Birot, M., Deleuze, H., Desforges, A. and Backov, R. Integrative chemistry toward the first spontaneous generation of gold nanoparticles within macrocellular polyHIPE supports (Au@polyHIPE) and their application to eosin reduction, *Reactive & Functional Polymers* **2007,** *67*, 1072-1082.

200. Liu, W., He, G. and He, Z. Polystyrene/magnetite hybrid foams prepared via 60Co γ-ray radiation of high internal phase emulsions, *J. Polym. Res.* **2012,** *19*, 1-9.

201. Ghosh, G., Vílchez, A., Esquena, J., Solans, C. and Rodríguez-Abreu, C. Preparation of porous magnetic nanocomposite materials using highly concentrated emulsions as templates, *C. Prog. Colloid Polym. Sci.* **2011,** *138*, 161-164.

202. Sun, G., Li, Z. and Ngai, T. Inversion of particle-stabilized emulsions to form high-internalphase emulsions, *Angew. Chem. Int. Ed.* **2010,** *49*, 2163-2166.

203. Li, Z. and Ngai, T. Macroporous polymer from core-shell particle-stabilized pickering emulsions, *Langmuir* **2010,** *26*, 5088-5092.

204. Ikem, V. O., Menner, A. and Bismarck, A. High-porosity macroporous polymers sythesized from titania-particle- stabilized medium and high internal phase emulsions, *Langmuir* **2010,** *26*, 8836-8841.

205. Zhang, S. and Chen, J. PMMA based foams made via surfactant-free high internal phase emulsion templates, *Chem. Commun.* **2009,** 2217-2219.

206. Gurevitch, I. and Silverstein, M. S. Polymerized pickering HIPEs: Effects of synthesis parameters on porous structure, *J. Polym. Sci. Pol. Chem.* **2010,** *48*, 1516-1525.

207. Menner, A., Verdejo, R., Shaffer, M. and Bismarck, A. Particle-stabilized surfactant-free medium internal phase emulsions as templates for porous nanocomposite materials: Poly-pickering-foams, *Langmuir* **2007,** *23*, 2398-2403.

208. Li, T., Liu, H., Zeng, L., Yang, S., Li, Z., Zhang, J. and Zhou, X. Macroporous magnetic poly(styrene-divinylbenzene) nanocomposites prepared via magnetite nanoparticles-stabilized high internal phase emulsions, *J. Mater. Chem.* **2011,** *21*, 12865-12872.

209. Gurevitch, I. and Silverstein, M. S. Nanoparticle-Based and Organic-Phase-Based AGET ATRP PolyHIPE Synthesis within Pickering HIPEs and Surfactant-Stabilized HIPEs, *Macromolecules* **2011,** *44*, 3398-3409.

210. Gurevitch, I. and Silverstein, M. S. One-pot synthesis of elastomeric monoliths filled with individually encapsulated liquid droplets, *Macromolecules* **2012,** *45*, 6450-6456.

211. Cameron, N. R., Sherrington, D. C., Albiston, L. and Gregory, D. P. Study of the formation of the open-cellular morphology of poly(styrene/divinylbenzene) polyHIPE materials by cryo-SEM, *Colloid Polym. Sci.* **1996,** *274*, 592-595.

212. Lépine, O., Birot, M. and Deleuze, H. Influence of emulsification process on structure-properties relationship of highly concentrated reverse emulsion-derived materials, *Colloid Polym. Sci.* **2008,** *286*, 1273-1280.

213. Williams, J. M. High internal phase water-in-oil emulsions: Influence of surfactants and cosurfactants on emulsion stability and foam quality, *Langmuir* **1991,** *7*, 1370-1377.

214. Cameron, N. R. and Barbetta, A. The influence of porogen type on the porosity, surface area and morphology of poly(divinylbenzene) polyHIPE foams, *J. Mater. Chem.* **2000,** *10*, 2466-2471.

215. Pulko, I., Wall, J., Krajnc, P. and Cameron, N. R. Ultra-high surface area functional porous polymers by emulsion templating and hypercrosslinking: Efficient nucleophilic catalyst supports, *Chem.-Eur. J.* **2010,** *16*, 2350-2354.

216. Collins, R. E., *Flow of fluids through porous materials*. Reinhold Publishing Corporation: USA, **1961**.

217. Wong, L. L. C., Ikem, V. O., Menner, A. and Bismarck, A. Macroporous Polymers with Hierarchical Pore Structure from Emulsion Templates Stabilised by Both Particles and Surfactants, *Macromol. Rapid Commun.* **2011,** *32*, 1563-1568.

218. Haibach, K., Menner, A., Powell, R. and Bismarck, A. Tailoring mechanical properties of highly porous polymer foams: Silica particle reinforced polymer foams via emulsion templating, *Polymer* **2006,** *47*, 4513-4519.

219. Ikem, V. O., Menner, A. and Bismarck, A. Tailoring the mechanical performance of highly permeable macroporous polymers synthesized via Pickering emulsion templating, *Soft Matter* **2011,** *7*.

220. Zou, H., Wu, S. and Shen, J. Polymer/Silica Nanocomposites: Preparation, Characterization, Properties, and Applications, *Chem. Rev.* **2008,** *108*, 3893-3957.

221. Normatov, J. and Silverstein, M. S. Silsesquioxane-cross-linked porous nanocomposites synthesized within high internal phase emulsions, *Macromolecules* **2007,** *40*, 8329-8335.

222. Menner, A., Salgueiro, M., Shaffer, M. S. P. and Bismarck, A. Nanocomposite foams obtained by polymerization of high internal phase emulsions, *J. Polym. Sci. Pol. Chem.* **2008,** *46*, 5708-5714.

223. Lépine, O., Birot, M. and Deleuze, H. Elaboration of open-cell microcellular nanocomposites, *J. Polym. Sci. Pol. Chem.* **2007,** *45*, 4193-4203.

224. Wu, R., Menner, A. and Bismarck, A. Tough interconnected polymerized medium and high internal phase emulsions reinforced by silica particles, *J. Polym. Sci. Part A: Polym. Chem.* **2010,** *48*, 1979-1989.

225. Normatov, J. and Silverstein, M. S. Porous interpenetrating network hybrids synthesized within high internal phase emulsions, *Polymer* **2007,** *48*, 6648-6655.

226. Bokobza, L. Reinforcement of elastomeric networks by fillers, *Macromol Symp.* **2001,** *171*, 163-170.

227. Sanchez, C., Belleville, P., Popall, M. and Nicole, L. Applications of advanced hybrid organic-inorganic nanomaterials: From laboratory to market, *Chem. Soc. Rev.* **2011,** *40*, 696-753.

228. Vidal-Vidal, J., Rivas, J. and López-Quintela, M. A. Synthesis of monodisperse maghemite nanoparticles by the microemulsion method, *Colloids. Surface. A* **2006,** *288*, 44-51.

229. Ramírez, L. P. and Landfester, K. Magnetic polystyrene nanoparticles with a high magnetite content obtained by miniemulsion processes, *Macromol. Chem. Phys.* **2003,** *204*, 22-31.

230. Scherrer, P. Bestimmung der Grösse und der inneren Struktur von Kolloidteilchen mittels Röntgenstrahlen, *Göttinger Nachrichten Gesell* **1918,** *2*, 98-100.

231. Brunauer, S., Emmett, P. H. and Teller, E. Adsorption of gases in multimolecular layers, *J. Am. Chem. Soc.* **1938,** *60*, 309-319.

232. Winkler, J., *Titanium dioxide*. Vincentz Network: Hannover, **2003**.

233. Lecomte du Noüy, P. A new apparatus for measuring surface tension, *J. Gen. Physiol.* **1919,** *1*, 521-524.

234. Vold, R. D. and Vold, M. J., *Colloid and Interface Chemistry*. Addison-Wesley Publishing Co: London, **1983**.

235. Drelich, J., Fang, C. and White, C. L., Measurement of interfacial tension in fluid-fluid systems. In *Encyclopedia of Surface and Colloid Science*, A. Hubbarb, Ed. Marcel Dekker: **2002**; pp 3152-3166.

236. Zuidema, H. H. and Waters, G. W. Ring method for the determination of interfacial tension, *Ind. Eng. Chem. Anal.* **1941,** *13*, 312-313.

237. Tate, T. On the magnitude of a drop of liquid formed under different circumstances, *Philos. Mag.* **1864,** *27*, 176-180.

238. Harkins, W. D. and Brown, F. E. The determination of surface tension (free surface energy), and the weight of falling drops: The surface tension of water and benzene by the capillary height method, *J. Am. Chem. Soc.* **1919,** *41*, 499-524.

239. Manley, S. Advances in Experimental Methods for Characterization of Porous Solids. Ph.D. Thesis, Imperial College: London, 2009.

240. Molina, R., Vílchez, A., Canal, C. and Esquena, J. Wetting properties of polystyrene/divinylbenzene crosslinked porous polymers obtained using W/O highly concentrated emulsions as templates, *Surf. Interface Anal.* **2009,** *41*, 371-377.

241. Carman, P. C., *Flow of Gases Through Porous Media*. Belfast, Butterworths Scientific Publications: **1956**.

242. Lian, S., Wang, E., Gao, L., Kang, Z., Wu, D., Lan, Y. and Xu, L. Growth of single-crystal magnetite nanowires from Fe_3O_4 nanoparticles in a surfactant-free hydrothermal process, *Solid State Commun.* **2004,** *132*, 375-378.

243. Shen, L., Laibinis, P. E. and Alan Hatton, T. Bilayer Surfactant Stabilized Magnetic Fluids: Synthesis and Interactions at Interfaces, *Langmuir* **1999,** *15*, 447-453.

244. Nakayama, N. and Hayashi, T. Preparation of TiO_2 nanoparticles surface-modified by both carboxylic acid and amine: Dispersibility and stabilization in organic solvents, *Colloids. Surface. A* **2008,** *317*, 543-550.

245. Qu, Q., Geng, H., Peng, R., Cui, Q., Gu, X., Li, F. and Wang, M. Chemically binding carboxylic acids onto TiO_2 nanoparticles with adjustable coverage by solvothermal strategy, *Langmuir* **2010,** *26*, 9539-9546.

246. Bini, R. A., Marques, R. F. C., Santos, F. J., Chaker, J. A. and Jafelicci Jr, M. Synthesis and functionalization of magnetite nanoparticles with different amino-functional alkoxysilanes, *J. Magn. Magn.* **2012,** *324*, 534-539.

247. Cornell, R. M. and Schwertmann, U., *The Iron Oxides: Structure, properties, reactions, occurences and uses*. Wiley-VCH: Weinheim, **2003**.

248. Berkowitz, A. E., Lahut, J. A., Jacobs, I. S., Levinson, L. M. and Forester, D. W. Spin pinning at ferrite-organic interfaces, *Phys. Rev. Lett.* **1975,** *34*, 594-597.

249. Yoon, K. Y., Li, Z., Neilson, B. M., Lee, W., Huh, C., Bryant, S. L., Bielawski, C. W. and Johnston, K. P. Effect of adsorbed amphiphilic copolymers on the interfacial activity of superparamagnetic nanoclusters and the emulsification of oil in water, *Macromolecules* **2012,** *45*, 5157-5166.

250. Vassiliou, J. K., Mehrotra, V., Russell, M. W., Giannelis, E. P., McMichael, R. D., Shull, R. D. and Ziolo, R. F. Magnetic and optical properties of γ-Fe_2O_3 nanocrystals, *J. Appl. Phys.* **1993,** *73*, 5109-5116.

251. Breulmann, M., Cölfen, H., Hentze, H. P., Antonietti, M., Walsh, D. and Mann, S. Elastic magnets: Template-controlled mineralization of iron oxide colloids in a sponge-like gel matrix, *Adv. Mater.* **1998,** *10*, 237-241.

252. Ding, J., Tsuzuki, T. and McCormick, P. G. Hematite powders synthesized by mechanochemical processing, *Nanostruct. Mater.* **1997,** *8*, 739-747.

253. Tsuzuki, T. and McCormick, P. G. Synthesis of Cr_2O_3 nanoparticles by mechanochemical processing, *Acta Mater.* **2000,** *48*, 2795-2801.

254. Dodd, A., McKinley, A., Tsuzuki, T. and Saunders, M. Optical and photocatalytic properties of nanocrystalline TiO_2 synthesised by solid-state chemical reaction, *J. Phys. Chem. Solids* **2007,** *68*, 2341-2348.

255. Koch, C. C., *Materials Science and Technology - A Comprehensive Treatment* VCH: Weinheim, **2001**; Vol. 15, p 193.

256. Salari, M., Rezaee, M., Marashi, S. P. H. and Aboutalebi, S. H. The role of the diluent phase in the mechanochemical preparation of TiO_2 nanoparticles, *Powder Technol.* **2009,** *192*, 54-57.

257. Salari, M., Mousavi khoie, S. M., Marashi, P. and Rezaee, M. Synthesis of TiO_2 nanoparticles via a novel mechanochemical method, *J. Alloy. Compd.* **2009,** *469*, 386-390.

258. Zhang, H. and Banfield, J. F. Understanding Polymorphic Phase Transformation Behavior during Growth of Nanocrystalline Aggregates: Insights from TiO_2, *J. Phys. Chem. B* **2000,** *104*, 3481-3487.

259. Yang, H. and McCormick, P. G. Mechanically activated reduction of nickel oxide with graphite, *Metall. Mater. Trans. B-Proc. Metall. Mater. Proc. Sci.* **1998,** *29*, 449-455.

260. Rouquerol, F., Rouquerol, J. and Sing, K., *Adsorption by powders and porous solids*. Academic Press: San Diego, USA, **1999**; p 204.

261. Sing, K. S. W., Everett, D. H., Haul, R. A. W., Moscou, L., Pierotti, R. A., Rouquerol, J. and Siemieniewska, T. Reporting Physisorption data for Gas/Solid Systems with Special Reference to the Determination of Surface Area and Porosity, *Pure Appl. Chem.* **1985,** *57*, 603-619.

262. Tsuzuki, T., Harrison, W. T. A. and McCormick, P. G. Synthesis of ultrafine gadolinium oxide powder by mechanochemical processing, *J. Alloy. Compd.* **1998,** *281*, 146-151.

263. Dodd, A., McKinley, A., Tsuzuki, T. and Saunders, M. Mechanochemical synthesis of nanoparticulate ZnO–$ZnWO_4$ powders and their photocatalytic activity, *J. Eur. Ceram. Soc.* **2009,** *29*, 139-144.

264. Szczepankiewicz, S. H., Colussi, A. J. and Hoffmann, M. R. Infrared spectra of photoinduced species on hydroxylated titania surfaces, *J. Phys. Chem. B* **2000,** *104*, 9842-9850.

265. Yu, J. G., Yu, H. G., Cheng, B., Zhao, X. J., Yu, J. C. and Ho, W. K. The Effect of Calcination Temperature on the Surface Microstructure and Photocatalytic Activity of TiO_2 Thin Films Prepared by Liquid Phase Deposition, *J. Phys. Chem. B* **2003,** *107*, 13871-13879.

266. Syoufian, A. and Nakashima, K. Degradation of methylene blue in aqueous dispersion of hollow titania photocatalyst: Study of reaction enhancement by various electron scavengers, *J. Colloid Interface Sci.* **2008,** *317*, 507-512.

267. Srinivasan, M. and White, T. Degradation of methylene blue by three-dimensionally ordered macroporous titania, *Environmental Science and Technology* **2007,** *41*, 4405-4409.

268. Desforges, A., Backov, R., Deleuze, H. and Mondain-Monval, O. Generation of palladium nanoparticles within macrocellular polymeric supports: Application to heterogeneous catalysis of the Suzuki-Miyaura coupling reaction, *Adv. Funct. Mater.* **2005,** *15*, 1689-1695.

269. Balazs, A. C., Emrick, T. and Russell, T. P. Nanoparticle polymer composites: Where two small worlds meet, *Science* **2006,** *314*, 1107-1110.

270. Jiang, L., Sun, W. and Kim, J. Preparation and characterization of w-functionalized polystyrene-magnetite nanocomposites, *Mater. Chem. Phys.* **2007,** *101*, 291-296.

271. Yan, F., Li, J., Zhang, J., Liu, F. and Yang, W. Preparation of Fe_3O_4/polystyrene composite particles from monolayer oleic acid modified Fe_3O_4 nanoparticles via miniemulsion polymerization, *J. Nanopart. Res.* **2009,** *11*, 289-296.

272. Landfester, K. Miniemulsion polymerization and the structure of polymer and hybrid nanoparticles, *Angew. Chem. Int. Ed.* **2009,** *48*, 4488-4508.

273. Neves, J. S., De Souza Jr, F. G., Suarez, P. A. Z., Umpierre, A. P. and MacHado, F. In situ production of polystyrene magnetic nanocomposites through a batch suspension polymerization process, *Macromol. Mater. Eng.* **2011,** *296*, 1107-1118.

274. Gyergyek, S., Makovec, D., Mertelj, A., Huskić, M. and Drofenik, M. Superparamagnetic nanocomposite particles synthesized using the mini-emulsion technique, *Colloids. Surface. A* **2010,** *366*, 113-119.

275. Duan, H., Wang, D., Sobal, N. S., Giersig, M., Kurth, D. G. and Möhwald, H. Magnetic colloidosomes derived from nanoparticle interfacial self-assembly, *Nano Letters* **2005,** *5*, 949-952.

276. Samanta, B., Patra, D., Subramani, C., Ofir, Y., Yesilbag, G., Sanyal, A. and Rotello, V. M. Stable magnetic colloidosomes via click-mediated crosslinking of nanoparticles at water-oil interfaces, *Small* **2009,** *5*, 685-688.

277. Sander, J. S. and Studart, A. R. Monodisperse functional colloidosomes with tailored nanoparticle shells, *Langmuir* **2011,** *27*, 3301-3307.

278. Bonini, M., Lenz, S., Falletta, E., Ridi, F., Carretti, E., Fratini, E., Wiedenmann, A. and Baglioni, P. Acrylamide-Based Magnetic Nanosponges: A New Smart Nanocomposite Material, *Langmuir* **2008,** *24*, 12644-12650.

279. Olsson, R. T., Azizi Samir, M. A. S., Salazar-Alvarez, G., Belova, L., Ström, V., Berglund, L. A., Ikkala, O., Nogués, J. and Gedde, U. W. Making flexible magnetic aerogels and stiff magnetic nanopaper using cellulose nanofibrils as templates, *Nat. Nanotechnol.* **2010,** *5*, 584-588.

280. Hoppe, C. E., Rivadulla, F., López-Quintela, M. A., Buján, M. C., Rivas, J., Serantes, D. and Baldomir, D. Effect of submicrometer clustering on the magnetic properties of free-standing superparamagnetic nanocomposites, *J. Phys. Chem. C* **2008,** *112*, 13099-13104.

281. Gass, J., Poddar, P., Almand, J., Srinath, S. and Srikanth, H. Superparamagnetic polymer nanocomposites with uniform Fe_3O_4 nanoparticle dispersions, *Adv. Funct. Mater.* **2006,** *16*, 71-75.

282. Ohno, K., Koh, K.-m., Tsujii, Y. and Fukuda, T. Synthesis of Gold Nanoparticles Coated with Well-Defined, High-Density Polymer Brushes by Surface-Initiated Living Radical Polymerization, *Macromolecules* **2002,** *35*, 8989-8993.

283. Frankamp, B. L., Boal, A. K. and Rotello, V. M. Controlled Interparticle Spacing through Self-Assembly of Au Nanoparticles and Poly(amidoamine) Dendrimers, *J. Am. Chem. Soc.* **2002,** *124*, 15146-15147.

284. Bockstaller, M. R., Lapetnikov, Y., Margel, S. and Thomas, E. L. Size-Selective Organization of Enthalpic Compatibilized Nanocrystals in Ternary Block Copolymer/Particle Mixtures, *J. Am. Chem. Soc.* **2003,** *125*, 5276-5277.

285. Romeo, H. E., Vílchez, A., Esquena, J., Hoppe, C. E. and Williams, R. J. J. Polymerization-induced phase separation as a one-step strategy to self-assemble alkanethiol-stabilized gold nanoparticles inside polystyrene domains dispersed in an epoxy matrix, *Eur. Polym. J.* **2012,** *48*, 1101-1109.

286. Shenhar, R., Norsten, T. B. and Rotello, V. M. Polymer-Mediated Nanoparticle Assembly: Structural Control and Applications, *Adv. Mater.* **2005,** *17*, 657-669.

287. Kunieda, H. and Shinoda, K. Solution behavior and hydrophile-lipophile balance temperature in the aerosol OT-isooctane-brine system: Correlation between microemulsions and ultralow interfacial tensions, *J. Colloid Interface Sci.* **1980,** *75*, 601-606.

288. Guardia, P., Batlle-Brugal, B., Roca, A. G., Iglesias, O., Morales, M. P., Serna, C. J., Labarta, A. and Batlle, X. Surfactant effects in magnetite nanoparticles of controlled size, *J. Magn. Magn.* **2007,** *316*, e756-e759.

289. Dormann, J. L., Fiorani, D. and Tronc, E. Magnetic relaxation in fine-particle systems. **1997**; Vol. 98, pp 283-494.

290. Frankamp, B. L., Boal, A. K., Tuominen, M. T. and Rotello, V. M. Direct control of the magnetic interaction between iron oxide nanoparticles through dendrimer-mediated self-assembly, *J. Am. Chem. Soc.* **2005,** *127*, 9731-9735.

291. Prene, P., Tronc, E., Jolivet, J.-P., Livage, J., Cherkaoui, R., Nogues, M., Dormann, J.-L. and Fiorani, D. Magnetic properties of isolated γ-Fe_2O_3 particles, *IEEE Trans. Magn.* **1993,** *29*, 2658-2660.

292. Zhou, J., Qiao, X., Binks, B. P., Sun, K., Bai, M., Li, Y. and Liu, Y. Magnetic Pickering Emulsions Stabilized by Fe_3O_4 Nanoparticles, *Langmuir* **2011,** 3308–3316.

293. Cui, Z. G., Cui, C. F., Zhu, Y. and Binks, B. P. Multiple phase inversion of emulsions stabilized by in situ surface activation of $CaCO_3$ nanoparticles via adsorption of fatty acids, *Langmuir* **2012,** *28*, 314-320.

294. Chibowski, E. and Hołłysz, L. Use of the Washburn equation for surface free energy determination, *Langmuir* **1992,** *8*, 710-716.

295. Hadjiiski, A., Dimova, R., Denkov, N. D., Ivanov, I. B. and Borwankar, R. Film trapping technique: Precise method for three-phase contact angle determination of solid and fluid particles of micrometer size, *Langmuir* **1996,** *12*, 6665-6675.

296. Li, Z., Giese, R. F., van Oss, C. J., Yvon, J. and Cases, J. The Surface Thermodynamic Properties of Talc Treated with Octadecylamine, *J. Colloid Interface Sci.* **1993,** *156*, 279-284.

297. Saien, J. and Akbari, S. Interfacial Tension of Toluene + Water + Sodium Dodecyl Sulfate from (20 to 50)°C and pH between 4 and 9, *J. Chem. Eng. Data* **2006,** *51*, 1832-1835.

298. Zoppe, J. O., Venditti, R. A. and Rojas, O. J. Pickering emulsions stabilized by cellulose nanocrystals grafted with thermo-responsive polymer brushes, *J. Colloid Interface Sci.* **2012,** *369*, 202-209.

299. Ingram, D. R., Kotsmar, C., Yoon, K. Y., Shao, S., Huh, C., Bryant, S. L., Milner, T. E. and Johnston, K. P. Superparamagnetic nanoclusters coated with oleic acid bilayers for stabilization of emulsions of water and oil at low concentration, *J. Colloid Interface Sci.* **2010,** *351*, 225-232.

300. Binks, B. P., Murakami, R., Armes, S. P. and Fujii, S. Temperature-induced inversion of nanoparticle-stabilized emulsions, *Angew. Chem. Int. Ed.* **2005,** *44*, 4795-4798.

301. Melle, S., Lask, M. and Fuller, G. G. Pickering Emulsions with Controllable Stability, *Langmuir* **2005,** *21*, 2158-2162.

302. Tao, P., Li, Y., Rungta, A., Viswanath, A., Gao, J., Benicewicz, B. C., Siegel, R. W. and Schadler, L. S. TiO_2 nanocomposites with high refractive index and transparency, *J. Mater. Chem.* **2011,** *21*, 18623-18629.

303. Zhang, Y., Wei, S., Zhang, W., Xu, Y. J., Liu, S., Su, D. S. and Xiao, F. S. Titania nanocrystals and adsorptive nanoporous polymer composites: An enrichment and degradation system, *ChemSusChem* **2009,** *2*, 867-872.

304. Zan, L., Fa, W. and Wang, S. Novel photodegradable low-density polyethylene-TiO_2 nanocomposite film, *Environmental Science and Technology* **2006,** *40*, 1681-1685.

305. Kim, S. H., Kwak, S. Y. and Suzuki, T. Photocatalytic degradation of flexible PVC/TiO_2 nanohybrid as an eco-friendly alternative to the current waste landfill and dioxin-emitting incineration of post-use PVC, *Polymer* **2006,** *47*, 3005-3016.

306. Shang, J., Chai, M. and Zhu, Y. Solid-phase photocatalytic degradation of polystyrene plastic with TiO_2 as photocatalyst, *Journal of Solid State Chemistry* **2003,** *174*, 104-110.

307. Zan, L., Tian, L., Liu, Z. and Peng, Z. A new polystyrene-TiO_2 nanocomposite film and its photocatalytic degradation, *Applied Catalysis A: General* **2004,** *264*, 237-242.

308. Nakayama, N. and Hayashi, T. Preparation and characterization of poly(L-lactic acid)/TiO_2 nanoparticle nanocomposite films with high transparency and efficient photodegradability, *Polymer Degradation and Stability* **2007,** *92*, 1255-1264.

309. Kumar, A. P., Depan, D., Singh Tomer, N. and Singh, R. P. Nanoscale particles for polymer degradation and stabilization-Trends and future perspectives, *Progress in Polymer Science (Oxford)* **2009,** *34*, 479-515.

310. Ghosh, G., Vílchez, A., Esquena, J., Solans, C. and Rodríguez-Abreu, C. Preparation of ultra-light magnetic nanocomposites using highly concentrated emulsions, *Mater. Chem. Phys.* **2011**.

311. Vílchez, A., Rodríguez-Abreu, C., Esquena, J., Menner, A. and Bismarck, A. Macroporous polymers obtained in highly concentrated emulsions stabilized solely with magnetic nanoparticles, *Langmuir* **2011,** *27*, 13342-13352.

312. Guo, Z., Lei, K., Li, Y., Ng, H. W., Prikhodko, S. and Hahn, H. T. Fabrication and characterization of iron oxide nanoparticles reinforced vinyl-ester resin nanocomposites, *Compos. Sci. Technol.* **2008,** *68*, 1513-1520.

313. Hoppe, C. E., Rivadulla, F., Vidal-Vidal, J., López-Quintela, M. A. and Rivas, J. Magnetic relaxation of y-Fe_2O_3 nanoparticles arrangements and electronic phase-segregated systems, *J. Nanosci. Nanotechnol.* **2008,** *8*, 2883-2890.

314. Vestal, C. R., Song, Q. and Zhang, Z. J. Effects of interparticle interactions upon the magnetic properties of $CoFe_2O_4$ and $MnFe_2O_4$ nanocrystals, *J. Phys. Chem. B* **2004,** *108*, 18222-18227.

315. Blundell, S., *Magnetism in Condensed Matter*. Oxford University Press: **2001**.

316. Destribats, M., Ravaine, S., Heroguez, V., Leal-Calderon, F. and Schmitt, V. Outstanding stability of poorly-protected pickering emulsions, *C. Prog. Colloid Polym. Sci.* **2010,** *137*, 13-18.

8 GLOSSARY

ABBREVIATIONS

ADVN	2,2’-Azobis-(2,4-dimethyl) valeronitrile
AIBN	Oil-soluble initiator α,α’-azoisobutyronitrile
AOP	Advanced Oxidation Processes
BET	Brunauer-Emmet-Teller
CMC	Critical Micelle Concentration
CNP_{32}	As-received commercial nanoparticles (average size is 32 nm)
CTAB	Cetyl Trimethyl Ammonium Bromide
DVB	Divinylbenzene
FC	Field-cooled
FTIR	Fourier Transform Infrared Spectroscopy
HIPE	High Internal Phase Emulsion
HLB	Hydrophilic-Lipophilic Balance
MAA	Methacrylic Acid
MB	Methylene blue
NIPAM	N-isopropylacrylamide
NMR	Nuclear Magnetic Resonance
NPs	Nanoparticles
NP_3	Oleic-acid surface modified nanoparticles prepared by a microemulsion method (average size is 3 nm)
NP_8	Oleic-acid surface modified nanoparticles prepared by a co-precipitation method (average size is 8 nm)
NP_{32}	Oleic-acid surface modified commercial nanoparticles (average size is 32 nm)
O/W	Oil-in-water
PIC	Phase Inversion Composition
PIT	Phase Inversion Temperature
PS	Polystyrene
polyHIPE	Polymerized High Internal Phase Emulsion
SAXS	Small Angle X-ray Scattering
SEM	Scanning Electron Microscopy
SDS	Sodium Dodecyl Sulphate
TEM	Transmission Electron Microscopy
TGA	Thermogravimetric analysis
UV	Ultraviolet radiation
UVA	Near ultraviolet radiation
W/O	Water-in-oil

XRD	X-ray Diffraction
ZFC	Zero-field-cooled

SYMBOLS

A	Interfacial area / Molecular interactions / Cross-sectional area
a	Surface area per molecule
b	Constant dependent on the packing exhibited by the particles. Used in the calculation of the maximum capillary pressure
C_p	Particle concentration
C_S	Surfactant concentration
C_0	Initial concentration
c_∞	Solubility of the dispersed phase into the continuous phase
D	Diffusion coefficient / Surfactant phase / Size of the crystalline domain
D_i	Diameter of droplet or particle i
D_m	Arithmetic mean diameter
$D[1,0]$	Droplet arithmetic mean size
E	Weight percent of the ethylene oxide group in a surfactant molecule / Young´s modulus
E_A	Magnetic anisotroy energy barrier
F	Force
f_D and f_N	Correction factors incorporated in the determination of interfacial tensions using the droplet-volume and Du Noüy methods, respectively.
g	Gravity acceleration
G_d	Free energy of detachment of a small spherical particle from the interface into (oil or water) the bulk phase
G_{form}	Free energy of emulsion formation
G^σ	Additional surface free energy
H	Applied magnetic field
H_c	Coercivity field
h	Compression length
K	Permeability coefficient
K_a	Uniaxial magnetic anisotropy
K_0	Knudsen permeability coefficient

K_{oil}	Constant (17 ºC) used in the determination of the Phase Inversion Temperature
k	Viscous permeability / reaction constant in a first order kinetics
k_B	Boltzmann's constant
L	Sample length in the permeability test
M	Gas molar mass / Magnetization
M_s	Remanence
M_s	Saturation magnetization
N	Total number of droplets
N_A	Avogadro´s number
N_{HLB}	Hydrophilic-Lipophilic Balance number
N_{oil}	Constant that quantifies the lipophilic degree of a given oil. Used in the determination of the Phase Inversion Temperature
P	Laplace Pressure / Percentage of droplets / Porosity
$P_{c,\max}$	Maximum capillary pressure
p	Three-phase contact line perimeter of the Du Noüy ring.
p_1 and p_2	Pressures on the inlet high and outlet low pressure sides of the sample in the permeability test
p_m	Mean pressure in the permeability test
Q_2	Volumetric flowrate
R	Ideal gas constant / Du Noüy ring radius
r	Needle radius / Du Noüy wire radius
r_D	Droplet radius
r_p	Particle radius
S	Entropy
S_{BET}	Specific surface area calculated using the BET method
$S_{average}$	Normalized surface area
T	Temperature
T_B	Blocking temperature
T_g	Glass transition temperature
t	Time
$\mathrm{T_{HLB}}$	Hydrophilic-Lipophilic Balance Temperature or Phase Inversion Temperature
U	Wetted length of the Du Noüy ring
V	Volume

V_D	Droplet volume
V_m	Molar volume of the solute
V_p	Particle volume
V_t	Total pore volume
$V_{\mu t}$	Total micropore volume
W	Work
W_E	Electrostatic repulsion potential
W_S	Steric repulsion potential
W_{VdW}	Van der Waals potential

GREEK SYMBOLS

α_{c}	Surface area per molecule
β	Corrected peak width. Used in Scherrer equation
Γ	Surface excess concentration
γ or γ_{ow}	Oil-water interfacial tension
γ_{ab}	Interaction energy between a and b molecules
γ_{po} and γ_{pw}	Interfacial tensions at the particle-oil and particle-water interface, respectively
η_o	Viscosity
θ	Contact angle / Diffraction angle
θ_{ow}	Contact angle that a particle makes with the oil-water interface
λ	Radiation wavelength
μ	Gas viscosity
v_0	Creaming or sedimentation velocity
ρ	Density
ρ_H and ρ_L	Densities of the heavy and light phases
ρ_s	Skeletal density
ρ_f	Foam or envelope density
σ	Standard deviation / Crush strength
σ_g	Geometric standard deviation
σ_s	Specific crush strength
τ_M	Characteristically experimental measured time

τ_M	Time constant for a given magnetic material
ϕ	Internal phase volume fraction. W and O subscripts indicate water and oil, respectively
ω	Oswald ripening velocity

9 SUMMARY IN SPANISH

1. INTRODUCCIÓN

Las emulsiones son dispersiones coloidales, termodinámicamente inestables, constituidas por dos fases inmiscibles, en que una de las fases (fase dispersa) se encuentra dispersa en forma de gotas en la otra (fase continua). Las emulsiones forman parte de nuestra vida cotidiana, y muchos productos alimentarios, como la leche y la salsa mayonesa, o productos cosméticos y de higiene personal, son emulsiones. Como indica la definición, las emulsiones son termodinámicamente inestables, por lo que su formación no es espontánea y una vez formadas, tienden a la separación de fases. Para retardar dicha separación, se añaden emulsionantes; los más frecuentes son, sin duda, los tensioactivos. Otros emulsionantes pueden ser macromoléculas o partículas finalmente divididas.

Las emulsiones se pueden clasificar en función de la naturaleza de sus fases en agua en aceite (W/O) o en aceite en agua (O/W). También se pueden clasificar según la fracción de volumen de fase dispersa en diluidas, concentradas, o altamente concentradas para fracciones menores del 20%, entre el 20% y el 74%, y mayores del 74%, respectivamente (Figura 1-1). En el presente trabajo se han empleado las emulsiones altamente concentradas para la preparación de materiales poliméricos macroporosos, como se detallará más adelante.

Debido a que la formación de emulsiones no es espontánea, es necesario aportar energía para su formación. En general, los métodos de preparación suelen clasificarse en métodos de alta y de baja energía, según la energía se aporta mediante agitación mecánica o mediante energía proveniente de la actividad química de los componentes de la emulsión, respectivamente. Otra consecuencia de la inestabilidad termodinámica es que las emulsiones tienden a la separación de fases, que puede ocurrir mediante distintos mecanismos de desestabilización. Dependiendo de diversos factores, las fases de las emulsiones pueden separar mediante: sedimentación, coalescencia, floculación y maduración de Ostwald. Cabe destacar que todos estos mecanismos de separación conducen a la completa desestabilización y separación de fases. Dichos mecanismos están representados en la Figura 1-5.

Los tensioactivos son compuestos que presentan dos partes claramente diferenciadas (Figura 1-7): la primera, generalmente denominada cadena hidrófila, con afinidad a solventes polares, y la segunda, conocida como cadena lipófila, con afinidad a compuestos apolares. Debido a esta propiedad, los tensioactivos son moléculas anfifílicas, ya que poseen afinidad por ambos tipos de solventes. La capacidad de los tensioactivos de adsorberse espontáneamente en las interfaces (aire-líquido, líquido-líquido, etc.) es responsable de la reducción de la tensión interfacial, que equivale a reducir la energía superficial. Dicha reducción facilita el proceso de emulsificación, ya que reduce la energía necesaria para la formación de gotas (ec. 1.1). Además, los tensioactivos no sólo facilitan la emulsificación, sino que, proporcionan estabilidad cinética debido a la formación de una monocapa en la superficie de las gotas. Otra característica típica mostrada por los tensioactivos es su capacidad para formar agregados supramoleculares (por ejemplo, micelas) a partir de concentraciones muy bajas de tensioactivo. De hecho, estas estructuras pueden aparecer a la concentración en la cual la superficie (o interfase) se satura de moléculas de tensioactivo, como se ilustra en la Figura 1-10.

En el presente estudio se han empleado tensioactivos no iónicos etoxilados. Estos tensioactivos se caracterizan por modificar su solubilidad en agua o en aceite dependiendo de la temperatura. Al aumentar la temperatura se produce una deshidratación de sus cadenas etoxiladas lo que aumenta la hidrofobicidad del tensioactivo (Figura 1-11). La temperatura de inversión de fases (o PIT) es la temperatura en la cual las propiedades lipófilas e hidrófilas se encuentran equilibradas. De acuerdo con este principio, se pueden formar emulsiones con tamaños de gota pequeños y homogéneos mediante un calentamiento (o enfriamiento) de una emulsión de tipo O/W (o W/O), formándose una emulsión de tipo W/O (o O/W) por inversión de fases. En este método se pasa por una temperatura intermedia (T = PIT), donde las propiedades hidrófilas y lipófilas de los sistemas están equilibradas, como se mencionó más arriba. Cabe subrayar que la tensión interfacial a la temperatura de inversiones de fases es mínima (por ej. 10^{-2} mN/m), por lo que empleando este método de emulsificación se logra obtener gotas más pequeñas que por métodos convencionales de alta energía.

En este trabajo de investigación también se han empleado nanopartículas de óxido de hierro y de dióxido de titanio como agentes emulsionantes. Aunque el descubrimiento de la capacidad de estabilizar emulsiones con sólidos finamente divididos (denominadas emulsiones de Pickering) fue descrito hace ya más de 100 años, la formación y estabilización de estas emulsiones ha sido estudiada extensamente durante los últimos veinte años, sobre todo por el grupo de Bernard Binks de la Universidad de Hull (U.K.). A diferencia de los tensioactivos, las partículas generalmente no son anfifílicas, y por tanto no reducen la tensión interfacial. No obstante, la energía superficial total puede reducirse cuando una partícula se adsorbe en la interfase y, consecuentemente, el área superficial de esta interfase disminuye. Esta es la principal causa que dificulta la obtención de emulsiones de Pickering con gotas de pequeño tamaño. Se ha demostrado que la adsorción de las partículas en las interfases está favorecida termodinámicamente (ec. 1.17), y que la energía necesaria para la extracción de una partícula desde dicha interfase a cualquiera de las dos fases (aceite o agua) puede ser de diversos grados de magnitud mayor que la energía térmica del sistema. Por lo tanto, la adsorción de partículas en la interfase puede ser prácticamente irreversible si dichas partículas poseen propiedades hidrófilas y lipófilas equilibradas en el sistema. Tanto teórica como experimentalmente, se ha demostrado que las partículas presentan mayor eficacia en la estabilización de emulsiones cuando sus ángulos de contacto con la interfase (θ_{ow}) son cercanos a 90 ºC (ver Figura 1-13). Por tanto, es necesario que las partículas estén parcialmente mojadas por las dos fases. Como regla general y en analogía con los tensioactivos, las partículas hidrófobas (θ_{ow}>90º) tenderán a formar emulsiones W/O, mientras que las partículas hidrófilas (θ_{ow}>90º) favorecerán la formación de emulsiones O/W. Otro aspecto a destacar es que la energía térmica puede desplazar a las partículas de las interfases si su tamaño es lo suficientemente pequeño (pocos nanómetros). Por ello, la estabilidad de las emulsiones Pickering suele aumentar con el tamaño de las partículas. Además, la estabilidad suele aumentar cuando las partículas poseen un determinado grado de agregación.

Debido a que la desorción de las partículas puede ser difícil cuando el ángulo de contacto es próximo a 90º, las emulsiones Pickering pueden poseer mayor estabilidad que las emulsiones estabilizadas con tensioactivos. Por otro lado, también se han observado emulsiones de Pickering estables en las que únicamente un cierto porcentaje de la superficie de las gotas está poblada por partículas. (Figura 1-15). Un aspecto importante estudiado en el presente trabajo de investigación es el estudio de la interacción entre partículas y tensioactivos, ya que dichas interacciones pueden aumentar o disminuir la estabilidad de los sistemas dependiendo de su naturaleza. Como ejemplo de la mejora de la estabilidad, el tensioactivo puede adsorberse en la superficie de las nanopartículas confiriendo cierta hidrofobicidad y favoreciendo su adsorción en las interfases. Por el contrario, ambos emulsionantes pueden competir por la adsorción en la interfase agua-aceite, causando el desplazamiento de uno de los dos (normalmente partículas) hacia una de las dos fases constituyentes de la emulsión.

Como se ha mencionado anteriormente, en esta Tesis se han estudiado emulsiones altamente concentradas (HIPEs). Estas emulsiones poseen una fracción de volumen de la fase interna igual o mayor al 74%, valor que corresponde al máximo empaquetamiento de esferas monodispersas. El alto porcentaje de fase dispersa provoca que las gotas se deformen y se compacten. Por ello, la estructura de estas emulsiones consiste en gotas poliédricas separadas por una película delgada constituida por la fase continua (ver Figura 1-21). Debido al elevado grado de compactación de las gotas, las emulsiones poseen una alta viscosidad.

Una de las posibles aplicaciones de las HIPEs es su utilización como plantilla para la preparación de materiales macroporosos poliméricos. Generalmente, este método se basa en incorporar uno o varios monómeros y/o entrecruzantes en la fase externa de dichas emulsiones (generalmente del tipo W/O) y llevar a cabo la polimerización de los monómeros. Un ejemplo de un material polimérico macroporoso se presenta en la Figura 1-22, donde se observa la textura macroporosa por microscopía electrónica de barrido (SEM). El material poroso, semejante a una espuma, posee poros interconectados que son réplicas (mismo tamaño, normalmente de 1 a 50 μm) de las gotas de la emulsión inicial, obteniendo densidades muy bajas de hasta 0,02 g/cm^3 y porosidades de hasta el 99%. La textura porosa depende principalmente de la fracción de volumen de fase interna, ya que el volumen contenido en las gotas equivale al volumen de aire de los materiales resultantes. El sistema más estudiado es el formado por el monómero estireno y el entrecruzante divinilbenceno, a pesar de que se ha publicado sobre una gran variedad de monómeros (tanto hidrófilos como hidrófobos). Este sistema modelo es, precisamente, el estudiado en este trabajo de investigación.

Tradicionalmente, las emulsiones utilizadas como plantilla se han estabilizado con tensioactivos. Recientemente, el mismo procedimiento ha sido adaptado para emulsiones estabilizadas con partículas, tanto orgánicas como inorgánicas. La Figura 1-23 muestra algunos de los ejemplos de los materiales obtenidos empleando emulsiones de Pickering. Una de las ventajas que esta propuesta conlleva es que cualquier funcionalidad que posean las partículas pasa a formar parte de los materiales macroporosos resultantes, ya que las partículas permanecen incorporadas en los materiales (Figura 1-23(c)). Como se puede observar en el ejemplo de la Figura 1-23(b), los materiales presentan macroporos de gran tamaño y que suelen ser cerrados, obteniéndose materiales de baja permeabilidad. Esto último se puede explicar por el mayor tamaño de las partículas con respecto a los tensioactivos, lo que produce que el film polimérico que separa dos poros nunca llegue a estrecharse lo suficiente para abrir conexiones entre los macroporos.

En el presente trabajo, se ha realizado un estudio en profundidad sobre estos aspectos, y se han preparado materiales porosos nanocompuestos utilizando distintos tipos de emulsiones altamente concentradas, como se describe en detalle en la sección de objetivos y plan de trabajo.

2. OBJETIVOS

La preparación de materiales constituidos por una matriz polimérica que contiene algún tipo de elemento inorgánico, como nanopartículas o nanotubos, ha generado durante los últimos años un enorme interés científico. Existen numerosas aplicaciones de los nanomateriales, como por ejemplo sensores ópticos o poliolefinas reforzadas con arcilla en la industria automovilística. Uno de los campos más innovadores es la fabricación de materiales porosos avanzados con aplicaciones en campos tan variados, como el de membranas, purificación de gases, almacenamiento de líquidos/gases o el de soportes catalíticos.

El objetivo principal de esta Tesis es la formación de nanocompuestos macroporosos con nanopartículas funcionales incorporadas, mediante el uso de emulsiones altamente concentradas del tipo W/O como plantilla. Con este propósito, se han utilizado las siguientes nanopartículas:

- Nanopartículas superparamagnéticas de óxido de hierro.
- Nanopartículas fotocatalíticas de dióxido de titanio.

La fase externa de las emulsiones está formada por una mezcla de estireno (monómero) y divinilbenceno (entrecruzante). Se ha llevado a cabo una polimerización por radicales libres en la fase externa de dichas emulsiones. Se han estudiado tres tipos de emulsiones, siguiendo diferentes metodologías:

(a) Emulsiones altamente concentradas (HIPEs) estabilizadas con tensioactivos, y preparadas por el método de temperatura de inversión de fases, conteniendo nanopartículas en el seno de la fase continua (sección 1.1).
(b) HIPEs estabilizadas con nanopartículas (Pickering HIPEs), en ausencia de tensioactivo (sección 4.3). La obtención de nanocompuestos macroporosos utilizando Pickering HIPEs como plantilla, constituye un método novedoso descrito por primera vez recientemente. [176]
(c) HIPEs estabilizadas con mezclas de nanopartículas y tensioactivo (sección 4.4).

El objetivo principal implica los siguientes objetivos parciales:

1. Selección del sistema tensioactivo, para preparar emulsiones estabilizadas con tensioactivos.

2. Preparación y modificación superficial de las nanopartículas con ácido oleico, para su utilización en la estabilización de emulsiones de Pickering de tipo W/O, estabilizadas con partículas.

3. Estudio de la interacción entre los dos emulsionantes empleados, nanopartículas y tensioactivos, y sus implicaciones en la estabilidad de las emulsiones altamente concentradas.

4. Estudio de la distribución de las nanopartículas en los materiales macroporosos obtenidos, en función de diversos parámetros como el tamaño o concentración de nanopartículas. Estudio de la influencia de dicha distribución en la permeabilidad de los materiales.

5. Comparación de las propiedades más importantes de los materiales, tales como textura macroporosa o propiedades mecánicas.

6. Estudio de las propiedades magnéticas y de la actividad fotocatalítica de los nanocompuestos, que contienen nanopartículas de óxido de hierro y de dióxido de titanio, respectivamente.

Plan de trabajo

Para lograr los objetivos mencionados más arriba, se ha llevado a cabo el siguiente plan de trabajo:

1. Preparación y caracterización de nanopartículas de óxido de hierro, con diferentes tamaños medios de partícula.

2. Preparación de nanopartículas de dióxido de titanio utilizando un método mecanoquímico en fase sólida.

3. Modificación superficial de las nanopartículas con ácido oleico.

4. Selección de la mezcla de tensioactivos en el sistema formado por agua / tensioactivos no iónicos etoxilados / aceite (conteniendo estireno y divinilbenceno).

5. Emulsificación por el método de temperatura de inversión de fases utilizando tensioactivos no iónicos etoxilados, y por el método de adición sucesiva de la fase interna, utilizando nanopartículas (Fe_3O_4 y TiO_2) y/o tensioactivo no iónico como emulsionantes.

6. Preparación de nanocompuestos macroporosos mediante la polimerización de la fase externa de emulsiones altamente concentradas (HIPEs) del tipo W/O.

7. Estudio de la interacción entre las nanopartículas de Fe_3O_4 y un tensioactivo polimérico no iónico, mediante determinaciones de tensión interfacial.

8. Caracterización estructural y morfológica de los nanocompuestos macroporosos. Con esta finalidad, se han empleado diversas técnicas: microscopía electrónica (SEM y TEM), picnometría, ensayos mecánicos y medidas de permeabilidad.

9. Evaluación de las propiedades magnéticas (magnetización de saturación y temperatura de bloqueo) de los materiales que contienen nanopartículas de Fe_3O_4.

10. Determinación de la actividad fotocatalítica de los materiales que contienen nanopartículas de TiO_2.

3. EXPERIMENTAL

A continuación se describen los tensioactivos y nanopartículas utilizadas a lo largo del estudio, así como los principales métodos y técnicas de caracterización:

Tensioactivos no iónicos: polietilenglicol alquil éteres de grado comercial, abreviados como R_mEO_n, donde *m* es el número de átomos de carbono de la parte hidrófoba, mientras que *n* es el número aproximado de grupos de óxido de etileno por molécula de tensioactivo. Estos tensioactivos se utilizaron para emulsionar mediante el método de temperatura de inversión de fases (método PIT). También se usó un tensioactivo polimérico de tribloque, Synperonic PE/L-64 (poli(etilenglicol)–poli(propilenglicol)–poli(etilenglicol)) para mejorar la estabilidad de las emulsiones. Por otra parte, las emulsiones preparadas por el método tradicional de adición sucesiva de la fase dispersa sobre la fase continua se estabilizaron con el tensioactivo Hypermer 2296 (HLB=4.9), que es una mezcla de ester de sorbitan y poliisobutenil succínico anhídrido.

Nanopartículas: en este trabajo se han empleado 3 tipos de nanopartículas de óxido de hierro, abreviadas como NP_x, en las que *x* indica el tamaño medio de partícula. Todas ellas fueron modificadas superficialmente con ácido oleico para proporcionar las propiedades hidrófilas y lipófilas adecuadas: NP_3 preparadas por el método de microemulsion, NP_8 sintetizadas por el método de coprecipitación de sales de hierro, y NP_{32}, que fueron adquiridas. Además, se sintetizaron nanopartículas de dióxido de titanio (TiO_2) por un método mecanoquímico de molienda en un molino de bolas de ZrO_2 (ver Figura 1-19 y Figura 3-1).

Métodos: las emulsiones altamente concentradas se han preparado mediante el método PIT y mediante el método clásico de adición lenta, con la ayuda de un agitador tipo vortex. La PIT se ha determinado a través de medidas de conductividad en función de la temperatura (ver Figura 3-2). Cabe mencionar que se han realizado mediciones de tensión interfacial entre las dos fases de las emulsiones que contienen tensioactivo y/o nanopartículas en la fase aceite, utilizando los métodos de volumen de gota y del anillo de Du Noüy.

Técnicas de caracterización: para caracterizar tanto las nanopartículas como los materiales porosos, se han utilizado principalmente técnicas de microscopia electrónica de barrido (SEM) y transmisión (TEM), picnometría (determinación de porosidad), compresibilidad (resistencia a la compresión), permeabilidad, difracción de rayos X (DRX), dispersión de rayos X de bajo ángulo (SAXS), adsorción de nitrógeno y magnetometría SQUID.

4. RESULTADOS, DISCUSIÓN

4.1 FUNCIONALIZACIÓN Y CARACTERIZACIÓN DE LAS NANOPARTÍCULAS

4.1.1 Nanopartículas de óxido de hierro

En este apartado (ver 4.1.1) se ha llevado a cabo una extensa caracterización de los tres tipos de nanopartículas obtenidas: NP_3, NP_8 y NP_{32}, con diámetros medios de partícula de 3, 8 y 32 nm, respectivamente, y todas ellas con predominio de morfología esférica (Figura 4-1). Respecto a la estructura cristalográfica, se ha confirmado mediante DRX que NP_8 y NP_{32} presentan estructuras cristalográficas pertenecientes a la fase magnetita (Fe_3O_4), mientras que en el caso de NP_3 no se pudo distinguir entre maghemita (Fe_2O_3) o Fe_3O_4 debido a la baja resolución de ciertos picos de difracción (ver Figura 10-1 en Apéndice). Para ser utilizadas como emulsionantes, las nanopartículas fueron funcionalizadas con distintas concentraciones de ácido oleico en su superficie. Para comparar el diferente grado de funcionalización, se calculó la adsorción superficial de moléculas de ácido oleico a partir de la fracción de materia orgánica determinada por termogravimetría. Los valores de adsorción superficial fueron de 5,9 (NP_3), 2,5

(NP_8) y 2,1 (NP_{32}) moléculas/nm^2, respectivamente (Tabla 4-1). Dicha adsorción se confirmó mediante espectroscopia infrarroja (Figura 4-3).

Tabla 4-1. Características principales de las nanopartículas de óxido de hierro utilizadas en este trabajo.

Muestra	Fase cristalina [a]	Tamaño medio de partícula (nm)[b]	Área superficial (m^2/g)[c]	Contenido ácido oleico (wt%)[d]	Adsorción superficial de ácido oleico (mol./nm^2)[e]	Dispersabilidad en ST/DVB
NP_3	Maghemita / Magnetita	3	-	45	5,9	Buena
NP_8	Magnetita	8	-	12,4 ± 1,6	2,5	Buena
CNP_{32}	Magnetita	32	48 ± 1	0	0	Mala
NP_{32}	Magnetita	32	-	4,2 ± 0,2	2,1	Mala

[a] Obtenida por difracción de rayos X (DRX). [b] Conteo directo a partir imágenes de microscopía electrónica.[c] A partir de medidas de sorción de nitrógeno (aproximación BET). [d] Obtenido a partir de TGA. [e] Calculado a partir de la densidad del óxido de hierro, de la distribución en tamaño de las nanopartículas y del contenido de ácido oleico de las partículas determinado por termogravimetría.

Otro aspecto que se evaluó cualitativamente fue la dispersión de las nanopartículas en la mezcla de monómeros (estireno y divinilbenceno) que constituye la fase continua en las emulsiones altamente concentradas. Se observó que las dispersiones de NP_3 y NP_8 se mantuvieron estables durante un mínimo de 24 horas, sin observarse sedimentación. No obstante, tanto CNP_{32} (hidrófilas) como NP_{32} (parcialmente hidrófobas), sedimentaron rápidamente, presentando una baja estabilidad. Finalmente, se procedió a la determinación de las propiedades magnéticas (magnetización de saturación (M_s) y temperatura de bloqueo (T_B)) de NP_8 y NP_{32}, utilizando magnetometría SQUID (ver Figura 4-4 y Tabla 4-2). Ambos tipos presentaron M_s elevadas a 300 K, correspondiendo 58.4 emu/g para NP_8 y 76.2 emu/g para NP_{32}. La disminución de M_s al reducir el tamaño de nanopartícula se puede explicar por la pérdida de magnetización debido al desorden de espines en la superficie. La ausencia de histéresis en el ciclo de magnetización indica que NP_8 son superparamagnéticas (T_B de 230 K).

4.1.2 Nanopartículas de óxido de titanio

Para la síntesis de las nanopartículas de TiO_2 se utilizó un método de reacción mecanoquímico en fase sólida y posterior calcinación. Dicho método constituye una alternativa rápida y eficaz a los métodos tradicionales en fase líquida. El precursor de titanio utilizado fue el titanil sulfato ($TiOSO_4$), y el procedimiento consistió en la reacción de este ácido de Lewis con una base (NaOH). Para controlar la liberación de calor durante las reacciones ácido-base muy exotérmicas, se añadió un diluyente sólido (Na_2SO_4). La reacción se inicia por acción mecanoquímica en un molino de bolas (ver Figura 3-1). En una reacción típica se obtienen óxidos de baja cristalinidad con cristales de pequeño tamaño insertados en una matriz de sal que después se elimina mediante un simple lavado con agua.

Este proceso en fase sólida sigue la siguiente reacción modelo:

$$TiOSO_4 \cdot 2H_2O + 2\,NaOH + Na_2SO_4 \rightarrow TiO_2 + 2Na_2SO_4 + 3H_2O$$

El dióxido de titanio se obtuvo en fase amorfa, no observándose picos en el espectro de DRX (Figura 4-6) de ninguna de las fases cristalinas del TiO_2 (anatasa, rutilo o broquita) al completarse la reacción. Debido a que el objetivo era obtener la fase fotocatalíticamente activa (anatasa) del TiO_2, las muestras se calcinaron a temperaturas de hasta 700 ºC. Los espectros de DRX revelaron que la fase anatasa empieza a formarse a los 400 ºC. Temperaturas más altas provocaron un aumento de la cristalinidad de las muestras que se refleja en el tamaño de cristal determinado por la ecuación de Scherrer (ec. 3.1). Dicho tamaño aumentó desde 6 hasta 20 nm al subir la temperatura de calcinación desde 400 hasta 700 ºC (ver Tabla 4-3). Los tamaños de cristal, calculados a partir de la ecuación de Scherrer, fueron muy parecidos a los tamaños de partícula observados por TEM (Figura 4-8 y Figura 4-9), lo que implica que las partículas son monocristalinas. Por otra parte, se determinaron las superficies específicas de las nanopartículas. Debido a la formación de agregados de partículas con tamaños comprendidos entre los 50 y 500 nm, las superficies específicas obtenidas fueron ligeramente inferiores a las superficies teóricas que se hubiesen obtenido para muestras de nanopartículas perfectamente dispersas y con toda su superficie expuesta al gas adsorbato. Dicha agregación fue causada probablemente por el aumento de temperatura durante la reacción mecanoquímica y por el elevado número de colisiones entre partículas. A pesar de ello, las superficies específicas fueron altas, obteniéndose valores de 298 m^2/g para las nanopartículas sin calcinar y 78 m^2/g para las nanopartículas calcinadas a 600 ºC.

Finalmente, se procedió a la evaluación de la actividad fotocatalítica de las nanopartículas en agua mediante la eliminación de un colorante modelo, el azul de metileno (Figura 4-13). El factor más influyente en la actividad catalítica fue la cristalinidad de la fase anatasa de las nanopartículas. La mayor actividad fue observada para el material calcinado a 600 ºC (Tabla 4-4). A pesar de que la superficie específica de estas nanopartículas (78 m^2/g) fue menor que la de las calcinadas a 400 ºC (170 m^2/g), su mayor tamaño de cristal explica la mayor eficacia en la degradación del colorante.

Las partículas de TiO_2 también se modificaron superficialmente con ácido oleico para conferirles hidrofobicidad y poder estabilizar emulsiones del tipo W/O.

4.2 INCORPORACIÓN DE NANOPARTÍCULAS DE ÓXIDO DE HIERRO (NP_3 Y NP_8) EN MATERIALES BASADOS EN POLIESTIRENO-DIVINILBENCENO

4.2.1 Polimerización en *bulk*

Debido a la buena dispersabilidad en solventes orgánicos, se eligieron las nanopartículas de óxido de hierro NP_3 y NP_8 para ser incorporadas en matrices poliméricas de poliestireno entrecruzado con divinilbenceno (monómeros en proporción 4:1). Antes de ser incorporadas directamente en la fase externa de HIPEs del tipo W/O, las nanopartículas se añadieron a la mezcla de monómeros. La polimerización de los monómeros se realizó con el iniciador ADVN (2,2'-Azobis-(2,4-dimetil) valeronitrilo) a 40 ºC. Los resultados indicaron que las nanopartículas NP_3 se incorporaron satisfactoriamente a las matrices poliméricas, y se obtuvieron monolitos no porosos sin separación de fases (ver Figura 4-15). Mediante observaciones de TEM de cortes ultrafinos preparados con un microtomo, se apreció una buena dispersión de las NP_3 dentro del polímero, con poco grado de agregación. Esto se atribuye a la estabilización mediante ácido oleico, que evita la agregación de las nanopartículas hidrófobas durante la polimerización. La concentración de las NP_3 se incrementó hasta el 49% en peso, observándose en este caso una clara segregación de las nanopartículas en dominios (Figura 4-16). No obstante, en dicha estructura las nanopartículas conservaron su individualidad y mediante SAXS se detectó un pico atribuible a la distancia media entre partículas (Figura 4-17). Este pico se desplazó a distancias más cortas al incrementar la concentración de NP_3. En cambio, cuando se repitieron los mismos experimentos con NP_8, los resultados obtenidos fueron distintos. Se alcanzó una menor concentración de NP_8 en el polímero (25%), ya que mayores concentraciones dieron lugar a materiales muy frágiles. Esto se puede atribuir al mayor tamaño de las nanopartículas. Además, en contraste con NP_3, no se detectaron picos de distancias de repetición en los espectros de SAXS. Se interpretó que la mayor polidispersidad de las nanopartículas impide cualquier ordenamiento de las nanopartículas dentro de la matriz.

4.2.2 Polimerización en la fase dispersa de emulsiones diluidas del tipo O/W

Las nanopartículas NP_3 fueron también incorporadas en la fase dispersa de emulsiones diluidas tipo O/W (estabilizadas con tensioactivo) con la mezcla de monómeros formando la fase dispersa. De nuevo, las nanopartículas mostraron una buena estabilidad en el seno de la fase dispersa, y después de la polimerización se confirmó su presencia en las micropartículas, resultantes de la polimerización de las gotas de la fase dispersa (Figura 4-19). Sorprendentemente, las nanopartículas se situaron preferentemente en la superficie de las micropartículas (Figura 4-20). Posiblemente, las nanopartículas se adsorben en la interfase, contribuyendo a la estabilidad de las emulsiones iniciales. Basándose en estos resultados, se estudió la estabilización de emulsiones con nanopartículas únicamente, experimentos que se describen más adelante.

4.2.3 Polimerización de la fase continua de emulsiones altamente concentradas (HIPEs) del tipo W/O preparadas por el método de temperatura de inversión de fases (PIT)

Se realizó la incorporación de las nanopartículas NP_3 y NP_8 en la fase externa de HIPEs del tipo W/O. En una primera etapa se ajustó la composición de la emulsión con el fin de controlar la PIT del sistema. Como se mencionó en la Introducción, este método se basa en el incremento brusco de temperatura de una emulsión inicial O/W (temperatura<PIT) para obtener una emulsión W/O (temperatura>PIT), en sistemas formados por agua, aceite y tensioactivos no iónicos etoxilados. En el presente trabajo se han utilizado tensioactivos de pureza comercial, que poseen polidispersidad en las longitudes de cadena de las partes hidrófila y lipófila.

Inicialmente, se determinó el número HLB (balance hidrófilo-lipófilo, N_{HLB}) de los tensioactivos comerciales $C_{12\text{-}14}(EO)_4$, $C_{13\text{-}15}(EO_5)$ y $C_{13\text{-}15}(EO)_6$ (Tabla 4-5) utilizando la ecuación desarrollada por Kunieda (ec. 4.4). El objetivo fue obtener una PIT ligeramente superior 0 ºC para poder manipular las emulsiones a temperatura ambiente y que las emulsiones fueran estables a 70 ºC, temperatura a la cual se llevarían a cabo las polimerizaciones. Las medidas de PIT se realizaron mediante conductividad en función de la temperatura. La ecuación de Kunieda permite predecir la PIT conociendo el aceite (parámetro N_{oil}) y las características del tensioactivo (N_{HLB}), aunque para tensioactivos comerciales, los valores experimentales pueden variar sustancialmente respecto a las predicciones teóricas. El hidrocarburo alifático tetradecano se añadió a la fase externa junto con los monómeros para aumentar el valor de la PIT. Ello fue necesario ya que si la fase continua se hubiese constituido con un 100% de monómeros, la PIT habría sido inferior a 0 ºC, y por tanto, no se podría realizar la inversión de fases. Se debe tener en cuenta, no obstante, que se requiere una concentración mínima de monómeros, ya que los materiales resultantes después de la polimerización deben ser suficientemente robustos para evitar que colapse su estructura. La concentración de monómero en la fase continua se fijó en un 55% en peso.

Se ha evaluado la influencia de distintos parámetros considerando los tensioactivos utilizados: concentración de monómeros en la fase continua de las emulsiones, fracción de volumen de la fase dispersa y velocidad de agitación del sistema (Figura 4-21 a Figura 4-24). Por ejemplo, dos sistemas tensioactivos con N_{HLB} similares, pero con distinta combinación de tensioactivos (por un lado 70% $C_{13\text{-}15}(EO)_5$ - 30% $C_{13\text{-}15}(EO)_6$ y por otro 25% $C_{12\text{-}14}(EO)_4$ - 75% $C_{13\text{-}15}(EO)_6$ mostraron comportamientos muy distintos aplicando las mismas condiciones de agitación. Mientras que con el primer sistema no se pudo lograr la inversión de fases más allá del 40% de monómeros en la fase continua de las emulsiones, la incorporación de un tensioactivo más hidrófobo ($C_{12\text{-}14}(EO)_4$) permitió alcanzar el 60%, demostrando que tensioactivos más hidrófobos facilitan la inversión de una emulsión O/W a otra W/O.

El sistema seleccionado para llevar a cabo las polimerizaciones fue el siguiente (las relaciones se indican en peso): H_2O / $K_2S_2O_8$ / $C_{12\text{-}14}(EO)_4$ / $C_{13\text{-}15}(EO)_6$ / Synperonic L-64 / estireno / divinilbenceno / tetradecano (89.9 / 0.1 / 0.95 / 2.85 / 0.2 / 2.88 / 0.72 / 2.4). El tamaño de gota de esta emulsión (Figura 4-25) fue más pequeño que los tamaños obtenidos por métodos de alta energía, debido a las bajas tensiones interfaciales que se dan a la temperatura de inversión. Aunque el tamaño de gota aumentó ligeramente durante la polimerización, probablemente debido a coalescencia, los tamaños de poro de los materiales obtenidos fueron pequeños, en el rango comprendido entre 1 y 5 µm (Figura 4-26). En las paredes de dichos poros se observaron conexiones (*pore throats*) (entre 0,1 hasta 2 µm). Como resultado, el material presentó un elevado grado de conectividad. El volumen total de poro de estos materiales fue de 20,5 cm^3/g y la porosidad y densidad del material fueron 95% y 0,05 g/cm^3, respectivamente. Las imágenes de SEM mostraron que la morfología macroporosa obtenida depende de la temperatura de polimerización de la emulsión (60, 65 o 70 ºC, Figura 4-27). Finalmente, también se caracterizó la superficie específica de las espumas. En todos los casos se obtuvieron valores cercanos a 50 m^2/g (Tabla 4-7). Cabe destacar, que estos valores son superiores a los que poseen otros materiales poliméricos macroporosos. Ello puede explicarse por el efecto de la adición del tetradecano en la fase continua de las emulsiones. Dicho compuesto actúa como agente porógeno al quedar atrapado en la red polimérica de estireno entrecruzado con divinilbenceno.

Después de fijar la composición de la emulsión estabilizada con tensioactivos, se procedió a la incorporación de las nanopartículas utilizadas anteriormente (NP_3 y NP_8) en la fase continua de dichas emulsiones. Los ensayos se han efectuado con concentraciones de nanopartículas cercanas al 7% en peso respecto a la fase continua. El primer paso consistió en evaluar el efecto que las nanopartículas tenían sobre la PIT del sistema. Para ello se utilizaron las nanopartículas NP_8. El resultado de las medidas de conductividad demostró que la inversión se produjo prácticamente a la misma temperatura (alrededor de los 9 ºC, Figura 4-29). Por tanto, se puede concluir que las nanopartículas no influyen sobre el proceso de inversión y que no compiten con el tensioactivo por la interfase.

Otro aspecto destacable, es que al incorporar nanopartículas en el seno de la fase continua de las emulsiones, la estructura macroporosa de las espumas no se vio alterada (Figura 4-30). La distribución de NP_3 y NP_8 en las paredes de los polímeros macroporosos se estudió mediante TEM, como en el caso de los materiales descritos previamente. De nuevo, se detectaron diferencias entre ellos. Mientas la distribución de NP_3 fue homogénea en todo el material poroso (Figura 4-31), observándose cierto grado de agregación, la formación de clústeres de nanopartículas fue más evidente en los materiales que contienen NP_8 (Figura 4-32). Esto podría indicar que durante el proceso de emulsificación y/o polimerización la agregación de NP_8 pudo estar favorecida. Finalmente, se determinó la magnetización de saturación (M_s) y la temperatura de bloqueo (T_B) de los nanocompuestos, tanto no porosos como porosos, y se compararon los valores con los obtenidos en las nanopartículas (Tabla 4-8). Como resultado importante cabe mencionar que el valor de M_s por gramo de material magnético es considerablemente menor en el caso de los nanocompuestos. Esto fue especialmente notorio en el caso de los materiales magnéticos que contienen NP_3. Este hecho fue atribuido a efectos oxidativos y superficiales de la polimerización sobre la magnetización de las nanopartículas de óxido de hierro.

4.3 POLÍMEROS MACROPOROSOS OBTENIDOS EN EMULSIONES ALTAMENTE CONCENTRADAS ESTABILIZADAS ÚNICAMENTE CON NANOPARTÍCULAS

4.3.1 Estudios preliminares: influencia de la funcionalización con ácido oleico, y medidas de tensión interfacial

En esta sección se ha estudiado en detalle la formación y estabilización de emulsiones altamente concentradas (HIPEs) con dos tipos de nanopartículas de óxido de hierro funcionalizadas con ácido oleico (NP_8 y NP_{32}). Estas se seleccionaron por poseer distintos tamaños y contenidos de ácido oleico, presentando comportamientos distintos en disolventes orgánicos, demostrando que las dispersiones de NP_8 se mantienen estables, mientras que NP_{32} presentan poca estabilidad y sedimentan rápidamente (ver Figura 4-37). Pese a estas diferencias, ambas nanopartículas permitieron estabilizar emulsiones, como se verá a continuación.

Inicialmente se realizó una serie de experimentos para verificar el papel que el ácido oleico adsorbido en la superficie de NP_8 y NP_{32} desempeña en la estabilización de las emulsiones. Se demostró (Figura 4-35) que 1,5% en peso de NP_8 y NP_{32} (con respecto a la fase continua), con 12,4 y 4,8% en peso de ácido oleico adsorbido en sus superficies, respectivamente, pueden estabilizar emulsiones del tipo W/O. Las emulsiones se prepararon con un 75% de agua (fase dispersa) y 25% de aceite (mezcla de estireno y divinilbenceno en proporción 1 a 1 en peso). Además, se demostró que se requiere la adsorción del ácido oleico sobre las partículas, para obtener emulsiones estables. Ello se confirmó al observar que emulsiones con la misma composición, eran inestables al utilizar únicamente ácido oleico, en ausencia de nanopartículas. Paralelamente, se confirmó la adsorción del ácido oleico por medidas cualitativas de ángulo de contacto, demostrando que las superficies de NP_8 y NP_{32} son parcialmente hidrófobas. Por otra parte, como cabría esperar, se obtuvieron emulsiones del tipo O/W cuando se utilizaron nanopartículas CNP_{32} como estabilizante (nanopartículas NP_{32} sin ácido oleico) debido a la hidrofilia de su superficie. Todas las emulsiones se prepararon mediante el método convencional de adición gota a gota.

Antes de aumentar la fracción en volumen de la fase dispersa (ϕ) de las emulsiones, se llevaron a cabo medidas de tensión interfacial utilizando el anillo de Du Nöuy para identificar un posible mecanismo de estabilización de las emulsiones. En sistemas compuestos de NP_8 dispersas en tolueno (simulando la mezcla de monómeros) y agua se confirmó que las nanopartículas hidrófobas no modifican la tensión interfacial del sistema. Los valores de la tensión interfacial entre el agua y el tolueno, con y sin nanopartículas, fueron cercanos a los 36 mN/m, valor que se corresponde con la tensión interfacial entre el agua y tolueno puros (Tabla 4-9). Por tanto, se pudo concluir que las NP_8 no favorecen la emulsificación debido a una reducción de la tensión interfacial.

4.3.2 Efecto del tamaño, contenido de ácido oleico y concentración de nanopartículas en la formación de las emulsiones

A continuación, se evaluó la máxima fracción de volumen de la fase dispersa (agua) alcanzada en las emulsiones (conocida como *emulsion capacity*, ver Figura 4-38), con diferentes concentraciones de partículas (C_p). Se observaron dos regímenes claramente distintos a valores de concentración de nanopartículas inferiores y superiores a l,5%, valor a partir del cual no se observó un aumento apreciable de la *emulsion capacity*. Esto sugiere que a dicha concentración es probable que la superficie de las gotas esté saturada de partículas. A bajas concentraciones de partículas, NP_8 se mostraron más eficientes que NP_{32}. A modo de ejemplo, únicamente con 0,25% de NP_8 se pudo estabilizar una emulsión W/O con el 82% en volumen de agua. Aunque el tamaño característico de gota fue extremadamente grande (del orden de milímetros), la emulsión fue estable por largos periodos de tiempo (Figura 4-38 (b)). En cambio, NP_8 mostraron una mayor eficacia a concentraciones de partículas más altas, obteniéndose emulsiones con un 92,5% de fase dispersa con un 3% de NP_{32}. Debido a la buena dispersión de NP_8 en la fase continua, se argumentó que a concentraciones de partículas bajas, la formación de un menor número de agregados de nanopartículas podría facilitar la estabilización de mayor superficie de gotas. En cambio, al aumentar la concentración de nanopartículas, la formación de agregados de NP_{32} de mayor tamaño formando una red alrededor de las gotas, en combinación con su menor contenido de ácido oleico, podría favorecer la emulsificación de mayores contenidos de fase dispersa. Cabe subrayar que la presencia de agregados de NP_{32} en la superficie de las gotas se confirmó por microscopía óptica (Figura 4-40).

Finalmente, se evaluó sistemáticamente la influencia del tamaño de nanopartícula en emulsiones con distintas concentraciones de fracción de volumen de la fase dispersa (de 75 a 92,5%, Figura 4-39). Como se ha descrito en la bibliografía, la disminución de tamaño de partícula mejoró la estabilidad de las emulsiones con respecto a la sedimentación. Es importante mencionar que, debido al carácter magnético de las partículas adsorbidas en la interfase agua-aceite, dichas emulsiones pudieron ser desestabilizadas rápidamente utilizando un imán (Figura 4-42).

4.3.3 Preparación de polímeros macroporosos a partir de emulsiones del tipo Pickering estabilizadas con nanopartículas de óxido de hierro (NP_8 y NP_{32})

Las mismas emulsiones descritas en el apartado anterior se utilizaron como plantilla para la síntesis de polímeros macroporosos mediante la polimerización de la fase continua de dichas emulsiones. En esta ocasión, se utilizó el iniciador AIBN (α,α’-azoisobutironitrilo) al 1% en peso con respecto al peso de los monómeros. Como ya se señaló en la introducción, si la mojabilidad de la superficie de las nanopartículas se ajusta correctamente, las partículas pueden quedar fuertemente adsorbidas en la interfase. En nuestro caso, se prepararon emulsiones con distintos valores de fracción en volumen de fase dispersa, estabilizadas con distintas concentraciones de NP_8 y NP_{32} (Tabla 4-10). La buena estabilidad de las emulsiones durante la polimerización permite la obtención de materiales porosos con tamaños de poro equivalentes a los tamaños de gota observados en las emulsiones (Figura 4-43). La presencia de nanopartículas en el polímero se confirmó por la atracción del material en forma de monolito a un imán. Una de las ventajas de este método es la obtención de monolitos con diversas formas, dependiendo del molde en el que se llevan a cabo las polimerizaciones.

Los materiales obtenidos poseen distribuciones de tamaño de poro bimodales, con un predominio de macroporos pequeños (de aproximadamente 20 μm), pero con presencia de macroporos más grandes, desde 120 hasta 800 μm. La población de poros más grandes disminuye al aumentar la concentración del emulsionante, tal como se puede apreciar en la (Figura 4-45(a)). Cabe destacar que estos tamaños tan grandes (mayores de 100 μm) suelen observarse en emulsiones de Pickering descritas por otros autores.[100]. En las emulsiones de Pickering, el mecanismo que controla el tamaño de las gotas a bajas concentraciones de partículas se denomina *limited coalescence*.[29] En dicho proceso, las gotas más pequeñas coalescen formando gotas más grandes hasta que el área interfacial entre el aceite y el agua queda totalmente recubierto por partículas.

La característica principal de los materiales obtenidos es que presentan una estructura de poros cerrada (*closed pores*). A diferencia de los sistemas preparados a partir de emulsiones estabilizadas con tensioactivo, no se observaron conexiones entre poros (Figura 4-44). Esto se explica por la estabilidad de los films formados entre gotas adyacentes durante la polimerización y por el mayor tamaño de las partículas en comparación con los tensioactivos, lo que produce un mayor grosor de las paredes entre macroporos. Esta estructura de poros cerrados limita enormemente el flujo de gases o líquidos. La Tabla 4-10 presenta los parámetros físicos más importantes de los materiales sintetizados. Su porosidad (P) es proporcional a la fracción de volumen de la fase dispersa inicial de las emulsiones, aunque los valores de P son siempre ligeramente superiores. Esto se debe al aumento de la densidad de la fase continua durante la polimerización. La densidad de las paredes (*skeletal density* (ρ_s)) aumenta y por tanto P es siempre algo mayor a la fracción de volumen de fase dispersa inicial. Respecto a los valores de la *skeletal density*, es interesante indicar que se obtuvieron valores (1,13 g/cm^3) superiores a la densidad del poliestireno (1,05 g/cm^3). Sin duda, ello es debido a la incorporación de las nanopartículas de óxido de hierro.

La estructura interna de las paredes poliméricas se caracterizó por microscopía electrónica de transmisión (TEM) en cortes ultrafinos (aprox. 60 nm) de los materiales. Los cortes se realizaron mediante ultramicrotomía. Las imágenes obtenidas por TEM permiten observar la adsorción de las partículas en la interfase (polímero-aire) y su estado de agregación. Llama la atención que se obtuvieron comportamientos distintos en los dos tipos de muestras estudiados. Por un lado se encontró que NP_{32} (Figura 4-46) se localizan exclusivamente en la superficie de los poros del polímero, lo que equivale a la interfase agua-aceite de la emulsión. A pesar del alto grado de agregación observado en las dispersiones de NP_{32}, estas nanopartículas son capaces de situarse en la interfase formando una capa gruesa. En las muestras estudiadas (1,5-5% de nanopartículas) la configuración encontrada siempre fue similar. Esto sugiere que, para lograr tamaños de gota más pequeños sean probablemente necesarias concentraciones muy altas de NP_{32}, y que la estabilización por monocapa sea improbable.

Por otra parte, aunque también se encontraron NP_8 en la interfase adoptando una estructura de multicapas, se detectó un número elevado de partículas en el interior de las paredes, lo que equivaldría a la fase continua de las emulsiones (Figura 4-47). Ello podría originarse por la combinación de varios factores: por una parte, debido a que las NP_8 poseen una mayor hidrofobicidad, es probable que puedan mantenerse dispersas en la fase oleosa en lugar de migrar a la interfase, reduciendo su capacidad como emulsionantes. Otra causa que explique la presencia de NP_8 en el seno de la fase continua, es que las partículas de menor tamaño pueden desorberse de la superficie con mayor facilidad.[63] Otra hipótesis sería que la funcionalización de la superficie de las NP_8 no hubiera sido homogénea, obteniéndose algunas partículas con más ácido oleico que otras.

Por último, se estudiaron las propiedades mecánicas de los monolitos obtenidos. Se determinó la resistencia a la compresión (σ) y el módulo de Young de los materiales mediante el test de compresión, en función de la concentración y tipo de nanopartícula y de la fracción en volumen de la fase dispersa en las emulsiones (Tabla 4-11). En el análisis de los resultados de las curvas de esfuerzo vs. deformación, se observó que la desviación estándar de los valores era muy elevada, especialmente en el caso de muestras preparadas con bajas concentraciones de partículas. Esto se atribuyó al drenaje de la fase continua durante la polimerización, por efecto de la gravedad, obteniéndose grosores distintos de las paredes de los films a la largo del eje vertical. Estas diferencias se minimizan cuando la concentración de nanopartículas en los materiales es alta (5%). Debido a este hecho, se decidió tomar como referencia la resistencia a la compresión específica (σ_s), calculada dividiendo σ por la densidad del material en cada zona estudiada. En relación a la concentración de nanopartículas, se observó que al aumentar la concentración de NP_8 desde 0,5 hasta 3% en peso, σ_s aumentó desde 0.006 hasta 0.017 $MPa \cdot m^3 \cdot Kg^{-1}$ (Figura 4-49). Este aumento se debió principalmente a la reducción del tamaño de poro, lo que mejora el comportamiento mecánico de los materiales. En otro experimento llevado a cabo, se mostró que los materiales preparados con NP_8 poseen valores de σ_s superiores (30-40%) a los materiales preparados con las NP_{32} (Figura 4-50). Se concluyó que la causa podría ser la presencia de un mayor número de nanopartículas, así como una distribución no sólo en la interfase sino también en el interior del polímero.

4.3.4 Preparación de polímeros macroporosos a partir de emulsiones del tipo Pickering estabilizadas con nanopartículas de dióxido de titanio (TiO_2)

El mismo procedimiento de emulsificación, basado en la adición gota a gota de la fase dispersa sobre la fase continua, fue adoptado en la obtención de materiales utilizando emulsiones de Pickering con nanopartículas de TiO_2. Estas nanopartículas fueron modificadas superficialmente de forma análoga a las NP_{32}. La concentración de ácido oleico fue ajustada para obtener emulsiones altamente concentradas (HIPEs) del tipo W/O. Como se mencionó anteriormente, las nanopartículas obtenidas mediante el método mecanoquímico, poseen un alto grado de agregación, formando clústeres de tamaños entre 50 y 500 nm. Se obtuvieron emulsiones empleando nanopartículas sin calcinar (superficie específica cercana a los 300 m^2/g) y calcinadas a 600 ºC (80 m^2/g de superficie específica). A su vez, estas emulsiones se utilizaron como plantilla para obtener los correspondientes polímeros macroporosos.

La elevada agregación de las nanopartículas parece limitar la efectividad emulsionante y no se apreciaron diferencias significativas en el tamaño de poro de los materiales obtenidos. Las imágenes de SEM (Figura 4-53) mostraron que los materiales están constituidos por numerosos poros de gran tamaño (alrededor de 700 μm) con algunos macroporos de menor tamaño (1-20 μm), situados en los *Plateau borders*. Comparando con otros resultados con la misma composición (3% de nanopartículas y 80 vol% de fase dispersa), los materiales preparados a partir de emulsiones estabilizadas con nanopartículas de óxido de hierro presentaron tamaños de poro mucho más pequeños. Esto demuestra que dichas partículas (Fe_3O_4), con menor agregación, son más eficaces para estabilizar interfases aceite-agua. El mayor tamaño de poro causó que los materiales monolíticos con nanopartículas de TiO_2 obtenidos fuesen frágiles Otro aspecto a destacar observado en las imágenes de SEM, es que las nanopartículas se sitúan en preferencialmente en el exterior de los poros, quedando parcialmente expuestas en las paredes de los materiales (Figura 4-53(c)).En conclusión, se puede afirmar que las partículas de TiO_2 estudiadas poseen un grado de agregación elevado y ello podría ser la causa de la baja estabilidad de emulsiones de Pickering preparadas con estas partículas.

Como se demostró anteriormente, las nanopartículas calcinadas a 600 ºC estaban formadas por cristales de anatasa de unos 13 nm (Tabla 4-3), por lo que dichas nanopartículas mostraron una alta eficacia fotocatalítica. Se realizaron los experimentos de degradación del colorante azul de metileno, utilizando los materiales macroporosos (Figura 4-54). Se comprobó que presentaban actividad fotocatalítica, aunque la cinética de degradación fue más lenta que en el caso de las nanopartículas solas.

4.4 POLÍMEROS MACROPOROSOS OBTENIDOS EN EMULSIONES ALTAMENTE CONCENTRADAS ESTABILIZADAS CON MEZCLAS DE NANOPARTÍCULAS DE ÓXIDO DE HIERRO Y TENSIOACTIVO NO IÓNICO

Los resultados anteriores de obtención de materiales porosos en emulsiones de Pickering, han mostrado que se obtienen materiales con poros cerrados. Por ello, se exploró la posibilidad de aumentar la interconectividad de los poros, añadiendo bajas concentraciones de tensioactivo. Esto se realizó mediante la adición de de un tensioactivo no iónico (Hypermer 2296) en las emulsiones iniciales de Pickering estabilizadas con nanopartículas de óxido de hierro (NP_8 y NP_{32}). En esta sección se describen dos estrategias: la primera ha consistido en preparar las emulsiones mezclando ambos emulsionantes en la fase continua antes de la emulsificación, mientras que en la segunda el tensioactivo se ha añadido sobre la emulsión de tipo Pickering una vez formada.

4.4.1 Medidas de tensión interfacial

En primer lugar, se procedió a la determinación de las tensiones interfaciales entre las fases de tolueno conteniendo el tensioactivo Hypermer 2296 a diferentes concentraciones (en presencia o en ausencia de las partículas NP_8, NP_{32} y CNP_{32}) y agua (Figura 4-55). La determinación de las tensiones interfaciales en la región de bajas concentraciones de tensioactivo se realizó con el anillo de Du Nöuy, mientras que para la región de altas concentraciones se utilizó el método del volumen de gota. El fundamento de ambas técnicas se haya descrito detalladamente en la parte experimental. En el sistema sin nanopartículas, únicamente con tensioactivo, se observó que la tensión disminuyó desde un valor inicial de 36,2 mN/m hasta 2,8 mN/m (4% de tensioactivo). No obstante, en el gráfico se observa que a partir de 0,1% de tensioactivo (5,9 mN/m) la tensión varía poco.

A continuación, se estudió la influencia de la adición de dicho tensioactivo en presencia de una concentración constante de nanopartículas (1,5%) en la fase de tolueno. Los resultados mostraron grandes diferencias entre los valores con/sin partículas a concentraciones inferiores al 1% de tensioactivo. A estas concentraciones, los valores de tensión interfacial en presencia de partículas (NP_8, NP_{32} y CNP_{32}) fueron más altos que los determinados sin nanopartículas. Las diferencias de tensión interfacial, en función de la concentración de tensioactivo, entre los sistemas con y sin partículas, se atribuyeron a la adsorción inicial de tensioactivo sobre la superficie de las partículas. Dicha adsorción se confirmó más adelante mediante medidas termogravimétricas (Figura 4-57). En el caso de CNP_{32} se alcanzó un valor de adsorción constante (0,068 g de tensioactivo por gramo de CNP_{32}) a una concentración de tensioactivo del 0,5%. La adsorción de tensioactivo sobre las partículas provocó que la superficie de éstas se volviera más hidrofóbica (Figura 4-58).

En el gráfico de tensiones interfaciales (Figura 4-55), se puede observar que en presencia de tensioactivo, la tensión disminuye muy poco hasta alcanzar concentraciones de tensioactivo elevadas. Se puede deducir que prácticamente todo el tensioactivo añadido, hasta una determinada concentración, se adsorbe en la superficie de las partículas y no contribuye a la disminución de tensión interfacial. También es importante destacar que se encontraron diferencias entre los tres sistemas: el tensioactivo se adsorbió más en la superficie de CNP_{32}, seguido por NP_8 y finalmente por NP_{32}. La mayor adsorción sobre CNP_{32} se puede atribuir a la mayor hidrofilia de la superficie de estas partículas, ya que no están funcionalizadas con ácido oleico. Al utilizar nanopartículas CNP_{32}, se necesitó una concentración de tensioactivo 2.5 ordenes de magnitud más elevada que en el sistema sin nanopartículas, para observar una reducción de los valores de tensión. De nuevo, ello se atribuye a que el tensioactivo añadido se adsorbe sobre las partículas y no contribuye a la reducción de la tensión. En referencia a los dos otros tipos de nanopartículas, el tensioactivo se adsorbió mayormente en NP_8 que en NP_{32}, posiblemente debido a la mayor superficie específica de NP_8. La Figura 4-56 muestra las diferencias de valores de tensión de cada sistema respecto al sistema de referencia sin nanopartículas: a modo de ejemplo, para una concentración de tensioactivo del 0,5%, los valores de las tensiones interfaciales aumentaron en 27,3 mN/m, 24,3 mN/m y 17.0 mN/m, con la adición de las nanopartículas CNP_{32}, NP_8 y NP_{32}, respectivamente.

En conclusión, los resultados comparativos de la tensión interfacial, en sistemas con mezclas de tensioactivo y nanopartículas, permiten deducir que el tensioactivo se adsorbe sobre las partículas y que ello influye enormemente sobre los valores de tensión interfacial.

4.4.2 Emulsiones altamente concentradas estabilizadas con mezclas de nanopartículas de óxido de hierro y tensioactivo no iónico

Debido a la adsorción del tensioactivo no iónico sobre las nanopartículas de óxido de hierro, se decidió investigar el efecto de dicha interacción sobre la estabilidad de HIPEs con 80% de fase acuosa, simulando las mismas concentraciones de emulsionantes que se utilizaron en las medidas de tensión interfacial. Los ensayos de estabilidad mostraron una buena correlación con los resultados obtenidos por tensiometría. Para simplificar, en este resumen únicamente se describirán los resultados obtenidos con las nanopartículas NP_8 y NP_{32}.

La estabilidad de las HIPEs con respecto al cremado, la sedimentación y la coalescencia se determinó midiendo las alturas de las fases separadas, así como de la emulsión residual a las 24 horas y a temperatura ambiente (Figura 4-59 y Figura 4-60). Como se describió anteriormente en ausencia de tensioactivo, NP_8 y NP_{32} fueron capaces de estabilizar por sí mismas HIPEs del tipo W/O, es decir, formando emulsiones de tipo Pickering. Al añadir concentraciones bajas de tensioactivo, se observó que el tamaño de gota de las emulsiones aumentaba notablemente (hasta valores de 1 mm, Figura 4-61), y se observó un gran aumento de la inestabilidad de los sistemas. A una determinada concentración de tensioactivo del 0,1 o 0,05%, en presencia de NP_8 o NP_{32}, respectivamente, se observó rápida separación de fases. Dichas concentraciones de tensioactivo corresponden aproximadamente a la situación de saturación del tensioactivo sobre las partículas. Ello produce un desplazamiento de las partículas lejos de la interfase, aumentando progresivamente la inestabilidad de las emulsiones. Se interpretó que la superficie de las nanopartículas se hidrofobiza progresivamente debido a la adsorción de tensioactivo en la partículas, lo que conlleva a la reducción de su capacidad para actuar como emulsionante. En consecuencia, según las predicciones teóricas la energía necesaria para la desorción de las partículas disminuye. Las nanopartículas son progresivamente eliminadas de la interfase, y se produce separación de fases al no haber suficiente concentración de tensioactivo para estabilizar las HIPEs.

Sin embargo, cuando la concentración de tensioactivo se aumentó hasta valores de aproximadamente del 1%, se obtuvieron de nuevo emulsiones estables del tipo W/O, aunque estabilizadas principalmente por tensioactivo, como revelan los menores tamaños de gota (1-50 μm) observados por microscopía óptica (Figura 4-62). Se observó una disminución gradual del tamaño de gota hasta un 4% de tensioactivo. Por tanto, se produce una transformación de emulsiones de tipo Pickering a emulsiones estabilizadas con tensioactivo pasando por una región intermedia de separación de fases (Figura 4-63).

La desorción de NP_{32} de la interfase de emulsiones estabilizadas con altas concentraciones de tensioactivo (>1%) se confirmó por imágenes de microscopía óptica (Figura 4-62(b)), ya que se detectaron agregados de nanopartículas de hasta 2 o 3 μm de tamaño en el seno de la fase continua de las emulsiones. La posición exacta del otro tipo de nanopartículas, NP_8, se examinó mediante TEM, como se describirá a continuación.

4.4.3 Polímeros macroporosos preparados a partir de emulsiones altamente concentradas estabilizadas con mezclas de nanopartículas de Fe_3O_4 y tensioactivo no iónico

Los dos tipos de emulsiones obtenidas en la sección anterior, estabilizadas con mezclas de nanopartículas y tensioactivo, se utilizaron como plantilla para la obtención de materiales macroporosos. Inicialmente, estos materiales se caracterizaron por microscopía electrónica de transmisión (TEM), con la finalidad de estudiar la distribución de las nanopartículas en el polímero.

En primer lugar, se observaron los materiales preparados con NP_{32} a diferentes concentraciones de tensioactivo en las emulsiones iniciales: 10^{-2}, 1,5 y 4%. De acuerdo con la Figura 4-61 (c), la adición de pequeñas concentraciones de tensioactivo produjo un aumento de tamaño de gota de las HIPEs. Después de la polimerización, se observó que aunque la mayor parte de las NP_{32} permanecen en la superficie de los poros, también aparecen agregados de NP_{32} adheridas a la interfase o en el polímero, indicando que algunas de las nanopartículas han sido expulsadas de la interfase (Figura 4-64(b-d)). Esto se atribuyó a la adsorción del tensioactivo sobre NP_{32}, produciendo un desplazamiento de las nanopartículas. Por tanto, se demuestra que la fracción de NP_{32} que no se haya adsorbida en la interfase, no contribuye a la estabilización de la emulsión, y por ello, dicha emulsión presenta mayores tamaños de gota. En concordancia con las imágenes obtenidas por microscopía óptica, las imágenes de TEM demostraron que a concentraciones de tensioactivo del 1,5%, todas las partículas han sido transferidas al interior de las paredes del polímero en forma de agregados (Figura 4-65). Por lo tanto, estas emulsiones están estabilizadas con tensioactivo. Cabe destacar, que la distribución de dichos aglomerados no fue homogénea, apreciándose zonas sin presencia de ningún agregado de NP_{32}.

Para los materiales preparados a partir de emulsiones de Pickering con NP_8, de nuevo se observó una fracción importante de NP_8 localizadas sobre la superficie de los macroporos, apreciándose también partículas individuales o pequeños agregados en el interior del polímero. Como en el caso de NP_{32}, al añadir pequeñas concentraciones de tensioactivo (0.01%), se detectaron algunos agregados de partículas en el seno del polímero, aunque cerca de la interfase polímero-aire (Figura 4-66(a-c)). Al aumentar la concentración de tensioactivo progresivamente hasta el 4%, se observó una expulsión gradual y casi completa de las nanopartículas fuera de dicha interfase (Figura 4-67), especialmente en los poros de gran tamaño. No obstante y a diferencia de NP_{32}, algunas NP_8 todavía permanecen adsorbidas en la superficie del polímero, principalmente en los poros de menor tamaño Figura 4-67(e)). Esto se debe probablemente a la mayor superficie específica de NP_8. Otra diferencia observada con los materiales que contienen NP_{32}, es que las nanopartículas (NP_8) expulsadas de la interfase se distribuyen homogéneamente en el seno del polímero, sin observarse aglomerados de gran tamaño. Se puede afirmar por tanto, que a pesar de utilizar una concentración de tensioactivo elevada (4%), una fracción de NP_8 todavía permanece adsorbida en la interfase aceite-agua.

A continuación, se caracterizaron sistemáticamente la estructura macroporosa, la resistencia a la compresión específica (σ_s) y la permeabilidad de los polímeros macroporosos preparados con mezclas de partículas y tensioactivo (Tabla 4-12). Confirmando lo observado en las imágenes de TEM, se observó por SEM que las paredes de los macroporos de los materiales preparados con 0.01% de tensioactivo no presentan conexiones, indicando que el tensioactivo no está situado en la interfase (Figura 4-68(b)). También se mostró que el tamaño de poro disminuyó rápidamente al aumentar la concentración de tensioactivo, y que los poros de mayor tamaño desaparecen (Figura 4-69 y Figura 4-70). Además, los poros presentan conexiones de entre 0,7 y 5 μm, características de los materiales preparados a partir de emulsiones estabilizadas con tensioactivo (Figura 4-69(c)). La reducción del tamaño de poro conllevó a la mejora de σ_s de 0,0066 a 0,0259 $MPa \cdot m^3 \cdot Kg^{-1}$ para materiales preparados únicamente con NP_8 o con una mezcla de NP_8 y 4% del tensioactivo no iónico Hypermer 2296 (Figura 4-71). Como resultado a destacar, la inclusión de sólo el 1,5% de NP_8 en una emulsión estabilizada con un 4% de tensioactivo, incrementó la σ_s en un 20% (Figura 4-73).

Todos estos resultados confirman que el aumento de la concentración de tensioactivo en emulsiones con concentración de nanopartículas constante, produce una transformación de emulsiones de Pickering a emulsiones estabilizadas con tensioactivo. Como ya se ha mencionado arriba, esto se debe al desplazamiento de las partículas que se desorben de la interfase.

Por otro lado, la permeabilidad no depende únicamente de las conexiones existentes entre los poros, sino que depende enormemente de la distribución de tamaño de poros. El valor máximo de permeabilidad (0,9 Da) se obtuvo en las muestras sintetizadas a partir de emulsiones con un 2% de tensioactivo (siempre con un 1,5 de NP_8). Al aumentar la concentración de tensioactivo al 4%, el valor de permeabilidad disminuyó un 33% debido a la disminución del tamaño de poro (Figura 4-71).

Por último, se determinó la magnetización de saturación (M_s) y la temperatura de bloqueo (T_B) de los polímeros macroporosos preparados con las nanopartículas superparamagnéticas NP_8, a partir de medidas magnetométricas (SQUID). Las medidas de magnetización vs. campo magnético aplicado (Figura 4-74) revelaron que la M_s es proporcional a la cantidad de nanopartículas magnéticas incorporadas en los materiales, independientemente del uso de emulsiones estabilizadas con nanopartículas (NP_8) o con mezclas de nanopartículas (NP_8) y tensioactivo (Hypermer 2296). Se puede concluir, por tanto, que el polímero no influye en la magnetización de las nanopartículas. Además, la ausencia de histéresis indica que los materiales retienen el comportamiento superparamagnético de NP_8.

Debido a las enormes diferencias respecto a la localización de las nanopartículas (NP_8) en función de la concentración de tensioactivo Hypemer 2296, se consideró oportuno evaluar el efecto de dicha localización en el valor de la temperatura de bloqueo (T_B) de NP_8 (Figura 4-75). Es conocido que las interacciones entre partículas (tipo dipolo-dipolo) modifican la barrera energética anisotrópica, alterando el comportamiento magnético de los sistemas nanoparticulados (ver ec. 4.6).[280] La T_B está directamente relacionada con dicha barrera. Mediante ciclos de *zero field-cooling* (ZFC) y *field cooling* (FC) se determinó que la T_B de las NP_8 es 230 K. Este valor disminuyó hasta 130 K para materiales preparados sólo con 1,5% de NP_8. Al aumentar la concentración de tensioactivo en las emulsiones, se obtuvieron T_B de 105 y 60 K para 2 y 4% de tensioactivo, respectivamente. Estos resultados demuestran que el desplazamiento de las NP_8 desde la interfase a la fase oleosa, produce que las interacciones entre partículas disminuyan y consecuentemente su T_B. Por tanto, se reduce la barrera energética para la transición superparamagnética de las NP_8.

4.4.4 Polímeros macroporosos preparados a partir de emulsiones altamente concentradas estabilizadas nanopartículas de Fe_3O_4 y posterior adición de tensioactivo no iónico

La adición de diferentes concentraciones del tensioactivo no iónico Hypermer 2296 a emulsiones altamente concentradas (HIPEs), descrita en el apartado anterior, provocó la transformación de una emulsión de tipo Pickering a una emulsión estabilizada con tensioactivo. Como resultado, se obtuvieron materiales macroporosos con poros de gran tamaño y con baja permeabilidad (a partir de emulsiones de Pickering), y materiales con poros de pequeño tamaño (1-30 μm) e interconectados (a partir de emulsiones estabilizadas con tensioactivo). No obstante, la permeabilidad de estos últimos materiales no es elevada, debido a que el diámetro de las conexiones entre poros es relativamente pequeño. Con el objetivo de obtener materiales con propiedades intermedias, es decir, que posean poros de gran tamaño y con elevada permeabilidad, se adoptó una metodología alternativa. Se partió de Pickering HIPEs del tipo W/O estabilizadas con NP_8 (1,5% en peso) y se añadieron pequeñas cantidades de tensioactivo (1-3% en peso) después de emulsionar. A continuación, se llevó a cabo la polimerización de la fase externa de dichas emulsiones. La estructura macroporosa de los polímeros se presenta en la

Figura 4-78(b). Sorprendentemente, la distribución de tamaño de los macroporos no se vio prácticamente modificada por la incorporación del tensioactivo, si la comparamos con una emulsión de Pickering (Figura 4-79). No obstante, se observó que las paredes de los poros poseen conexiones entre ellos. Esto es especialmente importante en los poros de mayor tamaño (Figura 4-78(b) y Figura 4-81).

Probablemente, la presencia de conexiones en las paredes de los poros indica que existen zonas en la interfase polímero-aire (o aceite-agua en la emulsión inicial) que están libres de partículas. Esto se confirmó por TEM (ver Figura 4-80). Las imágenes también demostraron que los poros de menor tamaño permanecen recubiertos por partículas. Se concluyó que la adición de poca concentración de tensioactivo (1%) con agitación leve, provoca que el tensioactivo se adsorba en la superficie de las nanopartículas, expulsándolas parcialmente de la interfase. Posiblemente, parte del tensioactivo también se adsorbe en la interfase, contribuyendo a la estabilidad de las emulsiones. El hecho de que el tamaño de poro no disminuya, podría explicarse por las condiciones suaves de agitación aplicadas durante la adición del tensioactivo.

Como resultado de la conexión entre los poros de mayor tamaño, estos materiales presentan permeabilidades altas (0,5 - 2,5 Da). Además, los valores de resistencia a la compresión son comparables a los de los sistemas preparados con emulsiones estabilizadas únicamente con tensioactivo (2 - 5 MPa) (ver Figura 4-82).

Por lo tanto, la adición posterior de tensioactivo a emulsiones de Pickering, permite aumentar la permeabilidad de los materiales macroporosos resultantes.

5. PRINCIPALES CONCLUSIONES

1. Preparación, caracterización y funcionalización de partículas de óxido de hierro

- Se han obtenido dos tipos de nanopartículas superparamagnéticas siguiendo métodos descritos en la literatura, basados en la co-precipitación de sales de hierro: NP_3 y NP_8, donde 3 y 8 indican el tamaño medio de partícula. Dichas nanopartículas y NP_{32} (adquiridas) fueron funcionalizadas superficialmente con ácido oleico. Se han obtenido distintos grados de adsorción superficial de ácido oleico (moléculas de ácido oleico/nm^2 de nanopartícula): 5,9, 2,5 y 2,1 para NP_3, NP_8 y NP_{32}, respectivamente.

2. Preparación, caracterización y funcionalización de partículas de dióxido de titanio

- Se han sintetizado nanopartículas de TiO_2 (fase anatasa) a partir de un método mecanoquímico en estado sólido, simple y efectivo. En ausencia de calcinación, se obtuvieron partículas no cristalinas. Como resultado del método de síntesis, las nanopartículas presentaron un elevado grado de agregación, observándose agregados de entre 50 y 500 nm.

- Las nanopartículas calcinadas a 600 ºC presentaron la mayor actividad fotocatalítica debido a su elevada cristalinidad (tamaño de cristal de anatasa de 20 nm). Estas nanopartículas también se funcionalizaron con ácido oleico, confiriendo hidrofobicidad a sus superficies.

3. Incorporación de partículas de óxido de hierro (NP_3 y NP_8) en materiales no porosos de poli(estireno-divinilbenceno)

- Las nanopartículas NP_3 y NP_8 se han incorporado con éxito en las matrices poliméricas no porosas hasta concentraciones de 49 y 25% en peso, respectivamente. Esto se atribuyó a la presencia del ácido oleico en su superficie, que previno un exceso de agregación de las nanopartículas y posterior separación de las partículas al polimerizar. NP_3 también se han incorporado en micropartículas poliméricas, observándose una localización preferencial en la interfase polímero-aire.

4. Incorporación de nanopartículas de óxido de hierro (NP_3 y NP_8) en materiales porosos de poli(estireno-divinilbenceno), utilizando emulsiones altamente concentradas preparadas por el método de temperatura de inversión de fases (PIT)

Selección del sistema tensioactivo mediante la determinación de la temperatura de inversión de fases en sistemas formados por agua/tensioactivos no iónicos/aceite

- La adición de NP_3 o NP_8 en la fase continua de las emulsiones altamente concentradas (HIPE) no modificó la PIT del sistema, demostrando que las nanopartículas no interfieren en el proceso de inversión de fases. Después de la polimerización, se observó que NP_3 se dispersan mejor que NP_{32} en las paredes del polímero. Cierta agregación pudo originarse durante el proceso de emulsificación.

- Los nanocompuestos macroporosos presentaron altos volúmenes de poro (20.5 cm^3/g) y bajas densidades (0.05 g/cm^3). Respecto a las propiedades magnéticas, tanto la saturación de magnetización, como la temperatura de bloqueo de las nanopartículas incorporados en los polímeros, disminuyeron en relación a las nanopartículas solas. Dichas disminuciones están asociadas a efectos superficiales y oxidativos durante la polimerización y a la reducción de las interacciones entre partículas, respectivamente.

5. Polímeros macroporosos obtenidos a partir de emulsiones altamente concentradas de tipo Pickering

Emulsiones altamente concentradas estabilizadas con nanopartículas de Fe_3O_4

- Se han estabilizado satisfactoriamente emulsiones altamente concentradas de Pickering (Pickering HIPEs) del tipo W/O con nanopartículas funcionalizadas con ácido oleico: NP_8 (12.4 wt%) y NP_{32} (4.4 wt%). La formación de las emulsiones se consiguió gracias a la hidrofobicidad parcial de las nanopartículas, debido a la adsorción del ácido oleico. Se han podido alcanzar elevados contendidos de fase dispersa (92,5 vol%).

- La adsorción de las partículas funcionalizadas sobre las gotas, impartiendo estabilidad estérica, parece ser el mecanismo principal de estabilidad de las emulsiones. Cabe destacar, que los valores de tensión interfacial entre la fase oleosa y la fase acuosa no se ven afectados por la presencia de nanopartículas.

Caracterización los materiales macroporosos que contienen las nanopartículas de Fe_3O_4

- Después de polimerizar en la fase externa de las emulsiones, los materiales mostraron una estructura de poros cerrada debido a la capa gruesa de nanopartículas que se forma alrededor de las gotas (poros). Se han obtenido materiales con elevada porosidad (77-95%) y con distribución de tamaño de poro bimodal. La población de poros pequeños posee tamaños de 10-20 µm, mientras que la población de poros grandes es de entre 100-700 µm.

- Por TEM se ha demostrado que las nanopartículas NP_{32} están localizadas exclusivamente en la interfase polímero-aire, mientras que numerosas NP_8 se encuentran también dispersas en el polímero. Esto se puede atribuir al mayor contenido de ácido oleico en la superficie de NP_8. Los valores de resistencia a la compresión de los materiales que contienen NP_8 fueron superiores a los mostrados por los materiales que contienen NP_{32}.

Materiales macroporosos preparados a partir de emulsiones de Pickering estabilizadas con nanopartículas de TiO_2

- El mismo procedimiento se utilizó para obtener nanocompuestos macroporosos con nanopartículas de TiO_2 contenidas en las paredes de los materiales. La elevada agregación de las nanopartículas limitó la eficiencia de las nanopartículas como emulsionantes. No obstante, los materiales retuvieron parte de la actividad fotocatalítica mostrada por las nanopartículas.

6. Nanocompuestos macroporosos obtenidos a partir de emulsiones altamente concentradas (HIPEs) estabilizadas con mezclas de nanopartículas de Fe_3O_4 i tensioactivo no iónico

Formación de Pickering HIPEs

- Se han observado tres regiones distintas al aumentar la concentración de un tensioactivo no iónico (Hypermer 2296) en Pickering HIPEs estabilizadas con 1,5% de nanopartículas de óxido de hierro. A bajas concentraciones**,** el tensioactivo se adsorbe preferentemente en las nanopartículas y estas son progresivamente expulsadas de la interfase. Esto provoca que un incremento de gota de las emulsiones. A una determinada concentración de tensioactivo, se produce una separación de fases de las emulsiones. A altas concentraciones de tensioactivo (1%), se obtienen de nuevo HIPEs del tipo W/O, pero en este caso estabilizadas con tensioactivo, ya que las nanopartículas hidrófobas permanecen en el seno de la fase continua.

Caracterización de los materiales

- El desplazamiento progresivo de las nanopartículas desde la interfase al seno de la fase continua, se ha confirmado por TEM. Se han encontrado diferencias significativas entre el comportamiento de NP_8 y NP_{32}. Mientras que la totalidad de NP_{32} son expulsadas de la interfase y se encuentran en forma de agregados en el seno de la fase continua, algunas NP_8 permanecen adheridas en la interfase, incluso a altas concentraciones de tensioactivo.

- Los materiales preparados a partir de las emulsiones estabilizadas con tensioactivo mejoran sus propiedades mecánicas debido a la reducción del tamaño de los poros. Además, debido a la aparición de conexiones entre poros estos materiales son permeables a los gases. No obstante el tamaño pequeño de dichas conexiones limita los valores de permeabilidad. En relación a las propiedades magnéticas, cabe destacar que la temperatura de bloqueo de NP_8 disminuye progresivamente al desplazar las nanopartículas de forma gradual, desde la interfase al seno de la fase continua de las emulsiones.

- La adición de una concentración baja del tensioactivo Hypermer 2296 a una emulsión de Pickering ya formada, acompañada de una leve agitación, permite la obtención de emulsiones con tamaños similares a los logrados en la emulsiones de Pickering. Esto produce que los materiales resultantes muestran elevadas permeabilidades (0,5-2,5 Da).

10 APPENDIX

10.1 SUPPORTING INFORMATION

10.2 PUBLICATIONS

10.1 SUPPORTING INFORMATION

X-ray diffraction patterns of iron oxide nanoparticles

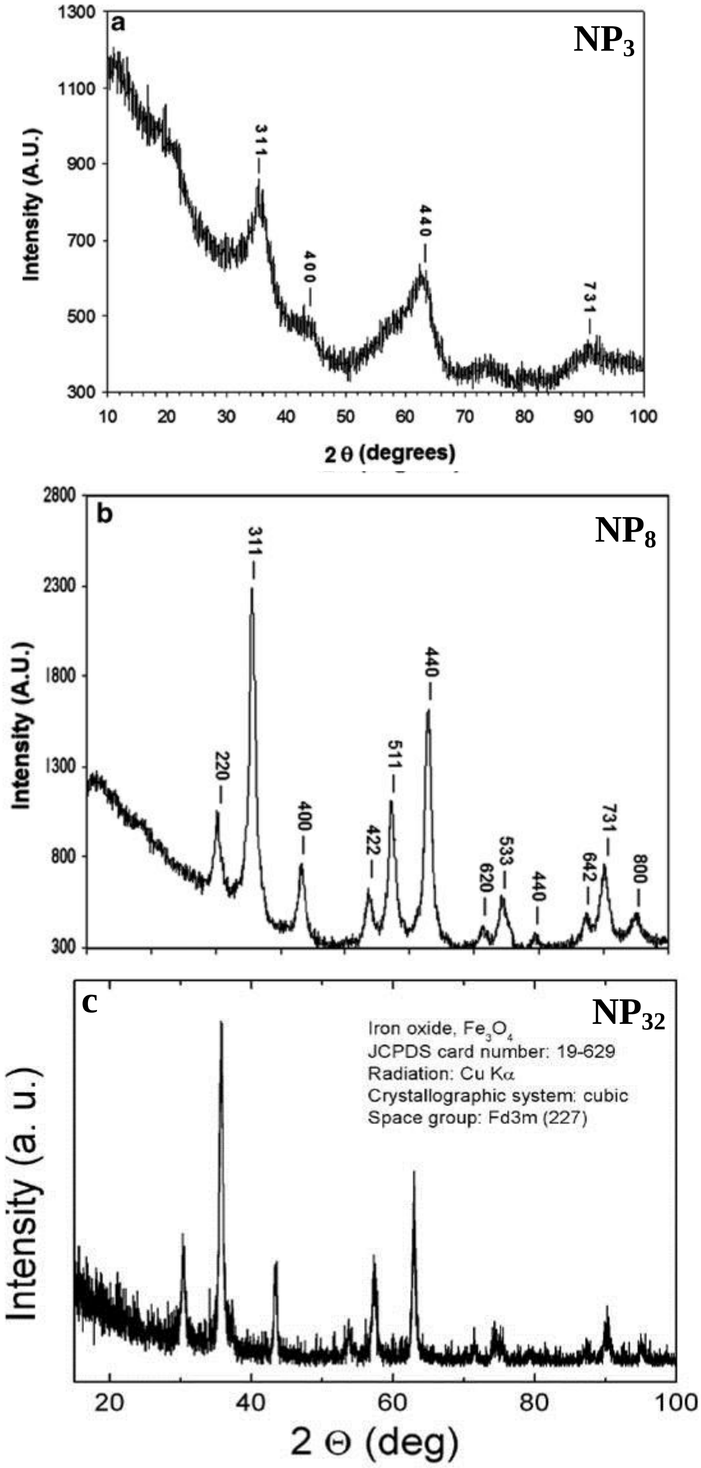

Figure 10-1. X-ray diffraction patterns for the different iron oxide nanoparticles used in this PhD thesis; (a) NP_3; (b) NP_8; (c) NP_{32}.

UV-visible adsorption spectra for nanocomposites containing Ag and Au nanoparticles

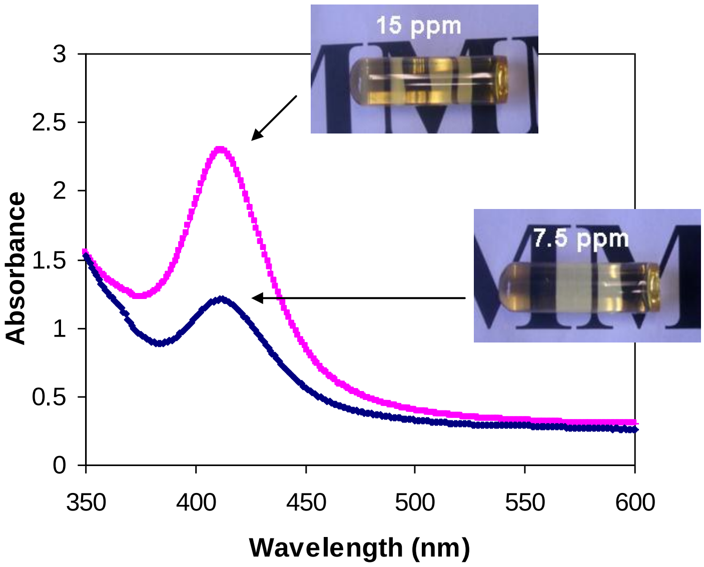

Figure 10-2. UV-visible absorption spectrum of poly(styrene-divinylbenzene) non-porous materials containing oleate capped Ag nanoparticles. The peak corresponds to the surface plasmon resonance of the nanoparticles.

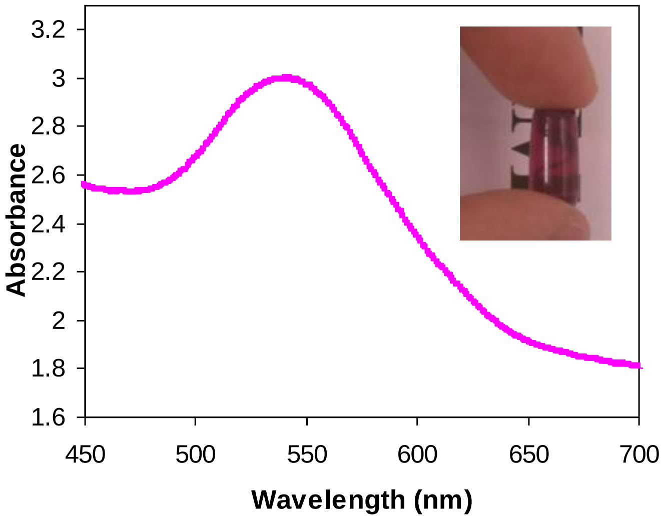

Figure 10-3. UV-visible absorption spectrum of poly(styrene-divinylbenzene) non-porous materials containing Au nanoparticles. The peak corresponds to the surface plasmon resonance of the nanoparticles. The nanoparticles were synthesized in situ using reverse reactive microemulsions.

Visual aspect of Pickering emulsions stabilized with NP_{32}

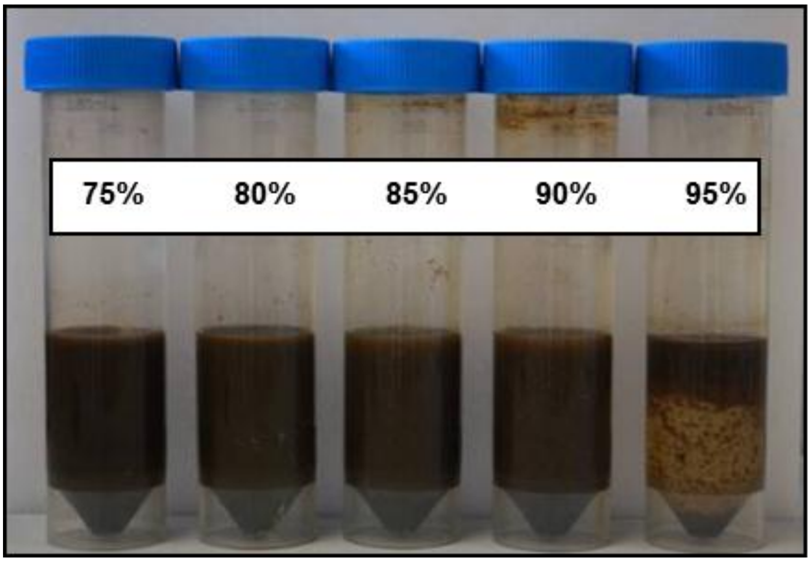

Figure 10-4. Emulsions with 1.5 wt% NP_{32} concentration as a function of the water volume fraction.

Thermogravimetric analysis of the TiO_2 nanoparticles functionalized with oleic acid

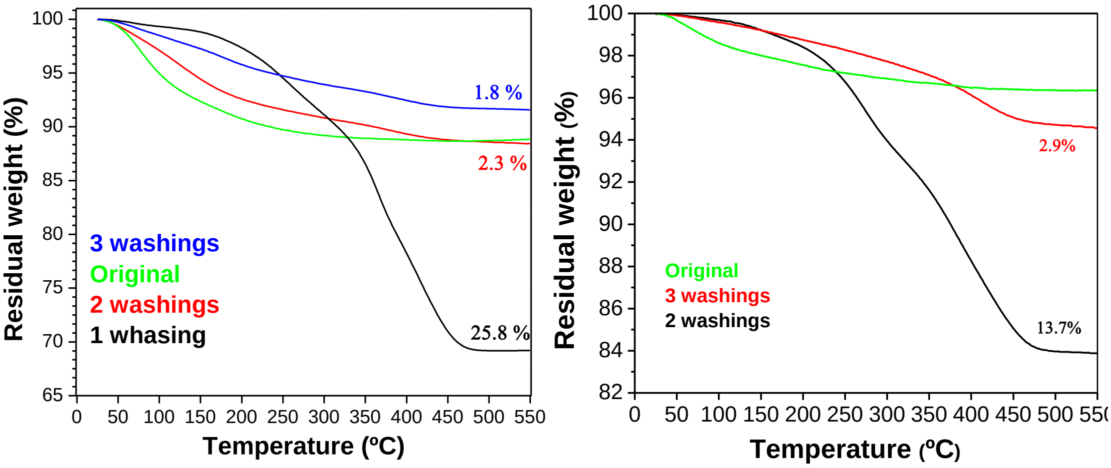

Figure 10-5. Thermogravimetric analysis for oleic acid surface-modified titanium dioxide nanoparticles (left) without calcination and (right) and calcined at 600 ºC after several washing cycles. Total weight loss is indicated above each curve. Oleic acid content was derived from the curves. Nanoparticles were prepared by a mechanochemical reaction.

Interfacial tension values: influence of nanoparticle addition

Table 10-1. Influence of particle addition on the toluene-water interfacial tension[a] values obtained at 25 ºC, for toluene solutions with increasing Hypermer 2296 concentration. in the presence (1.5 wt%) or the absence of different types of nanoparticles. Measurements in the NP_8 system were carried out with 1.5 wt% of NP_8 in the toluene phase. NP_{32} and CNP_{32}, with different surfactant concentration on their surfaces, were removed from toluene solutions (1.5 wt%) prior the measurements.

[Hypermer 2296]/wt%[b]	Hypermer 2296	CNP_{32}	NP_{32}	NP_8
0	36.2 ± 0.2	36.3 ± 0.3	36.3 ± 0.3	35.7 ± 0.2
1E-4	36.1 ± 0.2	36.3 ± 0.2	36.2 ± 0.2	35.6 ± 0.2
1E-3	30.5 ± 0.2	30.3 ± 0.2	36.3 ± 0.1	35.4 ± 0.2
2.5E-3	26.2 ± 0.1	-	-	-
5E-3	19.5 ± 0.1	-	-	-
1E-2	16.5 ± 0.1	36.1 ± 0.2	33.6 ± 0.3	35.2 ± 0.2
2.5E-2	11.7 ± 0.2	-	31.5 ± 0.2	-
5E-2	8.2 ± 0.4	35.5 ± 0.2	25.2 ± 0.2	32.6 ± 0.2
0.1	5.9 ± 0.1	32.4 ± 0.2	18.7 ± 0.1	27.9 ± 0.1
0.15	-	26.9 ± 0.2	-	25.1 ± 0.2
0.25	4.9 ± 0.2	14.6 ± 0.2	9.7 ± 0.1	15.2 ± 0.1
0.5	4.5 ± 0.2	7.3 ± 0.1	5.1 ± 0.1	9.0 ± 0.2
1.0	3.4 ± 0.1	3.6 ± 0.1	3.3 ± 0.1	4.33 ± 0.03
2.0	3.0 ± 0.1	2.97 ± 0.03	-	-
4.0	2.8 ± 0.1	2.6 ± 0.1	2.7 ± 0.1	3.7 ± 0.1

[a] The values above and behind the green line in the table were obtained using the Du Noüy ring and the drop-volume method, respectively. [b] Surfactant concentrations are expressed with respect to the toluene weight.

Interfacial tension and emulsion stability: influence of NP_8 concentration

From Figure 10-6 it can be seen that up to 1 wt% of NP_8, the interfacial tension value remain constant at approximately 3.5 mN/m. This is the lowest value reached for the system containing NP_8 (see Figure 10-1). The addition of more NP_8 increases the surface area available for surfactant adsorption, thus resulting in higher interfacial tensions due to the reduction of free surfactant molecules. At 3 wt% of NP_8 the interfacial value was 7.0 mN/m. These results confirm the depletion of the surfactant solution due to strong Hypermer 2296 adsorption onto the nanoparticle surfaces.

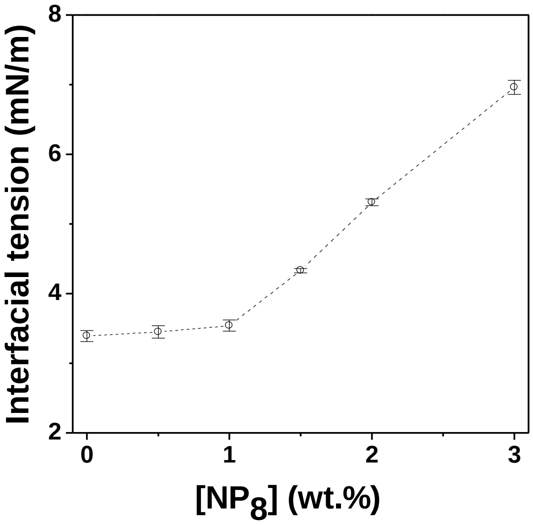

Figure 10-6. Toluene-water interfacial tension (25 ºC) vs. concentration of NP_8 in toluene, at 1 wt% Hypermer 2296 concentration. Lines are simply drawn to guide the eye.

Figure 10-7 shows the visual aspect of emulsions after 24 hours at 25 ºC, varying nanoparticle (from 0 to 3 wt% NP_8) concentration, but keeping the surfactant concentration constant (1 wt%). No sedimentation occurred up to 1.0 wt% Hypermer 2296. Above this concentration, the emulsions underwent sedimentation (destabilization), and a thin layer of monomer with NP_8 is released. Exactly the same concentrations of both emulsifiers were employed in the interfacial tension test described above (Figure 10-6). Both results are in general agreement.

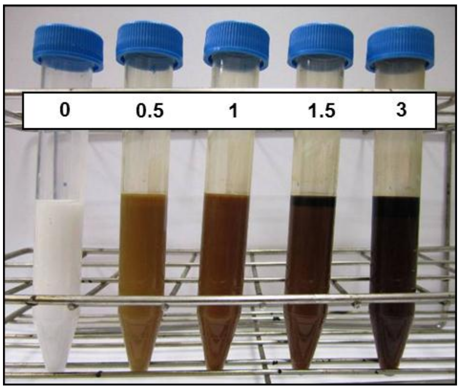

Figure 10-7. Appearance of emulsions 24 hours after its preparation (25 ºC), containing increasing NP_8 concentrations (ranging from 0 to 3 w.%) at constant Hypermer 2296 loading (1 wt%). The water-oil volume ratio was 80:20 in all cases.

Optical microscope images

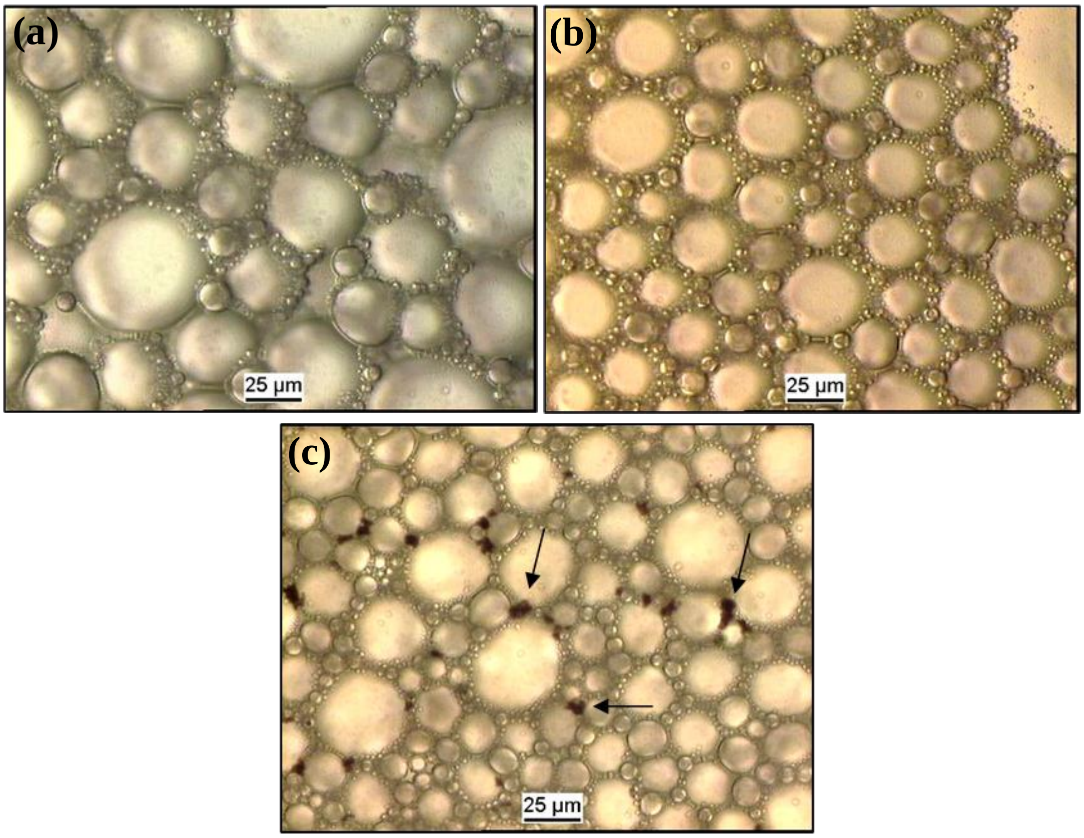

Figure 10-8. Optical microscope images of HIPEs having 80 % internal phase volume, and stabilized with (a) 1.5 and (b) 4 wt% Hypermer 2296 surfactant, and (c) with a mixture of 1.5 wt% surfactant and 1.5 wt% CNP_{32}. Black arrows indicate CNP_{32} aggregates.

Transmission electron microscopy (TEM) images

NP$_8$

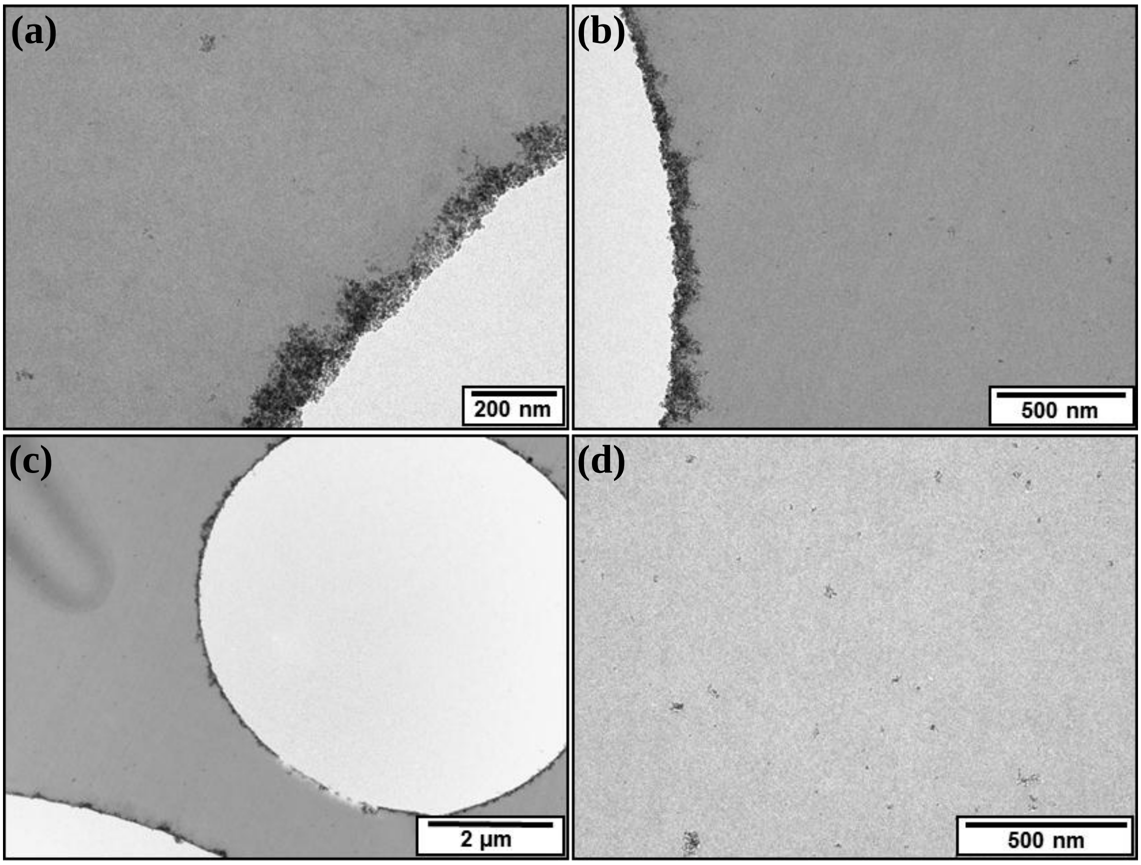

Figure 10-9. Representative TEM images of ultramicrotome slides (around 60 nm thick) showing how the nanoparticles (NP$_8$) are distributed in the polymer matrix of macroporous polymers. Samples were obtained from HIPEs with an 80 % internal phase volume and stabilized solely with 1.5 wt% NP$_8$; (a-c) Polymer-air interfaces; (d) polymer wall.

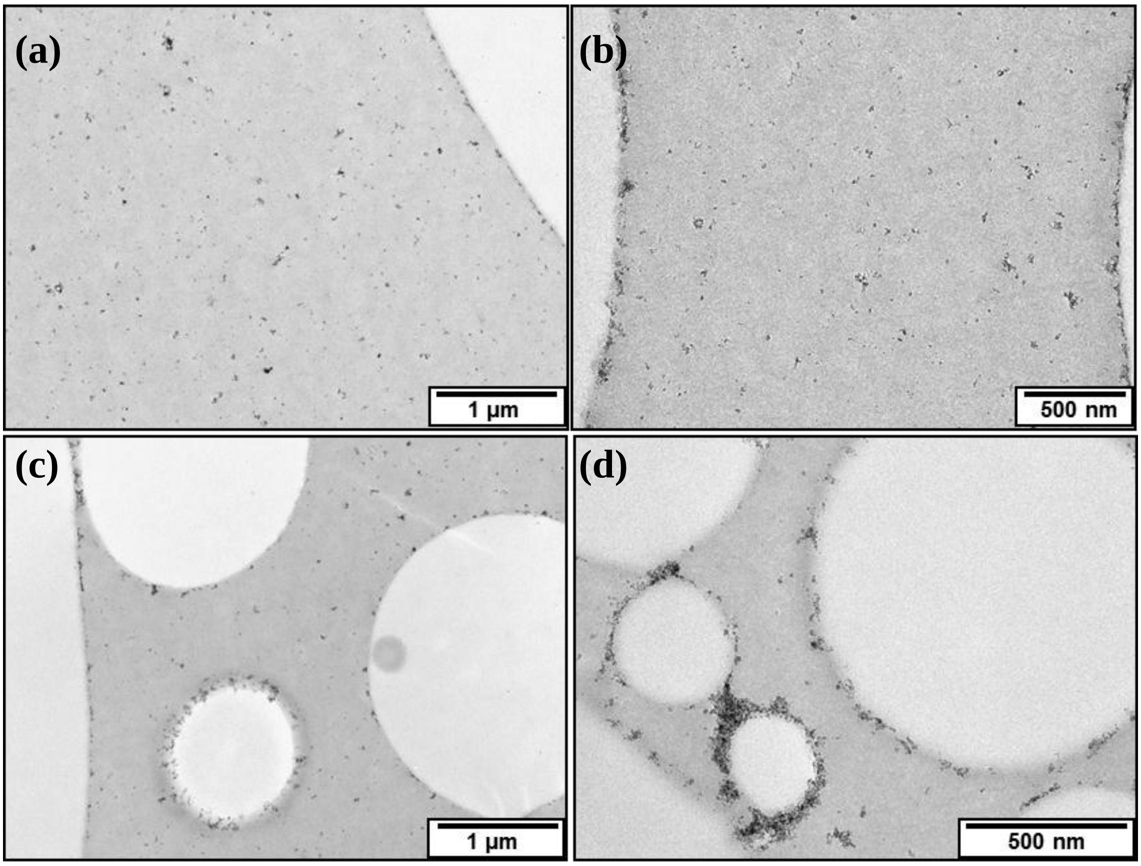

Figure 10-10. Representative TEM images of ultramicrotome slides (around 60 nm thick) showing how the nanoparticles (NP_8) are distributed in the polymer matrix of macroporous polymers. Samples were obtained from HIPEs with an 80 % internal phase volume and stabilized with a mixture of 1.5 wt% NP_8 and 1.5 wt% Hypermer 2296.

CNP_{32}

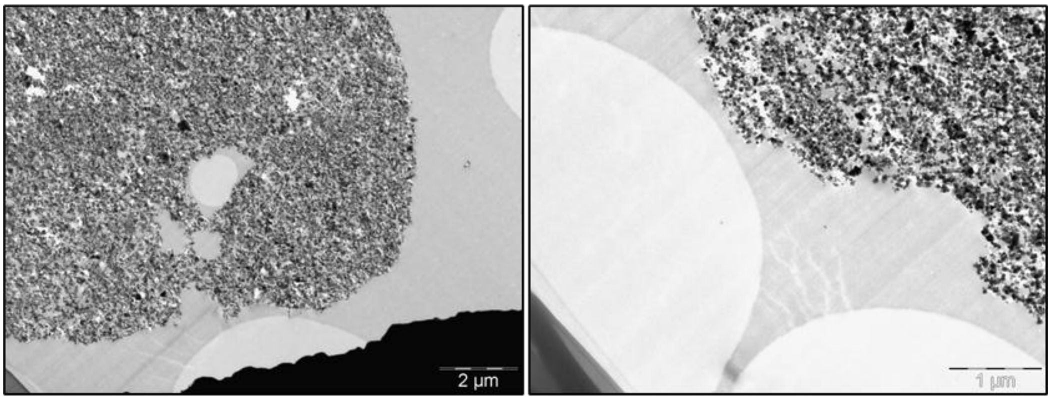

Figure 10-11. Representative TEM images of ultramicrotome slides (around 60 nm thick) showing how the nanoparticles (NP_{32}) are distributed in the polymer matrix of macroporous polymers. Samples were obtained from HIPEs with an 80 % internal phase volume and stabilized with a mixture of 1.5 wt% NP_{32} and 4 wt% Hypermer 2296.

Scanning electron microscopy images

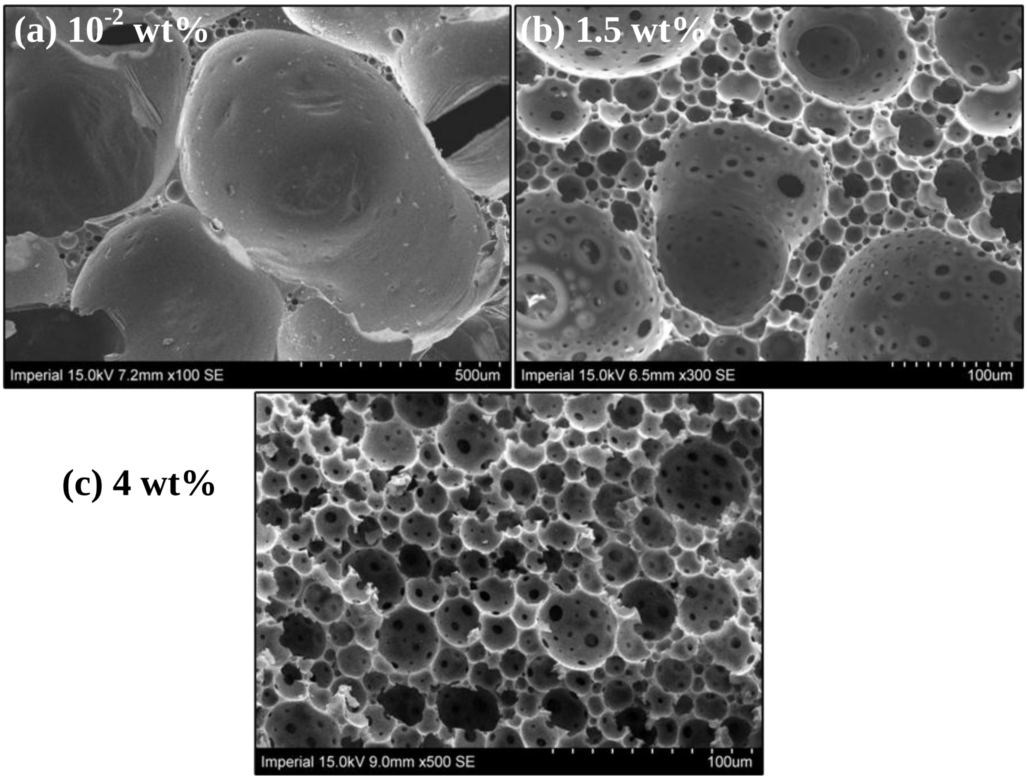

Figure 10-12. SEM images of macroporous polymers synthesized from HIPEs containing a mixture of NP_{32} nanoparticles (1.5 wt%) and Hypermer 2296 surfactant at different concentrations: (a) 10^{-2} wt%; (b) 1.5 wt%; (c) 4 wt%. In all cases the internal phase volume fraction of the emulsions was 80 %.

Magnetic properties: magnetization vs. magnetic field (M-H)

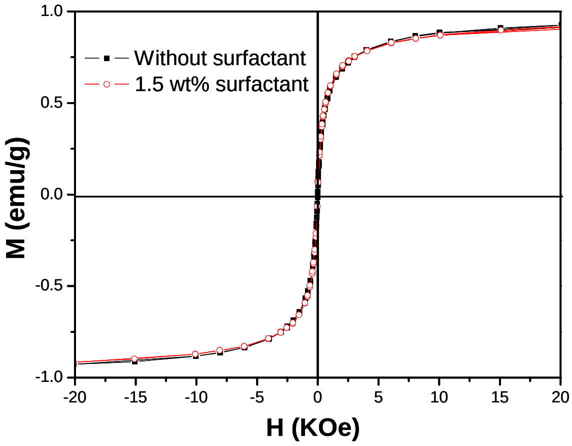

Figure 10-13. Magnetization per gram of material vs. applied magnetic field for macroporous polymers prepared from a Pickering HIPE stabilized with 1.5 NP_8 (without surfactant, black line), and from a HIPE containing a mixture of 1.5 wt% NP_8 and 2 wt% Hypermer 2296 surfactant (red line). The measurements were carried out at 300 K. Magnetization saturation is not modified by the incorporation of surfactant in the emulsions.

10.2 PUBLICATIONS

The work described in this thesis has so far led to the following journal paper, in which A.Vílchez was a corresponding author:

1. Vílchez, A., Rodríguez-Abreu, C., Esquena, J., Menner, A., Bismarck, A. Macroporous polymers obtained in highly concentrated emulsions stabilized solely with magnetic nanoparticles. *Langmuir*, **2011**, *27*, 13342-13352.

Other journal papers related to highly concentrated emulsions and to the incorporation of nanoparticles in polymer matrices, co-authored by A. Vilchez with great experimental contribution.

2. Ghosh, G., Vílchez, A**.**, Esquena, J., Solans, C., Rodríguez-Abreu, C. Preparation of ultra-light magnetic nanocomposites using highly concentrated emulsions**.** *Materials Chemistry and Physics*, **2011**, *130*, 786-793.

3. Ghosh, G., Vílchez, A., Esquena, J., Solans, C., Rodríguez-Abreu, C. Preparation of Porous Magnetic Nanocomposite Materials Using Highly Concentrated Emulsions as Templates. *Progress in Colloid and Polymer Science,* **2011**, Volume 138, 161-164.

4. Molina, R., Vílchez, A., Canal, C., Esquena, J. Wetting porperties of Polystyrene/Divinylbenzene Crosslinked Porous Polymers obtained from W/O Highly concentrated emulsions. *Surface and Interface Analysis*, **2009**, *41*, 371-377

5. Romeo, H.E., Vílchez, A**.**, Esquena, J., Hoppe, C.E., Williams, R.J.J. Polymerization-induced phase separation as a one-step strategy to self-assemble alkanethiol-stabilized gold nanoparticles inside polystyrene domains dispersed in an epoxy matrix. *European Polymer Journal*, **2012**, *48*, 1101-1109.

6. Nestor, J., Vílchez, A., Solans, C., Esquena, J. Facile Synthesis of Meso/Macroporous Dual Materials with Ordered Mesopores Using Highly Concentrated Emulsions Based on a Cubic Liquid Crystal. *Langmuir,* **2012**, DOI : 10.1021/la30380

The two first publications are annexed to the present PhD Thesis (see next pages) as part of the results described in these works are included in the present PhD thesis.

Langmuir
ARTICLE
pubs.acs.org/Langmuir

Macroporous Polymers Obtained in Highly Concentrated Emulsions Stabilized Solely with Magnetic Nanoparticles

Alejandro Vílchez,*[†,‡] Carlos Rodríguez-Abreu,[§] Jordi Esquena,[†] Angelika Menner,[‡] and Alexander Bismarck*[,‡]

[†]Institute for Advanced Chemistry of Catalonia, Consejo Superior de Investigaciones Científicas (IQAC-CSIC), CIBER de Bioingeniería, Biomateriales y Nanomedicina (CIBER-BBN), Jordi Girona 18-26, 08034 Barcelona, Spain

[‡]Department of Chemical Engineering, Polymer & Composite Engineering (PaCE) Group, Imperial College London, South Kensington Campus, London SW7 2AZ, U.K.

[§]International Iberian Nanotechnology Laboratory (INL), Av. Mestre José Veiga, 4715-310 Braga, Portugal

Supporting Information

ABSTRACT: Magnetic macroporous polymers have been successfully prepared using Pickering high internal phase ratio emulsions (HIPEs) as templates. To stabilize the HIPEs, two types of oleic acid-modified iron oxide nanoparticles (NPs) were used as emulsifiers. The results revealed that partially hydrophobic NPs could stabilize W/O HIPEs with an internal phase above 90%. Depending upon the oleic acid content, the nanoparticles showed either an arrangement at the oil−water interface or a partial dispersion into the oil phase. Such different abilities to migrate to the interface had significant effects on the maximum internal phase fraction achievable and the droplet size distribution of the emulsions. Highly macroporous composite polymers were obtained by polymerization in the external phase of these emulsions. The density, porosity, pore morphology and magnetic properties were characterized as a function of the oleic acid content, concentration of NPs, and internal phase volume of the initial HIPEs. SEM imaging indicated that a close-cell structure was obtained. Furthermore, the composite materials showed superparamagnetic behavior and a relatively high magnetic moment.

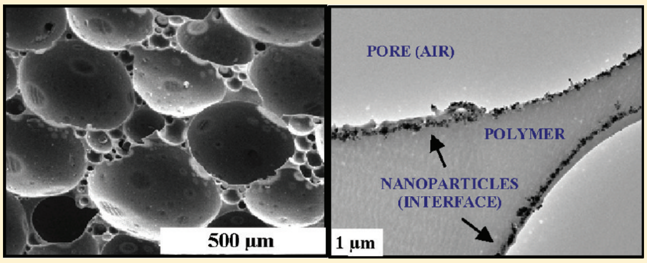

INTRODUCTION

Polymeric nanocomposites typically consist of a polymeric matrix possessing embedded particles with at least one characteristic length in the nanometer range. By combining both components in a single material, any additional property coming from the inorganic part can be directly imparted to the polymer. One of the advantages of such materials is the large nanoparticle−matrix interface. Because of the commercial interest in these materials, much research has been carried out in recent years.[1] It is well established that optical, mechanical, thermal, and chemical properties can be enhanced by using nanoparticles (NPs). Such advanced functional materials have applications as hydrogen storage systems, electrical conductors, or optical devices.[2]

Generally speaking, NP−polymer nanocomposites can be obtained in two different ways.[3] In the in situ approach, the NPs are synthesized using a monomer as the dispersion medium. However, in the ex situ technique the NPs are first synthesized and then embedded or incorporated into the medium before polymerization or cross-linking is carried out. Both techniques mentioned above have been applied either in the bulk,[4,5] in an emulsion,[6] or in highly concentrated emulsions[7] (as well as in gel systems[8,9]) in order to obtain nonporous (e.g., ultrathin films), particulate (e.g., latex), or macroporous nanocomposites, respectively.

Highly concentrated emulsions, also called high internal phase emulsions (HIPEs), are characterized by possessing a volume fraction of the disperse phase that exceeds 0.74, which corresponds to the critical value for the most compact packing of monodisperse spherical droplets.[10,11] HIPEs can be used as templates for the preparation of macroporous materials, also called polyHIPEs,[12] via the polymerization of the external (continuous) emulsion phase.[13,14] The first patent on the subject was registered by Unilever.[15] Over the past two decades, the research has been mainly focused on controlling the open-cell structure of polyHIPEs. The external phases of typical emulsion templates were in many cases formed by mixtures of styrene cross-linked with divinylbenzene.[16] The polymerized materials have typically densities of as low as 0.02 g/cm^3, porosities of up to 95%, and pore sizes ranging from 1 to 50 μm. More recently, several reports have proposed the integration of metal nanostructures (such as gold[17] or palladium NPs[18]) in already formed polyHIPEs. Such materials were used as catalyst supports. However, their synthesis processes consisted of a two-step method. An alternative approach based on a single-step method

Received: August 19, 2011
Published: September 09, 2011

Table 1. Composition of HIPEs and Physical Properties of Poly-Pickering HIPEs after the Polymerization of the Continuous Phase of the HIPEs[a]

sample	Φ (vol)[b]	Cp (w/w %)[c]	ρb (g/cm^3)[d]	P (%)[e]	average diameter (μm)[f]	average diameter (μm)[g]
PNP1	75	0.5	1.09 ± 0.01	79.5 ± 0.7	21 ± 12	436 ± 108
PNP2	75	1.5	1.09 ± 0.01	78.3 ± 0.4	22 ± 16	154 ± 38
PNP3	75	3.0	1.13 ± 0.01	80.1 ± 0.4	18 ± 13	124 ± 38
CNP4	75	3.0	1.12 ± 0.01	81.1 ± 1.0	37 ± 22	237 ± 92
CNP5	85	3.0	1.13 ± 0.01	88.7 ± 1.2	32 ± 22	310 ± 83
CNP6	92.5	3.0	1.13 ± 0.01	94.0 ± 1.3[h]	27 ± 15	669 ± 189
CNP7	85	5.0	1.13 ± 0.01	87.5 ± 0.6	30 ± 19	287 ± 75
PNP8	85	5.0	1.13 ± 0.01	88.2 ± 1.0	24 ± 15	378 ± 98

[a] PNP and CNP indicate the use of synthesized and commercial magnetite nanoparticles, respectively. [b] Internal phase volume. [c] Nanoparticle weight percentage with respect to the total monomer weight. [d] Bulk or skeletal density. [e] Porosity. [f] Average pore diameter corresponding to the smaller size populations. [g] Average pore diameter corresponding to the larger size populations. [h] Estimated by mass/volume measurements.

has been developed by Menner et al. and described in a sequence of articles. In the first stage, they started adding SiO_2 nanoparticles,[19] carbon nanotubes, and TiO_2 NPs[20] to the external phase of W/O HIPEs, giving rise to polyHIPEs with enhanced mechanical properties. Subsequently, they took advantage of the ability of the nanoparticles to stabilize emulsions (typically denoted as Pickering emulsions[21]). Pickering HIPEs with high internal phase volume contents were stabilized using small amounts of oleic acid surface-modified SiO_2 (HIPEs with up to 92% internal phase)[22] and TiO_2[23,24] nanoparticles. After the polymerization of the template, poly-Pickering-HIPE nanocomposites with high porosities, containing nanoparticles embedded in the walls, were obtained. These macroporous polymers had a typical close-cell structure. Such close-cell polymer foams are commonly used as thermal insulators.[25] It is well known from the literature that particles, by analogy to surfactants, can adsorb strongly at oil—water interfaces, acting as an efficient barrier against droplet coalescence.[26] However, to obtain stable emulsions some requirements are necessary: interalia, the contact angle of the nanoparticles at the oil—water interface, must be near 90°.[27] Consequently, the nanoparticles should be partially wetted by both oil and water phases. The phase that preferentially wets the particles will be the external phase.[28] The stability of Pickering emulsions depends on various factors such the nanoparticle concentration,[29] their size, and their wettability.[26] Although a large variety of inorganic nanoparticles have been used to stabilize emulsions,[27,30,31] only a few (SiO_2[22,32] and TiO_2[24] NPs) have been used to stabilize Pickering HIPEs, which then have been used as templates for the preparation of poly-Pickering-HIPE nanocomposites. Other types of nanoparticles and aspects such as their size and hydrophobicity have not been studied in depth in such systems.

Even though numerous investigations have been incorporated into the design of magnetic polymeric particles,[6,33] little work has been done concerning magnetic macroporous polymeric materials.[7−9] Here, we report the stabilization of Pickering W/O HIPEs with iron oxide NPs and the use of these HIPEs as templates for the preparation of macroporous polymer foams with a magnetic response. We undertook a more systematic study of the applicability of the oleic acid surface-modified NPs initiated by Menner et al.[23] Two types of NPs with different sizes and different oleic acid contents have been chosen. The ability of both NPs to act as efficient emulsifiers has been compared. The results have revealed that partially hydrophobic magnetic NPs can stabilize HIPEs with an internal phase content of up to 92.5%. Consequently, highly porous polymer foams have been obtained. The density, porosity, cell morphology, nanoparticle arrangement, and magnetic properties were characterized as a function of the nature of NPs, the oleic acid content and concentration of NPs, and the internal phase volume of the emulsions used to prepare the poly-Pickering HIPEs.

MATERIALS AND METHODS

Materials. Styrene (≥99%), oleic acid (≥90%), iron(III) chloride hexahydrate ($FeCl_3 \cdot 6H_2O$, ≥ 98%), and anhydrous iron(II) chloride ($FeCl_2$, ≥ 99%) were purchased from Sigma-Aldrich. Oil-soluble initiator α,α'-azoisobutyronitrile (AIBN, ≥ 96%), cross-linker divinylbenzene (technical grade, 50%), and ammonium hydroxide (32 wt % NH_3) were purchased from Merck. Styrene and divinylbenzene were purified before use by passing through neutral chromatographic aluminum oxide in order to remove polymerization inhibitors. The rest of the chemicals were used as received. In all experiments, Milli-Q water was used. One of the two types of iron oxide nanoparticles, used in this work, was acquired from Sigma-Aldrich (nanopowder, <50 nm). According to the supplier's X-ray diffraction pattern, the nanoparticles' crystalline phase corresponded to magnetite (Fe_3O_4).

Preparation, Surface Modification, and Characterization of Iron Oxide Nanoparticles. Two kinds of iron oxide nanoparticles with different size distributions have been employed in this work. Small iron oxide nanoparticles were synthesized using a coprecipitation method, following the literature.[6] The nanoparticles were coprecipitated from an aqueous solution of Fe^{3+}/Fe^{2+} salts (in a 3:2 molar ratio) using excess ammonium hydroxide (NH_4OH). To hydrophobize the nanoparticle surfaces and prevent aggregation, oleic acid was added as a capping agent. Additionally, as-received commercial Fe_3O_4 nanoparticles were also functionalized with oleic acid, as described in previous work using silica and titania nanoparticles.[22,24] First, iron oxide nanoparticles were dispersed in a mixture of chloroform/oleic acid (1:2 molar ratio), stirred for 3 h, and precipitated from solution with methanol. Then, excess oleic acid was removed by repeating the dispersion of the nanoparticles in chloroform and precipitating again with methanol prior to drying at 70 °C. In both types of nanoparticles, the weight content of the capping agent was determined by thermogravimetric analysis (TGA). The measurements were performed in a TGA/SDTA 851 unit (Mettler Toledo, US) in the temperature range of 25−550 °C using 100 μL aluminum crucibles and a heating rate of 10 °C/min in a N_2 atmosphere. Field emission scanning and transmission electron microscopy observations were carried out using Gemini LEO 1525 FEGSEM (Carl Zeiss, Netherlands) and JEM 2011 (JEOL, Japan) instruments, respectively. The particle sizes and polydispersity were calculated from

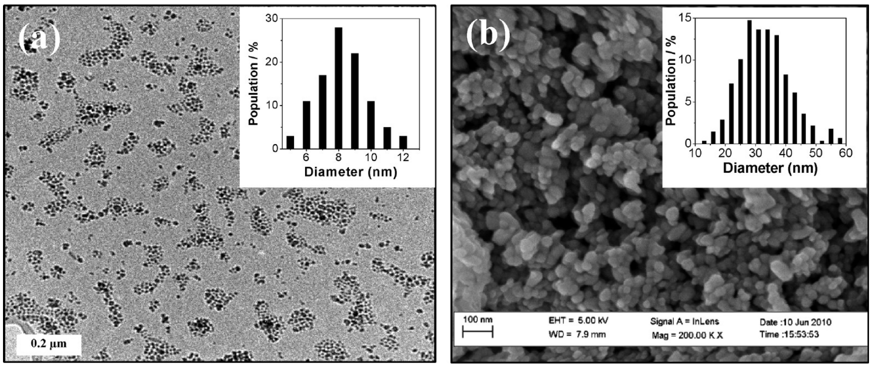

Figure 1. (a) TEM and (b) SEM images for synthesized (PNPs) and commercial (CNPs) iron oxide nanoparticles, respectively. The inset graphs show the average particle sizes for both kinds of nanoparticles.

the microscopy images; for improved statistics, at least 500 NPs were measured using ImageJ software. X-ray diffraction measurements were performed using an X'Pert PRO MPD θ/θ (PANalytical, Netherlands) Bragg–Brentano diffractometer with Cu Kα radiation (λ = 1.54 Å). The angle range was 2θ = 5–120°. The crystalline size was calculated using the Scherrer equation.[34]

Preparation and Characterization of HIPEs. Before emulsification, similar to that described elsewhere,[22–24] the dried iron oxide nanoparticles were dispersed in the oil phase of the emulsion (mixture of styrene and the divinylbenzene cross-linker in a 1:1 weight ratio) using a sonication bath for 10 min. Then, the oil-soluble initiator for the free-radical polymerization of AIBN was added to this solution (1 mol %). Both nanoparticle and initiator concentrations were calculated with respect to the total weight of the monomers. Afterward, the internal phase formed exclusively by water was added dropwise to the external phase under gentle and continuous stirring for 5 min using a Vortex Topmix FB15024 (Fisher Scientific, U.K.). The viscous water-in-oil (W/O), highly concentrated emulsions (HIPEs) were prepared directly in 50 mL standing polypropylene centrifuge (Falcon) tubes. After the emulsification was finished, the tubes were placed into an oven for polymerization at 70 °C for 24 h. Then, the resulting polymer foams were dried until constant weights were reached using a vacuum oven (Heraeus VT5036, Heraeus Instruments, Germany) at 120 °C for 12 h. The influence of the type and concentration of NPs and the internal phase volume fraction on the poly-Pickering-HIPE properties was examined. Details regarding the original composition of the W/O HIPEs prepared in this study are provided in Table 1. The nature of the emulsion (W/O or O/W) was assessed by the drop test and conductivity measurements, whereas its stability against sedimentation and phase separation was evaluated visually over several days after emulsion formation. To observe the structure of the HIPEs, digital images were captured using a Reichert Polyvar microscope (Leica, Germany).

Characterization of Poly-Pickering HIPEs. Scanning electron microscopy (SEM) micrographs of the poly-Pickering HIPEs were acquired using either a TM-1000 tabletop instrument (Hitachi, Germany) at 15 kV or a JSM-5610 LV (JEOL, Japan) microscope. For observation, samples were placed inside a Scan Coat Six (Edwards Ltd., U.K), where they were coated with a gold layer (ca. 60 nm thick) in an argon atmosphere to achieve the necessary electrical conductivity.

The pore size distribution was determined by measuring at least 300 pores from different regions of the sample using ImageJ software.

The skeletal density (ρ_s), foam density (ρ_f), and porosity (P) of the materials were determined using pycnometry, as reported in detail in previous work.[19] First, the skeletal density of the pore walls of the poly-Pickering HIPEs was obtained using a helium pycnometer (Accupic 1330, Micromeritics, U.K.) based on a gas displacement technique. Then, P was calculated by means of an envelope density analyzer (GeoPyc 1360, Micrometrics, U.K.), which determines the volume and density of a solid by the displacement of a solid medium, composed of small and rigid spheres that close pack efficiently around the object. P was calculated using the following equation:

$$P = \left(1 - \frac{\rho_f}{\rho_s}\right) \times 100 \qquad (1)$$

At least five pieces of approximately 3 cm^3 each were analyzed to obtain statistically relevant data. Polymeric foam samples for transmission electron microscopy (TEM) were embedded in a Spurr epoxy resin of low viscosity (60 cps) and then cut into slices of about 60 nm thickness using a Reichert Jung ultramicrotome (Seefeld, Germany). Then, these slices were placed on a holey copper grid coated with a carbon film. The TEM observations were performed on a JEM 2011F (JEOL, Japan) instrument working at 200 kV.

The final nanoparticle content of some poly-Pickering HIPEs was determined by thermogravimetric analysis (TGA). The measurements were performed following the same conditions as described for the nanoparticle characterization.

The magnetic properties of both poly-Pickering HIPEs and iron oxide nanoparticles were studied using an MPMS XL superconducting quantum interference device (SQUID) magnetometer (Quantum Design, US) at fields ranging from −20 to 20 kOe and at temperatures ranging from 2 to 300 K.

■ RESULTS AND DISCUSSION

Preparation and Characterization of Iron Oxide Nanoparticles. Two kinds of iron oxide nanoparticles with different average particle sizes were selected for this research in order to study their ability to stabilize W/O highly concentrated emulsions: (a) polydisperse commercial nanoparticles (CNPs) and (b) nanoparticles synthesized by a coprecipitation method (PNPs); these were synthesized following the method described in the Materials and Methods section. A TEM image of a PNP sample is shown in Figure 1a, and an SEM image of an as-received CNP sample is shown in Figure 1b. In both cases, the nanoparticles are almost spherical. However, these two NP samples had rather distinct sizes because the size of the PNPs was between 5 and 12 nm, with a dominant population at 8 nm, whereas the size of the CNPs was in the range of 10–70 nm, with a dominant population at 35 nm (inset graphs in Figure 1). Because of the small size of PNP particles, XRD peaks were very broad, making it difficult to differentiate between Fe_2O_3 and Fe_3O_4[35] iron oxide phases. For such PNPs, the crystalline size was estimated to be 7.3 nm using the Scherrer equation,[34] which is in fair agreement with the TEM observations (Figure 1a) and points to single-domain crystalline nanoparticles. As noted in the Materials and Methods section, CNPs were assigned to the magnetite phase (Fe_3O_4).

Because of the hydrophilicity of metal oxide nanoparticles, one would require more lipophilic particle surfaces for the preparation of W/O Pickering emulsions. For this reason, both kinds of iron oxide nanoparticles were surface modified with oleic acid. It is well established that particles that are more wetted by water than by oil can stabilize O/W emulsions, and inversely, particles preferentially wetted by oil can be good emulsifiers for W/O emulsions.[26] Therefore, the contact angle that the nanoparticles exhibit at the oil−water interface plays an important role in the stability of Pickering emulsions. Among the factors that affect this contact angle, the most important are the surface chemistry of the nanoparticles and the nature of the oil. We have modified the surface of iron oxide nanoparticles providing hydrophobicity in order to optimize the stability of W/O HIPEs.

First, and as pointed out in the Methods and Materials section, oleic acid was added as a capping agent to increase the hydrophobicity of PNPs and enhance their dispersibility in oil during the synthesis step. This modification could thus favor the adsorption of the nanoparticles at the water−oil interface, allowing for the preparation of stable W/O Pickering emulsions.[36,37] TGA measurements (Supporting Information, Figure S1) revealed that after the washing process the total content of oleic acid attached to PNP surfaces was 12.4 wt %. Two different mass loss steps were detected between 100 and 260 °C and between 260 and 450 °C. This indicates that different species of oleic acid are in the sample and are most likely disposed on the particles as a multilayer.[6]

Second, as-received CNPs were also functionalized with oleic acid. Figure S1 included in the Supporting Information shows TGA curves of CNPs before and after several cycles of washing. After the first washing cycle, CNPs contained 8.9 wt % oleic acid. Similar to that observed for PNPs, the TGA plot was also characterized by mass losses with two different steps, probably indicating adsorption in multilayers. Successive washing cycles further reduced the content of oleic acid progressively. If not otherwise mentioned, CNPs capped with 4.4 wt % oleic acid (after two cycles) were used for all emulsions. These CNPs showed only one TGA mass loss step, suggesting an arrangement of oleic acid molecules closer to a monolayer. Taking into account the residual mass of iron oxide nanoparticles determined by TGA, 5.16 g/cm^3 as the density of iron oxide, and the average particle size obtained from TEM images, we estimated the surface area per molecule of the primary layer of oleic acid for CNPs as 47 Å^2/molecule. Compared to this value, monolayer films with packed straight-chain fatty acids on water require a smaller molecular cross-sectional area of 20−22 Å^2/molecule.[38] This implies that the CNP surfaces are not fully covered by this first monolayer. It should be pointed out that in any case the surface coverage of the PNPs is considerably higher than for CNP, as deduced from the TGA curves. We will see below that despite this difference oleic acid-functionalized PNPs and CNPs are both efficient emulsifiers for stabilizing W/O HIPEs.

W/O HIPE Formation. The stability of Pickering emulsions, prepared using as-received CNPs as a stabilizer, was compared to that using CNPs functionalized with oleic acid (4.4 wt %). This proof-of-concept experiment was carried out to ensure that W/O emulsions could not be stabilized using solely unmodified CNPs. In such experiment, two mixtures of 50% water and 50% oil phase (1:1 w/w styrene/divinylbenzene) were prepared, containing 1.5 wt % original or modified CNPs with 4.4 wt % oleic acid attached to their surfaces, respectively. Then, the samples were shaken by hand. Photographs of the samples, just after mixing, are shown in Figure 2a. Sample 1 contains the as-received CNPs. An O/W emulsion is formed (Figure 2b), which is consistent with the hydrophilicity of the nanoparticles.[31] Even though this emulsion creamed rapidly, it did not experience coalescence, at least for 1 month. By contrast, emulsification failure was observed in the sample containing oleic acid-modified CNPs (sample 2 in Figure 2a) possibly because of the lack of efficiency in the emulsification process, leading to complete phase separation. Nonetheless, most of the particles were placed at the water−oil interface, and the brown color of the continuous phase could be attributed to the dispersion of some iron oxide nanoparticles. Moreover, the surface-modified CNPs did not partition into water. By contrast, W/O concentrated and highly concentrated emulsions were successfully prepared by adding the internal phase dropwise into the external phase using either CNPs with a 4.4 wt % oleic acid loading or PNPs as emulsifiers.

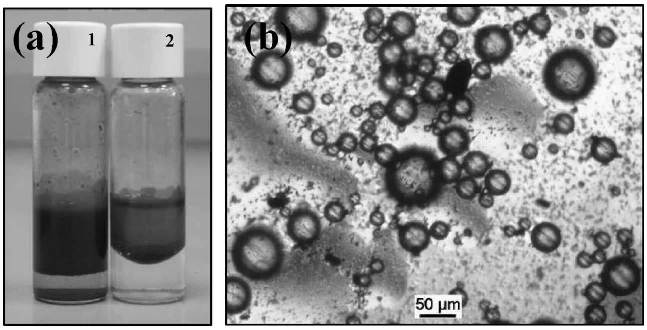

Figure 2. (a) Photograph of samples consisting of 50% water and 50% oil phase (1:1 w/w styrene/divinylbenzene), 1.5 wt % as-received CNPs (sample 1), and 1.5 wt % 4.4% oleic acid-modified CNPs (sample 2). The nanoparticle concentration is expressed with respect to the total monomer content. The picture was taken 15 min after mixing. Sample 1 is an O/W emulsion that has partially creamed, and sample 2 has two separated phases. (b) Optical microscope image of the O/W emulsion depicted in sample 1 of Figure 2a.

In Figure 3a, we plot the maximum internal phase volume of the W/O Pickering emulsions that can be reached using different concentrations of surface-modified CNPs and PNPs. The emulsion type was inferred from conductivity measurements. It was observed that with 3 wt % CNPs the maximum achievable internal phase volume was 92.5%. Recently, in a similar study, Ikem et al.[22] reported the stabilization of W/O HIPEs with a 92% internal phase volume using oleic acid-modified silica nanoparticles. The value corresponding to PNPs is slightly lower than that found for CNPs, which corresponds to around 89% using a 5 wt % nanoparticle concentration. Concentrations of water above the data points in Figure 3a lead to droplet coalescence and fast phase separation. For both types of nanoparticles, the maximum water content reached an asymptotic value at ca. 1.5 wt % NP concentration, suggesting that the surfaces of all droplets were covered by nanoparticles, and increasing the NP concentration leads to an increase in the viscosity of the emulsion. Attempts to use 10 wt % of either CNPs or PNPs failed because of the impossibility of emulsifying even small amounts of water. This could be explained by the high viscosity of the continuous phase of the emulsion,[22] which could be related to the fact that the

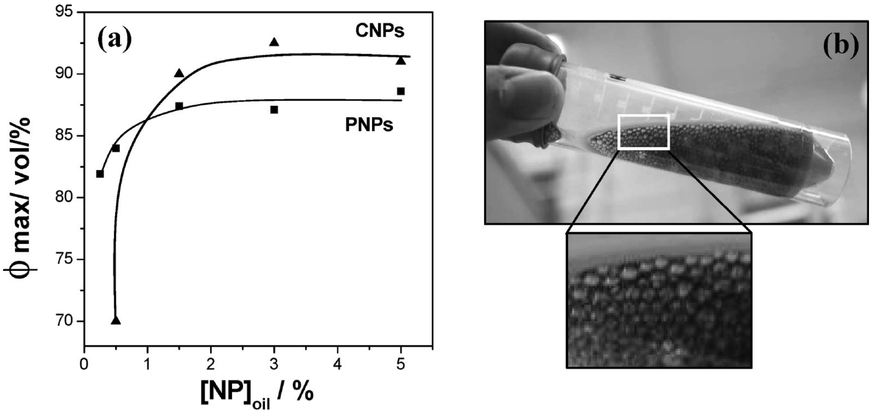

Figure 3. (a) Maximum internal phase volume reached using different concentrations of PNPs that contain (■) 12.4 wt % oleic acid and (▲) 4.4 wt % oleic acid-modified CNPs. The lines are simply drawn to guide the eye. (b) Images of a Pickering HIPE with an 82% internal phase volume stabilized with only 0.25 wt % PNP.

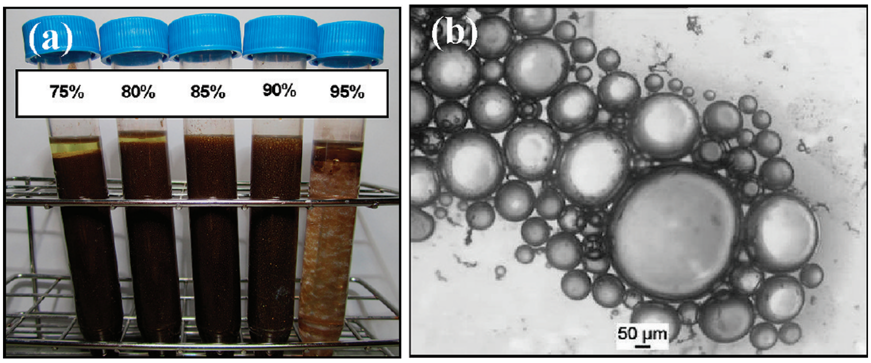

Figure 4. (a) Emulsions with a 1.5 wt % CNP concentration as a function of the water fraction. (b) Optical microscope image of a Pickering HIPE with an 80% internal phase volume using a 3 wt % CNP concentration.

emulsions are unstable under shear and higher viscosities would require stronger shear rates. The tendency observed in the region of low nanoparticle concentrations (<1.5 wt %) can be interpreted as the fact that the smaller number of particles is the factor that limits the stabilized interfacial area. Consequently, emulsions with large droplet sizes were obtained in this region, as observed in Figure 3b. It should be noted that 0.25 wt % PNPs was enough to stabilize emulsions with an 82% internal phase volume, and 0.5 wt % CNPs was necessary to stabilize HIPE emulsions with a 70% internal phase volume. However, it is evident from the results that CNPs were more effective when the nanoparticle concentration was increased.

Before emulsification, the nanoparticles were dried and redispersed in the oil phase using sonication. As expected, the dispersions containing PNPs were significantly more stable than those containing CNPs without any extent of sedimentation when starting emulsification. However, larger agglomerates of nanoparticles were observed in the case of CNPs leading to quick sedimentation. Such agglomerates can attach to the oil—water interface as water is added, preventing droplet coalescence. We reasoned that smaller PNPs compared to CNPs formed smaller and fewer aggregates, giving rise to a higher interfacial area covered by the nanoparticles. However, these aggregates can interact to form a 3-D network of nanoparticles surrounding the droplets upon increasing the nanoparticle concentration. This may lead to an increase in the emulsion viscosity. This is another accepted stabilization mechanism for Pickering emulsions,[39] and it is more likely to occur for CNPs, allowing us to obtain emulsions with larger amounts of incorporated water. Another point that should be taken into account is the different wettability of the nanoparticles. A higher content of oleic acid covering the PNPs surface may induce a preferential dispersion in the oil phase rather than a preferential adsorption in the oil—water interface. This could reduce the ability to stabilize emulsions with higher contents of water compared to CNPs when the concentration of nanoparticles was high enough. The TEM observations (discussed in the next section) provided evidence for different distributions of both types of nanoparticles into both the interface and the oil phase.

W/O Pickering HIPEs with a 1.5 wt % CNP concentration were chosen for a systematic study. Figure 4a shows images of emulsions, just after emulsification, as a function of the water volume fraction. The higher the internal phase volume, the larger the droplet size for a constant nanoparticle concentration in the oil. This was expected because the total concentration of nanoparticles decreases upon increasing the internal phase volume. Consequently, an extra oil—water interface cannot be covered with a sufficient number of adsorbed particles. Water droplets in emulsions with 75 and 80% internal phase volumes partially sedimented and a thin layer of supernatant oil was observed. Above these water fractions, the emulsions were stable against sedimentation. This is due to the high packing of emulsion droplets upon raising the internal-phase volume fraction.[22]

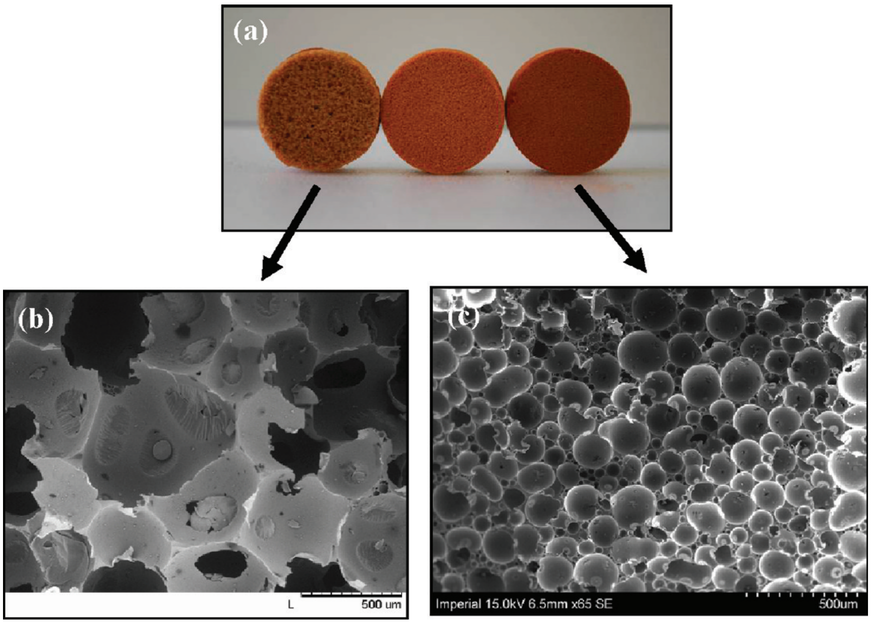

Figure 5. (a) Photograph of poly-Pickering HIPEs synthesized from Pickering HIPEs containing a 75 vol % internal phase (water) stabilized with 0.5, 1.5 and 3.0% PNPs. (b, c) SEM images of poly-Pickering HIPEs synthesized from Pickering HIPEs with a 75% internal phase volume stabilized with 0.5 and 3.0%, respectively.

Furthermore, when the concentration of CNPs was increased (not shown here) to 3.0 wt %, the W/O Pickering HIPEs did not experience sedimentation in the course of time. This feature is common in Pickering emulsions and is generally attributed to the fact that the viscosity of the external phase increases, retarding or suppressing the sedimentation of water drops in the case of W/O emulsions.[39] In samples stabilized with 1.5 wt % PNPs, emulsion sedimentation was not observed. This result was in good agreement with the observations made by Binks and Lumsdon.[40] In their work, a decrease in particle diameter led to a decrease in the sedimentation extent of W/O Pickering emulsions. Despite this, all emulsions prepared with both CNPs and PNPs were stable to coalescence for over 3 months.

Figure 4b shows an optical microscopy image corresponding to a W/O Pickering HIPE containing an 80% internal phase and stabilized with 3 wt % CNPs. This emulsion possessed a wide droplet size distribution ranging from 10 to 300 μm. It has been observed that samples with water contents higher than 80% presented a bimodal droplet size distribution, as shown in Figure 4b (which will discussed further in the next section). The diameter of the population with larger sizes increases progressively upon decreasing the total nanoparticle concentration. In such HIPEs, the process that is considered to control the droplet size in the low-particle-concentration region is the so-called limited coalescence. Arditty et al.[41] studied the formation of Pickering HIPEs with low particle concentrations, describing that smaller droplets coalesce to form larger droplets until a certain limit in which the interfacial area between oil and water was totally covered with nanoparticles. Moreover, they also found that the polydispersity was relatively narrow. This could be the case in the system shown in Figure 3b. Generally, the typical droplet size of Pickering emulsions containing similar contents of water and oil is in the range of 0.2 to 50 μm.[29,37,39,40] However, the extent of droplet growth by coalescence rises upon increasing the internal phase volume of the emulsions.

Coming back to the sequence shown in Figure 4a, it can be clearly observed that the emulsion containing 95% water experiences complete phase separation. It should be pointed out that in all emulsions stabilized using either PNPs or CNPs (with 12.4 and 4.4% oleic acid, respectively), catastrophic phase inversion[39] did not occur during the addition of the internal phase. As described in the literature, such an inversion is expected to take place in emulsions stabilized with particles either partially hydrophilic or hydrophobic. This inversion can be controlled in most cases by changing the internal phase volume,[39] modulating the hydrophobicity of the particle surface,[42] or modifying the pH.[36,43] To evaluate the degree of CNP hydrophobicity, emulsions were prepared by varying the oleic acid content on the CNP surface while keeping all other parameters constant. CNPs covered with 2.2 wt % oleic acid were used. This oleic acid loading was achieved after five washing cycles. From TGA analysis, the surface area per molecule was estimated to be 71.8 Å^2/molecule. Interestingly, in this case a phase inversion from a W/O to an O/W emulsion was observed when approximately 70% of the internal phase volume was added, which was consistent with the results reported by Binks.[39] Here, the phase inversion took place when the volume fraction (70%) of dispersed water reached the close-packing condition, which is close to 74% and is the value generally defined as the limit for highly concentrated emulsions.[10,11] Figure S2 (Supporting Information) shows the product of a diluted polymerized O/W Pickering emulsion resulting from catastrophic inversion and leading to cross-linked polystyrene microparticles. Consequently, we can control the formation of both W/O Pickering HIPEs and O/W diluted Pickering emulsions by adjusting the oleic acid coverage on the nanoparticle surface.

Preparation and Characterization of Poly-Pickering HIPEs. In this section, we evaluate the influence of several synthesis parameters (i.e., type and concentration of iron oxide nanoparticles and amount of the internal phase (Table 1)) on the physical properties of poly-Pickering HIPEs. Following the method described in the Materials and Methods section, poly-Pickering

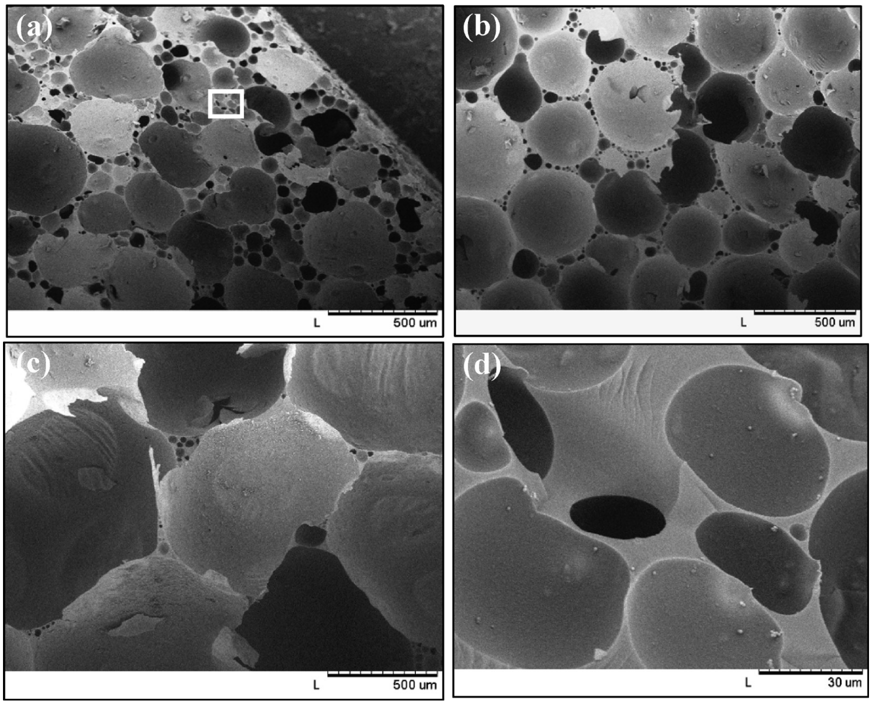

Figure 6. SEM images of poly-Pickering HIPEs synthesized from Pickering HIPEs containing (a) 75, (b) 85, and (c) 92.5% internal phase volumes stabilized with 3.0% CNPs. (d) Higher-magnification image of the region delimited with a box in the sample shown in a.

HIPEs were obtained by free-radical polymerization in the continuous phase of W/O Pickering HIPEs, composed of a mixture of styrene and divinylbenzene (1:1 w/w), in sealed tubes. As a result, macroporous polymers with no significant shrinkage were obtained after drying. No time-consuming purification was needed because the emulsions did not contain any surfactant. The appearance of the foams is shown in Figure 5a. It is important to mention that the homogeneity of the brown color along the sample was the first indication of the good dispersion of nanoparticles in the polymer matrix. Furthermore, the dried foams were easily attracted to a magnet, suggesting that the materials had a high level of magnetization.

The image shown in Figure 5a presents the sample sequence PNP1, PNP2, PNP3 in which the PNP concentrations were 0.5, 1.5, and 3.0, respectively, keeping the internal phase volume (75%) constant. The larger pores can clearly be seen, especially in the samples made with a low NP concentration. The bulk density and porosity of PNP1, PNP2, and PNP3 were determined by means of pycnometry. The bulk density increased from 1.09 to 1.13 g/cm^3 upon increasing the nanoparticle concentration. Such densities were higher than that of pure polystyrene (1.05 g/cm^3) because of the incorporation of inorganic nanoparticles into the polymer structure. The porosities (near 80%) were higher than the internal phase volume fractions of the initial emulsions templates, which were the same for all templates (75%). As we discussed above, the emulsions stabilized with PNPs did not experience sedimentation, so such difference could be attributed to an incomplete conversion of monomers to polymer. On the basis of gravimetric determinations, the polymerization yields were estimated to be in the range of 85−90%. This implies that the final amount of polymer was smaller than initially presumed; consequently, the concentration of nanoparticles in the nanocomposites would be slightly higher than predicted.

To study the pore morphology of the macroporous polymers, PNP1 and PNP3 were characterized by SEM. The structures displayed in Figure 5b,c are quite similar to other poly-Pickering HIPEs described in the literature.[23,24,32] These macroporous polymers have a close-cell structure. It is widely accepted that a dense film layer is formed by the nanoparticles at the O/W interface, creating a rigid film between adjacent droplets. In comparing the images in Figure 5b,c, it is clearly visible that with increasing nanoparticle concentration the pore size decreased gradually because of the stabilization of a larger interfacial area. The characteristic pore size ranged from several μm to 800 μm in the case of PNP1 and to less than 300 μm for PNP3, which was stabilized by 3 wt % PNPs. The water volume fraction in all systems was higher than 0.74, which is considered to be the maximum compact ratio for monodisperse spheres.[11] Therefore, the polyhedral pore shape is due to the high droplet packing.[10] This was more visible in the large pores in the poly-Pickering HIPEs made from templates stabilized with smaller nanoparticle concentrations (Figure 5b).

Apart from the nanoparticle concentration, the second most important parameter affecting the droplet size in Pickering emulsions is the volume percentage of the internal phase. The influence of this parameter, studied in poly-Pickering HIPEs made from HIPE templates stabilized with CNPs, is shown in Figure 6. In this study, emulsions with 75% (CNP4), 85% (CNP5), and 92.5% (CNP6) water were prepared by keeping the CNP concentration constant (3 wt %). The highest internal phase volume stabilized was 92.5%. The resulting values of bulk density and porosity (Table 1) were consistent with the values calculated for poly-Pickering HIPEs containing PNPs. First, the bulk density values remained constant at 1.13 g/cm^3 when using the same nanoparticle concentration. Second, the porosities were again slightly higher than the internal-phase volume fraction of the initial emulsions. Because poly-Pickering HIPE CNP6 was too brittle and broke during the measurement, the porosity of foam CNP6 could not be determined using pycnometry.

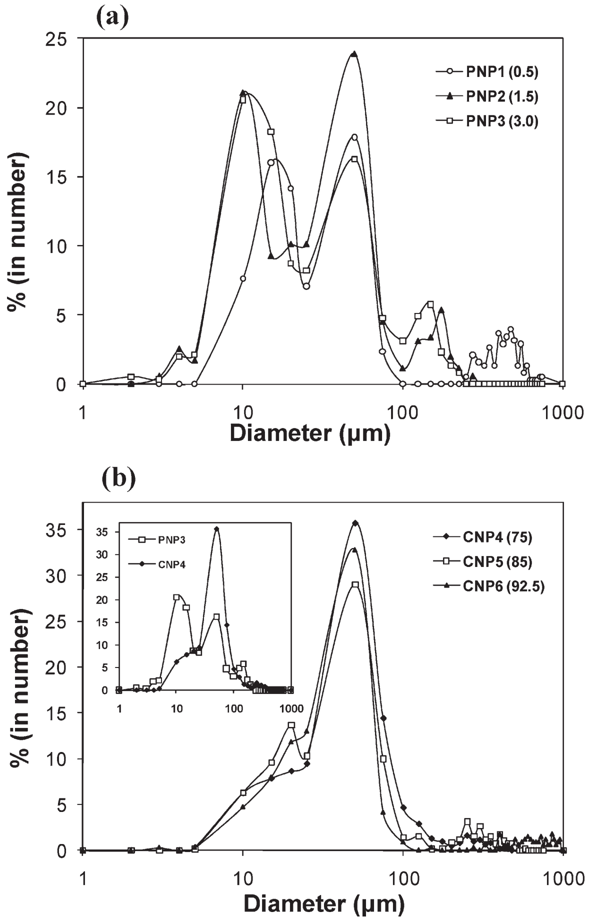

Figure 7. Pore size distributions for (a) poly-Pickering HIPEs PNP1, PNP2, and PNP3, which contain the same internal-phase volume fraction (75%), showing the influence of nanoparticle concentration and for (b) poly-Pickering HIPEs CNP4, CNP5, and CNP6 demonstrating the influence of the internal-phase volume (water) for samples with the same CNP content (3 wt %). The values included in the legend indicate (a) the NP weight percent concentration and (b) the internal-phase percentage added to precursor HIPEs. The inset in b compares the pore size distribution for PNP3 and CNP4, which are samples with the same composition but prepared with the two different NPs used in this study.

However, the porosity was estimated to be 94% by measuring the weight and approximate volume of three pieces corresponding to one sample.

Regarding the microstructure, the SEM images shown in Figure 6 revealed that the features observed for poly-Pickering HIPEs made from HIPEs stabilized with CNPs were essentially the same as those stabilized using PNPs. It is noteworthy that the integrity of the macroporous structure was not affected, even though the size of the CNPs is significantly larger than for PNPs. In all cases, SEM analysis showed a considerably higher percentage of the number of smaller pores, in line with optical microscope observations of the initial HIPEs. A magnified image of the smallest pores in the CNP4 sample is shown in Figure 6d. Closed small pores are placed at the plateau borders of larger droplets in poly-Pickering HIPEs, and they are separated by polymer walls that are about 200−300 nm thick.

The emulsion droplets and the pores were similar in size, demonstrating that no destabilization occurred during the polymerization step. As mentioned before, two well-defined pore populations were clearly observed, indicating a bimodal pore size distribution. A quantitative analysis of both small and large pore size distributions was carried out in order to study in more detail the differences between samples. The analysis is given in Figure 7. Small and large pore size average values are listed in Table 1. The values of the internal phase volume fraction will be always referenced to the initial HIPEs. The data included in Figure 7a, measured on samples PNP1, PNP2, and PNP3, showed that the size of the population of the larger pores, which are easily observed in Figure 5, dropped from values near 420 to 120 μm when the nanoparticle concentration increased from 0.5 wt % (PNP1) to 3 wt % (PNP3), respectively (keeping the internal phase volume percentage constant at 75%). This means that the extent of coalescence in the HIPEs decreased gradually. Therefore, the size of the larger pores can be used as a qualitative measurement of the emulsion stability. Figure 7b shows the influence of changing the internal phase volume of the systems depicted in Figure 6. Even though the presence of the number of small pores (with a maximum peak at around 40 μm) is considerably more important in all cases, the size of the large pores shifts to higher values when the internal phase volume increased from 75% (CNP4) to 92.5% (CNP6). Pores with large sizes, greater than 1000 μm, were found in sample CNP6, leading to the brittleness of the sample.

The inset graph included in Figure 7b shows a comparison of the pore size distribution of the two samples (PNP3 and CNP4) made from emulsion templates with the same composition (75% water and 3 wt % nanoparticles) but stabilized by the two different types of nanoparticles used in this work. Both samples exhibit a similar pattern with two important differences: first, CNP4 does not show any pore size population centered at around 10 μm, and the distribution of the smaller pores is slightly shifted to higher values compared to those for PNP3. This fact is more evident when comparing the values of the average pore sizes, indicated in Table 1. Second, CNP4 possesses larger pores than does PNP3. According to the following equation,[40]

$$r_e = \frac{4\phi_w r_p}{\phi_p} \qquad (2)$$

the radius of a Pickering emulsion droplet (r_e) depends on the nanoparticle radius (r_p), the volume fraction of water (ϕ_w), and the initial nanoparticle concentration (ϕ_p) in the emulsion. This implies that the larger the nanoparticle radius, the larger the droplet size, when all other parameters are kept constant. In our case, CNPs led to emulsions with larger droplet sizes when the internal phase volume was 75%. Nevertheless, the macroporous polymers prepared from HIPEs with an internal phase volume percentage in the range of 75−85% had smaller average sizes of the larger pores compared to the macroporous polymers made from HIPEs stabilized with PNPs. The average size of these larger pores increased moderately, from 237 to 310 μm (31%), whereas a significant 285% increment (from 124 to 488 μm) was observed in the poly-Pickering HIPEs made from PNP-stabilized templates. This behavior cannot be explained by eq 2 and possibly stems from the difference in the surface coverage of the nanoparticles with oleic acid, and it may not be caused by the different nanoparticle size. This means that their wettability and thus their ability to migrate to the oil−water interface is different. As we discussed in the previous section, CNPs can stabilize emulsions with higher contents of water when the CNP

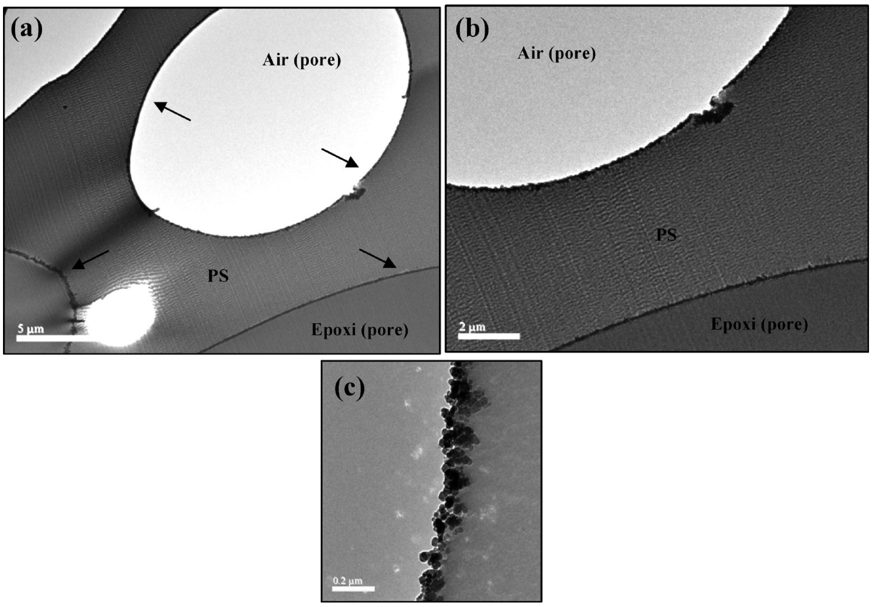

Figure 8. Representative TEM images of ultramicrotome slides (around 60 nm thick) showing how the nanoparticles are distributed in the polymer matrix of poly-Pickering HIPEs obtained from HIPEs with an 85% internal phase volume stabilized with 5% CNPs.

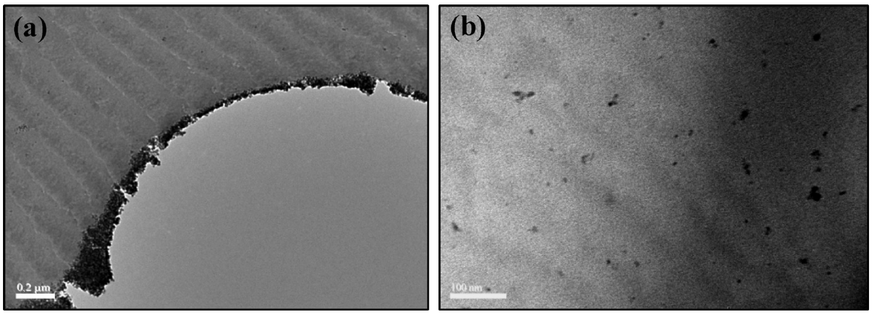

Figure 9. Representative TEM images of poly-Pickering HIPEs obtained from HIPEs with an 85% internal phase volume stabilized with 5% PNPs showing that most nanoparticles are located at the interface but many are embedded in the polymer matrix.

concentration is high enough, which was attributed to the lower hydrophobicity of the nanoparticles compared to that of the PNPs. Here, it is evident that PNPs can stabilize emulsions with smaller droplet sizes when the water content is relatively small, but when the water volume fraction increases, the emulsions are not as stable as with CNPs.

To study the internal structure of the polymeric materials, TEM images of two poly-Pickering HIPE thin sections embedded in an epoxy resin were taken. Many TEM images were obtained, and the same textures were observed. Figure 8a shows a representative example with all of the different regions observed in the ultramicrotome slides. In agreement with the SEM micrographs, several micrometer-sized pores are surrounded by polymer walls (indicated in the figure as PS); iron oxide nanoparticles (indicated with black arrows) are clearly visible at the pore—polymer interface. It is important to note that the pores are not always filled with the epoxy resin used before the cutting process, and air remained trapped inside the pores. The low permeability of the materials with respect to such a resin could be explained by the close-cell structure of the poly-Pickering HIPEs (Figure 6). In any case, the epoxy resin exhibits a different texture and contrast than does the polymer matrix, allowing us to differentiate the two phases (clearly visible in Figure 8b). The samples (CNP7 and PNP8, see Table 1) selected for this analysis were prepared from HIPEs with an 85% internal phase volume and 5 wt % nanoparticles using both CNPs and PNPs. As indicated before, the final concentration of nanoparticles in the nanocomposites exceeded the initial concentration to some extent, being close to 11%. This was confirmed by TGA determinations.

TEM images undoubtedly revealed two different patterns. First, CNPs were located exclusively on the polymer surface (i.e., the former W/O interface in the HIPE template, Figure 8a—c). Defined layers formed by several CNPs on both sides of the pore wall (i.e., at the surface) are clearly seen in Figure 8a,b. Hardly any CNPs could be found inside the pore wall. Therefore, the nanoparticles did not change their wettability during polymerization. Despite the CNPs being partially agglomerated, it was easy to distinguish individual nanoparticles (Figure 8c). Such partial agglomeration can improve the emulsion stability. The arrangement exhibited by these nanoparticles was consistent with the observations made by Gurevitch in a recent paper.[44]

In contrast to CNPs and even though most of the smaller PNPs were located at the polymer—air interface (Figure 9a), the

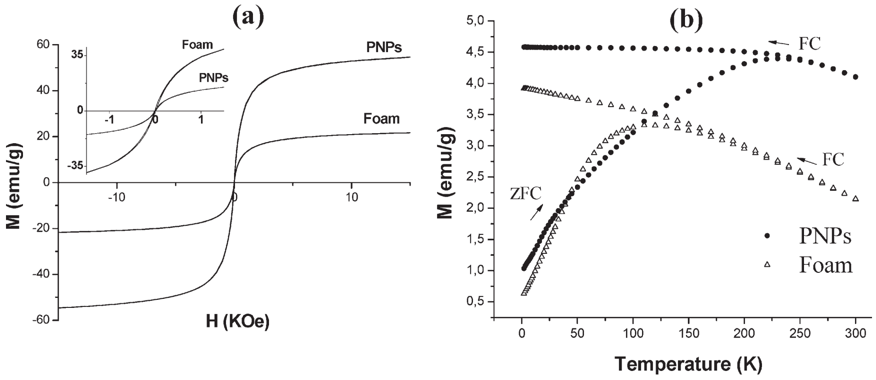

Figure 10. (a) Magnetization vs applied magnetic field and (b) temperature for original PNPs and for poly-Pickering HIPEs prepared from Pickering HIPEs containing an 85% internal phase volume stabilized with 5 wt % PNPs. (a) Measurements carried out at 300 K. The inset shows the same results on a larger scale. (b) Measurements carried out at 50 Oe.

number of PNPs embedded in the polymer walls was significant (Figure 9b). Figure 9a shows a polymer wall and a pore with a layer of PNPs on the pore surface. The PNPs were also located in layers of several units of nanoparticles at the interface, being partially agglomerated but distributed along the polymer surface. Moreover, the inner part of the polymer walls also contained PNPs (Figure 9b). Such PNPs were individual nanoparticles, which were homogenously dispersed. This evidence indicated that some PNPs had a higher affinity for the continuous phase of the W/O HIPEs and they could be effectively dispersed into the oil phase. Therefore, it can be assumed that the presence of the oleic acid multilayer acted as a capping agent for preventing the agglomeration of PNPs in the polymer. These results strongly confirm previous observations during the formation of the HIPEs. The ability of the CNPs to absorb more effectively at the W/O interface (compared to PNPs) is most likely the reason for the better capacity to incorporate larger internal phase volumes in the HIPEs. It is important to note that independently of the initial state of dispersion of both solids (CNPs and PNPs) they could act as a efficient emulsifiers.

Finally, the magnetization of both nanoparticles and porous nanocomposites was studied as a function of the applied magnetic field and temperature. Magnetization versus applied field (M-H) was measured at 300 K. The plot for PNPs (Figure 10a) showed that these nanoparticles, as expected, were superparamagnetic, as indicated by the lack of a hysteresis loop and coercivity (nanoparticles do not retain magnetization in the absence of a magnetic field) and the high magnetization value reached. The saturation magnetization value (M_s), represented per gram of magnetic material, was 56 emu/g. This value is appreciably lower than that for bulk magnetite (89 emu/g). The reduction of the total magnetization arises from the reduction of the particle size, which increases the surface spin disorder.[45] However, the M_s for CNP was 74 emu/g, which was higher than for PNPs because of the larger nanoparticles. Moreover, in the case of CNPs, a hysteresis loop was observed in the $M-H$ curves (coercitivity and remanence were 8.7 emu/g and 0.08 kOe, respectively). To detect the transition to the superparamagnetic state, we measured the field-cooled (FC) and the zero-field-cooled (ZFC) magnetization versus temperature at a field of H = 50 Oe. Confirming the results obtained in $M-H$ plots, no blocking temperature (T_B) could be detected for CNPs, which demonstrates that CNPs do not show superparamagnetic behavior at room temperature. For PNPs, a maximum in the ZFC magnetization (Figure 10b) was observed at 230 K, which could be attributed to T_B.[46] One of the properties of the single-domain superparamagnetic nanoscopic iron oxide particles is its dependency on temperature.[8] It is hence evident that the different magnetic behaviors of PNPs and CNPs are associated with their different sizes. Finally, the same characterization as detailed above was carried out for the poly-Pickering HIPEs studied in Figure 9.

Figure 10a shows the $M-H$ curve for the solid foam containing PNPs (PNP8). Compared with the values for the raw nanoparticles, the M_s value decreased by 60%, reaching a value of 22 emu/g. The percentage reduction of M_s for the CNP7 polyHIPE was similar, reaching a value of 33 emu/g. These reductions could be explained by the diamagnetic contribution from the polymer matrix.[6,33] However, the superparamagnetic behavior was retained for the nanocomposite containing PNP. Additionally, a temperature-dependent magnetization plot (ZFC and FC curves, see Figure 10b) revealed a reduction in the blocking temperature of PNPs, from 230 to 115 K. This could indicate a reduction in the particle−particle interaction as already reported in recent work.[47] Moreover, both the high collapse temperature at around 190 K (corresponding to the intersection of ZFC and FC curves) and the broadness of the maximum at around T_B in the ZFC could be used to gauge the particle anisotropy distribution in the polymer foam,[48] which was consistent with the TEM observations.

■ CONCLUSIONS

Water-in-oil HIPEs have been successfully prepared using two kinds of oleic acid surface-modified iron oxide nanoparticles. Both the size and the oleic surface coverage on the nanoparticles have a significant effect on the properties of the prepared emulsions. Superparamagnetic nanoparticles (PNPs, with sizes ranging from 5 to 12 nm) coated with a multilayer of oleic acid were compared with nonsuperparamagnetic nanoparticles (CNPs with an average size of 35 nm), which were not fully coated with a monolayer of oleic acid. Using the emulsion-templating approach, poly-Pickering HIPEs with a typical close-cell structure were obtained by a straightforward procedure that enabled us to produce macroporous cross-linked polystyrene magnetic foams with high porosities (>80%) and low envelope densities. As expected, neither nanoparticle showed the same efficiency as emulsifiers for HIPEs. The results demonstrate the feasibility of incorporating large amounts of the internal phase in the emulsions. The emulsion droplet size ranged from 5 μm (minimum size reached) to over 1000 μm depending on the initial composition. In spite of the large droplet sizes, the emulsions presented excellent stability with time. Furthermore, an increase in the droplet sizes was observed when the nanoparticle concentration was reduced or when the internal-phase volume was increased. PNPs were more effective as emulsifiers in the low nanoparticle concentration range. This leads to emulsions with an 80% internal phase volume stabilized solely with 0.25 wt % PNPs. However, CNPs could emulsify as much as a 92.5% internal phase volume when the CNP concentration was increased to 3 wt %. The different behavior was attributed first to the larger size of the CNPs and second to the suitable wettability exhibited by CNPs. TEM of poly-Pickering HIPEs revealed two clear patterns in agreement with predictions. CNPs were located exclusively at the polymer−air interface, whereas PNPs were placed mainly at that interface but also in the inner part of the polymer walls. This finding confirmed the higher hydrophobicity of PNPs and implied that an important fraction of PNPs did not act as a emulsifier. Regarding the magnetic properties, the M_s for the nanocomposite containing PNPs was lower (22 emu/g) than that for raw PNPs (56 emu/g). However, the PNP nanocomposites retained their superparamagnetic behavior at room temperature, as exhibited by the original PNPs.

■ ASSOCIATED CONTENT

Ⓢ Supporting Information. (S1) Thermogravimetric analysis in which the total oleic acid content attached to the particle surfaces is derived from the curves. (S2) SEM image of a polymerized sample after catastrophic inversion from a highly concentrated Pickering W/O to a O/W diluted Pickering emulsion. This material is available free of charge via the Internet at http://pubs.acs.org.

■ AUTHOR INFORMATION

Corresponding Author

*E-mail: avvqst@cid.csic.es and a.bismarck@imperial.ac.uk.

■ ACKNOWLEDGMENT

We greatly acknowledge the financial support from the Spanish Ministry of Science and Innovation (projects CTQ2008-06892-C03-01 and CTQ2008-01979/BQU and grant BES-2009-027271). We are grateful to Dr. Goutam Ghosh for help with nanoparticles synthesis and Mercè Moncusí (Universitat Rovira I Virgili) for valuable help with the TEM sample preparation.

■ REFERENCES

(1) Koo, J. H. *Polymer Nanocomposites: Processing, Characterization and Applications*; McGraw-Hill: New York, 2006; p 9.

(2) Carotenuto, G.; Nicolais, L. Nanocomposites, Metal-Filled. In *Encyclopedia of Polymer Science and Technology*; Mark, H. F., Ed.; John Wiley & Sons: New York, 2004; Vol. 10, p 484.

(3) Carotenuto, G.; Nicolais, L.; Martorana, B.; Perlo, P. Metal-Polymer Nanocomposite Synthesis: Novel Ex Situ and In Situ Approaches. In *Metal-Polymer Nanocomposites*; Nicolais, L., Carotenuto, G., Eds.; Wiley-Interscience: Hoboken, NJ, 2005; p 155.

(4) Althues, H.; Henle, J.; Kaskel, S. *Chem. Soc. Rev.* **2007**, *36*, 1454.

(5) Hoppe, C. E.; Rodriguez-Abreu, C.; Lazzari, M.; Lopez-Quintela, M. A.; Solans, C. *Phys. Status Solidi A* **2008**, *205*, 1455.

(6) Ramírez, L. P.; Landfester, K. *Macromol. Chem. Phys.* **2003**, *204*, 22.

(7) Ghosh, G.; Vílchez, A.; Esquena, J.; Solans, C.; Rodríguez-Abreu, C. *Prog. Colloid Polym. Sci.* **2011**, *138*, 161.

(8) Breulmann, M.; Cölfen, H.; Hentze, H. P.; Antonietti, M.; Walsh, D.; Mann, S. *Adv. Mater.* **1998**, *10*, 237.

(9) Bonini, M.; Lenz, S.; Falletta, E.; Ridi, F.; Carretti, E.; Fratini, E.; Wiedenmann, A.; Baglioni, P. *Langmuir* **2008**, *24*, 12644.

(10) Lissant, K. J. *J. Colloid Interface Sci.* **1966**, *22*, 462.

(11) Princen, H. M. *J. Colloid Interface Sci.* **1983**, *91*, 160.

(12) Brun, N.; Ungureanu, S.; Deleuze, H.; Backov, R. *Chem. Soc. Rev.* **2011**, *40*, 771.

(13) Williams, J. M.; Wrobleski, D. A. *Langmuir* **1988**, *4*, 656.

(14) Ruckenstein, E.; Park, J. S. *Polymer* **1992**, *33*, 405.

(15) Barby, D.; Haq, Z. Eur. Patent 0060138, 1982.

(16) Esquena, J.; Ravi Sankar, G. S. R.; Solans, C. *Langmuir* **2003**, *19*, 2983.

(17) Feral-Martin, C.; Birot, M.; Deleuze, H.; Desforges, A.; Backov, R. *React. Funct. Polym.* **2007**, *67*, 1072.

(18) Desforges, A.; Backov, R.; Deleuze, H.; Mondain-Monval, O. *Adv. Funct. Mater.* **2005**, *15*, 1689.

(19) Menner, A.; Haibach, K.; Powell, R.; Bismarck, A. *Polymer* **2006**, *47*, 7628.

(20) Menner, A.; Salgueiro, M.; Shaffer, M. S. P.; Bismarck, A. *J. Polym. Sci., Polym. Chem.* **2008**, *46*, 5708.

(21) Pickering, S. U. *J. Chem. Soc.* **2001**, *91*, 907.

(22) Ikem, V. O.; Menner, A.; Bismarck, A. *Angew. Chem., Int. Ed.* **2008**, *47*, 8277.

(23) Menner, A.; Ikem, V.; Salgueiro, M.; Shaffer, M. S. P.; Bismarck, A. *Chem. Commun.* **2007**, 4274.

(24) Ikem, V. O.; Menner, A.; Bismarck, A. *Langmuir* **2010**, *26*, 8836.

(25) Park, C. P. B., M. J.; Georges, E.; Michael, S. E.; Jean-Francois, K. U.S. Patent 6,583,193, 2003.

(26) Binks, B. P. *Curr. Opin. Colloid Interface Sci.* **2002**, *7*, 21.

(27) Schulman, J. H.; Leja, J. *Trans. Faraday Soc.* **1954**, *50*, 598.

(28) Finkle, P.; Draper, H. D.; Hildebrand, J. H. *J. Am. Chem. Soc.* **1923**, *45*, 2780.

(29) Frelichowska, J.; Bolzinger, M. A.; Chevalier, Y. *J. Colloid Interface Sci.* **2010**, *351*, 348.

(30) Bachinger, A.; Kickelbick, G. *Monatsh. Chem.* **2010**, *141*, 685.

(31) Zhou, J.; Qiao, X.; Binks, B. P.; Sun, K.; Bai, M.; Li, Y.; Liu, Y. *Langmuir* **2011**, *27*, 3308.

(32) Gurevitch, I.; Silverstein, M. S. *J. Polym. Sci., Polym. Chem.* **2010**, *48*, 1516.

(33) Yan, F.; Li, J.; Zhang, J.; Liu, F.; Yang, W. *J. Nanopart. Res.* **2009**, *11*, 289.

(34) Scherrer, P. *Göttinger Nachrichten Gesell* **1918**, *2*, 98.

(35) Lian, S.; Wang, E.; Gao, L.; Kang, Z.; Wu, D.; Lan, Y.; Xu, L. *Solid State Commun.* **2004**, *132*, 375.

(36) Lan, Q.; Liu, C.; Yang, F.; Liu, S.; Xu, J.; Sun, D. *J. Colloid Interface Sci.* **2007**, *310*, 260.

(37) Ingram, D. R.; Kotsmar, C.; Yoon, K. Y.; Shao, S.; Huh, C.; Bryant, S. L.; Milner, T. E.; Johnston, K. P. *J. Colloid Interface Sci.* **2010**, *351*, 225.

(38) Shen, L.; Laibinis, P. E.; Hatton, T. A. *Langmuir* **1999**, *15*, 447.

(39) Binks, B. P.; Lumsdon, S. O. *Langmuir* **2000**, *16*, 2539.

(40) Binks, B. P.; Lumsdon, S. O. *Langmuir* **2001**, *17*, 4540.

(41) Arditty, S.; Whitby, C. P.; Binks, B. P.; Schmitt, V.; Leal-Calderon, F. *Eur. Phys. J. E* **2003**, *11*, 273.

(42) Binks, B. P.; Lumsdon, S. O. *Langmuir* **2000**, *16*, 3748.

(43) Binks, B. P.; Rodrigues, J. A. *Angew. Chem., Int. Ed.* **2005**, *44*, 441.

(44) Gurevitch, I.; Silverstein, M. S. *Macromolecules* **2011**, *44*, 3398.

(45) Jiang, L.; Sun, W.; Kim, J. *Mater. Chem. Phys.* **2007**, *101*, 291.

(46) Vassiliou, J. K.; Mehrotra, V.; Russell, M. W.; Giannelis, E. P.; McMichael, R. D.; Shull, R. D.; Ziolo, R. F. *J. Appl. Phys.* **1993**, *73*, 5109.

(47) Ghosh, G.; Vílchez, A.; Esquena, J.; Solans, C.; Rodríguez-Abreu, C. *Mater. Chem. Phys.* **2011**, *130*, 786.

(48) Sohn, B. H.; Cohen, R. E.; Papaefthymiou, G. C. *J. Magn. Magn. Mater.* **1998**, *182*, 216.

Materials Chemistry and Physics 130 (2011) 786–793

Contents lists available at ScienceDirect

Materials Chemistry and Physics

journal homepage: www.elsevier.com/locate/matchemphys

Preparation of ultra-light magnetic nanocomposites using highly concentrated emulsions

Goutam Ghosh[a,1], Alejandro Vilchez[a], Jordi Esquena[a], Conxita Solans[a], Carlos Rodríguez-Abreu[a,b,*]

[a] Instituto de Química Avanzada de Cataluña, Consejo Superior de Investigaciones Científicas (IQAC-CSIC), Jordi Girona 18-26, 08034 Barcelona, Spain
[b] International Iberian Nanotechnology Laboratory (INL), Av. Mestre José Veiga, 4715-330 Braga, Portugal

ARTICLE INFO

Article history:
Received 21 December 2010
Received in revised form 18 June 2011
Accepted 26 July 2011

Keywords:
Composite materials
Magnetic materials
Nanostructures
Polymers

ABSTRACT

Hybrid inorganic–organic ultra-light magnetic solid foams with iron oxide nanoparticles embedded in a divinylbenzene–polystyrene matrix were prepared using a highly concentrated emulsion polymerization method. Iron oxide nanoparticles with diameters of 3 and 10 nm were synthesized using two different methods. For comparison purposes, nanocomposites with magnetite nanoparticles dispersed in a non-porous polymeric matrix obtained by bulk polymerization were also investigated. Materials were characterized using several techniques such as dynamic light scattering (DLS), X-ray diffraction (XRD), thermogravimetric analysis (TGA), small angle X-ray scattering (SAXS), scanning electron microscopy (SEM), transmission electron microscopy (TEM), Fourier transform infrared spectroscopy (FTIR) and magnetization measurements. SEM and TEM images showed that solid foams are made of well-defined macro pores with nanoparticles embedded in the walls. The density of the solid foams was ca. 50–70 kg m^{-3}, which is about 20 times lighter than the non-porous monoliths. The magnetic measurements show that both nanocomposites are superparamagnetic, and that there are differences regarding the interparticle interactions depending on matrix porosity. The synthesized materials may find applications in adsorbents, tissue reparation, enzyme supports, microreactors, or in water decontamination.

1. Introduction

The synthesis of organic–inorganic hybrid materials composed of magnetic particles and polymer matrices have gained increasing attention for emerging applications as sensors, imaging devices, storage media, and catalysis [1–3]. Furthermore, the synthesis of biocompatible superparamagnetic materials has also been of interest in biomedical applications including magnetic drug targeting, hyperthermia anticancer strategy, and enzyme immobilization [4]. Advances in polymer science have demonstrated the ability to prepare a vast array of materials exhibiting controllable mechanical, thermal, and electro active properties. However, the preparation of organic polymeric materials possessing high magnetic moments and susceptibilities comparable to inorganic systems remains a challenge. To overcome the inherent problems in fabrication of magnetic polymer nanocomposites various synthetic routes have been suggested to combine organic polymers and inorganic magnetic nanoparticles [5]. Emulsion and dispersed media polymerization have been utilized to encapsulate iron oxide nanoparticles into polymeric micro- and nano-spheres. These materials typically trap numerous iron oxide nanoparticles in polymeric matrices prepared by free radical polymerizable monomers [6].

On the other hand, macroporous materials and molecular sieves attract much attention due to their remarkable characteristics; they possess large surface area and high sorption capacity compared to non-porous objects, as well as the possibility to perform selective sorption of various substrates by regulation of pore diameter or chemical modification [7–9]. Though there are many reports on synthesis of magnetic non-porous nanocomposites, not much literature can be found on the synthesis of magnetic porous nanocomposite materials. Kolotilov et al. [10] recently reported the synthesis of molecular sieve MCM-41 in the presence of Fe_3O_4 nanoparticles. However, there are only few reports on template assisted synthesis of magnetic nanocomposite materials [11–13].

Highly concentrated emulsions have been successfully used as templates for the preparation of organic macroporous materials by polymerization in the continuous phase followed by the removal of the dispersed phase [14–18]. Highly concentrated emulsions, which consist of close-packed deformed and/or polydisperse droplets separated by a thin film of continuous phase (a structure resembling gas–liquid foams) [19,20], have proved to be very versatile as templating systems for the preparation of low-density

---

* Corresponding author. Current address: International Iberian Nanotechnology Laboratory (INL), Braga, Portugal.
E-mail address: carlos.rodriguez@inl.int (C. Rodríguez-Abreu).

[1] On leave from UGC-DAE Consortium for Scientific Research, Trombay, Mumbai 400085, India.

0254-0584/$ – see front matter © 2011 Elsevier B.V. All rights reserved.
doi:10.1016/j.matchemphys.2011.07.068

Table 1
Characteristics of iron oxide nanoparticles. Sample NP3 was prepared by using water-in-oil (W/O) microemulsion droplets as templates (Ref. [33]) whereas sample NP10 was prepared by a non-templated co-precipitation method (Ref. [34]).

Sample name	Phase[a]	Hydrodynamic diameter (nm)[b]	Crystalline domain size (nm)[c]	Mean particle diameter (nm)[d]	Oleic acid capping (wt%)[e]
NP3	Magnetite/maghemite	3	2.8	3	45
NP10	Magnetite	10.8	7.3	8	13

[a] As reported in Refs. [31,32].
[b] From DLS.
[c] From XRD using Scherrer formula.
[d] From TEM (see Figs. S1a and S1b in supporting information).
[e] From TGA.

macroporous materials, with high pore volume fraction and controlled pore size [21]. These macroporous solid foams have found successful applications as supports for catalysts, immobilization of enzymes, selective membranes, templates for the preparation of other materials, etc. [16,17,22–25]. The properties of the materials obtained using this technology (average pore size and pore size distribution, surface area, macroscopic density, etc.) were improved with respect to those obtained by other methods. However, their structures were still difficult to control due to the high polydispersity of the precursor emulsions. Emulsification by the phase inversion temperature (PIT) method [26], results in highly concentrated emulsions with smaller and more homogeneous droplet size [27,28]. The phase inversion temperature (PIT) is the temperature at which poly(oxyethylene)nonionic surfactants change their preferential solubility from water (oil) to oil (water) and inversion from O/W to W/O emulsions or vice versa is produced. Macroporous solid foams with improved mechanical properties and lower densities [21] are obtained by templating in emulsions prepared by the PIT method.

More recently, it has been demonstrated that nanocomposite macroporous materials can be obtained by polymerizing in highly concentrated emulsions, in which the external phase consists of a nanoparticle dispersion in a monomer mixture [29–31]. This method has been applied for the preparation of polystyrene nanocomposite foams, containing silica nanoparticles embedded in the polystyrene pore walls. The presence of such nanoparticles leads to improved mechanical properties [32].

In this context, we report on the preparation of macroporous magnetic nanocomposite materials through polymerization in highly concentrated water-in-oil emulsions. To our knowledge this is the first report on the synthesis of ultra-light macroporous nanocomposite material with relatively high magnetic moment. Porous, ultralight magnetic nanocomposites can find applications in adsorbents, tissue reparation, enzyme supports, microreactors, or in water decontamination.

2. Experimental

2.1. Materials

Iron (III) chloride hexahydrate ($FeCl_3$, $6H_2O$) and anhydrous iron (II) chloride ($FeCl_2$) were purchased from Sigma–Aldrich. Ammonium hydroxide (32 wt% NH_3) and oleic acid were purchased from Merck and Fluka, respectively. Styrene and divinylbenzene, either from Merck or Aldrich, were purified by passing through neutral chromatographic aluminium oxide, in order to eliminate polymerization inhibitors. Acrylic acid was obtained from Merck. 2,2′-Azobis-(2,4-dimethyl) valeronitrile (ADVN, soluble in oil phase), courtesy of DuPont Ibérica S.A., was used as initiator in the case of bulk polymerization. Potassium persulfate 99%, used as initiator in emulsion polymerization, was obtained from Merck.

Hexaethylene glycol n-hexadecyl ether and octaethylene glycol n-dodecyl ether non-ionic surfactants, abbreviated as $C_{16}(EO)_6$ and $C_{12}(EO)_8$, respectively, were purchased from Nikko Chemicals Co (Japan). The poly(ethylene glycol)–poly(propylene glycol)–poly(ethylene glycol) $(EO)_{13}$, $(PO)_{30}$, $(EO)_{13}$ triblock copolymer surfactant (Synperonic L64) was obtained from Uniqema (United Kingdom). All surfactants were used without further purification. Tetradecane 99% was obtained from Aldrich. Milli-Q water was used in all the experiments.

2.2. Synthesis

2.2.1. Nanoparticles and non-porous monolithic nanocomposites

Iron oxide nanoparticles capped with oleic acid were synthesized using water-in-oil (W/O) microemulsion droplets as templates [33] as well as by a non-templated co-precipitation method [34] following the literature. The characteristics of samples are shown in Table 1. Samples of nanoparticles are abbreviated hereafter as NPX, where *X* is the average size of nanoparticles. Oleic acid capping was confirmed by FTIR.

For the preparation of monolithic, non-porous nanocomposites, oleic-acid-capped nanoparticles (synthesized as indicated above) were dried at 50 °C and then dispersed in a mixture of styrene and divinylbenzene (1:4 ratios); divinylbenzene was used as a crosslinker to increase the mechanical strength of nanocomposites (for data on nanoparticle size and concentrations, see Table 2). To improve the compatibility of Fe_3O_4 nanoparticles with respect to the polymer matrix, acrylic acid was added to the monomer mixture (nanoparticles/acrylic acid mass ratio = 1:1). The concentration of initiator (ADVN) was 1 wt% with respect to the total initial monomer weight. Samples were kept in glass test tubes at 60 °C for 24 h for polymerization to complete. Non-porous nanocomposites are abbreviated hereafter as NCX-Y, where *X* is the average size of embedded nanoparticles and *Y* is a sample number.

2.2.2. Porous nanocomposites

Styrene and divinylbenzene were polymerized in the continuous phase of water-in-oil (W/O) highly concentrated emulsions prepared using the phase inversion temperature (PIT) method [18] (see Scheme 1). Emulsions were prepared in the system $H_2O/K_2S_2O_8/C_{16}(EO)_6/C_{12}(EO)_8$/Synperonic L-64/styrene/divinylbenzene/tetradecane with the following weight ratios 89.9/0.1/1.2/0.7/0.1/4.0/1.0/3 following a recipe from the literature [18]. Oleic-acid-capped nanoparticles (synthesized as indicated above) and acrylic acid were dispersed by a vortex mixer in styrene/divinylbenzene and then mixed with tetradecane to form the continuous phase of the emulsion (for data on nanoparticle size and concentrations, see Table 2). After adding the aqueous phase, samples were mixed thoroughly in an ice bath for 10 min and then put in a 70 °C bath with strong shaking until the samples became highly viscous. The viscous emulsion was then kept in a constant temperature bath at 70 °C for 48 h for polymerization and crosslinking to obtain solid foams. The solid foams (i.e. porous nanocomposites) were washed with ethanol and water to remove surfactants, tetradecane and unreacted monomers, and then freeze-dried to remove the aqueous dispersed phase. Porous nanocomposites are abbreviated hereafter as PNCX, where *X* is the average size of embedded nanoparticles.

Table 2
Nanoparticle (NP) type and concentrations in non-porous nanocomposites (NC) and porous (PNC) nanocomposites. The concentrations are expressed as amount of iron oxide in the polymer matrix.

Nanocomposites with NP3	NP3 concentration (wt%)	Nanocomposites with NP10	NP10 concentration (wt%)
NC3-1	0.6	NC10-1	0.4
NC3-2	3.0	NC10-2	10.0[a]
NC3-3	16.0[a]	NC10-3	25.0[a]
NC3-4	29.0[a]	PNC10	6.4
NC3-5	46.0[a]		
PNC3	6.4		

[a] Confirmed by TGA.

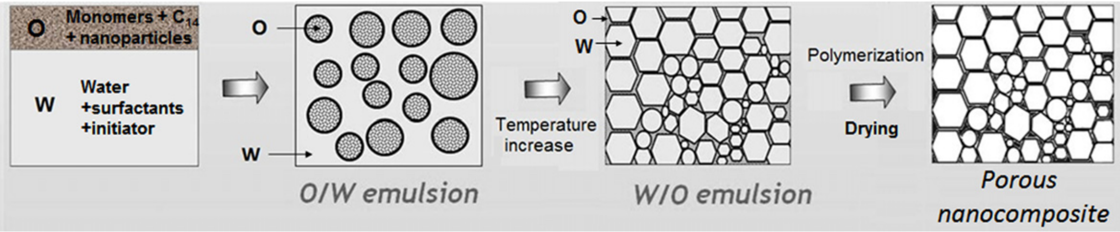

Scheme 1. Scheme of the method for the preparation of porous magnetic nanocomposites. *O* stands for an organic phase whereas *W* stands for an aqueous phase.

3. Characterization techniques

3.1. Thermo gravimetric analysis (TGA)

Measurements were carried out in a Mettler Toledo TGA/DTA 851 instrument. The temperature range measured was between 25 and 650 °C at 10 °C min^{-1} heating rate.

3.2. Fourier-transform infrared spectrophotometry (FTIR)

Samples were analysed by Fourier transform infrared spectroscopy (FTIR) with a Nicolet 510 spectrophotometer. Spectra were collected at 4 cm^{-1} resolution with 64 averaged scans.

3.3. Dynamic light scattering (DLS)

Dynamic light scattering (DLS) measurements were carried out using a cross-correlation DLS instrument (3D DLS from LS Instruments, Switzerland). The light source is a vertically polarized monochromatic He–Ne (λ = 632.8 nm) laser. The detectors used are photo diodes (APD). Temperature was maintained at 25 °C using a thermostated water circulator.

3.4. X-ray diffraction (XRD)

A PANalytical X'Pert PRO MPD θ/θ Bragg–Brentano diffractometer with CuK$_\alpha$ radiation (λ = 1.54 Å) was used for the measurements. The angle range was $2\theta = 5$–$120°$. Nanoparticles were finely ground and loaded in a grooved (541) cut silicon substrate. The average crystal size of the iron oxide was determined according to the Scherrer equation [35] using the full width at half maximum of peaks after correcting the instrumental broadening.

3.5. Small angle X-ray scattering (SAXS)

Small angle X-ray scattering (SAXS) was performed in a S3 MICRO instrument (Hecus X-ray Systems, Graz, Austria) equipped with a GENIX microfocus X-ray source and a FOX 2D point-focusing element (both from Xenocs, Grenoble). The instrument is equipped with a Peltier device for temperature control. The scattering vector was calculated from $q = 4\pi \sin(\theta/2)/\lambda$, where λ = 1.54 Å is the wavelength and θ the scattering angle. The d-spacings from scattering maxima were estimated as $d = 2\pi/q$.

3.6. Scanning electron microscopy (SEM)

Micrographs of solid foams were acquired using a Hitachi TM-1000 tabletop scanning electron microscopy (SEM) instrument at 15 kV. For observation, samples were coated with a gold layer.

3.7. Transmission electron microscopy (TEM)

Transmission electron microscopy (TEM) images of nanoparticles were taken with a JEOL JEM 1010 microscope at 100 kV. Samples were prepared by evaporating a droplet of the dispersion of magnetite nanoparticles on a standard TEM copper grid covered with Formvar polymer. For nanocomposites, samples embedded in an epoxy resin were cut with a Reichert Jung ultramicrotome in slices with a thickness of ca. 60 nm. The slices were placed on holey copper grids for observation.

3.8. Magnetic measurements

A Quantum Design, USA, SQUID magnetometer was used. Maximum field used for the magnetization (*M*) versus magnetic field (*H*) measurements was 20 kOe. The field used for the magnetization (*M*) measurements at the field cooled (FC) and the zero-field cooled (ZFC) modes in temperature range of 2–300 K was 50 Oe.

4. Results and discussion

4.1. Preparation and characterization of monolithic non-porous and porous nanocomposites

We first synthesized non-porous nanocomposites to study the dispersion of nanoparticles in crosslinked styrene–divinylbenzene matrices, which would constitute the walls in the porous nanocomposites. Different concentrations of nanoparticles (samples NP3 and NP10) were used to prepare the non-porous nanocomposites materials; sample compositions are shown in Table 2.

It is to be mentioned again here that we added acrylic acid to give better compatibility between the oleic acid layer on the nanoparticles surfaces and the styrene monomers. Samples with no added acrylic acid appeared opaque and turbid due to macroscopic phase separation.

Porous nanocomposites were prepared from highly concentrated emulsions (for data on nanoparticle size and concentrations, see Table 2). It is to be pointed out that the composition of the external phase of the emulsion (excluding nanoparticles) and the composition of the solutions used to form the non-porous monoliths are almost equal, and that the pores are a replica of the emulsion droplets. Besides the initiator, the only difference concerning the continuous phase is tetradecane that is used to control the phase inversion temperature during emulsification. The oil phase carrying the nanoparticles changes from the internal phase (O/W emulsion) to the continuous phase (W/O emulsion) when the sample is heated above the PIT. Using both aqueous ($K_2S_2O_8$) and non-aqueous (ADVN) initiators the polymerization was fast and there was no emulsion destabilization. During washing the nanoparticles remain in the structure, and there is almost no shrinkage of the matrix during freeze-drying.

Fig. 1 shows the SAXS intensity profiles for samples NC3s. It is observed that a correlation peak appeared in the presence of

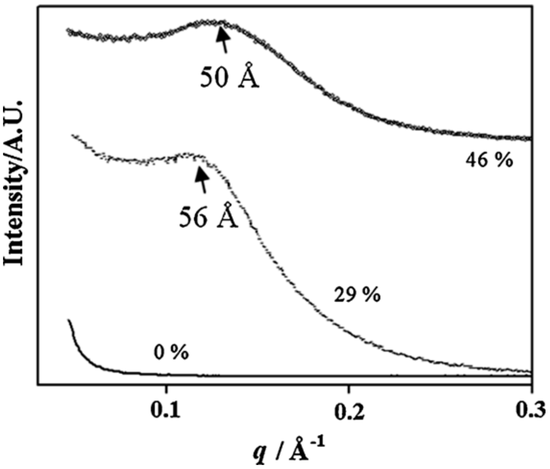

Fig. 1. Small angle X-ray scattering (SAXS) intensity versus scattering vector (q) plots for nonporous nanocomposites with 3 nm nanoparticles (NC3) at different concentrations as indicated in the figure. Peak positions indicate the particle–particle distance of dispersed nanoparticles in the polymer matrix. Increasing concentration of nanoparticles results in shorter particle–particle distance.

nanoparticles. This correlation peak comes from randomly, closely placed nanoparticles in the polymer matrix; the particle–particle average distance can be associated to the d-spacing at the intensity maximum, which is about 5 nm. On the other hand, no correlation peak was found within the experimental q-range for samples NC10-1 (0.4% NPs) and NC10-3 (25% NPs) (results not shown). We cannot rule out that a correlation peak may appear at q values beyond the range of the instrument, as expected for larger nanoparticles. No correlation peaks were observed either for PNC3 and PNC10 porous composite samples within the experimental q-range.

Fig. 2a shows the scanning electron microscopy (SEM) image of the solid foam without nanoparticles, and Fig. 2b and c shows samples PNC3 and PNC10, respectively. A macroporous structure with interconnected pores is clearly visible. The pore sizes are within the 1–5 μm range.

All porous samples were ultra-light in weight. The bulk densities of the solid foams without and with 6.4 wt% nanoparticle concentration were measured gravimetrically to be 50 kg m^{-3} and 70 kg m^{-3}, respectively, almost 20 times less than the density (e.g., ~1100 kg m^{-3} without nanoparticle) of non-porous monoliths (NCs). The difference in densities is due to the high volume fraction of pores.

Fig. 3 shows the TEM images for NC3 and PNC3 samples with different nanoparticle concentrations.

For the 29 wt% nanoparticle sample (NC3, Fig. 3a), partially segregated domains with higher nanoparticle local concentration are observed. The number density of the domains increases further for the 46 wt% nanocomposites (inset of Fig. 3a). Those domains give rise to the SAXS correlations peaks observed in Fig. 1. The TEM pictures of porous nanocomposites PNC3 (Fig. 3b and c) show the walls surrounding micron-sized pores; nanoparticles are distributed within the polymer walls.

Fig. 4a–d shows TEM images for nanocomposites with 10 nm nanoparticles at different concentrations, e.g., 10 (NC10-2) and 25 wt% (NC10-3) non-porous monoliths, and 6.4 wt% (PNC10) porous monoliths. In contrast to Fig. 3, we observe in Fig. 4a and b an homogeneous (random) distribution of 10 nm nanoparticles (NP10) in non-porous polymer matrices at concentrations of 10 and 25 wt%, respectively, with no evidence of micro-segregation. On the other hand, Fig. 4c and d shows clearly that nanoparticles are embedded in the pore walls of the composite solid foams. The brighter zones surrounded by dark walls (polymer matrix with embedded nanoparticles) are macro pores, as seen in SEM images

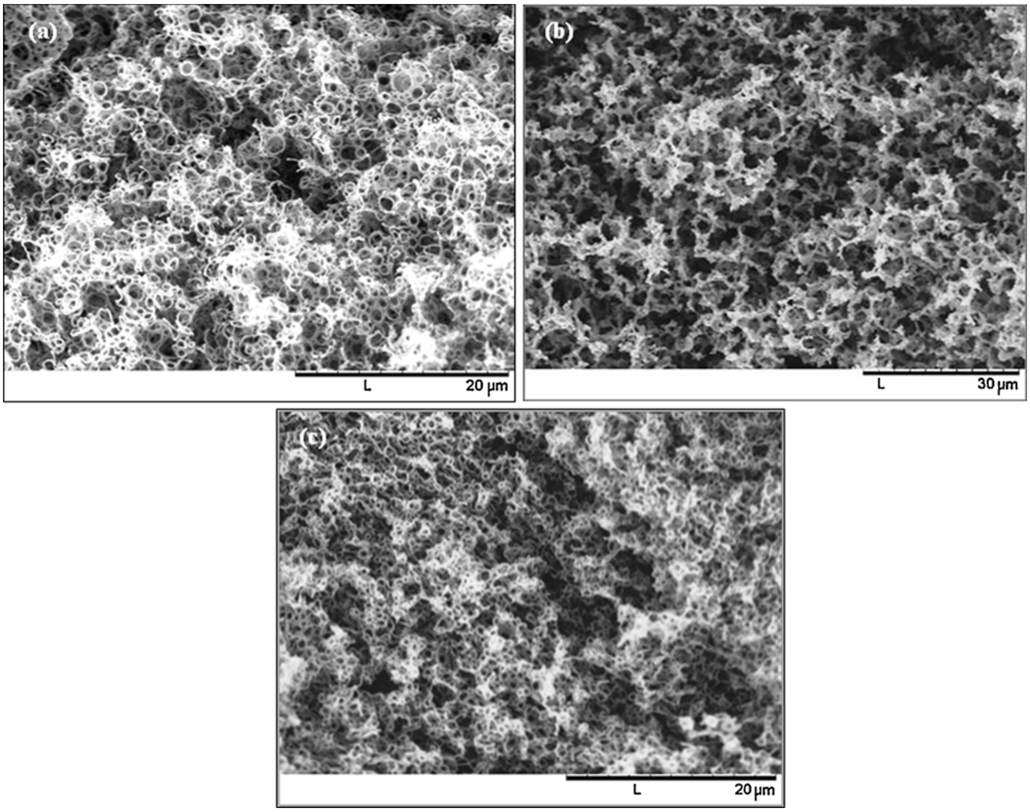

Fig. 2. Scanning electron microscopy (SEM) images of porous nanocomposites: (a) without nanoparticles and with 6.4 wt% nanoparticles of size, (b) 3 nm (PNC3) and (c) 10 nm (PNC10).

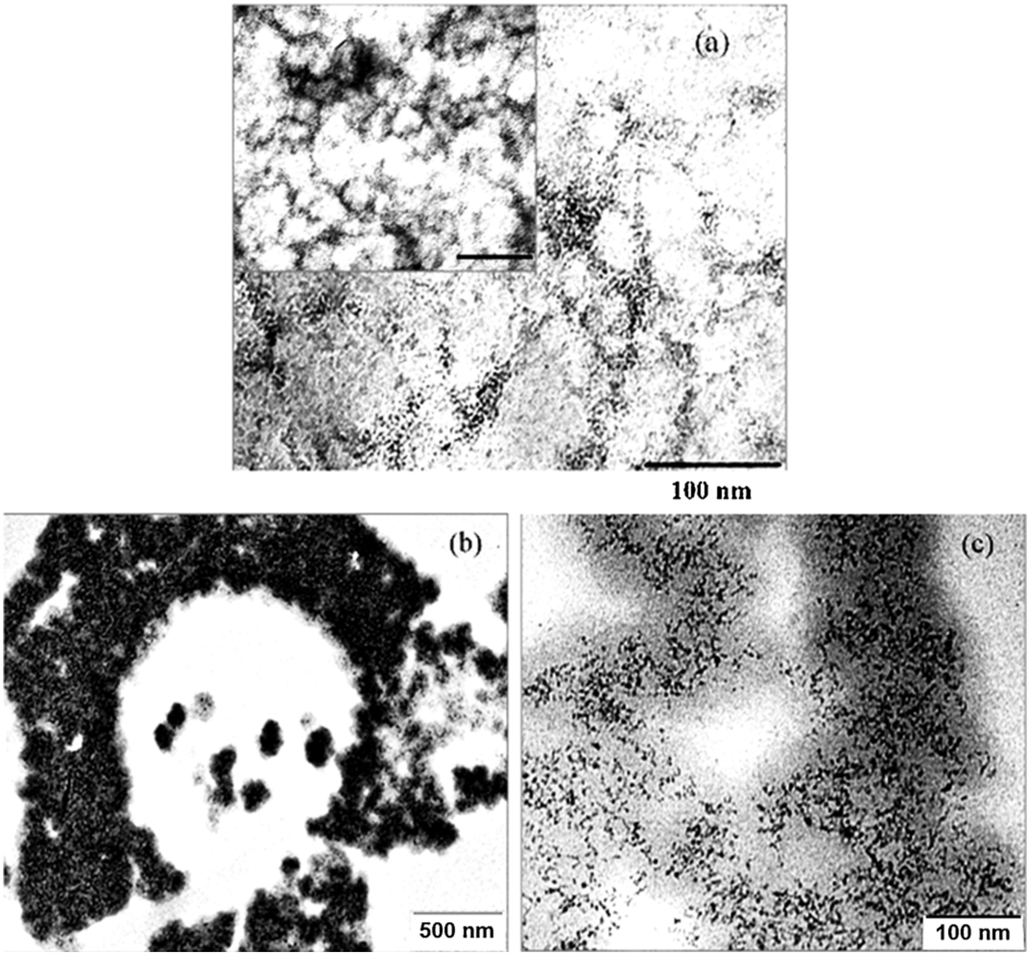

Fig. 3. Transmission electron microscopy (TEM) images of composites with 3 nm nanoparticles. (a) Non-porous nanocomposite with 29 wt% nanoparticles (NC3-4). The inset shows a sample with 46 wt% nanoparticles (NC3-5, scale bar = 100 nm). (b and c) Porous nanocomposites with 6.4 wt% nanoparticles (PNC3) at two magnifications. Brighter zones in (b) correspond to pores obtained from dispersed water droplets in highly concentrated water-in-oil (W/O) emulsion after drying the foam. Darker zones correspond to the polymer walls containing dispersed nanoparticles. Black dots in (c) are the nanoparticles dispersed in the polymer walls.

also, and are the replica of water droplets in water-in-oil (W/O) emulsions using as templates for polymerization. The exact reason of micro domain formation in NC3s is not clear; however weak van der Waals interaction forces may influence this segregation more strongly in the case of smaller particles.

4.2. Magnetic properties

4.2.1. Measurements of magnetization (M) versus field (H) at constant temperature

We have measured the magnetization (M) versus applied magnetic field (H) at 5 K for both non-porous and porous nanocomposites (see Fig. 5). The maximum field applied was 20 kOe. Fig. 5a shows the M–H curves for NC3-3 (16 wt% 3 nm NP) and NC10-2 (10 wt% 10 nm NP). The saturation magnetizations (M_s) were estimated by fitting experimental points with the approximate saturation law [36] and the obtained values are shown in Table 3. The lower value of M_s in NC3-3 is due to the smaller size of nanoparticles [5]. As the size of magnetic particle decreases the surface area increases, and as a result, the magnetization is lost due to surface spin disorder. Below a critical size (ca. 20 nm), the magnetic nanoparticle becomes a single domain state with uniaxial anisotropy [37] and becomes superparamagnetic. It is to be noted here that the M_s of bulk magnetite is around 92 emu g^{-1} and the M_s measured from M–H curve for NP10 at 300 K (see supporting information, Fig. S2) and 5 K were about 58.3 and 66.5 emu g^{-1}, respectively. The diamagnetic contribution from polymer matrix in nanocomposites causes further reduction in the M_s value. Fig. 5b shows the M–H loop for PNC3 and PNC10. The values of M_s for PNC3 and PNC10 are shown in Table 3. Though the size of nanoparticles is same in NC3-3 and PNC3 the saturation magnetization (M_s) in the latter case is 2.5 times more; this is an unexpected result, as the nanoparticle concentration in PNC3 is lower than in NC3-3. We still do not have an explanation for that, although interactions and surface effects might be playing a role.

Surprisingly, the M_s in the case of NC10-2 and PNC10 are same. The coercive fields (H_c) measured for nanocomposites are shown in Table 3. The values of H_c for NC10-2 and PNC10 are similar to that for 10 nm magnetite nanoparticles at 5 K reported by another group [38]. The coercivity

Table 3
Magnetic properties of nanoparticles and nanocomposites at 5 K.

Sample	M_s (emu g^{-1} magnetite)	H_c (Oe)
NP10	66 (58[a])	285
NC3-3	15	20
NC10-2	52	300
PNC3	38	60
PNC10	52	350

[a] Value at 300 K.

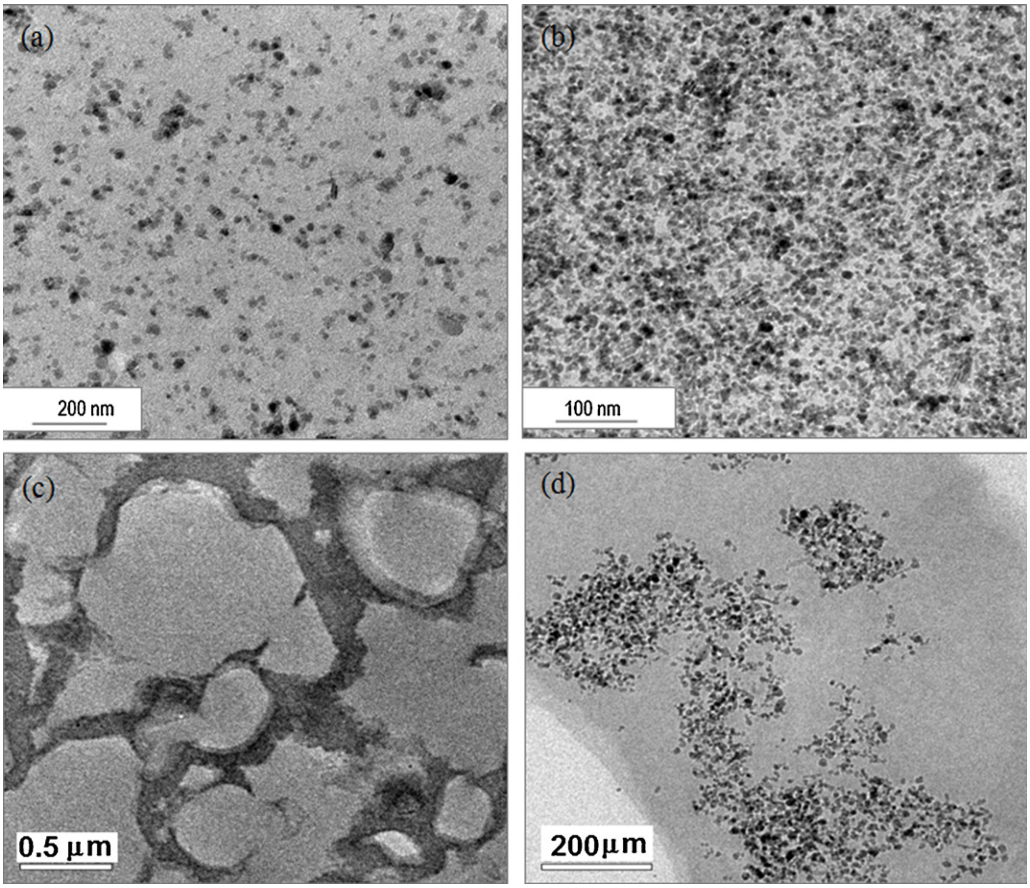

Fig. 4. Transmission electron microscopy (TEM) images of composites with 10 nm nanoparticles. (a) Non-porous composite with 10 wt% nanoparticles (NC10-2). (b) Non-porous composite with 25 wt% nanoparticles (NC10-3). (c and d) Porous nanocomposites with 6.4 wt% nanoparticles (PNC10) at two magnifications. Brighter zones in (c) correspond to pores obtained from dispersed water droplets in highly concentrated water-in-oil (W/O) emulsion after drying the foam. Darker zones correspond to the polymer walls containing dispersed nanoparticles. Black dots in (d) are the nanoparticles dispersed in the polymer walls.

disappears above the blocking temperature (T_B) and, therefore, all these nanocomposites will show superparamagnetic behaviour [39]. Note that both non-porous and porous nanocomposites are attracted to a strong magnet (see insets in Fig. 5).

4.2.2. Measurements of field-cooled (FC) and zero field-cooled (ZFC) magnetization (M) versus temperature (T) at constant field

We measured the field-cooled (FC) and the zero field-cooled (ZFC) magnetization (M) versus temperature (T) for 10 nm particles (NP10) at a field H = 50 Oe (see Fig. S3 in supporting information)

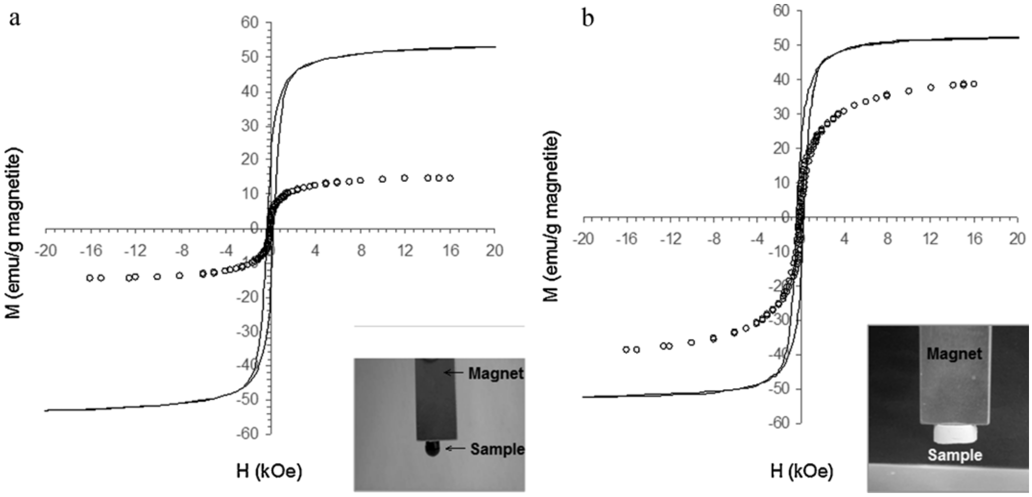

Fig. 5. Magnetization (M) versus applied field (H) plots at 5 K for (a) non-porous nanocomposites with 16 wt% 3 nm (NC3-3) (open circle) and 10 wt% 10 nm (NC10-2) (solid line) nanoparticles, and for (b) porous nanocomposites with 6.4 wt% 3 nm (PNC3) (open circle) and 6.4 wt% 10 nm (PNC10) (solid line) nanoparticles. The insets show the nanocomposites attracted to a magnet, e.g. (a) non-porous monolith with 46 wt% 3 nm nanoparticles (NC3-5) and (b) porous monolith with 6.4 wt% 3 nm nanoparticles (PNC3).

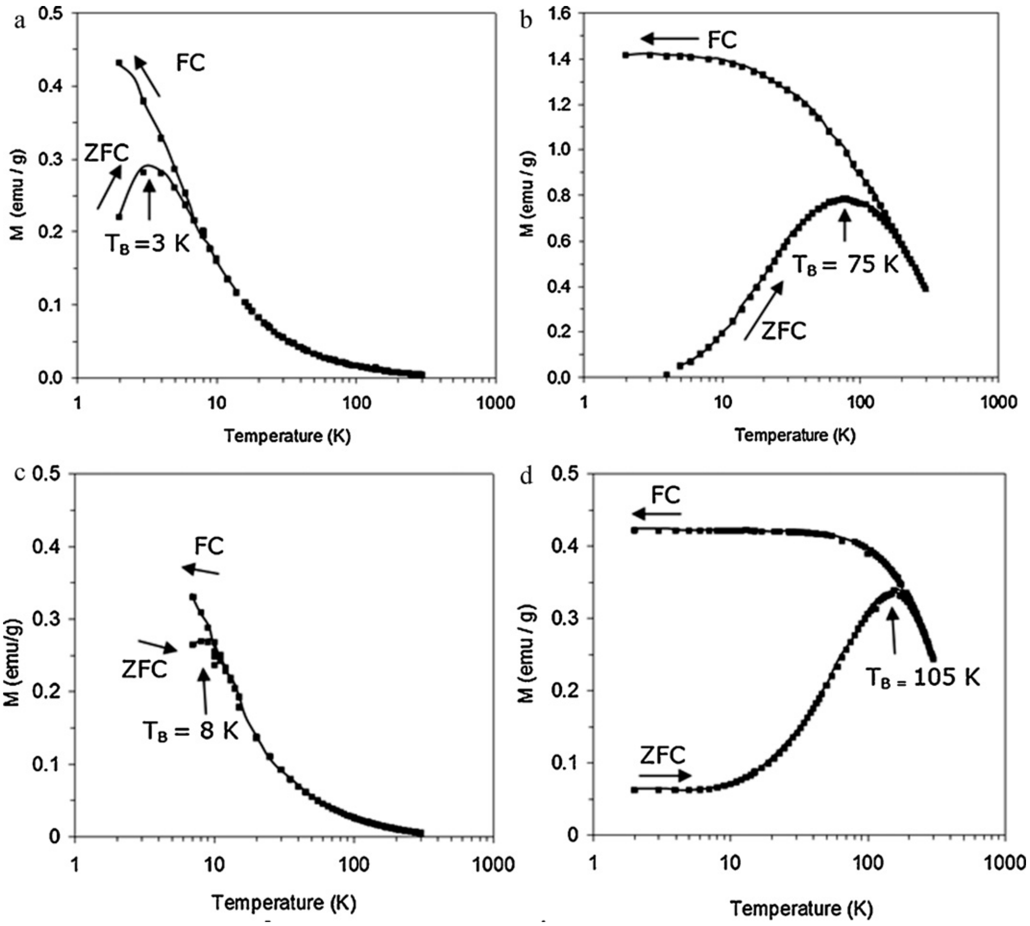

Fig. 6. Magnetization (M) versus temperature (T) plots of non-porous nanocomposites (a) NC3-3 and (b) NC10-2 and of porous nanocomposites (c) PNC3 and (d) PNC10 for zero-field cooled (ZFC) and field cooled (FC) experiments at $H = 50$ Oe. Solid lines are only visual guides.

and estimated the blocking temperature (T_B) to be 215 K, which is close to 210 K for 7-nm nanoparticles as reported earlier [40].

The measurements of field cooled (FC) and zero field cooled (ZFC) magnetization (M) with temperature (T) were also carried out for non-porous and porous nanocomposites to study if there is any change in interaction between nanoparticles from non-porous composite to porous composite. Fig. 6 shows the FC and ZFC magnetization for non-porous composite and porous nanocomposites (solid foams). The blocking temperature T_B (associated with the peak in the ZFC data) is higher for porous nanocomposites as compared to non-porous ones. We can interpret that the increase of T_B is associated with a higher contribution of the particle–particle magnetic interaction. The saturation below T_B as well as the proximity between T_B and the FC-ZFC branching temperature also point to stronger interactions in the case of porous nanocomposites [41]. Probably, the emulsification procedure to prepare the porous nanocomposites favours some particle agglomeration. It should also be noted here that the T_B values in 10 nm nanocomposites are lower than that of sample NP10 consisting of dried, neat nanoparticles (see supporting information, Fig. S3), indicating less interactions when nanoparticles are embedded in the polymer matrix.

5. Conclusions

We report the syntheses of hybrid magnetic nanocomposites through bulk and highly concentrated emulsion polymerization. Iron oxide nanoparticles capped with acrylic acid can be uniformly dispersed in crosslinked poly(styrene–divinylbenzene) matrices obtained by free radical polymerization. When the polymerization is carried out in highly concentrated emulsions used as templates, ultra-light porous nanocomposites are obtained, in which nanoparticles are embedded in the micron-sized pore walls. The nanocomposites show superparamagnetic behaviour, and the experimental results suggest stronger particle–particle interaction in porous nanocomposites as compared to non-porous ones. Porous nanocomposites (solid foams) show a relatively high magnetic moment.

Acknowledgements

G. Ghosh acknowledges a JAE-Doc 2008 postdoctoral grant from CSIC, Spain. C.R.-A. is grateful to the Ministerio de Ciencia e Innovación, Spain (Project CTQ2008-01979/BQU) and the bilateral cooperation program “Luis Santaló” between Spain (CSIC) and Argentina (CONICET) for financial support. Authors are grateful to Prof. Francisco Rivadulla, Jorge Vidal and Manuel Bañobre (Universidad de Santiago de Compostela, Spain) and Roberto Zysler (Centro Atomico Bariloche, Argentina) for useful discussions and help on nanoparticle synthesis and magnetic measurements.

Appendix A. Supplementary data

Supplementary data associated with this article can be found, in the online version, at doi:10.1016/j.matchemphys.2011.07.068.

References

[1] M.T. Klem, M. Young, T. Douglas, Mater. Today 8 (2005) 28–37.
[2] J. Pyun, Polym. Rev. 47 (2007) 231–263.
[3] H. Gu, K. Xu, C. Xu, B. Xu, Chem. Commun. 9 (2006) 941–949.
[4] D.K. Kim, Y. Zhang, J. Kehr, T. Kalson, B. Bjelke, M. Muhammad, J. Magn. Magn. Mater. 225 (2001) 256–261.
[5] D. Leslie-Pelecky, R.D. Rieke, Chem. Mater. 8 (1996) 1770–1783.
[6] H. Bao, Z. Chen, W. Xu, P. Wu, Y. Wang, B. Gao, J. Liu, Colloid J. 68 (2006) 644–647.
[7] R. Szostak, Molecular Sieves, Blackie Academic, London, 1998.
[8] K.J. Balkus, Prog. Inorg. Chem. 50 (2001) 217–268.
[9] T.D. Tilley, J. Mol. Catal. A: Chem. 182–183 (2002) 17–24.
[10] S.V. Kolotilov, O. Shvets, O. Cador, N. Kasian, V.G. Pavlov, L. Ouahab, V.G. Ilyin, V.V. Pavlishchuk, J. Solid State Chem. 179 (2006) 2426–2432.
[11] P. Wu, J. Zhu, Z. Xu, Adv. Funct. Mater. 14 (2004) 345–351.
[12] N. Andersson, R.W. Corkery, P.C.A. Alberius, J. Mater. Chem. 17 (2007) 2700–2705.
[13] P. Wang, I.M.C. Lo, Water Res. 43 (2009) 3727–3734.
[14] D. Barby, Z. Haq, European Patent No. 0060138 (Unilever), 1982.
[15] J.M. Williams, Langmuir 4 (1988) 44–49.
[16] E. Ruckenstein, J.S. Park, Polymer 33 (1992) 405–417.
[17] N.R. Cameron, D.C. Sherington, L. Albiston, D.P. Gregory, Colloid. Polym. Sci. 274 (1996) 592–595.
[18] J. Esquena, G.S.R. Ravi-Sankar, C. Solans, Langmuir 19 (2003) 2983–2988.
[19] K.J. Lissant, J. Colloid Interface Sci. 22 (1966) 462–468.
[20] H.M. Princen, J. Colloid Interface Sci. 71 (1979) 55–66.
[21] C. Solans, J. Esquena, N. Azemar, Curr. Opin. Colloid Interface Sci. 8 (2003) 156–163.
[22] P. Hainey, I.M. Huxham, B. Rowatt, D.C. Sherington, L. Tetley, Macromolecules 24 (1991) 117–121.
[23] E. Ruckenstein, Adv. Polym. Sci. 127 (1997) 1–58.
[24] N.R. Cameron, D.C. Sherrington, Adv. Polym. Sci. 126 (1996) 163–214.
[25] H. Maekawa, J. Esquena, S. Bishop, C. Solans, B.F. Chmelka, Adv. Mater. 15 (2003) 591–596.
[26] K. Shinoda, H. Saito, J. Colloid Interface Sci. 26 (1968) 70–74.
[27] R. Pons, I. Carrera, P. Erra, H. Kunieda, C. Solans, Colloids Surf. A 91 (1994) 259–266.
[28] H. Kunieda, Y. Fukui, H. Uchiyama, C. Solans, Langmuir 12 (1996) 2136–2140.
[29] B.P. Binks, Adv. Mater. 14 (2002) 1824–1827.
[30] A. Menner, M. Salgueiro, M.S.P. Shaffer, A. Bismarck, J. Polym. Sci. A: Polym. Chem. 46 (2008) 5708–5714.
[31] A. Menner, K. Haibach, R. Powell, A. Bismarck, Polymer 47 (2006) 7628–7635.
[32] W.U. Ranking, A. Menner, A. Bismarck, J. Polym. Sci. A: Polym. Chem. 48 (2010) 1979–1989.
[33] J. Vidal-Vidal, J. Rivas, M.A. López Quintela, Colloid Surf. A 288 (2006) 44–51.
[34] L.P. Ramirez, K. Landfester, Macromol. Chem. Phys. 204 (2003) 22–31.
[35] L. Jiang, W. Suna, J. Kim, Mater. Chem. Phys. 101 (2007) 291–296.
[36] A.H. Morris, The Physical Principles of Magnetism, IEEE Press, New York, 2001.
[37] S.-Y. Zhao, D.K. Lee, C.W. Kim, H.G. Cha, Y.H. Kim, Y.S. Kang, Bull. Korean Chem. Soc. 27 (2006) 237–242.
[38] (a) R.Y. Hong, T.T. Pana, H.Z. Li, J. Magn. Magn. Mater. 303 (2006) 60–68;
(b) P. Guardia, B. Batlle-Brugal, A.G. Roca, O. Iglesias, M.P. Morales, C.J. Serna, A. Labarta, X. Batlle, J. Magn. Magn. Mater. 316 (2007) e756–e759.
[39] L. Neel, Ann. Geophys. 5 (1949) 99–136.
[40] J.A. López Pérez, M.A. López Quintela, J. Mira, J. Rivas, S.W. Charles, J. Phys. Chem. B101 (1997) 8045–8047.
[41] P. Prené, E. Tronc, J.-P. Jolivet, J. Livage, R. Cherkaoui, M. Nogués, J.-L. Dormann, IEEE Trans. Magn. 29 (1993) 2658–2660.